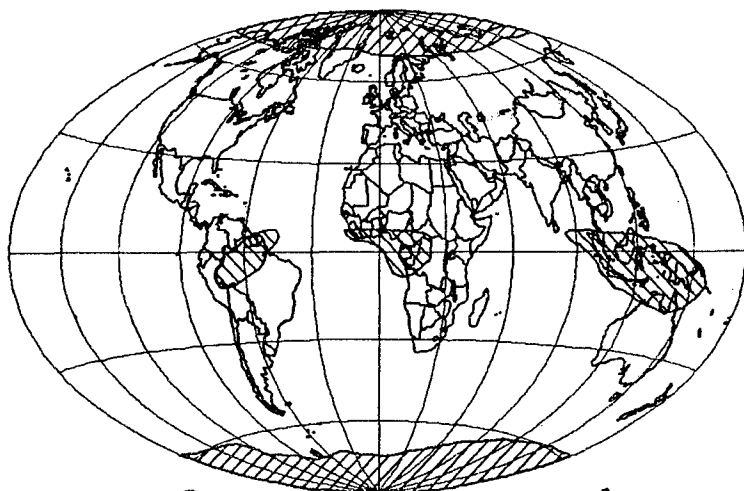


Open Symposium

Pre-prints of papers

Colloque Ouvert

Communications à présenter

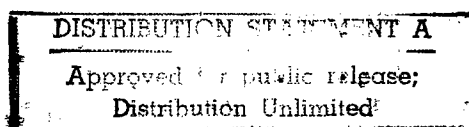


CLIMPARA94

19990204 012

Climatic Parameters in Radiowave Propagation Prediction

Reproduced From
Best Available Copy



Moscow

31 May - 3 June 1994

AB F99-05-0859

REPORT DOCUMENTATION PAGE

Form Approved OMB No. 0704-0188

Public reporting burden for this collection of information is estimated to average 1 hour per response, including the time for reviewing instructions, searching existing data sources, gathering and maintaining the data needed, and completing and reviewing the collection of information. Send comments regarding this burden estimate or any other aspect of this collection of information, including suggestions for reducing this burden to Washington Headquarters Services, Directorate for Information Operations and Reports, 1215 Jefferson Davis Highway, Suite 1204, Arlington, VA 22202-4302, and to the Office of Management and Budget, Paperwork Reduction Project (0704-0188), Washington, DC 20503.

1. AGENCY USE ONLY (Leave blank)		2. REPORT DATE 1994	3. REPORT TYPE AND DATES COVERED Conference Proceedings	
4. TITLE AND SUBTITLE Climpara 94, Climatic Parameters in Radiowave Propagation Prediction			5. FUNDING NUMBERS F6170894W0574	
6. AUTHOR(S) Conference Committee				
7. PERFORMING ORGANIZATION NAME(S) AND ADDRESS(ES) Rutherford Appleton Laboratory Chilton Didcot OX11 0QX United Kingdom			8. PERFORMING ORGANIZATION REPORT NUMBER N/A	
9. SPONSORING/MONITORING AGENCY NAME(S) AND ADDRESS(ES) EOARD PSC 802 BOX 14 FPO 09499-0200			10. SPONSORING/MONITORING AGENCY REPORT NUMBER CSP 94-1028	
11. SUPPLEMENTARY NOTES				
12a. DISTRIBUTION/AVAILABILITY STATEMENT Approved for public release; distribution is unlimited.			12b. DISTRIBUTION CODE A	
13. ABSTRACT (Maximum 200 words) The Final Proceedings for Climpara 94, Climatic Parameters in Radiowave Propagation Prediction, 31 May 1994 - 3 June 1994				
14. SUBJECT TERMS EOARD			15. NUMBER OF PAGES Too Many to Count	
			16. PRICE CODE N/A	
17. SECURITY CLASSIFICATION OF REPORT UNCLASSIFIED	18. SECURITY CLASSIFICATION OF THIS PAGE UNCLASSIFIED	19. SECURITY CLASSIFICATION OF ABSTRACT UNCLASSIFIED	20. LIMITATION OF ABSTRACT UL	

NSN 7540-01-280-5500

Standard Form 298 (Rev. 2-89)
Prescribed by ANSI Std. Z39-18
298-102



Open Symposium

Pre-prints of papers

CLIMATIC PARAMETERS
IN RADIOWAVE PROPAGATION PREDICTION

CLIMPARA'94

31 May - 3 June 1994, Moscow

Under the auspices of:

Department of Research and Development Ministry
Telecommunication Russia, Moscow

Sponsor:

International Union of Radio Science

Organised:

Radio Research and Development Institute (NIIR),
Moscow

Organising Committee (OC):

Prof. Y.B. Zoubarev (chairmen), Mr. M.P.M. Hall, Mr. S.L. Mishencov, Mr. Dr. A.P. Pavliouk, Dr. V.N. Pozhidayev, Dr. V.N. Troitsky.

Scientific Programme Committee:

Mr. M.P.M. Hall and Mr. J.P.V. Poiares Baptista (Co-chairmen), Prof. N.A. Armand, Dr. S. Benedict, Dr. F. Dintelmann, Dr. A.J. Kalinin, Dr. V.N. Troitsky.

Ladies and gentlemen, distinguished guests!

I am very much pleased to welcome the participants of the Climpara-94 International Symposium in Moscow on behalf of the NIIR management.

It was no accident that NIIR was among those who initiated and organized this Symposium. During many decades the Institute has been a diversified scientific and research center of the Ministry of the Posts and Telecommunications in the former USSR, and at present the Ministry of Telecommunications of the Russian Federation; it has been and is responsible for the development and introduction of terrestrial and satellite radio communication and broadcasting systems. Obviously, the creation of these radio systems would have been impossible without input data on radio wave propagation over the vast territory of the former USSR with a great variety of climatic and topographical conditions.

NIIR began to study metric, decimetric and centimeter waves in the late 40-s in the context of designing analogue line-of-sight radio relay systems and terrestrial television and sound broadcasting systems.

As regards line-of-sight radio relay systems, radio wave propagation experiments were carried out in the frequency range of 2-30 GHz in the central European areas of Russia, in the Volga region, the Baltic Republics, Belorussia, Ukraine, the Black Sea coast in the Caucasus, in the Alpine areas in Kirgizia. The experiments were conducted on more than 60 paths. Beside studies on signal and noise statistics, aerological tropospheric sounding data were statistically processed and rain rates were measured for a detailed mapping of the USSR territory based on vertical refractive gradient distributions and precipitation rates. As a result of these studies, a calculation procedure for line-of-sight radio relay links was developed. This procedure allows for various fading mechanisms (diffraction, tropospheric and surface refraction, rain attenuation).

The above procedure was widely used in the former USSR by all organizations and institutions engaged in designing line-of-sight radio relay links having a total length of about 200000 km. At present the procedure is being updated to include the fading frequency selectivity effect on high-rate digital microwave systems in different climatic regions.

The second important direction in the experimental studies covered forward tropospheric propagation. These studies began in the late 40-s and were made over the whole territory of the former USSR: in the central European areas of Russia, in Siberia, the Far East, the Baltic Republics, over the Caspian and Black Seas as well as in the polar regions on different paths ranging from 50 km to 1100 km. They were used as a basis for developing a calculation method for tropospheric communication links. Presently, the total length of operating troposcatter links in Russia designed by this method is about 14 000 km. The first tropospheric link was commissioned in 1956.

There were also studies on centimeter and decimetric wave diffraction and scattering by mountain ridges at a distance of up to 800 km. These studies contributed to the construction of high-capacity long-distance communication links, in particular a 800 km link between the USSR and India.

Comprehensive studies on anomalous troposcatter propagation were carried out with reference to electromagnetic compatibility problems. The studies of many years were performed in different areas of the former USSR at frequencies ranging from 6 GHz to 60 MHz over the sea and over the land on paths of up to 1000 km. As a result, a technique for calculating interfering signals was designed for the entire country allowing for climatic and geographical features of different areas.

Long-term investigations were also conducted at the International Experimental Satellite Communication Center (IESCC) in Dubna that was built within the framework of the Intercosmos Cooperation Program for the countries of Eastern Europe and was a NIIR division. The Center was put into operation in 1982 and experts from Bulgaria, Hungary, Germany, Poland, Russia and Czechia participated in the experiments.

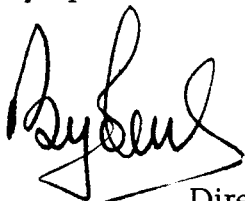
In 1983-1990 the down-link radio wave propagation at 11 GHz was studied in Dubna and in the Black Sea coast in the Caucasus and experiments on terrestrial paths were carried out at 11 GHz, 20 GHz and 30 GHz with concurrent rain rate and hydrometeors measurements. Radiometric attenuation measurements at 12 GHz were also made.

These experimental studies resulted in a large amount of information that was used for the development of procedures required for a computation of satellite and terrestrial link attenuation statistics.

The above investigations were to a great extent concerned with a study of climatic effects on radio wave propagation which is the subject matter of the present Symposium.

Ladies and gentlemen, I believe that this summary of the activities that were and are conducted in NIIR on the tropospheric radio wave propagation is expedient because the results of these studies apply to various radio climatic zones and conditions and, hopefully, they will be useful for the participants of the Symposium in developing methods for global predictions of tropospheric propagation conditions.

In conclusion I wish the Symposium every success.



Y.B. Zoubarev

Director of the NIIR, Professor

PREFACE

This symposium comes at a time when there is great potential for the mapping of climate-dependant radiometeorological parameters that are needed for the prediction of performance of radiowave communications. The same parameters have similar value to those involved in climatic studies and hydrological forecasting. Russia has considerable data relevant to these studies and we are fortunate to have the Radio Research and Development Institute (NIIR) as hosts.

Commission F (Wave Propagation and Remote Sensing) of the International Union for Radio Science (URSI) is closely concerned with various aspects of the scientific research described at this symposium which is sponsored by URSI Commission F, by the World Climatic Research Programme and by URSI Young Scientist funding. In addition, we wish to thank the US Air Force European Office of Aerospace Research and Development for its contribution to the success of this conference. The work is very relevant to the needs of the Radiocommunication Sector of the International Telecommunications Union (ITU-R), but, whilst the whole objective is towards practical predictions, the symposium is essentially science-oriented. The background is outlined in the opening paper.

CONTENTS

TABLE DES MATIERES

Session 1: Introduction

- 1.1 "Climatic Parameters in Radiowave Propagation" — M.P.M.Hall (RAL.UK), S.E.Benedict (WCRP, Switzerland), J.P.V.Poiars Baptista (ESA/ESTEC, Netherlands)

Session 2: Precipitation I

- 2.1 "Climatically — related parameters for prediction of attenuation and cross — polarisation in rainfall" — P.A.Watson — Univ.York, UK
- 2.2 "Precipitation retrieval from spaceborne microwave radiometers: motivation, potential and applications of a maximum likelihood profile algorithm" — A.Mugnai, F.S.Marzano — IFA, Italy, N.Pierdicca — Universita "La Sapienza", Italy.
- 2.3 "Climatic parameters required for the prediction of interference due to precipitation scatter" — M.Thurai — RAL, UK.
- 2.4 "Some aspects of Ku band radiometer measurement results and thunderstorm activities in Nigeria" — G.O. Ajayi, B.C.O.Onime — Nigeria.
- 2.5 "On the accuracy of raingauge measurements" — M.S.Assis — Brazil
- 2.6 "Rain rate and its temporal variability measured for a period of eight years at Darmstadt" — G.Ortgies — FTZ, Darmstadt, Germany.
- 2.7 "Precipitation retrieval from the high frequency SODAR measurements" — Shixuan Pang, H.Grassl — MPI, Hamburg, Germany.

Session 3: Precipitation II

- 3.1 "Rain height and cell diameter from rain and attenuation exceedences" — L.Watai, Q.Pan, G.H.Bryant — Lae, Papua New Guinea.
- 3.2 "A prediction method for the joint cumulative distribution of radiowave rain attenuation on space diversified paths" — Ye.V.Sukhonin — IRE, Moscow, Russia.
- 3.3 "The meteorological fronts and their influence on the design and exploitation of reconfigurable antenna pattern in satellite based area services" — A.Paraboni, M.Binaghi, A.Pawllina (CSTS, Italy), D.Brain (ERA,UK), J.P.V.Poiars Baptista (ESTEC,NL).
- 3.4 "Lidar Technique for cloudiness parameters monitoring on slant communication links with geostationary satellite" — V.V.Efremenko, A.V.Zubkov, L.N.Kornilov, A.V.Moshkov, V.N.Pozhidayev (IRE,Moscow, Russia), F.Dintelmann (FTZ, Germany).
- 3.5 "First results of 30 GHz radiometric and rain measurements in the Moscow area" — G.Heyer, S.Szuppa, H.Trommer, F.Dintelmann (FTZ, Germany), V.L.Bykow, V.V.Svjatogor (ISC, Dubna, Russia).

Session 4: Precipitation III

- 4.1 "Millimeter and centimeter wave attenuation variations due to cloudy atmospheres" — G.A.Andreyev, V.M.Pletchikov, O.K.Stankevich — IRE, Moscow, Russia.
- 4.2 "Statistics of clear — air attenuation, precipitable water and cloud liquid" — G.Ortgies — FTZ, Darmstadt, Germany.
- 4.3 "Concurrent occurrences of deep fadings due to hydrometeors and heavy rain intensities on a 15 km path in the 15 GHz" — V.Kvicera — TESTCOM, Prague, Czech Republic.

- 4.4 "Radar investigation of melting layer" — A.V.Kochin — CAO, Moscow, Russia.
- 4.5 "Derivation of path integrated rain rates and drop size distributions from attenuation, radiometer and radar measurements" — A.Hornbostel, M.Chandra, A.Schroth — DLR, Oberpfafenhöfen, Germany.

Session 5: Precipitation IV

- 5.1 "Long-term 0° C isotherm height characteristics in Warsaw region (preliminary results)" — A.Kawecki — Inst.Tel., Warsaw, Poland.
- 5.2 "On two mechanisms of signal scintillation by wavefield propagation in precipitations" — V.L.Kouznetsov — MSTUCA, Moscow, Russia.
- 5.3 "The experimental results of radio wave attenuation investigations on slant communication links in climatic conditions of Russia" — V.L.Bykov, V.V.Svjatogor (NIIR, Moscow), V.N.Pozhdayev — IRE, Moscow, Russia.
- 5.4 "The evaporation of rain drops and its influence on the microwave slant path attenuation" — O.Fiser — TESTCOM, Prague, Czech Republic.
- 5.5 "Analysis of the interference due to differential rain attenuation induced by adjacent path on a multiple site diversity Earth-space system of dual polarisation" — J.D.Kanellopoulos, C.N.Vezouras — NTU, Athens, Greece.
- 5.6 "Variations of 0° C isotherm height during rain in Berlin" — H.Trommer, S.Szuppa, G.Heyer — FTZ, Berlin, Germany.
- 5.7 "Radiometric measurements of effective rain height" — M.S.Pontes, L.A.R.Silva Mello, R.S.L.Souza — CETUC, Brazil
- 5.8 "The raincell climatology across the world and its impact in the prediction of various rain-dependent propagation parameters" — C.Capsoni, M.D'Amico, A.Paraboni, F.Zaccarini — Politecnico Milan, Italy.
- 5.9 "Separating absorption — from scintillation — phenomena in satellite radio links: Theory, experimental data and predictions" — C.Riva, A.Paraboni — Politecnico Milan, Italy.
- 5.10 "Rain areas on horizontal radar rain maps: new collection, new insight into spatial intensity distribution" — A.Pawlina Bonati — CSTS, Milan, Italy.
- 5.11 "A study of the relationship $\gamma = aR^b$ for rain attenuation at millimetric wavelengths" — C.J.Gibbins — RAL, UK.
- 5.12 "Rain attenuation measurements in South-East Asia" — R.Lekkla (CAT, Thailand), S.L.Lim (STP, Singapore), J.Wachja (PT Telkom, Indonesia), K.S.McCormick (CRC, Canada).

Session 6: Clear air I

- 6.1 "Climatic parameters in clear air propagation modelling" — K.Craig (RAL, UK), T.Tjelta (Tele Research, Kjeller, Norway), B.Segal (CRC, Canada).
- 6.2 "Investigation of climatic factors influence on abnormal radio propagation" — V.N.Troitsky — NIIR, Moscow, Russia.

Session 7: Clear air II

- 7.1 "On acoustic remote sensing for climatologic study of microwave propagation in the atmospheric boundary layer" — M.A.Kallistratova, IAP, Moscow, Russia.
- 7.2 "Mapping of zones in which clear air fading and interference may occur" — G.Fengler — Germany.

- 7.3 Climatic factor in statistics of the fade duration on line-of-sight paths" — L.Nadenenko — NIIR, Moscow, Russia.
- 7.4 "Database of radiometeorological parameters" — M.E.Rovkin — CSR, Tomsk, Russia.
- 7.5 "Clear air propagation measurements in Brazil" — N.R.Dhein, C.M.Einloft, M.S.Pontes, L.A.R.Silva Mello, G.L.Siqueira — CETUC, Brazil.

Session 8: Clear air III

- 8.1 "Climatologic study of microwave active turbulence behaviour over a big city by Sodar" — I.V.Petenko, A.N.Bedulin, M.A.Kallistratova, M.S.Pekour — IAP, Moscow, Russia.
- 8.2 "Line-of-sight microwave propagation and clear air climatic conditions for coastal regions under the northern polar circle" — T.Tjelta and S.Lystad — Tele Research, Norway.
- 8.3 "The experimental results of 11–35 GHz radio wave attenuation investigations on terrestrial links in Bulgaria, Poland and Russia" — E.Alexandrova (Inst.Telecom Bulgaria), A.Kawecki (Inst. Telecom, Poland), V.V.Svjatogor (NIIR, Russia), V.N.Pozhidayev (IRE, Moscow, Russia).
- 8.4 "Radiometeorological parameters and signal fluctuation characteristics of the tropospheric paths of the Pacific Ocean's coast" — E.V.Batueva, D.D.Darizhapov — Ulan-Ude, Russia.

Session 9: Clear air IV

- 9.1 "Algorithm for computing trajectory parameters of EM waves in a spherically stratified atmosphere" — V.A.Parshukov, A.Yu.Zrazhevski, Ye.P.Novichikhin — IRE, Moscow, Russia.
- 9.2 "Statistical characterisation of radio refractivity in Cairo" — A.K.Farrag and A.A.Hassan — Nat.Tel.Inst., Cairo, Egypt.
- 9.3 "Radiometeorological parameters model over Russia region" — G.S.Zhamsueva, D.D.Darizhapov — Ulan-Ude, Russia.
- 9.4 "Transhorizon wave scattering and the problem of prediction of field nonenergetical characteristics" — J.P.Akulichev, V.A.Butko, M.E.Rovkin — CSR, Tomsk, Russia.
- 9.5 "Prediction of attenuation factor hour median for UHF microwave tropospheric over sea propagation using meteorological parameters" — O.N.Kiselev, V.N.Kovalev, G.S.Sharygin, B.P.Dudko — CSR, Tomsk, Russia.
- 9.6 "The results of non-stop measurements of atmospheric boundary layer temperature profile by using 5mm radiometer" — M.Khaikin, E.Kadygrov, M.Sorokin — CAO, Moscow, Russia.
- 9.7 "The estimation of refractivity structure function by the optical propagation along the slant path near the ground" — T.I.Arsenyan, N.N.Fedotov, P.V.Korolenko, E.A.Kuliagina — MSU, Moscow, Russia.
- 9.8 Millimeter-wave scattering due to atmospheric turbulent inhomogeneities" — G.A.Andreyev, E.V.Frolova — IRE, Moscow, Russia.

Session 10: Mapping I

- 10.1 "Global precipitation climatological data base" — B.Rudolf — GPCC, Deutscher Wetterdienst, Germany.
- 10.2 "Mapping of super-refractive and ducting layer statistics from radiosonde data" — K.H.Craig, T.G.Hayton — RAL, UK.

Session 11: Mapping II

- 11.1 "Rainrate distributions in Spain related to climatic characteristics" — L.Mercader (UPN, Pamplona, Spain), A.Benarroch, (UPM, Spain).

- 11.2 "Radiometeorological database of Russia with graphic mappings" – D.D.Darizhapov, E.V.Batueva, G.S.Zhamsueva – Ulan-Ude, Russia.
- 11.3 "Oceanic rain rate parameters derived from SSM/I" – L.S.Chiu, A.T.C.Chang – NASA/GSFC, USA.
- 11.4 "Mesoscale modelling of refractive index and troposphere path-loss variations" – O.N.Kiselev, S.G.Gosenchenko, A.A.Mescheryakov – CSR, Tomsk, Russia.

Session 12: Mapping III

- 12.1 "Data from numerical weather forecast systems – useful input for propagation predictions?" – E.Salonen (HUT, Finland), S.Uppala (FMI, Finland), S.Kahru (VTT, Finland), J.P.V.Poiars Baptista (ESA/ESTEC, NL).
- 12.2 "Prediction of attenuation on satellite–earth links for systems operating with low fade margins" – P.A.Watson (Univ. York, UK), Y.F.Hu (Univ. Bradford, UK).
- 12.3 "Radioclimatic maps of UHF radiowave over–sea propagation parameters for the Pacific Ocean" – G.S.Sharygin, V.I.Slutski, B.P.Dudko, O.N.Kiselev, I.L.Korneev, M.V.Krutikov – CSR, Tomsk, Russia.
- 12.4 "Freezing level characteristics at selected stations across Canada" – E.Kochtubajda (Univ. Alberta, Canada) and D.V.Rogers (CRC, Canada).

Session 13: Mapping IV

- 13.1 Application of maximum entropy method for prediction mutual content at atmospheric ozone ear Moscow" – A.V.Shabelnikov, V.V.Efremenko, K.G.Kirjanov, A.V.Moshkov – IRE, Moscow, Russia.
- 13.2 "The potential of a spaceborne radar to measure various cloud types at 94 GHz" – A.D.Papatsoris and P.A.Watson – Univ. York, UK.
- 13.3 "Satellite probing of Earth's ozone layer at millimeter wavelengths" – G.M.Strelkov – IRE, Moscow, Russia.
- 13.4 "Analysis of the rain intensity statistics in the north coast of Spain" – I.F.Anitzine, C.S.Yaldi, UPV, Bilbao, Spain, A.Benazzoch – Polytechnic University of Madrid, L.Mercader – UPNA Public University of Navarre, Spain.

Session 14: Concluding Session

Author Index

- Ajayi, G.O. 2.4
 Akulinichev, J.P. 9.4
 Alexandrova, E. 8.3
 Andreyev, G.A. 4.1, 9.8
 Anitzine, I.F. 13.4
 Arsenyan, T.I. 9.7
 Assis, M.S. 2.5
 Batueva, E.V. 8.4, 11.2
 Bedulin, A.N. 8.1
 Benarroch, A. 11.1, 13.4
 Benedict, S.E. 1.1
 Binaghi, M. 3.3
 Brain, D. 3.3
 Bryant, G.H. 3.1
 Butko, V.A. 9.4
 Bykow, V.L. 3.5, 5.3
 Capsoni, C. 5.81
 Chandra, M. 4.5
 Chang, A.T.C. 11.3
 Chiu, L.S. 11.3
 Craig, K. 6.1, 10.3
 D'Amico, M. 5.81
 Darizhapov, D.D. 8.4, 9.3, 11.2
 Dhein, N.R. 7.5
 Dintelmann, F. 3.4, 3.5
 Dudko, B.P. 9.5, 12.3
 Efremenko, V.V. 3.4, 13.1
 Einloft, C.M. 7.5
 Ekuwem, E.E. 14.1
 Farrag, A.K. 9.2
 Fedotov, N.N. 9.7
 Fengler, G. 7.2
 Fiser, O. 5.4
 Frolova, E.V. 9.8
 Ghaloul, F. 11.1
 Gibbins, C.J. 5.11
 Gosenchenko, S.G. 11.4
 Grassl, H. 2.7
 Hall, M.P.M. 1.1
 Hassan, A.A. 9.2
 Hayton, T.G. 10.3
 Heyer, G. 3.5, 5.6
 Hornbostel, A. 4.5
 Hu, Y.F. 12.2
 Kadygrov, E. 9.6
 Kallistratova, M.A. 7.1, 8.1
 Kanellopoulos, J.D. 5.5
 Karhu, S. 12.2
 Kaweck, A. 5.1, 8.3
 Khaikin, M. 9.6
 Kirjanov, K.G. 13.1
 Kiselev, O.N. 9.5, 12.3
 Kochin, A.V. 4.4
 Kochtubajda, E. 12.4
 Korneev, I.L. 12.3
 Kornilov, L.N. 3.4
 Korolenko, P.V. 9.7
 Kouznetsov, V.L. 5.2
 Kovalev, V.N. 9.5
 Krutikov, M.V. 12.3
 Kuliagina, E.A. 9.7
 Kvicera, V. 4.3
 Lekla, R. 5.12
 Lim, S.L. 5.12
 Lystad, S. 8.2
 Marzano, F.S. 2.2
 McCormick, K.S. 5.12
 Mercader, L. 11.1
 Mescheryakov, A.A. 11.4
 Moshkov, A.V. 3.4, 13.1
 Mugnai, A. 2.2
 Nadenenko, L. 7.3
 Novichikhin, Ye.P. 9.1
 Onime, B.C.O. 2.4
 Ortgies, G. 2.6, 4.2
 Pan, Q. 3.1
 Pang, Shixuan 2.7
 Papatsoris, A.D. 13.2
 Paraboni, A. 3.3, 5.8, 5.9
 Parshukov, V.A. 9.1
 Pawlina, A. 3.3, 5.10
 Pekour, M.S. 8.2
 Petenko, I.V. 8.1
 Pierdicca, N. 2.2
 Pletchikov, V.M. 4.1
 Poiars Baptista, J.P.V. 1.1, 3.3, 12.2
 Pontes, M.S. 5.7, 7.5
 Pozhidayev, V.N. 3.4, 5.3, 8.3
 Riva, C. 5.12
 Rogers, D.V. 12.4
 Rovkin, M.E. 7.4, 9.4
 Rudolf, B. 10.1
 Salonen, E. 12.1
 Schroth, A. 4.5
 Segal, B. 6.1
 Shabelnikov, A.V. 13.1
 Sharygin, G.S. 9.5, 12.3
 Silva Mello, L.A.R. 5.7, 7.5
 Siqueira, G.L. 7.5
 Slutski, V.I. 12.3
 Sorokin, M. 9.6
 Souza, R.S.L. 5.7
 Stankevich, O.K. 4.1
 Strelkov, G.M. 13.3
 Sukhonin, Ye.V. 3.2
 Svjatogor, V.V. 3.5, 5.3, 8.3
 Szuppa, S. 3.5, 5.6
 Thurai, M. 2.3
 Tjelta, T. 6.1, 8.2
 Troitsky, V.N. 6.2
 Trommer, H. 3.5, 5.6
 Uppala, S. 12.1
 Vezouras, C.N. 5.5
 Wachja, J. 5.12
 Watai, L. 3.1
 Watson, P.A. 2.1, 12.2, 13.2
 Zaccarini, F. 5.81
 Zhamsueva, G.S. 9.3, 11.2
 Zrazhevski, A.Yu. 9.1
 Zubkov, A.V. 3.4

Session 1: Introduction

CLIMATIC PARAMETERS IN RADIOWAVE PROPAGATION PREDICTION - WORKSHOP OBJECTIVES

M.P.M. Hall¹, S.E. Benedict², J.P.V. Poiars Baptista³

- 1 - Rutherford Appleton Laboratory, Chilton, Didcot, Oxon. OX11 0QX, UK
Phone: +44 235 446650, Fax: +44 235 446140, E-mail: martin.hall@rutherford.ac.uk
- 2 - World Climate Research Programme, Av. Giuseppe Motta 21, CH-1211 Geneva 2
Phone: +41-22-730-8247, Fax: +41-22-734-2326
- 3 - ESA/ESTEC, PO Box 299, 2200 AZ Noordwijk, Netherlands
Phone: +31 1719 84319, Fax: +31 1719 84999, E-mail: pedro@xe.estec.esa.nl

ABSTRACT

This paper summarizes the objectives of CLIMPARA'94 and the framework of the workshop. The areas of possible scientific cooperation and exchange between workers in the areas of radiowave propagation, remote sensing, meteorology and climatology are reviewed.

Keywords: Workshop Objectives, Radiowave propagation, Climatology, Meteorology, Remote Sensing

1. INTRODUCTION

This paper is intended to set the scene for the symposium and to outline some objectives. The purpose is to examine what radio-meteorological parameters may best be used to predict radiowave propagation characteristics, how they vary with climate and how best they may be mapped on a world scale. Also, consideration should be given to how climatologists and hydrologists may gain from (and contribute to) these studies. Presentation sessions, poster sessions and workshop sessions will be used to exchange ideas and information between the following different scientific communities:

- Those conducting radiowave propagation measurements and/or related ground-based remote sensing of the atmosphere (e.g. of precipitation, precipitable water, cloud liquid water, refractive index, etc.) and concerned with preparing climatic maps of parameters relevant to the prediction of radiowave propagation characteristics, notably through the Radiocommunications Sector of the ITU (ITU-R) and URSI.

- Those performing research in atmospheric physics using numerical techniques relevant to precipitation, cloud physics, meso-scale

modelling, global circulation models (GCMs), hydrology, climatology, etc., notably through the WMO's World Climate Research Programme (WCRP), GEWEX, and the Global Precipitation Climatology Project (GPCP).

- Those concerned with related space-borne remote sensing of the atmosphere using both active and passive instruments.

The radio-science and radio-engineering communities around the world have expended much energy, ingenuity and expertise in developing methods for the prediction of various characteristics or the propagation of radiowaves in non-ionised media. However, the extent to which these characteristics may be expected to vary from one region of the world to another is still far from clear.

In the field of meteorology, the development of sophisticated numerical meso-scale models that increase the resolution of current operational numerical forecast algorithms may be in the near future supply very powerful tools also for the area of radiometeorology or wave propagation. Very early attempts with resolutions of around 100 km yield already very encouraging results even for forecasting propagation losses (Ref. 1).

On the other hand, the high time resolution data observed for long periods by the wave propagation community may be of interest to the climatology scientific community in projects like the Global Precipitation Climatology Project (Ref. 2, 3 4).

New spacecraft or instruments like the joint NASA/NASDA TRMM or ESA's MIMR (that will fly in METOP) will offer new opportunities to measure globally meteorological and climatological parameters that are also of interest to wave propagation.

The present symposium should give a forum to

compare experiences and exchange points of view between these different communities and especially with our colleagues in Central and Eastern Europe.

2. CLIMATIC PARAMETERS

Most of the electromagnetic effects due to atmospheric phenomena are well understood; however, most of the models used are either empirical or physico-empirical, i.e. they are based on relevant physical parameters (some of which are radiometeorological) but made to fit propagation data, for areas where data are available, through the use of suitable coefficients. Suitable choices of coefficients and physical parameters, in general, should enable good predictions to be made of a radio variable on a given path if the related radiometeorological data are available for that path. This can be done for areas where there is sufficiently good statistical data collected for both the radio variable and the radiometeorological parameters.

This approach is dictated by both the limited knowledge of atmospheric conditions at any instant and by the resources necessary to derive the complete statistical information from the complete instantaneous data if the latter were available.

The radiometeorological variables vary with climate and may be called "Climatic Parameters". The development of the computing capability as well as space-borne remote sensing and numerical meteorology may before long yield global data for these Climatic Parameters.

Progress and understanding in examining effects of Climatic Parameters may be most advanced on attenuation due to rain. During the last two decades, a number of methods have been produced for the prediction of cumulative distribution statistics of such attenuation at frequencies above 10 GHz, (ITU-R having to produce one for universal application). For terrestrial paths, most methods start from (i) the rainfall rate at a point that is exceeded for a given time percentage of concern and (ii) the effective proportion of the path over which that rainfall rate may be assumed to apply. For Earth-space paths, an additional factor has been used to give (iii) the effective height over which the rainfall rate may be assumed to exist. The first of these may already be mapped on a world-wide basis, but characteristics of raincell widths, separation and heights are less well known. Due to the serious lack of sufficient measured rainfall and path attenuation data from various areas of the world from which model improvements might be made, the prediction methods have generally not been able to take numerical account of a priori differences between climates (e.g. prevalence of monsoon or cyclone rain).

A number of new measurements in low-latitude

regions are now beginning to produce results, and these were the basis for an URSI Commission F Special Open Symposium on "Regional Factors in Predicting Radiowave Attenuation due to Rain" which was held in Rio de Janeiro in December 1990 (Ref. 5). The 51 participants at the Open Symposium came from 15 countries, and it was arranged that the symposium was followed immediately by two concurrent meetings of those closely concerned with these issues in two Working Parties of ITU-R Study Group 5. This enhanced the exchange of ideas and information on the theme of the symposium between the URSI and ITU-R communities.

Prediction of attenuation due to rain has had a large amount of attention in both ITU-R and URSI Commission F, and the databases now have considerable information to draw it on, but quantifying its climatic variability in terms of a set of Climatic Parameters is still an area that requires a lot of effort. Many people have worked hard to produce good maps of rainfall rate data, but something similar may be needed to characterise the horizontal and vertical structures of rain to take account of tropical storms and monsoons and to contrast these with rain structures of temperate regions. Clearly this is not a simple matter, and the means of collection of data need a lot of attention. Due to its global approach, remote sensing of the atmosphere from space may in the future be a prime source for this type of data. Numerical meteorology, with its drive towards ever increasing spatial and time resolutions, may also bring very important contributions in the near future.

Very comparable considerations have now become apparent in the prediction of signal levels likely to cause transhorizon co-channel interference, with a reappraisal of data and prediction methods. World mapping of radio refractive index parameters is giving a means of steering prediction methods for interference in clear-air conditions in terms of Climatic Parameters. In addition, both within URSI and ITU-R there are those interested in collaborating on Climatic Parameters in relation to other refractive index effects (notably multipath), but it is still difficult to see what will be the radio-meteorological steering parameters. Obvious ones are (i) surface refractivity (which may largely be an indication of high humidity), (ii) probability of occurrence of refractive index lapse-rates in excess of 100 N/km in the first 100 m height (which may need to be remapped with new and improved data from around the world) and (iii) refractive index lapse-rates in the first kilometre. Any climatic variability in diameter and height of raincells is important in the prediction of interference levels that may occur due to scatter from rain and other hydrometeors.

All these considerations of the influence of Climatic Parameters are at an early stage, but exploration of the

potential for such factors was the basis for a Workshop held immediately following on the Commission F Triennial Symposium at Ravenscar in the UK in June 1992 (Ref. 6). The objective of the Workshop was to examine the extent to which radio-meteorological parameters needed for world-wide methods of predicting radiowave propagation characteristics in non-ionised media can be characterised on a climatic basis. Some 42 people participated, from 23 organisations in 15 countries, and discussion was in the areas of (i) rain effects (attenuation and scatter) and (ii) clear-air effects (ducting and multipath). It was recognised that only an initial examination of the situation could be made at this short Workshop meeting.

In the matter of attenuation due to rain, there was some doubt as to whether the horizontal and vertical distributions of rainfall rate were of any major concern compared with the dependence on radio frequency and rainfall rate. Better world-wide mapping of the latter is essential. On Earth-space paths, the effects of elevation angle in intercepting one or more raincells was felt to be of major importance. A considerable difficulty was in getting stable data for comparison between regions, the time and spatial variability (and possibly microclimate effects) being large. This problem is less severe when, for instance, investigating effects of rainfall rates using concurrent data. Lack of data to test prediction methods, together with uncertainty of rain cell sizes, was a major bar to developing Climatic Parameters for hydrometeor scatter. Many such Parameters were considered to be important.

Climatic Parameters certainly strongly influence the magnitude and occurrence of clear-air effects, but there is a marked scarcity of data. For modelling of both transhorizon ducting and line-of sight multipath effects, use was made of the percentage of time that refractive index gradients in the first 100 m height were more negative than 100 N/km, but it seemed likely that the height of the duct should also be a strong influence. The nature of this influence was unclear, as was the means of determining or even specifying the height. (Again there might be some difficulty with variability due to microclimate).

In the remarks made in this section, some Climatic Parameters are directly-measured meteorological parameters, e.g. rainfall rate at a point. Others are simply derived radiometeorological parameters e.g. radio refractive index derived from atmospheric pressure, temperature and humidity. Others sound equally simple (e.g. radio refractive index gradient in the first kilometer or 100 m) but must be derived by interpolation after careful screening of radiosonde data (or other means). Others may also sound simple (e.g. effective rain height of effective rain distance), but are derived empirically from radio data and an assumed

model. In this case, it may be that future 3D rainfall measurements from space will enable very good global data to be derived of such a parameter, despite the fact that it does not necessarily constitute a continuous column of rain up to that height.

In principle, if all relevant radiometeorological parameters had been measured over 3D space with sufficient time-space sampling and for a sufficient length of time, forward prediction for a radio path by a mathematical wave model could be as dependable as using direct statistics of past data from radio statistics. In practice it is expected that Climatic Parameters will be needed with prediction models, possibly as a direct input (just as a terrain database may be used as a direct input).

3. MAPPING

Rainfall may be mapped on a world-wide basis. Examples of such an exercise are the ITU-R rainzone and the GPCP rain height maps, and the several rain climatologies available in the literature; however, with the exception of the GPCP maps, they all lack a consistent approach based on rain data and not on other related general climatological parameters to define the rain regimes or rainfall characteristics. Unfortunately, the time resolution of the GPCP maps is, at the moment, not high enough for radio-meteorological applications.

Any prediction model is only as good as its input parameters. This obvious statement leads to the development of accurate radio-climatological/meteorological mapping if any basic improvement in the accuracy of prediction models is to be achieved. Prediction models, however, change and have their own evolution especially in terms of planning needs of the regulatory agencies (e.g. ITU-R). By contrast, in the frame of URSI and other scientific organizations or programmes (e.g. WCRP, IBGP), a basic groundwork in terms of a global general climatology based strictly on geophysical parameters is necessary. It may be useful to take into account, to some degree, the requirements of agencies like the ITU-R; however, due to the effort of globally mapping a variable, it makes no sense to carry it out with empirical parameters that may change from one prediction model revision to another. We hope that in this context, the URSI community will be able to contribute to other scientific efforts (e.g. GPCP) and to draw contributions from other scientific communities.

The whole basis of using climatic parameters for prediction of radiowave propagation characteristics may lie in the use of high space resolution digital maps of the key parameters that are exceeded for given time percentages (e.g. 0.001, 0.01, 0.1, 1, 10, 50, 90, 99, 99.9, 99.99). They will need to be stored on a world-wide basis where the original data is documented and

always accessible, and where the preprocessing needed to arrive at the mapped parameter is clear. Such a digital database may be directly linked to a prediction procedure so that, for instance, signal level may be predicted for one of the time percentages for which data are stored.

In order to achieve this goal several problems, also facing the meteorology/climatology scientific communities, need to be solved.

The first one is related to the representation of the data in terms of coordinate systems, sampling and sampling functions. Any choices in terms of the density of points on the surface of the Earth, the total number of points and how they are distributed are bound to have an impact on how the data are assimilated and later used. A choice that has a flexible basis, even at the risk of "overdriving" the total number of points, is very important.

The second one is the problem of assimilating new data as it becomes available; new measurements and results will have to be incorporated in the digital map taking into account the data accuracy, period of measurement and representativeness. Sophisticated data analysis and assimilation techniques have been developed in the frame of numerical weather forecast algorithms and may be of help.

A third problem is related to the use of the data included in such a data base. Spatial filtering techniques in the frame coordinate system will have to be investigated for this purpose.

An associated global digital topographical (i.e. terrain-height) database, is also necessary in order to either normalize the climatological variables themselves to altitude or to understand their behaviour when not normalized. This type of database is already available in some form; however, they are not "public-domain" and some are known to contain undocumented errors for several regions of the world.

We hope that the present workshop will not only raise and discuss all of these questions but will also point directions of research and development and, of course, sources of data.

4. CONCLUSION

This then is the background to the present symposium. The first of the main areas of the meeting will be concerned with modelling and climatic parameters relating to precipitation, such as (i) rain, clouds and snow; (ii) rain cell and cloud structure, size and height; (iii) global and meso-scale modelling; (iv) attenuation (rainfall rate, rain/melt/ice, rain height) on terrestrial and Earth-space paths; (v) cross

polarisation (rainfall rate, hydrometeor type, rain height); (vi) interference from hydrometeor scatter (rainfall rate, cell size, rain height); and (vii) sky noise from clouds. It will also involve data available, measurements and instruments.

The second area will be concerned with modelling and climatic parameters relating to clear-air conditions, such as (i) the structure of the atmosphere (water vapour, temperature, pressure and gases, and radio refractive index); (ii) turbulence; (iii) global and meso-scale modelling; (iv) ducting (intensity, thickness, base height, β_0) of transhorizon microwave signals; (v) layering (intensity, thickness, height P_L) giving atmospheric multipath microwave line-of-sight paths; (vi) scintillation ($\langle \delta N^2 \rangle$, C_n^2), especially on Earth-space paths; (vii) tropospheric scatter ($\langle \delta N^2 \rangle$, C_n^2); and (ix) refraction. Again, it will also involve data available, measurements and instruments.

The third area will be concerned with mapping processes of meteorological and radio-meteorological parameters, notably (i) sampling; (ii) data analysis; (iii) data assimilation; (iv) interpolation and (v) spatial filtering.

All of this promises development of a new stage of radiowave propagation prediction, taking into account the influence of Climatic Parameters.

5. REFERENCES

1. Salonen et al. 1994, Improved Propagation Predictions ..., Technical University Helsinki, ESA/ESTEC Contract N. 9455 Final Report
2. Rudolf B. 1993, Global area-mean monthly precipitation totals for the year 1988, Global Precipitation Climatology Center, Deutscher Wetterdienst, Offenbach am Main, July 1993, ISBN 3-88148-289-X
3. WCRP 1992, Analysis Methods of Precipitation on a Global Scale, Report of a GEWEX Workshop, Koblenz, Germany - WCRP-Report 81, WMO/TD-N.558, Genf., June 1993.
4. Rudolf B. 1993, Management and analysis of precipitation data on a routine basis, Proc. WMO Int. Symp. on Precipitation and Evaporation, Bratislava, 20-24/9/93 (Ed. Lapin, B. Sevruk), Vol. 1, S. 69-76, Slovak Hydromet. Inst., Bratislava, Sept. 1993
5. Hall M P M 1991, Regional factors in predicting radiowave attenuation due to rain, URSI Information Bulletin No. 257, pp23-26.
6. Hall M P M 1992, Climatic factors in the prediction of radiowave propagation factors, URSI Information Bulletin No 263, pp17-20.

Session 2: Precipitation I

CLIMATICALLY-RELATED PARAMETERS FOR PREDICTION OF ATTENUATION AND CROSS-POLARISATION IN RAINFALL

P A Watson

Department of Electronics, University of York, Heslington, York, YO1 5DD
Tel + 0904 432338, Fax +0904 432335, E-mail paw@ohm.york.ac.uk

ABSTRACT

Approaches to prediction of attenuation and cross-polarisation from rainfall, on microwave and millimetre-wave radio links, are reviewed from the viewpoint of identifying the climatically-dependent variables necessary for prediction. Questions are raised as to the climatic classifications that should be used for such variables and as to whether or not the variables can or should be determinable by independent physical measurement, or simply by empirical means through model optimisation.

Key Words

Microwaves, millimetre-waves, attenuation, cross-polarisation, rainfall.

1. INTRODUCTION

The continuing demand for radio spectrum, in all regions of the world, maintains our interest in improving prediction techniques for attenuation and cross-polarisation. Interest for new systems now lies not only in the 11/14 GHz band, where considerable operational data are now available, especially in temperate climates, but also in the 20/30 and 30/40 GHz regions, both for fixed and mobile applications.

In the past the majority of experimental studies and prediction techniques have addressed the lower frequency range (ie 11/14 GHz) where a much more limited range of physical phenomena need to be taken into account, associated with the occurrence of intense convective rainfall. As we move towards the 30/40 GHz frequency range, the effects of cloud and light rainfall must be considered, making the problem of prediction much more complex.

In this paper we will not assume that we can focus only on intense rainfalls effects, but attempt to include a wider range of physical phenomena.

PHYSICAL MODELLING OR EMPIRICISM?

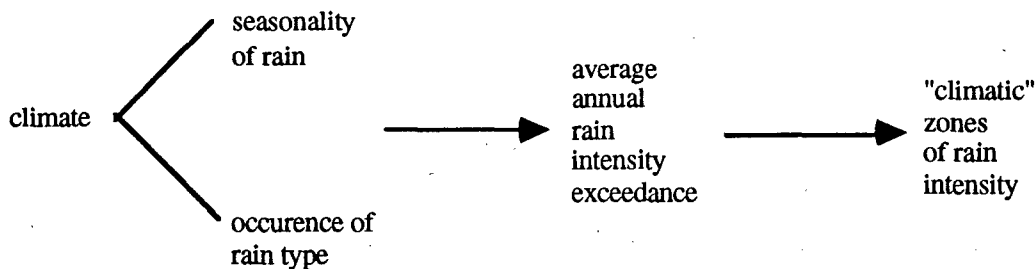
This debate has many aspects but is central to our theme. Radio data are now being accumulated from all parts of the globe in the ITU-R database. The fundamental questions are: (i) How many

climatologically-dependent variables are needed to scale such data with frequency and path length into a common pool? (ii) Can such variables be determined by independent physical measurement or must they be determined empirically by comparing predictions from models with measured data?

At present the ITU instantiates only one such variable (annual average rain intensity exceedance) in the context of attenuation (and cross-polarisation) prediction. Furthermore the climatic classification of the variable is not made strictly on an independent climatological basis, but on an empirical basis, comparing statistics of intensity exceedance. Should we extend this empiricism further? Or should we attempt to go back to the classifications of climate as put forward by climatologists and evolve a set of climatologically related parameters based on physical modelling of each climate?

In the extreme empirical approach we may decide that there are N climatologically dependent variables, each with a maximum of n independent classifications, where the variables N , have a loose physical significance (but may not be directly measurable) but the n independent classifications have no physical meaning or commonality. This could clearly get out of hand.

Let us illustrate the problem with reference to the one "climatic" variable that ITU currently instantiates, for attenuation prediction in rainfall, namely annual exceedance of 1 minute ground rainfall intensity. This variable can be measured directly, especially for high rainfall intensities, though it is often predicted (using empirically derived conversions) from data measured over periods longer than 1 minute. It is nevertheless a directly useful variable for prediction, especially on terrestrial paths and for frequencies ≤ 20 GHz. However the approach that we use of simply classifying similar exceedance distributions into climatic zones of rainfall intensity does lead to difficulty for Earth-space prediction. Questions on seasonality and monthly distributions of rain intensity (related of course to climate) are hidden within the one variable, but can be adjusted to some extent using a worst-month factor (which is currently not climatically classified). Questions on rain-type are also hidden within the same variable, which is a considerable problem for Earth-space



prediction, since the vertical extent of rainstorms is very dependent on rain type, which in turn has pronounced seasonal and climatic dependence. The picture is thus as illustrated above.

One approach would be to designate the worst month ratio as a prediction variable for climatic classification. Alternatively we should perhaps question the classification of rainfall intensity according to arbitrary "climatic zones" and perhaps go back to the features of climate that give a more comprehensive description of rainfall, including type of rain and seasonality. Not only do these features bear directly upon average yearly rain intensity distributions but also upon other contributory factors to attenuation, such as vertical and horizontal structure, drop-size distribution, rain cloud structure and occurrence of the melting zone. This approach draws upon physical modelling, linked to climatic classifications, so as to be able to make comparisons between data collected in different climates.

CLIMATIC CLASSIFICATIONS

The classification of climate is not an exact science, it depends to some extent on the application for which it is intended. Nevertheless, there are some well established systems of classification, mostly in terms of the critical factors for plant growth [1, 2] (especially rainfall and temperature). The question is, should we use such classifications as a basis for pooling data (with appropriate modelling parameters for each region) or should we ignore such classifications and build up our own, based on climatic variables unique to our application?

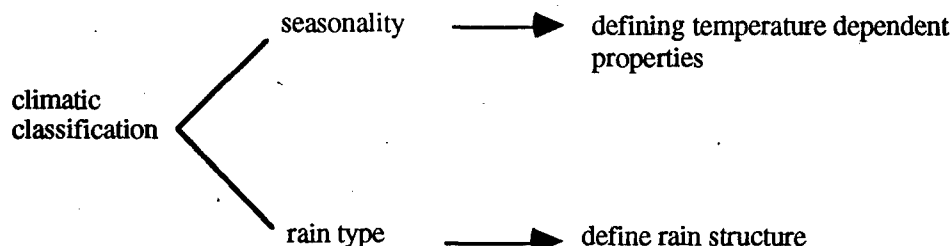
The main climatic classifications of Koeppen [1], (the most commonly used system) are given in

table 1, which must be read in association with a key of classification criteria (see for example [3]. Taking as an illustration the Interior Mediterranean climate, then Csa signifies: C, an average temperature of the warmest month $>50^{\circ}\text{F}$ and coldest between 64 and 32°F ; s, precipitation in the driest month of the summer half of the year <4 cms and less than one-third the amount in the wettest winter month and; a, average temperature of the warmest month $>71.6^{\circ}\text{F}$.

Hence the use of such an approach to climatic classification would seem to address some of our problems of prediction to do with rain type and seasonality. The approach is illustrated below.

CLASSIFICATION OF RAINSTORM TYPES

We are interested in rain types from the point of view of being able to model structure, whereas climatologists usually classify rain according to the process of generation, leading to essentially four categories, namely orographic, convective, frontal and cyclonic, with their well known meanings. Meteorologists still seem to be content to identify structure within two main categories [4] (stratiform and convective) but it is to be noted that these categories of structure do not map simply onto the categories related to growth. For example, extra-tropical cyclones should be considered as essentially stratiform structures [4] whereas tropical cyclones are basically convective, though strong stratiform features can emerge in late development. Warm frontal rains are essentially stratiform, but embedded convection is frequently seen. This is also especially the case with narrow cold frontal rainbands.



It may thus be satisfactory to relate categories of structure directly to climate, rather than to involve the categories of growth. We will thus stick to the usual stratiform and convective categories, but we perhaps ought also to identify two special rain types with pronounced structural features, namely drizzle and so-called "warm" rain. Wexler [20] has pointed out that precipitation from clouds entirely above freezing temperatures is observed over and near oceans, generally in tropical regions.

An important, and as yet not improved upon, approach to linking rain type to climate is that developed by Rice and Holmberg [5] and later implemented by Dutton and Dougherty [6]. Here two rain modes are distinguished (approximity to convective and stratiform rains) with a weighting that is determined in the main by the thunderstorm index. This gives us an ability to predict rain-type occurrence (for example see [7]) but does not help with seasonality.

At first sight it might seem that the seasonality of rain is only of very minor importance, especially if we are interested in average annual statistics of attenuation. However for satellite-Earth links, the effective rain height, which in some climates varies dramatically with season, has a strong influence on slant path attenuation.

A further complication which may be of interest to system designers is the pronounced diurnal variation of tropical rainfall [20].

MODELLING PARAMETERS FOR RAIN ATTENUATION PREDICTION

Table 2 identifies the most obvious modelling parameters, some specific and well established (for example 1 min ground rain intensity) and others more generic in nature (eg rain height) requiring closer specification. Various approaches to modelling rain height and rain horizontal structure are given in the literature (eg references [8] to [14]), but there is still considerable scope for development, especially in tropical regions, where it is hoped that radar studies will be undertaken. There is also some scope for making the variables necessary to define rain vertical and horizontal structure physically based, relating to parameters that can be directly measured (usually by radar).

COMBINATION OF FACTORS

The number of factors contributing to attenuation during rainfall increases, as we increase in frequency, a situation which is exaggerated by any shift of systems interest to lower link availabilities.

Once we move to 30/40 GHz and above, we must consider contributions from rain clouds and the (probably saturated) water upon contribution in addition to contributions from widespread and showery rain. These aspects have been studied by Salonen et al [15], Karhu et al [16] and Watson and Hu [7].

The method of combining factors makes a very significant difference to the attenuation predicted.

RECENT WORK ON ATTENUATION PREDICTION

Low Latitude High Rainfall Regions

In a recent review of propagation experiments conducted by INTELSAT (Allnutt [17]) it is clear that current CCIR path attenuation prediction procedures are not adequate for rainy tropical areas. The modelling of variation with elevation (and by implication with rain structure) is a particular problem.

As a purely empirical development of the CCIR procedure Dissanayake and Allnutt [18] have analysed underlying trends in transformations between (lognormal) rain intensity and path attenuation statistics. An empirically determined path adjustment factor is used to account for the horizontal structure of rain, the use of which was tested for terrestrial path prediction and found to give a significant improvement over the original CCIR method. Vertical rain structure was included for slant path prediction in a more conventional way, with specially interpolated values for latitudes between 0° and 23°.

Low Elevation Predictions

Low elevation angle (5.8°) measurements performed over the years in Austin, Texas [19] have shown significantly higher fades than predicted by the CCIR procedure. This is in keeping with earlier findings by Casiraghi and Paraboni [20] on European data. An interpretation given by both authors is that the CCIR method essentially deals with a single rain cell. Point-to-path statistical transformations (ie not based on extrapolation of rain cell models eg [9]) are seen to perform much better in these circumstances [20].

Dintelmann and Ortgies [21] have proposed a simple semi-empirical method for simple prediction of cloud attenuation from meteorological observables measured at ground level, ie humidity and temperature. Salonen et al [15] have more recently made a detailed comparative study of approaches to cloud attenuation prediction and

report an improved approach determined from vertical profiles of humidity and temperature. They also reported an alternative approach based on cloud-type data. The vertical profile approach has the strongest physical base and is believed to give the most accurate predictions. For percentages of time between 0.1 and 1% it predicts significantly higher attenuation values than those predicted by the methods of Dintelmann and Ortgies [21] and by Altshuler and Marr [22].

One of the uncertainties in prediction of cloud attenuation is the frequency of presence of drizzle at base of stratiform clouds, which bear no precipitation at the ground.

PREDICTION OF CROSS POLARISATION IN RAINFALL

For terrestrial paths cross-polarisation in rainfall can be satisfactorily predicted from attenuation using the current ITU-R semi-empirical relationship [23]. Problems arise when considering Earth-space paths and the occurrence of depolarisation from (high altitude) ice particles. Such depolarisation is of increasing significance to systems as frequency increases.

It has been suggested for some time that climatic factors played a part in determining the frequency of occurrence of ice depolarisation. McEwan [24] in examining OTS data, noticed substantial variability from site-to-site, but owing to the quality of the data then available was unable to isolate the climatic features of importance. He did however notice a tendency for more pronounced occurrence in coastal regions. More recently Fukuchi [25] has examined data collected in Japan at 11, 20 and 35 GHz and concluded that ice depolarisation is more significant in climates dominated by stratiform rain. This is not contradictory to the earlier findings of McEwan, though it is well known that stratiform features do emerge in the tails of convective structures [4] and it might be expected that there could be considerably more ice aloft in such structures than in typical stratiform rain. Also the possibility of rain occurring in coastal tropical climates without an ice-phase [20], must be accounted for.

Fukuchi [25] has proposed extending the current ITU-R prediction method by defining an ice depolarisation ratio ρ and an ice depolarisation correction factors as follows:

$$\rho = \frac{P(XPD < x, A < a_x)}{P(XPD < x)} \times 100(\%)$$

where, $P(XPD < x, A < a_x)$ is the percentage of time that XPD and attenuation are less than x and a_x respectively, where a_x is the theoretical attenuation that corresponds to XPD, x . Also:

$$\delta = \frac{100}{100 - \rho}$$

The ice depolarisation ratio could simply be determined empirically for a range of climates, or following up the findings of Fukuchi on the rainfall type dependence, could be linked to standard climatic classifications.

CONCLUSIONS

This paper has drawn attention to weaknesses in our ability to predict attenuation and cross-polarisation during rainfall in certain circumstances, especially in rainy tropical climates (for all frequencies above 10 GHz) but also in most climates for frequencies above 30 GHz.

The modelling parameters that are required for prediction have been identified in a general way, but require a more detailed treatment for accurate prediction. A key question is whether or not the detailed treatment of these parameters should be physically based, linked to rainfall type and an established climatic classification. The alternative approach, based on empirical interpolations for ranges of new (and unconventional) climatic variables becomes increasingly difficult as the number of variables increases.

REFERENCES

- [1] Koeppen W "Das geographische system der klimate" Vol 1 Part C of "Handbook der Klimatologie", Gebruder Borntraeger, Berlin, 1936.
- [2] Thornthwaite C W "The climates of North America according to a new classification" Geog Rev 21, 4, Oct 1931, 633-55.
- [3] Critchfield H J "General climatology" Prentice Hall 2nd Ed, 1966.
- [4] Houze P A "Structure of atmospheric precipitation systems : A global survey" Radio Science 16 5 Sept/Oct 1981, 671-690.
- [5] Rice P L and Holmberg N R "Cumulative time statistics of surface point rainfall rates" IEEE Trans Comms CoM-21, (10), 1973.
- [6] Dutton E J, Dougherty H T and Martin R F "Prediction of European rainfall and link

- performance coefficients at 8 to 30 GHz" Tech Report ACC-ACO-16-74, Institute for Telecommunications Sciences USA, Aug 1974.
- [7] Watson P A and Hu Y F "Prediction of attenuation on satellite-Earth links for systems operating with low fade margin." (This symposium)
 - [8] R K Crane "A two component rain model for prediction of attenuation statistics" Radio Science, 17 (6) Nov/Dec 1982, 1371-1387.
 - [9] Leitao M J and Watson P A "Method for prediction of attenuation on Earth-space links based on radar measurement of the physical structure of rainfall" Proc IEE PtF 133, (4) 1986, 429-440.
 - [10] Capsoni C, Fedi F, Magistroni C, Paraboni A and Pawlina A "Data and theory for a new model of the horizontal structure of raincells for propagation applications" Radio Science 22, (3) 1987 395-404.
 - [11] Watson P A, Leitao M J, Sathiaselen V, Gunes M, Poyares Baptista J P V, Potter B A, Sengupta N, Turney O and Brussaard G "Prediction of attenuation on satellite-Earth links in the European region" Proc IEE PtF 134 (6), 1987, 583-596.
 - [12] Morita K and Higuti I "Statistical studies in electromagnetic wave attenuation due to rain" Rev of Elec Comm Lab. Japan 19 (7-8) 1971 798-842.
 - [13] Lin S H "A method for calculating rain attenuation distribution on microwave paths" BSTJ 54, 1975, 1051-86.
 - [14] Stutzman W L and Yon K M "A simple rain attenuation model for Earth-space radio links operating at 10-34 GHz" Radio Science 21, (1) 1986, 65-72.
 - [15] Salonen E, Karhu S, Jokela P, Zhang W, Uppala J, Aulamo H, Sarkkula S and Poyares Baptista J P V "Modelling and calculation of atmospheric attenuation for low-fade-margin satellite communications" ESA Journal 16, 1992 299-317.
 - [16] Karhu S, Salonen E, Hyvonen R, Uppala S and Poyares Baptista J P V "Prediction of rain attenuation at low-availabilities using models and data of widespread and convective rains" IEE conf on Antennas and Propagation (ICAP) IEE Conference Publication 370, April 1993 1.56-1.59.
 - [17] Allnutt J E "INTELSAT propagation experiments : The focus and results of recent campaigns" Proc IEEE 81 (6) June 1993, 856-864.
 - [18] Dissanayake A W and Allnutt J E "Prediction of rain attenuation in low-latitude regions" URSI Commun F Open Symposium on Wave Propagation and Remote Sensing, Ravenscar UK, June 1992 Pre-points 6.4.1-6.4.6.
 - [19] Vogel W J, Torrence G W and Allnutt J E "Rain fades on low elevation angle Earth-satellite paths : comparative assessment of the Austin, Texas 11.2 GHz experiment" Proc IEEE 81 (6) June 1993 885-896.
 - [20] Casiraghi E and Paraboni A "An update on the modern techniques for predicting slant path attenuation beyond 10 GHz in different world regions and experimental conditions" URSI Commun F Open Symposium on Wave Propagation and Remote Sensing, La Londe-les-Maures France 1989, Proc 1-2-1-1-2-7.
 - [21] Dintelmann F and Ortgies G "Semi-empirical model for cloud attenuation prediction," Elec Lects 25, 1989 1487-1488.
 - [22] Altshuler E and Marr R "Cloud attenuation at millimetre wavelengths" IEEE Trans AP- 37 1989 1473-1479.
 - [23] ITU-R Recommendations 618-2 "Propagation data and prediction methods required for the design of Earth-space telecommunications systems" (1986/1990/1992).
 - [24] McEwan N J "Propagation Experiments with the OTS Satellite" Section 2 of report to EUTELSAT P/TEC'83/1 1983.
 - [25] Fukuchi H "Prediction of depolarisation distributions in Earth-space paths" Proc IEE B7 Pt-H (6) Dec 1990, 325-330.

TABLE 1 MAIN CLIMATIC TYPES OF THE KOEPPEN CLASSIFICATION

Af	Tropical rain forest. Hot; rainy in all seasons
Am	Tropical monsoon. Hot; seasonally excessive rainfall
Aw	Tropical savanna. Hot; seasonally dry (usually winter)
BSb	Tropical steppe. Semiarid; hot
BSk	Mid-latitude steppe. Semiarid; cool or cold
BWh	Tropical desert. Arid; hot
BWk	Mid-latitude desert. Arid; cool or cold
Cfa	Humid subtropical. Mild winter; moist all seasons; long, hot summer
Cfb	Marine. Mild winter; moist all seasons; warm summer
Cfc	Marine. Mild winter; moist all seasons; short cool summer
Csa	Interior Mediterranean. Mild winter; dry summer; hot summer
Csb	Coastal Mediterranean. Mild winter; dry summer, short warm summer
Cwa	Subtropical monsoon. Mild winter; dry winter; hot summer
Cwb	Tropical upland. Mild winter; dry winter; short, warm summer
Dfa	Humid continental. Severe winter; moist all seasons; long, hot summer
Dfb	Humid continental. Severe winter; moist all seasons; short, warm summer
Dfc	Subarctic. Severe winter; moist all seasons; short cool summer
Dfd	Subarctic. Extremely cold winter; moist all seasons; short summer
Dwa	Humid continental. Severe winter; dry winter; long hot summer
Dwb	Humid continental. Severe winter; dry winter; warm summer
Dwc	Subarctic. Severe winter; dry winter; short, cool summer
Dwd	Subarctic. Extremely cold winter; dry winter; short, cool summer
ET	Tundra. Very short summer
EF	Perpetual ice and snow
H	Undifferentiated highland climates

TABLE 2 COMMENTS ON POSSIBLE MODELLING PARAMETERS FOR ATTENUATION PREDICTION

Parameter	1 minute ground rainfall intensity	Rain vertical structure	Rain height	Rain horizontal structure	Rain drop-size distribution
Rain Type					
Convective/ Showery	Attenuation prediction possible both from directly measured data and (less accurately) from predicted 1 min intensities from long term data.	Fall velocity variations with barometric pressure in rain region (5 to 10% error over uniform case).	Considerable variability with continentality. Effects of clouds important above ~30 GHz.	Characterised by model cells (or cells plus debris) or point-to-path transformations.	Intensity-related on-average functions appear to be satisfactory (included in AR ^B constants). Variability < 10%.
Stratiform/ Widespread	Attenuation less accurately predicted from gauges designed for intense short duration rains. Longer term data may be better	Smaller range of dsd and fall velocity variations, but coalescence towards ground may be significant especially in coastal tropical climates ("warm" rain).	Melting zone must be included (proportionally less significant as frequency increases). Effects of clouds important above ~40 GHz. Uncertainty in tropical climates over occurrence of "warm" rain below 0° isotherm.	Different point-to-path transformations required. Simple uniform models probably not adequate owing to small zones of embedded convection.	Intensity-related dsd becomes dubious for light rains, which for higher frequencies are of some significance.

PRECIPITATION RETRIEVAL FROM SPACEBORNE MICROWAVE RADIOMETERS: DESCRIPTION AND APPLICATION OF A MAXIMUM LIKELIHOOD PROFILE ALGORITHM

A. Mugnai¹, F. S. Marzano² and N. Pierdicca²

¹ Istituto di Fisica dell'Atmosfera, Consiglio Nazionale delle Ricerche, Via G. Galilei - 00044 Frascati (Italy)
Tel. ++39-6-94186215; Fax. ++39-6-94186266; E-mail: mugnai@hp.ifs.fra.cnr.it

² Dipartimento di Ingegneria Elettronica, Università "La Sapienza", Via Eudossiana, 18 - 00184 Roma (Italy)
Tel. ++39-6-44585845; Fax. ++39-6-4742647; E-mail: franko@palatino1.ing.uniroma1.it

ABSTRACT

This paper illustrates a statistical inversion technique for retrieving hydrometeor vertical profiles of precipitating clouds and associated surface rainrates from spaceborne multifrequency microwave radiometers. The retrieval scheme uses the maximum-likelihood discriminant analysis trained on a physically-constrained and statistically-generated cloud-radiation database. This algorithm is applied to a precipitating cloud system over the Italian peninsula, observed by the Special Sensor Microwave Imager (SSM/I).

Keywords: Microwave radiometry, Spaceborne remote sensing, Precipitation retrieval

various hydrometeors and absorbing gases (Refs. 4 and 5).

In this paper, we describe a new precipitation-profile retrieval algorithm that is based on the use of a large number of cloud structures (i.e., the vertical profiles of different kind of hydrometeor contents and of the relevant meteorological quantities) and of their related brightness temperatures; this cloud-radiation database, is statistically generated so as to be physically consistent with a three-dimensional cloud mesoscale model. The statistical inversion is accomplished by applying a maximum likelihood discriminant method that selects the solution set of hydrometeor profiles from the database. The algorithm is applied to a rainfall event over central Italy and rainrate estimates are compared with available raingauge measurements.

1. INTRODUCTION

Spaceborne multifrequency microwave radiometry has shown to be an effective tool for measuring precipitation which is an important parameter for climate and radiowave propagation researches. Various simulation studies have been carried out in order to provide an interpretation of remotely sensed microwave measurements in precipitating atmospheres. Consequently, several retrieval algorithms have been developed having different characteristics and potential (Ref. 8).

Most of the algorithms are designed to retrieve only the surface rainrate (RR). However, in the last years, spaceborne passive microwave observations have been exploited to retrieve cloud and precipitation profiles, i.e. the vertical distributions of the equivalent water contents (EWC's) of the various hydrometeors in different phases (Ref. 6). This capability arises from the fact that the upwelling microwave radiation emerging from a cloud is responsive to precipitation microphysics. Specifically, the measured brightness temperatures (T_B 's) respond, in a frequency dependent fashion, to scattering and absorption processes within the cloud, so that they result correlated to the vertical distribution of the

2. MAXIMUM LIKELIHOOD RETRIEVAL OF PRECIPITATING CLOUD STRUCTURE

The retrieval algorithm is based on the use of cloud-radiation models and of multivariate statistical analysis (Ref. 1). As compared to other methods inferring the vertical structure of the precipitating cloud, it adopts a maximum likelihood criterion to identify the actual profile; moreover it exhibits fairly good performance in terms of processing time since the algorithm itself is not iterative and the time consuming task of solving the radiative transfer equation is accomplished only once, when generating the cloud-radiation database.

The maximum likelihood estimation can be expressed rigorously by matrix notation (Ref. 1). The set of hydrometeor vertical profiles is identified by a vector g , consisting of EWC's at different altitudes of the various hydrometeor species, while the multi-frequency T_B measurement is expressed by vector t . Then the inverse solution is found by searching the most probable cloud structure within the cloud-radiation database, i.e. by maximizing the following discriminant function with respect to g :

$$d(t, g) = \ln[p(t|g)] + \ln[p(g)] - \ln[p(t)] \quad (1)$$

where $p(t|g)$ is the conditional probability density function (pdf) of t conditioned to g , and $p(g)$ and $p(t)$ are the pdf's of g and t , respectively. Eq. (1) has been derived by means of the Bayes theorem that allows to express the posterior pdf $p(g|t)$ as a function of the prior pdf $p(t|g)$. Assuming a Gaussian multidimensional joint-distribution of vector g , the covariance matrix C_g and the mean vector m are sufficient to describe the statistics of g , and its probability density function is given by:

$$p(g) = \frac{1}{(2\pi)^{D/2} \sqrt{\det(C_g)}} \exp\left[-\frac{1}{2}(g-m)^T C_g^{-1}(g-m)\right] \quad (2)$$

where $\det(C_g)$ and C_g^{-1} indicate the determinant and the inverse matrix of C_g , respectively. If t' is the T_B vector associated to g by the radiative transfer, and the measurement errors $(t-t')$ are assumed uncorrelated at the different frequency bands with the same variance σ_t^2 , by substituting Eq. (2) into Eq.(1) and considering that $p(t)$ is a common term, it results:

$$d(t, g) = -\frac{1}{2\sigma_t^2}(t-t')^T(t-t') - \frac{1}{2}\ln[\det(C_g)] - \frac{1}{2}(g-m)^T C_g^{-1}(g-m) \quad (3)$$

where "T" represents the transpose operator. Once the vector g has been selected, the most probable surface rainfall rate is computed from the retrieved hydrometeor profiles by means of a fallout model (Ref. 5). Note that Eq. (2) can be applied to the whole dataset as well to a classified dataset, by inserting the class probability into the equation itself and by calculating m and C_g for each class. It is interesting to point out that both the measured brightness temperatures and the knowledge about the statistics of each class contribute to the discriminant function. In particular, if the radiometric measurements are assumed free of error (i.e., in Eq. (3): $\sigma_t^2=0$), the first term on the right will prevail and the cloud structure will be selected on the basis of a minimum Euclidean distance criterion in the space of brightness temperatures. On the other hand, if σ_t^2 becomes infinite, the second and third terms on the right will prevail with respect to the first one and, in this case, the minimization of $d(t, g)$ is accomplished

by selecting the mean cloud profile. If several classes are considered, the decision rule will select the class having the minimum determinant of the covariance matrix, i.e., the class that exhibits minimum variances of hydrometeor EWC's and profiles having large correlation coefficients.

In Eq. (3), the covariance matrix C_g and the mean vector g must be specified. In principle, they may be derived either from outputs of a mesoscale cloud model, or from experimental data (radar profile retrievals and/or *in situ* measurements). In this work, for generating the cloud database, we have used the three-dimensional time-dependent cloud/mesoscale model named University of Wisconsin - Nonhydrostatic Modeling System (UW-NMS) (Ref. 7), explicitly presenting four species of hydrometeors: cloud droplets, rain drops, graupel particles and ice crystal-aggregate particles. The number of cloud layers has been reduced in an automatic way to at most seven homogeneous layers in order to deal with manageable covariance matrices and to reduce the redundancy of the cloud structures with respect to the information carried by the microwave frequencies currently used. The primary dataset has been classified into various cloud typologies and the mean m and matrix C_g have been estimated for each identified class. Moreover, it has been extended, class by class, by means of a pseudo-random multidimensional Gaussian generator of a random vector g , having mean m and covariance matrix C_g . By applying a plane-parallel radiative transfer scheme to the extended cloud database, the vector of simulated brightness temperatures t' is associated to each generated precipitating cloud structure. Therefore, a cloud-radiation database (consisting of five thousand cloud structures and the associated T_B 's) is generated; in the algorithm, this database is considered as a random sample of the brightness temperatures emerging from precipitating clouds (Ref. 2). Of course, by using a plane-parallel radiative transfer, the performed estimation is valid under the assumption of horizontal homogeneity of the precipitating cloud within the radiometer antenna beam.

We have tested the retrieval algorithm on simulated data. To this end, the choice of parameter σ_t^2 is a critical point since we can make fairly good assumption on the radiometer noise, but we do not know the errors associated with the radiative transfer modeling. In order to best evaluate σ_t^2 , the discriminant function of Eq. (3) has been applied to the T_B 's of the cloud-radiation database by adding an instrumental noise. The variance of the additive instrumental noise (equal to 1 K) has been preliminarily assumed for σ_t^2 , but

the analysis of the residual errors in the estimation of rain rate has shown that $\sigma_1^2=4$ gives the best accuracy. From this simulation, we have found for the surface rainrate a residual r.m.s. error of 5.1 mm/h using the four Special Sensor Microwave Imager (SSM/I) frequencies.

One limitation of the proposed method is due to the fact that the solution profile is searched within a discrete number of cloud structures from the cloud radiation database. On the other hand, increasing the number of generated cloud structures would grow the computational load of the technique. However, this limitation can be partially overcome if, in general, we consider that the discriminant function $d(t,g)$ does not differ significantly from a statistical point of view for a number of profiles close to the maximum likelihood profile. Thus, the solution can be given by the average of these profiles, while their standard deviation can be interpreted as the accuracy of the final solution. The same procedure applies to the associated surface rainrate and, in this case, the residual r.m.s. error is of 4.5 mm/h. It must be noted that we can also estimate the integrated parameters from the retrieved vertical profile, such as the columnar EWC's of rain and ice hydrometeors. The accuracy we have found for the cloud, rain, graupel, and ice CEWC's is 0.6 Kg/m², 0.8 Kg/m², 0.3 Kg/m², and 0.9 Kg/m², respectively.

3. APPLICATION TO SSM/I DATA

In the past, the algorithm has been applied to airborne microwave radiometer measurements with high ground resolution (order of kilometers); retrieval results have shown fairly good agreement

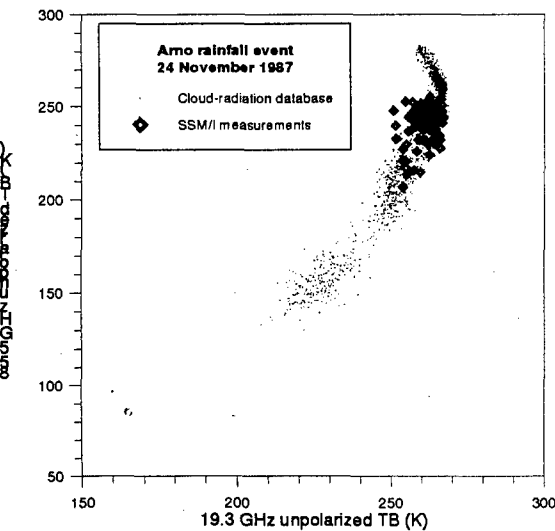


Figure 1: Spectral signature of the cloud-radiation database compared to SSM/I measurements for the

Arno rainfall event. with those obtained by radar measurements (Ref. 3). This section presents a case study where the algorithm has been applied to SSM/I measurements over the Mediterranean area, in order to show its potential for spaceborne precipitation retrieval.

The case study refers to a cold front passed over Italy on 24 November 1987; quite intense precipitation over land was observed, particularly in the area of the Tuscany region (about 43 Nord, 12 East) corresponding to the Arno river catchment basin, where a raingauge network is present. The adequateness of the used cloud-radiation database to represent the SSM/I microwave spectral signature of the considered event must be first verified. Figure 1 shows the comparison of the brightness temperatures in the precipitation area extracted from the SSM/I T_B's at 19.3 and 85.5 GHz with the T_B's from the cloud-radiation database. The correspondence can be considered fairly good, except for a few image pixels. In particular, at lower frequencies, the effect of Earth surface emissivity can be significant and probably requires an improved model. We point out that these encouraging results are obtained by applying a deconvolution procedure that has enhanced the lower ground resolution to that one of the 85.5 GHz (order of 15 Kilometers).

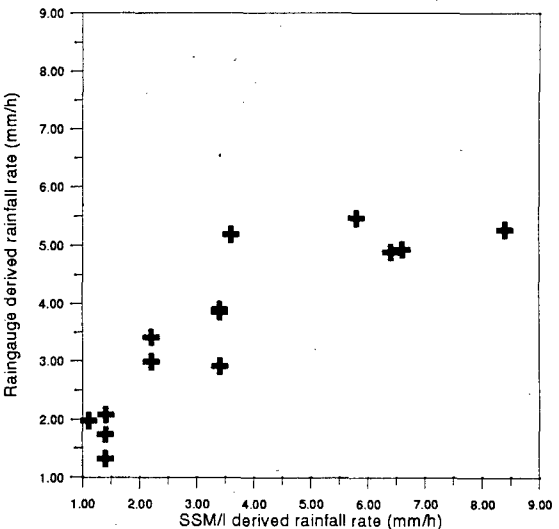


Figure 2: Comparison of SSM/I derived rainfall rate and raingauge measurements for the Arno rainfall event.

Comparison of rain rates derived from spaceborne radiometers with raingauge network measurements is always difficult. The two kinds of sensors have different spatial resolutions; moreover, the raingauges provide hour-cumulative values while instantaneous values are derived from satellites. Nevertheless, Figure 2 shows the comparison

between SSM/I-estimated surface rainfall rate and raingauge-derived RR. The agreement is fairly good in an average sense; the retrievals based on SSM/I tend to overestimate RR of about 3 mm/h with respect to raingauges.

5 - CONCLUSIONS

In this paper, we have shown how the use of a statistically-generated cloud-radiation database can lead to a proper modeling framework for statistical retrieval of precipitating cloud structures. We have described a maximum likelihood estimation algorithm, that is able to assimilate the information deduced from the simulated dataset in an effective and efficient way. The potential of the proposed retrieval algorithm has been shown and a preliminary comparison with rain-gauge measurements has given encouraging results. Noteworthy, our participation to the second phase of the Precipitation Intercomparison Project (PIP-2), organized by the NASA WetNet, will represent a precious chance to examine the algorithm performances in many precipitation conditions.

Acknowledgments: this research has been supported by Gruppo Nazionale per la Difesa dalle Catastrofi Idrogeologiche, by Agenzia Spaziale Italiana and by Commission of the European Communities (contract EV5V-CT92-0167) within research program Climatology and Natural Hazards of the EC ENVIRONMENT Programme 1991-1994.

REFERENCES

1. Basili, P., Ciotti, P., d'Auria, G., Marzano, F.S., Pierdicca, N., Mugnai, A., 1994: Precipitation retrieval from spaceborne microwave radiometers based on maximum likelihood discriminant analysis. *IEEE Trans. Geosci. Remote Sens.*, submitted.
2. Marzano, F.S., Mugnai, A., Turk, J., Vivekanandan, J., Smith, E.A., Xiang, X., 1994: Active and passive microwave remote sensing of precipitating storms during CaPE. Part II: Intercomparison of AMPR and CP-2 retrievals. *Meteorol. Atmos. Phys.*, in press.
3. Marzano, F.S., Mugnai, A., Pierdicca N., Smith, E.A., Turk, J., Vivekanandan, J., 1994: Precipitation profile retrieval from airborne microwave radiometers: a case study over ocean during CaPE, submitted to the Specialist meeting on microwave radiometry and Rem. Sens. of the Envirom., 14-17 Feb., Rome.
4. Mugnai, A., Smith, E.A., Tripoli, G.J., 1993: Foundations for statistical-physical precipitation retrieval from passive microwave satellite measurements. Part II: Emission source and generalized weighting function properties of a time- dependent cloud-radiation model. *J. Appl. Meteor.*, 31, 6, 506-531.
5. Smith, E.A., Mugnai, A., Cooper, H.J., Tripoli, G.J., Xiang, X., 1992: Foundations for statistical-physical precipitation retrieval from passive microwave satellite measurements. Part I: Brightness-temperature properties of a time-dependent cloud-radiation model. *J. Appl. Meteor.*, 31, 6, 506-531.
6. Smith, E.A., Kummerow, C. and Mugnai, A., 1994: The emergence of inversion-type profile algorithms for estimation of precipitation from satellite passive microwave measurements. *Remote Sens. Rev.*, in press.
7. Tripoli, G.J., 1992: A nonhydrostatic model designed to simulate scale interaction. *Mon. Wea. Rev.*, 120, 1342-1359.
8. Wilheit, T. R., Adler, S., Barret, E., Bauer, P., Berg, W., Chang, A., Ferriday, J., Grody, N., Goodman, S., Kidd, C., Kniveton, D., Kummerow, C., Mugnai, A., Olson, W., Petty, G., Shibata, A., Smith, E., and Spencer, R. 1994: Algorithms for the retrieval of rainfall from passive microwave measurements. *Remote Sens. Rev.*, in press.

CLIMATIC PARAMETERS REQUIRED FOR THE PREDICTION OF INTERFERENCE DUE TO PRECIPITATION SCATTER

M. Thurai

Rutherford Appleton Laboratory
Chilton, Didcot, Oxon OX11 0QX, UK
Tel : +44 235 44 5770, Fax : +44 235 44 6140,
E-mail : m.thurai@rutherford.ac.uk

ABSTRACT

This paper discusses the climatic parameters that are required for hydrometeor scatter interference prediction. Five parameters regarding the large scale spatial structure of precipitation are identified. On a microscopic level, the rain drop size distribution is also identified as an important parameter. The role of meteorological radar in providing such information is examined and, in particular, the advantages of multi-parameter systems are highlighted. For regions not covered by ground based radars, data sets which will become available from future satellite rain radar systems seem to provide the best alternative.

Key words: Hydrometeor scatter interference, precipitation structure, meteorological radar, dropsizes distribution.

1. INTRODUCTION

The increasing need for different microwave terrestrial systems, satellite communications and broadcast systems to share frequencies has produced a correspondingly greater likelihood of interference. The mechanisms of such interference can be several, one being the scattering of microwaves from rain and other hydrometeors. A particular aspect of this interference is that it can occur for several geometries (i.e. for different antenna bearings) owing to the omni-directional nature of precipitation scatter. In general, however, maximum interference occurs for geometries for which there is considerable overlap between the two antenna mainlobes. A typical rain scatter interference scenario is depicted in Figure 1.

The problem of rain scatter interference was addressed within the framework of COST Project 210 [1] European collaborative programme. It led to the development of a prediction procedure to evaluate its statistical significance, on the basis of input data regarding path geometry, antenna characteristics and climatic data. The method was

tested against statistical data obtained from several long-term experiments conducted in Western Europe, with varying geometries, frequencies and terminal separations. The results showed that when coupling occurs as a consequence of main-lobe intersection, the predicted levels of interference agree well with experimental measurements. As a result, the method formed the basis of the ITU-R recommended procedure [2].

From the point of view of climatic parameters, the prediction method requires meteorological characteristics of precipitation which include both rainrate statistics and the spatial structure. Whilst the former can be obtained from the multitude of rain gauges, distrometers, etc. currently installed throughout the world, the latter is much more difficult to quantify without the use of specialised meteorological radars. This paper addresses all parameters that are required for the prediction of hydrometeor scatter interference and discusses the ways in which current and future weather radar systems can contribute by characterising precipitation structure in climatic regions for which there are very little data available at present.

2. PREDICTION METHOD AND ITS CLIMATIC PARAMETERS

For a given geometry, the interference signal level depends not only on the amount of directional scatter produced within the 'common volume' but also on the attenuation along the interference path. In general, both these factors increase with rain rate, i.e. the higher the rainfall rate, the higher the scattered power and higher the path attenuation. Since these have opposing effects on the signal strength, the interference level does not increase monotonically with rain rate. It follows that for the prediction of interference levels, the statistics of point rainfall are not sufficient by themselves. We need to know their large scale spatial structure too.

Prediction methods fall into two categories; they are either rigorous or semi-empirical. Several

rigorous methods have been developed in the past (see for example [3-5]), however, the computational time required for their evaluation is often large for operational uses. For this reason, the COST 210 procedure adopted a semi-empirical approach. Although the method is based on the bistatic radar equation [6] to evaluate the received power of the interference signal, the position and parameters of the rain cell are assumed fixed for a given rainfall rate. The rain cell model is a statistically representative one, consisting of (a) a constant rainfall cylindrical core whose diameter 'd_c' is given by

$$d_c = 3.3 R^{-0.08} \quad (i)$$

where R is the rain fall rate in mm/hr and (b) an exponentially decaying function outside the centre whose rate of decay depends on the scaling distance 'r_m' which is empirically related to the peak rain rate by

$$r_m = 600 R^{-0.05} 10^{-(R+1)^{0.19}} \text{ km} \quad (ii)$$

Like the bistatic radar equation, the model evaluates both the scatter within the common volume (CV) and the attenuation along the two paths (i.e. tx to CV and rx to CV). The scatter is assumed to take place only within the cylindrical rain cell whilst the attenuation is computed both inside this cell and outside. The unit volume rain scatter reflectivity factor Z_r below the melting layer is given by

$$Z_r = 400 R^{1.4} \quad (iii)$$

which is subsequently converted to the bistatic radar reflectivity by taking into account polarisation decoupling and any deviation from Rayleigh scattering, particularly for frequencies greater than 10 GHz. The reflectivity is assumed constant with height in the rain region; above the melting layer, it is supposed to fall off at a rate of 6.5 dB/km. Note, the coefficients in equation (iii) apply only for a Marshall-Palmer dropsizes distribution, which tends to be a good statistical representation for North-west European climate

As for the height of the melting layer, the model recognises that it is a variable quantity and hence is represented by a distribution rather than a single value. For the mean height, H_{fr}, the expression

$$H_{fr} = 5800 - 72.6\theta \quad (iv)$$

is used, where θ is the latitude in degrees and H_{fr} is in units of metres above sea level. For middle latitudes, i.e. when 35 < θ < 70, the expression has been shown to be accurate to within 100 metres [7].

The attenuation along the bistatic path is computed from the rain-intensity dependent specific attenuation, γ, given by [8]:

$$\gamma = k R^\alpha \quad (v)$$

where the coefficients k and α depend on frequency, polarisation and the direction of propagation vector. As in the case of the Z - R relationship (equation [iii]), these coefficients also assume a certain function for the rain drop size distribution. The main point to note here is that if the annual statistics of DSD is climate dependent, then both Z - R and γ - R coefficients would need to be changed accordingly.

In summary, the evaluation of hydrometeor scatter interference requires five basic input parameters which are related to the spatial structure of precipitation. In the horizontal dimension, the model requires (i) the width of the rain cell in terms of the peak rainrate and (ii) the exponential function which can statistically approximate the intensity decay with distance (in particular, the parameter r_m). In the vertical direction, the model requires (i) the mean height of the melting layer, (ii) its annual distribution and (iii) the mean reflectivity-height profile (below and above the melting layer). On a microscopic level, the raindrop size distribution needs to be characterised so that the appropriate Z - R and γ - R relationships can be derived accordingly. Since the prime objective of the interference method is to derive interference statistics, its input parameters regarding the rain cell model should also be derived statistically.

3. USE OF METEOROLOGICAL RADAR

During the development stages of the prediction method, it became clear that the spatial structure of precipitation was best obtained from meteorological radars. As a result, several analysis studies were conducted using radar data. In particular, three radar systems were used for this study, located at (a) Milan, Italy, (b) Delft, Netherlands and (c) Chilbolton in Southern UK.

3.1 Vertical structure

Figure 2 shows an example of the results using the Chilbolton radar data, collected over a two year period. During the two-year campaign, the radar was used to scan vertical (RHI) planes on a statistical basis. From these scans, the reflectivity statistics were derived for various heights relative to the local 0 deg isotherm.

The four profiles shown in Figure 2 show very similar behaviour, viz. constant reflectivity within the rain region, a clear enhancement of approximately 5 dB in the melting region and a subsequent decrease in reflectivity at almost a constant rate of 6.5 dB/km in the ice region. The curves, although generated on a statistical basis, are very similar to individual profiles exhibited by a typical stratiform precipitation, indicating that the vertical structure of rain is dominated by the characteristics of such stratiform events, at least for the UK.

In tropical climates, convective activity is far more prevalent where strong vertical air motions give rise to large scale mixing of frozen, liquid and partially melted hydrometeors. Convection also results in supercooled drops or wet hail being present at large heights, giving rise to high reflectivity values. An example of radar measurements taken through a convective storm is given in Figure 3. The measurements were made from an airborne radar at near-nadir incidence [9]. The aircraft was flying along a straight line at an altitude of 12 km above sea level, over a typhoon event in the western Pacific ocean. Top figure shows the radar reflectivity at X-band and the bottom figure shows the cross-polar back scatter, given in terms of L_{dr} defined as

$$L_{dr} = 10 \log_{10} \left(\frac{Z_{VH}}{Z_{HH}} \right) \quad (vi)$$

where Z_{VH} and Z_{HH} are the cross-polar and co-polar back scatter reflectivities (in linear units) for horizontally polarised transmission.

The L_{dr} signatures show three clear regions; the first is a tall thin column at 06:17 GMT which corresponds to a convective cell, with a maximum L_{dr} of around -16 dB; the second is a clear enhancement in the melting region of the stratiform part of the event; the third is a combination of the first two, i.e. a bright-band

enhancement which extends from the zero deg isotherm down to the sea surface.

It is clear that for a nadir-looking radar, the combination of co-polar and cross-polar reflectivity measurements can provide a potentially useful method of identifying hydrometeors and, in particular, the regions of melting particles. This may have implications for future satellite systems, (see section 3.3)

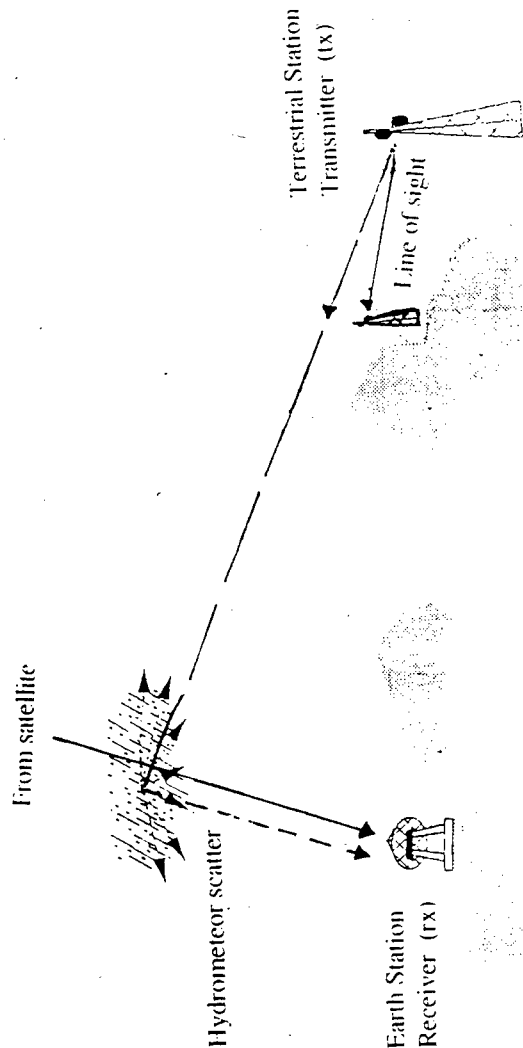
3.2 Horizontal structure

Many countries, particularly those in Western Europe, North America and some parts of Asia, already have ground based radar systems, often installed as part of their national research into atmospheric science. As a result, the spatial structure of precipitation in these regions are fairly well defined. For example, Capsoni et al [10] have used an extensive database with more than 6000 horizontal sections of rain cells (i.e PPI scans) collected by an S-band radar at Spino d'Adda, near Milan, to derive the parameters for a (statistical) model rain cell. The rain model has an exponential shape starting from the centre, with a rate of decay which is a function of the peak rain rate. Like the ITU-R model, the rain cell is parameterised by its peak intensity, cell size and rate of decay. The authors also propose an algorithm for adapting the cell model to other regions, on the basis of the local cumulative statistics of point rainfall rate. The algorithm can indeed be tested by performing a similar analysis on statistically collected PPI scans in other locations.

3.3 Satellite weather radar

For regions not covered by ground based radar, satellite systems may provide an adequate solution. Up till now, the main instruments used for satellite weather monitoring have been radiometers, ranging from microwaves to infra-red and visible frequencies. Although active instruments have had well recognised advantages, it was not possible to develop such systems (until recently) because of such factors as cost, weight, power and reliability.

With the advent of the necessary technology (e.g. efficient and reliable microwave power amplifiers with space specifications, low noise receivers, advances in antenna technology), spaceborne weather radar is now under serious consideration [11]. Missions such as TRMM (Tropical Rainfall Measuring Mission) are now designed to carry a



2.3.4

Figure 1 : A typical hydrometeor scatter interference scenario. Solid lines represent wanted signals and dashed line represents interference signal

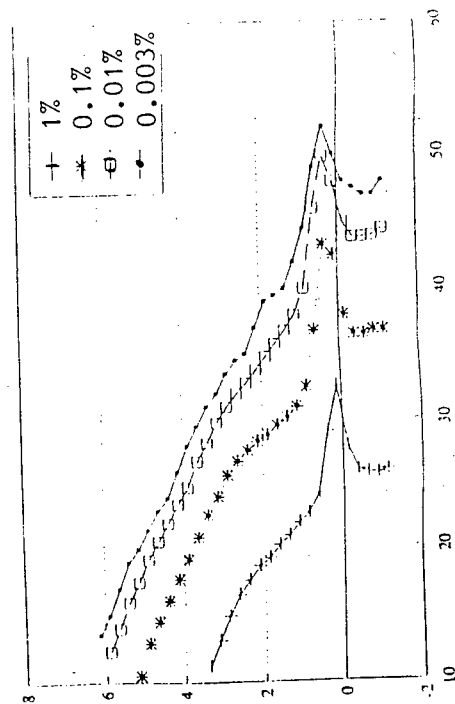


Figure 2 : Reflectivity variation with height relative to freezing level for various time percentages

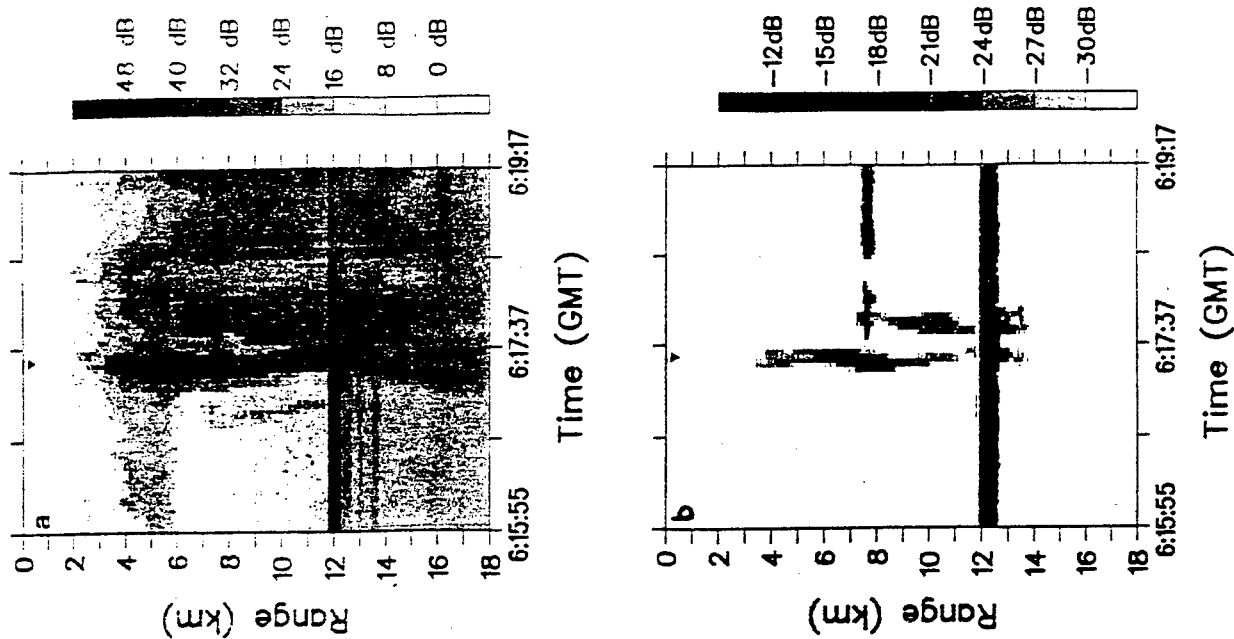


Fig 3 : Airborne radar measurements at 10 GHz of a typhoon event (a) dBZ and (b) Ldr. The sharp echo at 12.5 km (from aircraft) is due to sea-surface back scatter. Mirror image of rain is seen below.

'rain package' which includes a rain radar as the prime instrument to give vertical profiles of rain intensity. In most cases, the radar measurements are meant to complement the radiometer by distinguishing rain, ice and melting layer, and in the case of convective storms, by providing information on the storm height and intensity profiles. Although the mission objectives are oriented towards global climatology, the datasets which will become available in due course are directly relevant to interference predictions.

3.3.1 TRMM Radar

TRMM is a joint US-Japan space project, designed to measure precipitation in the tropical and sub-tropical climates [12]. The satellite is to be launched in August 1997, with a design lifetime of three years. Some relevant information is given in Table 1.

The radar will enable the 3-D rainfall distribution to be estimated, both over land and over sea. From an altitude of 350 km (with an orbit inclination of 35°), the antenna will be scanned over a swath width of 220 km, with a horizontal resolution at nadir of about 4 km. At nadir, a range resolution of 250 m will be used to obtain vertical storm structure. For off-nadir angles, a degraded range resolution will be used in order to reduce the dwell time while maintaining an adequate number of independent samples.

Table 1 : TRMM radar and orbit characteristics

Radar type	active phased-array (electronic scanning)
Frequency	13.796, 13.802 GHz (2-channel freq. agility)
Swath width	~ 220 km
Observable range	from surface to 15 km
Range resolution	250 m
Horizontal resolution	4.3 km (at nadir)
Sensitivity	S/N per pulse > 0 dB for 0.5 mm/hr at rain top
Number of independent samples	64
PRF	2773 Hz
Peak power	> 578 W
Dynamic range	~ 70 dB
Pulse width	1.67 μ s x 2 channels
Scan angle	\pm 17 deg
Beam width	0.71 deg x 0.71 deg
Orbit	35 deg inclination
Altitude	350 km (high res)
	Rapid precession

3.3.2 Radar data products

The main goal of TRMM is to estimate the path-averaged rainrates and the liquid water content, particularly near the surface. Others include (i) a quick-look display of the radar derived rain rates based on a standard Z-R relationship; (2) fractional area coverage of rain rates exceeding certain specified rainrate thresholds; (3) a library of surface cross section measurements over both land and ocean. The products derived from radar data are classified into several levels. These are summarised in Table 2.

Table 2 : Radar products classified by processing level

Level	Qualitative data	Quantitative data
Level 1 B		Measured Z profiles and surface echo
Level 2A	Rain / No rain Rain classifier stratiform convective and transition type Identify warm rain Global rain rate using Z-R (quick look)	Bright band height Effective height of storm Path averaged rain rate, LWC (IFOV basis) Profiled rain rate, LWC (IFOV basis) Library of surface back scatter cross-section (land, ocean)
Level 3		Averaged rain rates over various space-time domain Rainfall totals over various time domains

3.3.3 TRMM Validation Programme

Another relevant feature of the TRMM programme is that, as part of its validation campaign, several ground-truth experiments are to be conducted on a world-wide basis [13]. Several pre-mission studies are already under way. Through cooperative arrangements, routine collection of radar and rain gauge data have begun at : (i) Darwin, Australia; (ii) the Marshall Island Atoll of Kwajalein, (iii) the Cape Canaveral Center of Florida, (iv) Phuket in Thailand, (v) Israel, (vi) Taiwan and (vii) southern Brazil. In addition, potential sites for locating future ground truth facilities have been identified at eight other locations.

The purpose of the validation programme is not only to provide reliable ground truth estimates of rain intensities but also to conduct climatology research in tropical regimes. Studies will focus on two issues : (i) the mesoscale structure, referring to sizes, lifetimes and spatial structure of rain producing systems; and (ii) their microphysical properties, referring to raindrop formation processes and their drops size distribution.

It is fortuitous that the TRMM programme and its associated research will provide quantitative information on the same parameters as those required by the interference prediction method. The mission will provide a rare opportunity to get these data in regions where such information is very limited at present.

4. RAIN MICROSTRUCTURE

By microstructure, we often mean the statistical distribution of drop size, shape and orientations. This is a highly variable quantity, which as we saw earlier, is an important parameter for deriving bistatic reflectivity and specific attenuation.

Satellite radar measurements at a single frequency are not generally sufficient to determine rain drops size distribution (DSD). Certain retrieval methods apply a surface reference technique to infer the parameters governing the DSD [14,15]. The methods give fairly accurate predictions for stratiform rain with moderate rainrates. Convective events are more difficult to analyse because of the large uncertainties associated with their melting process.

4.1 Dual-polarisation methods

For ground based radars, with near-horizontal incidence, the DSD is best estimated by switching both transmitter and receiver polarisations. The additional parameter, namely the differential reflectivity (Z_{dr}), gives a direct estimate for the median value of the DSD [16]. This together with the co-polar reflectivity will characterise the DSD, given by the gamma function :

$$N(D) = N_0 D^m \exp \left[-\frac{3.67 + m}{D_0} D \right] \quad (\text{vii})$$

where $N(D)$ represents the number of particles with diameter D , N_0 is a scaling factor and ' m ' is the dispersion factor which is often fixed for simplicity

and when set to zero, gives rise to an exponential function. With the DSD estimated, it is straight forward to obtain the $Z - R$ and $k - R$ coefficients mentioned in Section 2.

Z_{dr} also provides information on the height of the melting layer. Compared with rain drops, dry ice particles exhibit a much reduced polarisation difference for a similar shape. Many forms of ice, such as needles, snowflakes and hail exhibit only a small Z_{dr} signature, until they begin to melt [17]. As melting begins, they show a pronounced signature resulting from the combined effect of significant asymmetry in shapes and the increases dielectric constant.

The Z_{dr} technique works for near horizontal incidence because rain drops, as they fall, take up (almost) an oblate spheroidal shape, due to the effects of gravity, air resistance and surface tension. When viewed vertically, (ie. nadir or zenith) the drops appear symmetrical. For this reason, the Z_{dr} method is not suitable for satellite radar. The L_{dr} technique offers more information, as we saw earlier, because it is particularly sensitive to the presence of wet ice and is a reliable indicator of the wet snow flakes responsible for the bright band.

4.2 Doppler Radars

Doppler radars operate on the principle that moving scatterers produce a frequency shift, the mean of which can be determined from the time variation of the phase of the pulse-to-pulse back scatter signal. These measurements are particularly useful for vertically pointing radar in that they provide estimates of the fall velocity spectrum which in turn can be used to determine DSD [18]. The spectrum however may be distorted by turbulence effects, but these can be filtered out by employing various correction procedures.

For radar elevations of around 30 deg, Russchenberg [19] has proposed a complete characterisation of the DSD using Z_H , Z_{dr} , L_{dr} , Doppler mean velocity ' v ' and its spectrum width ' W_d '. Turbulence effects are estimated by obtaining canting angle distribution from Z_{dr} and L_{dr} measurements. These effects are removed from the velocity measurements so that the resultant spectrum contains only the component due to the distribution of fall velocities. Then, using Z_H , Z_{dr} and W_d , the three parameters defining the gamma distribution are obtained.

For a thorough review of polarisation radar and Doppler radar, readers are referred to [20] and [21] respectively.

4.3 Differential Phase

The oblateness of raindrops causes another phenomenon, namely the differential propagation phase, Φ_{dp} , between horizontally and vertically polarised signals (see [22]). There are in fact two components to the differential phase of the return signal, viz. the propagation phase and the back scatter phase. At 3 GHz, the difference in the back scatter phase between the two orthogonal polarisations can be neglected (at least for rain), hence only the propagation phase contributes. Since this is a measure of the cumulative effect of propagation between the radar and the target volume, parameters such as averaged rainfall rate and integrated path attenuation caused by the intervening medium can be directly estimated. Differential phase measurements can also provide a useful means of identifying melting regions (see Figure 4). In vigorous convective storms, Φ_{dp} has the added advantage that it is sensitive only to the rain component (and not tumbling hailstones for example) whilst Z_H can be dominated by the contribution from hail. Finally, Φ_{dp} data provides an accurate calibration technique for weather radars [23], a critically important issue that concerns all radar meteorologists.

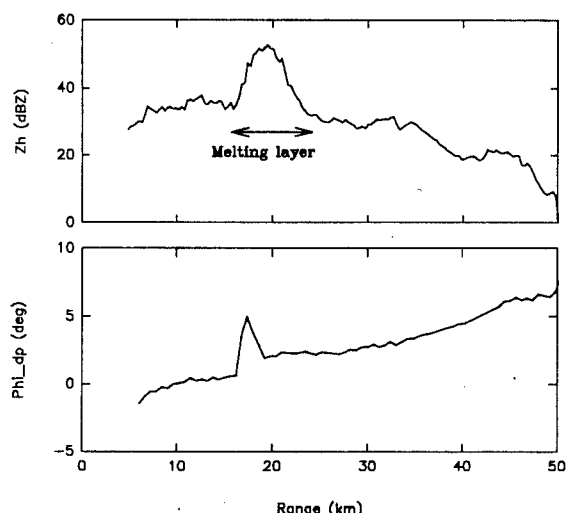


Figure 4 : Range variation of reflectivity (top) and differential phase (bottom) from Chilbolton radar, taken through a stratiform event at 5 deg elevation. (25 second dwell)

5. CONCLUSIONS

The prediction method for hydrometeor scatter interference requires, as its input, five parameters relating to the precipitation spatial structure. These extend to both horizontal and vertical dimensions. For the vertical case, the specific parameters required are (i) the mean height of the melting layer, (ii) its annual distribution and (iii) the mean reflectivity-height profile (below and above the melting layer). In the horizontal dimension, it is necessary to have (i) the width of the rain cell in terms of the peak rainrate and (ii) the exponential function which can statistically approximate the intensity decay with distance.

Apart from (perhaps) the melting layer height, it is clear that such information on precipitation spatial structure can only be obtained from meteorological radars. Such systems already exist in many countries, and as a result, the precipitation characteristics in these regions can be very well defined. For the rest of the climatic zones, the data are perhaps best obtained from satellite-borne radar, such as the system currently being built as part of the Tropical Rainfall Measuring Mission (TRMM), due to be launched in 1997. Although its objectives are oriented towards global climatology, the data sets of tropical and sub-tropical rainfall measurements which will become available in due course are directly relevant to interference predictions.

On a more microscopic level, the prediction method requires the characterisation of rain drop size distribution (DSD). These can only be obtained from advanced meteorological radars which have either polarisation diversity or Doppler capabilities (preferably both). For satellite systems such as the TRMM radar, DSD estimates can be made for stratiform rain if the retrieval algorithms employ surface reference constraint. For convective events, it is hoped that the second generation systems would have either cross-polar or Doppler measurements, both of which provide additional valuable information.

ACKNOWLEDGEMENTS

The author wishes to thank Dr Hiroshi Kumagai at Communications Research Laboratory, Tokyo for giving permission to publish their airborne data. Other measurements reported in this paper were obtained from the Chilbolton radar, funded by the UK Radiocommunications Agency of the DTI, under the National Radio Propagation Programme.

REFERENCES

- [1] COST 210 Final Report 1991: Influence of the atmosphere on interference between radio communication systems at frequencies above 1 GHz, EUR 13407 EN, Commission of the European Countires, Brussels
- [2] ITU-R Recommendation 452-5, 1992 : Prediction procedure for the evaluation of microwave interference between stations on the surface of the earth at frequencies above about 0.7 GHz, pp 301-303
- [3] Awaka J 1984 : A prediction method for the received power from rain scattering, Radio Science Vol 19, No 2, pp 643-651
- [4] Capsoni C, Fedi F and Paraboni A 1987 : A comprehensive meteorology oriented methodology for the prediction of wave propagation parameters in telecommunication applications beyond 10 GHz, Radio Science, Vol 22, pp 387-393
- [5] Crane R K 1974 : Bistatic scatter from rain, IEEE Trans. Ant. and Propag. AP-22, pp 462-465
- [6] Ishimaru A 1978 : Wave propagation and scattering in random media, Vol 1, Chapter 4, Academic Press, New York
- [7] Watson P A 1991 : Earth-space propagation path predictions from VHF to millimetre waves, in 'Radiowave Propagation' Peter Peregrinus Ltd, IEE Electromagnetic waves series 30, Edited by Hall M P M and Barclay L W
- [8] Allnutt J E 1989 : Satellite-to-ground radiowave propagation, Peter Peregrinus Ltd, IEE Electromagnetic waves series 29 (pp 156-164)
- [9] Kumagai H, Meneghini R and Koza T 1993 : Preliminary results from multiparameter airborne radar measurement in the Western Pacific, J. Applied Meteorology, Vol 32, No 2, pp 431-440.
- [10] Capsoni C et al 1987 : Data and theory for a new model of the horizontal structure of the rain cells for propagation applications, Radio Science, Vol 22, No 33, pp 395-404
- [11] Meneghini R and Koza T 1990 : Spaceborne weather radar, Artech House, Boston.
- [12] Simpson J, Adler R F and North G 1988 : A proposed Tropical Rainfall Measuring Mission satellite, Bull. Amer. Meteor. Soc, Vol 69, 278-295
- [13] Theon J S 1992 : The tropical rainfall measuring mission, in 'The global role of tropical rainfall', Deepak publishing, Virginia, USA edited by Theon J S et al, pp 216-219.
- [14] Koza T et al 1991 : Dual parameter radar rainfall measurement from space : a test result from an aircraft experiment, IEEE Trans. Geosci. and Remote Sens., GE-29, pp 690-703.
- [15] Thurai M, Kumagai H and Koza T 1993 : Improvements to a range profiling algorithm proposed for spaceborne rain-radar, Proc IGARSS'93, pp 838-840.
- [16] Seliga T A and Bringi V N 1976 : Potential use of radar differential reflectivity measurements at orthogonal polarisations for measuring precipitation, J. Appl. Meteor. Vol 15, pp 69-76
- [17] Hall M P M, Goddard J W F and Cherry S M 1984 : Identification of hydrometeors and other targets by dual-polarisation radar, Radio Science, Vol 19, pp 132-140
- [18] Hauser D and Amayenc P 1984 : Raindrop size distributions and vertical air motions as inferred from zenith-pointing Doppler radar with the RONSARD system, Radio Science Vol 19, No 1, pp 185-192 (Chapter 29 a).
- [19] Russchenberg H W J 1993 : Doppler polarimetric radar measurements of the gamma drop size distribution of rain, J. Applied Meteor. Vol 32, No 12, pp 1816-1825.
- [20] Bringi V N and Hendry A 1990 : Technology of polarisation diversity radars for meteorology, Chapter 19a in 'Radar in Meteorology' Edited by D. Atlas, Americal Meteorological Society, Boston.
- [21] Doviak R J and Zrníc D S 1992 : Doppler radar and weather observations, Academic press.
- [22] Sachidananda M and Zrníc D S 1986 : Differential propagation phase shift and rainfall estimation, Radio Science Vol 21, pp 235-247.
- [23] Goddard J W F, Tan J and Thurai M 1994 : A technique for the calibration of meteorological radars using differential phase, Electronics Letters, Vol 30, No 2, pp 166-167.

SOME ASPECTS OF Ku BAND RADIOMETER MEASUREMENT RESULTS AND THUNDERSTORM ACTIVITIES IN NIGERIA.

G.O. Ajayi and E.C.O Onime
Department of Electronic and Electrical Engineering,
Obafemi Awolowo University, Ile-Ife, Nigeria.

1. ABSTRACT

The joint Ku-band radiometric measurement of slant path attenuation due to rain at a frequency of 11.6 GHz was carried out at three locations in Africa for a period of two years. The site of the experiment in Nigeria was Obafemi Awolowo University, Ile-Ife. Thunderstorm activities in Nigeria have been studied from the monthly average number of thunderstorm days over thirty meteorological stations in Nigeria. Some results of the Ku-band radiometric measurement are discussed in terms of seasonal variations of rainfall rate and attenuation in relation to the thunderstorm activities.

Keywords: Radiometric Measurement, Slant path Attenuation, Thunderstorm Activities.

2. CCIR RADIO PROPAGATION MEASUREMENT CAMPAIGN IN AFRICA

There is generally a dearth of radio propagation data in the tropical regions especially Africa. Figure 1 shows a representative block diagram of the ex-CCIR (ITU-R) radio propagation measurement campaign in Africa. In 1979, the World Administrative Radio Conference WARC-79 adopted Resolutions and Recommendations calling upon "the CCIR to promote the study of radio wave propagation in developing countries, particularly those in tropical areas". As shown in Fig. 1 the WARC-79 declarations have been followed by other CCIR resolutions and recommendations including those adopted at WARC-92 calling for radio propagation measurements in Africa. The ITU and ex-CCIR initiated a radio wave propagation measurement campaign in Africa in 1984 as a follow-up of the ex-CCIR Propagation Seminar held

in Lome, Togo during the World Communication Year (1983). The measurement campaign was to cover two broad areas, viz: clear air effects and rain related measurements.

The joint Radiometer Rain Attenuation Measurement was initiated in 1986 in three Africa Countries - Cameroon (Douala), Kenya (Nairobi) and Nigeria (Ile-Ife). The participation of the parties is as follows:-

(i) ITU and ex-CCIR solicited for financial and technical support.

(ii) INTELSAT and COMSAT - supplied the equipment and provided the technical support before and during the measurement.

(iii) Nigerian Telecommunications Plc. (NITEL) provided local financial support.

(iv) Obafemi Awolowo University, Ile-Ife was the site of the experiment. The university provided site facilities and infrastructure for the project.

(v) Data analysis which was organised by and based at INTELSAT, with some collaborations from other parties.

3. THE RADIOMETRIC MEASUREMENT.

The equipment which arrived at Ile-Ife in April 1987 was installed, tested and calibrated. The measurement started on July 1, 1987 for a period of two years. The experiment took place at Ile-Ife, with site coordinates of 4.34°E, 7.33°N and altitude 274 m. The elevation angle was 48.3° at an azimuth of 257.25° clockwise with true North. In effect the antenna of the radiometer was pointing approximately in the direction of the INTELSAT AOR (Atlantic Ocean Region) satellite which is used in Nigeria

for International Communication by NITEL.

The hardware subsystem consisted of the 11.6 GHz radiometer receiver (Dicke Switch type), data collection system, uninterruptible power-line supply and a back-up system and spare parts. The data acquisition system consists of the IBM PC-AT compatible personal computer, signal conditioner unit and a 2 channel recorder for analogue recording of the sky noise temperature and the rain gauge tip count. The data recording during the experiment was controlled by the Data Acquisition System (DAS) software. The DAS recorded the sky noise temperature, the rain tips, the other temperatures e.g T_{box} , T_{amb} , T_{feed} etc and other data that will be useful in data analysis. Apart from recorded data, a log file was provided for observations made during the recording that could be useful during the data analysis.

A medium temperature, T_m of 285K and an antenna integration factor H of 0.9 were assumed in the analysis.

4. THUNDERSTORM ACTIVITIES

In our attempt to identify other climatological parameters responsible for the rain attenuation characteristics along the slant path, thunderstorm activities in Nigeria have been studied from the monthly average number of thunderstorm days over a period of thirty years from over thirty meteorological stations in Nigeria. In addition the variation of the monthly average total precipitation over a period of thirty years for the coastal (Coast to latitude 7°N) and the inland (latitude 10°N to latitude 13°N) areas over Nigeria has been considered in order to discuss the seasonal variation in the slant path attenuation.

5. RESULTS.

Table 1 shows the comparison of some factors related to the radiometer measurements at the three sites in Africa. The percentage observation times at the three locations were

high ($> 99\%$) except for Douala where the observation time for the radiometer was 84.15%. The observation time at Ile-Ife was 99.90% for rain and 99.79% for radiometer. Although the total rain accumulation is highest in Douala, the convective factor, which was lower than that for Ile-Ife, made the rain rate exceeded for 0.01% of the year comparable at Douala and Ile-Ife.

The results of the first year of measurement at a frequency of 11.6 GHz are available in McCarthy et al, 1992. The first year covered July 1987 to June 1988. The relevant data for the first year are available in the ITU-R data bank.

The cumulative distributions for rain rate, sky noise temperature and attenuation have been reported. However the seasonal variation of the rain rate, sky noise temperature and attenuation is considered mainly in this paper.

5.1 Seasonal variations.

The seasonal variations of rain rate, sky noise temperature and attenuation were investigated by dividing the whole year into four climatological seasons. November to January represents the Harmattan period (season 1) which is a dry season, February to April represents the transition from dry season to rainy season (season 2), May to July represents the rainy months with monsoon type of rainfall (season 3), whilst August to October is the end of the rainy season (season 4) characterized by intense convective rainfall. Figs. 2 and 3 show the seasonal variation in the cumulative distributions of rainfall rate and sky noise temperature respectively. Fig. 4 shows the seasonal variation in the cumulative distribution of the slant path attenuation as obtained from the measured sky noise temperature.

There was no rain in November 1987 and January 1988 and this made the cumulative distributions of rainfall rate, sky noise temperature and slant path attenuation for the dry season (season 1) to be remarkably different from those of the other seasons. The four months that contributed to

the worst month statistics are July, August 1987 and May, June 1988 (Ref. 1). Three of these months fall into the season (3) i.e the rainy season (May - July). It can be observed that the rainfall rate, the sky noise temperature and slant path attenuation for the percentages of time of interest for season (3) are highest in figures 2,3 and 4 for the May - July season.

The variations in the CD of rainfall rate, sky noise temperature and attenuation for seasons 2,3 and 4 show similar patterns with the lowest value for season 2 (February - April) for the percentage of time of interest.

5.2 Thunderstorm activities

Fig. 5 shows that for a station such as Ile-Ife, the thunderstorm activities are maximum in April, May. There is a minimum in August when the intertropical discontinuity ITD moves to the northern part of Nigeria. There is a large peak in the thunderstorm activities in October. The thunderstorm activities are high from March to June. Earlier results (Ref.2) showed that the highest rainfall rate occurred during season (3) i.e. August to October towards the end of the rainy season which includes October, the month with the highest thunderstorm activities. The rainfall pattern in the first year of measurement does not represent the average rainfall pattern in Ile-Ife. For example, the month of August, which is supposed to be a dry month within the rainy season had a lot of precipitation. However the rainy months had the highest rainfall rate, sky noise temperature and slant path attenuation. A clear correlation has not emerged between the thunderstorm activities and the slant path attenuation as well as rainfall rate. Fig. 5 shows a variation for total mean monthly precipitation, which has a peak in June and July, a minimum in August and another maximum in September.

6. CONCLUSION

The results of the first year data have shown that season 3 (May -

July) the rainy season with monsoon type of rainfall has the highest rainfall rate, slant path attenuation and sky noise temperature at equal probability level. The analysis has not yet revealed clear correlation between the rain rate, slant path attenuation and thunderstorm activities.

7. REFERENCES

1. McCarthy, D.K., J.E. Allnut, W.E. Salazer, E.C. Omeata, B.R. Owolabi, T. Oladiran, G.O. Ajayi, T.I. Raji, and C. Zaks: Results of 11.6 GHz Radiometric Experiment in Nigeria, *Electronics Letters*, 28, 3, 318-319, 1992.
2. Ajayi G.O., Statistical properties of tropical rainfall intensity measured in Nigeria. *Ann. Telecommun.*, 37, 447-483, (1982).

Country	Cameroun	Kenya	Nigeria
Location	Douala	Nairobi	Ile-Ife
Latitude	4° 03'N	1° 18'S	7° 33'N
Longitude	9° 42'E	36° 45'E	4° 34'E
Altitude(m)	15	1800	274
Elevation	47.0°	56.9°	48.3°
Azimuth	263.6°	83.8°	257.25°
Annual Total Precipitation (mm)	3213	1042.4	1703.6
Convective Factor	0.43	0.23	0.6
CCIR climatic region	Q	K	N & P
T _m (K)	285	285	285
Antenna Factor H	0.9	0.9	0.9
Rain observation time	99.08	99.76	99.90
Radiometer observation time	84.15	99.62	99.79

Table 1 - Comparison of some factors at the 3 radiometer sites in Africa.

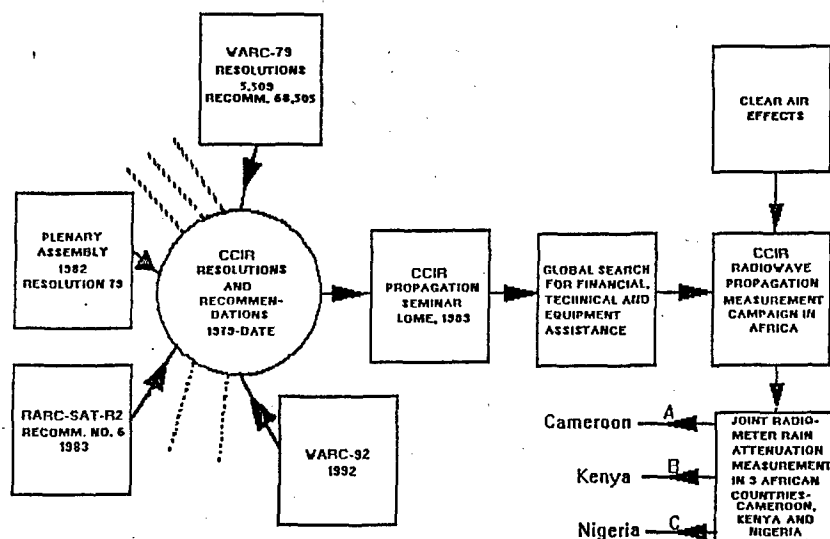


FIG. 1 CCIR RADIO PROPAGATION MEASUREMENT CAMPAIGN IN AFRICA

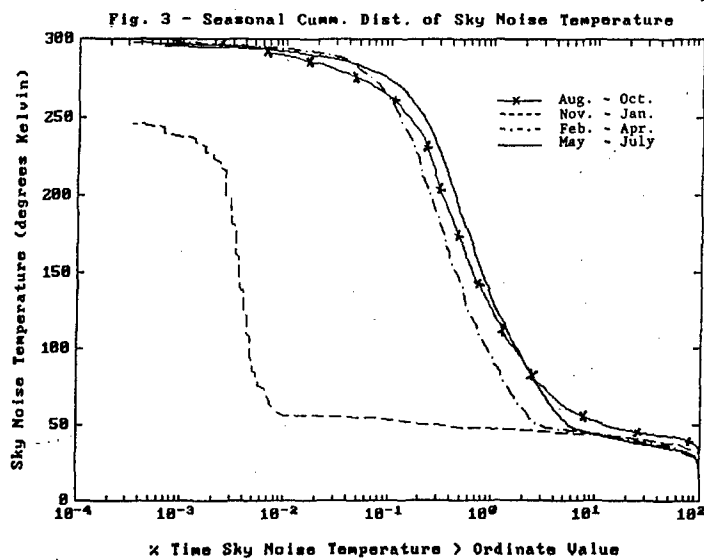
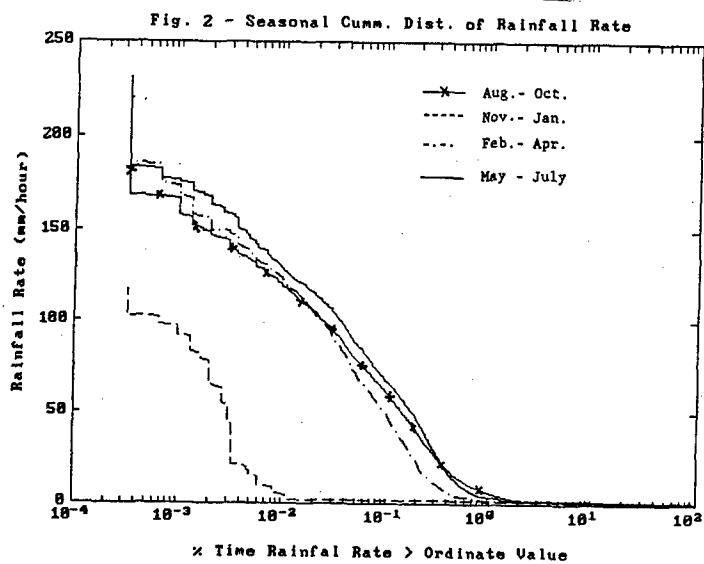


Fig. 4 - Seasonal Cum. Dist. of Attenuation

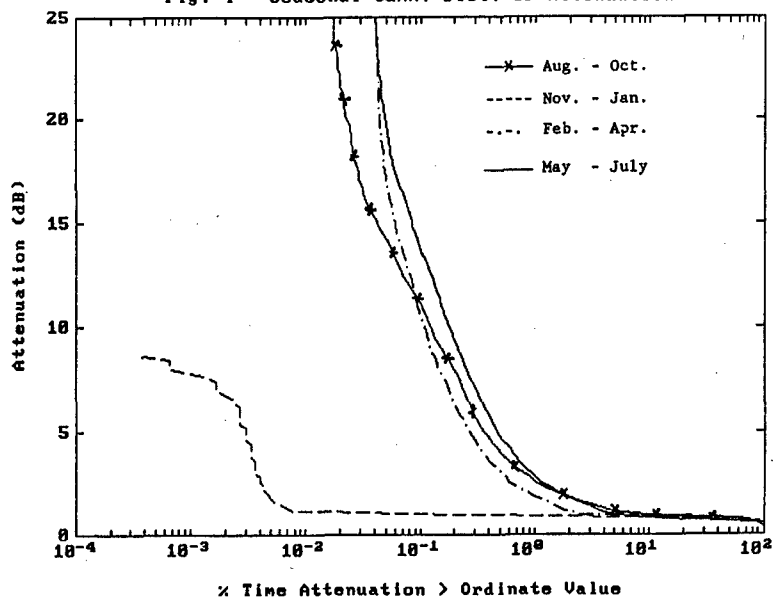
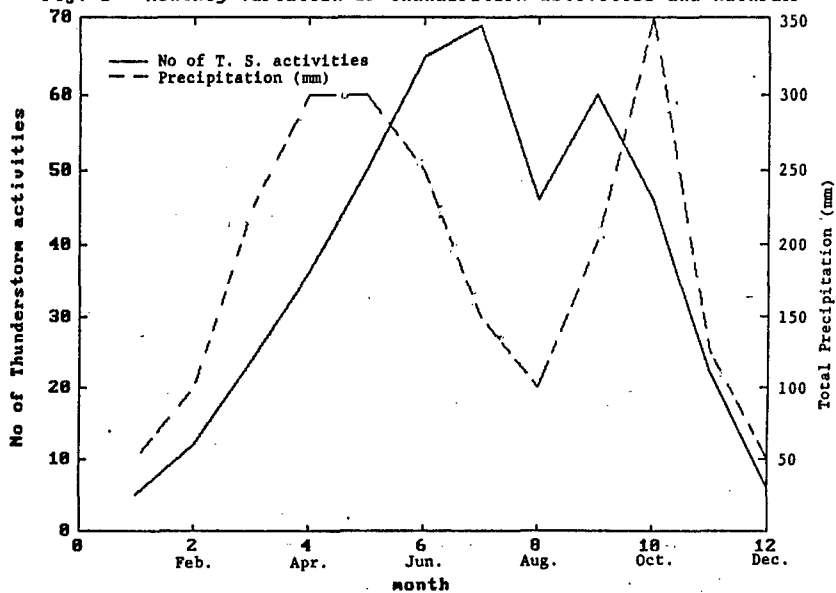


Fig. 5 - Monthly variation of Thunderstorm activities and Rainfall



ON THE ACCURACY OF RAINGAUGE MEASUREMENTS

Mauro S. Assis

Ministry of Communications - Rio de Janeiro Division
Rua Primeiro de Março 6 - 11 andar, 20010-000 Rio de Janeiro, Brazil
Tel: + 55-21-2248045, Fax: +55-21-2168685

ABSTRACT

This paper deals with the problem of raingauge measurement errors and their effect on radio system availability. The study is mostly based on experimental data from tropical locations. Instrumental as well as errors due to high winds are considered in this analysis.

Keywords: Raingauge. Rainfall rate. Wind speed. Tropical climates. Availability.

1. INTRODUCTION

The analysis of cumulative distributions of rainfall rate from several locations has evidenced the existence of a break point, around 80~100mm/h, where the curve for rainfall rate versus percentage of time changes its slope. Considering that the physical saturation of the rainfall process has a much higher limit, the break point may be attributed only to measurement errors. The origin of these errors, as well as their effects on the prediction of rain attenuation in the tropics are discussed in this paper. The variability of the yearly rainfall rate statistics is also considered.

2. RAINFALL RATE STATISTICS

Figure 1 shows some examples of yearly distributions of rainfall rate measured in low latitude areas (Ref. 1). In this figure, as commented in the previous section, the existence of a break point is evident. This point does not occur in precipitation data from temperate climates, since the maximum observed rainfall rate is, in most cases around or below 80mm/h (0.001% of time in average year). The break point is probably due to one or both of the following sources of error: a) Raingauge inaccuracy for measuring high rainfall rates; b) Effect of high winds usually associated to strong convective storms.

On the other hand, the annual cumulative distribution of precipitation rate in the tropics may

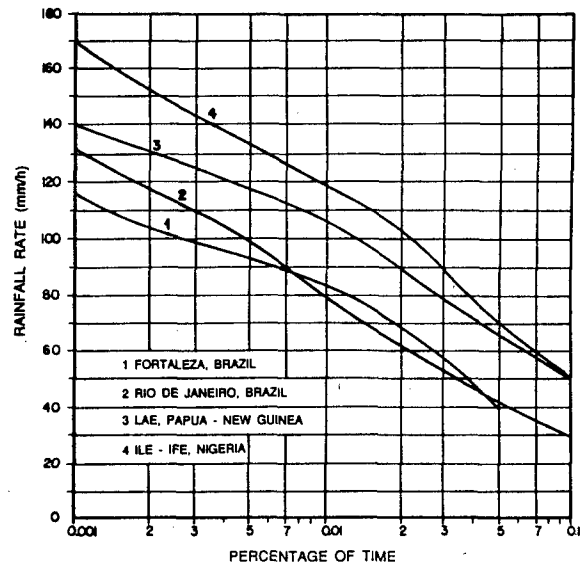


Figure 1: Rainfall rate in the tropics

exhibit a great variability, particularly in the range from 0.01 to 0.001% of time. As an example of this variability, measurements corresponding to a period of 4 years in Rio de Janeiro, Brazil (22 55 S ; 43 30 W) are shown in figure 2 (Ref. 2). These measurements were carried out with a 5-minute integration time raingauge.

3. INSTRUMENTAL ERRORS

At present, most rainfall intensity measurements use tipping bucket raingauges. The error introduced by this type of gauge is due to the time required for tipping. As this time is constant regardless of the precipitation rate, there is a loss of rain while the bucket is tipping. For instance, if the gauge tips when 1 mm of rain is accumulated in the bucket and the time for tipping is 0.2s, in the case of a precipitation rate equal to 180mm/h, there will be a loss of 6s for each minute of rain. The corresponding error will be 10%. A careful calibration of the gauge in a laboratory, through the simulation of different rainfall rates, may reduce this type of error.

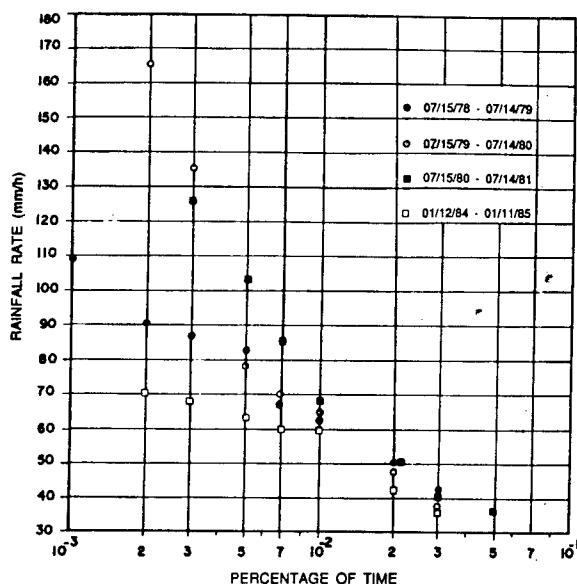


Figure 2 : Yearly variability of rainfall rate

The difficulty of measuring high rainfall rates is also true for drop-counter gauges. In this case, the maximum rate to be measured is limited by the value where the flow becomes a continuous jet. In general, the maximum measurable rate is around 150~200mm/h. It should be pointed out that there is a compromise between this limit and the minimum advisable catching area of the gauge.

4. EFFECT OF WIND ON RAINFALL RATE MEASUREMENTS

Certainly the wind is the main source of error in measuring rainfall rate and the most difficult to be controlled. In a gusty wind the precipitation is blown over and around the gauge and the corresponding collector area coefficient may decrease substantially. This coefficient is given by the ratio between the quantity of water collected by the pluviograph in given period of time and the quantity of water available, without the pluviograph, in an area equal to the aperture of the gauge collector at the same period of time.

The problem of rainfall measuring error due to wind effect was first pointed out by Jevons in 1861 (Ref. 3). Since then, several experimental studies were carried out, both open air and wind tunnel measurements being used. Based on the available results, to minimize this effect, the World

Meteorological Organization (WMO) recommends locating the collector aperture of the gauge nearly one meter above the ground.

However, the relation between wind speed and the collector area coefficient is not well established. According to author's knowledge, in the radiocommunication area, only two papers dealing with this question were published in the past. The problem was first raised by Misme (Ref. 4) and some experimental data were presented by Damosso et alli. (Ref. 5). In the present paper, in using data from figure 1 of Misme's paper, the following approximated solution is proposed,

$$\rho = 1.85v^{-0.3} \quad (1)$$

where ρ is the collector area coefficient and v is the wind speed in km/h.

5. EFFECT OF RAIN ON RADIO SYSTEM AVAILABILITY

As a consequence of the increasing demand for communication, the use of frequencies above 10GHz is growing fastly. At these frequencies, particularly in the tropics, rain is usually the most important source of signal degradation. Systems designers must have adequate technical information at their disposal to evaluate the effect of rain on radio path availability. In this context, rainfall rate measuring errors, as well as the yearly variability of precipitation rate statistics are serious constraints to development of an accurate rain attenuation prediction model.

A better understanding of the break point appears to be a fundamental matter to define the philosophy to be adopted in the derivation of the prediction model. Below this point, i.e. for percentages higher than 0.01% in low latitude climates, there is a reasonable correlation between the precipitation rate and the rain attenuation. Then, in the range from 0.1 to 0.01% a model which evaluates rain attenuation in point-to-point basis seems to be an acceptable option. Above this point, considering the additional problem associated to the yearly variability of rainfall rate (see figure 2), another alternative should be adopted. For instance, a model based on the best fit to the experimental data. However, in this case a higher standard deviation is expected.

As a support to the above comments, figure 3 shows the rain attenuation measured during the same period as of figure 2, in an urban terrestrial link, 8.6 km long, operating at 11GHz and located

in Rio de Janeiro (Ref. 2). It must be noted that the yearly variations of rain attenuation of rain attenuation are lesser than the corresponding variations of precipitation rate in all observed range (0.1 to 0.001%). In the range $0.1 \geq p \geq 0.01\%$ the correlation coefficient between rainfall rate and rain attenuation is 0.75. In the range $0.01 > p \geq 0.001\%$ this coefficient decreases to 0.67.

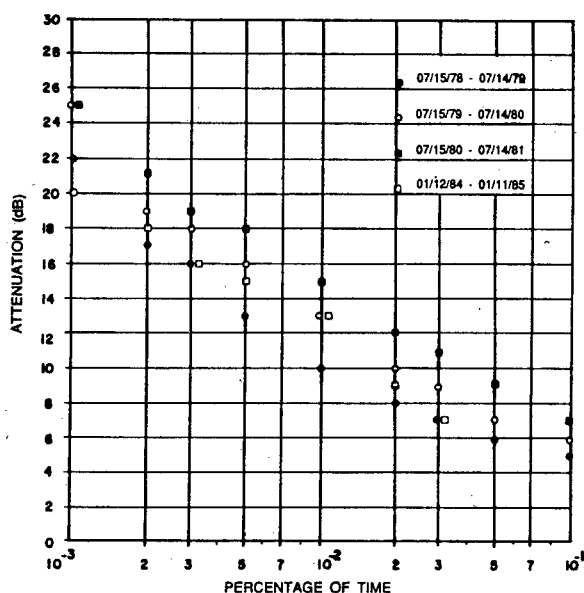


Figure 3: Yearly variability of rain attenuation

6. CONCLUDING REMARKS

The accuracy of raingauges when measuring rainfall rates in the tropics⁹ has been discussed, instrumental error and wind effect being considered in the analysis. The former source of error can be minimized through a careful calibration of the gauge. The later, however, is a quite complicated issue. An approximate relation between wind speed and the raingauge collector area coefficient was proposed. Nevertheless, taking into account the lack of experimental data, complementary studies including simultaneous measurements with raingauges and anemometers at different heights are needed. Regarding radio system availability, the range from 99.9 to 99.99% was pointed out as the one where accurate rain attenuation prediction models may be derived.

7. REFERENCES

1. ITU-R , Acquisition, presentation and analysis of data in studies of tropospheric propagation, *Recommendation 311-7*, Geneva 1994
2. IWP 5/2, Rain attenuation and rain rate measurements in Brazil, *Doc. 89/54*, Tokyo 1989
3. Jevons, W. S. 1861, On the deficiency of rain in an elevated rain gauge caused by wind, *Philosophical Magazine*, 22, pp. 421-443
4. Misme, P. 1978. Affaiblissement dus à la pluie. Résultats expérimentaux, calculs et prévisions, *Ann. Télécommunic.* 33, 9-10, pp. 341-362
5. Damosso et alli. 1981, Influence of the integration time and the height of rain-gauge on rainfall rate statistics, *CSELT Rapport Tecnici*, VIII, 4, pp. 299-302

RAIN RATE AND ITS TEMPORAL VARIABILITY MEASURED AT DARMSTADT FOR A PERIOD OF EIGHT YEARS

Gerd Ortgies

Forschungs- und Technologiezentrum der Deutschen Bundespost Telekom, D-64276 Darmstadt, Germany
Tel: +49-6151-833848, Fax: +49-6151-834031, E-mail: fz233a@vmxa.fz.telekom.de

ABSTRACT

This contribution reports on statistical results of rain rate measurements carried out at Darmstadt for a period of eight years. Besides a statistical analysis of the year-to-year variability, statistics for the worst-month and the seasonal and diurnal variability of rain intensity is presented.

Keywords: Rain Rate, Risk Analysis, Worst-Month, Temporal Variability, Rain Attenuation

1. INTRODUCTION

Rain attenuation is the most severe meteorological parameter which may cause transmission degradation in satellite communications. Its importance increases with increasing frequency, following roughly an $f^{1.8}$ -law. Therefore, rain intensity, respectively its statistics, is an essential quantity to describe the climatic conditions for planning telecommunication links via satellite.

Rain rate measurements have been carried out at Darmstadt since many years using a combination of a drop counter (low rain rates) and a tipping bucket (high rain rates). The integration time is one minute. In the present paper, statistical results of rain rate measurements carried out for a period of eight consecutive years will be discussed. The variability of annual cumulative statistics, the worst-month behaviour, as well as the diurnal and seasonal variation of the measured rain rates are of particular interest. Results will be compared with recent models.

2. YEAR-TO-YEAR VARIABILITY

Cumulative statistics of measured rain rates are presented in Fig. 1 for a period of eight consecutive

years. In the ITU-R map (Ref. 1), Darmstadt is located at the border between rain zones E and H. Therefore, cumulative statistics for these rain climatic zones are depicted for comparison. It can be clearly recognised, that zone E parameters underestimate the measured long-term averages for exceedance probabilities below about 0.1%, whereas zone H parameters fit the experimental data quite well.

Fig. 2 represents the variability of annual cumulative statistics. It can be seen, that for probability levels above about 0.1%, the rain rate statistics do not vary significantly from year to year, whereas the spread in the distributions increases with decreasing exceedance probabilities, e.g. for 0.01% of the year, the recorded data vary between 24 and 47 mm/h and even between 57 and 100 mm/h for an exceedance level of 0.001% of the time.

A few years ago, Crane (Ref. 2) published results on the variability of annual rain rate and attenuation statistics. From an analysis of data in the ITU-R data banks, he showed, that, caused by temporal variations within the same climatic zone, rain intensities exceeded at fixed time percentages could be described by a log-normal distribution. This distribution can be characterised by its standard deviation, $\sigma_{\ln(R/\bar{R})}$, where R is the annual rain intensity exceeded for a given time percentage and \bar{R} is the long-term mean intensity for the same time fraction of excess. For a probability level of 0.01%, he estimated a value of 0.21 for $\sigma_{\ln(R/\bar{R})}$. Our results based on an eight-years period can be read from Fig. 3. The value for 0.01% of the time agrees well with the value estimated by Crane. For lower probability levels, $\sigma_{\ln(R/\bar{R})}$ was found to be nearly constant, slightly below a value of about 0.2. For larger probabilities, $\sigma_{\ln(R/\bar{R})}$ decreases to a value of about 0.1, which reflects the lower variability at lower rain rates. With $\sigma_{\ln(R/\bar{R})}$ known, and assuming a log-normal distribution for the year-to-year variability,

the risk of exceeding a rain rate threshold for a given annual exceedance probability can be estimated.

A similar analysis was carried out by Trommer et al. (Ref. 3), but the values found there were by a factor of about two higher. The results in Ref. 3 are based on data measured at six different stations along a 19 km line of sight path in the Berlin area (rain zone H) over a period of 10 years. Since the orography changes from site to site (hilly region with many lakes), it is assumed that the higher standard deviation reflects besides the annual variability also the spatial variability.

3. WORST-MONTH

In the planning of satellite telecommunications systems, the concept of the "worst-month" plays an important role, particularly, if a system has to meet agreed performance criteria in any month of the year. The worst-month in this context is related to a given threshold which is exceeded with the highest monthly probability in the course of 12 consecutive calendar months or 30-days periods, i.e. the cumulative distribution for the worst-month is the envelope of 12 monthly cumulative distributions.

Fig. 4 shows the cumulative distribution of the worst-month of the eight-years period, i.e. the average of the annual worst-month statistics for the eight years. For comparison, also the cumulative statistic for the average year is depicted for the same period. It can be seen, that it is much more stringent to meet a quality criterion, e.g. that a specified attenuation threshold must not be exceeded for a given time percentage, for any month which is considered the worst-month than for the average year.

In system planning, it is convenient to relate worst-month statistics to that of the average year by means of a conversion factor Q , which is the ratio of exceedances for which the same threshold is exceeded during the worst-month and the average year. This conversion factor is depicted in Fig. 5 as a function of the exceedance probability, p . Following ITU-R Rec. 841 (Ref. 4), Q can be expressed over a large range of exceedance probabilities by a power law, i.e.

$$Q = Q_1 p^{-\beta} \quad (1)$$

which was confirmed by several experiments (e.g. Refs. 5, 6). It can be seen from Fig. 5, that this relation holds also for our experimental data, but only up to exceedance levels of about 0.5%. Above this value, Q is nearly constant. This upper limit is significantly lower than the respective value given by ITU-R Rec. 841, where a value of 3% is recommended as an upper limit for the validity range for the power-law relation. For global planning purposes, ITU-R gives values of 2.85 and 0.13 for Q_1 and β , respectively. From our experiments, we found for the probability range between 0.002 and 0.5% values of 1.84 for Q_1 and 0.22 for β . Extending the range to 2%, the corresponding values are 2.1 and 0.19, respectively. A comparison with the respective parameters compiled in ITU-R Rec. 841 for different geographical regions shows, that our data based on an eight-years period fall into the range of reported values for Q_1 and β , but differ by about 25 to 30% from the values recommended for global planning purposes.

4. DIURNAL AND SEASONAL VARIATION

Besides its year-to-year variability, the diurnal and seasonal variations of rain were investigated as well. To analyse whether rain exhibits a diurnal pattern, statistics for four six-hour intervals per day were derived. Such statistics are based in the following on calendar months, on 12-months periods and on the whole eight-years period, respectively.

The analysis of single months showed significantly higher rain rates during the time interval 12.00 to 18.00 hours for exceedance levels below 0.1% in more than 40% of the evaluated months, whereas for the remaining months, the highest rain rates occurred equally distributed over the other three six-hours periods.

The investigation of annual periods stresses this trend. In each of the eight years, the highest rain rates occurred in the interval 12.00 to 18.00 hours. Their respective cumulative distributions were significantly higher than the corresponding average cumulative distribution. It is quite obvious, that for these reasons, in six out of eight years, the distributions for all of the other three periods 00.00 to 06.00, 06.00 to 12.00 hours and 18.00 to 24.00 hours were found to be lower than the average distribution. Only in two years, the distribution representing the interval 06.00 to 12.00 hours is similar to the average distribution.

The respective results for the eight-years period is presented in Fig. 7. Similarly to the annual results, the highest rain intensities were found in the afternoon, whereas the lowest rain rates occurred in the first six hours after midnight. The distributions for the intervals 06.00 to 12.00 hours and 18.00 to 24.00 hours fell into the range between the average and the early morning distributions.

The seasonal rain intensity variation is presented in Fig. 7 for the period from January 1986 to December 1993. Rain intensities are given for thresholds exceeded in 1% and 0.01% of the respective month. Strong seasonal variations can be recognised for the 0.01% exceedance probability, whereas the distribution for the 1% level is nearly uniform. As a rule of thumb it can be stated that for 0.01% of the time, rain rates are about a factor of five to six, in extreme cases up to by ten times, higher than in winter. The minima occurring in winter do not vary significantly from year to year and are of the order of 10 mm/h for an exceedance level of 0.01%. Maxima were found during the summer months, as expected, in our climate, since thunderstorms associated with high rain intensities occur mainly during this season.

It has been stated earlier, that cumulative rain intensity statistics may vary significantly from year to year. This behaviour can also be read from Fig. 7. Values of rain intensities exceeded in 0.01% of the respective month were found in the range from slightly more than 40 to about 100 mm/h during the eight-years period. Since the annual total amount of precipitation is fairly constant, as a consequence, the monthly distribution of rain intensities is much broader in a year exhibiting lower maximum rain rates than for a year with very high peak intensities.

6. CONCLUSION

Rain intensities measured for a period of eight consecutive years were analysed with respect to their year-to-year variability, their worst-month behaviour, and their diurnal and seasonal variations. Significant annual variations were found with a standard deviation, $\sigma_{\ln(R/\bar{R})}$, of about 0.2 for exceedance levels below 0.01% of the annual distribution, which decrease to a value of about 0.1 for higher probability levels. The conversion factor between long-term average and worst-month statistics was found to decrease with increasing probability levels following a power-law relation. The diurnal variation exhibits a pronounced preference of high

rain intensities to occur in the afternoon. The seasonal distribution showed high peaks in the summer months and minima during winter being by a factor of about five to six lower.

7. REFERENCES

1. ITU-R Rec. 837 1992, Characteristics of precipitation for propagation modelling.
2. Crane, R K 1990, Rain attenuation measurements, *Radio Science* 25, 4, pp. 455-473
3. Trommer, H et al. 1992, A comparison of results obtained from concurrent measurements with colocated rain gauges of different types, *Pre-Prints of URSI Commission F Open Colloquium on Wave Propagation and Remote Sensing*, Ravenscar, pp. 1.1.1-1.1.4
4. ITU-R Rec. 841 1992, Conversion of annual statistics to worst-month statistics.
5. Dintelmann, F 1984, Worst-month statistics, *Electronics Letters*, 20, 21, pp. 890-892
6. Dintelmann, F et al. 1991, Year-to-year variability and worst-month statistics of long-term rain rate measurements in Germany, *Electronics Letters*, 27, 8, pp. 617-618

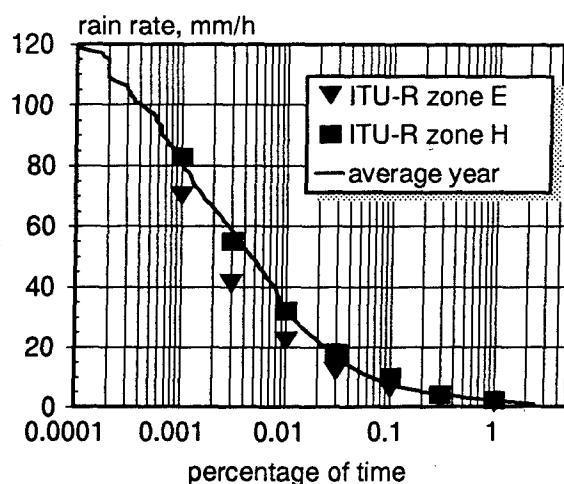


Figure 1: Cumulative distribution of long-term rain intensities(1986-1993) together with respective statistics for ITU-R rain climatic zones E and H.

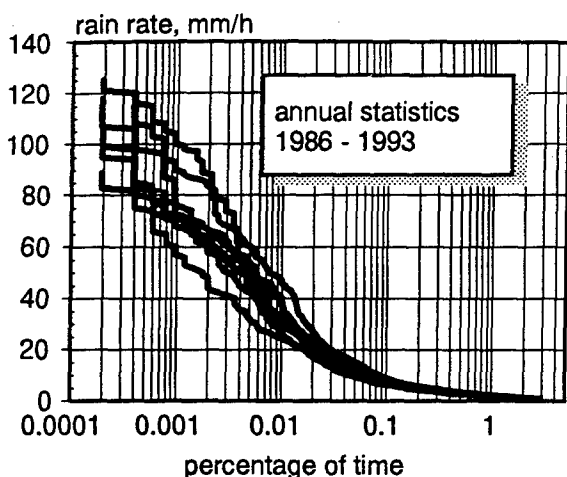


Figure 2: Year-to-year variability of annual cumulative statistics of measured rain intensities for the years 1986 to 1993.

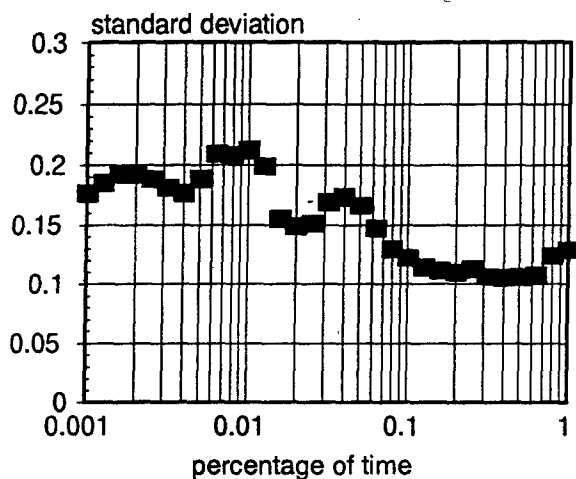


Figure 3: Standard deviation $\sigma_{\ln(R/\bar{R})}$ of eight annual cumulative rain intensity distributions.

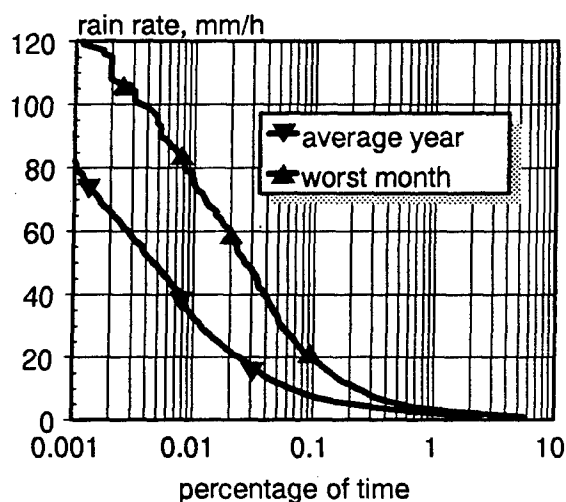


Figure 4: Comparison of cumulative rain intensity statistics for the long-term average year and statistics for the long-term worst-month (1986 to 1993).

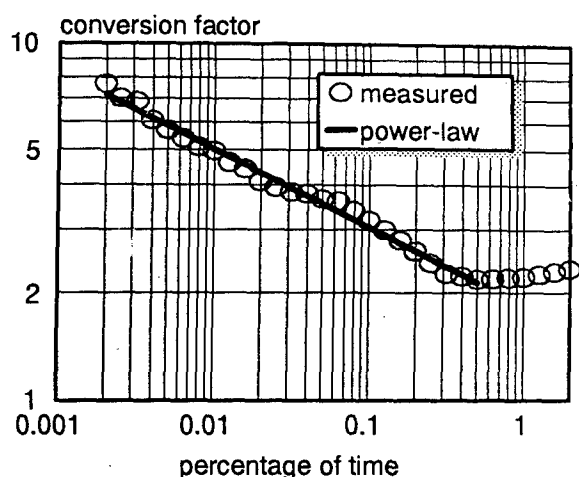


Figure 5: Conversion factor between average annual cumulative rain intensity statistics and the corresponding worst-month statistics.

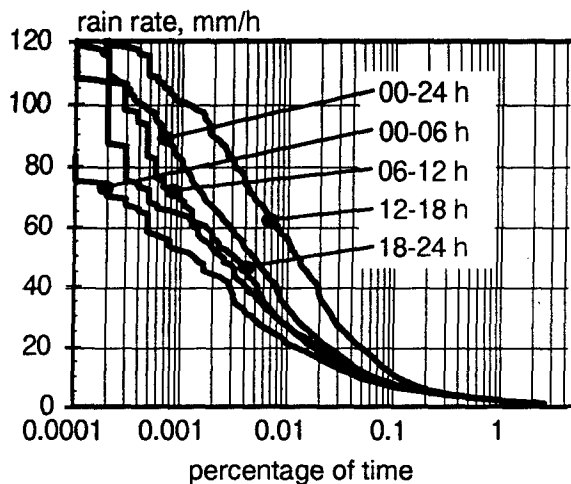


Figure 6: Diurnal variations of cumulative rain intensity statistics for a period of 8 consecutive years.

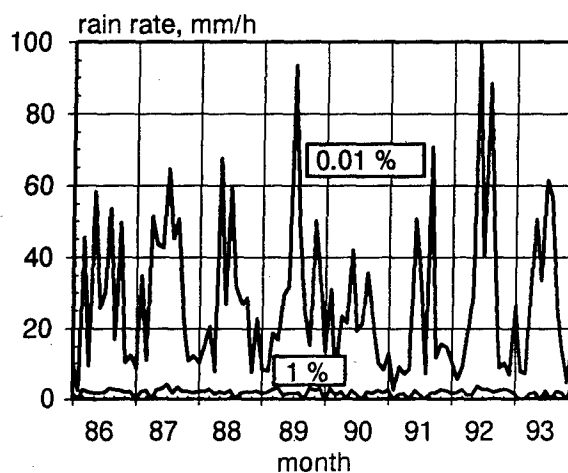


Figure 7: Seasonal variation of rain intensities exceeded for 1% and 0.01% of the respective month over period of eight years.

THE PRECIPITATION RETRIEVAL FROM HIGH-FREQUENCY SODAR MEASUREMENTS

Shixuan Pang¹ and Hartmut Graßl^{1,2}

¹Max-Planck-Institut für Meteorologie, Bundesstraße 55, D-20146 Hamburg, Germany

²Meteorologisches Institut, Universität Hamburg, Bundesstraße 55, D-20146 Hamburg, Germany

ABSTRACT

A clear separation of the rainfall Doppler and the turbulence spectra can be obtained by a high frequency sodar, which additionally provides a possibility to remove the effects of mean vertical wind on rainfall parameters. However, the imperfect precipitation response function I_p has to be introduced into this correction. Based on 6.4kHz sodar data most of rain drop size distributions $N(D)$ retrieved were nearly exponential, but the overlap between rainfall and turbulence spectra influences considerably the retrieval accuracy for drops smaller than about 0.5 mm.

One main characteristic of a high frequency sodar, strong acoustic attenuation, can - under certain assumptions - be turned into a new algorithm for attenuation coefficient α and thus temperature profile retrieval in the surface layer. Increasing frequency will essentially improve the $N(D)$ and α retrieval accuracies.

The high frequency sodar-disdrometer may both provide ground truth for rain gauges or correspondent satellite experiments and become a useful tool for investigating micrometeorological process in the surface layer.

Keywords: High frequency sodar-disdrometer, Imperfect precipitation response function

1. INTRODUCTION

Over more than tens years precipitation remote sensing techniques have been developed. However, they often can not demonstrate that they measure rainfall correctly, unless mean vertical wind effects can be accounted for (see e.g. Refs. 1, 2). Lee (1988) (Ref. 3) concluded that for radar precipitation measurement by either absorption or backscatter techniques the high potential accuracy fails due to the bias through vertical air velocity, which may cause a factor of 2 error in rain estimation. The simultaneously measurement of the turbulence spectrum to derive mean vertical wind velocity \bar{w} is essential for high accuracy. C. Richter (1993) (Ref.4), University of Hamburg, combined Doppler radar measurements of droplet spectra and rainfall with a RASS (Radio Acoustic Sounding System) to get the vertical wind correction. This study will show that the high frequency sodar is a promising technique to reach this goal in the only one system.

Since the backscattering from raindrops is proportional to λ^{-4} (here λ is the acoustic wave length), and turbulence only to $\lambda^{-1/3}$, increasing frequency enables a simultaneously measurement of both rainfall Doppler and turbulence spectra. However, the question still remains: how to remove the mean vertical velocity effect? The assumption of a perfect precipitation response to turbulent air motion is not correct. We, therefore, introduce an *imperfect response function* I_p into the drop size distribution $N(D)$ retrieval algorithm accounting for the effects of turbulent motion on the falling speed of drops.

At high sodar frequency the strong acoustic attenuation may be utilized for a new algorithm to derive the attenuation coefficient and thus also temperature profile retrieval in the surface layer. An advantage is its freedom from absolute sodar calibration.

In order to evaluate the capability of a high frequency sodar for $N(D)$, rain rate R and other meteorological parameters, a 6.4kHz sodar was operated at Hungrifer Wolf, Northern Germany, from 4th to 6th of Jan. 1993. By comparison with a 3.3kHz emitter used by the same sodar setting, the 6.4 kHz data show a far higher signal with a separate 15 to 20 dB peak for rain. However, the overlap between rainfall Doppler and turbulence spectra is still large at $D_{min} \approx 1mm$, which will significantly influence the retrieval accuracy for small drops and light rain. The best way to reduce the overlap is increasing sounding frequency, for instance, to 20 kHz, which would shift D_{min} to about 0.5mm.

2. RAINFALL PARAMETER RETRIEVAL

The retrieval method of rain drop size distribution $N(D)$ based on sodar Doppler spectra (Ref. 5) is similar to that of radar.

From the sodar equation the backscattered power spectrum $P_r(f)$ as a function of Doppler frequency f is related to the combination spectrum $S'(f)$ associated with backscattering from both precipitation particles and turbulence by

$$P_r(w) = P_t L e^{-\int_0^r 2\alpha(r) dr} A_v S'(w)/r^2 \quad (1)$$

where P_t is the effective power transmitted into the solid angle subtending the scattering volume V of length L , $\alpha(r)$ is the acoustic attenuation coefficient depending on the local temperature and

humidity, A_v is the effective area of the receiver antenna, and r is the distance from transmitter to scattering volume, $P_r(f)$ and the Doppler spectrum $S'(f)$ may also be expressed by $P_r(w)$ and $S'(w)$ as a function of vertical Doppler velocity w .

If in presence of a perfect response we assume that all size precipitation particles instantly follow the turbulence air motion, $S'(w)$ can be expressed as the convolution of a rainfall Doppler spectrum $S(w)$ and a turbulence spectrum $S_t(w)$ shifted by mean vertical wind velocity \bar{w} . As a first approximation we consider the turbulence spectrum to be a δ -function and a simple summation of two spectra is assumed,

$$S'(w) = p_1 S(w \pm \bar{w}) + p_2 S_t(w \pm \bar{w}) \quad (2)$$

where p_1 and p_2 are the echo power intensities from precipitation particles and turbulence, respectively, and counting an downward velocity positive. For Rayleigh scattering the rainfall Doppler spectrum $S(w)$ is related to D by

$$S(w) = A \cdot N(D) \frac{25\pi^5}{36\lambda^4} D^6 \frac{dD}{dw} \quad (3)$$

where A is a frequency dependent calibration factor. With a widely used empirical expression of drop terminal velocity related to D , $w = 9.65 - 10.30e^{-6D}$, where w is in ms^{-1} , and D in cm , $N(D)$ can be retrieved from measured Doppler spectra $S'(w)$, thus rainfall integral parameters as well.

First an average of Doppler power spectrum over at least 40 single spectra, i.e. over 1 min average, was calculated to reduce the variance. Secondly, for additional smoothing we use a least-square 3rd degree polynomial 5-point fitting. Then we utilize the optimal (Wiener) filter method to remove the system filter response effect as well as the noise "tail". Finally, we calculate $N(D)$ with vertical wind correction also considering the imperfect precipitation response, and from $N(D)$ we calculated the integral rain parameters. The $N(D)$ retrieved were almost exponential and show an agreement with M-P distribution or Gamma distributions. Figure 1 yields a rainfall Doppler and turbulence spectra. The correspondent distributions $N(D)$ retrieved at different heights are shown in figure 2. It is clearly seen that without removing the \bar{w} effect and particularly also with no attenuation coefficient α correction (in fact, the α used in retrieval was smaller than the real one) these $N(D)$ distributions show a rather large scatter.

3. ACCOUNT OF IMPERFECT PRECIPITATION RESPONSE FUNCTION AND MEAN VERTICAL WIND VELOCITY

Although the mean vertical wind velocity \bar{w} is decreasing as height reduces, for 1 min averages

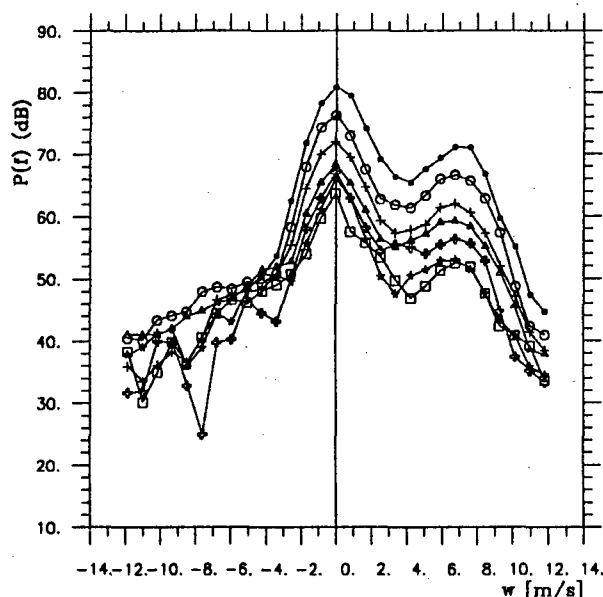


Figure 1 Sodar Doppler relative power spectrum. The middle part is the turbulence spectrum while the rainfall Doppler-spectrum is on the right side (positive velocity). The abscissa is in velocities w corresponding to Doppler frequency with $w = cf/(2f_a)$ (here f_a , c are the acoustic frequency and velocity, respectively), downward motion is positive. The spectra are 10 min averages from 002202 to 003202(UTC) on 6th Jan. 1993, at an average rainrate of 3.1mm/h.

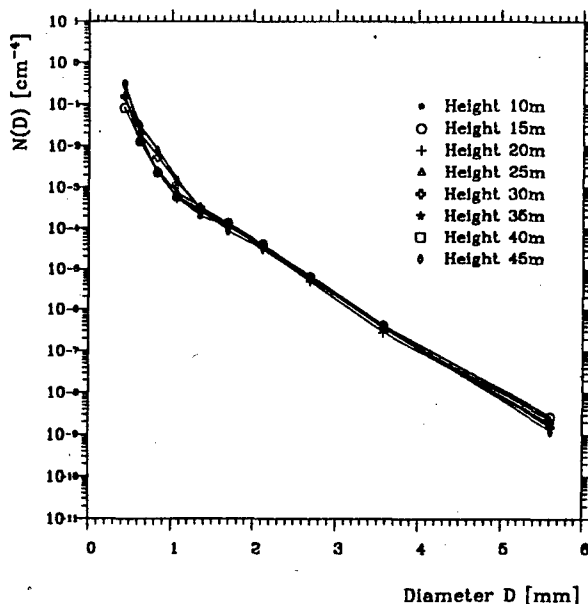


Figure 2 Raindrop size distribution $N(D)$ derived from rainfall Doppler spectra in Fig.1 but without α and \bar{w} corrections. The overestimation at small diameters is due to the overlap with turbulence spectra.

$\bar{w} > 0.5 \text{ m/s}$ was still often observed at heights of 15m to 30m even at night. And $\bar{w} = 0.1 \text{ m/s}$ will cause about a 5% to 12% error in rainrate R . Based on 6.4kHz sodar data and a perfect response the retrieved distributions $N(D)$ in different heights with a correction for \bar{w} were close to each other for small drops but showed a large scatter for big drops. The imperfect response thus should be introduced to remove this error. Since the ratio of rain water density to air density $\rho_d/\rho_a \gg 1$, and using the steady state drag formulas to describe the hydrodynamic resistance experienced by the drops, considering only one vertical dimension, the equation of motion for a spherical drop with mass m_d and instantaneous velocity V_d is (Ref. 6)

$$m_d \frac{dV_d}{dt} = m_d g \left(1 - \frac{\rho_a}{\rho_d}\right) - F_D \quad (4)$$

with the drag force $F_D = 3\pi D\eta \left(\frac{C_D N_{Re}}{24}\right) (V_d - V_a)$, where V_a is the undisturbed air velocity in the vicinity of the particle, kinematic viscosity η and gravitational acceleration g , $N_{Re} = D\rho_a(V_d - V_a)/\eta$ is the Reynold number of the drop. For a steady state the solution of Eq.4 results in an approximate Imperfect response function I_p

$$I_p = \Delta V_d / \bar{w} \approx 1 / (1 + K_z^2 V_T^4 g^{-2})^{1/2} \quad (5)$$

where $\Delta V_d = V_d - V_T$ is the drop speed increment caused by turbulent motion, V_T is the particle terminal fall speed, K_z is related to turbulence vertical apparent scale λ_a , $K_z = 2\pi/\lambda_a$. Figure 3 yields the characteristics of the imperfect response function I_p versus D related to different heights with an empirical relationship in the surface layer, $\lambda_a \approx 0.35r_i$. It is clear that as the particle size increases the response I_p is reduced. In the rain parameter retrieval algorithm $I_p \bar{w}$ (i.e. ΔV_d) should be used rather than \bar{w} . The comparisons between $N(D)$ retrieved without wind correction, with \bar{w} , and with $I_p \bar{w}$ correction the latter gave $N(D)$ in different heights of 15m to 30m coinciding most.

4. RETRIEVAL ALGORITHM FOR ACOUSTIC COEFFICIENT AND TEMPERATURE PROFILE

The main obstacle for high frequency sodar to be practical is the significant attenuation in air and also its variation depending on local temperature and/or humidity change. However, the strong attenuation may be utilized to derive the acoustic attenuation coefficient α_i and thus the temperature profile T_i if a height independent rain rate may be assumed.

From $N(D)$ the rainrate R_i can be easily determined by $R_i = \frac{\pi}{6} \int N_i(D) D^3 w(D) dD$. If we introduce a mean attenuation coefficient $\alpha_{im} = (\int_0^{r_i} \alpha(r) dr) / r_i$, we find that the retrieved R_i is

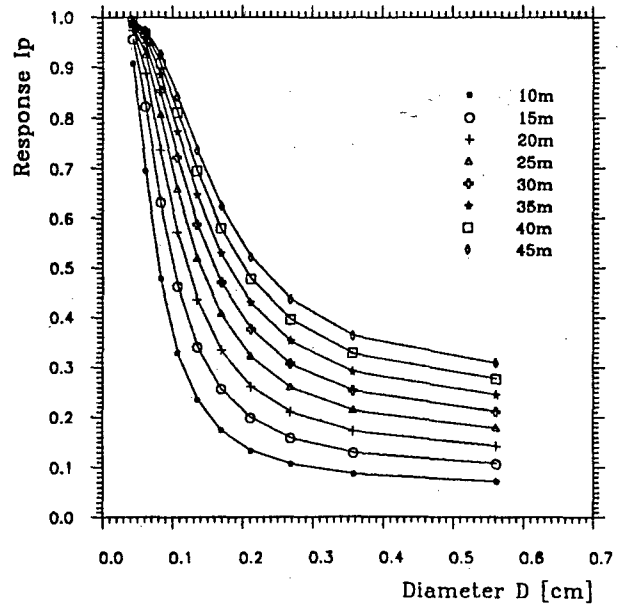


Figure 3 Imperfect precipitation response function $I_p(D, \lambda_a)$ as a function of drop diameter D in cm. Using the empirical relationship, $\lambda_a \approx 0.35r_i$, the 8 curves correspond to different heights from 10m to 45m.

proportional to $e^{-2(\alpha_{im} - \alpha_0)r_i}$, here the α_{im} are unknown mean values of the attenuation coefficient and α_0 is the attenuation coefficient used in retrieval which depends on the surface measurements of temperature and humidity. With the assumption of a constant rain intensity with height, which could hold for averages over at least one minute in the surface layer below about 50m, particularly for stratiform rain, a practical retrieval algorithm is using the logarithm of the ratio R_i/R_1 , $Y_i = \ln \frac{R_i}{R_1}$. We get

$$Y_i = 2(\alpha_0 - \alpha_{im})r_i - 2(\alpha_0 - \alpha_{1m})r_1 \quad (6)$$

where R_1 is the rain rate in the lowest range gate. Utilizing the ratio $\frac{R_i}{R_1}$ as a criterion we delete the possible influence of an imperfect sodar calibration. As only the ratio of "relative" rainrates is required for the retrieval, it may also avoid the complication caused by measurements of factors such as antenna characteristics, system frequency response and other height independent fluctuation factors. Moreover, a small different temperature T_i from T_1 causes a large percentage change of $\ln \frac{R_i}{R_1}$, therefore, rises the retrieval accuracy.

After calculating the curve $Y_i = \ln \frac{R_i}{R_1}$ versus r_i , the retrieval allows to determine Y_0 for $r_0 = 0$ by extrapolation. From Eq.6 then α_{im} can be calculated. Further, with the assumption of a linear temperature distribution in a range gate the attenuation coefficient α_i at height r_i can also be

derived by

$$\alpha_i = \frac{2(i+1)}{2i+1} \alpha_{im} - \frac{2i}{2i+1} \alpha_{(i-1)m} + \frac{2i-1}{2i+1} \alpha_{i-1} \quad (7)$$

Finally, we can utilize the strong dependence of α on temperature to derive temperature profiles. In a temperature region of few degree we may assume that α_i changes linearly with temperature by a constant gradient β , $\alpha_i = \alpha_{i-1} + \beta \Delta T$, where ΔT is the temperature increment over a range gate. Then, the temperature T_i at height r_i may be expressed as $T_i = T_{i-1} - \frac{\alpha_i - \alpha_{i-1}}{\beta}$. Normally, the laboratory values β measured by Harris (1966) (Ref. 7) are likely to be too small due to excess attenuation. Therefore, the coefficient β , should be carefully calibrated through the direct measurement of a vertical temperature distribution. In figure 4 temperature profiles retrieved during one night with rain are shown.

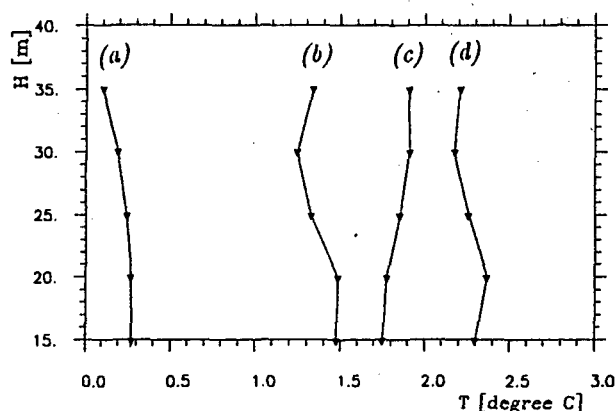


Figure 4 The temperature profiles retrieved from rainfall Doppler spectra averaged over 30 min, starting time from 185302(UTC) for (a), 233502 for (b), 005502 for (c) on 4th of Jan 1993, and 025502 for (d) on 5th of Jan 1993.

5. DISCUSSION AND SUMMARY

- (1). A 6.4 kHz sodar clearly allows the separation of raindrop and turbulence spectra for rainrates above 1 mm/h with a spectral minimum corresponding to $D_{min} \approx 1mm$.
- (2). Introduction of an imperfect precipitation response function into the retrieval algorithm improves the retrieval accuracy. The imperfect response depends on both turbulence scale and precipitation particle size.

(3). With the new retrieval algorithm developed in this study the real acoustic attenuation coefficient and thus the temperature profile in surface layer may be derived.

Our first attempt to derive the temperature profile in the surface layer clearly shows the feasibility for a 6.4kHz sodar. A larger scattering volume would give more reliable results.

(4). A Doppler sodar at higher acoustic frequencies ($> 15kHz$) should be able to give surface rainrate, drop size distribution, mean vertical wind velocity and temperature profile in the Prandtl layer. The first attempt with a 6.4kHz sodar was so promising, that we plan to construct a new high frequency sodar disdrometer.

Acknowledgement

We gratefully acknowledge the help of METEK GmbH, Hamburg, in providing the 6.4kHz sodar. Our thanks also go to Dr.H.Jeske and Dr.G.Peters, University of Hamburg, for helpful discussions.

References

1. Atlas, D., R.C. Srivastava and R.S. Sekon 1973, Doppler radar characteristics of precipitation at vertical incidence, *Rev. Geophys. Space Phys.*, 11, pp.1-35
2. Ulbrich, C.W. 1992, Algorithm for determination of rainfall integral parameters using reflectivity factor and mean Doppler fall speed at vertical incidence, *J. Atmos. Oceanic Technol.*, 9, pp.120-128
3. Lee, A.C.L. 1988, The influence of vertical air velocity on the remote microwave measurement of rain, *J. Atmos. Oceanic Technol.*, 5, pp.727-735
4. Richter, C., 1993, A combined Doppler radar/RASS system as rain gauge, *26th International Conference on Radar Meteorology*, 24-28th May 93, Norman, Oklahoma
5. Little, C.G. 1972, On the detectability of fog, cloud, rain and snow by acoustic echosounding methods, *J. Atmos. Sci.*, 29, pp.748-755
6. Wang, P.K. and H.R. Pruppacher 1977, Acceleration to terminal velocity of cloud and raindrops, *J. Appl. Meteor.*, 16, pp.275-280
7. Harris, C.M. 1966, Absorption of sound in air versus humidity and temperature, *J. Acoust. Soc. Am.*, 40, pp.148-159

Session 3: Precipitation II

MODEL FOR TROPICAL RAIN

L. Watai, Q.W. Pan and G.H. Bryant

Department of Electrical and Communications Engineering
The Papua New Guinea University of Technology
Lae, Papua New Guinea

ABSTRACT

Analysis of the annual rainrate and attenuation exceedences measured at the University of Technology in Lae. for the years of 1991/92 and 1992/93, has led to the proposal of a new model for tropical rainfall.

INTRODUCTION

An experiment has been running at the University of Technology in Lae, Papua New Guinea, since 1991 to measure rainrate and slant path attenuation at 12GHz from a satellite at 73 degrees elevation. The annual rainrate and attenuation exceedences for the years of 1991/92 and 1992/93, are shown in figure 1. Figure 2 has a tipping bucket rain gauge sited at the receive antenna and a slant path length determined by the rain patterns. Three distributions can be identified according to the range of rainrates.

A MODEL FOR RAINFALL IN A HIGH ELEVATION PROPAGATION PATH

Figure 3(a) shows all possible raincell positions that cause rain collection in the bucket. The rain falling on the raingauge must be within the circle of radius D centred on it. The set of circles within this radius indicates cells that just touch the raingauge at their circumferences and for which it rains at the cell and simultaneously introduces attenuation into the beam. Figure 3(b) shows all possible raincell positions that interact only with the slant path and therefore give attenuation even though no rain is recorded at the raingauge. There is an effective increase in the attenuation time for those cells on the raingauge. This can be accounted for by increasing the slant path by μ . Hansson(1) has defined a ratio as the accumulation time factor (ACCF) as

$$ACCF = \frac{L + \mu}{D} = L/D + x \quad (1)$$

x is the point to line factor; and remains constant at 0.636 when $D/L \geq 1$, whilst when $L/D = 1$ the ACCF = 1.636.

RAIN AND ATTENUATION STATISTICS

Hansson(1) has shown the relation between the rainfall and attenuation exceedences depends upon the rain height and cell diameter. Moupfouma(2) has noted the presence of a breakpoint in the rain exceedences at the 0.01 percentage level. A similar breakpoint in the attenuation exceedences, first noted by Bryant(3) has been used by Pan and Bryant (4) to estimate raincell diameter and height at 105mm/hr, the measured breakpoint at Lae.

These breaks in the slope are clearly visible in figure 1. In order to find a correspondence between the rainfall rate and the attenuation exceedences we may adjust the length of each scale to make points coincident at the low rainfall rates, where we may expect an ACCF of 1 given the widespread nature of the rain. The two curves are shown in figure 5 for the year 1992/93.

TIME SPECTRAL DENSITY DISTRIBUTION OF RAINRATE

Exceedences have been calculated from the experimental data at rainrate intervals of 5mm/hr. to give the time spectral density, $H(R)$ or percentage of time per mm/hr. From the regression a best fit curve can be derived for $H(R)$, and this is shown in figure 6. It is possible now to recalculate the rainrate exceedences $E(R)$ from the integral of $H(R)$. Calculated and measured rainrate exceedences are shown in figure 7.

MEAN RAINCELL DIAMETER

For those raincells that are cut by the slant path along a diameter, the diameter can be found from the measured attenuation, $A(R)$, and the specific attenuation, $S(R)$, at that rainrate as

$$D(R) = A(R)/S(R) \quad (3)$$

In practice, raincells are equally likely to cross the slant path on any chord, including the diameter. For any chord, other than the diameter, and for a given attenuation, the rainrate will be higher in

those cells interacting along a chord. We can calculate a mean cell diameter at the raingauge from the corresponding pairs of measured attenuation and rainrates in figure 5. The probability of occurrence of a given rainrate is proportional to its time spectral density, given in figure 6, to give a mean cell diameter of

$$\overline{D(R)} = 2 \cos(EL) \frac{\sum_R \{ [A(R)/S(R)] H(R) \}}{\sum_R H(R)}$$

Where EL is the elevation angle and the summations are from the rainrate R to the highest measured rainrate exceedence. The mean diameter can be inserted into equation 1 for the ACCF.

TIME SPECTRAL DENSITY DISTRIBUTION OF ATTENUATION

The time spectral density for attenuation can be calculated in a similar way to that for rainrate by subtracting adjacent exceedences at intervals of 1dB. The time spectral density distribution, H(A), is shown in figure 8. A regression calculation, similar to that used for rainrate spectral density, gives a corrected attenuation exceedences curve, E(A), as shown in figure 9.

ACCF, CELL DIAMETER AND HEIGHT

The ratio of E(A) to E(R) gives the ACCF and

the $L/D(R)$ can be calculated from equation 3. At $L/D = 1$ ACCF is 1.63622. This occurs in the data at 70mm/hr. Above that the quantity x remains constant at 0.63622 and L/D can be found from equation 1. Figure 10 is a plot of calculated E(A), E(R) and ACCF. The figure shows that the ACCF is 1 at a rainfall rate close to 40mm/hr.

BREAKPOINT AND RAIN HEIGHT

We have seen that up to 70mm/hr only one raincell may exist within the beam. At some point it may be possible for two cells to be present within the beam. When a single cell breaks into two the effective diameter at the rain gauge is halved compared to that in the beam, assuming all the raincells have the same diameter. The breakpoint may be interpreted as the onset of these multiple cells. The two cells may cut the beam at any chord with equal probability, but they are independent random events and therefore we may expect a smaller change of slope at the breakpoint in E(A) than occurs in E(R). We can progressively reduce the mean cell diameter at a given rainrate in the ratio of the ACCF at that

rainrate to the ACCF at the breakpoint. Such a calculation shows that below the breakpoint at 105mm/hr only 1 cell exists, whereas there are 6 at 195mm/hr. When the ACCF adjusted mean diameters are multiplied with L/D the final projected path length, L, and the height, H, can then be found. These results are plotted in figure 11.

CONCLUSION

We may use figure 11 to distinguish the three rain conditions. In the low rainfall range, from 5 to about 40mm/hr, rain is widespread. At about 70mm/hr the raincell diameter has increased to 2.5km from 2km at 5mm/hr. At this point the diameter equals the projected slant path length. Higher rainfall is achieved by convection to increased height with smaller diameters. Above the breakpoint, higher rate can only be obtained by further reducing the diameters as there is insufficient water in the sky above the 12 to 15km level(8). It is unlikely that well formed columns exist, rather, there is a vertical striation of a widespread lower rainfall rate that concentrates the highest intensities into smaller and smaller cross sections. Supporting evidence of striated or ragged formation in a background of lower rainrate is available from radar measurements of tropical rainfall made from a satellite reported as part of the Tropical Rainfall Mission(7).

REFERENCES

- 1 Hansson, L., "New concept used to predict slant path rain attenuation statistics", Proc. IEE, Pt. H, Vol. 137, No. 2, pp. 89-93, April 1990.
- 2 Moupfouma, F., "More about rainfall rates and their prediction for radio systems engineering", Proc. IEE, Pt. H, Vol. 134, No. 6, pp. 524-537, Dec. 1987.
- 3 Bryant, G.H., "The structure of tropical rain from attenuation and rain exceedences", Proceedings of ISAP, Sapporo, Japan, 1992, pp. 877-880.
- 4 Pan, Q.W. and Bryant, G.H., "Results of 12GHz Propagation Measurements in Lae (PNG)", Electronics Letters, Vol. 28, No. 21, pp. 2022-2024, October 1992.

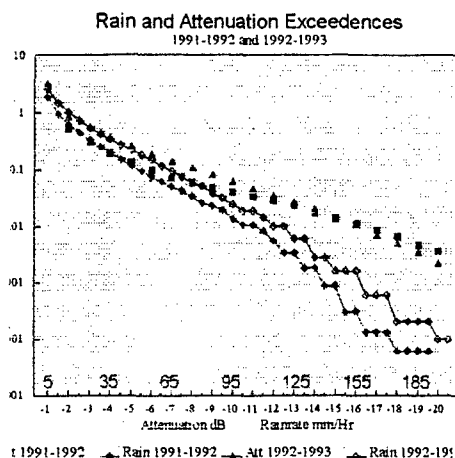
5 Allnutt, J.E., "Satellite-to-ground radiowave propagation", Peter Peregrinus Ltd. on behalf of the IEE., 1989, p.156.

6 Recommendations and Reports of the CCIR, Volume 5: Report 563-1 ITU/CCIR Geneva, 1978.

7 Report of the Science Steering Group for a Tropical Rainfall Measuring Mission (TRMM). Editor Joanne Simpson, Goddard Space Flight Center, Greenbelt, Maryland 20771, National Aeronautics and Space Administration, August 1988.

8 Li, H.J., and Zhang, Z.W., "The statistics of original altitudes of rain and their effects on microwave propagation", Third International Conference on Antennas and Propagation, 12-15 April 1983 pp. 2-65, 2-68.

work reported here forms part of the ongoing research activities of INTELSAT and The Papua New Guinea University of Technology. Any views expressed are not necessarily those of either organisation.



ACKNOWLEDGEMENTS

The authors would like to acknowledge the support of Dr. J.E. Allnutt, of INTELSAT. The

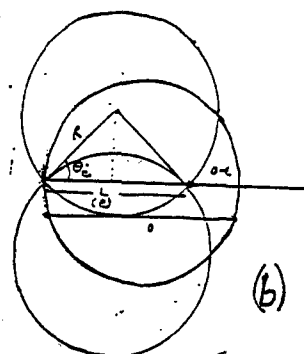
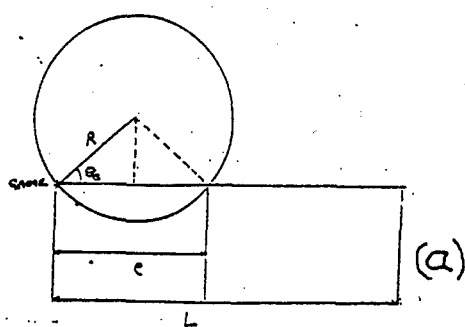
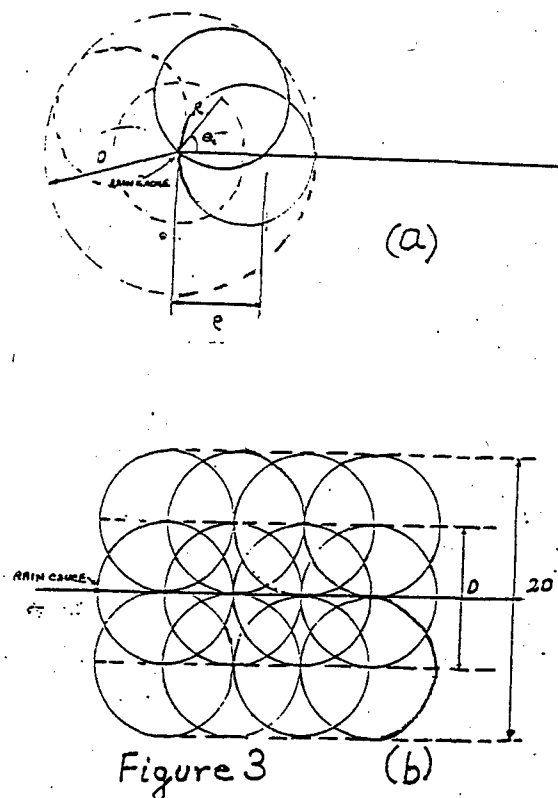
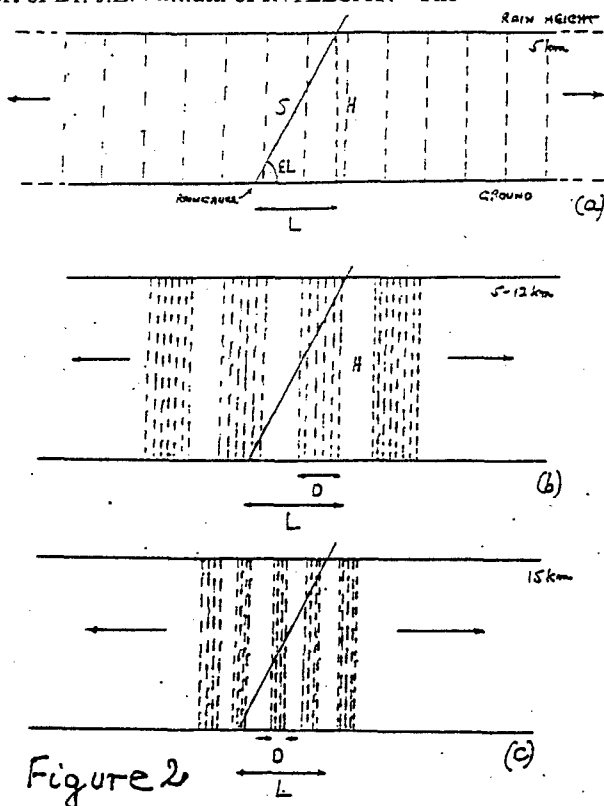
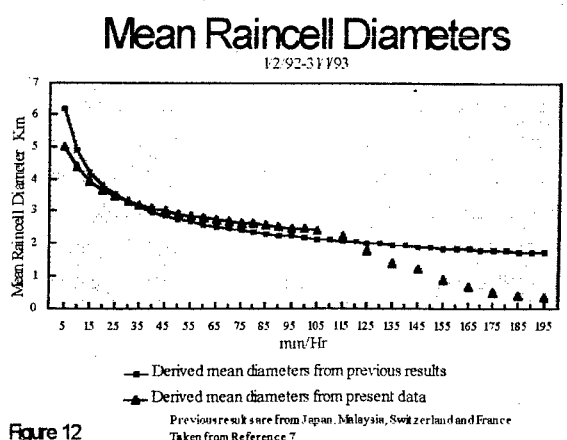
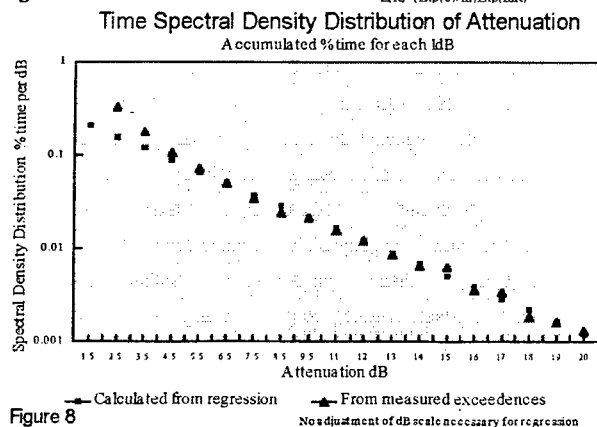
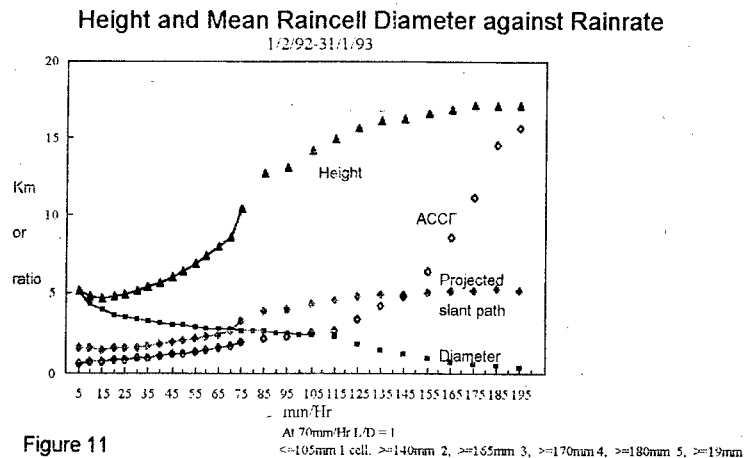
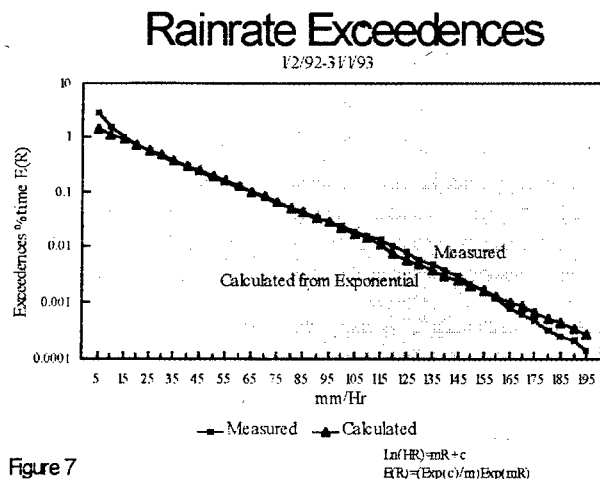
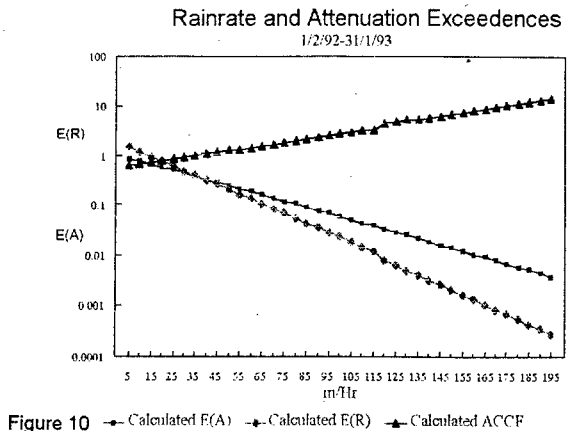
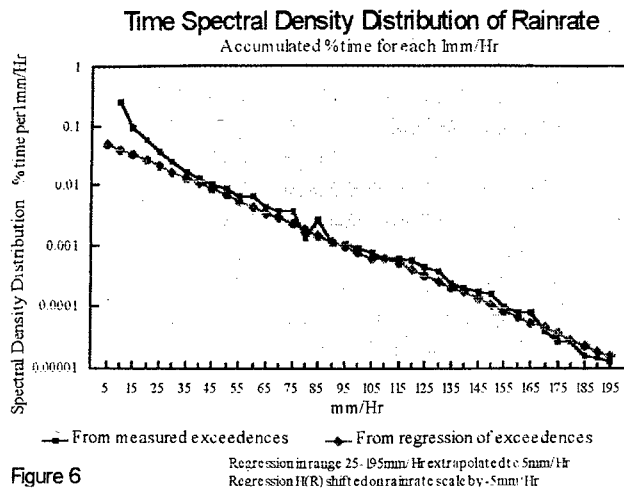
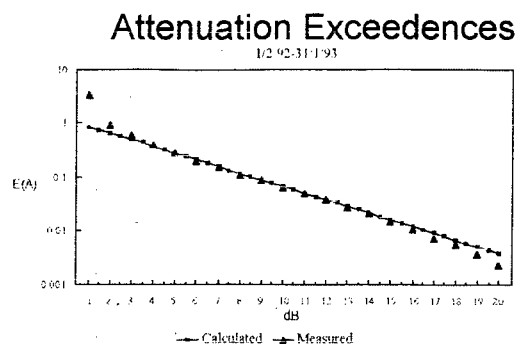
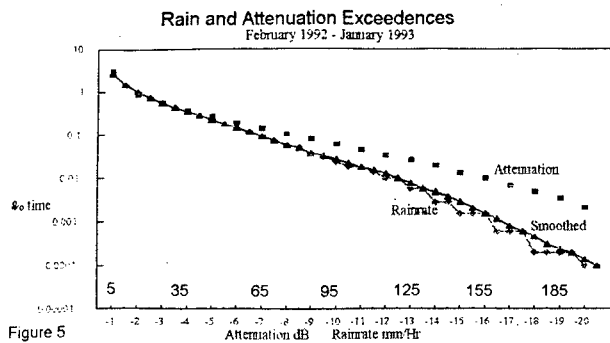


Figure 4



A PREDICTION METHOD FOR THE JOINT CUMULATIVE DISTRIBUTION OF RADIOWAVE RAIN ATTENUATION ON SPACE DIVERSED PATHS

Ye.V. Sukhonin

Institute of Radioengineering and Electronics of RAS,
Marx avenue 18, Moscow, Russia
Tel: +7-095-5269262, Fax: +7-095-2038414

ABSTRACT

The known rain model of P.Misne is generalized to develop the prediction method of the joint long-term radiowave rain attenuation cumulative distributions for space diversified paths. The results of radiometrical measurements of rain zenithal attenuation statistics at $\lambda=8.2$ mm are shown to be in good agreement with the prediction results.

Keywords: Rain, Models, Microwaves, Forecasting, Attenuation.

1. INTRODUCTION

More than 30 rain models describing its spatial and temporal structure have been developed for prediction of microwave attenuation statistics on terrestrial and slant paths. A lot of the models and the methods are empirical because they use the rain effective path lengths obtained from the rain attenuation measurements at different frequencies. Only one model (Ref.1) has a simple physical meaning. Moreover, according to (Ref.2) the model (Ref.1) allows to predict the long-term rain attenuation statistics with higher accuracy than the other models.

The model (Ref.1) was modified that allowed to explain the dependence of rain attenuati-

on distributions on direction of radiowave propagation path or path diversity (Ref.3). The models (Refs.1,3) are used usually for prediction of the rain attenuation statistics on single paths. However a generalized rain model can be developed by using these models for prediction of the joint rain attenuation statistics on space diversified paths (Ref.4) when the additional data on space autocorrelation function of rainfall rate are not required.

This work is devoted to development of such generalized physical rain model and its application for prediction of attenuation statistics on the zenithal paths.

2. DESCRIPTION OF THE RAIN MODELS

In (Ref.1) the rain zone is modeled as the two circular coaxial cylinders of different diameters with height H depending on rainfall rate R . The inner cylinder diameter d_c (km) restricting the rain cell (shower part) with R_c (mm/h) is described by the equation

$$d_c = 2.2(R_c/100)^{-0.4} \quad (1)$$

The outer cylinder diameter d_{bg} restricting the background part of the rain zone is taken to be equal to 33 km.

In (Ref.3) the rain zone in

horizontal section is assumed to consist of the two different geometrical figures with a common centre, a central circle of diameter d_c described by Eq.1 and an ellipse with the axes ratio $a/b = 2$ characterizing the rain background part ($2a=46,2$ km and $2b=23,1$ km). The rainfall rate in the background part R_{bg} (mm/h) is described by equation

$$R_{bg} = 10[1 - \exp(-0,0105R_c)] \quad (2)$$

as in the model (Ref.1). Moreover, in (Ref.3) it is proved that the elliptical rain zone is oriented relatively to prevailing wind direction at the height of 3 km above the sea level in a given geographical region in such a way that in average the ellipse major axis is perpendicular to the wind direction.

In the case of slant paths the models (Ref.3) is transformed to the two coaxial cylinders, inner circular and outer elliptical with rain layer height H depending on R (Ref.1).

3. GENERALIZED RAIN MODEL

Let us formulate a problem. Let rain be in two points diversified by distance D . One needs to find the probability $p_j(R)$ that the least rainfall rate in the points is equal to R . The value of $p_j(R)$ depends on where the diversified points are located, inside the shower or background parts of rain or one point inside the first part and another point in the second one. It can be shown that the value $p_j(R)$ is described by equation

$$p_j(R) = p_c(R)p(c|c,R) + p_{bg}[f(R)] + p_c[f(R)]p(bg+0|c,f(R)) \quad (3)$$

$$p_z[f(R)]p(0|z,f(R))$$

where $p_c(R)$ is probability that the observation point is in the rain shower part with rainfall rate R , $p_c[f(R)]$, $p_{bg}[f(R)]$ and $p_z[f(R)]$ are probabilities that the observation point is respectively in the shower part, the background part and the zone of rain. The value of rainfall rate $f(R)$ in the rain shower part means that in the background part the value of rainfall rate is equal to R . (It follows from Eq.2 that $f(R) = \ln(1-R/10) \cdot 10^2$ mm/h). Since the least rainfall rate is equal to R in the rain background part then according to Eq.2 the value $R < 10$ mm/h in Eq.3.

For simplicity we shall consider the model (Ref.1) when the outer cylinder is a circular one. If $10 < D < 33$ km Eq.3 is considerably simplified and one can obtain the joint cumulative rainfall rate distribution $R \geq r$ (Ref.4) for diversity distance D between points 1 and 2 as

$$P_{1,2}(R \geq r) = \int_z^{10} p_z[f(R)] F(D, d_{bg}) dr = = P(R \geq r) [1 - 2 \arcsin(D/d_{bg}) / \pi] \quad (4)$$

where $P(R \geq r)$ is cumulative rainfall rate distribution $R \geq r$ in one point. In the case of model (Ref.3) the value d_{bg} in Eq.4 must be replaced by the lengths of the rain elliptical zone axes $2a$ and $2b$ in point diversity direction perpendicular and parallel accordingly the prevailing wind direction at the height of 3 km above the sea level.

Therefore to calculate a long-term joint cumulative rain attenuation distribution for two diversified paths one can use the algorithm (Ref.1) of rain attenuation statistics calculation for a single path and

Eq.4. As in the case of single paths (Ref.1) only the rainfall rate statistics in a given point is required. To account for influence of the diversity direction on the diversity gain the model (Ref.3) must be used with the elliptical rain background part.

4. COMPARISON OF MEASUREMENT AND PREDICTION RESULTS

In June-August of 1985 the radiometric measurements of the rain zenithal attenuation at wavelength $\lambda=8.2$ mm were carried out simultaneously at the two sites located in Nizhnij Novgorod and Zimenki and diversified by distance $D=24$ km. The total measurement time was equal to 25 hours. Besides the rainfall rate R was measured in the points by using the tipping bucket rain gauges. The both measured R cumulative distributions in the two points coincided practically. It means that the obtained statistics can be regarded as representative. On the basis of these R -distributions the rain zenithal attenuation Γ_r^2 distributions were calculated for the single and space diversified paths using the suggested generalized rain model (Ref.4). For statistics prediction the rain layer heights H_0 and H_z (Ref.1) and the effective rain attenuation heights (Ref.5) were used. It should be noted that the predicted values of Γ_r^2 at small probability levels on the basis of H_0 and H_z exceeded the measured ones by 2 times. Therefore the models (Refs.1,3) are not of use for prediction of millimetre wave rain zenithal attenuation. Probably this is due to the fact that the rain region is

really inclined relative to the vertical by $\sim 30^\circ$. The results of measurements and prediction of Γ_r^2 -distributions for the single paths and the joint distribution for the two diversified paths are given in the Figure. One can see from the Figure that the results of prediction and measurements are in good agreement.

5. REFERENCES

1. Misme P and Waldteufel P 1980, A model for attenuation by precipitation on microwave earth-space link, *Radio Science*, 15, 3, pp.655-665
2. Macchiarella G 1985, A comparative analysis of some prediction methods for rain attenuation statistics in earth-to-space links, *Radio Science*, 20, 1, pp.35-49
3. Sukhonin Ye V 1990, Prediction of millimetre wave attenuation in the atmosphere, *Itogi nauki i tekhniki, Series Radio-tehnika*, Moscow VINITI, 41, pp.3-68 (in Russian)
4. Korotkov V A, Rukina A N and Sukhonin Ye V 1989, Generalized rain model for prediction of radiowave attenuation statistics on single and space diversified paths, *Radioengineering and Electron Physics*, 34, 6, pp.1127-1134
5. Babkin Yu S, Chernyshev V I and Sukhonin Ye V 1980, On prediction of MMW attenuation in the atmosphere on the slant paths, *Proc. 3-rd Allunion Symposium on MM and subMM Waves*, Gorkij IAP RAS, pp.273-274

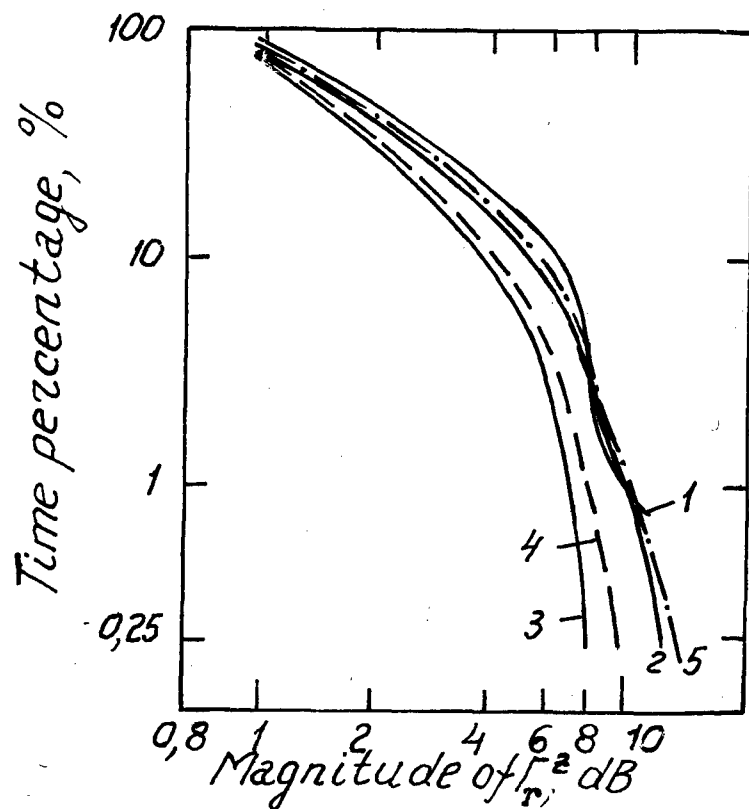


Figure: The measured and predicted rain zenithal attenuation. Γ_r^2 distributions at $\lambda=8,2$ mm. The curves 1 and 2 are the measured distributions on the single paths, the curve 3 is the joint measured distribution. The curves 4 and 5 are the calculated distributions respectively for the two diversified paths by using the generalized rain model and for the single paths.

THE METEOROLOGICAL FRONTS AND THEIR INFLUENCE ON THE DESIGN AND EXPLOITATION OF RECONFIGURABLE ANTENNA PATTERN IN SATELLITE-BASED AREA SERVICES

By A. Paraboni, M. Binaghi and A. Pawlina¹, D. Brain², J.P.V. Poiars Baptista³

¹ - Politecnico di Milano, Piazza L. da Vinci 32, I-20133 Milano, Italy

² - ERA Technology Ltd, Cleeve road, Leatherhead, Surrey KT22 7SA, England

³ - ESA/ESTEC XEP Division, Keplerlaan 1, P.O. Box 299, NL-2200 AG Noordwijk, The Netherlands

ABSTRACT

This paper presents the result of a study aiming at assessing the main properties of the meteorological fronts and demonstrating their possible utilisation in future satellite-based area services; as an example the attention has been focused on a radio system which is going to assume great importance in the near future: the direct TV broadcasting from satellite. It is shown how elements collected with raingauges and meteorological radars can be brought in the context of a single model which provides parameters of direct use both for the system design and its day-by-day management.

1. INTRODUCTION

The meteorological fronts are weather systems in which air masses at different temperature encounter each other during their movement within the general atmospheric circulation; the masses at warmer temperature are then lifted by the colder ones and the water vapour contained in them is cooled and transformed into rain. Along the fronts (stripes of a few hundreds kms width and some thousands kms length) the rain, both of stratified and convective nature, is much more probable than elsewhere.

The characteristics of the fronts are of particular interest for the design of future satellite-based area services like the mobile radio or the direct broadcasting. In the present paper, after presenting some of the particular characteristics of the fronts, it is shown how they can be exploited in the design of high-definition TV direct broadcasting systems at 20 GHz foreseen in the next future. In particular the problem of the efficient use of the on-board available power is considered and it is shown how the policy of concentrating most of the power flux along the fronts, at expenses of the external regions where it is likely to be less necessary, allows a

significant reduction of the outage time due to rain in the case of extended countries such as, e.g., Italy. This technique, made possible today thanks to the most recent advances in the field of the reconfigurable-pattern antenna technology, will require achieving from the meteorological offices a continuous information on the position of the fronts and their motion.

2. THE METEOROLOGICAL FRONTS

The impact of the meteorological fronts on the prediction of rain attenuation for the design of advanced telecommunication systems received some attention some years ago in occasion of the design of satellite based TLC systems with a "common resource", i.e. systems possessing the possibility of assisting one (or a few more) earth terminal undergoing particularly severe weather conditions.

The way in which this form of assisted condition was realised (a steerable high gain antenna, a lower frequency beacon, a lengthened time window in the bit stream etc.) was relatively little important in the basic design of the system, being instead of more importance the assessment of the probability that a number of earth terminals greater than the available resources would request the assisted condition.

Studies on the joint exceedance probability of rain attenuation in multiple sites were then undertaken using rain and beacon data [1,2,3]. In figure 1 [3] a scatterplot giving the joint exceedance probability of the rain intensity as a function of the distance is represented. The probability, in ordinate, is normalised to the value it would assume in the case of statistical independence.

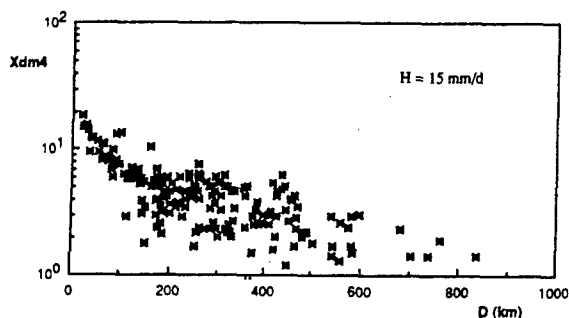


Figure 1: Scatterplot giving the joint probability to exceed the indicated value of rain intensity in couples of sites separated as in abscissas. The joint probabilities are normalised to the value of statistical independence.

From figure 1 three distinct subranges of distance can be distinguished:

- 0 to 100 kms: the joint probability decreases quickly from the initial value (single-site probability at 0 distance);
- 100 to 600 kms: the joint probability decreases much slower than in the previous range; a stationary average (*plateau*), instead of a decreasing slope, accompanied by a much wider spread of values can be perhaps considered a better model;
- 600 to 1000 kms: the normalised joint probability tends to unity, so indicating a tendency towards the statistical independence beyond this limit.

The first subrange is typical of couples of points within the same rainy area (as the systems of our concern here are typically low margin systems, we consider extended areas of very light rain, often of stratified type, stretching over distances of many tens of kms). The second subrange is typical of couples of points for which the higher joint probability with respect to the statistical independence value can only be explained from the fact that the points are within a region in which rain is more probable than in the average. This region is evidently a meteorological front. The spread can be explained by the different orientation of the line joining the two points with respect to the preferred orientation of the fronts. In the third subrange the statistical dependence drops gradually to unity so giving indication of the typical length of part of the fronts intercepted by Italy.

3. THE FRONT CHARACTERISTICS

The most relevant parameters describing the fronts, as far as direct broadcasting systems are concerned, are the following:

- the *actual* fractional area of the fronts, F , i.e. the ratio between the part of the territory covered by the front(s) and the total area;
- the *average* fractional area over all the actual fractional areas in a long observation period, $\langle F \rangle$; (this parameter, in the case of a phenomenon statistically uniform in space, is equal to the fractional area over a territory of infinite extension which, in turn, is equal to the probability P_f that a point of the region is within a front: $\langle F \rangle = P_f$;
- the relative raincell density within the fronts, with respect to the average raincell density, μ ;
- the front depth, s_f ;
- the front orientation, ϑ_f ;
- the front velocity, v_f .

All these parameters are of interest in statistical sense being their knowledge necessary for the system design; some of them, moreover, are needed for the system management and must be known in any time for the optimisation of the reconfigurable antenna pattern.

4. ASSESSMENT OF THE FRONT PARAMETERS

Figure 2 shows a synoptic meteorological map, taken by a newspaper, in which the fronts are drawn together with a dashed area indicating the enhanced probability of rain in it. This map confirms a data well known by the meteorologists about the fronts, namely that they are about 150-200 kms thick (in average). Here we will assume:

$$s_f = 300 \text{ km} \quad (1)$$

Figure 3 shows a cumulative distribution of the frontal fractions F obtained by the authors from a limited but significant set of days in Italy during the summer-autumn 1993 (front depth 300 km).

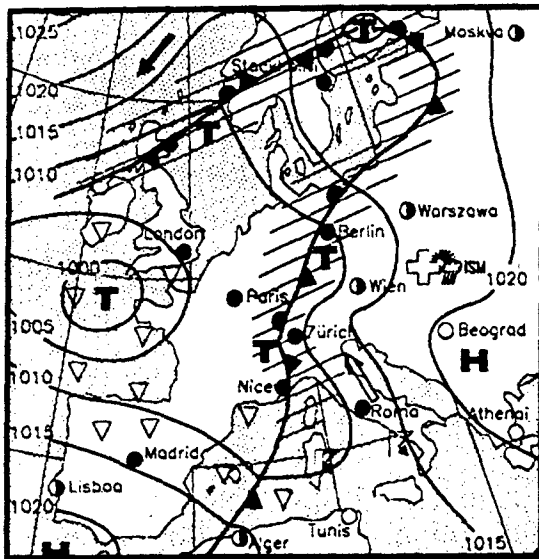


Figure 2: Standard meteorological map showing the presence of a front covering the eastern part of Italy. The dashed portion is an estimate of the front depth.

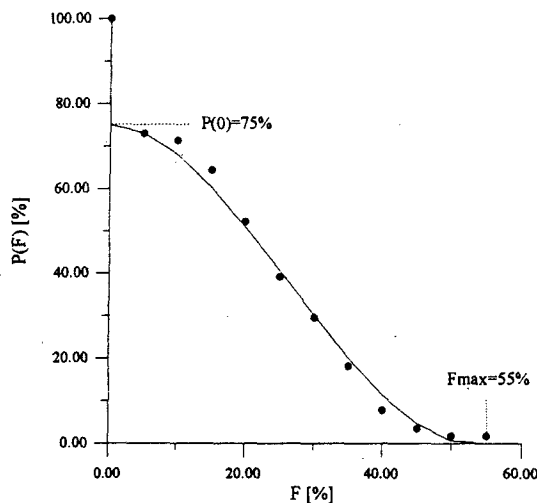


Figure 3: Cumulative distribution of the frontal fractions of the Italian territory covered by a front.

From the figure it appears that almost never more than 50% of the Italian territory was under a front ($F_{\max} = 0.50$) and that in the 75% of the observations some front intersected the Italian territory ($P(F > 0^+) \equiv P(0) = 0.75$). The following simple model was fitted on the data:

$$P(F) = P(0) \left[2(F/F_{\max})^3 - 3(F/F_{\max})^2 + 1 \right] \quad (2)$$

(probability to exceed F in the range $0 < F < F_{\max}$)

$$p(F) = -dP(F)/dF = (1 - P(0))\delta(0) + P(0) \left[6(F/F_{\max}) - 6(F/F_{\max})^2 \right] / F_{\max} \quad (3)$$

(probability density of F , $\delta(0)$ = Dirac function)

From these models the average fraction has been easily worked out:

$$\langle F \rangle = P_f \approx 0.2 \quad (4)$$

It is interesting to note that, as it has been demonstrated in [4], P_f must be equal to the inverse of the plateau value which characterises the normalised joint probability. This property is fully confirmed from figure 1, so indirectly proving the correctness of the assumption $s_f = 300$ km.

As for the raincells density, it is difficult to assess rigorously the effect of "concentrating rain" in the fronts, also because the lifting of warm airmasses is not a unique prerogative of the cold masses wedging themselves beneath the warm ones; convective instabilities can occur spontaneously in presence of strong temperature gradients and also orographic effects can have an important role in some countries.

Provided that adequate margins of power are assumed, one can make the hypothesis that the frontal effect is maximum, with the consequence that practically all the raincells are assumed to be internal to the fronts (*maximum frontal density hypothesis*): with this hypothesis all the raincells are assumed to be concentrated in an area P_f times smaller than the total with the consequence that the concentration increases of a factor

$$\mu = 1/P_f \quad (5)$$

As for the actual front parameters, they may be provided by the meteorological offices: it is of extreme importance that their actual values are estimated with great care and sufficient frequency, as the movement and the deformation of the fronts can be relatively fast and forecasting based on too long time intervals can reveal itself inadequate.

Of these parameters the front orientation and the translational velocity are the most important even though the depth, the eventual curvature and presence of areas of possible instabilities can make more effective the choice of the antenna pattern in a given circumstance.

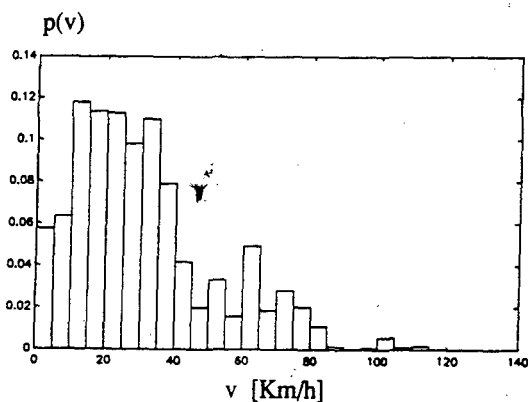


Figure 4: Histogram of the front velocities in Italy.

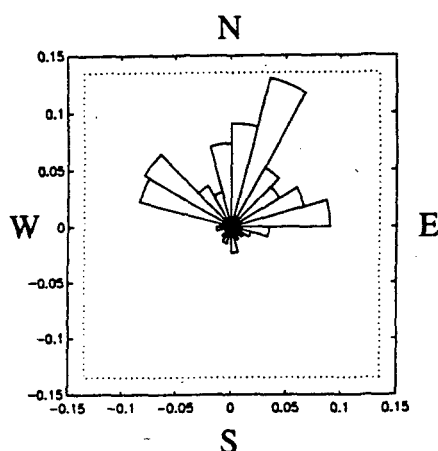


Figure 5: Histogram of the front orientations in Italy.

Studies performed by means of a meteorological radar located at Spino d'Adda, near Milano [5] provided some statistical information on the front velocities and orientations: these are reported in figures 4 and 5.

From figure 4 it appears that the translational velocity of the fronts is characterised by a large spread; this means that the value of this parameter can not at all be assumed as a fixed one when extrapolating the position of the front in the interval between two consecutive updating. On the contrary an accurate assessment must be made, especially if the updating can not be performed at time intervals shorter than some 5-6 hours.

From figure 5 it seems that the fronts tend not to be completely aligned with the main orientation of the Italian territory: this condition is the more favourable as large fractional areas covered by a front are so prevented owing to the elongated

nature of Italy. This effect is confirmed from figure 3, in which a coverage exceeding the 50% were never observed.

5. THE DIRECT BROADCASTING SYSTEM

in line of principle, a satellite broadcasting system disposing of a reconfigurable antenna pattern could take advantage by the possibility of increasing the radiated power towards the sub-regions of the served territory in which, owing to the rain attenuation, the power demand is greater. In practice it is not possible, however, with the present state of the art in the earth surveillance, to know at any instant the exact contours of the rainy areas; moreover, if even this were the case, it would be impossible to tailor the footprint exactly along these contours owing to the obvious restrictions existing in the present antenna technology and in the physical size of the on-board antenna, which determines the spatial detail of the footprint contours.

A more feasible approach to the problem consists in radiating more power where rain is more likely to occur, i.e. along the fronts. The time and space variations of these weather systems are certainly less pronounced and within the possibility to be tracked by the adaptive antenna contours.

The basic principle of the system consists then in setting apart a certain fraction of the power available on board (*movable fraction*), with the aim of redirect it towards the frontal region, where it is more likely to be exploited. Obviously the remaining fraction of power is fixed (*fixed fraction*) and devoted to assure a minimum necessary power density level over the whole region, taking into account contribution of attenuation other than rain. This level can never be reduced, whichever pattern configuration is assumed. Only if the movable power exceeds the actual request, the excess can be "spent" otherwise (e.g. re-distributed over the served region, radiated out of the region, or spared).

6. THE SYSTEM PERFORMANCE

In this section the expected improvement of the system is assessed assuming two simplifying hypotheses:

- statistically uniform region
- maximum frontal density (no rain outside the fronts)

Let us call:

- $\ell_0 [W/m^2]$: reference power flux, the power flux density necessary to cope with the quality objectives taking into account all the contributions of attenuation *other than rain* as if these were due to permanent causes (gaseous absorption, scintillations, etc.). This power density is the one which would arrive to the user if the fixed fraction of power were uniformly radiated across the territory;
- $u \ell_0$: average power flux, the enhanced power flux which would arrive to the users if the whole power (movable plus fixed fractions) were uniformly radiated across the territory;
- u, u_f, u_{nf} : average margin, frontal margin and non-frontal margin respectively (not in dB here);
- F : actual fraction of the territory covered by a front;
- $P(A)$: long term probability to exceed a given rain attenuation A ;
- $\mu P(A)$: probability to exceed attenuation A conditioned to being within a front.

Let us firstly suppose that the whole power available on board is radiated. In this case the margins must obey to the relationship:

$$u = F u_f + (1 - F) u_{nf} \quad (6)$$

Having assumed the maximum frontal density hypothesis, it turns out $u_{nf} = 1$ (because there is no need of margin out of the fronts) and then:

$$u_f = 1 + (u - 1) / F \quad (7)$$

An user is considered "non served" whenever he receives, while being in a front, a power flux density less than $u_f \ell_0$, i.e. when $A > 10 \log_{10} u_f$.

The conditional fraction of non served users $P_{out}(u, F)$ is then given, on long term basis, by the expression:

$$\begin{aligned} P_{out}(u, F) &= F \mu P(10 \log_{10} u_f) = \\ &= F \mu P \left[10 \log_{10} \left(1 + \frac{u-1}{F} \right) \right] \end{aligned} \quad (8)$$

De-conditioning the probability with respect to the parameter F we finally obtain the average long term probability of non being served:

$$\langle P_{out}(u) \rangle = \int_0^1 P_{out}(u, F) p(F) dF \quad (9)$$

which can be solved utilising the probability density (3) and a cumulative probability density of attenuation significative, in average, of the territory under study.

We assume here a simple model fitting fairly well the average distribution in the high probabilities range for frequency equal to 22 GHz and average elevation equal to about 37 degs.

$$P(A) = 4 A^{-2} \% \quad (10)$$

Expression (9) is of interest not so much for the absolute value it provides, but rather for the comparison it allows with the case of non-adaptive case; this case is directly represented by Eq. (10) (naturally the two expressions may be both represented as a function of the same parameter: A or u ; here we chose A , as customary when talking about attenuation).

Expressions (9) and (10) are plotted in figure 6, where also the cases of a system "clipping" the power density within the fronts when it exceeds the

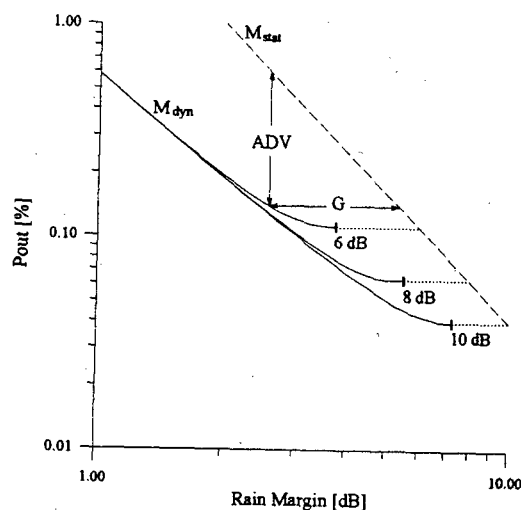


Figure 6: Outage probability of users as a function of the system margin set apart for rain. The curves on the left give the outage probability in the case of dynamic allocation of the power density, with margin "clipped" at the values indicated. The curve on the right gives the outage in the case of static allocation (extra power spread uniformly across the territory).

indicated value, are considered (a possibility pointed out in the previous section but not deepened here for conciseness).

From figure 6 two significant parameters can be extracted: the *adaptivity gain* and the *adaptivity advantage*, with meaning similar to the corresponding ones in use for space diversity systems. The adaptivity gain is the difference in dB between the margins which would be necessary with the two types of systems, fixing the outage objective; by converse the adaptivity advantage is the ratio between the outage probabilities when a system with a given margin uses it statically or dynamically.

From figure 6 it comes out that, with a maximum power flux density clipped at 6 dB over the no-rain value, an outage of 0.15% (about 13 hours per year) can be reached with a rain margin of 2.5 dB with the dynamic system, and of 5 dB with the static system; the adaptivity gain is in this case of 2.5 dB.

By fixing the rain margin at 2.5 dB (the margin due for other causes like gaseous absorption etc. is not included here), the system, if used statically, gives an outage probability of about 0.6% (52.5 hours). This corresponds to an adaptivity advantage of 4 for the adaptive system.

7. CONCLUSIONS

The tendency of the rain to concentrate along the meteorological fronts makes it possible to make an "intelligent" use of the power available on board in satellite-based direct broadcasting systems; this goal can be achieved, resorting to modern antenna technologies, by distributing the power flux density where rain is more likely to happen, i.e. along the fronts themselves. According to a preliminary analysis performed in this paper, a margin gain of 2.5 dB, for outages of the order of 13 hours per year can be obtained through this technique.

8. REFERENCES

- 1 Barbaliscia F, Ravaioli G, Paraboni A, Characteristics of the spatial statistical dependence of rainfall rate over large areas, *IEEE Trans. on Antennas and Propagation*, vol. 40, n. 1, Jan. 1992.
- 2 Acampora A S, A shared resource TDMA approach to increase the rain margin of 12-14 GHz satellite systems, *Bell Syst. Tech. J.*, vol. 58, pp. 2097-2111, 1979.
- 3 *Fading correlation study*, final report of a research activity carried out by Fondazione Ugo Bordoni for ESA/ESTEC, contract n. 6825/86/NL/DG, March 1988.
- 4 Binaghi M, Capsoni C, Paraboni A, Pawlina A, Use of a conventional meteorological radar together with external sources for the assessment of structural properties of rain over large scale, *Proceedings International Workshop on Multi-Parameter Radar Applied to Microwave Propagation*, Graz (Austria), Sept. 3-6, 1991.
- 5 Pawlina A, Binaghi M, Statistical dependence of rain occurrence in multiple site case modelled with dynamical radar derived parameters, *Proceedings ISAP '92 (International Symposium on Antennas and Propagation)*, Sapporo (Japan), Sept. 22-25, 1992.

LIDAR TECHNIQUE FOR CLOUDINESS PARAMETERS MONITORING ON SLANT COMMUNICATION LINKS WITH GEOSTATIONARY SATELLITE

V.V. Efremenko, L.N. Kornilov, A.V. Moshkov,
V.N. Pozhidayev, A.V. Zubkov, F. Dintelmann*

IRE RAS, 11 Mokhovaja str., Moscow, 103907, RUSSIA

Tel: (095) 203-49-96, Fax: (095) 203-60-78, E-mail: efr@ire.uucp.free.msk.su

*FTZ DBP TELEKOM, Am Kavalleriesand 3, D-64276 Darmstadt, GERMANY

Tel: +49-6151-832-530, Fax: +49-6151-834031, E-mail: fi33@vmxa.fz.telekom.de

ABSTRACT

In this contribution the physical connections between atmosphere noise temperature and optical properties were under investigation. A lidar technique was used to measure the light back scattering from different meteorological phenomena influencing radio wave attenuation and phase distortion along a slant communication link. The test measurements were performed in parallel with the 30-GHz radiometer. The experiments as well as numerical modeling confirmed the expected correlation between cloudiness and precipitation parameters measured by lidar and radiometer and proved to be potentially useful for monitoring of meteorological conditions on satellite links.

Keywords: Lidar, Sky noise temperature, Radio wave attenuation, Atmospheric monitoring.

1. INTRODUCTION

It is well known that both, radio wave attenuation on communication links in the atmosphere and signal phase distortions depend on the combined influence of different meteorological and aerological phenomena along a path. That is why are trying to bring the radio wave distortions into correlation with atmospheric conditions, since one has to be aware of the spatial atmospheric data along the path.

Sometimes it is possible to avoid taking account of the instantaneous atmospheric conditions for estimation of radio wave distortions. One way is to use a statistical approach. Accumulating experimental data on radio wave distortions (generally attenuation) for a long time and combining these with meteorological data, we can create some statistical model of the link or the bounds for

estimation of the annual and worst month attenuation statistics [1]. Moreover, a basic correlation between the atmosphere noise temperature and microwave atmospheric extinction gives us a possibility to simplify an experimental setup and measure the sky noise temperature by means of a microwave radiometer [2] instead of the signal level on a real satellite link. There are semi-empirical methods linking wave attenuation with noise temperature and describing frequency dependencies of them for the clear atmosphere. There are also some approaches to describe the relation for clouds and precipitation but in this case one has to take into account not only radio wave absorption in the atmosphere but scattering also. As was shown [3] we may neglect the scattering effects for extinction calculations if the ratio scattering-to-extinction-coefficients, $-\kappa$ is less than 0,1 and the atmospheric optical depth, $-\tau$, for the wave length is not more than 0,5. For precipitation of mean intensity and $\lambda < 3,2$, cm we have $\kappa > 0,2$ and $\tau > 1$. Similar situation exists for some clouds and clouds with rain.

This means that we have to take into account for the sky noise temperature single and multiple scattering effects and their influence on the connection between radio wave attenuation and noise temperature. On the other hand, the atmosphere may cause phase distortions of a radio wave beam due to its inhomogeneous structure, phase shifts by drops, etc. Some of them as multi-path propagation in the atmosphere with a temperature inversion may change the signal level, others are modifying signal's spectral structure and this may limit the link bandwidth. But they can not be recognized by means of sky noise temperature measurements according to their integral nature and because the spatial scattering features do not become apparent in atmosphere optical depth measurements.

From this point, it seemed interesting to sup

plement the traditional technique for the study of radio wave propagation in the atmosphere with a new tool that could bring us additional information on scattering properties of the atmosphere and its spatial structure. A lidar proved to be such a tool. The physical base of electromagnetic wave absorption and scattering in the atmosphere is the same in either bands be it optical or radio, but due to the short wave length the light is more sensible to scattering by small particles.

- light pulse energy - 140 mJ;
- pulse duration - 20 ns;
- light beam divergence - 2 mrad;
- receiver aperture diameter - 100 mm;
- filter band width - 1,5 nm.

The lidar's axis is roughly matched with the radiometer's one. Both of them have PC-controlled data acquisition systems and run synchronously.

Lidar signatures or back-scattered light profiles along the laser beam path contain the spatial information on the atmospheric scatterers which may have no equivalent response in the radiometer signal.

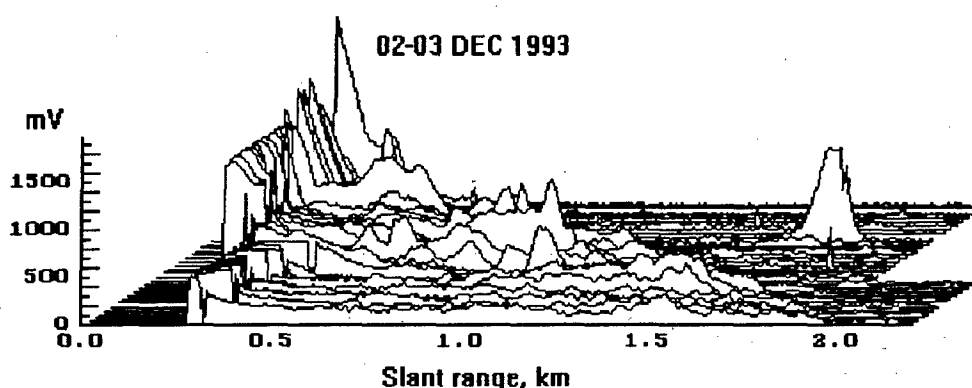


Figure 1: *Temperature inversion development. Profiling at half an hour intervals.*

2. TECHNICAL DESCRIPTION

2.1 The experimental set up

As the basis we use long term measurements of the sky noise temperature being performed along a slant communication link in Dubna. The *radiometer* has the following main parameters:

- frequency - 29,6 GHz;
- band width - 140 MHz;
- time constant - 1 s;
- antenna angle width - 2 dg;
- min. noise temperature - 10 K;
- measurement periodicity - 10 s;
- auto-calibration periodicity - 10 s;
- antenna zenith angle - 65 dg.

The radiometer is placed outdoors and pointed along a satellite link.

The *lidar* has a Q-switched ruby laser and it's parameters are as follows:

- wave length - 694,3 nm;

Fig.1 shows the development of a night temperature inversion of the atmosphere which was not accompanied with noise temperature changes but could cause multi-path radio wave propagation, e.g. on a LOS path.

2.2 The inversion problem

An early and continuing goal of lidar research has been to devise an inversion method whereby profiles of optical parameters such as attenuation and backscatter coefficient in an inhomogeneous atmosphere can be quickly and accurately deduced from the signature of a monostatic single-wave-length lidar. The main difficulties follow from theoretical requirements of the inversion process. For a monostatic single-wave-length pulsed lidar, the basic is the single-scattering lidar equation, linking the received backscattered light signal to optical parameters of the atmosphere, i.e. extinction and backscattering coefficients.

$$Y(z) = \frac{c\delta}{2} A \frac{\beta(z)}{z^2} \exp\left[-2 \int_0^z \sigma(z') dz'\right], \quad (1)$$

where:

$Y(z) = P(z)/P_0$ - a lidar signature;

$P(z)$ - the instantaneous received light power;

P_0 - the transmitted power at time t_0 ;

c - the velocity of light;

δ - the pulse duration;

A - constant connected with the lidar's technical parameters;

$z = c(t - t_0)/2$ - the range;

$\beta(z)$ and $\sigma(z)$ - are the volume backscatter and attenuation coefficients of the atmosphere.

Unfortunately, analytical solutions of (1) are not well justified for many situations of interest, e.g., under conditions of dense cloud, fog, rain, etc. Even under the relatively stable conditions prevailing in fog, significant local heterogeneities occur. Such microstructure variations along the lidar beam path could easily lead to relatively large fluctuations in $d\beta/dz$ and, as result to an unstable solution.

Several observational and theoretical studies have been published that show that under a wide range of circumstances for which particularly backscattering dominates, β and σ can in fact be related approximately by a power law of the form

$$\beta = b \sigma^k, \quad (2)$$

where $b = \text{const.}$ and k depends on the lidar wavelength and various properties of the scatterers. Reported values of the exponent are generally in the interval $0.67 \leq k \leq 1.0$. It was experimentally shown [4] that for clouds of different type and microstructure $k=1$, and b is a function of liquid water content.

The relation in Eq.2 was used to develop two stable inversion procedures for Eq.1. The first one is based on the approach proposed in [5] and deals with the logarithmic range-adjusted power, defined as

$S(z) = \ln[z^2 P(z)]$. The main and brilliant point of the study [6] is the offer to change the direction of recovering and to integrate from the cloud to the lidar. Moreover, Eq.1 in terms of $S(z)$ does not contain the constant A , which has to be measured experimentally.

The second iterative procedure recovers $\sigma(z)$ from the usual form of Eq.1. To use it, the lidar's const. $-A$ was measured.

To check the computer codes based on the two procedures in presence of the different meteorological phenomena (aerosols, clouds, rain) the special simulating program has been developed. It takes the vertical profiles of the molecular and aerosol extinction and scattering coefficients provided by the LOWTRAN model for the different visibility ranges at ground level, calculates these coefficients for the clouds with the different drop size distributions at top and bottom heights, taking into consideration the different shapes of the cloud liquid water content distributions, and calculates these coefficients for rain with different rain rates at top and bottom heights. After that this program calculates the signature Y for different distances along the path.

The tests have demonstrated good agreement between initial and recovered values of σ for both procedures.

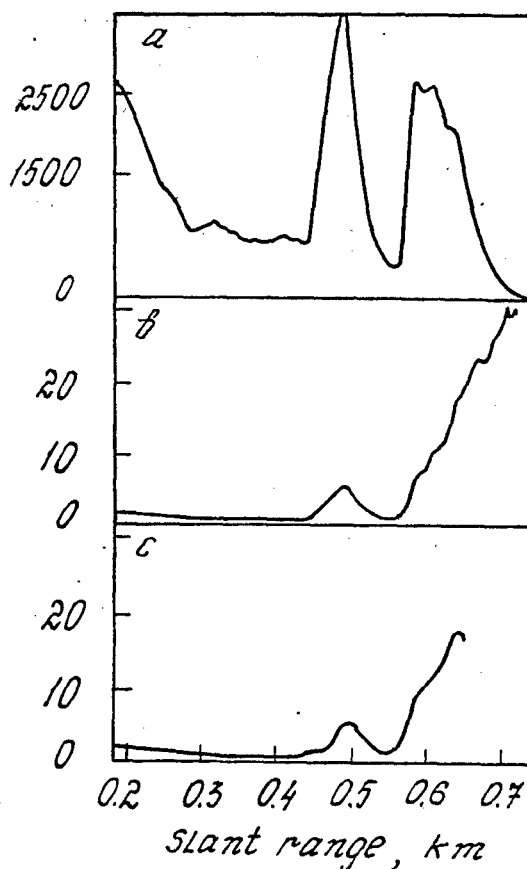


Figure 2: a- A real signature of the stratified cloud (mV). b,c- The profiles of σ (1/km) recovered by S- method (b) and iterative method (c) from the signature above (a).

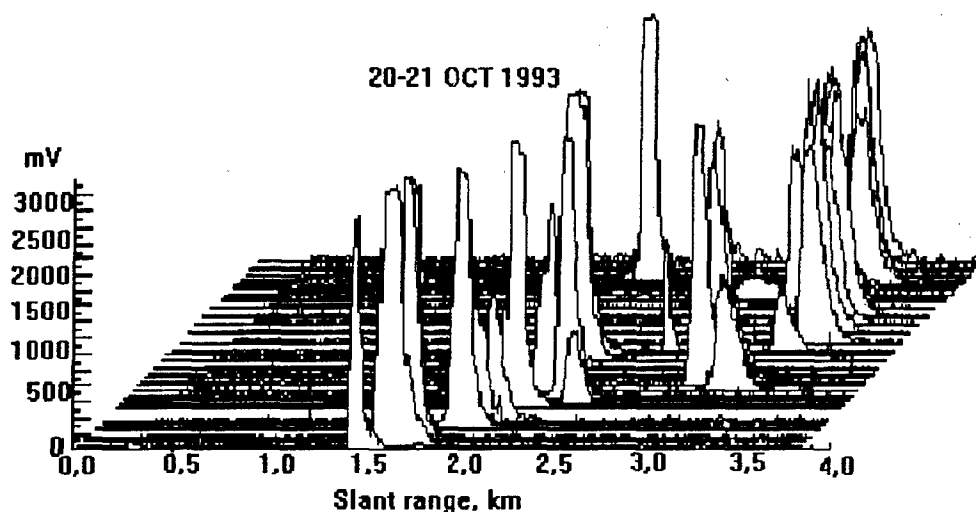


Figure 3: *The cloudiness changes in lidar signatures. Profiling at half an hour intervals.*

Fig. 2 illustrates the results of the extinction coefficient recovered from the real signature of the stratified cloud by means of the two algorithms.

3. RESULTS AND DISCUSSION

To correlate sky noise temperature and

optical parameters of the atmosphere recovered from the lidar signatures and the noise temperature for different meteorological conditions, the test round-the-clock measurement cycles were performed in Dubna last year. Besides lidar and radiometer data, all available meteorological information was collected. Subsequent data processing had the objective

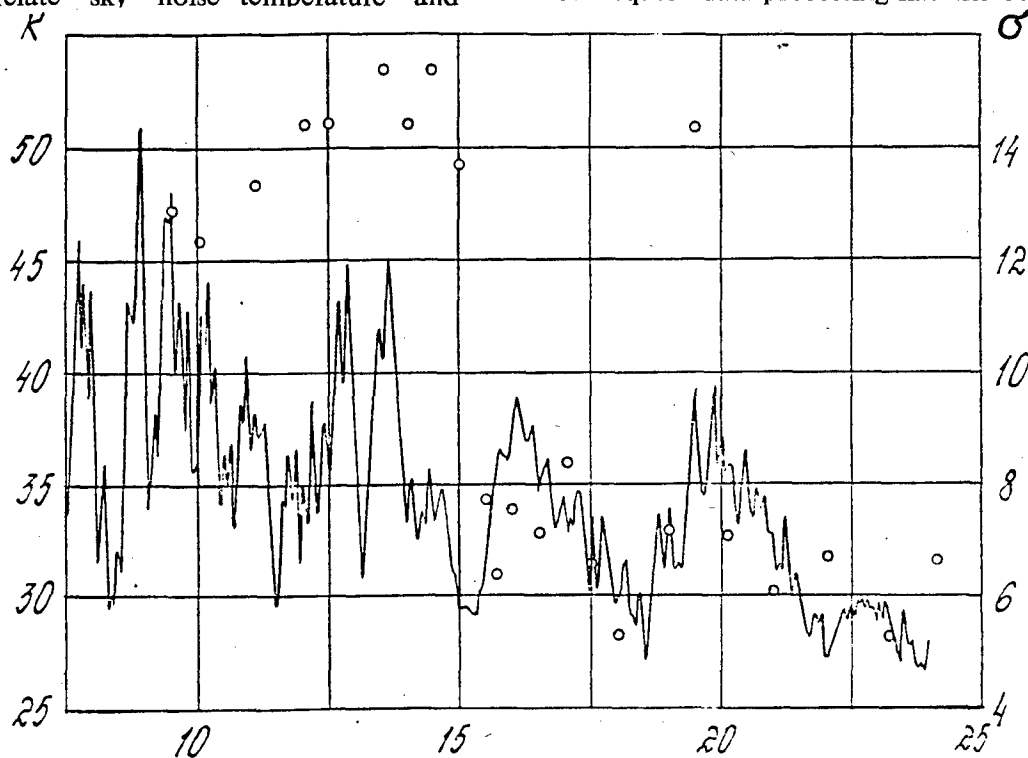


Figure 4: *Time dependency of the sky noise temperature (K) - solid line, and light extinction (1/km) - small circles, for one of the round-the-clock cycle. The time scale is in hours.*

to compare the parameters of the atmosphere taken from the two different bands.

The first results show that a lidar running in parallel to a radiometer allows to solve two problems. The first one is the monitoring of the current meteorological conditions along a link. Analyzing the shape of lidar's signatures, it is possible to distinguish the presence of clouds, clouds with rain, clouds with snow, etc., and to improve models of attenuation prediction by means of statistics for different phenomena separation.

The second one is the measurement of cloudiness parameters. In the optical band, the light extinction coefficient in a cloud can be roughly estimated as

$$\sigma \approx 2\pi 10^{-6} N \frac{(\mu+1)(\mu+2)}{\mu^2} r_m^2, [1/m] \quad (3)$$

where $N, [\text{cm}^{-3}]$ is the cloud drop concentration, μ and $r_m, [\mu\text{m}]$ are the cloud microstructure parameters assuming a γ -distribution. Cloud water content relates to the same parameters

$$q \approx \frac{4}{3} \pi 10^{-6} N \frac{(\mu+1)(\mu+2)(\mu+3)}{\mu^3} r_m^3, [\text{g}/\text{m}^3] \quad (4)$$

Combining Eq.3 with Eq.4 we can relate the light extinction to cloud water content:

$$q \approx \sigma \frac{2(\mu+3)r_m}{3\mu} \quad (5)$$

Eq.5 is valid along the distance of laser pulse penetration depth into a cloud. For stratified clouds with $\mu=4$ and $r_m=2$, the water content is $q \approx 2,33\sigma$.

On the other hand the cloud water content is related to radio wave attenuation and sky noise temperature. The attenuation A in the cloud is related to cloud noise temperature T_a , by the equation

$$A = 10 \lg \frac{T_m - T_c}{T_m - T_a}, \quad (6)$$

where T_m is the mean effective temperature of the atmosphere and T_c is the cosmic background temperature of about 2,6 K. The attenuation is connected also with the cloud water content and effective length of the cloud:

$$A = qK(F, T)L_{\text{eff}}, \quad (7)$$

where the coefficient $K(F, T)$ contains the complex water refractive index for frequency F and water temperature T .

In the case of mono-frequency measurements, we can not resolve the two parameters

q and L_{eff} . The use of a lidar allows us to measure the backscatter coefficient of the cloud and estimate with some assumptions the water content independently. So, the mutual lidar and radiometer running is a way to measure both, the cloud's water content and its effective length.

The lidar profiling shown in Fig.3 was performed during a round-the-clock cycle of measurements. It was cloudy without rain. Cloudiness power and height were changing in wide intervals. The corresponding values of light extinction in the bottom layers of the clouds recovered from the signatures are shown in Fig.4 together with the radiometer record. The results demonstrate some synchronism in changing of sky noise temperature and light extinction that corresponds to the relations in Eq.5 and 7.

In our opinion the first results of mutual measurements of the atmospheric parameters by means of a lidar and microwave radiometer proved to be sufficient ground for subsequent regular investigations in the field with an improved experimental set up and a better developed theoretical base.

4. REFERENCES

1. Pozhidayev V.N. 1993, *Proc. of 18th Meeting of OPEX*, p.102.
2. Dintelmann F., Ortgies G. 1989, A semi-empirical model for cloud attenuation prediction, *Electr. Lett.*, vol. 25, p.1487.
3. Волчок Б. А., Черняк М. М. 1968, *Труды ГГО*, вып.22, с.83.
4. Dubinsky R.H. et al. 1985, Determination of cloud microphysical properties by laser backscattering and extinction measurements, *Applied optics*, v.11, No.11, p.1614.
5. Klett J.D. 1981, Stable analytical inversion solution for processing lidar returns, *Applied optics*, v.20, No.2, p.211.

FIRST RESULTS OF 30-GHZ RADIOMETRIC AND RAIN MEASUREMENTS IN THE MOSCOW AREA

G. Heyer¹, S. Szuppa¹, H. Trommer¹, F. Dintelmann², V. L. Bykov³, V. V. Svjatogor³

1-Forschungs- und Technologiezentrum, Ring 19, 15752 Kolberg, Germany

Tel: +49-30-768-87320, Fax: +49-33768-87246

2-Forschungs- und Technologiezentrum, Am Kavalleriesand 3, 64295 Darmstadt, Germany

Tel: +49-6151-832530, Fax: +49-5161-834031

3-NIIR, Kasakova ul. 16, 103064 Moskwa, Russia

Tel: +70-95-2610273, Fax: +70-95-2610273

ABSTRACT

Results of one-year 30-GHz radiometric sky noise temperature and rain rate measurements near Moscow, Russian Federation, are presented and discussed. The derived attenuation is compared with similar measurements performed in Germany.

Keywords: atmospheric attenuation, satellite links, K_a-band, rain rate, ITU-R climatic zones

1. INTRODUCTION

Taking into account the fast growth of the need for communication and information in Russia, there will be a corresponding growth for communication links. Geostationary satellite systems are a powerful means to achieve this goal within a short time period at relatively low costs. In order to make best use of new frequency ranges, propagation measurements are inevitable tools for adequate system planning.

Although Russia has a long tradition in satellite propagation research, it only slowly followed the recent tendency towards the use of higher frequencies, e.g., the 20/30 GHz bands. In order to speed up, NIIR Moscow, and the Research Centre of German Telekom have embarked on a long-term co-operation in the field of satellite communications with a propagation experiment which began 1992. The main objectives are investigations in radio wave propagation and measurements of meteorological parameters at the International Experimental Centre for Satellite Communication of the Radio Research and Development Institute (NIIR) in Russia. In autumn 1992, we relocated a 30-GHz-Radiometer from Germany to Dubna (ITU-R climatic

zone E, $\varphi = 56.6^\circ\text{N}$, $\lambda = 37.20^\circ\text{E}$, altitude 120 m msl), 120 km north-east of Moscow. The operation and a first evaluation of the data is done at Dubna, further evaluation is carried out at Kolberg and Darmstadt. Measurement results for the 30-GHz noise temperature are available for the period November 1992 until October 1993. Rain rate measurements from a tipping bucket rain gauge have been gathered in parallel.

When operating outdoor measuring equipment in the Moscow-area, the particular climatic conditions have to be taken into account. The frost period with temperatures down to -35°C generally begins in October and ends in April, while heavy rain storms with intensities up to about 150 mm/h occur during the summer months.

To monitor the course of the experiment and to transfer the data to Germany, we use a VSAT link from Dubna to Kolberg once a day. This link serves also for the exchange of information between both sites.

2. TECHNICAL DESCRIPTION

2.1 Radiometer measurements

The equipment consists of a total power radiometer in connection with temperature and humidity sensors. A 60-cm parabolic antenna with a half power beam width of 1.2° is pointed under an elevation angle of 25° in direction south west. This pointing is a compromise between the angle under which a potential geostationary satellite would appear and the attainable accuracy of the measurements, i.e. the unavoidable noise radiation picked up from the environment. An antenna efficiency factor, varying between $\eta = 0.93$ in winter and $\eta = 0.95$ during the rest of the year, is used to correct this additional pick-up.

The radiometer has an integration time of 10 s, the resolution is 1 K. Calibration of the receiver gain is done every 5 minutes by switching the input of the RF unit to a reference load kept at constant temperature. During this cycle, ambient temperature and humidity are gathered in addition. Over-all calibrations are done by the tip curve procedure, carried out regularly under clear-sky conditions. The output signal is a voltage proportional to both, the sky noise temperature and the noise figure of the receiver. The complete data acquisition and the control functions for the device are done by a PC, an additional strip chart recorder for the analogue output is used as a back-up medium. An accurate time synchronisation of the equipment is realised with the aid of a radio-clock, receiving the DCF-77 standard time transmissions at least once a day.

2.2 Rain-rate measurements

The measurement of rain intensity can only be carried out in the frost-free period. The equipment used regularly at Dubna consists of a tipping bucket rain gauge with an operating range from about 2.5 mm/h up to 150 mm/h. Rain intensities are recorded by means of a computer and a strip chart recorder.

3. RESULTS FROM ONE-YEAR MEASUREMENTS

The key result from our radiometer measurement is primarily the sky noise temperature. The corresponding attenuation is calculated with the help of the radiometric equation (Ref. 1)

$$A = 10 \log \frac{T_m - T_c}{T_m - T_{sky}} \quad (1)$$

The medium temperature T_m is obtained from

$$T_m = a \cdot T_0 + (1 - a) \cdot T_0 \cdot e^{\beta(T_{sky} - T_0)} \quad (2)$$

(Ref. 2) with:

- T_0 - ambient temperature
- T_{sky} - noise temperature received
- $T_c = 2.7$ K (cosmic background radiation)
- $a = 0.91643$) for 30 GHz.
- $b = 0.038293$)

The calculated atmospheric attenuation is considered valid in a range from 0 up to about 12 dB. The cumulative distributions of attenuation for 12 months are shown in Fig. 1. A remarkable difference between a group of months with a high range (May to September) and another one with a low range of attenuations (October to April) can be recognised. This corresponds to the rain intensities, shown in Fig. 2, from May to October. In this period, rain measurements have been carried out. Some minor events took place also in April, as can be seen in the attenuation statistics. Fig. 3 shows the cumulative distributions of attenuation for the average year, the worst month and for the two periods of the year as mentioned above.

4. EVALUATION OF RESULTS

The variation of attenuation during the measurement period is very strong as can be seen in Fig. 3. To compare this results with the 30-GHz radiometric attenuation measured at an elevation angle of 30° at Kolberg (south-east of Berlin, Germany), we have calculated the adequate attenuation for Dubna. The elevation conversion factor for this operation is 0.843. Table 1 lists some representative values for the average year and the worst month.

%	average year		worst month	
	Dubna	Kolberg	Dubna	Kolberg
10	1.6 dB	1.0 dB	2.0 dB	1.5 dB
5	2.8 dB	1.5 dB	3.0 dB	2.2 dB
1	3.5 dB	3.1 dB	6.5 dB	5.7 dB
0.5	5.0 dB	4.2 dB	9.5 dB	8.2 dB

Table 1: Attenuation statistics for the average year and the worst month for Dubna and Kolberg (elevation angle: 30°)

Although the average attenuation does not exceed 3.5 dB for 1% of the time, we have for the same percentage of time an attenuation of about 6.5 dB for the worst month. For 0.5% of the time, these values are 5 dB and 9.5 dB, respectively.

Comparing these results with attenuation statistics obtained from similar measurements carried out at Kolberg (Fig. 4), we found constantly higher attenuations at Dubna than at Kolberg for

the same time percentages. With respect to the ITU-R rain climatic zones E and H (Ref. 3), one would expect the opposite behaviour. That is the reason, why we compared also the rain statistics measured at both locations (Fig. 5). We evaluated the concurrent cumulative rain distribution and a long-term average (1984-1990) for Kolberg. For the purpose of comparison, the cumulative distributions describing rain zones E and H are added. The long-term average year distribution and also the distribution for the considered period show for Kolberg distinctly lower values than one would predict from ITU-R rain zone data. The reason may be the very close location of Kolberg to the border between zones H and E.

5. CONCLUSIONS

There is no doubt that for the prediction of propagation characteristics, a measuring period of at least several years is necessary to describe the underlying meteorological effects. Hence,

these first results can be regarded only as preliminary. Nevertheless, we do believe that some of the trends observed are real. Therefore, we continue and will expand our experiment in order to produce results with better statistical significance.

6. REFERENCES

1. Brussard, G. 1985, Radiometry, a useful prediction tool? PhD Thesis, Univ. Catholique de Louvain, ESA SP-1071
2. Zhang, G.F., Li, H.J. 1985, An analytical model for effective medium temperature and its application, Proc. of ISAP Japan 1985, pp. 293-296
3. ITU-R, Recommendation 837, Geneva 1992, Characteristics of precipitation for propagation modelling

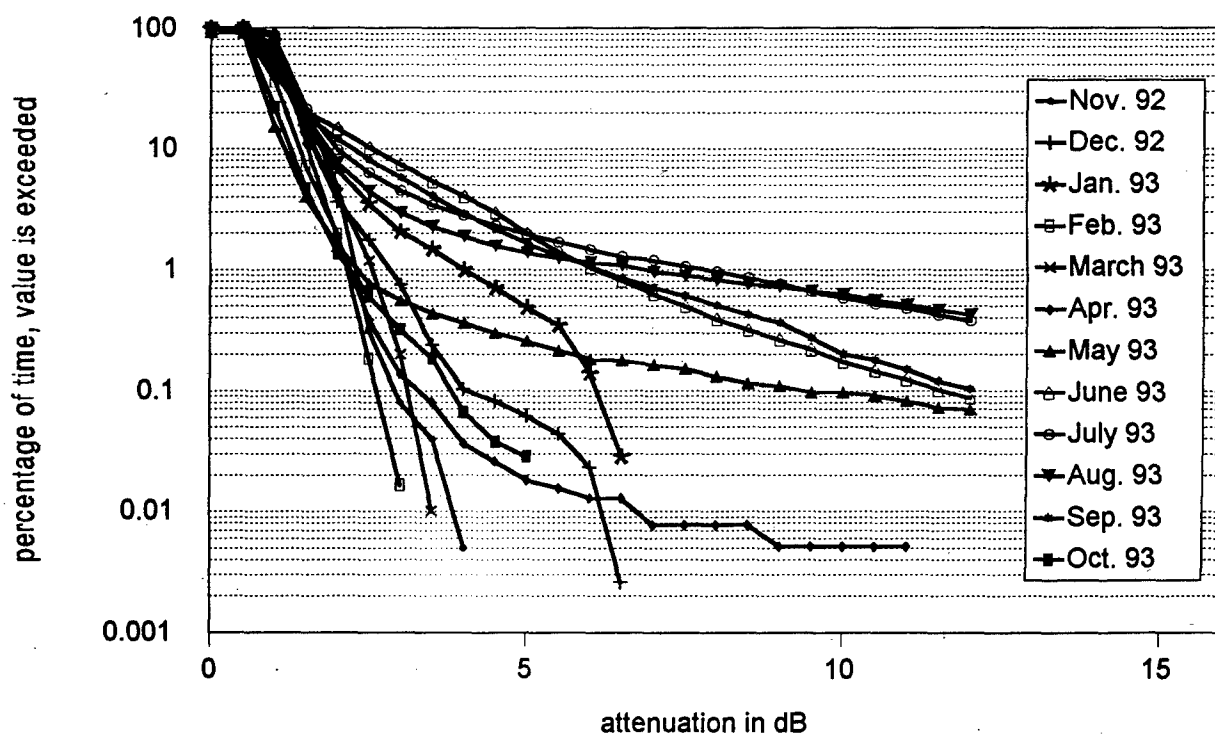


Figure 1: Cumulative distribution of attenuation at Dubna, November 1992 to October 1993

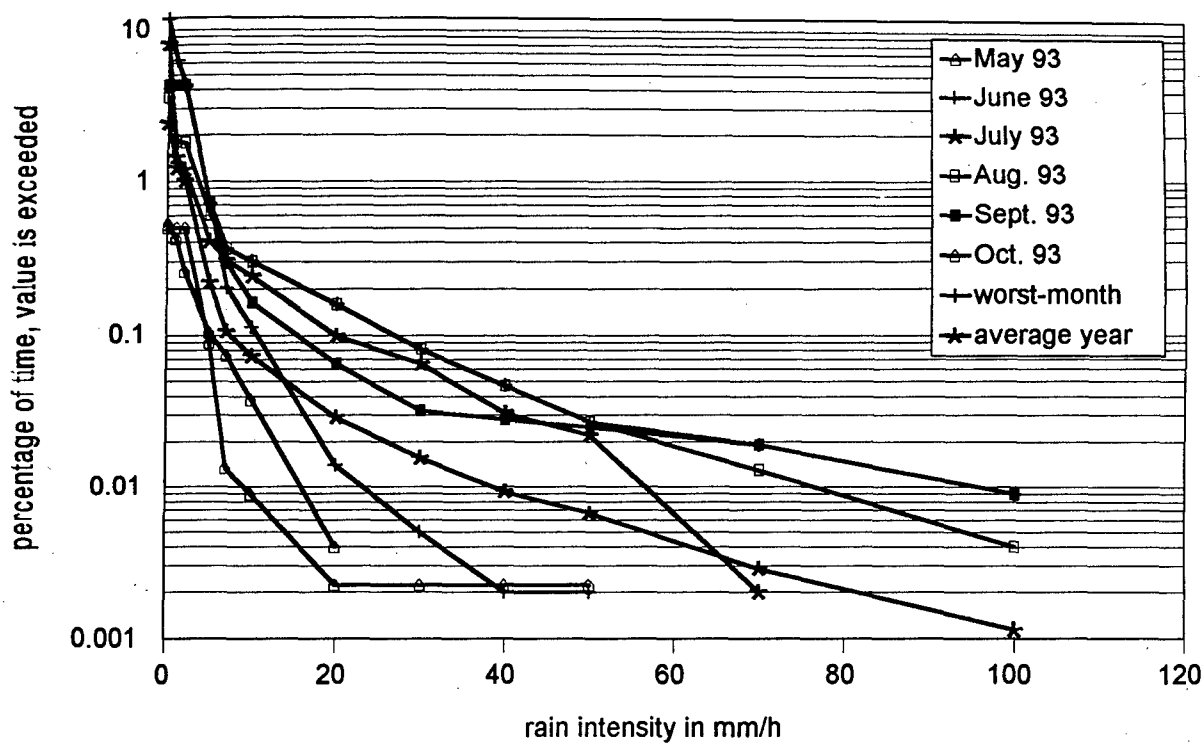


Figure 2: Cumulative distribution of rain intensities at Dubna, May to October 1993

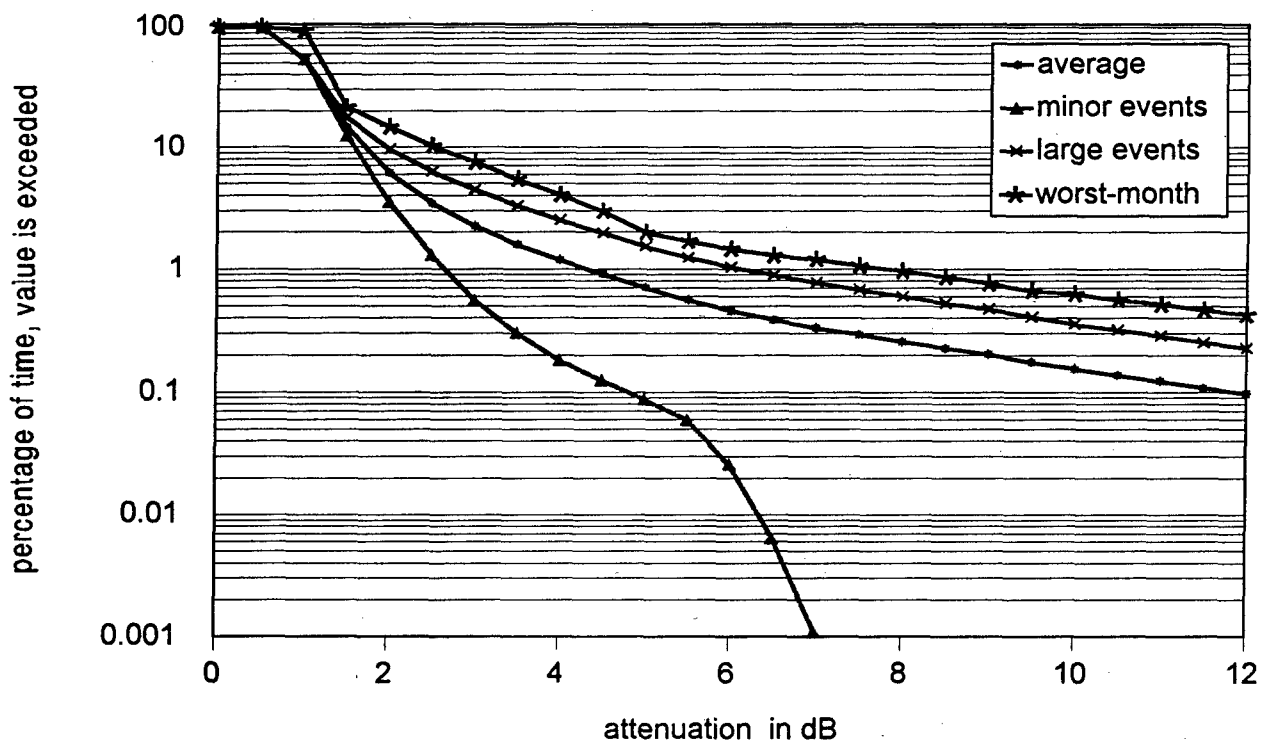


Figure 3: Cumulative distribution of attenuation for two periods:
 minor events: October 1993, November 1992 - April 1993
 large events: May 1993 - September 1993

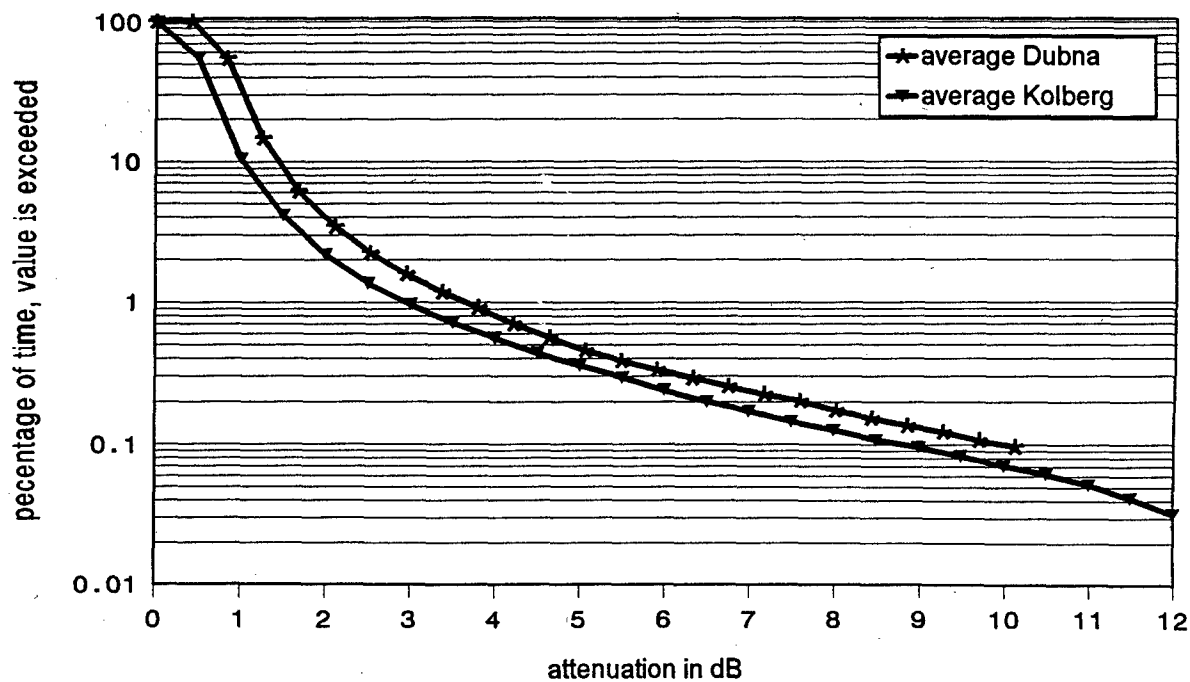


Figure 4: Cumulative distribution of attenuation at Dubna and Kolberg, elevation angle 30°

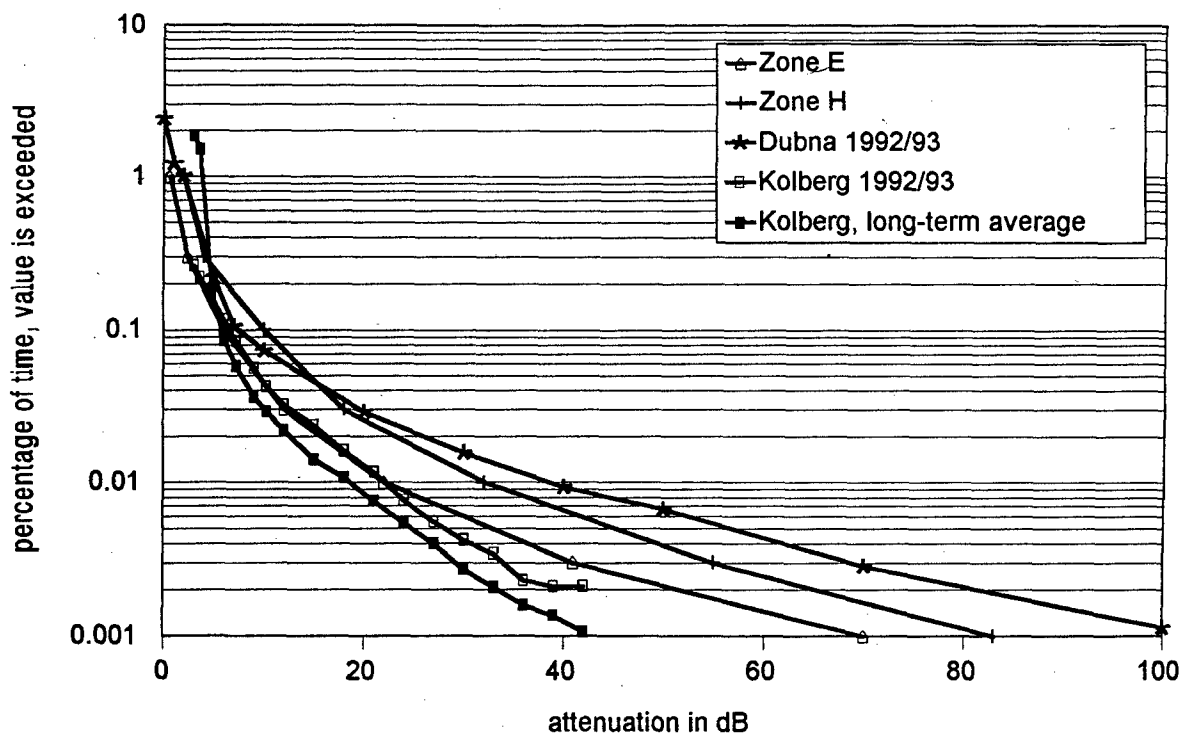


Figure 5: Cumulative distribution of rain intensities at Dubna and Kolberg with respect to ITU-R rain zones down to 0.001 % of time

Session 4: Precipitation III

MILLIMETER AND CENTIMETER WAVE ATTENUATION VARIATIONS DUE TO CLOUDY ATMOSPHERE

G.A.Andreyev¹, V.M.Plechkov, and O.K.Stankevich¹

¹ - Institute of Radioengineering and Electronics of the Russian Academy of Sciences

11 Mokhovaya St., GSP-3, Moscow 103907 Russia

Phone: (+7 095) 202-1591, Fax: (+7 095) 203-8414, e-mail: L112@uucp.ire.free.msk.su

ABSTRACT

For the prompt diagnostics of integral attenuation variations $\delta\Gamma$ in [dB] of clouded atmosphere thickness it is appropriate to estimate δT_B on the basis of radiobrightness temperature variations relatively to the minimal value T_- . It was derived the analytical dependence $\delta\Gamma = \delta\Gamma[\delta T_B, \bar{T}, \alpha_-(0, \lambda)]$, and the appropriate calculations carried out. As follows from theoretical evaluations, the variations of (radio) brightness temperature at wavelength $8 \cdot 10^{-3}$ m are more intensive than the variations at $13.5 \cdot 10^{-3}$ m. The data of the simultaneous measurements of brightness temperature at wavelengths of $8 \cdot 10^{-3}$ m and $13.5 \cdot 10^{-3}$ m are presented, under conditions of bulky cumulus cloudiness (Cu-cong).

Keywords: Diagnostics, variations, radiobrightness temperature, MM-Wave integral attenuation, cloudy atmosphere.

INTRODUCTION

Changes of cloud water contents of bulky convective and cumulus-nimbi clouds cause the integral attenuation variations, that leads to the essential variations of antenna temperature in radiometric systems and fading in Earth-space satellite communication systems (Ref.1-4). This fading can be reduced with the usage of adaptive receiving, but however it requires the expeditious data concerning the depth of random modulation, and correlation interval of radiobrightness temperature variations. There is good reason to obtain promptly this data from the radiophysical method of remote probing of

atmosphere thickness - by down-tending thermal radiation.

The aims of the paper were the following:

- to reveal theoretical dependence between radiobrightness temperature variations and integral attenuation of a layered-inhomogeneous thickness of cloudy atmosphere;
- to carry out the experimental testing of the methodics of prompt diagnostics of integral attenuation variations by the variations of clouded atmosphere brightness temperature;
- accumulating of experimental data concerning the depth of random modulation, and coefficients of auto- and mutual correlation of radiobrightness temperatures at two wavelengths.

Using the solution of transition equation radiation in cloudy atmosphere (Ref. 2), the expression of brightness temperature variations δT_B can be presented as follows:

$$\delta T_B(\lambda, \Theta) = \bar{T} \{1 - \exp(-\delta\alpha_w(\lambda, \Theta)) \cdot \exp(-\alpha_-(\lambda, \Theta))\}, \quad (1)$$

where $\bar{T} =$

$$\frac{\int_0^{\infty} \alpha(z) T(z) \exp(-\sec \Theta \int_0^z \alpha(z') dz') dz}{\int_0^{\infty} \alpha(z) \cdot \exp(-\sec \Theta \int_0^z \alpha(z') dz') dz}. \quad (2)$$

$\delta\alpha_w$ - integral attenuation variations of cloudy atmosphere, α_- - minimal integral attenuation at moisture Q and water W_- contents corresponding to the

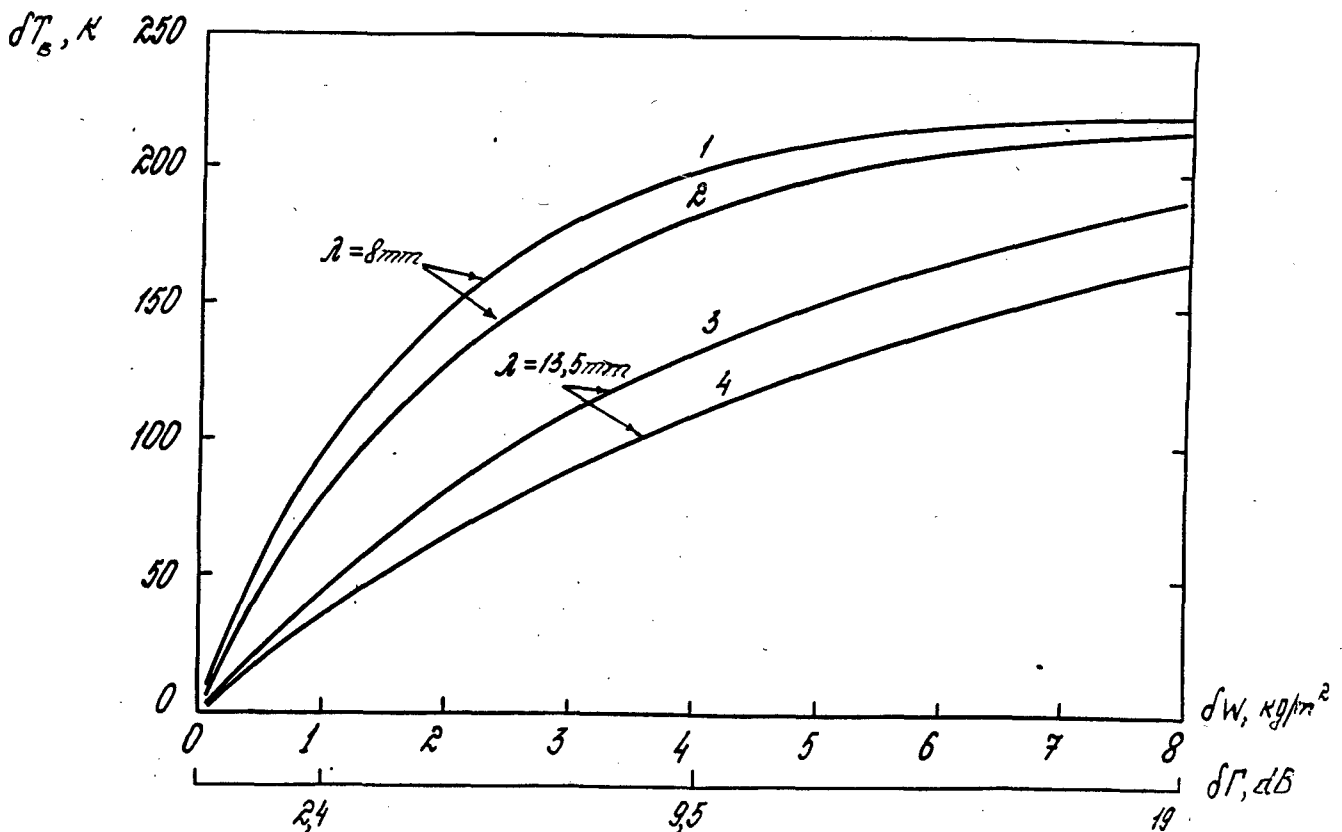


Figure 1. The dependence of radiobrightness temperature variations δT_B and corresponding integral attenuation variations $\delta \Gamma$, and water contents variations δW .

minimal values of brightness temperature. For the variations of absorption $\delta \Gamma_w$ in dB one can derive the following expression:

$$\delta \Gamma_w = 4.34 \ln \left(\frac{\bar{T}}{\bar{T} - \delta T_B e^{-\alpha_-(\lambda, \Theta)}} \right), [dB]. (3)$$

Fig.1 shows theoretical dependences of radiobrightness temperature variations δT_B versus the integral attenuation variations $\delta \Gamma_w = K_w \delta W$ corresponding to the water contents variations δW under the following conditions: $\bar{T} = 282K$, $\Theta = 60^\circ$, $\alpha_- = \alpha_z \sec \Theta = 2\alpha_z = 0.315$ for $\lambda = 8 \cdot 10^{-3}m$ (curves 1, 2), and $\alpha_- = 0.26$ for $\lambda = 13.5 \cdot 10^{-3}m$ (curves 3, 4).

As follows from theoretical estimations and data of Fig.1, at the change of cloud water contents from 0.08 to 8, the average temperature of atmosphere thickness $\bar{T} = 282K$, average cloud temperature $T_0 = 273K$ and zenith angle $\Theta = 60^\circ$, the variations of radiobrightness temperature at wavelength $8 \cdot 10^{-3}m$ can result

$\delta T_B = 9 \dots 206K$, and at wavelength $13.5 \cdot 10^{-3}m$ $\delta T_B = 3.5 \dots 176K$. This corresponds to the following attenuation variations: $\delta \Gamma_w = 0.19 \dots 19$ dB and $\delta \Gamma = 0.07 \dots 7$ dB.

The measurements of variations were carried out in summer and winter in Crimea at Caradag at a height approximately 50 above sea level. Fig.2 shows the simultaneous recordings of radiobrightness temperatures of clouded atmosphere at wavelengths $8 \cdot 10^{-3}m$ and $13.5 \cdot 10^{-3}m$, correspondingly, at the zenith angles $\Theta = 60^\circ$ and 62° in summer when it was the movement of bulky cumulus clouds (Cu Cong). The terrestrial temperature $T = 294K$. At the temporal intervals about 60 and 110 min the radiobrightness temperature at wavelength $8 \cdot 10^{-3}m$ exceeded 170K - i.e. the upper boundary of recording range achieved at wavelength $13.5 \cdot 10^{-3}m$. Attenuation Γ are presented in dB at the second ordinate axis for wavelength $8 \cdot 10^{-3}m$ at $\bar{T} = 282K$. The scale of Γ along the ordinate axis for wavelength $13.5 \cdot 10^{-3}m$ is practically the same due to negligible difference between $\bar{T}_{13.5}$ and \bar{T}_8 . At

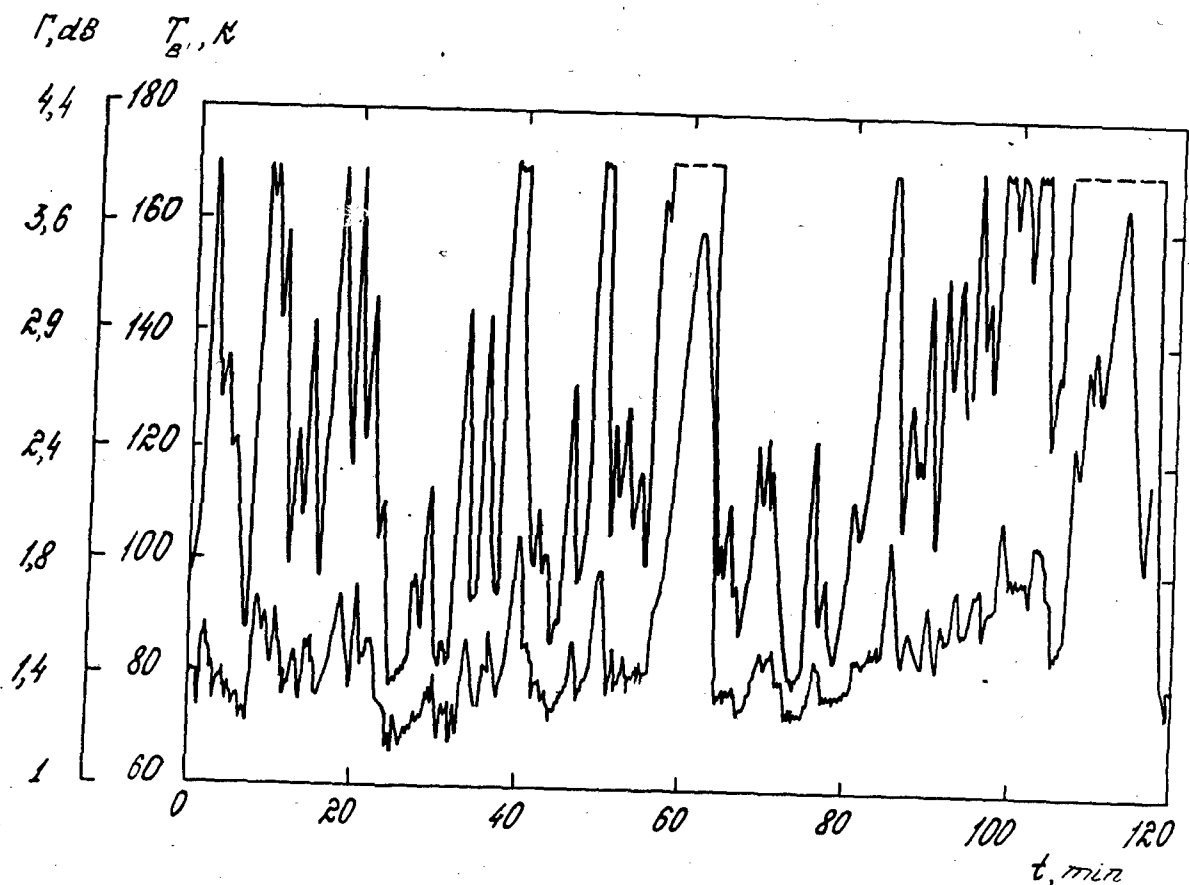


Figure 2. The recordings of fluctuated signals at the radiometers output under conditions of bulky cumulus cloudiness (Cu-cong). The upper curve corresponds to $\lambda = 8 \cdot 10^{-3} \text{ m}$, $\Theta = 60^\circ$. The lower curve corresponds to $\lambda = 13.5 \cdot 10^{-3} \text{ m}$, $\Theta = 62^\circ$.

the time about 24 min in Fig.2 for the experimental variation $\delta T_B = T_B - T_- = 140\text{K} - 80\text{K} = 60\text{K}$ at wavelength $8 \cdot 10^{-3} \text{ m}$ the variation of absorption $\delta \Gamma_w = 2.9\text{dB} - 1.4\text{dB} = 1.5\text{dB}$, and at wavelength $13.5 \cdot 10^{-3} \text{ m}$ is correspondingly, $\delta T_B = 88\text{K} - 68\text{K} = 20\text{K}$, and recording of radiobrightness temperature at wavelength $8 \cdot 10^{-3} \text{ m}$ was carried out with limitation, and at wavelength $13.5 \cdot 10^{-3} \text{ m}$ without it. At wavelength $13.5 \cdot 10^{-3} \text{ m}$ the temperature variations account for $\delta T_B = 158\text{K} - 68\text{K} = 90\text{K}$, and corresponded attenuation variations are $\delta \Gamma_w = 3.6\text{dB} - 1.13\text{dB} = 2.47\text{dB}$, water contents is $\delta W = 3.65 \text{ kg/m}^2$. For wavelength $\lambda = 8 \cdot 10^{-3} \text{ m}$ one can find that $\delta \Gamma_w = 2.47 \cdot 3.5 = 8.64\text{dB}$, that corresponds to $\delta T_B = 175\text{K}$. Fig.3 shows the autocorrelation coefficient of stationarized variations at wavelength $\lambda = 8 \cdot 10^{-3} \text{ m}$ (presented in Fig.2). The process of stationarization consisted of surge elimination within the temporal intervals of 60 and 110 min. and smoothing by Hamming with averaging time

$\delta \Gamma_w = 0.4\text{dB}$. It follows from theoretical estimations and the curves in Fig.1 that these radiobrightness temperature variations are corresponded to cloud attenuation variations with the average temperature a little bit more than 10°C . At the time about 60 min the interval of 10 min. As follows from correlation analysis, the correlation interval τ_x accounts for 2.3 min at wavelength $8 \cdot 10^{-3} \text{ m}$. The average temperature within the 110 min temporal interval was $T = 121\text{K}$ at wavelength $8 \cdot 10^{-3} \text{ m}$, the r.m.s. value is $\sigma_T = 26.6\text{K}$, and experimental variational factor $m_T = \sigma_T / \langle T \rangle = 0.21$.

The appropriate values at wavelength $13.5 \cdot 10^{-3} \text{ m}$ are the following: $\langle T \rangle = 81\text{K}$, $\sigma_T = 7\text{K}$, $m_T = 0.08$.

Therefore, the variations at wavelength $8 \cdot 10^{-3} \text{ m}$ are 2.5 times more intensive than at wavelength of $13.5 \cdot 10^{-3} \text{ m}$, and this coincides well with theoretical estimations.

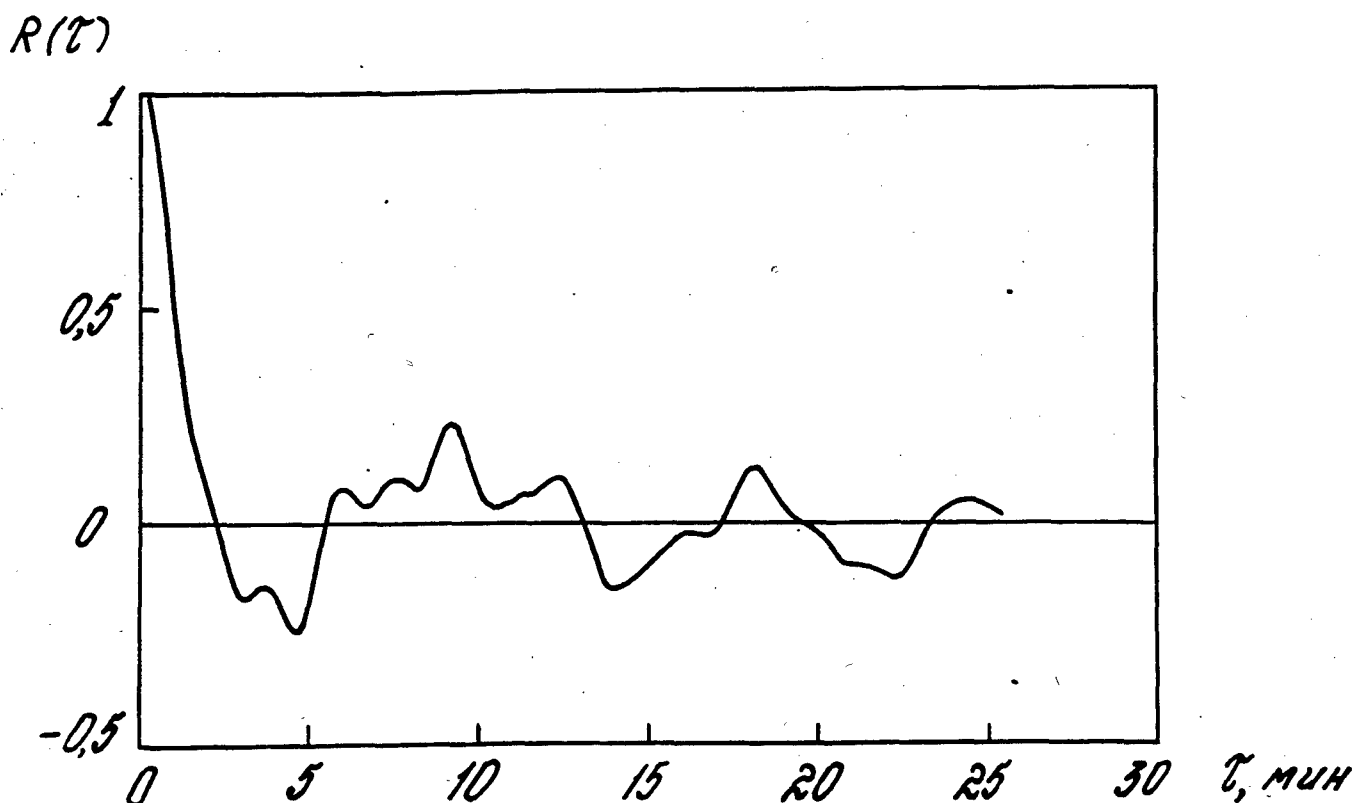


Figure 3. The autocorrelation coefficient of the stationarized variations from Figure 2.

CONCLUSION

The following main results were obtained:

- the dependence between radiobrightness temperature variations and integral absorption of conventional atmosphere thickness was derived;
- the found dependences made the basis for the methodics of experimental determination of integral attenuation of atmosphere thickness by the relative and absolute measurements of its own radiobrightness temperatures;
- the synchronous measurements at wavelengths $8 \cdot 10^{-3}$ m and $13.5 \cdot 10^{-3}$ m of radiobrightness temperature variations with the usage of derived relationships proved the possibility of an instant evaluation of integral attenuation in cloudy weather, and determination of moisture and water contents. For example, at variations of $\delta T = 10 \dots 175$ K at wavelength $8 \cdot 10^{-3}$ m and $\delta T = 5 \dots 90$ K at wavelength $13.5 \cdot 10^{-3}$ m the attenuation variations account for $\delta \Gamma_w = 0.2 \dots 8.64$ dB and $\delta \Gamma_w = 0.1 \dots 2.5$ dB, accordingly, that corresponds to the following

variations of a water contents: δW is up to 3.65 kg/m^2 at the values of moisture and minimal water contents: $Q = 20.6 \text{ kg/m}^2$ and $W = 1.1 \text{ kg/m}^2$, correspondingly.

REFERENCES

1. G.A. Andreyev, V.A. Golunov, V.A. Timofeev, In: Proc. 7th Colloq. Microwave Commun. (6 - 10 Nov. 1982, Budapest, Hungary).
2. G.A. Andreyev, O.K. Stankevich, In: Proc. JSEMC (8-10 Sept. 1989, Nagoya Japan), pp. 220.
3. G.A. Andreyev, V.M. Plechkov, O.K. Stankevich, In: Proc. 3rd All-Union School on MMW and Sub MMW Atmosph. Propagat. (Khar'kov, 1989), p. 159 (in Russian).
4. G.A. Andreyev, V.M. Plechkov, O.K. Stankevich, In: Proc. 16th All-Union Conf. on Radiowave Propag. (Khar'kov, 1990), p. 13 (in Russian).

STATISTICS OF CLEAR-AIR ATTENUATION, PRECIPITABLE WATER AND CLOUD LIQUID

Gerd Ortgies

Forschungs- und Technologiezentrum der Deutschen Bundespost Telekom, D-64276 Darmstadt, Germany
Tel: +49-6151-833848, Fax: +49-6151-834031, E-mail: fz233a@vmxa.fz.telekom.de

ABSTRACT

In this contribution it will be shown that a multi-frequency radiometer is a powerful tool to continuously monitor the cloud liquid and water vapour content of the atmosphere. Statistics of attenuation caused by these quantities including their seasonal and diurnal variations will be presented based on a data set of two years.

Keywords: Attenuation, Clouds, Water Vapour, Rain, Radiometer, Satellite Communications

1. INTRODUCTION

While clear-air attenuation can be neglected for most applications in satellite communications at lower frequencies, this is no longer the case when moving to higher frequency bands. Clear-air attenuation is mainly due to water vapour and oxygen absorption and occasionally also to clouds. Attenuation caused by these tropospheric constituents prevails for large fractions of time. Statistics for the larger time percentages are of particular interest to the planning of low-margin systems.

Besides its impact on satellite communications, liquid water and water vapour are important components for many meteorological processes in the atmosphere. Unfortunately, there is a lack of information on quantities like cloud liquid and its temporal and spatial variability. In the past, it was shown that the liquid water content in clouds as well as the ubiquitous water vapour can be determined from radiometer measurements carried out simultaneously at two different frequencies at least (Refs. 1-3). However, statistics are only available for short time periods.

2. SEPARATION OF ATTENUATION CAUSES

Radiometrically determined brightness temperatures, T_b , can be converted to attenuation, A , using the "radiometer equation"

$$A = 10 \log_{10} \frac{T_m - T_c}{T_m - T_b} \quad (1)$$

with T_m and T_c being the effective medium and the cosmic background temperatures, respectively. The total attenuation measured during clear-sky conditions on an earth-satellite path is the sum of contributions from, e.g., liquid water in clouds, from water vapour and from oxygen, i.e.

$$A(f) = a(f)L + b(f)V + c(f) \quad (2)$$

where L describes the columnar liquid water content and V the columnar water vapour content. The coefficients a , b and c are frequency dependent, with c being the oxygen attenuation. Values for these parameters can be calculated, e.g., from relations given in ITU-R recommendations (Ref. 4). From radiometer measurements carried out simultaneously at two different frequencies, preferably with one of which being more sensitive to water vapour attenuation, while attenuation at the other should be dominated by liquid water, a set of two linear equations based on Eq. 2 can be formulated and solved for L and V .

A three-frequency radiometer has been operated at Darmstadt, Germany, since summer 1991. Attenuation contributions caused by cloud liquid and water vapour have been separated on the basis of 1-

min mean values from the brightness temperatures measured at 21.3 and 31.7 GHz. In addition, a third frequency (23.6 GHz) is available at the radiometer, which has been used independently to judge the reliability from a comparison of results from different frequency pairs. Data have been evaluated separately for clear-sky periods and for periods with rain present on the propagation path. To distinguish between these periods, it was assumed that the onset of a rain event did not occur earlier than 20 minutes prior to the recording of the first rain drop on ground by a fast response rain gauge. Similarly, it was assumed that the rain event did not last longer than 20 minutes after the last rain drop was recorded.

An example of time series data of liquid water and water vapour attenuations at 31.7 GHz is presented in Fig. 1 for a period of one day. It should be noted that Eq. 2 is strictly valid only for clear-air periods. Nevertheless, it could be proved that the solutions of Eq. 2 are also meaningful during light rain. In this case, liquid water attenuation is caused by a mixture of rain drops and cloud droplets. For strong rain, the solutions for V are getting instable. Therefore, for these periods, V was estimated by interpolating between stable solutions and L was recalculated afterwards.

3. STATISTICAL RESULTS

Data were analysed for a period of 24 consecutive months starting with September 1991. For clear-sky conditions, cumulative statistics are shown in Figs. 2 and 3 for water vapour and cloud attenuation at 21.3 and 31.7 GHz, respectively. Attenuations measured on a 30° elevated path were transformed to zenith attenuation. The solid lines represent two periods of 12 consecutive months, respectively. For exceedance probabilities down to 0.01%, nearly no year-to-year variability can be observed for water vapour attenuation. For cloud attenuation at 31.7 GHz, annual cumulative statistics vary only by about 0.07 dB. For comparison, results of an earlier study (Ref. 2) are included as well, which were derived from simultaneous measurements with radiometers at 20 and 30 GHz at the same site for the period from July 1988 to June 1989. These data are in good agreement with the present results.

The seasonal variation of water vapour attenuation during clear-air intervals at 21.3 GHz is depicted in Fig. 4 for three exceedance probability levels for a period of two years. A strong seasonal attenuation

dependence was found, showing maximum values in summer and minimum values in winter. This behaviour could be expected, since, caused by higher ambient temperatures in summer, more water is evaporated into the atmosphere than in winter. For fixed exceedance levels, attenuations vary by a factor of about two in the course of a year. Apparently, the annual pattern does not change significantly from year to year. The results were compared with a similar evaluation for the same period but including time intervals with rain as well. No significant difference was found, neither for the magnitude of attenuations nor for their seasonal distributions.

For cloud attenuation during clear-air periods, the seasonal dependence is not that distinct as for water vapour attenuation. For monthly exceedance probabilities of 0.1 and 1% of the time, a tendency towards higher values was found for October to January, while lower cloud attenuations were found in spring and early summer. This behaviour can be explained by more frequent cloud coverage occurring in late autumn and winter. For low exceedance probabilities, however, this trend is not well marked. Very high values were found in this case in summer, reflecting heavy clouds just before the occurrence of thunderstorms.

A similar analysis for the total measuring period including rain showers showed similar results. In this case, the liquid water attenuation is caused by a mixture of rain and clouds. As a consequence, attenuations are significantly higher for the same exceedance levels as compared to the clear-air period.

In addition to the seasonal dependence of attenuation components, their diurnal distribution was investigated as well. To this end, statistics for eight three-hour time intervals per day were derived. Such statistics based on calendar months showed no uniform distributions neither for cloud nor for water vapour attenuation. Therefore, the diurnal distribution was calculated for the complete 24-months period as a whole. Statistics were derived separately for clear-air periods, for pure rain time intervals and for the total measuring period. Examples of results are presented for liquid water and for water vapour attenuation in Figs. 5 and 6 for the clear-air case.

Water vapour attenuation (Fig. 5) exhibits no pronounced diurnal pattern. Instead, the data appear to be independent of the time of the day. As stated earlier, no significant differences could be observed

between clear-air and rain periods being the basis for the statistics. For liquid water attenuation (Fig. 6), the situation is different. For clear-air periods, again, no diurnal pattern was found for exceedance levels greater than about 1% of the time. For lower exceedance probabilities, however, a trend towards higher values was observed for the afternoon and the early evening. Considering only periods with rain, this trend gets more pronounced which is in agreement with results of an analysis of rain data over a period of eight years (Ref. 5).

4. CONCLUSION

It could be shown that a multi-frequency radiometer is a powerful tool to continuously monitor the liquid water and water vapour attenuations on earth-satellite paths. Statistics for these quantities including their seasonal and diurnal variations were presented for a period of 24 consecutive months showing a sinusoidal annual distribution of water vapour attenuation with maximum values in summer. No diurnal pattern was found for water vapour attenuation, while for liquid water attenuation, a tendency towards higher values in the afternoon can be observed for low exceedance probabilities. Its seasonal distribution exhibits lower values for spring and early summer than for late autumn and winter.

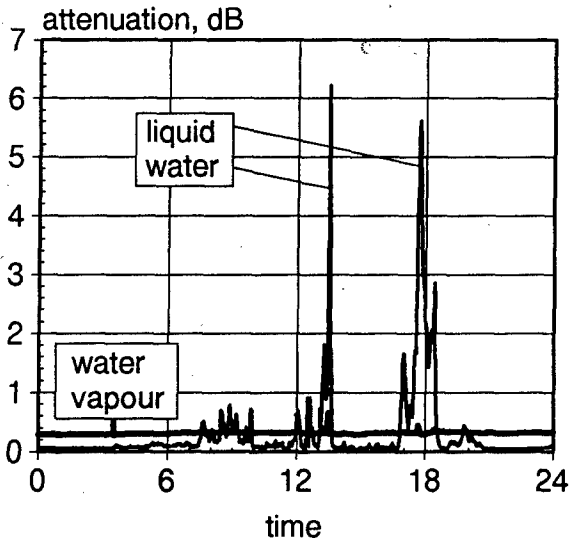


Figure 1: Time series data of radiometrically determined attenuation at 31.7 GHz and its contributions from liquid water and water vapour (elevation angle 30°).

5. REFERENCES

1. Guiraud, F O et al. 1979, A dual-channel microwave radiometer for measurement of precipitable water and liquid, *IEEE Transactions on Geoscience Electronics*, GE-17,4, pp. 129-136
2. Ortgies, G 1990, Statistics of clear-air attenuation on satellite links at 20 and 30 GHz, *Electronics Letters* 26,6, pp. 358-360
3. Fionda, E et al. 1991 Attenuation statistics at 20.6, 31.65 and 52.85 GHz derived from emission measurements by ground-based microwave radiometers, *IEE Proceedings-H*, 138,1, pp. 46-50
4. ITU-R Rec. 676-1 1992, Attenuation by atmospheric gases in the frequency range 1-350 GHz.
5. Ortgies, G 1994, Rain rate and its temporal variability measured for a period of eight years at Darmstadt, this issue

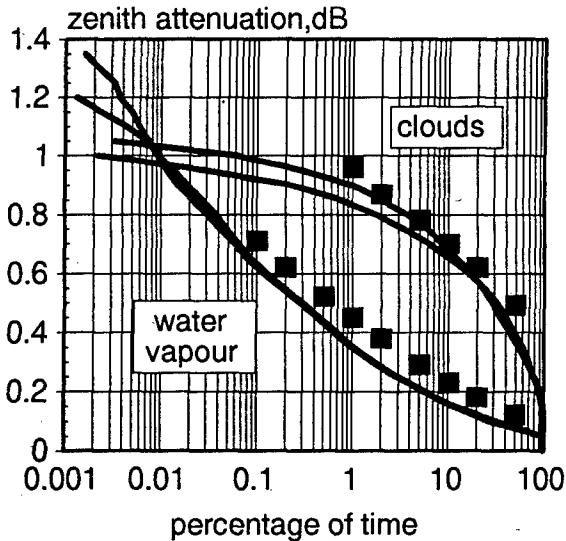


Figure 2: Annual cumulative distributions of clear-air water vapour and cloud liquid attenuation at 21.3 GHz (Squares: data from Ref. 2, see text).

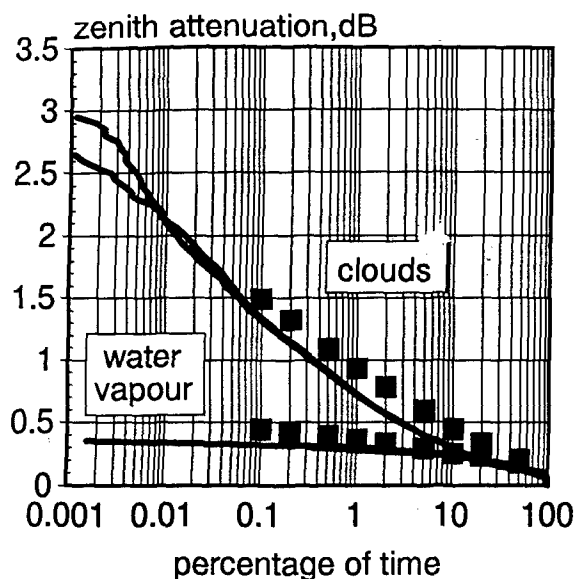


Figure 3: Annual cumulative distributions of clear-air water vapour and cloud liquid attenuation at 31.7 GHz. (Squares: data from Ref. 2, see text).

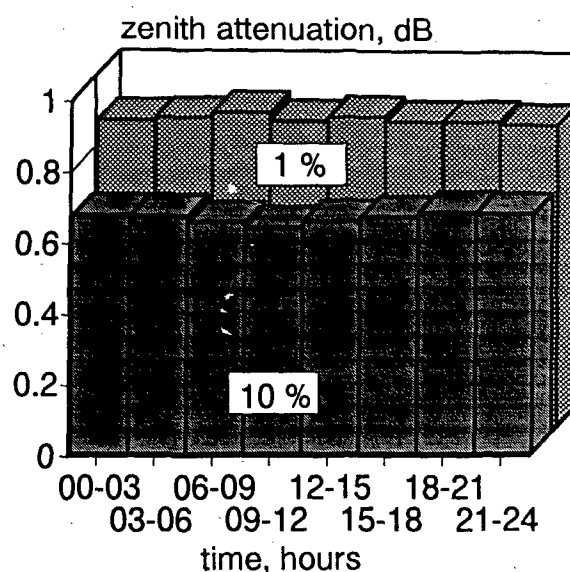


Figure 5: Diurnal distribution of water vapour attenuation exceeded for 10 and 1 % of the clear-air periods for 21.3 GHz.

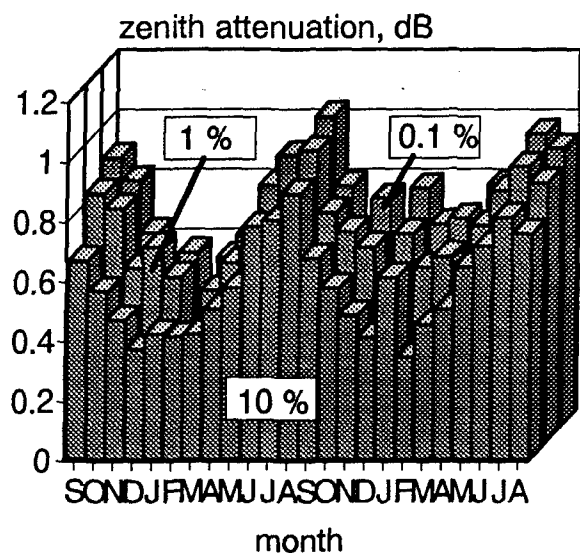


Figure 4: Seasonal variation of water vapour attenuation exceeded for 10, 1, and 0.1 % of the clear-air periods for 21.3 GHz.

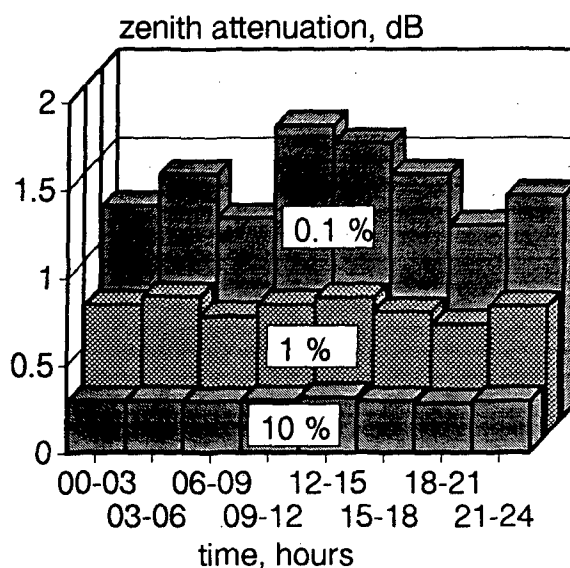


Figure 6: Diurnal distribution of cloud attenuation exceeded for 10, 1, and 0.1% of the clear-air periods for 31.7 GHz.

CONCURRENT OCCURRENCES OF DEEP FADINGS DUE TO HYDROMETEORS AND HEAVY RAIN INTENSITIES ON A 15 km PATH AT 15 GHz

V. Kvičera

TESTCOM, Hvožd'anská 3, 148 00 Praha 4, Czech Republic
Tel: + 42 2 7992 225, Fax: + 42 2 7992 318

ABSTRACT

The experimental research of electromagnetic wave propagation was performed on a 15 km line-of-sight path at 15 GHz with H polarization. Rain intensities were measured by a syphon raingauge. Experimentally obtained time distributions of fadings due to hydrometeors as well as rain intensities for the worst month of the individual years are analysed.

Keywords: Attenuation due to hydrometeors, rain intensity

1. INTRODUCTION

For 5 consequent years (1988-1992), the PTT Research Institute Prague (now TESTCOM) performed experimental research of electromagnetic wave propagation on a line-of-sight path, 15.3 km long, at the frequency 14 920 MHz with H polarization. Off-set antennas of ϕ 50 cm were used. Rain intensities were measured by a syphon raingauge placed at one end of the path.

2. EXPERIMENTAL RESULTS

Both maximum fading due to hydrometeors and maximum average 5-minute rain intensity for the worst month, their date and time of occurrence, duration, concurrent rain intensity and fading for individual years are presented in Tables 1 to 5.

Table 1 Maxima of both rain intensity and fading due to hydrometeors for the worst month 1988

1988 - WM	A_{\max}	$R(5)_{\max}$
value	> 36 dB	129 mm/h
date	Aug 12	Jul 24
time	17.08	21.05
duration	2.8'	5'
concurrent $R(5), A$	0 mm/h	0 dB

Table 2 Maxima of both rain intensity and fading due to hydrometeors for the worst month 1989

1989 - WM	A_{\max}	$R(5)_{\max}$
value	> 37 dB	185 mm/h
date	Jul 18	Jul 26
time	13.22	16.10
duration	0.2'	5'
concurrent $R(5), A$	0 mm/h	16 dB

Table 3 Maxima of both rain intensity and fading due to hydrometeors for the worst month 1990

1990 - WM	A_{\max}	$R(5)_{\max}$
value	> 37 dB	69 mm/h
date	May 16	Aug 15
time	19.37	14.10
duration	0.5'	5'
concurrent $R(5), A$	0 mm/h	12 dB

(i.e. for $A > 6$ dB) was composed of fadings in August and June.

1989

In 1989, the worst month for fadings due to hydrometeors was derived from July for fadings greater than 15 dB as well as from 1 to 7 dB, and from May for fadings in the range 8 to 14 dB.

In July, fadings greater than 15 dB were composed of two fade events:

- 1) on July 18 from 13.21 to 13.25; fading greater than 37 dB occurred at 13.22,
- 2) on July 26 from 15.54 to 16.10; fading up to 36 dB occurred at 16.05.

From records of rain intensities it follows:

- 1) on July 18 rain occurred from 13.25 to 13.35 with rain intensity of 1 mm/h,
- 2) on July 26 rain occurred from 15.45 to 16.50 with maximum rain intensity of 185 mm/h at 16.10.

The worst month for rain intensities was derived from July for intensities from 3 to 185 mm/h, and from September for intensity of 1 mm/h.

Although fadings due to hydrometeors greater than 15 dB for the worst month were composed of events on July 18 and 26, the heavy rain intensities for the worst month were composed of events on July 26.

The time distribution of rain intensities for the worst month and for percentages of time smaller than 0.64% (i.e. for $R(5) > 3$ mm/h) was composed of rain intensities only during July while the time distribution of fadings due to hydrometeors for the worst month and for the same percentages of time (i.e. for $A > 4$ dB) was composed of fadings in July and May.

1990

In 1990, the worst month for fadings due to hydrometeors was derived from May for fadings greater than 29 dB, and from June for fadings in the range 5 to 28 dB.

In May, fadings greater than 29 dB were composed of one fade event on May 16 from 19.37 to 19.39; fading greater than 37 dB occurred at 19.37.

From records of rain intensities it follows that rain occurred on May 16 from 19.25 to 19.35 with maximum rain intensity of 5 mm/h at 19.30.

The worst month for rain intensities was derived from August for intensities from 23 to 69 mm/h, from May for intensity of 21 mm/h, and from June in the range 3 to 15 mm/h.

Although fadings due to hydrometeors greater than 29 dB for the worst month were composed of event on May 16, the heavy rain intensities for the worst month were composed of events on August 15, May 9, June 8, 21 and 28.

The time distribution of rain intensities for the worst month and for percentages of time smaller than 0.6% (i.e. for $R(5) > 3$ mm/h) was composed of rain intensities during August, May and June while the time distribution of fadings due to hydrometeors for the worst month and for the same percentages of time (i.e. for $A > 4$ dB) was composed of fadings in May and June.

1991

In 1991, the worst month for fadings due to hydrometeors was derived from August for fadings greater than 32 dB as well as from 1 to 5 dB, and from July for fadings in the range 6 to 31 dB.

In August, fadings greater than 32 dB were composed of one fade event on August 1 from 17.40 to 17.57; fading greater than 39 dB occurred from 17.42 to 17.52.

From records of rain intensities it follows that rain occurred on August 1 from 17.30 to 18.50 with maximum rain intensity of 19 mm/h at 17.50,

The worst month for rain intensities was derived from July for intensities from 11 to 55 mm/h, and from June for intensities up to 9 mm/h.

Although fadings due to hydrometeors greater than 32 dB for the worst month were composed of event on August 1, the heavy rain intensities for the worst month were composed of events on July 13.

The time distribution of rain intensities for the worst month and for percentages of time smaller than 1% (i.e. for $R(5) > 3$ mm/h) was composed of rain intensities during June and July while the time distribution of fadings due to hydrometeors for the worst month and for the same percentages of time (i.e. for $A > 4$ dB) was composed of fadings in August and July.

Table 4 Maxima of both rain intensity and fading due to hydrometeors for the worst month 1991

1991 - WM	A_{\max}	$R(5)_{\max}$
value	> 39 dB	55 mm/h
date	Aug 1	Jul 13
time	17.42	8.55
duration	9.7'	5'
concurrent $R(5), A$	20 mm/h	5 dB

Table 5 Maxima of both rain intensity and fading due to hydrometeors for the worst month 1992

1992 - WM	A_{\max}	$R(5)_{\max}$
value	> 37 dB	61 mm/h
date	Jun 6	Aug 10
time	10.36 10.48	18.35
duration	6.6'	5'
concurrent $R(5), A$	0 mm/h	25 dB

The measured time distributions of fadings due to hydrometeors for the worst month during the warm period (from April to October) of the individual years are drawn in Fig. 1.

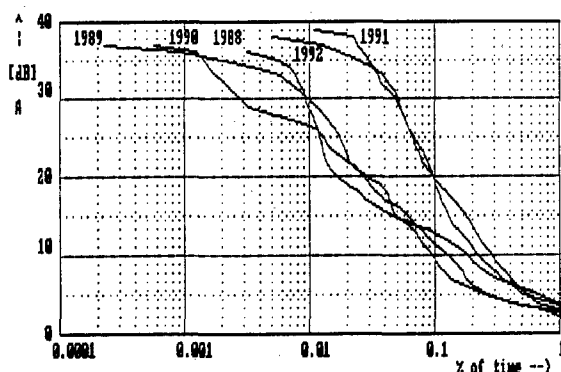


Fig. 1 The measured time distributions of fadings due to hydrometeors for the worst month of the individual years

The measured time distributions of average 5-minute rain intensities for the worst month of observation from April to October of the individual years are shown in Fig. 2.

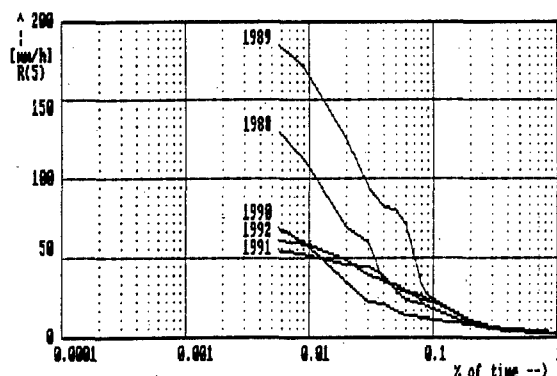


Fig. 2 The measured time distributions of average 5-minute rain intensities for the worst month of the individual years

1988

In 1988, the worst month for fadings due to hydrometeors was derived from August for fadings greater than 20 dB as well as from 8 to 14 dB, and from June for fadings in the range 16 to 18 dB.

In August, fadings greater than 20 dB were composed of two fade events:

- 1) on August 12 from 17.07 to 17.13; fading greater than 36 dB occurred at 17.08,
- 2) on August 16 from 17.25 to 17.27; fading up to 21 dB occurred at 17.26.

From records of rain intensities it follows:

- 1) on August 12 rain occurred from 14.20 to 14.50 with maximum rain intensity of 31 mm/h at 14.35,
- 2) on August 16 rain occurred from 17.05 to 17.35 with maximum rain intensity of 25 mm/h at 17.10.

The worst month for rain intensities was derived from July for intensities from 5 to 129 mm/h, and from June for intensities in the range 1 to 3 mm/h.

Although fadings due to hydrometeors greater than 20 dB for the worst month were composed of events on August 12 and 16, the heavy rain intensities for the worst month were composed of events on July 24 (for the same probabilities).

The time distribution of rain intensities for the worst month and for percentages of time smaller than 0.48% (i.e. for $R(5) > 5$ mm/h) was composed of rain intensities during July while the time distribution of fadings due to hydrometeors for the worst month and for the same percentages of time

1992

In 1992, the worst month for fadings due to hydrometeors was derived from June for fadings greater than 37 dB as well as from 12 to 21 dB, and from August for fadings from 22 to 36 dB as well as up to 11 dB.

In June, fadings greater than 37 dB were composed of two fade events on June 6 from 10.36 to 10.41 and from 10.48 to 10.50.

In August, fadings from 22 to 36 dB were composed of two fade events:

- 1) on August 4 from 3.24 to 3.29; fading up to 36 dB occurred at 3.26,
- 2) on August 10 from 18.11 to 18.53; fading up to 36 dB occurred at 18.51.

From records of rain intensities it follows:

- 1) on June 6 rain occurred from 10.50 to 12.45 with maximum rain intensity of 25 mm/h at 11.30,
- 2) on August 4 rain occurred from 3.20 to 7.45 with maximum rain intensity of 31 mm/h at 3.25,
- 3) on August 10 rain occurred from 16.40 to 19.10 with maximum rain intensity of 61 mm/h at 18.35.

The worst month for rain intensities was derived from August for intensities from 7 to 61 mm/h and from June for intensities in the range 3 to 5 mm/h.

Although fadings due to hydrometeors greater than 37 dB for the worst month were composed of events on June 6, the heavy rain intensities for the worst month were composed of events on August 10.

Both the time distribution of rain intensities and the time distribution of fadings due to hydrometeors for the worst month and for percentages of time smaller than 0.75% (i.e. for $R(5) > 3$ mm/h and $A > 4$ dB) was composed of August and June.

The PTT Research Institute Prague performed the investigation of fadings due to hydrometeors on a line-of-sight path, 43.8 km long, on the frequency 13 143 MHz with V polarization. The investigation was performed from 1988 to 1992. The path was situated in the south of Slovakia, from Mostová to Bratislava - Kamzík. Rain intensities were measured by 2 syphon raingauges. One raingauge was placed near Bratislava - Kamzík (Bratislava - Airport) the other one was placed in

about the middle of the path (Kráľová pri Senci), in the same climatic zone.

The gained time distributions of 5-minute rain intensities for an average year as well as for an average worst month are drawn jointly in Fig. 3 (marked 2 and 3). There are also the time distributions of 5-minute rain intensities for an average year and for an average worst month for the same period 1988 - 1992 gained by the processing of 5-year measurements of rain intensities in PTT Prague (marked 1).

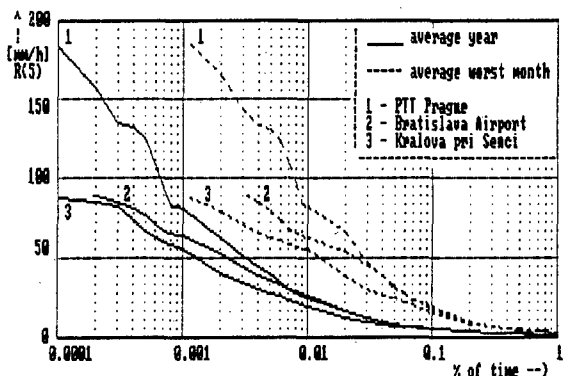


Fig. 3 Time distributions of rain intensities

Differences reach up to 18 mm/h between the time distributions gained in the same climatic zone in the south of Slovakia (station 2 and 3). Rain intensities in the PTT station (station 1) were much greater than rain rates in the Slovakia.

3. CONCLUSION

It was found that during rain events, the maximum fade and maximum rain rate were not strictly concurrent, i.e. coincident in time. This fact may be explained by the small rain cell diameters for the high rain rates. The great year variability of the time distributions of rain intensities as well as rain attenuations was shown. The climatic dependence of the time distributions of rain intensities is evident. Our results support the necessity of the long-term experimental investigations of both fadings and rain rates to gain the representative distributions for the specific climatic conditions.

RADAR INVESTIGATION OF MELTING LAYER

Alexander V. Kochin

CAO, 141700, Dolgoprudny, Moscow region, Russia

Tel: 7 095 408 7460 Fax: 7 095 576 3327

ABSTRACT

Result of the melting layer investigation by polarization and Doppler radar is given. On basis of the radar data the conclusion is made about presence in lower part of melting layer the region, in which breaking drops give the greater contribution to the reflectivity than other hydrometeors. The analysis of the possible enlargement of hydrometeors size distribution is presented on the basis of the capture drops by melting ice crystals. The theoretical model is proposed to calculate the reflectivity, differential reflectivity and Doppler velocity profiles in the melting layer.

Keywords: Melting Layer, Differential Reflectivity, Breaking Drops.

1. INTRODUCTION.

The melting layer is called in the radiometeorology bright band (Ref.1), because in this region the reflectivity increases significantly in comparison with regions above and below melting layer. Last investigation of melting layer by polarization and Doppler radar is showed, that the maxims of differential reflectivity and Doppler velocity profiles are presented in lower part of bright band. In spite of many theoretical and experimental works the successful explanation of this has not been obtained yet. This work is an attempt to explain this phenomena by backscatter from large breaking drops.

2. RADAR EQUIPMENT.

The experimental investigation of melting layer by polarization radar was made by the author in middle of 80-th by using experimental polarization weather X-band radar, (Refs.2,3). The radar repetition frequency was 600 Hz, the pulse length was 1.0 ms. The beamwidth was 0.75 deg, the switch polarization isolation was 26 dB. The beamwidth at horizontal

and vertical polarizations were identical in order to avoid the error in measuring differential reflectivity (Ref.4), when there was a high gradient of reflectivity in examining volume. The averaging time was 1 s and the total accuracy of measuring differential reflectivity was 0.25 dB. The differential reflectivity is defined as the ratio of reflectivity on horizontal polarization to vertical one expressed in dB.

Doppler data were obtained by using X-band radar with repetition frequency 2 Hz, pulse length 0.3 ms and pulse-pair processing system, but system processing permitted space resolution 240 m. The beamwidth was 0.75 deg. Experiments were made in summer and fall 1993

3. EXPERIMENTAL DATA.

The investigation of bright band by polarization radar had shown that in its lower part there is maximum of differential reflectivity (ZDR). The value of ZDR is 0.5...3.5 dB. An effect was practically observed in the all types of clouds leading to the precipitation. For instance, it takes place in the powerful connective clouds and even in the thunderstorm in a period of lighting activity. The height of layer with increasing ZDR is about hundred meters and its location is lower part of bright band. An example of vertical profile of ZDR is given on fig. 1.

Doppler radar data was received by Doppler weather radar with vertically oriented antenna. Vertical profilers of reflectivity and Doppler velocity is shown on fig.1. Both profiles were averaging on 360 individual profiles of reflectivity and Doppler velocity respectively. The total averaging time was 200 s. Polarization and Doppler data were not received simultaneously, because of this the combination of data on fig.1 was made to coincidence maximum of reflectivity. The rain rate was similar in both cases about 3 mm/h. The values of decreasing of reflectivity, maximum ZDR and maximum Doppler velocity were 12 dB, 2 dB and 9 m/s respectively. Similar data were obtained by many other research groups (Refs. 5,7).

The measurement form of Doppler

spectrum in melting layer were made by Pinsky, (Ref.8). The Doppler spectrum above bright band had one maximum, in middle of bright band had two maxima, in lower part of bright had three maxima and under bright band had one maximum. The third high frequency maximum in lower part of bright band had central velocity 9 m/s, which corresponds the terminal velocity fall of drops with diameter 4 mm.

4. ANALYSIS OF THEORY OF BRIGHT BAND.

An increase of radar reflectivity in bright band is conditioned by following mechanism. First, the ice particles melt without essential change of their form approximately the 90% of ice will melted and then they transform into the drops. Since a dielectric constant of water is higher one of ice, a radar reflectivity increases. Indeed, a particle velocity of fall changes not very essentially before its transformation into drop. Hence, a concentration hydrometeors does not change. After the melting the velocity of fall increases drastically, the concentration slow down and as a result the reflectivity decreases. Besides of the above effects, the increase of reflectivity gives 6dB(Ref 1). Ordinary the increase of reflectivity in the bright band gives the value 10...14dB.

It can explained by the particle's aggregation or the large scattering of semimulted particles (Ref.6)

The investigation of bright band by polarization radar has shown there is a reflection of radiowaves from nonspherical particles having horizontally big axis the reflectivity in the horizontal polarization is turned out to be higher in vertical one in lower part of bright band. This can not explained by scattering on the semimulted crystals (Refs.5,7), since the investigation of the orientation of falling crystals and snow flakes has shown that the orientation at fall is noticed only for definite crystals of simple enough forms and small sizes for which the Reynolds number is not large and the streamline is laminar. For the large particles the streamline will be turbulent. Therefore they will be rotated chaotically at fall independently on their form. There was a attempt to explain above effect taking into account idea that the ice crystals are transformed into the large drops with diameter 2...3 mm which then will dry till the size 1...1.5 m (Ref.10). Such an explanation is incredible since the band of higher differential reflectivity ZDR has a height almost 100 m. It excludes a possibility of

above change the size in process of evaporation even in absolutely dry air. This situation is quite impossible in the case when the lower boundary of the cloud is situated below the melting layer. However the height of the layer with higher ZDR does not change.

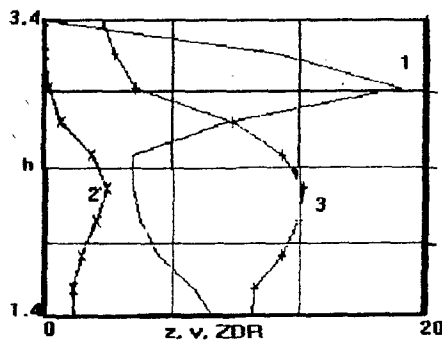
5. DISTRIBUTION OF DROPS AND SNOWFLAKES IN MELTING LAYER.

Consider snowflake or ice crystal which falls in region with positive temperature and calculate the distance to full melting of ice. If this process is defined only by heat transfer from air to particles and condensations not considered, then the distance is given by the equation

$$L = \sqrt{\frac{C_m \rho_w U(D)}{6 \gamma K}} \sqrt{\frac{\rho_{ice}}{\rho_w}} D(1)$$

where L is the distance of full melting, C_m is latent heat of melting, ρ_w is the density of water, $U(D)$ is the fall velocity, γ is vertical temperature gradient, K is the heat conductivity of air, ρ_{ice} is density of ice particle, D is diameter of drop with volume equal to ice particles.

According ice particle. This equation gives a simple estimate of melting distance, only because many factors are neglected (Ref.9). However, it gives the possibility to consider a melting layer as a spatial filter where on each height smaller hydrometeors with diameters from 0 to $D(h)$ are drops and lower hydrometeors at



1-reflectivity, 2-Doppler velocity, 3- ZDR.

Figure 1: Experimental data 6 July 1993. The time of averaging is 2 minutes. The distance between points is 240 m. ZDR data were obtained earlier.

$P(h)$ to D_{\max} are melting ice particles. According to Eq.1 $D(h)$ is given a linear function of height. Respectively the backscatter on each height are given by mixture of drops and melting ice particles. In lower part of melting layer there are no small crystals and only drops and large crystals give backscatter. Indeed there are only drops, under melting layer. Drops with diameters larger than 4...5 mm are unstable and break up. If hydrometeors size distribution has large crystals which have equal volumes with unstable drops, these crystals give thin layer with breaking drops in low part of melting layer. The consideration of backscatter by this layer explains of radar data.

6. EXPLANATION OF RADAR DATA.

Breaking large drops is a well knowing process, (Ref.11). After the first stage a drop transfers into a thin disk with the diameter of 2...3 cm. Then the central part of the disk becomes a form like a parachute and breaks into several hundred of small drops. After that the periphery ring breaks into 4...5 relatively large drops. The breaking time is about 0.02 s. The reflectivity of breaking drops is $10^4 \dots 10^5$ as great as that of the initial drop. Because of this, drops give large backscatter signals. The reflectivity of a horizontally polarized signal is greater than of a vertically polarized signal and ZDR is positive. The velocity of breaking drop is equal to initial velocity because the drops which arise by breaking a drop keep initial velocity over breaking time. Therefore they give a maximum in the profile of vertical Doppler velocity.

Above the melting layer, ice crystals and snow flakes give one maximum in Doppler spectrum. In the middle of the melting layer snowflakes and drops give two maxima in the Doppler spectrum. In the low part of melting layer show flakes, drops, and breaking drops give three maxima in the Doppler spectrum. Under melting layer drops give one maximum.

7. EMPIRICAL MODEL OF BACKSCATTER BY MELTING LAYER.

The backscattering cross - section of breaking drops is not determined yet. However, the theoretical evaluation is possible by calculating observed profile of radar data. The profiles of Doppler velocity is measured more exactly than other profile. Because of that the

calculation at the first stage was made to make consistent experimental and theoretical profiles of Doppler velocity. It needs that the backscatter of breaking drops were greater at 6...10dB than at drops. After this ZDR profiles was made by substitution of the value of ZDR 3.5dB to breaking drops because the maximum ZDR value in lower part of melting layer which was observed in our experiments was 3.5dB. The theoretical ZDR profiler was in a good agreement with experimental one. By this conditions the theoretical profiles of reflectivity had two maxims. The analysis of data of aircraft weather radar with high resolution shows the presence of this phenomena in melting layer.

8. CAPTURE DROPS BY SNOW-FLAKES.

It is doubtful that very large crystals constantly exist in stratiform clouds upper melting layer. But radar data showed exactly that these crystals exist in lower part of melting layer.

In order to make it clear, the author studied one more mechanism of forming these crystals. There was considered a possibility of capture of already melted show flakes (drops) by the ice particles of different sizes. Since the ice particles have a lower velocity of fall then the drops and since they also have a bigger surface because of lower volume density, the increase of the particle volume with equivalent diameter C^* may be defined as a layer of the precipitation falling the crosssection $s(C^*)$ moving down with the velocity $g(C^*)$. It leads to

$$\frac{dv}{dt} = \frac{\pi}{6} \int_0^D N(d)[U(d) - g(C^*)]dd \quad (2)$$

where D is maximum diameter of already melted snow flakes, d is diameter of drops, $N(d)$ is their distribution over sizes, $U(d)$ is a velocity of fall.

Considering the all parameters in the Eq.2 we can conclude:

- i. the particles with $D < 0.5$ mm do not change.
- ii. for the particles with $0.5 < D$ a volume of joined water is proportional to a diameter in fourth power. Moreover, for D about 1.5 mm the volume of joined water has the same value as initial one and for particles with $D > 1.5$ mm the form size spectrum already changes significantly. Corresponding distribution can be described (supposing that the initial spectrum is described by the Marshall-Palmer distribution) by the

formula

$$N(D) = 0.4NI^{-1.5}D^{-0.33}\exp(-D^{0.67}I^{-0.43}) \quad (3)$$

where N is the parameter of the initial distribution, I is intensity of precipitation. The total number of unstable drops is 30...100 times greater than in initial size distribution. However equation was made under suggestion needs that value of capture coefficient is equal unity. This suggestion needs future research to correct evaluate this process.

9. CONCLUSION.

The melting layer is the region with complex mixture of semimelted ice particles and drops. Besides, lower part contains the layer with breaking large unstable drops. The backscattering signals from this layer are 6...10dB greater than those from drops. That is confirmed by Doppler and polarisation radar data. The wave propagation through the layer with breaking drops is not investigated and future research of this phenomena should be made to predict the wave attenuation there.

10. REFERENCE.

1. Austin P.M. Bemis H.C. 1950. A quantitative study of the bright band in radar precipitation echoes. *Journal of Applied Meteorology* Vol.7.
2. Kochin A.V. 1989 Determination of rain drops size by using differential reflectivity. *Proceedings of 7-th All-Union Conference on Radar Meteorology* pp.208-210. (in Russia)
3. Kochin A.V. 1989. Investigation of melting layer by polarization radar. *Proceedings of 7-th All-Union Conference on Radar Meteorology* pp.187-189 (in Russia).
4. Kochin A.V. Megalinsky V.R. 1989. Using scalar horn in antenna of weather radar. *Proceedings of 7-th All-Union Conference on Radar Meteorology* pp.146-148. (in Russia).
5. Bringi V.N. Seliga T.A. Hall M.P.M. Cherry S.M. Goddard G.W.F. Kennedy G.R. 1981. Dual-polarization radar: technics and application. *Recent progress in radar meteorology* No.13. pp 33-45.
6. Russchenberg H.W.J. 1991. Doppler-polarimetric radar measurement of the melting layer of precipitation. *7-th International Conference on Antennas and Propagation*
7. D.S.Zrnic N.Balachrishnan C.L.Ziegler V.N. Bringi K.Aydin T.Mateika. 1993. Polarimetric Signatures in the stratiform Region of a mesoscale Convective System. *Journal of Applied Meteorology* Vol.32. No.4. pp.678-693.
8. Pinsky M.B. 1991. The Thesis: Computer processing the Doppler weather radar signals. *CAO. Dolgoprudny* p.161.
9. Mitra S.K. Vohl O. Ahr M Pruppacher H.R. 1990. A wind tunnel and theoretical study of melting behaviour of atmospheric ice particle. IV. Experimental and theory for snow flakes. *Journal of Atmospheric Sciences*. Vol.47, No 5, pp.584-591.
10. Moniger W.R. Bringi V.N. Detman T.R. Jordan I.R. Seliga T.A. Aydin K. 1984. Melting layer observations during MAYPOLE. *22-th Conference Radar Meteorology* pp.364-369.
11. Cotton N.R. Goknale N.R. 1967. Collision, coalescence and break-up of large water drops in a vertical wind tunnel. *Journal of Geophysics Research* Vol.72, No.16. pp.4041-4040.

Derivation of Path Integrated Rain Rates and Drop Size Distributions from Attenuation, Radiometer and Radar Measurements

A. Hornbostel, M. Chandra and A. Schroth
DLR, Institute of Radio Frequency Technology
P.O. Box 1116
D-82230 Oberpfaffenhofen, Germany

1 Introduction

Due to the high correlation of sky noise temperature with rain rate and path attenuation, it is possible to determine both parameters by radiometer measurements. However, the relationship of brightness temperature with rain rate and attenuation is non-linear, and for high values of both the radiometer is saturated. In direct comparisons it has to be regarded, that brightness temperature and attenuation are both path integrated values, but the rain rate and other ground measurements are measured at one point [1, 2].

As a special feature, the DLR-radiometer is able to measure the sky temperature in two linear orthogonal polarizations. For horizontally aligned rain drops the largest polarization difference is measured by use of horizontal and vertical linear polarization. For a plane-parallel homogeneous rain slab of known thickness, the drop size distribution has a strong influence on the differential temperature. An algorithm has been developed to derive a path integrated two-parameter exponential drop size distribution and the corresponding rain rate by measurements of brightness temperature and differential brightness temperature of a precipitating atmosphere. Rain rates and drop size distributions obtained by this method are compared with ground measurements and volume integrated values derived from polarimetric radar reflectivity measurements.

Cumulative distributions and equal-probability statistics of 20 GHz beacon attenuation, 19 GHz sky noise and rain rate

of summer 1992 had been produced in the frame work of the Olympus propagation experiment (OPEX), to investigate the relationships between the three measurement values. The results are compared with radiative transfer simulations and CCIR-models.

2 Radiative Transfer Model

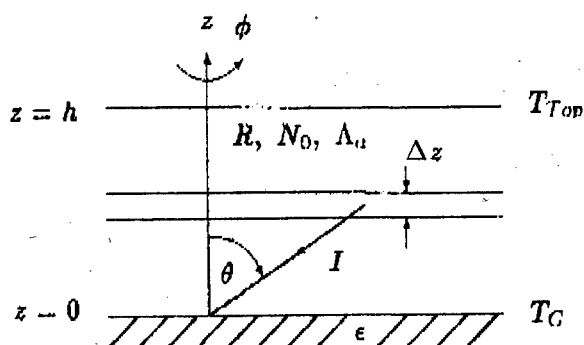


Figure 1: Modelling of a rain slab by a plane-parallel atmosphere with azimuth symmetry.

Fig.1 shows the model of a homogeneous rain slab of height h above the ground surface with linear temperature profile from ground temperature T_G and cloud temperature T_{Top} . ϵ is the emissivity of the ground surface, and Λ_a denotes the specific absorption by water vapour and oxygen.

Mathematically, this model is described by the equation of radiative transfer for a plane-parallel atmosphere with azimuth symmetry. This equation is solved in its

full vector form using the method of successive orders of scattering and the Gauss quadrature technique [4, 3]. Basic input values are the bistatic scattering coefficients of spheroidal oblate rain drops with Pruppacher-Fitter axial ratio, which are computed with the Waterman T-Matrix method. These coefficients are integrated with a two parameter exponential drop size distribution:

$$N(D_c) = N_0 e^{-3.87 D_c / D_0} \quad (1)$$

D_c is the equivolumetric drop diameter. The constants N_0 and D_0 are varied corresponding to rain rates R from 1 to 100 mm/h.

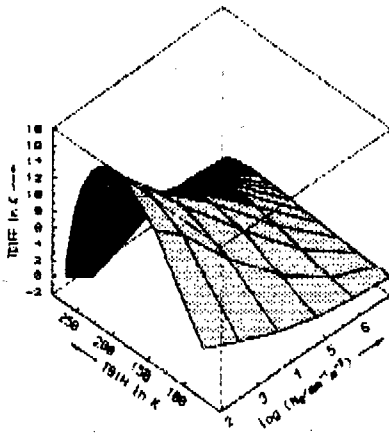


Figure 2: Differential temperature $TDIFF$ vs. brightness temperature in horizontal polarization $TB1H$ and partikel number density N_0 . Elevation 27.3° , $h = 2.5$ km, $T_G = 293$ K, $T_{top} = 273$ K, $\epsilon = 0.96$, $A_a = 0.035$ Np/km, $R = 1 - 100$ mm/h.

As an example Fig. 2 shows the differential brightness temperatures $TDIFF$ at 19 GHz for a path elevation of $90^\circ - \theta = 27.3^\circ$ in dependence of the downwelling brightness temperature in horizontal polarization $TB1H$ and the drop size distribution parameter N_0 . The lines represent curves of constant N_0 and constant rain rates R . Further simulations are shown in [4].

3 Radiometer Measurements

The following figures show the analysis of a convective event measured on 17th June 1993. First, Figs. 3 and 4 show the brightness temperature in horizontal polarisation $TB1H$ and the differential temperature $TDIFF$ versus time measured at 19 GHz with a path elevation of 27.6° .

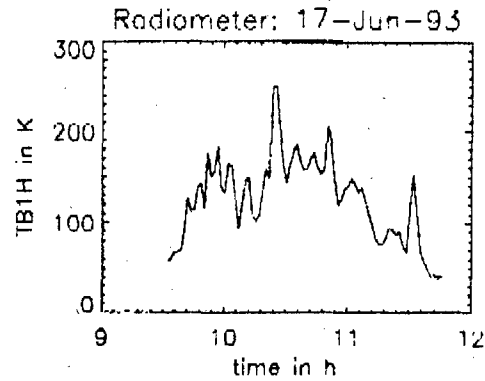


Figure 3: Brightness temperature measured along horizontal polarization $TB1H$ on 17th June 1993 vs. time.

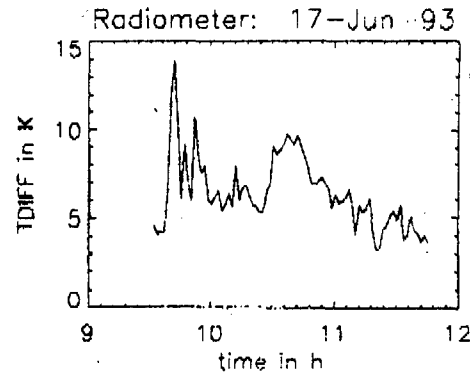


Figure 4: Differential temperature $TDIFF$ measured on 17th June 1993 vs. time.

In Figs. 5, 6 and 7 the rain rates delivered by the rain gauge and drop size parameters N_0 and D_0 delivered by distrometer measurements (solid lines) are compared with values computed by inversion of the theoretical relations underlying Fig. 2 (dashed lines).

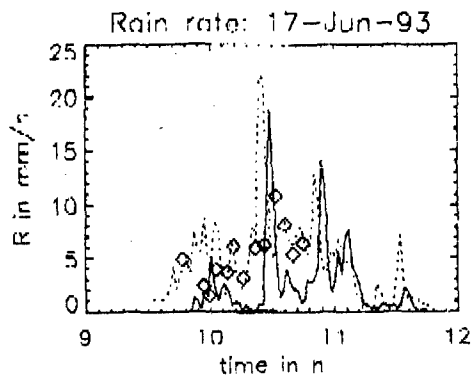


Figure 5: Rain rate R vs. time on 17th June 1993. Solid line: Rain gauge. Dashed line: Retrieval from radiometer. Symbols: Retrieval from radar.

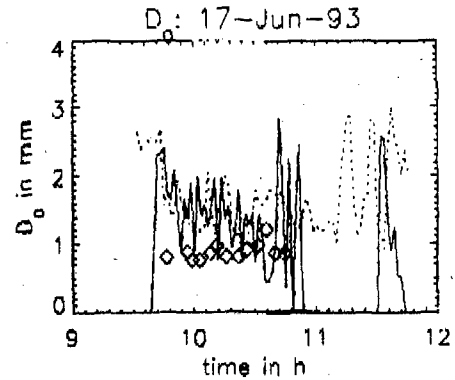


Figure 7: Volume median drop diameter D_0 vs. time on 17th June 1993. Solid line: Distrometer. Dashed line: Retrieval from radiometer. Symbols: Retrieval from radar.

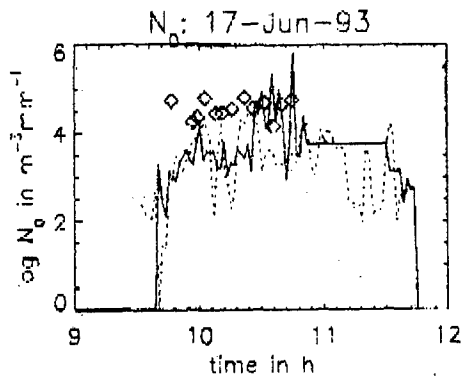


Figure 6: Partikel number density N_0 vs. time on 17th June 1993. Solid line: Distrometer. Dashed line: Retrieval from radiometer. Symbols: Retrieval from radar.

Briefly, the inversion algorithm looks for the two points on the curves in Fig. 2, which are closest to the measured values of $TB1H$ and $TDIFF$, and does a linear interpolation between the corresponding values of N_0 , D_0 and R . With the exception of some spikes the agreement in all three figures is good, although here path integrated (effective) values are compared with point measurements.

4 Radar Measurements

The symbols in Fig. 5, 6 and 7 are radar predictions of volume averaged rain rates and drop size distribution parameters, which were obtained with the following procedure:

1. RHI-scans at 5.5 GHz threading the radiometer path were made concurrently in time. These scans include as a subset some portions of the precipitation on the radiometer path.
2. From the dual polar radar data of these RHI-scans, the volume averages of Z_H and Z_{DR} , i.e. $\langle Z_H \rangle$ and $\langle Z_{DR} \rangle$ were obtained using the following averaging-formula:

$$\langle x \rangle = \frac{\int x dV}{\int dV} \quad (2)$$

3. The $\langle Z_H \rangle$ and $\langle Z_{DR} \rangle$ values were used to get the rain rate from the dual polar technique, i.e. the relationship $R = f(Z_H, Z_{DR})$ due to the Seliga and Bringi method [9]. In a similar way also the N_0 and D_0 values were obtained.

The comparison of the radar derived rain rates with the radiometer results reveals a

very good agreement, bearing in mind that the radar results are volume averages that are not identical to the volume averaging of the radiometer path. The corresponding radar derived values of N_0 and D_0 however, reveal a noticeable departure from the radiometer and distrometer results. Although this effect is not seen in the rain rate results, this issue needs further investigation.

5 Statistical Results

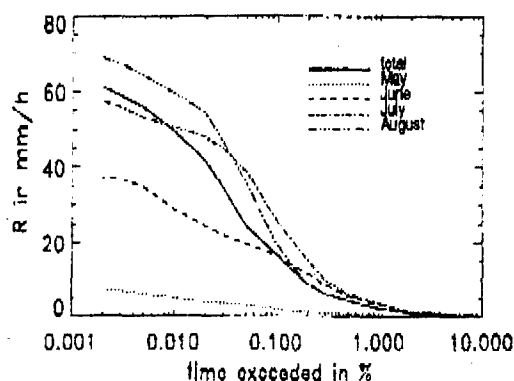


Figure 8: Cumulative distributions of the rain rate.

Fig. 8 shows monthly cumulative distributions (CD) of the rain rate for the months May, June, July and August 1992. The solid lines represent the CD of the total time period. The curves are generated from 1 minute mean values (moving average) of tipping bucket and drop counter measurements with an integration time of 10 seconds.

In Fig. 9 values of 10.77 GHz attenuation CDs, derived from Olympus beacon measurements, are plotted versus the rain rate values of Fig. 8 corresponding to the same percentages of time (equal probability statistic). The values of the total period are fitted with power law regression curves of the form

$$CPA = a R^b \quad (3)$$

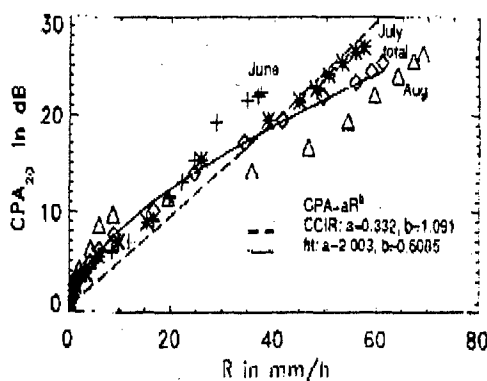


Figure 9: 20 GHz copolar attenuation versus rain rate and regression curves. Elevation 27.6° .

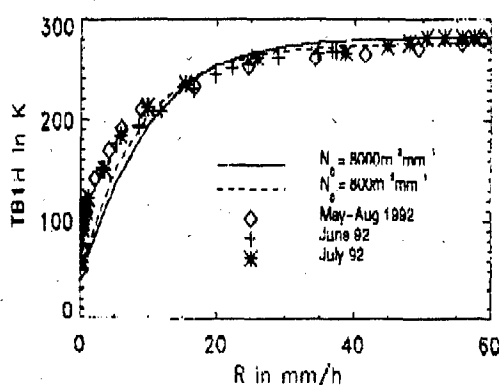


Figure 10: Sky noise temperature versus rain rate with model curves for a homogeneous plan-parallel atmosphere of thickness 2.5km. Elevation 27.6° .

for minimum absolute deviation. For comparison the dashed line shows the same relation with the coefficients given by Olson [7] and CCIR [8] and a path length of 4.5 km. This curve shows good agreement with the measured values of July, but generally underestimates the attenuation for low and medium rain rates and overestimates the attenuation for high rain rates. The reasons for the differences between the singles months are possibly different effective path lengths due to path inhomogeneities and different rain height and rain cell sizes, and the existence of hail for some events. The effect of drop size distribution has less influence in this case ([6]).

Fig. 10 shows equal probability statistics of 19 GHz sky noise temperature and rain rate.

The data are taken from the CDs of the single months and the total period. For comparison two curves computed with the radiative transfer model described in section 2 are shown. In this case, a homogeneous plan-parallel atmosphere with a thickness of 2.5 km, surface temperature 288 K, temperature at the top 273 K and Lambert-Surface with emissivity 0.96 is assumed.

6 Conclusion

Radiometer and attenuation measurements allow to derive path integrated rain rates for statistical purposes and for event analysis. However, if simple regression formulae are used, there are uncertainties due to changing meteorological conditions. Path integrated rain rates and drop size distributions derived from polarimetric radiometer measurements show good agreement with rain gauge and distrometer measurements. Rain rates obtained from volume integrated polarimetric reflectivity measurements fit the radiometer values well. However, this is not the case for the drop size distributions, which show a noticeable departure. The advantage of the radiometer in comparison to the radar is, that the measurements can be done with low effort and a high sample rate. On the other hand the radar can scan large areas and derive rain rates also in regions which are in a large distance from the antenna.

References

- [1] Hornbostel, A., Schroth, A.: "Statistical and Event Based Analysis of 20 GHz Attenuation on the Earth-Olympus Satellite Path". Proc. of ICAP'93 Edinburgh, 1993, Conf. Publication No. 370, part 1, pp. 131-134.
- [2] Hornbostel, A., Schroth, A.: "Propagation Research on the 20 GHz Earth-Olympus Satellite Path". To be published in Journal of Electromagnetic Waves and Applications soon.
- [3] Liou, K.-N., "An Introduction to Atmospheric Radiation", Int. Geophysics Series, Vol. 26, Academic Press 1980.
- [4] Hornbostel, A., Schroth, A. and Kutuza, B. G.: "Polarimetric Measurements and Model Calculations of Downwelling Rain Brighness Temperature", Proceedings of μ rad'94 Rome, Febr. 1994, to be published by VSP.
- [5] Schuabl, G.: "Tropospheric Influences on Satellite-Earth Paths and Their Determination by Means of Radar Measurements", ESA-TT-1143, translation of DFVLR-FB 88-53, 1988.
- [6] Hornbostel, A.: "Rain Rate, Sky Noise and Attenuation Measurements in the Summer of 1992", Proceedings of OPEX 20, Darmstadt, Nov. 1993, edited by ESA/ESTEC.
- [7] Olsen, R. L., Rogers, D. V., Hodge, D. B.: "The uR^b relation in the calculation of rain attenuation", IEEE Trans. Ant. Prop., Vol AP-26, 2, p.318-329.
- [8] CCIR Recommendations and Reports, Rep. 564-4, 1990.
- [9] Seliga T.A., Bringi, V. A.: "Potential use of radar differential reflectivity measurements at orthogonal polarisations for measuring precipitation", J. Appl. Meteor., 15, pp. 66-76, 1976.

Session 5: Precipitation IV

LONG TERM 0°C ISOTHERM HEIGHTS CHARACTERISTICS IN WARSAW REGION. (PRELIMINARY RESULTS)

Arnold Kawecki

INSTITUTE OF TELECOMMUNICATIONS, Szachowa 1, 04-894 Warszawa, Poland
Tel: +48 22 128362, Fax: +48 22 128180

ABSTRACT:

The radiosonde-atmospheric soundings, performed from 1961 to 1987, have been used to estimate the average 0°C isotherm height in months and in decades of month. Separate assessments have been made for midday and midnight soundings. At the next step the assessments have been made in four separate collections:

- a) - the soundings performed during the days without rain,
- (b) - during the days with widespread rain,
- (c)- during the days with showers and
- (d)- during the days with mixed type of rain.

In result one can conclude that average of monthly 0°C isotherm heights during rainy days is lower ca 300 m than the average of 0°C isotherm heights during the days without rain.

1. INTRODUCTION.

The characteristics of 0°C isotherm heights have been specified using the results of balloon-atmospheric soundings conducted by Meteorological Service at noon and at midday in Aerological Station in Legionowo (near Warsaw). For this purpose the period 1961-87 of 27 year long has been selected, [1].

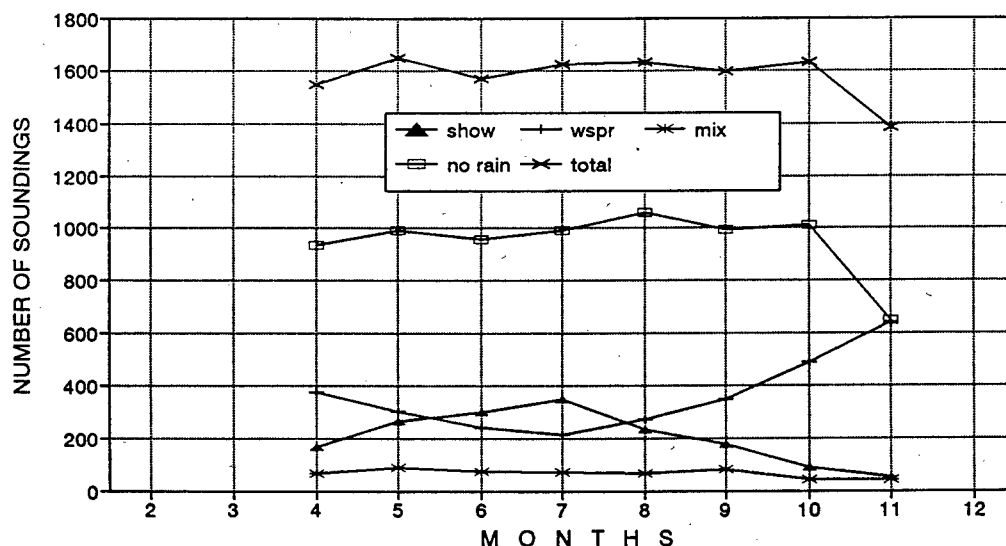


Fig.1. Number of soundings in months from April to November performed during 27-years period in Legionowo (total) and numbers of soundings performed during weather without rain (no rain) and during rainy weather: in case of showers (show), widespread rain (wspr) and mixed type of rain (mix).

At the first approach to the problem the average 0°C isotherm heights in months H_m and in

decades H_d of the months have been specified as well as the standard deviation of these heights.

Such computation has been made also for midnight soundings and noon soundings separately. The average height H was estimated using the relation

$$H = \frac{1}{n} \sum_{i=1}^n h_i, \quad i = 1, 2, \dots, n$$

where h_i - i -th height and n - the number of soundings in decade/month or in decade/month in 27 years period. Similarly the standard deviation σ was evaluated using the relation

$$\sigma = \left[\frac{1}{n} \sum (h_i - H)^2 \right]^{0.5}$$

At the next approach to the problem the effect of weather conditions on 0°C isotherm height has been evaluated. Four situations were

considered: the day and night soundings in clear weather, - in periods with spread rain, - in periods with showers and in periods with mixed rainfall types. This approach forced to create separate data collections for everyone type of weather conditions.

2. THE RESULTS.

The whole collection of height data can be characterized with diagrams presented in figures from 1 to 4.

The numbers of soundings per month, performed in different weather conditions during 27 years, are presented in Fig.1. Fig.2 presents average of monthly values H_m in period of 27 years and possible deviations of decade values H_d around monthly average value. H_{dm} denotes average of maximal decade values in month and H_{di} denotes average value of minimal H_d values in months in the same period. The maximal decade value of H_d found in given month in 27 years period, is denoted H_{dxx} and minimal value - H_{dii} .

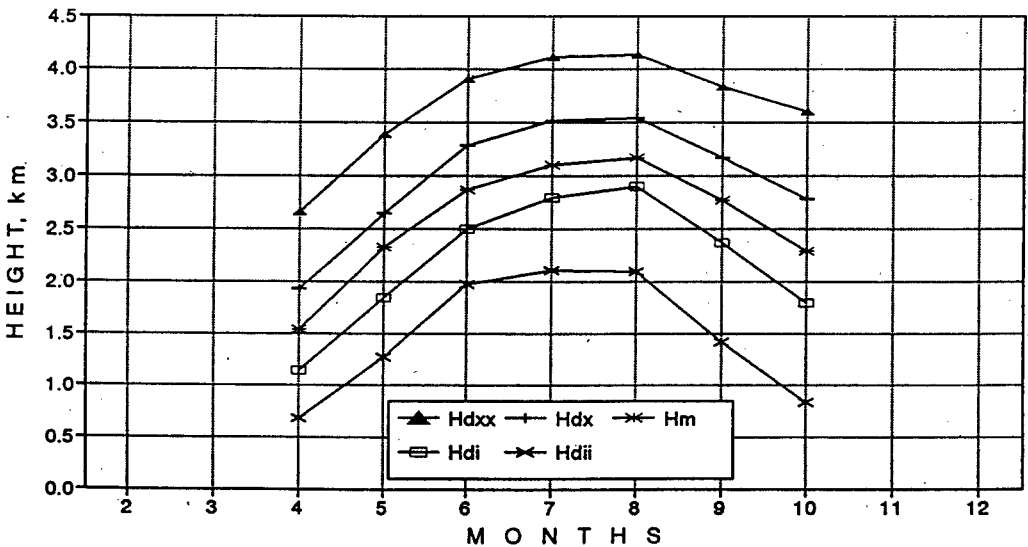


Fig.2. Deviation of 0°C isotherm heights averaged in decades of month H_d , about average height in month H_m during 27-years period: maximal and minimal H_d values in month averaged in 27-years interval (H_{dxx} H_{dii}) and maximal and minimal H_d values which occurred during this period (H_{dxx} H_{dii}).

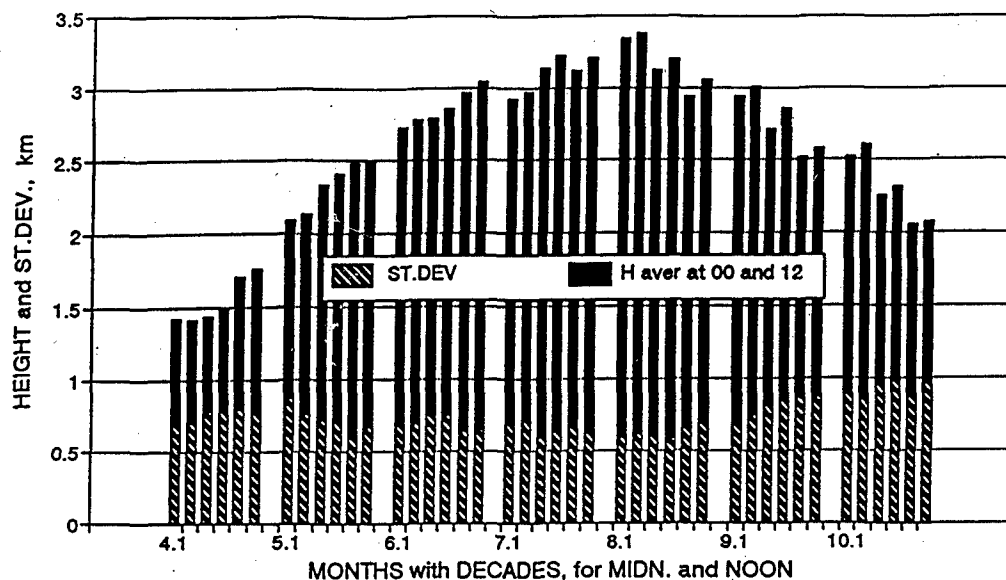


Fig.3. Height of 0°C isotherm averaged in decades of months and in 27-years period for midnight and noon soundings performed from April to October.

The average value and standard deviation of 0°C isotherm heights in decades (H_d) from April to October in 27 years cross-section for midday and midnight soundings are presented in Fig.3. The lower part of H-bars presents σ , which value is approximately constant (about 700 m) during warm period and in October raises to 1 km. The first bar in decade relates to midnight soundings and the second one - to midday

soundings. H_d values in April are distorted due to the fact, that in some days the air temperature at the ground was lower than 0°C. In such cases the soundings were removed from the collections and from this reason the bar in first decade of April is considerably higher than expected. The changes from year to year of average monthly H_m values in period from 1971 to 1980 presents Fig.4.

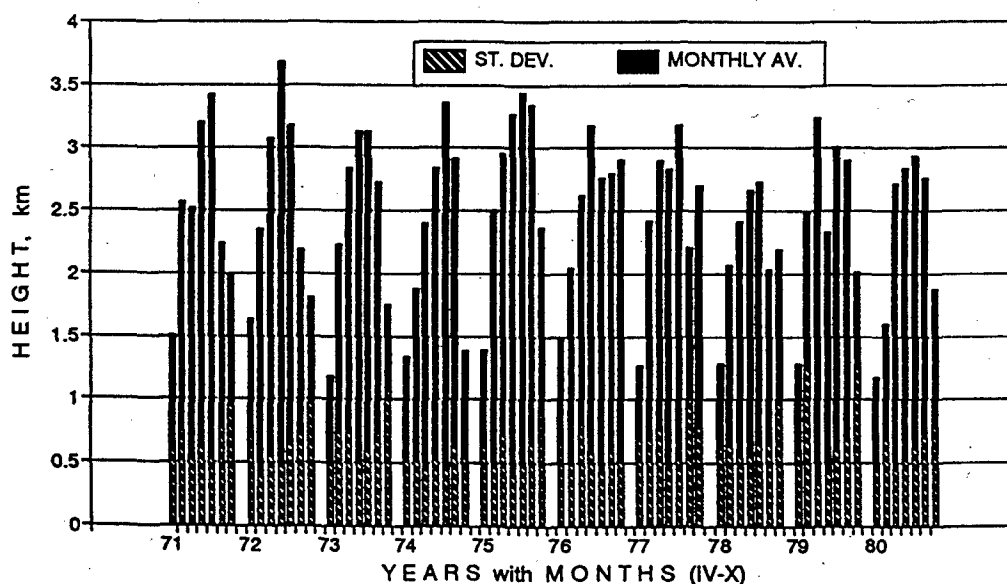


Fig.4. Average height of 0°C isotherm in months from April to October for years from 1971 to 1980.

The average monthly 0°C isotherm height values in different weather conditions are presented in Fig.5. It reveals that in rainy periods the 0°C isotherm height is situated ca 300 m lower than the level of the same isotherm in clear weather

conditions. The asymmetrical course of this difference during the average year can't be explained at the present moment. Also the low number of soundings makes the assessments not satisfactory confident.

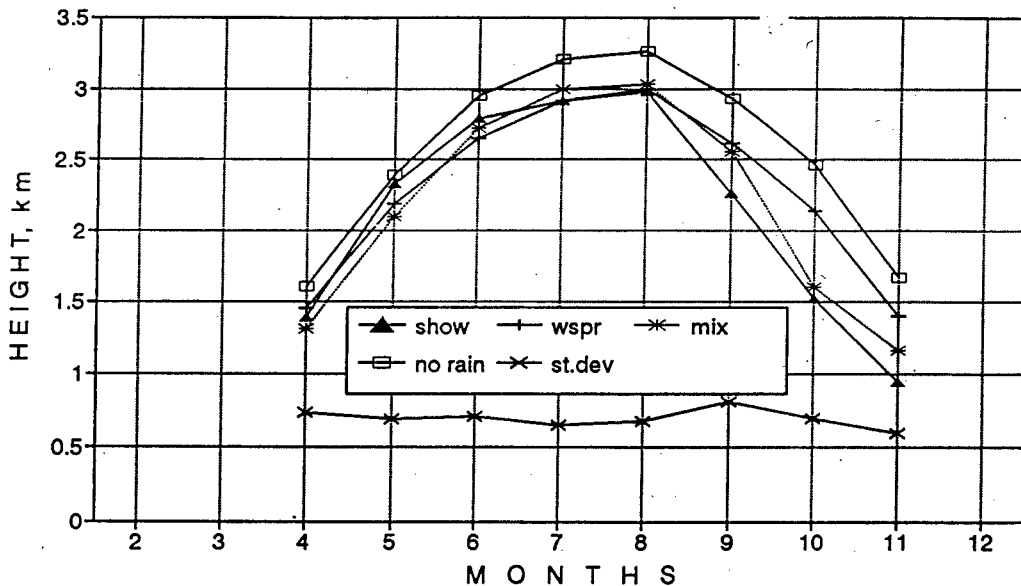


Fig.5. Average 0°C isotherm height in months from April to November and in 27-years period at different weather conditions: during showers (show), widespread rain (wspr), mixed type of rain (mix) and during weather without rain (no rain).

3.CONCLUDING REMARKS.

The average 0°C isotherm height at any weather conditions in most intense rainfall period from June to August has the value of 3.05 km. In case of days and nights with rain this value is reduced to ca 2.9 km.

The measured 0°C isotherm height in weather with showers relates most frequently to the zone between precipitation columns and not inside the columns. However inside the Cumulonimbus cloud, in the stream of rising up air, warmer than the air outside, the 0°C isotherm is raised above the level of the same isotherm outside the cloud.

In case of widespread rain the measured 0°C isotherm height is more frequently related to the zone of rain.

Much more information from data contained in four soundings collections can be extracted. For

example long-term distributions of 0°C isotherm heights related to different rain types could be useful for prediction models applying such statistical representation of 0°C isotherm heights behaviour.

One can note that although the total number of sounding is comparatively high, in case of selected weather conditions this number is rather moderate. More sounding data are desired for example in order to explain the asymmetry of curves at the spring and the autumn.

4. REFERENCE

1. A.Kawecki, 3-5 May 1992, Some characteristics of 0°C isotherm height in Warsaw region, *Proc.17-th Meeting of Olympus Prop.Experiment*, Stockholm/Helsinki.

ON TWO MECHANISMS OF SIGNALS SCINTILLATION BY WAVEFIELD PROPAGATION IN PRECIPITATIONS

V.L. Kouznetsov

MSTUCA; Kronstadtsky Bld., 20, 125838, Moscow, Russia
Tel: 007.095.459 04 40, Fax: 007.095.457 12 02

ABSTRACT

Rain as the cause of scintillations origin in communication radioline is considered. The effect of small-scale fluctuations of raindrops concentration and space macroinhomogeneity of precipitation intensity on the transformation of angular wavefield spectrum of the signal is analysed. A compact expressions allowing to estimate the value of relative signal fluctuations by rain are obtained.

Keywords: Wave Propagation, Rain, Random Media and Phase Screen, Scintillation.

1. INTRODUCTION

The substantial by various geophysical and meteorological factors effect critically on the quality of information exchange in exposed communication channels. These effects determine both energy losses of signal and origin of scintillations which are comparatively fast amplitude and phase fluctuations of the wave incident on the receiving antenna. By the signal amplitude fluctuations the mean probability of the signal reception error increases. That is why the study of all factors and mechanisms resulting in signal fluctuations origin in communication channels is of considerable interest.

Precipitations are a random inhomogeneous medium characterized by macro- and microinhomogeneities. Microinhomogeneities are caused by the random perturbations of the hydrometeors concentration; macroinhomogeneities are associated with structure and formation of clouds and manifest themselves in cell (centre) structure of rain. Electromagnetic field of a signal in the process of interaction with precipitations is scattered and transformed. This causes the fluctuations of amplitude and angle of wave incidence on the receiving antenna. Such is the general picture of scintillations formation. By the quantitative analysis of the fluctuations of receiving antenna response it is convenient to present the incident field as a plane

waves spectrum (angular spectrum)
 $E(\vec{q}, z) = \int d\rho E(\vec{\rho}, z) e^{-i\vec{\rho}\vec{q}}$. \vec{q} is the projection

of plane wave vector \vec{k} on the aperture plane of receiving antenna, z is the coordinate of receiving antenna location in the coordinate system, the origin of which is at the transmitting antenna. Then the received signal value U is determined by the expression

$$U = \int G(\vec{q}) E(\vec{q}, z) d\vec{q}, \quad (1)$$

where $G(\vec{q})$ is the directional pattern of receiving antenna.

The value of relativ signal fluctuations, calculated according to formula

$$\frac{\delta U}{U} = \left[\frac{\langle U \cdot U^* \rangle - \langle U \rangle \langle U^* \rangle}{\langle U \rangle \langle U^* \rangle} \right]^{1/2}, \quad (2)$$

is determined by two first moments of angular field spectrum $\langle E(\vec{q}, z) \rangle$ and $\langle E(\vec{q}_1, z) E^*(\vec{q}_2, z) \rangle = K(\vec{q}_1, \vec{q}_2; z)$ - the latter will be called below correlator. For calculating these values, consider the problem of wave propagation between transmitting and receiving antennas in the presence of precipitations in the way of waves. Let us suppose that precipitations are localised in the slab with the width L_0 of at the distances L_1 and L_2 from transmitting and receiving antennas, respectively. The total length of the signal path is L_x .

2. THE FIRST MECHANISM. THE EFFECT OF MICROINHOMOGENEITIES

In order to estimate the effect associated with wave scattering on microinhomogeneities of drops concentration let us consider a simple rain model having a form of a plane layer with the thickness L_0 randomly filled by discrete scatterers with constant mean concentration n_0 .

Using the equations system for angular spectrum correlator (Refs 1,2), the following integral equation is obtained:

$$K_x(\vec{\mu}, \vec{a}; z) = K_{\text{ext}}(\vec{\mu}, \vec{a}; L_1) e^{i\alpha(\vec{\mu}, \vec{a})z} + \gamma(\vec{\mu}, \vec{a}) \int_{L_1}^{L_1+L_0} d\xi e^{i\alpha(\vec{\mu}, \vec{a})(z-\xi)} \cdot J(\vec{a}, \xi) \quad (3)$$

Here $K_x(\cdot)$ is the sum of two correlators for waves propagating forward and scattered backwards.

$$J(\bar{a}, z) = \int d\bar{\mu} K_x(\bar{\mu}, \bar{a}; z), \quad \bar{\mu} = \frac{\bar{q}_1 + \bar{q}_2}{2},$$

$$\bar{a} = \frac{\bar{q}_1 - \bar{q}_2}{2}, \quad \tilde{k}_z(\bar{q}_1) = \sqrt{\varepsilon k_0^2 - q^2},$$

$$\alpha(\bar{\mu}, \bar{a}) = \tilde{k}_z(\bar{\mu} + \bar{a}) - \tilde{k}_z^*(\bar{\mu} - \bar{a})$$

Here ε is the mean dielectric permeability of a medium filled by hydrometeors.

$K_{env}(\cdot)$ is the correlator value when the wave enters the precipitation slab. It is the product of two deterministic (unrandom) components of angular spectrum of the wave emitted by the antenna.

The augend of Eq.3 describes the space change in correlator ignoring the interaction between field components. It means that components which form this value do not interact between themselves but only are attenuated by incoherent scattering and adsorbing. The addend of Eq.3 describes the energy transport through the angular spectrum because of the scattering process. The factor $\gamma(\bar{\mu}, \bar{a}) \approx \gamma_0 = \frac{3}{8\pi} \cdot \frac{1}{k_0 L_{ph}}$.

Here $L_{ph} = \frac{1}{n_0 \sigma_s}$ - is the mean free path of photon in scattering but not absorbing medium (σ_s is the scattering section of the drop).

This process take place in the whole layer volume. It corresponds to the integration in Eq.3 between the limits from L_1 to $L_1 + L_0$.

Notice that this interaction between angular field components is absent in the equations for mean field in consequence of scattered waves incoherency. In Eq.3 the scattered waves incoherency manifests itself in the fact that, on the average, only those plane waves in pairs, which have $\bar{q}_1 - \bar{q}_2 = 2\bar{a} = \text{const}$ (vector \bar{a} in Eq.3 is the parameter), interact between themselves.

When $a \rightarrow 0$, the solution of Eq.3 has a singularity, $K_x \rightarrow \infty$. Consider this interval in detail. After integrating Eq.3 with respect to $\bar{\mu}$ and shifting the origin of coordinates ($z = 0$) to the rain slab border we obtain the following integral equation for $J(a, z)$ in approximation of forward scattering:

$$J(a, z) = J_{env}(a, z) + 2\pi\gamma_0 \int_0^z K_0(2a|z - \xi|) \cdot J(a, \xi) d\xi \quad (4)$$

Here $K_0(\cdot)$ is the McDonald function.

Taking the Laplace transform of Eq.4, obtain:

$$J_p(a) = \frac{J_{env}(a; p)}{1 - \pi \frac{\gamma_0 k_0}{a} \cdot \frac{\arccos(pk_0 / 2a)}{\sqrt{1 - (pk_0 / 2a)^2}}} \quad (5)$$

Recovering the original function, choose the branch of $\arccos(pk_0 / 2a)$ with cut on the real axis $(-\infty, 2a / k_0]$. In this case $-\pi \leq \text{Re} \arccos(pk_0 / 2a) \leq \pi$ and denominator of Eq.5 has a pole singularity determined by non-zero roots of transcendental equation

$$\pi \frac{\gamma_0 k_0}{a} \cdot y = \text{sh } y \quad (6)$$

Eq.6 has such roots only when

$$a < \pi\gamma_0 k_0 \approx \frac{3}{8} L_{ph}^{-1} \quad (7)$$

It may be demonstrated that by $a \rightarrow 0$ the main contribution to the value

$$J(a, z) = \frac{1}{2\pi i} \int e^{pz} J_p(a) dp \quad (8)$$

makes a residue in pole and

$$J(a, z) \approx \left(\frac{2\pi\gamma_0 k_0}{a} \right)^{2\pi\gamma_0 k_0 z} \quad (9)$$

Eqs.1,3,9 make it possible to obtain the estimation for the conditions when the incoherent component of radiation starts playing first fiddle by forming the value of received signal

$$\pi\gamma_0 k_0 L_0 = \frac{3}{8} \cdot \frac{L_0}{L_{ph}} \approx 1 \quad (10)$$

The physical meaning of Eq.10 is sufficiently obvious: incoherent scattering must be taken into account in case the free path of photon is on the same level as the rain slab width.

The condition formulated in Eq.10 can be realised very seldom. Thus, for precipitations with rain rate of $R = 100 \text{ mm/h}$ and radiation wave length of $\lambda = 0,03 \text{ m}$ the rain slab width has to be of $L_0 = 10^4 \text{ m}$.

It should be noticed that by the increase of transmitting system frequency the nonlinear increase of raindrops scattering section $\sigma_s = \sigma_s(f)$ results in considerable rise of incoherent scattering contribution. This is in accord with Oguchi's results, obtained by research of the radiative transfer equation (Ref.3).

Exepting very narrow interval of $\bar{a}(|\bar{a}| / k_0 < \pi\gamma_0)$, where the solution of Eq.3 has a singularity, the unknown value can be obtained by using the typical iteration procedure. In this case the value (L_0 / L_{ph}) may be taken as the small parameter.

Supposing the identity of transmitting and receiving antennas and approximating their directional pattern with Gauss plot with semiwidth

$\theta \ll 1$, one can obtain the following analytical dependencies:

$$\begin{aligned} \langle |U|^2 \rangle - \langle U \rangle \langle U^* \rangle &= \frac{\pi \gamma_0 A_1^2 A_2^2 e^{-2 \operatorname{Im} \sqrt{\epsilon} k_0 L_0}}{\sqrt{8 + (4 L_x k_0 \theta^2)^2}} \\ &\times \arctg \left\{ \frac{2 k_0 L_0 \sqrt{0,5 \cdot \theta^4 + (k_0 L_x)^2}}{0,5 \cdot \theta^4 + k_0^2 [L_x^2 + (L_1 - L_2)^2 - L_0^2]} \right\} \quad (11) \\ \langle U \rangle \langle U^* \rangle &= \frac{A_1^2 A_2^2 e^{-2 \operatorname{Im} \sqrt{\epsilon} k_0 L_0}}{2 + (2 \theta^2 k_0 L_x)^2} \end{aligned}$$

Assuming that $0,5 \theta^4 \ll k_0 L_0$, Eqs.11 can be simplified some more and the following estimation for relative fluctuations of received signal can be obtained.

$$\frac{\delta U}{U} \approx 20 \sqrt{\pi \gamma_0 k_0 L_0} \approx \theta \sqrt{\frac{3}{2} \cdot \frac{L_0}{L_{ph}}} \quad (12)$$

Presented expression is the first member in total solution expansion in terms of powers of small parameter (L_0 / L_{ph}) .

The estimations show that by rain rate of $R = 50 \text{ mm/h}$ and rain slab width of $L_0 = 10^3 \text{ m}$ the value of relative signal fluctuations on the frequency of 30 GHz adds up to 15%. When $R = 15 \text{ mm/h}$ and $L_0 = 10^4 \text{ m}$ ($\delta U / U$) decreases to 5%

3. THE SECOND MECHANISM. THE EFFECT OF MACROINHOMOGENEITIES

Analysing the second mechanism of scintillations occurrence, let us replace the precipitations slab with a collection of localised centres with inherent structure of precipitations intensity R_i that can be described by Gauss distribution:

$$R_i(\bar{\rho}) = R_{0i} \exp \left\{ -\frac{(\bar{\rho} - \bar{\rho}_i)^2}{2 d_i^2} \right\} \quad (13)$$

Here $\bar{\rho}_i$ is the coordinate of centre of i 'th cell, R_{0i} - is the maximum precepitation intensity in the centre, d_i - is the effective width of a rain cell. Centres of cells are located inside the slab with the width L_0 . Small-scale fluctuations are not considered in this model.

In this case characteristic size of dielectric permeability change - d (the semiwidth of distribution in Eq.6) is well more than wave length λ , and the approximation of geometry optics and the concept of rays can be used by describing the wave propagation.

Infinitesimal of value $(\epsilon - 1)$ causes the fact that in the rain slab with the length of L_0 the rays

deviate from unperturbed trajectories slightly. The phase shift of the signal wavefield in the rain slab prove to be substantial but can not appear on relatively small rain slab. The value of this phase shift can be determined by integrating the perturbations of wave vector over the unperturbed ray trajectory:

$$\Delta \Phi = (2\pi)^{3/2} k_0 \sum_{i=1}^N \kappa_i n_{0i} d_i \exp \left\{ (x - x_i)^2 / 2 d^2 \right\} \quad (14)$$

Here κ_i is the mean polarizability of hydrometeors of i 'th rain cell, n_{0i} - is the concentration of drops in the centre of this cell. The summation in Eq.14 is extended over the total number N of cells that fall at the precipitations front with the extent of D . This corresponds to the cells density $m = N / D$.

Taking into account the fact that κ is the complex value, one can easily get certain that Eq.14 includes both the additional phase shift and the wave attenuation in precipitations.

The reason that was set forth above motivates the use of a random phase screen, having complex transparency coefficient $t(x) = e^{i \Delta \Phi(x)}$, and locating at the distance $z_0 = L_1 + L_0 / 2$ from the transmitting antenna.

Passing over this phase screen, the electromagnetic wavefield gets transformed:

$$\begin{aligned} E \left(x, y, L_1 + \frac{L_0}{2} + 0 \right) \\ = E \left(x, y, L_1 + \frac{L_0}{2} - 0 \right) e^{i \Delta \Phi(x)} \end{aligned} \quad (15)$$

Each component of the angular field spectrum of the incident wave after passing over the screen is not a plane wave any more and can be expanded in an angular spectrum. Such is the process of field energy redistribution in the angular spectrum.

Using (just as by the analysis of the first mechanism) the Gauss approximation for the directional radiation pattern of receiving and transmitting antenna, the random value of receiving antenna response can be calculated:

$$U \approx \tilde{A} \exp \left\{ i \sqrt{2 / \pi \Omega} \sum_j e^{-x_j^2 / 2 \delta^2} \right\} \quad (16)$$

Here

$$\begin{aligned} \tilde{A} &= A_1 A_2 e^{i k_0 L_x} \frac{\pi}{\beta}, \quad \beta = [1 / k_0^2 \theta^2 + i L_x / k_0], \\ \delta^2 &= \{ d^2 + 1 / 2 k_0^2 \theta^2 \}, \quad \Omega = 2 \pi^2 \kappa k_0 d^2 / \delta \end{aligned}$$

A_1 and A_2 are the coefficients which depend on transmitted signal power and antenna systems characteristics.

For making further analytical estimations, let us replace Gauss functions in exponent (Eq.16) with rectangular strobe

$$\frac{1}{\sqrt{2\pi\delta^2}} e^{-\frac{x_j^2}{2\delta^2}} \Rightarrow \frac{1}{2\delta} \{ \theta(x_j + \delta) - \theta(x_j - \delta) \} \quad (17)$$

$$= \frac{1}{2\delta} S(x_j; \delta)$$

Here $\theta(\cdot)$ is the generalized Heavyside function.

The mean value of receiving antenna response may be calculated by averaging Eq.16 over the coordinates of rain centres:

$$\langle U \rangle = \tilde{A} \prod_{j=1}^N \int_{-D}^D \frac{1}{2D} dx_j e^{i\Omega S(x_j; \delta)}$$

$$= \tilde{A} \left[1 - d/D (1 - e^{-i\Omega d}) \right]^N \quad (18)$$

Passing to the limit $N \rightarrow \infty$, $D \rightarrow \infty$, $N/D = m = \text{const}$, obtain

$$\langle U \rangle = \tilde{A} \exp \left[-md(1 - e^{-i\Omega d}) \right] \quad (19)$$

When deriving this expression, it was taken into account that $\lim_{N \rightarrow \infty} (1 + 1/N)^N = e$

Eq.19 makes it possible to estimate the mean attenuation in rain slab

$$-20 \lg e \cdot md \{ 1 - \cos(\text{Re } \Omega) e^{-\text{Im } \Omega} \} \quad (20)$$

and the mean additional phase shift

$$md \sin(\text{Re } \Omega) \quad (21)$$

The second moment of receiving antenna response may be calculated by analogy

$$\langle U \cdot U^* \rangle = |\tilde{A}|^2 \exp \left[-md(1 - e^{-2\text{Im } \Omega}) \right] \quad (22)$$

Eqs.19,22 in line with Eq.2 allow to obtain the estimation for the relative fluctuations caused by precipitations in the second model

$$\frac{\delta U}{U} = \left\{ \exp \left[md \sin^2(\text{Re } \Omega) \right] \cdot \exp \left[md \cos(\text{Re } \Omega) - e^{-\text{Im } \Omega} \right]^2 - 1 \right\}^{1/2} \quad (23)$$

This estimation does not depend in an explicit form on the width of precipitations slab L_0 because of the fact that this value is effectively taken into account in m . In case the attenuation in precipitations is 1dB, the rain rate in the centres of cells is 15 mm/h and the cell size is $d \approx 10^2 \text{ m}$, the value of m is $7,5 \cdot 10^{-2} \text{ m}^{-1}$.

The value of relative fluctuations determined from Eq.22 at the frequency of $f=10 \text{ GHz}$ will be 43%.

4. DISCUSSION AND CONCLUSION

In the paper the dynamics of fluctuations has not been considered. However, it is evident from the general reasoning that the mechanisms de-

scribed above generate the signal scintillations in different frequency ranges.

Characteristic time of the first mechanism is determined by the dispersal time of micro-scale inhomogeneity with characteristic size that depends on radiation wave length λ .

This time is of the same order of magnitude as the correlation time of sequential echoes received by remote exploration of precipitations and is on the order of tens of milliseconds.

The characteristic time of the second mechanism is determined by space size of rain cells and their propagation velocity. The order of magnitude of this time is of units of seconds.

That is why the first mechanism cannot be ignored, although the intensities of mechanisms are different, and fluctuations caused by macroinhomogeneities are greater than those concerned with microstructure of the rain.

The given analysis of mechanisms in precipitation has shown the following:

1 Small-scale fluctuations of hydrometeors concentration can generate relatively fast fluctuations of the amplitude of received signal, the value of which (in case the precipitations are not intensive) can be determined by Eq.12.

2. The conditions formulated in Eq.10 determine the boundary of the range where incoherent scattering is a factor. When $\pi \gamma_0 k_0 L_0 \ll 1$, the contribution of incoherent scattering is insignificant and Eq.12 is quite correct.

3. The macroinhomogeneities of rain originate rather smooth fluctuations, the relative value of which may be calculated according to Eq.23.

REFERENCES

1. V.L.Kouznetsov, V.G.Budanov, 1988, "Polarisation characteristics of electromagnetic radiation which undergo multiple scattering in the cloud of small particles": Radiofizika, vol.31, No 4, p.493 (in russian)
2. C.H.L. Rino, H.D. Ngo, K.A. Haycock, 1990, A spectral domain method for multiple scattering in discrete random media: IEEE Trans. Antennas Propagat. vol.38, No 7, p.1018
3. T.Oguchi, 1991, Effects of incoherent scattering on microwave and millimetre wave communications through rain: Electronics Letters, vol.27, No 9, p.759

THE EXPERIMENTAL RESULTS OF RADIO WAVE ATTENUATION INVESTIGATIONS ON SLANT COMMUNICATION LINKS IN CLIMATIC CONDITIONS OF RUSSIA

V.L.Bykov¹, V.V.Svjatogor¹, V.N.Pozhidayev²

1 - NIIR, 16 Kazakova Str., Moscow, 103064, RUSSIA

Tel: (095) 261-02-73, Fax: (095) 261-02-73, E-mail:

2 - IRE, 11 Mokhovaja Str., Moscow, 103907, RUSSIA

Tel: (095) 203-49-96, Fax: (095) 203-60-78, E-mail: efr@ire.uucp.free.msk.su

ABSTRACT

The results of 4 years measurements of 11.5 GHz radio wave attenuation at the International experimental area are presented in this report. The approximation coefficients for some empirical relations have been determined. Basing on measured statistics some prediction methods had been checked. The measured drop-size distributions in rains had permitted to calculate k and α coefficients for some frequencies and compare it with CCIR recommendations.

Keywords: Attenuation Statistics,
Rain Rate Statistics

The results of 4 years measurements of 11.5 GHz radio wave attenuation at the International experimental area which were a part of "INTER-COSMOS" program are presented in this report. The receiving ground stations were located in the center of the European part of Russia (site # 1: 56.67°N, 37.1°E, Dubna, 130 km north from Moscow, the height above the sea level is 0.12 km) and on the Black sea coast of the Caucasus mountains (site # 4: 43.75°N, 39.6°E, 50 km north-west from Sochi, the height above the sea level is 0.1 km). For the attenuation measurements the active repeater had been used on board of the geostationary satellite located at 14°W, so that elevation angles for the both sites were 12° and 18°. The carrier frequency 14.1 GHz had been emitted to the satellite from Dubna and had been retransmitted back to the Earth

on 11.52 GHz (Ref.1).

Such experimental set had required to elaborate the special technique to eliminate the influence of the atmosphere on the "up"-link so one can measure the attenuation statistics on the "down"-link only. The dynamic ranges for the attenuations measured in Dubna and Sochi were about 12-13 dB and 20 dB. The accuracy of our measurements was about 1 dB.

Simultaneously to the radio wave attenuation measurements the rain rate statistics had been recorded also near the ground stations. The tipping bucket rain gauges had been used as a standard equipment and an additional rain gauge (capacitor type) had been installed in Dubna also. More of it, the rain rate had been recorded at the distances 3 and 12.6 km from the ground station in Dubna along the terrestrial projection of the communication link to the satellite. A self-made photo-optical device for measuring the drop-size distributions in rains had been installed on the both sites as an extra experiment to clarify $\gamma = kR^\alpha$ relation for the real rains.

The sampling rates for the attenuation and rain rate measurements were 1 s and 1 m. The radio wave attenuation statistics in Dubna has been recorded from Jan. 1987 to Dec. 1990 (registration time is 96.4 % of the total time of the 4-years period). The same statistics in Sochi has been recorded from June 1987 to May 1990 (registration time is 91.5 % of the total time of the 3-years

Table 1.

Attenuation statistics on the two slant links for the period 1987-1990 (R - rain rate in mm/hour, A - attenuation in dB)

DUBNA

SOCHI

Probability of exceed.,%	w.month		year-av.	
	R	A	R	A
3.0	2.2	2.1		
2.0	3.0	2.3		
1.0	4.5	2.7		
0.7	6.0	3.0		
0.5	7.7	3.5	2.9	2.3
0.3	11.0	4.6	3.9	2.6
0.2	14.6	6.4	4.6	3.0
0.1			7.3	3.9
0.07			9.6	4.6
0.05			11.5	5.3
0.04			13.5	6.0
0.02			16.8	7.3
0.03			22.1	9.6

Probability of exceed.,%	w.month		year-av.	
	R	A	R	A
1.0	5.0	3.6		
0.5	11.5	4.9	5.0	2.6
0.3	20.0	5.5	8.5	3.4
0.2	28.0	6.8	13.5	4.1
0.1	40.0	9.0	24.0	5.3
0.07	47.2	10.2	30.5	6.0
0.05	54.5	11.5	34.0	6.7
0.03	66.7	14.4	40.0	8.2
0.02			45.0	9.3
0.01			54.0	11.6
0.005			67.0	14.2
0.003			82.0	18.0

period). The resulting statistics are presented in the Table 1 both the year-averaged and for the worst month.

At the site # 1 the most serious attenuations have been observed in summer time (most likely in July) and they are correlated with rains. At the site # 4 the worst events are in autumn time (most likely in September - October) and they are caused by rains too. In the winter time the attenuations due to the wet snowfalls were usually less than 2 dB but the single peaks were about 4 dB.

The year-to-year variance of the attenuation statistics at the site # 1 is quite large: for the probability range 0.05 - 0.2 % the ratio $(A_{\max} - A_{\min})/2A_{\text{mean}}$ is about ± 32 % for the year and ± 36 % for the worst month. For the site # 4 in the probability range 0.01 - 1.0 % these values are ± 15 % for the year and ± 17 % for the worst month.

One of the important purposes of our experiments was to check the different methods of how to predict

the attenuation statistics from rainfall rate data. Comparisons of measured and predicted distributions $P(A \geq A)$ for Dubna and Sochi have been carried out according to 8 methods. Eight methods for different locations are marked in Table 2, which contains our results in estimating r.m.s. values of prediction errors. The abbreviations for the following methods are: Svjatogor - Sv; Lin - Li; Stutzman & Dishman - St; CCIR - CC; Misme & Waldteufel - Mi; Assis & Einloft - As; Leitao & Watson - Le; Capsoni & Fedi - Ca (Ref.2).

Our results show that "the best" method (method which gives the best fit of predicted to measured data) is different for different locations: Svjatogor's method for Dubna and P.Misme's method for Sochi. So, for any location where no measured statistics are available, it is impossible to say beforehand what "the best" method is which should be used. So our preposition to predict attenuation statistics for rain is to use three different methods with subsequent averaging of results. In our opinion "the best" methods for the moment are: V.Svjatogor, CCIR

Table 2.

R.m.s. values for the different prediction methods

Nr	Location	Time interval	Sv	Li	St	CC	Mi	As	Le	Ca
1	Dubna	year-averaged	12.9	65.7	75.2	34.8	35.5	73.9	37.4	51.9
2	Dubna	worst-month	14.3	73.6	82.2	68.7	44.1	82.1	37.4	63.3
3	Sochi	year-averaged	14.0	34.3	24.5	10.0	6.7	19.5	17.8	20.1
4	Sochi	worst-month	24.0	44.3	38.0	24.9	11.8	35.5	25.4	14.6

and P.Misme. Data in Table 2 support this conclusion.

At site # 1 both slant and terrestrial links looking at the same azimuth have been used, so we have tried to estimate the validity of the transformation from one attenuation statistics into another. We have used the following expression for equal probabilities: $A_{sp} = m \cdot A_{ter}^n$, where A_{sp} and A_{ter} are attenuations for space and terrestrial links. The coefficient values are: $m=0.376$, $n=0.4$ with correlation between data as 0.9.

The comparison between the attenuation statistics for the worst month and year-averaged shows that the expression proposed by CCIR for such relation is acceptable:

$$Q = \frac{P_{wm}}{P_y} = B P_y^{-\beta},$$

where B и β are numerical coefficients. Their exact values for our sites are:

site # 1 (Dubna): $B=4.18$, $\beta=0.081$

site # 4 (Sochi): $B=3.16$, $\beta=0.12$.

The difference between them is supposed to match the climatic conditions between Moscow and sea coast.

To investigate the climatic influence on rains the drop-size distributions measurements had been carried out during one season at both sites. We had examined 1254 distributions (44 days with rains from

May to September) recorded in Dubna and 820 distributions (35 days from April to October) in Sochi. For each individual distribution we had calculated rain rate value (R) and the specific attenuation value (γ) for given frequency (Ref.3). After that using the regression least-square method we can get the values for the coefficients k and α at this location. Changing the frequency and repeating the calculations we can find all needed values which are presented in Table 3. As a draft conclusion one can say that the sea coast has much more small droplets than the continental area, and the real drop-size distributions are different from the statistically averaged model distributions.

CONCLUSIONS

The conclusions based on these experiments are:

- 1) the attenuation statistics for the center of the European part of the Black sea coast and it corresponds to the different rain rate statistics;
- 2) the worst-months for the European part of Russia are in summer (June, July) and the worst-months for the Black sea coast are in autumn (September, October);
- 3) the variations of year-averaged rain attenuation statistics from year to year are from -33% to 29 % and for the worst-month they are from -41% to 39%;

Table 3.

The values of k и α according to our experiments and calculations (R^* is the regression coefficient for Sochi)

F (GHz)	Dubna		Sochi		
	k	α	k	α	R^*
10	0.00939	1.270	0.00858	1.204	0.919
15	0.0259	1.267	0.0242	1.216	0.976
20	0.0577	1.162	0.0505	1.190	0.989
25	0.0993	1.093	0.0883	1.141	0.993
30	0.1501	1.045	0.1356	1.105	0.994
40	0.2829	0.967	0.2624	1.050	0.994
50	0.4533	0.889	0.4349	0.995	0.990
60	0.6403	0.817	0.6456	0.934	0.985
70	0.8206	0.755	0.8775	0.873	0.978
80	0.9830	0.704	1.108	0.816	0.970
90	1.126	0.663	1.319	0.767	0.962
100	1.250	0.630	1.498	0.728	0.953
150	1.505	0.563	1.872	0.650	0.924
200	1.473	0.559	1.887	0.640	0.918
250	1.430	0.559	1.851	0.636	0.916
300	1.390	0.559	1.797	0.638	0.916
350			1.755	0.638	0.917

4) the prediction method proposed by V.Svjatogor gives the best fit to the experimental rain attenuation statistics.

5) the specific attenuation of radio waves in rains depends on drop-size distributions for a particular place, but this influence starts to be significant ($\pm 20 - 25\%$) at the frequencies above 100 GHz.

REFERENCES

1. Alexandrova E. et al. Slant path rain attenuation distribution at frequencies above 10 GHz - correlation between some propagation models and results of long-term measurements in the Intercosmos programme. *41st Congress of the International Astronautical Federation*, 6 - 12 October, 1990, Dresden, GDR.
2. Pozhidayev V. 1993, A program package for prediction of radiowave attenuation statistics along slant communication links between ground station in Europe and geostationary satellites, *Proc. XX-OPEX Meeting*, Darmstadt, pp.165-170.
3. Zakharyan M.V. et al. 1989, Raindrops size-distribution measurements and evaluation of the radio wave specific attenuation, *Radiotekhnica i elektronika*, 34, 10, pp.2017-2022, (in Russian).

THE EVAPORATION OF RAINDROPS AND IT'S INFLUENCE ON THE MICROWAVE SLANT PATH ATTENUATION

Ondřej Fišer

TESTCOM, Hvoždanská 3, Praha 4, Czech Republic
Tel: +42-2-7992264, Fax: +42-2-7992318

ABSTRACT

As the drop falls we have to accept the rain drop evaporation as a physical phenomena. Within the rain attenuation computation on slant paths is this phenomena usually neglected. The purpose of this contribution is to answer the following question: is this simplification justified?

Keywords: satellite communication, rain attenuation, evaporation of rain drops

1. INTRODUCTION

Let us assume the International Standard Atmosphere model in order to study the evaporation of rain drops together with it's influence on the height dependence of the specific rain attenuation. For the temperature height profile let us suppose:

$$T(h) = 15^{\circ}\text{C} - 6.5 h [^{\circ}\text{C}, \text{km}] \quad (1)$$

For the air pressure we consider:

$$p(h) = p(0) \left[1 - \frac{6.5 h}{T_0 - 273.15} \right]^{5.24} [\text{mb}, \text{mb}, \text{km}, ^{\circ}\text{C}] \quad (2)$$

After checking many air humidity height profiles and in accordance with Ref.6 we suppose the value of air humidity to be independent of the height. Similarly after discussions with meteorologists, we neglect the changes of raindrop water density with the height supposing it to be 1 g/cm^3 .

Let us repeat the formula for specific rain attenuation supposing the raindrops canting angle being zero (according Ref.5):

$$\alpha(h, R) \approx 8.686 \cdot 10^5 \int_{0.025}^{0.35} f(a) N(a, h, R) da [\text{dB/km}] \quad (3)$$

[a] = cm

2. THE EVAPORATION OF RAINDROPS

We have created the program to compute the evaporation of raindrops in which the required parameters are: the initial equivolumetric rain drop radius in certain heights, the air pressure and humidity, the ventilation factor (which typical value is closed to 0.24) and the temperature. The differential equation has been published by Mason (Ref.6) and the numerical approximations given in Ref.2 enabled us to formulate the evaporation equation solely in the dependence on the above mentioned parameters:

$$\frac{da}{dh} = f(a, \varphi, T, p, \rho_w) \quad (4)$$

We have selected the Runge-Kutta method of order 4 (step dh being 100 m) to solve Eq.4.

For illustration Fig.1 shows the radius decrements of raindrops during it's fall while the air humidity of 80% was set (having studied the air humidity values in Sedlec - Czech Republic during a sufficiently long time period we concluded that the mean value of it is 80% while it's standard deviation being 13.5%).

When the air humidity was 80% (or less), the drop of the initial radius 0.025 cm was completely evaporated during it's fall from tested heights (1, 2, 3, 4, and 5 km).

3. HEIGHT PROFILE OF THE RAINDROPS SPECTRUM

For the height profile of the raindrops spectrum it is considered (cf. Ref.3 or Ref. 4):

$$N(a,h,R) = N(a,0,R) \frac{v(a,0)}{v(a,h)} \quad (5)$$

where $N(a,0,R)$ is the drop spectrum usually published supposing (silently) to be valid at the zero sea level.

It would be useful to define the falling factor $b(h,a)$:

$$b(h,a) = \frac{v(a,0)}{v(a,h)} \quad (6)$$

Using the exact formulas for the fall velocity of raindrops (Ref. 2) under the condition of the International Standard Atmosphere we have found the following approximation for b :

$$b(h,a) \approx 1 - 0.035 (a+1) h \quad [1, \text{cm}, \text{km}] \quad (7)$$

3.1 Influence of evaporation on the rain falling factor

Considering the evaporation of the falling raindrops, we can modify Eq. 5:

$$\omega(a,h) = \frac{v(a-\Delta a,0)}{v(a,h)} \quad (8)$$

where Δa is the equivolumetric rain drop radius decrement between heights h and 0 km (known from the solution of Eq. 4) and $\omega(a,h)$ we can call the modified falling factor). We can rewrite the formula (5) in the following form:

$$\omega(a,h) = \frac{v(a-\Delta a,0)}{v(a,0)} b(a-\Delta a,h) \quad (9)$$

The first fraction is easily evaluable by the formulas for the terminal rain drop fall velocity (at the zero sea level) while b is known from the approximation (7) if we do not prefer to use the

accurate expressions given in Ref. 2.

In the Tab.1 we can compare the top values (in heights h or zero respectively) of the fall velocity of raindrops as well as the drop falling factor b with the modified falling factor considering the evaporation. It is obvious, that the evaporation numerically plays the more part the smaller rain drop we consider.

3.2 Rain drop spectrum shift due to evaporation

The rain drop evaporation also has an influence on the "shift" of the rain drop spectrum. This is caused through the fact, that the spectrum (Eq. 5) at the height h and for drop radius being a , corresponds to the rain drop radius $\{a - \Delta a\}$ (this radius is considered to occur at the zero sea level) instead of the origin $\{a\}$.

$$N(a,h,R) = N(a-\Delta a,0,R) \quad (10)$$

On the other hand, the scattering function corresponds to the real equivolumetric rain drop radius of $\{a\}$.

3.3 Total influence of evaporation on the spectrum

When we combine the influence of the modified falling factor (Eq. 8) as well as of the "shift" of the spectrum (Eq. 10), we finally can define the height dependence of the rain drop spectrum, which used in the formula to compute the specific rain attenuation (3) gives us the height dependence of the rain drop spectrum considering the rain drop evaporation:

$$N(a,h,R) = N(a-\Delta a,0,R) \omega(a,h) \quad (11)$$

The spectrum value for the initial rain drop radius being 0.025 cm was estimated to be 0.01 cm^{-4} through the method of the graphical extrapolation.

4. PRACTICAL INFLUENCE OF THE EVAPORATION OF RAINDROPS ON THE SPECIFIC RAIN ATTENUATION ON SLANT PATHS

Having respected the described rain drop spectrum changes with the height due to the evaporation and having used the formulas (8) and (11) and the scattering functions according Ref.5 we have

computed the specific rain attenuation at heights 1,2,3,4 and 5 km for rain intensities 5,20, 40,60, 100,120 and 150 mm/h, for required frequencies, in our example for 11,20 and 30GHz; the used rain drop spectrum was the Marshall-Palmer one. In order only to study the influence of the evaporation the influence of the temperature and elevation angle on the scattering function is not included. For the "evaporated" raindrop of the radius being 0.025 cm we have tested the influence of the dispersion of the estimated spectrum within the interval $1 - 10^{-3}$ and we concluded that the choice of the value from this interval is negligible in the influence on the attenuation.

In Fig.2 you can observe the influence of the evaporation on the specific rain attenuation seeing the ratio of the specific rain attenuation computed through the Eqs.3 and 10 (i.e. considering the evaporation) to the specific rain attenuation value computed by methods neglecting the evaporation on frequencies 11 - 30 GHz. Similar results for frequency 20 GHz you can see on Tab.3 (for humidity 0.8) and on Tab.4 (for humidity 0.85).

The air humidity will increase through the evaporated water. We have derived the equation of the time dependence of the air humidity while the rain intensity is the parameter (Fig. 3). It is obvious, that the humidity quickly increases to the saturated stage where the evaporation is no more possible. The evaporation of raindrops has the influence on the rain attenuation only at the beginning of the rain event.

7. EXPLANATION OF SYMBOLS

α [dB/km]	specific rain attenuation
T [°C]	temperature
h [km]	height above sea level
a [cm]	equivolumetric drop radius
R [mm/h]	rain intensity
f [cm]	scattering function (Ref. 5)
N [cm ⁻⁴]	spectrum of raindrops
b [-]	falling factor
ω [-]	modified falling factor
ρ_w [g/cm ³]	the water density
φ [-]	the relative air humidity
p [mb]	the air pressure
v [cm/s]	fall velocity of raindrop

8. REFERENCES:

1. Pišer O. 1986: Influence of atmosphere status to rain attenuation on slant microwave path: examples...Proc. URSI, Budapest, 96p
2. Pruppacher Klett 1980, Microphysics of clouds and precipitation, D.Reidel Publishing Company
3. Misme P.,Waldteufel P. 1980 , A model for attenuation by precipitation on a microwave earth - space link, Ra.Sci., 15, 655p
4. Pišer O. 1986, Interaction of Electromagnetic Field with Rain Medium with Respect to Satellite Links Rain Attenuation Prediction in Frequency Range above 10 GHz, Dissertation, Czech Technical University
5. Uzunoglu at al. 1977, scattering of electromagnetic radiation by precipitation particles and propagation characteristics of terrestrial and space communication systems, Proc. IEE,124,No 5, 417p
6. Mason B.J. 1971, The Physics of Clouds, Clarendon Press-Oxford, 312p

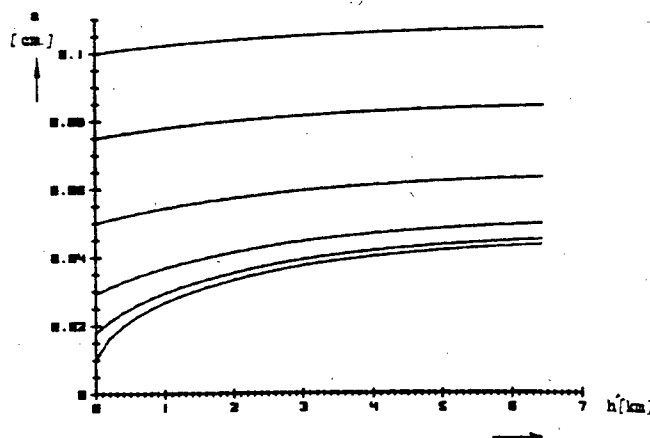


Figure 1: The height profiles of the radiuses of the falling raindrops changed due to the evaporation ($\varphi=80\%$)

$a(h)=0.05\text{cm}; X=v(0.05, h); Y=v(0.05, 0); Z=v(0.05-a, 0)$						
h [km]	$a(0)$ [cm]	X	Y	Z	$b(a, h)$	$\frac{\omega(a, h)}{b(a, h)}$
		[cm/s]				
1	0.045	419	403	368	0.963	0.879
2	0.041	438	403	335	0.921	0.766
3	0.037	460	403	306	0.878	0.666
4	0.034	484	403	282	0.833	0.582
5	0.032	512	403	262	0.788	0.512

Tab. 1: Fall velocities, falling factor, modified falling factor and their ratio for raindrop of the equivolumetric radius 0.05 cm during evaporation (the air humidity equals to 0.8)

$a(h)=0.075\text{ cm}$			$a(h)=0.1\text{ cm}$		
h [km]	$a(0)$ [cm]	$b(a, h)$ $\omega(a, h)$	$a(0)$ [cm]	$b(a, h)$ $\omega(a, h)$	
1	0.072	0.961 0.934	0.098	0.960 0.947	
2	0.069	0.917 0.870	0.096	0.915 0.892	
3	0.067	0.872 0.811	0.094	0.869 0.839	
4	0.066	0.825 0.756	0.093	0.822 0.788	
5	0.065	0.777 0.704	0.093	0.773 0.737	

Tab. 2: Falling factors, modified falling factors for raindrops of the initial equivolumetric radius 0.075 and 0.1 cm during evaporation (the air humidity equals to 0.8)

h [km]	R [mm/h]						
	5	20	40	60	100	120	150
1	0.5	2.3	4.8	7.2	11.9	14.1	17.4
1*	0.5	2.4	4.9	7.3	12.0	14.2	17.4
2	0.5	2.3	4.8	7.2	11.9	14.1	17.4
2*	0.6	2.5	5.0	7.3	11.9	14.0	17.2
3	0.5	2.3	4.8	7.2	11.9	14.1	17.4
3*	0.6	2.5	4.9	7.2	11.6	13.7	16.7
4	0.5	2.3	4.8	7.2	11.9	14.1	17.4
4*	0.6	2.4	4.8	7.0	11.2	13.2	16.0
5	0.5	2.3	4.8	7.2	11.9	14.1	17.4
5*	0.6	2.4	4.6	6.7	10.6	12.5	15.2

Tab. 3 Specific rain attenuation at frequency 20 GHz computed by methods considering the rain drop evaporation (labeled by asterisk) and computed by methods neglecting it, while the air humidity is 0.8.

h [km]	R [mm/h]						
	5	20	40	60	100	120	150
1	1.08	1.03	1.01	1.00	1.0	0.99	0.99
2	1.15	1.04	1.00	0.99	0.98	0.97	0.97
3	1.16	1.02	0.98	0.96	0.94	0.94	0.93
4	1.17	1.0	0.95	0.93	0.91	0.90	0.89
5	1.13	0.95	0.90	0.88	0.86	0.85	0.84

Tab. 4 Ratio of the specific rain attenuation computed through methods considering the evaporation to the specific rain attenuation computed by methods neglecting it, frequency is 20 GHz, the air relative humidity was chosen to be 0.85.

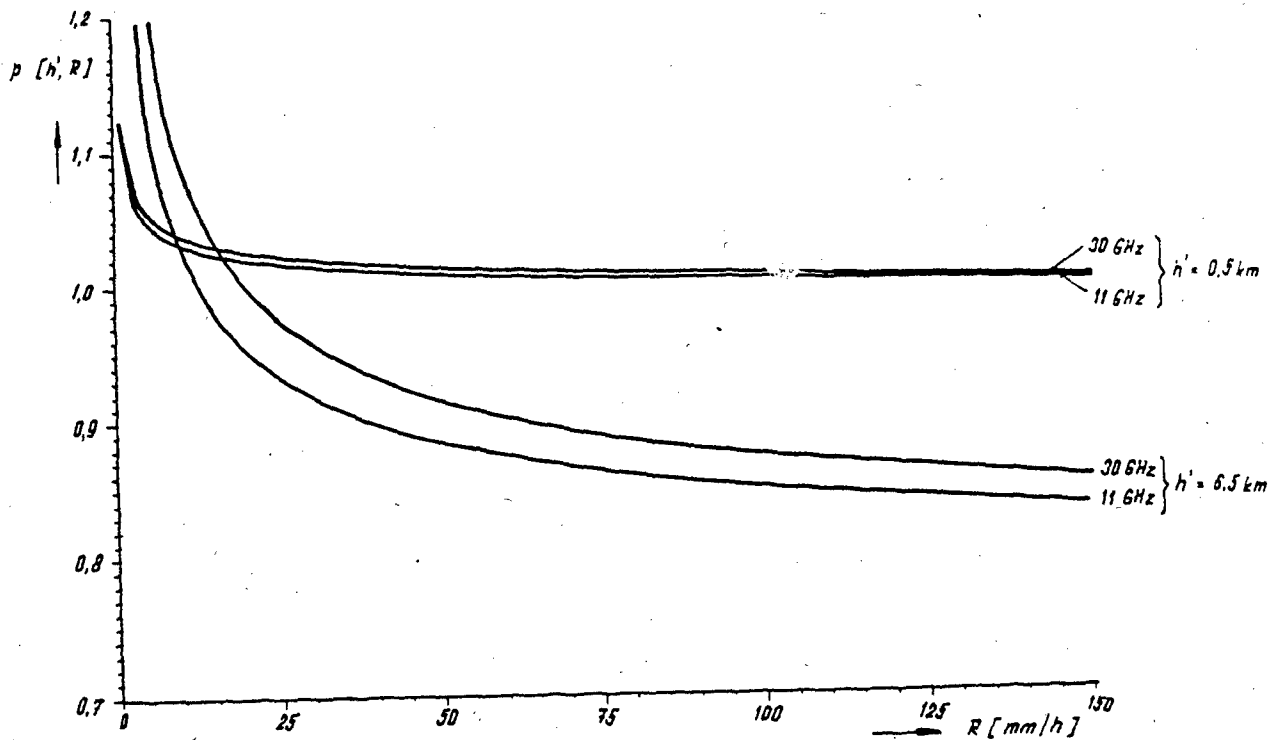


Figure 2: The relative changes of the specific rain attenuation respecting the rain drop evaporation with respect to its values at the zero sea level

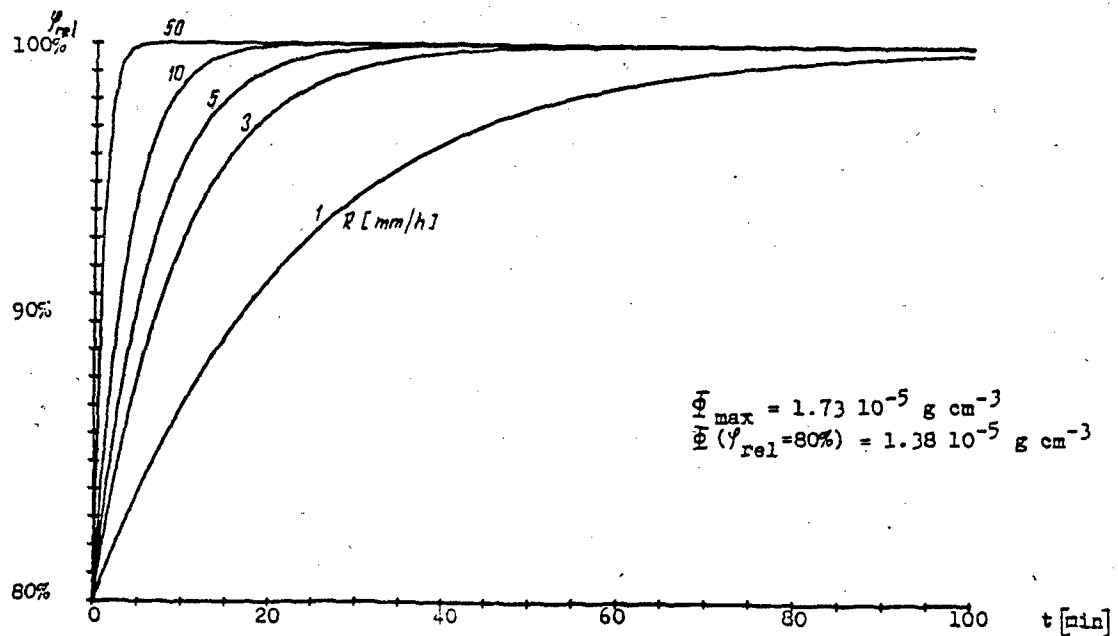


Figure 3: The increase of the relative air humidity due to the rain drop evaporation while the initial humidity is considered to be 80 %; the rain intensity is the parameter

ANALYSIS OF THE INTERFERENCE DUE TO DIFFERENTIAL RAIN ATTENUATION INDUCED BY AN ADJACENT PATH ON A MULTIPLE SITE DIVERSITY EARTH-SPACE SYSTEM OF DUAL POLARIZATION

J.D. Kanellopoulos¹ and C.N. Vazouras¹

1 - NTUA, Iroon Polytechniou Str. 9, Athens, Greece

Tel: +301-3691355, Fax: +301-3626792, E-mail: chvazour@macedonia.ntua.gr

ABSTRACT

In the present paper a method to predict the rain differential attenuation statistics valid for single earth-space systems, is extended to include multiple site diversity systems of dual polarization. The extended method is again based on a model of convective raincells as well as the lognormal model for the point rainfall statistics. Numerical results are presented and some useful conclusions are deduced.

Keywords: Interference, Multiple-Site Systems, Dual polarization.

1. INTRODUCTION

Frequencies above 10 GHz will be of high importance in future satellite systems as they will allow high antenna directivities and high communication capacities. In this band of frequencies the propagation is adversely affected by rain, which is a basic limiting factor concerning the outage performance of the radio system, especially in heavy rain climatic regions. In such cases, the double site diversity as an adaptive method to reduce the outage time has been introduced.

Further, the complete analysis of a communication system requires also the consideration of the interference effects which are of utmost importance for earth-space systems. Several types of interference can exist in this band of frequencies, but the main sources are the following: interference from adjacent satellites into the earth station due to differential attenuation and crosstalk between the orthogonally polarized signals for frequency-sharing systems. Both sources are crucially dependent upon the rainfall conditions.

As far as the predictive analysis for this kind of problems is concerned, several techniques have been developed for the evaluation of the cross-polarization discrimination (XPD) for frequency-sharing systems with no interference from adjacent satellites (Ref. 1). On the other hand, Rogers et al. (Ref. 2) have first proposed a semi-empirical model for the rain differential attenuation at the 1% conditional probability level. Later, Kanellopoulos and Houdjoumis (Ref. 3) have presented a more general method for the prediction of the interference due to differential attenuation induced on a single earth-space system.

The method is based on a model of convective raincells for the rainfall medium and the lognormal assumption for the point rainfall rate statistics. Next, the more complicated problems of the consideration of two unintended signals caused from both the cross-polarization and differential rain attenuation (Ref. 4) as well as the interference induced by an adjacent path on a multiple site diversity earth-space system (Ref. 5), have been treated.

The subject of the present paper is a combination of the latter models (Refs. 4-5) in order to include the interference case referring to a multiple site diversity earth-space system of dual polarization. The proposed technique is quite flexible and it is oriented to be applicable to any location of the world where the assumptions of convectivity for the raincells and lognormality for the point rainfall statistics are satisfied. Numerical results using the above technique are presented and some useful conclusions are deduced.

2. THE ANALYSIS

The configuration of the problem under consideration is shown in Figure 1. Two earth stations E_1 and E_2 are in communication with a satellite S_1 , forming a double-site diversity protection scheme. A second satellite S_2 , operating at the same frequency, is in orbit close to S_1 , the two subtending an angle θ to E_1 and E_2 . For the proceeding following values of attenuation are important: the attenuations A_{C1} and A_{C2} of the wanted signal referring to earth stations E_1 and E_2 , the corresponding attenuations A_{I1} , A_{I2} of the potential interfering signal and the system margins M_1 , M_2 available for rain attenuation. For reasons of simplicity, we will adopt here the balanced diversity systems, and this leads to the assumption of $M_1 = M_2 = M$.

For interference calculations, the following conditional probability should be evaluated

$$P = \frac{P_1 + P_2}{P_3 + P_4} \quad (1)$$

where

$$P_1 = P\left[\left(\frac{C}{I}\right)_1 \leq r, 0.5 \leq A_{C1} \leq M, A_{C1} \leq A_{C2}\right] \quad (2)$$

$$P_2 = P\left[\left(\frac{C}{I}\right)_2 \leq r, 0.5 \leq A_{C2} \leq M, A_{C2} \leq A_{C1}\right] \quad (3)$$

$$P_3 = P[0.5 \leq A_{C1} \leq M, A_{C1} \leq A_{C2}] \quad (4)$$

$$P_4 = P[0.5 \leq A_{C2} \leq M, A_{C2} \leq A_{C1}] \quad (5)$$

where the following carrier-to-interference ratios $(C/I)_1$ (for station 1) and $(C/I)_2$ (for station 2) under rain fading condition can be expressed by combining the effects of cross-polarization and differential rain attenuation as

$$(C/I)_i = C(A_{Ci}, A_{Ii}) = \left(\frac{C}{I} \right)_{i, \text{nom0}} - A_{Ci} + A_{Ii} - 10 \log \left\{ 1 + 10^{C_{X,i}/10} \right\} \quad i = 1, 2 \quad (6)$$

with

$$C_{X,i} = \left(\frac{C}{I} \right)_{i, \text{nom0}} - A_{Ci} + A_{Ii} - (XPD)_i \quad (7)$$

in terms of the A_{C1} , A_{C2} and A_{I1} , A_{I2} . The $(C/I)_{i, \text{nom0}}$ parameters (in dB) are related to the nominal parameters through

$$10 \frac{(C/I)_{i, \text{nom}}}{10} = 10 \frac{(C/I)_{i, \text{nom0}}}{10} + 10 \frac{(XPD)_{i, \text{nom}}}{10} \quad (8)$$

where $(C/I)_{i, \text{nom}}$ and $(XPD)_{i, \text{nom}}$ are the carrier to interference power ratio (dB) and the cross polarization discrimination during nominal (clear sky) conditions for the i th station ($i = 1, 2$), respectively. Further, the the cross polarization $(XPD)_i$ during rain fade can be expressed as

$$(XPD)_i = U - V \log A_{Ci} \quad i = 1, 2 \quad (9)$$

where the U and V are dependent upon system and rain medium parameters (Ref. 1).

2.1 General considerations

The following assumptions, which are required for the analysis, are taken into account:

1. The lognormal form for the point rainfall rate R and attenuation A is adopted (Ref. 6).
2. The slant paths corresponding to the wanted and potential interfering signal have generally different elevation angles given by ϕ_1 and ϕ_2 , respectively (See Figure 1).
3. Crane's simplified considerations for the vertical variation of the rainfall structure are

employed (Ref. 7). This leads to the assumption of uniform rain structure from the ground up to an effective rain height H given by the following expression

$$H = 4.8 \text{ km} \quad \Lambda \leq 30^\circ \\ H = 7.8 - 0.1|\Lambda| \text{ km} \quad \Lambda > 30^\circ \quad (10)$$

where Λ is the latitude of the specific location in degrees.

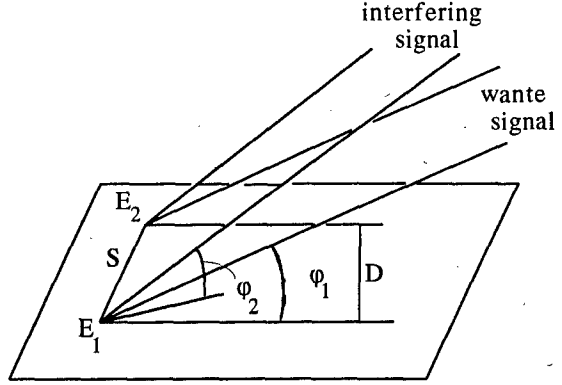


Figure 1: Configuration of the system

According to the above considerations, the single and joint exceedance probabilities for the slant paths can be obtained as

$$P_i = P \left[C \left(\frac{A_{Ci}'}{\cos \phi_1}, \frac{A_{Ii}'}{\cos \phi_2} \right) \leq r, \right. \\ \left. 0.5 \leq \frac{A_{Ci}'}{\cos \phi_1} \leq M, A_{Ci}' \leq A_{Cj}' \right] \quad (11)$$

for $i = 1, 2$, where j is 2 (if $i = 1$) or 1 (if $i = 2$), and the function $C(x, y)$ is as defined in Eq. 6, with Eqs. 7-9 taken into account. Also,

$$P_3 = P_4 = P \left[0.5 \leq \frac{A_{C1}'}{\cos \phi_1} \leq M, A_{C1}' \leq A_{C2}' \right] \quad (12)$$

where A_{Ci}' , A_{Ii}' ($i = 1, 2$) are the attenuations calculated for hypothetical terrestrial links (the projections of the slant paths).

The other assumptions concerning the specific rain attenuation A_0 and the horizontal variation of the rainfall spatial structure are the same as those presented elsewhere (Ref. 3).

2.2 Evaluation of the Conditional Probability

The calculation of the probability P_3 or P_4 is carried out as in (Ref. 5). Next, we can proceed to the calculation of P_1 and P_2 by using the joint probability density function $f(x,y,z)$ of the lognormal variables A_{C1}' , A_{C2}' and A_{II}' for P_1 , or A_{C2}' , A_{C1}' and A_{I2}' for P_2 (Ref. 8). The final results for P_1 are only presented here, because P_2 has quite analogous form.

$$P_1 = \frac{1}{2} \int_{u_{lk}}^{u_{lp}} \int_{-\infty}^{u_{2p}} f_{U_1 U_2}(u_1, u_2) \times \operatorname{erfc} \left[\frac{u_1 - \mu_3}{\sqrt{2}\sigma_3} \right] du_2 du_1 \quad (13)$$

where

$$u_{lk} = \begin{cases} \frac{\ln(0.5 \cos \phi_1 - m_1)}{S_1}, & x_0 \leq 0.5 \cos \phi_1 \\ \frac{\ln x_0 - m_1}{S_1}, & 0.5 \cos \phi_1 \leq x_0 \leq M \cos \phi_1 \\ u_{lp}, & x_0 \leq M \cos \phi_1 \end{cases} \quad (14)$$

and x_0 is the root of the transcendental equation

$$C \left(\frac{x_0}{\cos \phi_1}, 0 \right) = r \quad (15)$$

In (Eq. 14) u_{lp} , u_{2p} are defined through

$$u_{lp} = \frac{\ln(M \cos \phi_1 - m_1)}{S_1} \quad (16)$$

$$u_{2p} = \frac{\ln(A_{lp}'(u_1) - m_2)}{S_2} \quad (17)$$

and the $A_{lp}'(x)$ level is defined as follows: For each value of x , setting

$$A_{C1}'(x) = \exp(S_1 x + m_1) \quad (18)$$

the $A_{lp}'(x)$ level is found by solving the transcendental equation

$$C \left(\frac{A_{C1}'(x)}{\cos \phi_1}, \frac{A_{lp}'(x)}{\cos \phi_2} \right) = r \quad (19)$$

Further, μ_3 , σ_3 and $f_{U_1 U_2}$ are given by

$$\mu_3 = \frac{\rho_{n13} - \rho_{n12}\rho_{n23}}{1 - \rho_{n12}^2} u_1 + \frac{\rho_{n23} - \rho_{n13}\rho_{n12}}{1 - \rho_{n12}^2} u_2 \quad (20)$$

$$\sigma_3^2 = \frac{1 - \rho_{n12}^2 - \rho_{n23}^2 - \rho_{n13}^2 + 2\rho_{n12}\rho_{n23}\rho_{n13}}{1 - \rho_{n12}^2} \quad (21)$$

$$f_{U_1 U_2}(u_1, u_2) = \frac{1}{2\pi\sqrt{1 - \rho_{n12}^2}} \times \exp \left[-\frac{u_1^2 + u_2^2 - 2\rho_{n12}u_1u_2}{2(1 - \rho_{n12}^2)} \right] \quad (22)$$

In the previous expressions, m_1 , S_1 , m_2 , S_2 and m_3 , S_3 are the lognormal statistical parameters of the attenuations corresponding to the A_{C1}' , A_{II}' and A_{C2}' signals, respectively. Further, ρ_{n12} is the correlation coefficient between $\ln(A_{C1}')$, $\ln(A_{II}')$ and A_{C2}' signals, respectively. Further, ρ_{n12} is the correlation coefficient between $\ln(A_{C1}')$, $\ln(A_{II}')$, ρ_{n23} between $\ln(A_{II}')$, $\ln(A_{C2}')$ and ρ_{n13} between $\ln(A_{C1}')$, $\ln(A_{C2}')$. Following their definitions and after a tedious but straightforward mathematical analysis, one is able to obtain complicated but closed-form expressions for these parameters, in terms of the point rainfall parameters R_m , S_r , the constants a and b of the specific attenuation and the characteristic distance G of the spatial rainfall structure.

3. NUMERICAL RESULTS AND DISCUSSION

Due to lack of available experimental data of this kind, numerical results are only presented corresponding to realistic dual-site diversity systems suffering from differential attenuation interference, under the hypothesis of using both single and double polarization.

In Figures 2 and 3 the predictive results for an 20 GHz dual-site diversity system located in the Japan area, in the form of conditional probability versus r , for various values of $(C/I)_{nom}$ are presented. Two cases of potentially existing dual site diversity systems are shown, with separation distances $S = 10$ (Figure 2) and 30 km (Figure 3). In the same figure, the results for the single and the corresponding (i.e. the one with the same $(C/I)_{nom0}$ level) double polarization system are also shown. As it has also been indicated in the single-site system (Ref. 4),

the increase of the parameter $(C/I)_{nom0}$ results in a more pronounced impact of the depolarization.

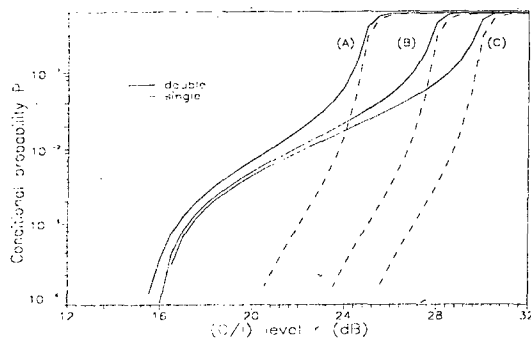


Figure 2 : Conditional probability versus r for a dual-site diversity system with $S = 10$ km. The $(C/I)_{nom0}$ parameter is 25 dB (A), 28 dB (B), and 30 dB (C), with $(XPD)_{nom} = 35$ dB and a polarization angle of 45° from horizontal.

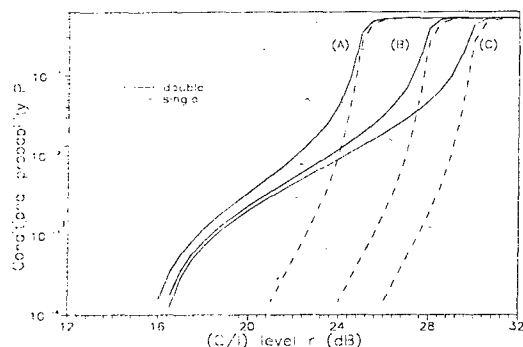


Figure 3 : Conditional probability versus r for a dual site diversity with $S = 30$ km. The other parameters are the same as above.

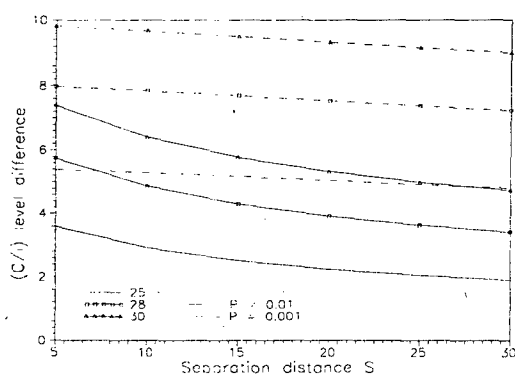


Figure 4: Threshold difference versus the separation distance S for various probability levels and $(C/I)_{nom0} = 25, 28$ and 30 dB. $(XPD)_{nom}$ is 35 dB.

In Figure 4, the above difference of (C/I) for a prescribed probability level and various $(C/I)_{nom0}$ versus the separation distances is examined.

4. CONCLUSIONS

In conclusion, a predictive procedure for the evaluation of the total interference for a multiple site diversity system of dual polarization caused by the cross polar signals and the differential rain attenuation from an adjacent satellite path, is proposed. The procedure is based on the convective raincell model and it is quite flexible to be applicable to any location of the world where the lognormal form for the rainfall distribution can be adopted. The numerical results taken from the proposed procedure are employed to deduce some useful results with regard to the interference problem under consideration.

5. REFERENCES

1. Gaines J. et al. 1982, Modelling the joint statistics of satellite path XPD and attenuation, *IEEE Trans. Antennas Propagat.*, AP-30, 4, pp. 815-817.
2. Rogers R. et al. 1982, Statistics of differential rain attenuation on adjacent earth-space propagation paths, *Ann. Telecommun.*, 37, 11-12, pp. 445-452.
3. Kanellopoulos J. et al. 1990, A model for the prediction of differential rain attenuation on adjacent earth-space propagation paths, *Radio Sci.*, 25, 5, pp. 853-864.
4. Kanellopoulos J. et al. 1993, Analysis of the interference on a dual polarized earth-space path due to differential rain attenuation from an adjacent satellite system, *23rd EuMC Proceedings*, Madrid, Spain, pp. 961-963.
5. Kanellopoulos J. et al. 1994, Analysis of the interference due to Differential Rain Attenuation Induced by an Adjacent Path on a Multiple Site Diversity System, *MELECON '94 Proceedings*, Antalya, Turkey.
6. Kanellopoulos J. et al. 1987, Analysis of rain outage performance of route diversity systems, *Radio Sci.*, 22, 4, pp. 549-565.
7. Crane R. 1980, Prediction of attenuation by rain, *IEEE Trans. Commun.*, COM-28, pp. 1717-1733.
8. Kanellopoulos J. et al. 1990, Prediction of Triple-Site Diversity Performance in Earth-Space Communication, *Journal of Electr. Waves and Appl.*, 4, 4, pp. 341-358.

VARIATIONS OF 0° C ISOTHERM HEIGHT DURING RAIN IN THE BERLIN AREA

H. Trommer, S. Szuppa, G. Heyer

Forschungs- und Technologiezentrum, Deutsche Bundespost Telekom, Ring 19, 15752 Kolberg, Germany
Tel: +49-33768-87320, Fax: +49-33768-87246

ABSTRACT

Results of a statistical analysis of 0° C isotherm heights on the basis of radiosonde ascents in connection with rain intensity measurements are presented for a five-year period for the Berlin area.

Keywords: rain attenuation, satellite links, 0° C isotherm height

1. INTRODUCTION

In many models for prediction of rain attenuation along slant paths, the effective path length through rain is one of the important input parameters. It is closely related to the effective rain height. In temperate climates, it is common practice to substitute the height of the 0° C isotherm for the height during rainy conditions, h_{FR} , since it is believed that liquid water will not occur much above this height at lower temperatures. This hypothesis is only a first approach because the temperature of liquid water can be much lower than 0° C.

The ITU-R Recommendation PN 839 (Ref.1) gives a formula how to estimate this height as a function of geographical latitude. We have compared the predictions by this formula with measurements by means of radiosonde ascents, carried out during a five-year period. Concurrently, rain rate was measured continuously by means of a water wheel rain gauge.

2. DATA EVALUATION

2.1 Data set

Radiosonde measurements were made four times a day at 0, 6, 12 and 18 h UTC during seven months per year, i.e., from April to October at Lindenberg Observatory ($\varphi = 52.2^\circ$ N, $\lambda = 14.1^\circ$ E, south-east of Berlin) from 1984 to 1988. The data set includes the isotherm

heights for 0°, -5°, -10° and -15° C within the frost-free period of the years 1984 to 1988. The location where concurrent rain measurements were carried out is about 2 km west of Lindenberg.

In order to better assess weather conditions, we also used weather maps, indicating the current weather situation and sequence of events (temperature, rain, thunderstorm, etc.) at Lindenberg for the same hours of observation. In case of temperature inversion, we always took the lower value of the 0° C isotherm height for our calculations.

2.2 Average height of 0° C isotherm

The statistical analysis of this data set yields an average value of the 0° C isotherm height during the summer months, i.e. June, July and August, of $h_{FS} = 2911$ m, with a standard deviation of 706 m. This value is to be compared with that of about 3300 m as calculated from the respective figure of Reference 1. The corresponding average 0° C isotherm height for the total period (April to October) is 2527 m. When analysing the monthly averages, the month of August turns out to be the one with the largest value of the 0° C isotherm height with one exception in 1987. These values range from 2999 to 3255 m, the average value being 3167 m (see Table 1).

The corresponding average height for the total period (April to October) is 2527 m.

2.3 Rainy conditions

The measured height of the 0° C isotherm during rainy conditions, h_{FR} , from April to October, for Lindenberg is 2300 m. It might be even slightly lower, if values for the colder period, i.e. November to March, would be included. However, these measurements are not available. Nevertheless, the value is significantly lower than that expected on the basis of Ref. 1, which predicts a h_{FR} - value of 2810 m.

Predictions based on more recent work of Ito (Ref. 2), i.e.

$$h_{FR}(km) = 5.2 - 0.092(\varphi - 26) \\ (\text{for } \varphi \geq 26^\circ),$$

would result in only a slightly lower value (2790 m).

Fig.1 gives, for example, the average 0° C isotherm height in 1985 during rainy conditions for the hours of observation 0, 6, 12, 18 h UTC and a daily average value.

If, however, the height of the 0° C isotherm during rainy conditions is evaluated only for the summer months (June, July and August), its value increases to about 2690 m. On average, the level of the 0° C isotherm height decreases by about 250 m in summer during rain and by about 320 m during thunderstorms. The latter difference was evaluated from an analysis of 87 events of thunderstorm with rain.

A particularly remarkable day is the 5th of June, 1984. On this day, the 0° C isotherm height was going down from 3317 m to only 300 m within 6 hours. The wheather situation on that particular day was as follows: A cold front moved across Central Europe with a very distinct boundary between cold and warm air-masses associated with heavy rain showers (rain intensity at Lindenberg 72 mm/h) and a temperature decrease of 15 degree. We have disregarded this day in the evaluation of average value.

2.4 0° Isotherm height and temperature at ground level

Fig. 2 shows for each year the daily average of the 0° C isotherm height as a function of ambient temperature. In Fig. 3 also the average curve for rainy days is depicted for 1988. The slope of the curve for rainy days is higher by 20 % higher than for the average.

3. CONCLUSIONS

In summer months measured average values of 0° C isotherm heights in the Berlin area are lower than predicted by the ITU-R, Rec. PN 839. For rainy conditions, the value h_{FR} , decreases by about 250 m during rain, and 320 m during thunderstorms.

4. REFERENCES

1. ITU-R, Rec. PN 839, Geneva, 1992, Rain height model for prediction methods
2. Ito, S. 1989, Dependence of the 0° C isotherm height on temperature at ground level in rain, Trans. DEICE, E72(1989)2, pp. 98 - 100

Table 1:
Average 0° C isotherm heights and standard deviations at Lindenberg

	1984		1985		1986		1987		1988	
	av.	σ	av.	σ	av.	σ	av.	σ	av.	σ
April	1359	565	1452	753	1561	943	1716	657	1540	736
May	2131	546	2493	812	2627	652	1913	523	2492	522
June	2314	671	2327	610	2970	899	2575	702	2798	375
July	2725	746	3067	551	2967	742	3182	642	3147	583
Aug.	3255	423	3198	546	2999	756	2923	789	3217	644
Sept.	2316	576	2754	625	2393	613	2827	804	2787	631
Oct.	2349	627	2471	914	2571	891	2420	729	2508	1010

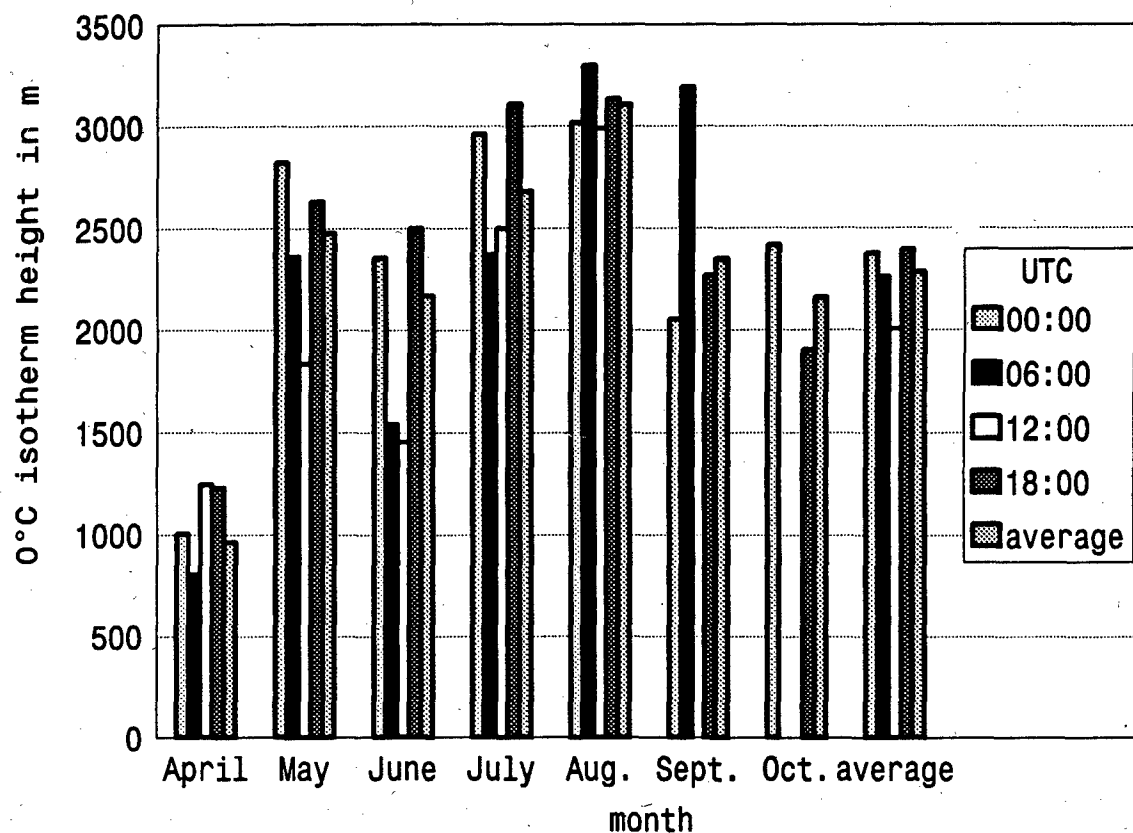


Figure 1: Average 0°C isotherm height during rain (1985)

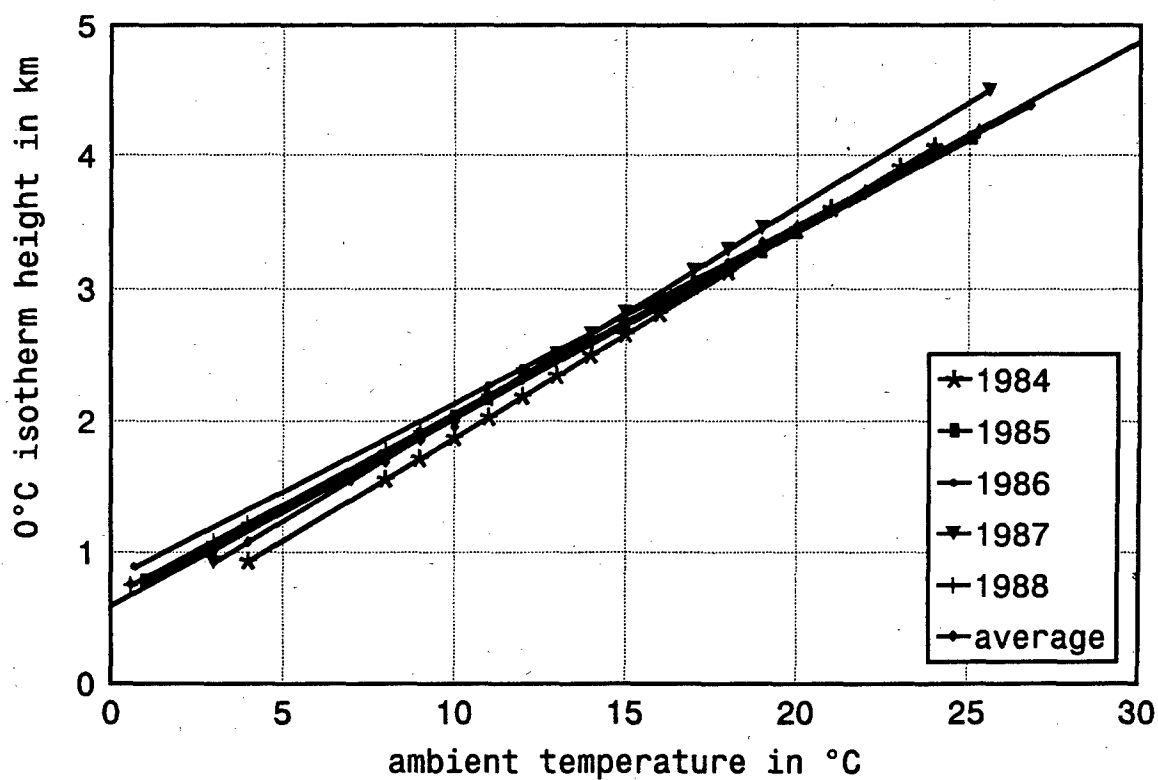


Figure 2: Average 0°C isotherm height versus ambient temperature (1984 - 1988)

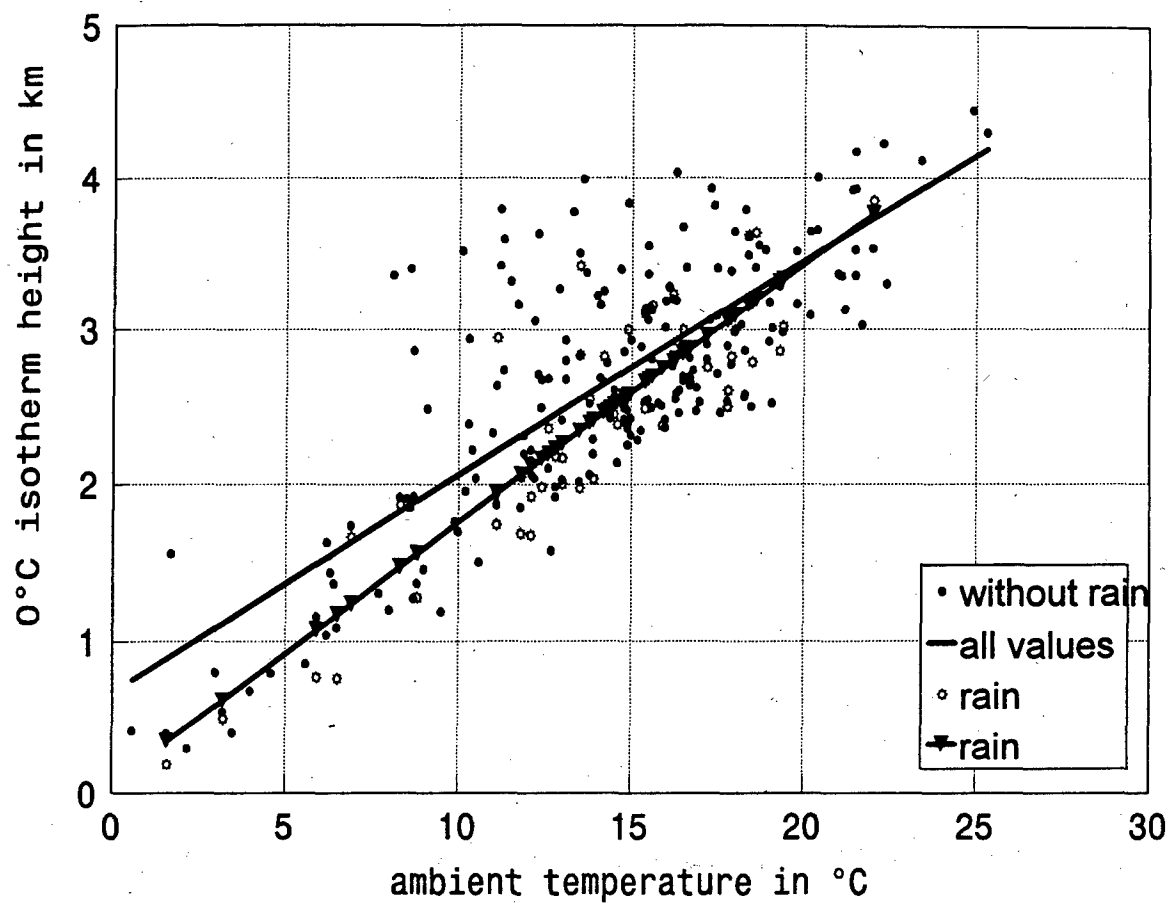


Figure 3: Average 0° C isotherm height versus ambient temperature (1988)

RADIOMETRIC MEASUREMENTS OF EFFECTIVE RAIN HEIGHT

M.S. Pontes, L.A.R. Silva Mello, R.S.L. Souza

CETUC-PUC/Rio, R. Marquês de S. Vicente 225, Rio de Janeiro, 22453-900, Brazil
Tel: +55-21-5299255, Fax: +55-21-2945748, E-mail: mspontes@cetuc.puc-rio.br

ABSTRACT

This paper presents the first results of an investigation of the quasi-instantaneous and statistical behaviour of the effective rain height for rain attenuation in satellite links. The results are derived from point rainfall rate and radiometric attenuation measurements.

Keywords: Satellite links, Rain attenuation, Rain height, Radiometry.

1. INTRODUCTION

The random nature of rainfall, both in space and time, poses a major difficult in the prediction of rain attenuation that affects terrestrial and slant path radio links operating in frequencies above 10 GHz. To overcome this difficulty, most prediction methods use the concept of an equivalent rain cell, that should produce the same path attenuation as the random rain clusters.

The rain attenuation prediction method currently recommended by the ITU-R (Ref. 1) is based on an uniform rainfall rate cell of rectangular cross section. The equivalent rain cell dimensions are the effective rain height, modelled as a function of the site latitude, and the effective cell length, which is a function of the point rainfall rate exceeded during 0.01% of the time at the site. Other methods attempt to model the equivalent rain cell using other characteristics of the path and the site, but some climatic dependence is usually implied.

In this paper, the behaviour of the effective rain height is investigated based on data obtained in concurrent measurements of point rainfall rate and radiometric attenuation at 12 GHz. The measurements were performed at Rio de Janeiro, in the tropical region of Brazil, using a radiometer pointing upwards and a tipping bucket raingauge. A second radiometer pointing with 53° elevation angle was also used, allowing the comparison between the effective rain height and the effective path length, which is dependent of the effective

cell length. Data from similar measurements with 83° elevation angle at Manaus are also available.

2. EFFECTIVE RAIN HEIGHT

Using the concept of an equivalent cell of uniform rain, the attenuation in a satellite link is given by

$$A(\text{dB}) = \gamma(\text{dB/km}) \cdot L_{\text{eff}}(\text{km}) \quad (1)$$

where L_{eff} the effective path length and γ is the specific attenuation, a function of rain rate, frequency and wave polarisation. The effective path length can be written as

$$L_{\text{eff}} = \frac{h_R - h_S}{\sin \theta} \cdot r_h \quad (2)$$

where h_S is the altitude of the site respectively to the mean sea level, θ is the elevation angle and r_h a reduction factor to take into account the non-uniformity of the rain intensity in the horizontal direction. The effects of the non-uniform vertical structure of rainfall are represented by the effective rain height h_R . For a 90° elevation path, the horizontal reduction factor equals 1 and the effective rain height is given simply by

$$h_R = \frac{A}{\gamma} + h_S \quad (3)$$

3. EVENT ANALYSIS

The measurements with the radiometer pointing upwards were conducted during two years, from January 1991 to January 1993. Data recorded consists of samples of the antenna noise temperature taken every 2 seconds and the date and time of each raingauge tip. The raingauge is a standard tipping bucket with a bucket volume corresponding to 0.2 mm of rain. The antenna noise temperature T_A is related to slant path attenuation by (Ref. 2) :

$$A(\text{dB}) = 10 \log \frac{T_m - T_{cs}}{T_m - T_A} \quad (4)$$

were T_m is the effective medium temperature and T_{cs} the clear sky temperature.

To analyse the behaviour of the effective rain height, the raingauge data were processed to calculate quasi-instantaneous rainfall rates, which were subsequently interpolated to provide time series of rain rate, similar to the radiometer data. Both series were filtered using a moving average of 30 samples, corresponding to a one minute window. The time series of effective rain height were then obtained using Eq. 3-4.

An example of rain attenuation event is shown in Figure 1. It is a long event, with a total duration of about 2 hours. The rainfall rate is below 20 mm/h during most of the event, having a peak value of 38 mm/h. There is very good correlation between the point rainfall rate and the attenuation, which never exceeds 2 dB. The effective rain height varies between 2 and 4 km during most of the time, with a peak value of approximately 6 km.

Figure 2 shows a scatterplot of instantaneous values of rain rate and effective rain height for this event. The points are well fitted by an exponential function, as shown in the figure. For rain rates above 8 mm/h, the effective rain height is always below 3 km. Higher values of effective rain height may be attributed, in this case, to the inaccuracy of the raingauge for very low rain rates.

A second example is shown in Figure 3. In this case it is a shorter event of heavy rain, with a total duration of about 30 minutes. The rainfall rate has a peak value of 92 mm/h, being above 20 mm/h during most of the event, and the attenuation reaches 10 dB. The instantaneous correlation between point rainfall rate and the attenuation is not as good as in the previous example. The effective rain height varies mostly between 2 and 6 km, with a peak value of approximately 8 km.

Figure 4 shows the corresponding scatterplot of instantaneous values of rain rate and effective rain height. A much higher spread relatively to the exponential fit is observed in this case. The higher values of effective rain height correspond to the first part of the event, before the rainfall rate has reached the peak value, as illustrated in Figure 5, that shows the same scatterplot as in Figure 4, but with the points corresponding to the first and second parts of the event represented by crosses and circles, respectively. Whether this result really indicates that the effective rain height is reduced as the event develops, or is due to the relatively slow response of the tipping bucket raingauge, is a matter for further investigation.

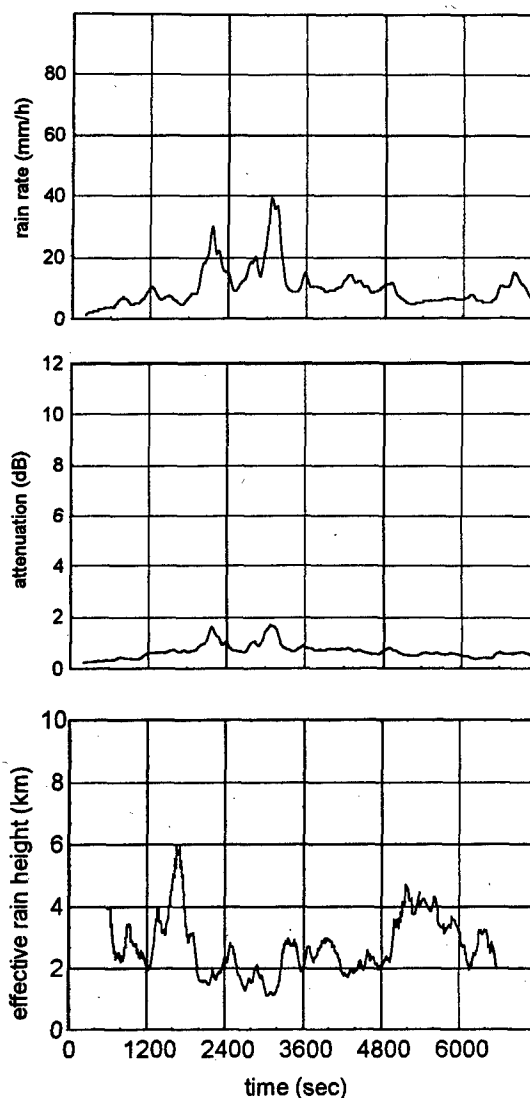


Figure 1: Rain event at Rio de Janeiro on 07 May 1991 - point rainfall rate (top), attenuation (middle) and effective rain height (bottom).

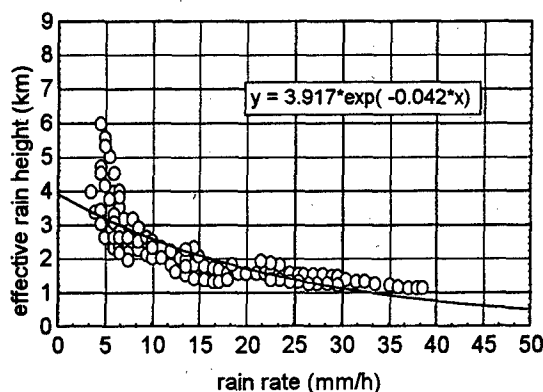


Figure 2: Instantaneous relation between point rainfall rate and effective rain height for the rain event at Rio de Janeiro on 07 May 1991.

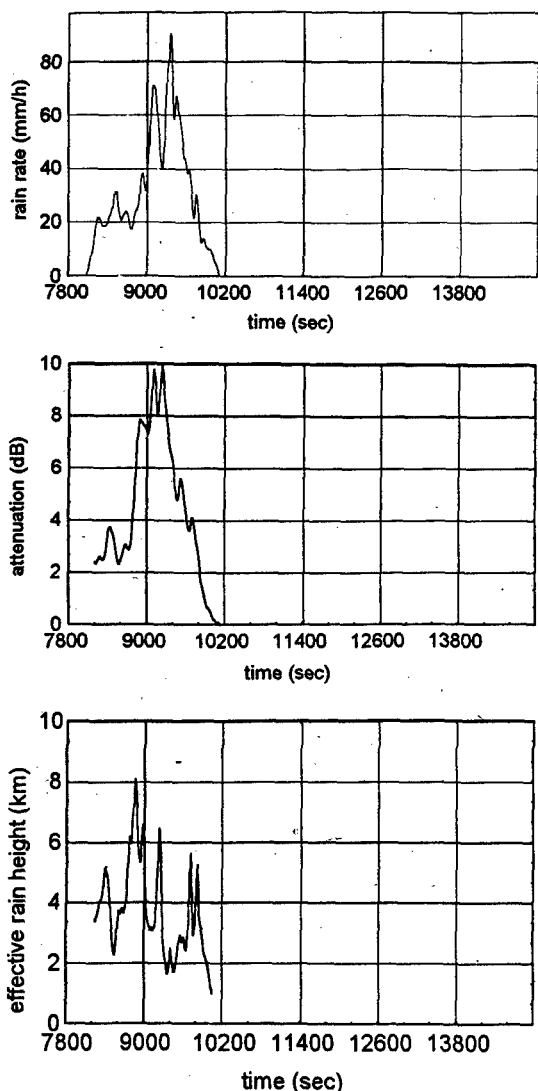


Figure 3: Rain event at Rio de Janeiro on 05 Feb. 1991 - point rainfall rate (top), attenuation (middle) and effective rain height (bottom).

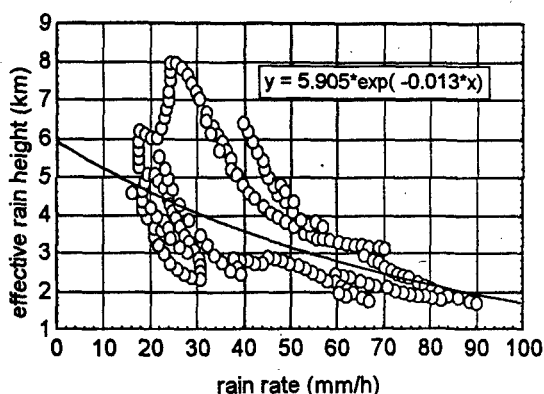


Figure 4: Instantaneous relation between point rainfall rate and effective rain height for the rain event at Rio de Janeiro on 05 Feb. 1991.

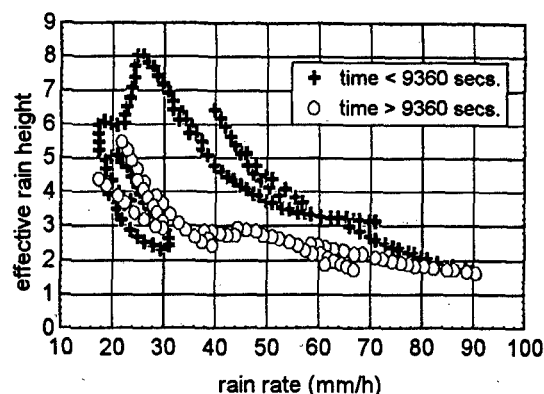


Figure 5: Instantaneous relation between point rainfall rate and effective rain height for the rain event at Rio de Janeiro on 05 Feb. 1991 (showing 1st and 2nd parts of the event).

4. STATISTICAL ANALYSIS

The data from Rio de Janeiro and Manaus were analysed to provide yearly cumulative distributions of rain rate and attenuation and conditional distributions of effective rain height during rain events.

As shown in Figure 6, Manaus, in the equatorial region of Brazil, is subjected to a very severe rain regime so that the attenuation exceeded at a given percentage of time is around 4 dB higher than the corresponding value for Rio de Janeiro. For this site, the attenuations measured with 53° elevation are slightly higher than the values measured with 90° elevation.

The distributions of effective rain height and effective path length were obtained conditioned to occurrence of rain rates higher than 20 mm/h. This procedure was adopted to minimise the measurement errors due to the tipping-bucket rain gauge time response.

As shown in Figures 7, the distributions are very well fitted by exponential functions. The median value of the effective rain height in Rio de Janeiro is 2.38 km. For low probabilities (or percentages of time) the effective path length is larger than the effective rain height, as could be expected.

Figure 8 shows the conditional distribution of effective path length for Manaus. Considering the very high elevation angle of 83°, the effective path length is approximately equal to the effective rain height at this site. The distribution is well fitted by an exponential function and the median value of the effective rain height is approximately equal to 2.49 km.

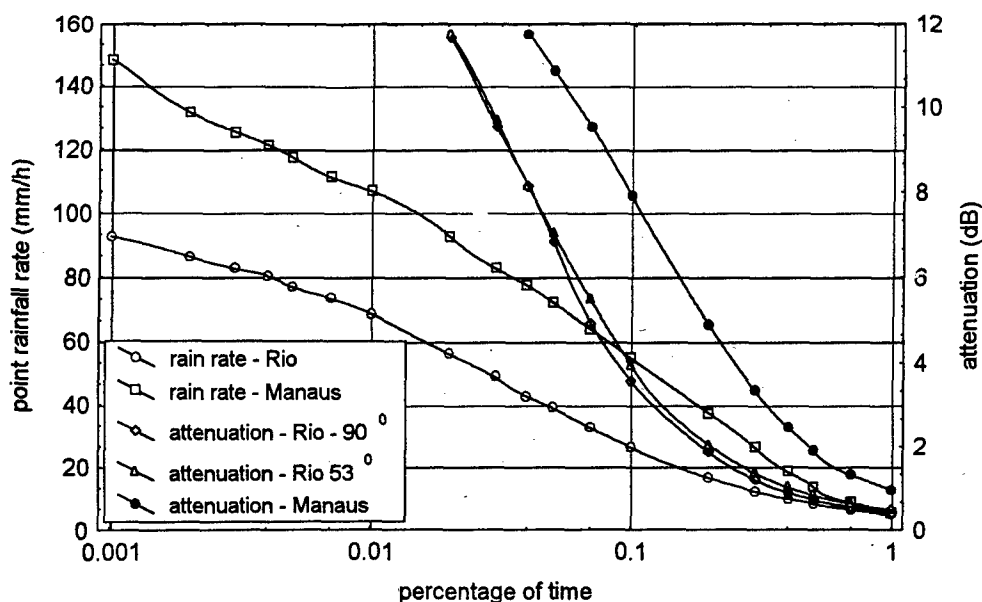


Figure 6: Cumulative probability distributions of point rainfall rate and slant path attenuation for Manaus (equatorial climate, 83° elevation angle) and Rio de Janeiro (tropical climate, 90° elevation angle).

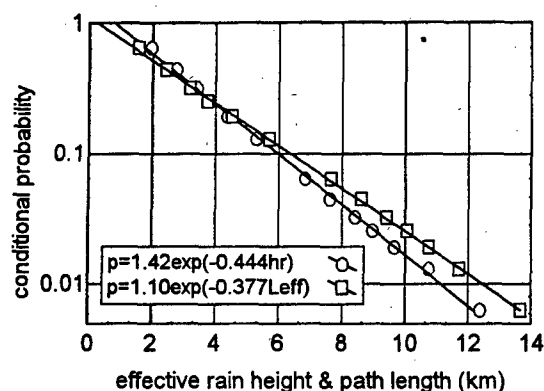


Figure 7: Conditional probability distributions of effective rain height and effective path length (Rio de Janeiro).

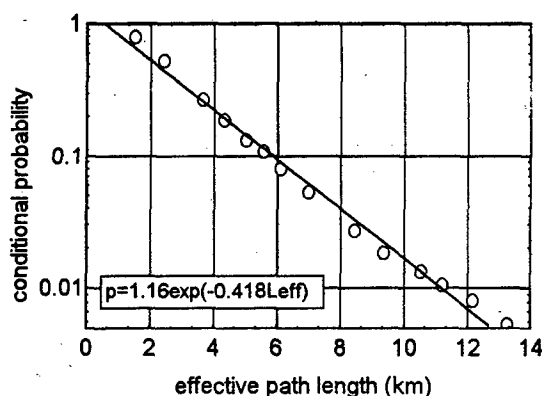


Figure 8: Conditional probability distributions of effective path length (Manaus).

5. CONCLUSIONS

Time series of effective rain height were obtained from data of concurrent measurements of point rainfall rate and radiometric attenuation.

The event based analysis indicated that it varies mostly in the range from 2 to 4 km during rain events. Scatterplots of instantaneous values of rain rate and effective rain height are well fitted by exponential functions, the effective rain height decreasing as the rain rate increases.

It was observed that in the beginning of the rain event, particularly for heavy storms, the time response of the rain gauge may induce measurement errors, leading to much higher values effective rain height, that must not be considered.

Conditional distributions of effective rain height, obtained for periods with measured rainfall rates above 20 mm/h, are well fitted by exponential functions. The distributions obtained for Rio de Janeiro, in a tropical climate, and Manaus, in a equatorial climate, are not very different, showing approximately the same median value.

6. REFERENCES

1. CCIR Recommendation 618-1, CCIR RPN Series, Geneva 1992.
2. Pontes M S et al. 1990, Ku Band Radiometric Measurements at Three Locations in Brazil, *Int. J. Sat. Com.*, 8, pp.127-132.

THE RAINGCELLS CLIMATOLOGY ACROSS THE WORLD AND ITS IMPACT IN THE PREDICTION OF VARIOUS RAIN DEPENDENT PROPAGATION PARAMETERS

C. Capsoni, M. D'Amico, A. Paraboni and F. Zaccarini

Politecnico di Milano, Piazza Leonardo da Vinci 32, I-20133 Milano, Italy

ABSTRACT

A more accurate characterization of the rain climatology seems to be the way to achieve more accurate predictions of propagation impairments. This paper illustrates the results of an investigation aimed to highlight the role of the stratified rain in determining the rain attenuation for different rain zones of the globe. The experimental measurements stored in the CCIR data bank, selected with a 'climatic' criterion, have been used to test, among the others, the EXCELL model.

1. INTRODUCTION

The prediction of rain induced propagation impairments (attenuation, interference etc.) starting from the cumulative distribution of the point rainfall intensity has been, in the last years, the subject of a big effort carried out by many researchers, owing to the strong impact of the rain phenomena on the design of modern satellite-based TLC systems. Despite this effort a prediction accuracy for rain attenuation better than some 30% (standard deviation in dB for the case of attenuation) seems hardly obtainable to-day. A better characterization of the rain climatology, and, as a consequence, the adoption of "better tuned" parameters in the prediction procedures seems the way to obtain a substantial improvement in the prediction performance. This is true, in particular, for the EXCELL rain model, a multipurpose model of the horizontal rain structure which has been developed by the Politecnico di Milano with the aim of predicting many propagation parameters related to rain. With reference to the EXCELL model, which reproduces the spatial density of the rain cells as a function of the peak intensity and cell-size, the paper aims at comparatively assessing the different influence of the ITU-R (ex CCIR SG5) rain zones on some propagation effects.

2. THE EXCELL MODEL

The EXCELL model is a model of the horizontal structure of the rain intensity which assumes the rain being organized in cells. Calling R the point rainfall intensity, its distribution is assumed to be exponential in space (hence the acronymus EXponential CELLS), i.e. obeying to the law:

$$R = R_M \exp(-\rho / \rho_0) \quad (1)$$

where ρ is the distance from the cell centre and the two parameters R_M (peak rain intensity) and ρ_0 (radius at $1/e$) are random variables characterized by a distribution giving the number of cells existing per unit area within unit range $d(\ln R_M)$ and $d\rho_0$.

According to observations made by the meteorological radar sited at Spino d'Adda, the distribution of ρ_0 can be modelled by an exponential function:

$$p(\rho_0 / <\rho_0>) = \exp(-\rho_0 / <\rho_0>) \quad (2)$$

$$<\rho_0> = 1.7 \left[(R_M / 6)^{-10} + (R_M / 6)^{-0.26} \right] \quad (3)$$

for $R_M > 4$ mm/h, while the number density of cells (number of cells per square km and per unit range of $\ln(R_M)$, regardless to ρ_0) is given by:

$$N(\ln R_M) = -P'''(\ln R_M) / (4\pi <\rho_0>^2) \quad (4)$$

where P''' is the third order derivative (with respect to $\ln(R)$) of the point rainfall intensity distribution characterizing the location of interest.

In addition to the cells a "plateau" of rain is assumed to account for the stratified rain surrounding the cell and/or the presence of fragmented rain structures of minor importance. This plateau is taken into account in evaluating the attenuation by adding a contribution equal to the one which would be produced by an uniform rain intensity along the path. This constant rain rate is fixed to the value 4 mm/h (leading to an attenuation $A_{plateau} = k4^\alpha L_s$ with k and α constants given by the CCIR and L_s =path length). For this reason the application of the model cannot be extended below 4 mm/h.

The third order derivative in (4) must be evaluated by approximating the actual $P(R)$ with a mathematical model. A convenient model is given by the "log-power-law" one:

$$P(R) = P_0 [\ln(R_{asint} / R)]^n \quad (5)$$

where P_0, R_{asint}, n are parameters to be fitted on the given cumulative distribution.

The third order derivative is then given by:

$$-P''' = n(n-1)(n-2)P_0 [\ln(R_{asint} / R_M)]^{n-3} \quad (6)$$

3.THE CLIMATIC INFLUENCE

In table 1 the parameters P_0, R_{asint} and n are given for each of the CCIR rain zones.

Once the distribution of cells has been determined for each rain zone, the statistical prediction of any propagation parameter depending on the spatial distribution of rain is possible by means of a simulation in which the cells are "swept" over the radio system and in each position the parameter is evaluated by assuming the simulated rain profile given by the cell in that particular position with

$$\text{respect to the system } (A_{cell} = \int_{pathlength} kR(x,y)^\alpha dl).$$

This is the basis of the EXCELL prediction model, which has been recently been applied to the prediction of site diversity attenuation [1] and to the problem of EM interference by rainscatter [2].

The EXCELL method has been recently tested, on behalf of the ITU-R (ex CCIR), against the CCIR attenuation data bank for various latitudes, elevations frequencies etc. In any case the performance was very good placing the the model always among the best performing ones.

The method is here tested for various CCIR rain zones. Unfortunately the data available in the CCIR data bank are far from being uniformly distributed and most of the zones are poorly covered by experiments; in order to preserve significativity to the test, only the rain zones with more than 10 experiments were considered, namely the E, K and M ones.

RZONE	R_{asint}	P_0	n
A	88	1.7E-4	4.86
B	128	1.2E-4	5.35
C	168	1.3E-4	5.31
D	168	8.0E-5	6.49
E	280	1.3E-4	5.02
F	312	1.4E-4	5.19
G	260	1.1E-4	6.01
H	332	1.7E-4	4.99
J	220	7.0E-5	8.14
K	400	1.6E-4	5.17
L	600	2.0E-4	4.82
M	480	1.9E-4	5.52
N	720	2.1E-4	5.39
P	1000	1.8E-4	6.02
Q	680	8.6E-5	8.23

Table 1: Parameters for the "log-power-law" rainfall intensity distribution (eq.5) for the various CCIR world rain zones. The same parameters apply for the distribution of raincells defined by eqs. 4 and 6.

The results of the test are reported in tables 2 to 5. Each table is divided in 2 sections: the first section gives the percentage error (according to the ITU-R definition) for the 3 best methods today available as a function of the probability (ensemble averages: Mean, RMS and standard deviation, over the subset of single-year attenuation data available in the CCIR data bank); the second section gives the errors averaged also across the probability range.

Table 2 gives the results pertaining to the whole set of experiments (134), table 3 the ones pertaining to zone E (34), table 4 the ones pertaining to zone K (73) and table 5 the ones pertaining to zone M (14).

The performance appears very good considering that the methods reported in the tables are already selected among the best methods appeared in the literature. In comparison with the other methods the EXCELL one presents a relatively high bias and is unable to predict at time percentages exceeding about 0.5 % of the time. This fact, which undoubtedly constitutes a drawback, is inherent in the nature of the method itself which is based on the concept of raincell and is less suited to work when the dominating scenario is the one of stratified rain. The method is in fact structured so as to refuse giving an answer when the low rain has a dominant role (see later) and has its optimum range of application to the high- and medium-availability radio telecommunication systems.

For what concerns the impact of the climatic zone the M one seems to give much worse results than the others: here again the fact that there are many measurements falling at the 1% probability (i.e. in the range where the performance is inherently poor) plays a role even though probably this is not the only reason of lower performance with respect to the other rainzones.

4. ABOUT THE SPATIAL RAINSTRUCTURE

As told in section 2, the rain horizontal distribution is assumed to be constituted by cells of various radiuses and peak rain intensities: in fig. 1 a bidimensional histogram shows, for each interval of radius and peak intensity, the cell density in log scale.

It is interesting to investigate about the relative contribution to the total exceedance time of each particular sub-population of cells. In order to simplify the problem only the influence of the rain peak R_M is here considered, as the variation with the radius is conceptually very similar. For this purpose all the cells with the same value of R_M have been grouped together and the variation with this parameter studied. The results are presented in figs. 2 and 3 which give the contribution to the probability of a sub-population of cells, per unit range of R_M . The experimental conditions assumed in the simulation are: attenuation due to raincell: 5 dB, frequencies: 11.6 and 30 GHz, rainy

path length: 6 kms, rainzones E, K and M. The total exceedance probabilities (i.e. the integral of the curves) are given in table 6:

GHz	E	K	M
11.6	2.45E-2	5.93E-2	7.7E-3
30.0	0.320	0.801	0.134

Table 6: Probability to exceed 5 dB attenuation in a rainy path length of 6 Km. Frequency 11.6 and 30 GHz. Rain zones E, K and M.

The figures show how different is the 11.6 GHz case from the 30 GHz one. In the first case indeed the most contributing cells are the ones characterized by very intense peak rain intensities i.e intensities in the approximate range 50 - 150 mm/h (points at "halved density" with respect to the maximum), with a maximum at about 80 mm/h. (one must consider however that these values are the ones reached by the "cuspex" of the exponential cell, a "zero extension" region. More probably these cells are in reality "clipped" around their peak and the real peak value is 30-40% lower). In the case of 30 GHz the range of contributing cells is much wider "invading", even though marginally, the range of stratified rain.

Diagrams like the ones of figs. 2 and 3 demonstrate that intense attenuations are mostly generated by cells of convective nature, being the role of stratified rain rather marginal below 0.2 % probability. The authors consider this range as the one in which the EXCELL method can be applied with great confidence, at least in the rain zones K and E.

5. CONCLUSIONS

The paper presents an investigation aimed at highlighting the role of the stratified rain in determining the rain attenuation in various climates.

Unfortunately, owing to the small number of propagation experiments in many CCIR rain zones, the analysis had to be restricted to three zones: E, M and K.

For all them zones the major contribution to the attenuation exceedance probability exceeded for a few hours per year, seems due to convective rain cells, being the role of the stratified rain marginal up to 0.2% probability.

0.001% PROBABILITY			
Method	MEAN	RMS	ST.DEV
CCIR91	-8.091	38.664	37.808
EXCELL	17.697	40.898	36.871
U.S.A.	2.782	32.697	32.579
0.01% PROBABILITY			
Method	MEAN	RMS	ST.DEV
CCIR91	-11.636	32.116	29.934
EXCELL	8.077	31.740	30.695
U.S.A.	-9.059	33.138	31.875
0.1% PROBABILITY			
Method	MEAN	RMS	ST.DEV
CCIR91	-1.501	37.421	37.391
EXCELL	12.991	34.480	31.939
U.S.A.	-4.652	29.587	29.219
1% PROBABILITY			
Method	MEAN	RMS	ST.DEV
CCIR91	-5.162	49.630	49.361
EXCELL	40.457	47.288	24.483
U.S.A.	-23.776	54.118	48.616

AVERAGED ERRORS SUMMARY			
Method	MEAN	RMS	ST.DEV
CCIR91	-6.340	38.484	37.959
EXCELL	13.159	35.494	32.965
U.S.A.	-7.886	36.308	35.441

Table 2: Testing results for all the 134 "Beacon and Single Year" experiments available in the database.

0.001% PROBABILITY			
Method	MEAN	RMS	ST.DEV
CCIR91	-18.695	40.999	36.488
EXCELL	18.779	41.512	37.021
U.S.A.	14.712	35.105	31.874
0.01% PROBABILITY			
Method	MEAN	RMS	ST.DEV
CCIR91	-17.230	35.494	31.031
EXCELL	6.837	28.587	27.757
U.S.A.	1.000	30.099	30.083

0.1% PROBABILITY			
Method	MEAN	RMS	ST.DEV
CCIR91	-0.719	38.705	38.699
EXCELL	19.866	38.941	33.492
U.S.A.	2.740	31.588	31.469
1% PROBABILITY			
Method	MEAN	RMS	ST.DEV
CCIR91	-36.989	43.318	22.545
EXCELL			
U.S.A.	-52.183	58.977	27.482

AVERAGED ERRORS SUMMARY			
Method	MEAN	RMS	ST.DEV
CCIR91	-14.128	38.685	36.013
EXCELL	13.845	35.756	32.967
U.S.A.	0.275	35.307	35.306

Table 3: Testing results for the 34 "Zone E and Single Year" experiments available in the database.

0.001% PROBABILITY			
Method	MEAN	RMS	ST.DEV
CCIR91	-1.499	35.046	35.013
EXCELL	17.024	38.126	34.114
U.S.A.	-6.423	32.424	31.781
0.01% PROBABILITY			
Method	MEAN	RMS	ST.DEV
CCIR91	-8.432	30.007	28.798
EXCELL	8.525	30.198	28.969
U.S.A.	-13.338	33.072	30.263
0.1% PROBABILITY			
Method	MEAN	RMS	ST.DEV
CCIR91	9.089	31.090	29.732
EXCELL	13.522	34.484	31.722
U.S.A.	-3.684	27.676	27.429
1% PROBABILITY			
Method	MEAN	RMS	ST.DEV
CCIR91	14.634	47.896	45.606
EXCELL	-17.360	17.360	0.000
U.S.A.	-9.313	51.266	50.413

AVERAGED ERRORS SUMMARY			
Method	MEAN	RMS	ST.DEV
CCIR91	2.690	34.671	34.566
EXCELL	12.071	33.571	31.326
U.S.A.	-8.116	34.892	33.935

Table 4: Testing results for the 73 "Zone K and Single Year" experiments available in the database.

0.001% PROBABILITY			
Method	MEAN	RMS	ST.DEV
CCIR91	5.661	5.661	0.000
EXCELL	29.172	29.172	0.000
U.S.A.	-21.553	21.553	0.000
0.01% PROBABILITY			
Method	MEAN	RMS	ST.DEV
CCIR91	-6.373	30.670	30.000
EXCELL	17.380	54.375	51.522
U.S.A.	-13.403	50.131	48.306
0.1% PROBABILITY			
Method	MEAN	RMS	ST.DEV
CCIR91	-14.458	40.761	38.111
EXCELL	20.812	31.133	23.154
U.S.A.	-1.472	12.908	12.824
1% PROBABILITY			
Method	MEAN	RMS	ST.DEV
CCIR91	-2.545	19.582	19.416
EXCELL	56.097	57.386	12.091
U.S.A.	-7.895	20.951	19.406

AVERAGED ERRORS SUMMARY			
Method	MEAN	RMS	ST.DEV
CCIR91	-9.029	33.605	32.369
EXCELL	25.970	42.585	33.750
U.S.A.	-6.352	27.354	26.606

Table 5: Testing results for the 14 "Zone M and Single Year" experiments available in the database.

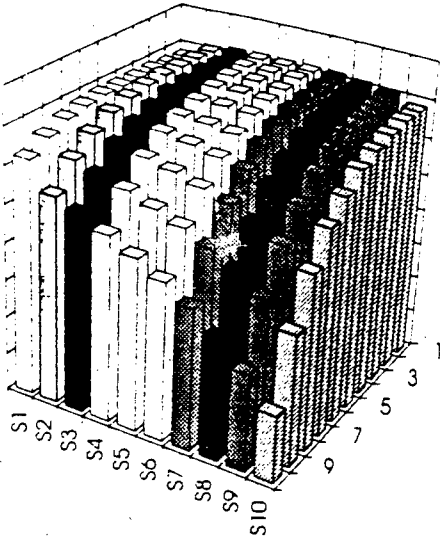


Figure 1: Histogram of the cell density as a function of radius ($S1 \div S10$) and peak rain intensity ($1 \div 10$). The S intervals are bounded by p_0 intervals making a ratio of 1.42 starting from 600 meters, the intensities are bounded by R_M intervals making a ratio of 1.55 starting from 5 mm/h. The ordinates give the number of cells per 100 Km² area in log scale (2 decades/div.) starting from 10^{-14} .

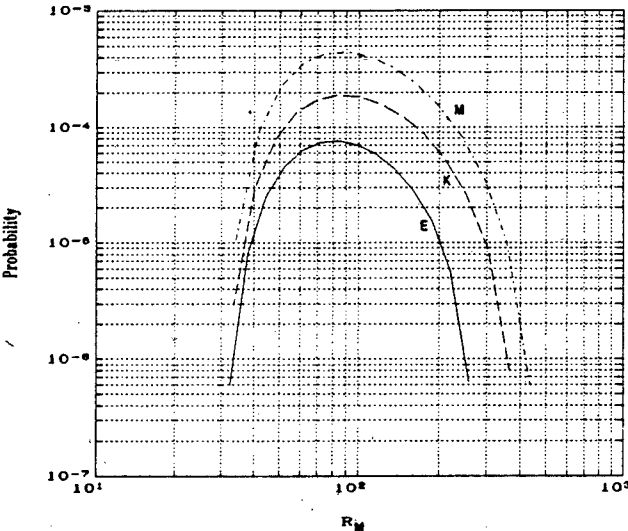


Figure 2: Contribution to the probability of a sub-population of cells, per unit range of R_M . Frequency 11.6 Ghz, path lenght 6 Km, attenuation 5 dB.

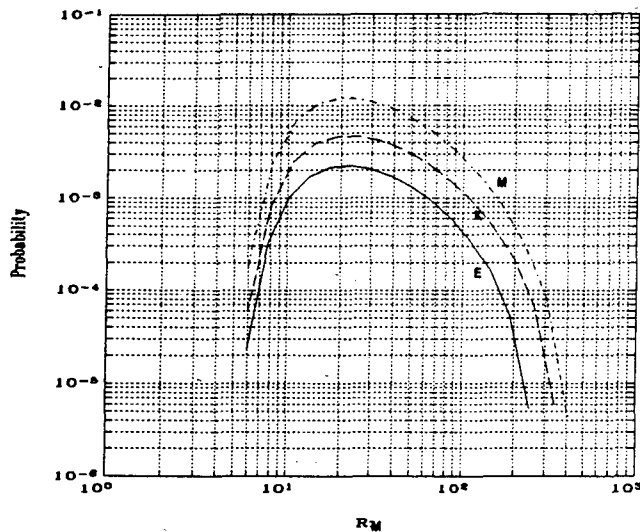


Figure 3: Contribution to the probability of a sub-population of cells, per unit range of R_M . Frequency 30 Ghz, path lenght 6 Km, atténuation 5 dB.

6. REFERENCES

- [1] Bosisio A.V., C. Capsoni, M. Matricciani, Comparisons among prediction methods of site diversity system performances, *VIII International Conference on Antennas and Propagation*, Edimburgh (UK), March 1993.
- [2] Capsoni C., M. D'Amico, A. Martellucci, L. Ordano, A. Paraboni, A 3-D Prediction method of scattering interference: complete procedure versus pencil beam approximation, *URSI Comm. F Open Symposium on Wave Propagation and Remote Sensing*, Ravenscar (UK), June 1992.
- [3] ITU-R - CCIR Recommendations, *Propagation in non-ionized media*. Geneva 1992.
- [4] Capsoni C., F. Fedi, C. Magistroni, A. Paraboni, A. Pawlina, Data and theory for a new model of the horizontal structure of rain cells for propagation applications, *Radio Science*, Vol. 22, N. 3, pp. 395-404, June 1987.
- [5] CCIR Study Groups, PG3 Doc. 92/8, USSG5C/1T, private communication.

**SEPARATING ABSORPTION FROM SCINTILLATIONS PHENOMENA
IN SATELLITE RADIO LINKS:
THEORY, EXPERIMENTAL DATA AND PREDICTIONS**

A. Paraboni¹ and C. Riva²

Politecnico di Milano, Piazza Leonardo da Vinci 32, I-20133 Milano, Italy
1 - Tel: +39-2-23993586, Fax: +39-2-23993413, E-mail: paraboni@elet.polimi.it
2 - Tel: +39-2-23993601, Fax: +39-2-23993413, E-mail: riva@elet.polimi.it

ABSTRACT

Separation of the fade due to rain absorption from the one due to scintillations is becoming an important issue in the design of satellite-based low margin systems. The paper presents some theoretical and experimental achievements based on the data collected in Italy by means of the two experiments OLYMPUS and ITALSAT.

Keywords: ITALSAT, OLYMPUS, Rain Attenuation, Scintillations

1. INTRODUCTION

In satellite communications at cm and mm waves, scintillations play an important role especially in low-margin systems and in the case of joint occurrence with rain: for time percentages of the order of 1% the two phenomena are of the same order of magnitude and the system design must therefore take into account both of them; being the physical causes of the two phenomena quite different, the necessity arises of separating the two effects for a better ability to predict their occurrence. This appears to be possible by resorting to the different dynamic behaviour and spectral characteristics of the two components of the signal amplitude.

A systematic activity aiming at the separate assessment of the two phenomena has been deemed one of the most important among those allowed by the two OLYMPUS (12, 20 and 30 GHz) and ITALSAT (20, 40 and 50 GHz) propagation experiments. In the paper the results of this activity, performed on systematic basis with OLYMPUS data and on sample basis with ITALSAT data, are presented. After separating the slow components due to rain from the turbulence-induced scintillations the relation between the two is studied.

**2. RAIN ATTENUATION AND
SCINTILLATIONS JOINT OCCURRENCE**

With the advent of the mm waves technology and of the satellite based low margin systems, the propagation activity has been lately more and more frequently devoted to the characterisation of the scintillations phenomena.

It is known since a long time that the convective activity in the atmosphere, a condition often accompanying rain, is associated to enhanced scintillations. Even though a relation between the two phenomena was expected, measurements and experimental results did not give, so far, an univocal indication on how to make a separate assessment of the relative effects.

A prediction method, allowing to account both for rain and scintillations has been given, some years ago, in [1] and successively adopted by the CCIR (now ITU-R); this approach tackles the problem from the statistical point of view but does not give any indication on how to separate the two phenomena on short term or event basis (as needed e.g. for the implementation of fading countermeasures). This aspect of the problem has been instead recently considered in [2] and is here briefly recalled. Naturally the combining procedure implies assuming that the separate effects of rain and scintillations are well identifiable. This is not at all a trivial matter, as the number of phenomena causing the signal fluctuations is very high (multipath, defocusing, variation of the angle of arrival, depolarization, quickly variable absorption, multiple scattering by raindrops etc.). Rather than try to guess the dominating mechanisms in each circumstance, a separation based on the spectral characteristics of the signal seems a more viable procedure to follow.

Let us assume that total fade depth a , [dB] can be expressed as a sum of the two well identifiable contributions, not necessarily statistically independent,

the one due to scintillations a_s and the one due to rain a_r :

$$a_t = a_r + a_{sc} \quad (1)$$

Assuming a_r as conditioning variable, the cumulative distribution function of a_t , i.e. the probability that a_t exceeds a fixed threshold $P(THR) \equiv P(a_t > THR)$ can always be expressed as a function of the conditional probability $P_{cond}(a_t > THR / a_r)$:

$$\begin{aligned} P(THR) &= \int_0^{\infty} P_{cond}(a_t > THR / a_r) p_{ar}(a_r) da_r \\ &= \int_0^{\infty} P_{cond}(a_{sc} > THR - a_r) p_{ar}(a_r) da_r \end{aligned} \quad (2)$$

where $P_{cond}(a_{sc} > THR - a_r)$ is the exceedance probability of scintillations *conditioned to rain*.

The second expression shows how the absolute exceedance probability can be expressed by the integral of the product of two functions, one having the quantity $THR - a_r$ as argument and the other a_r . The first function depends, in principle, by a_r (apart from the explicit dependence through $THR - a_r$). If this would not happen (i.e. scintillations were statistically independent from rain) equation (2) would be a bare convolution integral; however this does not correspond to reality, in the author's experience; in any case there are not conceptual differences in accounting for any possible statistical dependence in solving the integral (2) provided that the probability of scintillations conditioned to rain is known. The main purpose of this paper is to provide preliminary results about this quantity obtained with the two OLYMPUS and ITALSAT experiments.

3. OLYMPUS AND ITALSAT EXPERIMENT

The OLYMPUS and ITALSAT propagation experiments were conceived with the aim of assessing the physical background and the statistical behaviour of a large number of parameters regard-

ing the radio channel at 12.5, 20, 30, 40 and 50 GHz.

OLYMPUS main characteristics [3]:

- Frequencies: 12.5, 20 and 30
- European antenna coverage of the 20 and 30 GHz beacons with a minimum EIRP of 24dBW in Europe
- Visible earth full coverage for the 12.5 GHz beacon
- Coherence among all the transmitted signals
- Dual polarization transmission at 20 GHz with a 933 Hz switch rate.

The earth station installed in Politecnico di Milano provided for reception of 20 GHz beacon while the station in Spino d'Adda could receive all the three beacons. The sampling rate is 1 Hz.

The ITALSAT main characteristics [4]:

- Frequencies 20, 40 and 50 GHz
- European antenna coverage
- High EIRP value (27 dBW)
- Coherence among all the transmitted signals
- Dual polarization transmission at 50 GHz with a 933 Hz switch rate
- Angle modulation of the 40 GHz beacon (sidebands at 500 MHz from the centre frequency).

An earth-station, also located in Spino d'Adda receives all the beacons.

4. ANALYSIS

Four types of analyses were undertaken on the data:

- Spectral analysis
- Fade duration statistics analysis
- Correlation between scintillations and rain attenuation
- Frequency scaling of the scintillations standard deviation.

These are briefly summarized in the sequel.

4.1. Spectral Analysis

The spectra of scintillations and rain events possess some very clearly distinguished characteristics. The most relevant are:

- the spectral extension (up to some Hz the scintillations, limited to about 0.01 Hz the rain in most cases)

- the asymptotic behaviour: scintillations are characterized by a flat spectrum till a cut-off frequency, (in the range 0.1-1 Hz) [1,5], and then by an asymptotic behaviour (i.e. $\approx f^{-9/3}$). On the contrary [6], rain, in most cases, is characterized by a power spectrum of the type $[\sin(kf)/f]^2$.

This latter property can be understood by considering that the attenuation is roughly proportional to the integral of the rain intensity profile along the path. If the well known synthetic storm concept [7] were rigorously applicable (time exchangeable with space using a constant translation storm velocity), this would imply convolving, in the time domain, a rectangular unit function (representing the link averaging function) with the rain intensity time profile as would be recorded by a rain gauge. This corresponds, in the frequency domain, to the product of the Fourier Transform of the two functions. As the storm profile spectrum is larger than the rectangle spectrum, it is the latter to provide the shape of the signal spectrum.

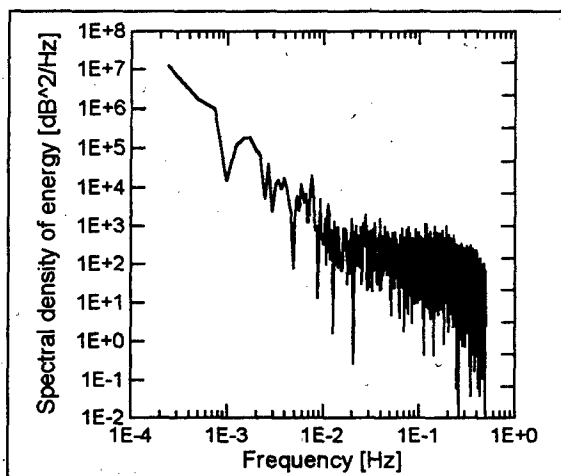


Figure 1: Typical signal spectrum with transition frequency between rain and scintillations effects at around 0.01 Hz.

The total signal spectrum is then characterized as in figure 1 where an observable *separation frequency* around 10^{-2} Hz is discernible. This value however is not fixed but depends on event intensity, storm translation speed and scintillations energy. In the author's opinion, the separation frequency is the most useful and effective signature to separate absorption from scintillations. It allows in fact to implement a filtering algorithm to remove the rain effects and assess the power of scintillations alone.

Due to the inherent spectrum fluctuations, the exact transition frequency is however not easily assessed by inspection of the spectrum, especially when few points are available in the low-frequency range; a zero estimator spectral technique was attempted by the authors [8] and a theoretical accuracy better than 10% obtained.

4.2. Fade Duration Statistics

Investigation on fade durations can also help in distinguishing rain induced fades from fades induced by atmospheric turbulence; it has been found indeed that:

- Short fades are mainly associated to scintillations and follow a power-law distribution
- Long fades are associated to the space-time rain structure and are log-normally distributed.

The two processes seem well separable especially at high thresholds as it appears from figure 2 which gives the cumulative distributions of fade durations for the 8 dB threshold; two different slopes separated by a particular duration, the *separation duration*, can be observed in the figure. This parameter is very near and probably related to the separation frequency [9].

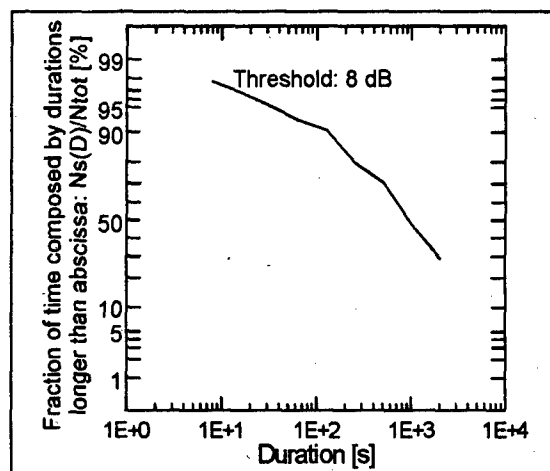


Figure 2: Cumulative distribution of fade duration for OLYMPUS experiment at 20 GHz; threshold 8 dB: exceedance time 5 hours.

4.3. Correlation between Rain Attenuation and Scintillations

Time series from OLYMPUS 20 GHz beacon recorded by the Politecnico di Milano were low-pass filtered to obtain the slow varying components due to rain and high-pass filtered to obtain the fast

varying ones due to turbulence as indicated in section 4.1.

Once the two time series were obtained for each block of 30 s (30 samples) the average level (attenuation) and the standard deviation (scintillations) were evaluated and a scatterplot drawn. This result is shown in figure 3 from which two different ranges of attenuation seem to reflect different behaviours of scintillations:

- High attenuation range (> 6 dB) in which a constant conditional average of about 0.2 dB seems to apply
- Lower range in which the average increases with increasing rain attenuation; more over the dispersion seems much larger than in high attenuation range.

These elements could be a preliminary input for modelling the conditional probability of scintillations as in equation (2).

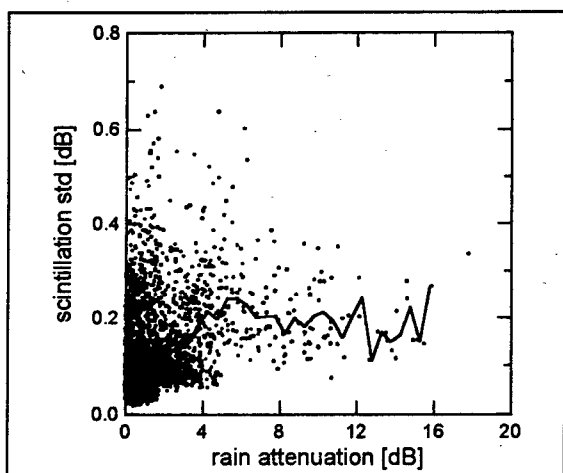


Figure 3: Scatterplot between standard deviation of scintillations calculated for 22 selected OLYMPUS events at 20 GHz; the continuous line represents the mean value of std conditioned to rain attenuation.

4.4. Frequency Scaling of Scintillations

Rain attenuation and scintillations scale differently in frequency; the rain attenuation A_1 at the frequency f_1 is related to A_2 at f_2 through the (approximate) equation [7]:

$$A_1/A_2 = (f_1/f_2)^{1.72} \quad (3)$$

As for scintillations, Tatarskii proposed the following theoretical relation [10]:

$$\sigma_1/\sigma_2 = (f_1/f_2)^{7/12} \quad (4)$$

The ratio between the standard deviations evaluated as described in the previous section has been put in relation with the ratio of the frequencies as in equation (4); the result is an exponent very near to 0.5 for the three couples of frequencies tested with ITALSAT at Spino d'Adda. The fact that the found exponent is much more similar to 0.5 than 1.72, which is typical of the rain attenuation, demonstrates that the observed scintillations are a multipath effect due to non-uniformity of the refraction index rather than a phenomenon of quickly variable absorption.

5. CONCLUSIONS

- Scintillations and rain attenuation are well separable processes which can be assessed separately.
- They do not seem statistically independent: a model to take the statistical dependence into account seems at hand
- Even though related to rain the nature of the scintillations seems the one of a typical phenomenon caused by non-uniformity of the refraction index.

6. REFERENCES

1. Karasawa Y. and T. Matsudo 1991, Characteristics of Fading on Low-Elevation Angle Earth-Space Paths with Concurrent Rain Attenuation and Scintillation, IEEE Transactions on Antennas and Propagation, Vol. AP-39, N° 5, pp. 657-661
2. Riva C. and J.P.V. Poiarés Baptista 1994, Outage probability due to rain and scintillations in earth-to-space links: a rigorous approach, submitted to *European Transactions on Telecommunications*
3. OLYMPUS satellite user's guide (ESA)
4. Paraboni A. et al., Planning of in-orbit-testing activity of the ITALSAT

- propagation experiment in the 20, 40 and 50 GHz bands, Supercomm. ICC '92 International Conference on Communications - IEEE Communication Society, Chicago 1992
5. Basili P. et al. 1990, Case Study of Intense Scintillation Events on the OTS Path, IEEE Transactions on Antennas and Propagation, Vol. AP-38, N° 1, pp. 107-112
 6. Matricciani E. 1994, A physical-mathematical model of the dynamics of rain attenuation with application to power spectrum, to be published on *Electronics Letters*
 7. Druifuca G. 1974, Rain Attenuation Statistics for Frequencies above 10 GHz from Raingauge Observations, *J. Rech. Atmos.*, Vol. 1-2, pp 399-411
 8. Riva C. 1994, *Un algoritmo per l'identificazione delle caratteristiche trasmissive di un canale radio per mezzo di tecniche spettrali*, Politecnico di Milano, Rapporto Interno N° 94-024
 9. Paraboni A. and C. Riva 1994, A new method for the prediction of fade duration statistics in satellite links beyond 10 GHz, to be published on *International Journal of Satellite Communications*
 10. Tatarskii V.I. 1961, *Wave propagation in a turbulent medium*, New York, McGraw-Hill

RAIN AREAS ON HORIZONTAL RADAR RAIN MAPS : NEW COLLECTION, NEW INSIGHT INTO SPATIAL INTENSITY DISTRIBUTION

A. Pawlina Bonati

CNR, Centro di Studio sulle Telecomunicazioni Spaziali
Politecnico di Milano, Piazza Leonardo da Vinci 32, I-20133 Milano, Italy
Tel: +39-2-23993586, Fax: +39-2-23993413, E-mail: pawlina@elet.polimi.it

ABSTRACT

New collection of rain clusters identified at various levels of intensity (ranging from 0.5 to 40 mm/h) on horizontal radar maps, characterized and organized into a hierarchical data base (HRM89) is presented along with primary statistical investigations addressing spatial distribution of rain intensity.

Keywords:

Horizontal Rain Map, mother rain cluster, inner rain cluster, cluster nesting

1. INTRODUCTION

With new requirements for "low availability" TLC systems in mind, calling for the knowledge of low intensity rain structures, and thanks to the upgrading of the meteorological radar system of Spino d'Adda in North Italy now measuring with greater space detail and down to lower intensity echoes, a vast collection of low elevation scans for the generation of horizontal rain maps was started in 1988 and is still carried on. The 1989 collection worked out in this contribution covers 32 rain events, lasting from 75 minutes up to 12 hours, contains more than 7000 Horizontal Rain Maps (HRM) with the total of 175 hours of rain exceeding 0.5 mm/h.

The present contribution aims to: (a) introduce the collection of rain clusters nested with respect to the intensity level, (b) present preliminary results of statistical enquiry on the spatial distribution (and organization) of rain intensity within the rain region.

2. HRM89 DATA SET

The relevant characteristics of the radar (Ref. 1) at the time of collection are reported in Table 1. Three full azimuth scans at elevations 3, 5, and 7° are completed in 90 seconds with range resolution of 150 m, azimuth resolution of 2°, maximum

range of 40 km, 32 time consecutive echoes averaged.

Table 1. *Spino d'Adda Radar Characteristics*

Geographical location	45.40° N, 9.5° E
Height	84 m asl
Type and frequency	conventional, 2.8 GHz
Resolution	2° - 75/150 m
Min. and max. range	350 m - 150 Km
Antenna	
Parabolic Reflector	3.6 m, rear feed
Gain	38.2 dB
Max rotational speed	30 degrees/sec.
Polarization	vertical
Receiver	
Noise figure	2.7 dB
Dynamic range	80 dB \pm 1 dB
Transmitter	
Type	magnetron
Pick power	475 KW
Pulse duration	0.5/1.5 μ s
Pulse repetition freq.	456/228 Hz
Outputs	
Analogic for PPI and digital for recording	

Three consecutive rings are taken of three azimuth scans, closest to the radar at 7° elevation, median at 5° and most distant at 3° and combined into one horizontal polar map, representing on average the layer around 1.5 km above the ground; it is then remapped onto cartesian grid, each 250 x 250 m square being assigned an average reflectivity, z , measured in the corresponding radar volume.

A radar image of 160 per 160 pixels obtained this way (eventually after conversion of reflectivity values to rain rate, R) is referred to as Horizontal Rain Map (HRM).

Measurement campagne of 1989 produced 7167 HRM's with rain greater than 0.5 mm/h, once the interferred or otherwise damaged scans were discarded. They cover 32 rain events: 17 in spring, (4530 maps), 8 in summer (1255), 3 in fall (367) and 4 in winter (1015). HRM's within an event are spaced by 90 seconds.

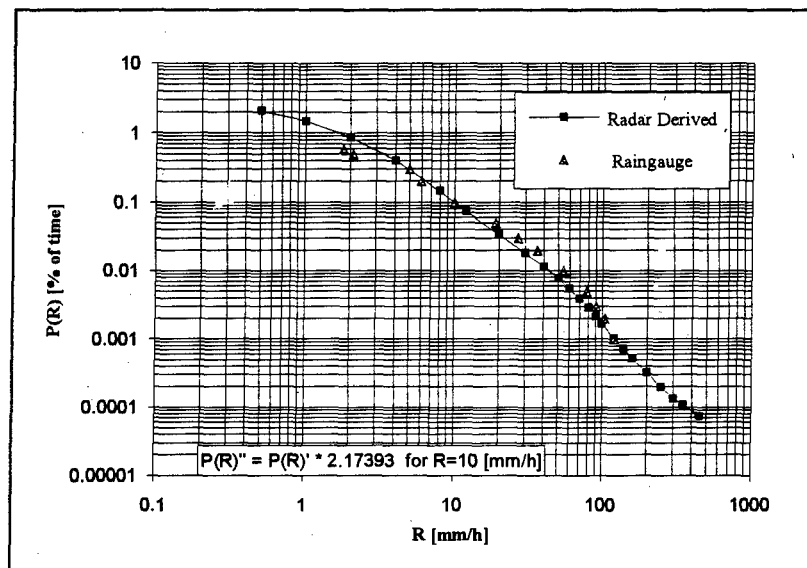


Figure 1. Radar derived and raingauge CD's.

For contrast, other similar data set (Ref.2) collected in 1980 contained about 1700 rain maps with space resolution of 1km per 1km, spaced by 6 minute time interval over the range from 3 to 80 km.

As regards the conversion $z - R$, known empirical relation [$z=200 R^{1.6}$] was adopted, tested as usual against long term raingauge data and working well

on average, as shown in Figure 1, which gives two Cumulative (probability) Distributions (CD), one for all data of HRM89 collection converted to rain rate and other for three years of the raingauge data (radar site).

An example of HRM belonging to the HRM89 set is shown in Figure 2.

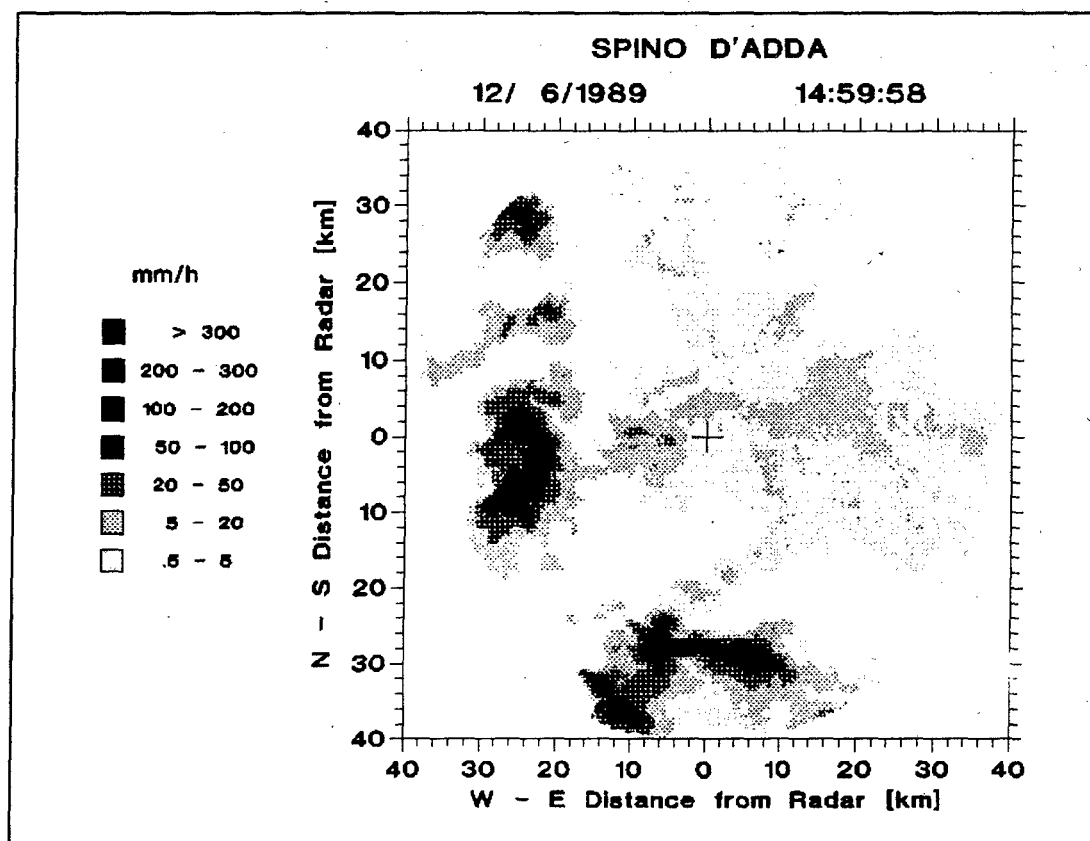


Figure 2. Example of Horizontal Rain Map in HRM89

2.1. Identification of horizontal rain clusters

The common terms used in reference to rain echoes observed on radar images are "rain pattern" and "rain cell". The first one, pretty general, applies to any type of rain echo while the second one is preferably used in modeling of propagation effects of rain. By rain cell on radar image one understands usually a form (spot) delimited by a (closed) contour, containing relatively intense rain. Two categories of contours that delimit a rain cell

Rain cluster at i -th intensity level is defined as a set of close enough i -th level rain structures; two structures are close enough when the minimum distance (in sense of Hausdorff) between their contours does not exceed a given value d (in pixels); an isolated rain structure is the case of cluster. The distance d in the HRM89 collection is (empirically) fixed to 4, ie. 1 km. See Ref. 5 for the details on algorithms.

Minimum detectable level (that guarantees an acceptable S/N) of rain intensity is, for HM89, of

Table 2. Clusters at various intensity levels

Level	0	1	2	3	4	5	6
Rainrate [mm/h]	0.5	1	2.5	5	10	20	40
N° of clusters	34356	81057	78760	39695	21068	8562	3617
Total Area[km2]	6685484	4863718	2187274	884184	288819	91683	29840

are used, absolute and relative ones (eg. Ref. 4). Example of the absolute contour is "20 dBz", of the relative one is "10 dBz down the local maximum". In both cases the structure (area) delimited by it is meant as internal to the contour, with the rain exceeding the contour (threshold) value. In this paper the term **rain structure** is preferred and applies to any set of adjacent pixels of rain exceeding given (absolute) contour level; we will identify structures at several intensity levels, so speaking of **i -th level structure** delimited by contour level i .

As rain structures cluster, ie. appear in aggregates and an aggregate may represent in fact a single structure if seen at slightly lower level (thresholding effects, not discussed here) rain clusters instead of cells will be identified and described.

18 dBz corresponding to the rain rate of 0.5 mm/h. It will be referred to as zero or "mother" level. Clusters are first identified at zero level on HRM, as **mother clusters**, and for each of them the **inner clusters** are found at next, higher intensity level; the process is repeated until the clusters at all intensity levels of interest are found. The threshold intensity levels for HM89 with total figures are in Table 2.

2.2. HHMR89 organization

HM89 multilevel rain cluster collection is organized in several files, the three of main interest here being:

- GM89: lists clusters with their descriptors,

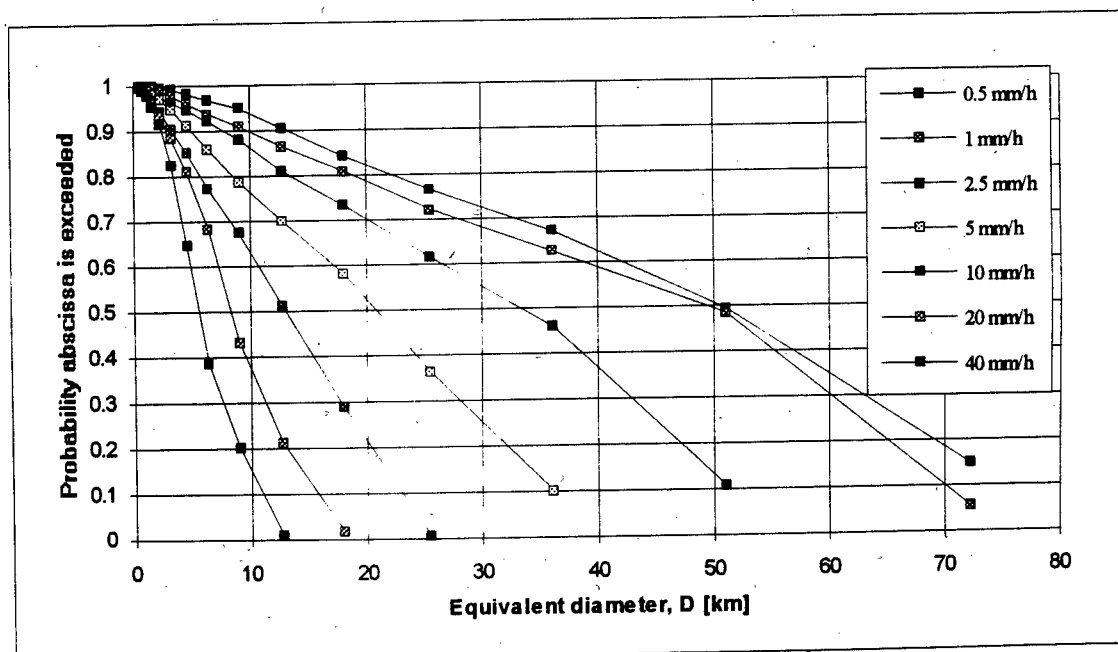


Figure 3. Extension of clusters in function of intensity level

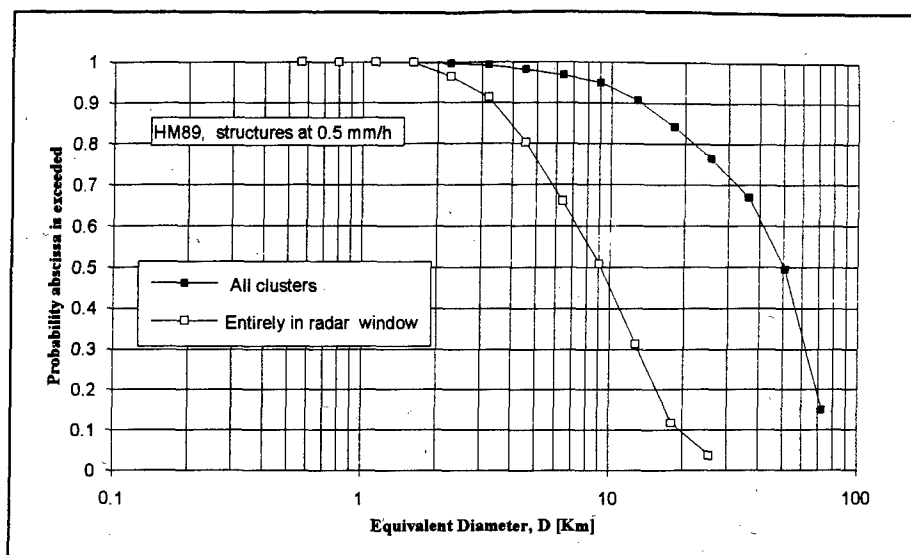


Figure 4. CD's of cluster extension for all clusters and for those entirely in radar window

organized in blocks, one block groups the clusters at all levels of one HRM: it is linked to other files through the HRM identifier.

- MM89: contains intensity data of mother clusters, it is a list of cluster windows, each cluster window is a matrix of pixels composing the cluster; it is linked to other files through the HRM identifier.
- SM89 is a list of HRM descriptors, one set of descriptors for each HRM, including identifier, date, time, number of mother clusters, total extension of rain, maximum and average intensity, radar conversion parameters etc.

Each inner i -th level cluster "knows" to what $(i-1)$ -th level (outer) cluster it is inner. In this way the exhaustive description of spatial distribution of rain intensity within the cluster is possible.

All, mother and inner clusters are "measured" and characterized by the essential morphological and physical descriptors (Ref. 3), such as: area, ellipticity, main axis orientation, barycenter coordinates, maximum, mean and effective intensity.

Particular morphological descriptors are the identification level and the pointer to the outer cluster.

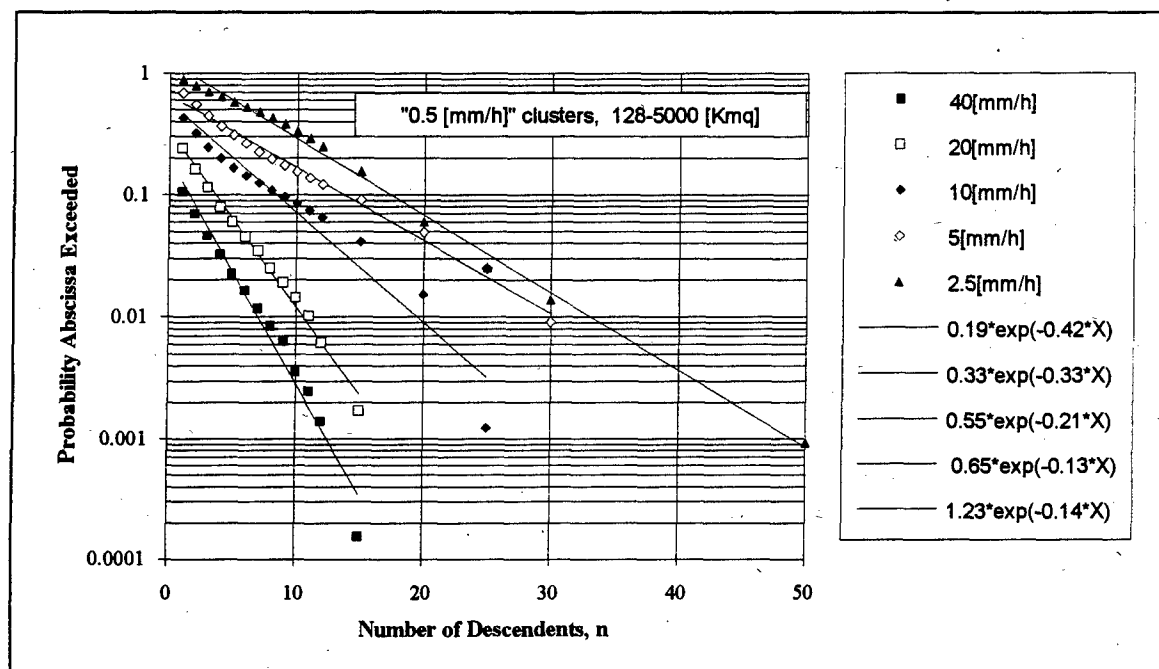


Figure 5. Occurrence of inner clusters of various intensity

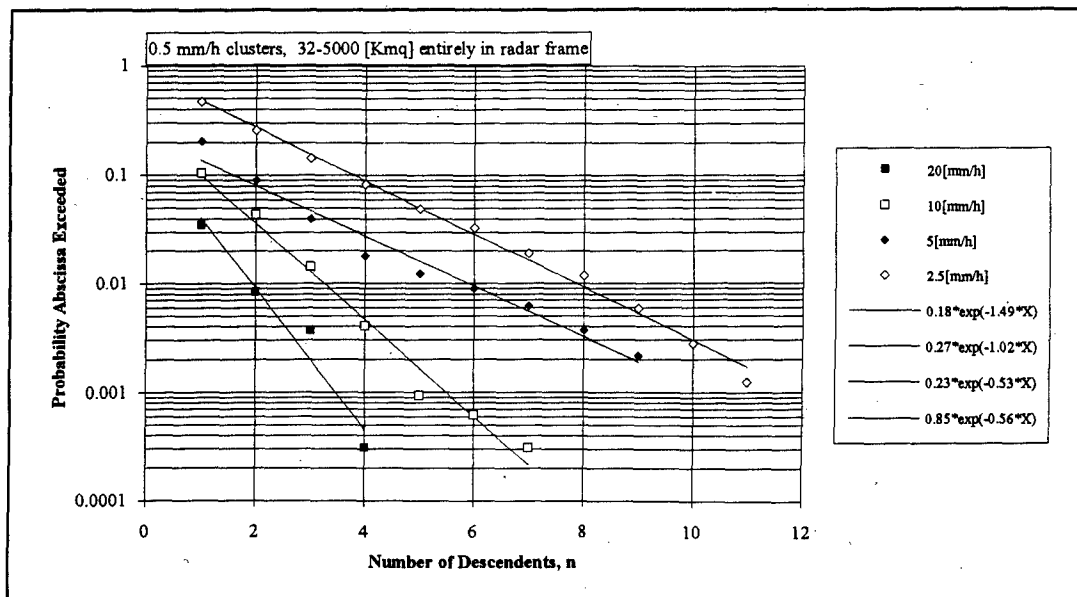


Figure 6. Occurrence of inner clusters of various intensity in a mother cluster

3. STATISTICAL INVESTIGATION.

In first place the estimation of probabilistic occurrence of rain clusters at various levels of intensity is carried out. This is expressed by the Table 2 and the curves of Figure 3.

It should be noted however that the dimension of mother clusters (and, to lower extent, clusters of next two levels) is biased by the fact that they may cross the border of radar observation window (a circle of 40 km in radius). Figure 4 shows the degree of underestimation of spatial extension in case only the clusters entirely contained in the observation window are considered. Thus 50 % of clusters at 0.5 mm/h level would have equivalent diameter greater than 10 km for those entirely visible and greater than 50 km for all clusters at that level. It seemed wiser to keep the bias instead of miting the analysis to entirely visible but necessarily much smaller structures.

As expected, more intense clusters have smaller dimensions at equiprobability levels; not so obvious the almost linear relation.

As regards spatial distribution of rain intensity within a cluster the primary investigation aims to adress the question like "what is the probability of occurrence of n inner clusters at specified intensity level ?".

The response is of type depicted in Figure 5 and 6 for a selected set of conditions. In Figure 6 small to medium mother clusters, entirely visible, show that there is 0.1, 0.02, 0.004 and 0.0003 probability that a

mother cluster will have at least 4 inner clusters at the 2.5, 5.0, 10.0, and 20 mm/h levels, respectively. The probabilities are at least 5 times greter if "entirely visible" condition is removed, as can be seen in Figure 5.

The carefull modellistic analysis of the statistics should be now carried on.

4. REFERENCES

1. Capsoni C et al. 1983, "Radar data analyses for propagation studies", *ESTEC Final Report 4680/81/NL/MS(SC)*, ESA/ESTEC Noord-wijk, NL
2. Pawlina A 1987, "Radar rain patterns: automatic extraction, collection and description for modeling purposes", *Alta Frequenza*, vol. LVI, n. 1-2, Jan-Apr., pp.153-159
3. Capsoni C et al. 1987, "Data and theory for a new model for the horizontal structure of rain cells for propagation applications", *Radio Science*, Vol.22, N. 3
4. Goldhirsh J and Musiani B, 1992 "Dimension Statistics of Rain Cell Cores and Associated Rain Rate Isoleths derived from Radar Measurements in the Mid-Atlantic Coast of the United States", *IEEE Trans. Geosci. Remote Sensing*, Vol. 30, No. 1, Jan
5. Mussio P Pawlina A 1990, "Modeling rain patterns: towards automatic interpretation of radar images", *Image and Vision Computing*, vol.8 no 3, pp.199-210

A STUDY OF THE RELATIONSHIP $\gamma = aR^b$ FOR RAIN ATTENUATION AT MILLIMETRIC WAVELENGTHS

C. J. Gibbins

Radio Communications Research Unit,
Rutherford Appleton Laboratory, Chilton, Didcot, Oxfordshire, OX11 0QX, UK
Tel: +44 235 446584, Fax: +44 235 446140

ABSTRACT

A number of rain attenuation events measured at 97 GHz over a twelve-month period have been analyzed in terms of the relationship attenuation (in dB km⁻¹) $\gamma = aR^b$, where R is the rainfall rate in mm h⁻¹ and a and b are coefficients deduced from the experimental measurements. These coefficients were found to vary considerably from event to event, and have been further examined in terms of various meteorological parameters, to investigate whether there are any climatological influences involved in rain attenuation processes. Little correlation has been found between the coefficients and those meteorological factors examined, but the coefficients themselves were found to be in anti-correlation, suggesting some degree of compensation in the power-law relationship.

Keywords: Rain attenuation, rainfall rates, millimetre wavelengths.

1. INTRODUCTION

The calculation of attenuation due to rain is a complex procedure, based generally on Mie scattering theory, for spherical raindrops, or on more elaborate procedures such as point matching, *etc.*, for non-spherical raindrops. For simplicity, however, power-law models have been developed, in the form of attenuation (in dB km⁻¹) $\gamma = aR^b$, where R is the rainfall rate in mm h⁻¹ and the coefficients a and b depend on frequency, temperature and, for non-spherical raindrops, polarization. Values for the coefficients a and b have been determined by fitting to extensive scattering calculations, for example by Olsen *et al.* (Ref. 1) for spherical raindrops and by Fedi (Ref. 2) and Maggiori (Ref. 3) for non-spherical raindrops. These latter calculations now form the basis for ITU-R Recommendation 838 for the calculation of rain attenuation (Ref. 4)

There is increasing evidence, however, that at frequencies above about 40 GHz, the ITU-R values for the coefficient a may be underestimated,

while those for b may be overestimated. The net effect of this is an underestimation of rain attenuation at frequencies higher than 40 GHz. The explanation for this has generally been sought from the raindrop size distribution employed in the calculations, and a number of workers have examined experimental, multi-frequency measurements of rain attenuation in order to derive information on the distribution of raindrops more appropriate to the millimetre-wave region of the spectrum (see, for example, Ref. 5)

Other experimental studies of the relation $\gamma = aR^b$ have also shown some variability in the values of a and b from one rain event to another, and the reasons for this are not fully understood, but are also considered to originate from differences in the distribution of raindrop sizes in different rain events. Another possibility, which is explored in this paper, is that there might be some other meteorological factors which could influence the attenuations produced by rain, which are not, at present, considered in the models.

This paper examines a number of rain events measured at 97 GHz over a 12-month period, in terms of various meteorological parameters, to investigate whether such meteorological factors could be significant.

2. EXPERIMENTAL MEASUREMENTS

The experimental measurements of attenuations and rainfall rates were made at the 500m Millimetre-Wave Experimental Range at Chilbolton (MWERAC) in Hampshire, UK (latitude 57° 8' N, longitude 1° 26' W, elevation 84m), operated by the Rutherford Appleton Laboratory. The range, which has been described in detail elsewhere (Ref. 6), is a well-instrumented open-air laboratory where transmissions of millimetre-wave, infra-red and visible signals are monitored at a rate of 0.1 Hz, simultaneously with a comprehensive set of meteorological observations. In the present work, attenuations measured at 97 GHz, with vertical polarization, have been used, together with rainfall rates measured with three rapid-response raingauges of

the drop-counting type, spaced 200m apart along the 500m range. The raingauges have an accuracy of about 10% and a minimum resolution of $\sim 1 \text{ mm h}^{-1}$, with an integration time of 10 s.

Twenty-five events distributed throughout a 12-month period have been used in the analysis, in order to encompass all seasons and a range of meteorological conditions. The events were selected to have a maximum rainfall rate in excess of 15 mm h^{-1} , representing an exceedance time percentage of 0.03% for the relevant ITU-R rain zone (zone F). Time series of attenuations measured at 97 GHz and the mean rainfall rate measured with the three raingauges were analyzed by regression to the relationship $\gamma = aR^b$. Values of attenuation less than 1 dB km^{-1} and rainfall rate less than 1 mm h^{-1} were eliminated from the analysis, since such small values tended to skew the results. An example of one such correlation is shown in Figure 1. In general, the power-law correlations were very good, with correlation coefficients typically higher than 80% and averaging 90%.

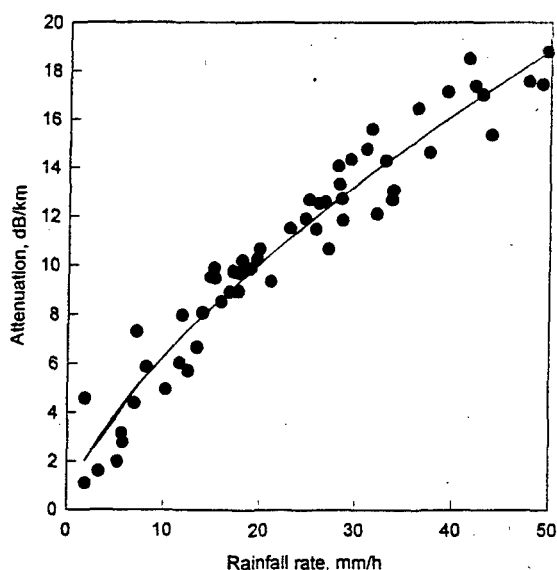


Figure 1: Example of correlation between attenuation at 97 GHz and rainfall rate. The regression line is $\gamma = 1.32R^{0.68}$

The values for the coefficients were found to vary over a wide range, with coefficient a ranging from 0.6 to 2.5; mean 1.30, standard deviation 0.38 and coefficient b from 0.5 to 1.1, mean 0.73, standard deviation 0.13. For comparison, the respective ITU-R values are $a = 1.04$ and $b = 0.75$

In order to investigate these variations in the coefficients, they have been correlated with several meteorological parameters which were also measured on the 500m range.

3. CORRELATION ANALYSIS

3.1 Correlation with Temperature

Temperatures were measured on the 500m range using a Pt resistance thermometer with a time constant of 30s and a sampling rate of 1min. For each event, the mean temperature was determined, and Figure 2 shows that there is little or no correlation between coefficient a and mean temperature. Similar conclusions were also found for the coefficient b . Figure 1 does show, however, the wide range of values in the coefficient which were deduced from the analysis. The temperature dependence of rain attenuation arises through the temperature dependence of the refractive index of water, and is not, in fact, expected to be very significant, especially at such high frequencies (e.g. Ref.1).

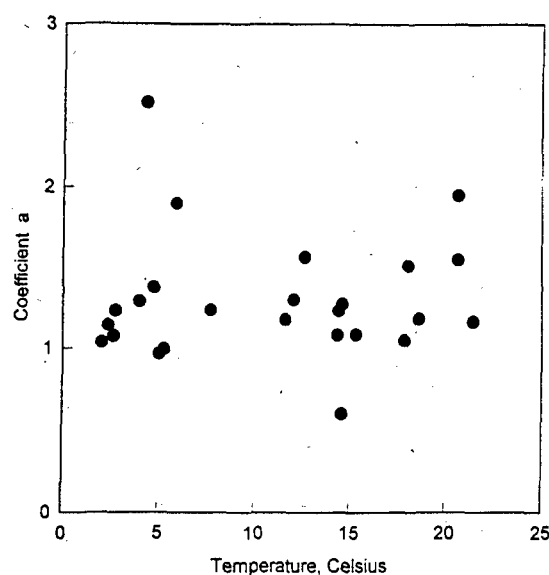


Figure 2: Correlation between the coefficient a and mean temperature.

3.2 Correlation with Wind Speed

With vertical polarization, forward scattering amplitudes for oblate spheroidal raindrops with zero canting angle will be a minimum, and will increase as the canting angle increases, thus implying that rain attenuations could also increase with increasing canting angle. Consequently, the values of the coefficients were examined in terms of the average wind speed measured during each event, in order to investigate whether there could be such effects present in the attenuation process.

Figure 3 shows the correlation between the coefficient a and the average wind speed,

measured with a cup anemometer, while Figure 4 shows the same correlation for the coefficient b.

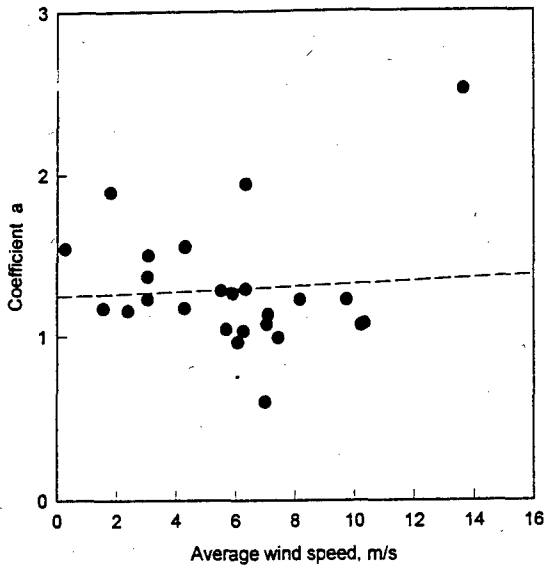


Figure 3: Correlation between the coefficient a and average wind speed, in $m\ s^{-1}$. The regression line is $a = 1.3 + 8 \times 10^{-3}w$, where w is the wind speed.

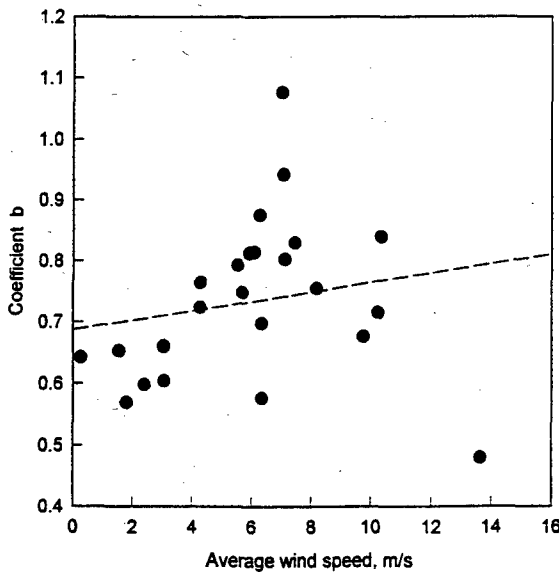


Figure 4: Correlation between the coefficient b and the average wind speed. The regression line is $b = 0.7 + 8 \times 10^{-3}w$.

The results indicate a marginal increase with wind speed in the values of both coefficients, which would suggest that attenuations could

increase with wind speed. However, the correlation coefficients were very small in both cases, implying that there is no statistically-significant dependence on wind speed.

3.3 Correlation with Maximum Rainfall Rate

It is expected that different type of rain could have different raindrop size distributions. For example, Olsen *et al.* (Ref. 1) used drops size distributions for different types of rain which yielded different values for the coefficients a and b. In the present work, it was not possible to characterize the rain in a similar way. However, as an indicator of the type of rain, the maximum rainfall rate in each event was used as a variable in the correlation analysis.

Figure 5 shows the correlation between the coefficient b and the maximum rain rate, indicating a decrease in the value with increasing rain rate. The correlation between the coefficient a and maximum rain rate was rather weaker, and positive. In both cases, the correlation coefficients were very small (8% for a, 17% for b) and are thus not considered statistically significant.

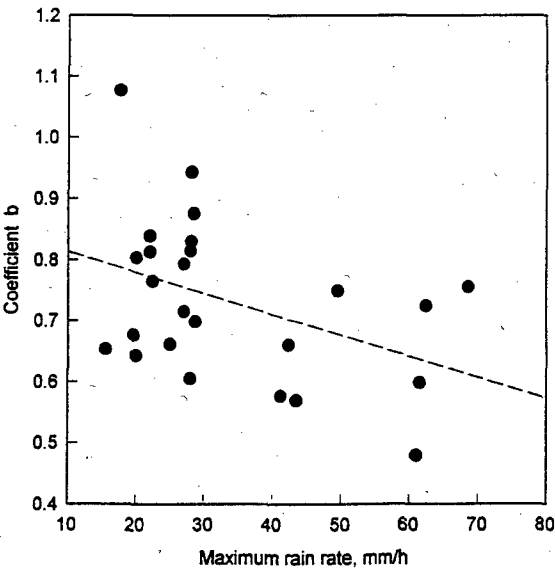


Figure 5: Correlation between the coefficient b and maximum rain rate. The regression line is $b = 0.8 - 4 \times 10^{-3}R_{max}$.

It is perhaps of some interest to note that Olsen *et al.* (Ref. 1) find the converse of this result, that the value of the coefficient a decreases for high rainfall rate distributions, while the coefficient b increases. However, the effect is again not very large.

3.4 Correlation Between the Coefficients

The final correlation considered in this paper is between the coefficients themselves. Figure 6 shows the correlation between the coefficient b and the coefficient a , and indicates quite a strong anti-correlation. The regression line can be represented by the linear expression $b = 1.05 - 0.25a$, with a correlation coefficient of 52%.

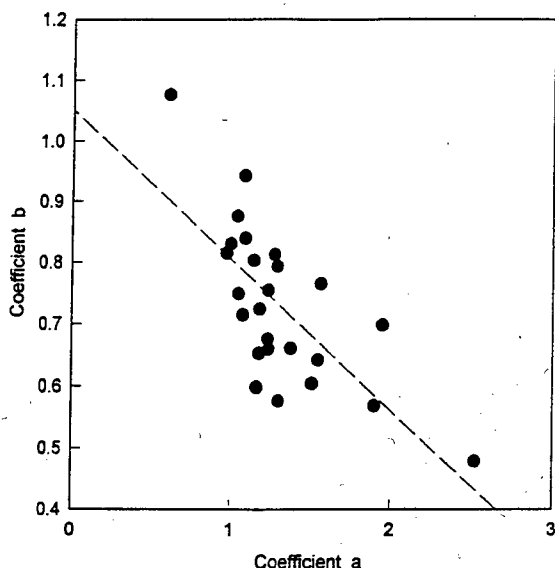


Figure 6: Correlation between the coefficient b and the coefficient a .

This suggests that, while there is considerable variation in the values of these coefficients deduced from different individual rain events, collectively the variability in the actual values of attenuation is somewhat less, since there appear to be some compensating mechanisms in the power-law model used in the analysis of rain attenuation.

4. SUMMARY

This paper has presented the results of an analysis of rain events in terms of the relationship $\gamma = aR^b$. The coefficients a and b have been examined in respect of various meteorological parameters, to investigate whether there are any climatological factors in the rain attenuation process. Little evidence was found for the data used, although there was considerable variability in the values of the coefficients. This variability may be due to differences in the raindrop size distributions in the individual rain events. Such dependencies were not examined in the present

work, but will form part of the next stage in these analyses.

While there were indeed wide variations in the values of the coefficients, they appear to be in anti-correlation, thus suggesting some form of compensating mechanism in the model, resulting in somewhat smaller variations in the actual rain attenuations.

For example, to take two extremes from this analysis, using values for the coefficient $a = 1$ and $a = 2$, encompassing most of the results, the predicted attenuations at a rain rate of 25 mm h^{-1} are 13 and 12 dB km^{-1} , while at 50 mm h^{-1} the differences become a little more pronounced, with predictions of 23 and 17 dB km^{-1} , respectively.

4. ACKNOWLEDGEMENTS

The author is grateful to Mr. Adil M Ahmed for his assistance in carrying out the initial aR^b analyses. This work was carried out as part of the National Radio Propagation Programme and has been funded by the Radiocommunications Agency of the DTI.

5. REFERENCES

1. Olsen *et al.* 1978, The aR^b relation in the calculation of rain attenuation, *IEEE Trans Ant Prop*, **AP-26**, pp 318 - 329
2. Fedi F 1979, Attenuation due to rain on a terrestrial path, *Alta Frequenza*, **48**, pp 167 - 184
3. Maggiori D 1981, Computed transmission through rain in the 1 - 400 GHz frequency range for spherical and elliptical drops and any polarization, *ibid*, **50**, pp 262 - 273
4. ITU-R Recommendation 838. 1992 - CCIR Recommendations, RPN Series, Propagation in Non-Ionized Media, ITU, Geneva.
5. Gibbins C J 1992, Studies of millimetre-wave propagation and related meteorology over a 500m path, *Proc. URSI Commission F Open Symposium on Wave Propagation and Remote Sensing*, Ravenscar, North Yorkshire, UK, 8 - 12 June.
6. Gibbins C J *et al.* 1987, A 500m experimental range for propagation studies at millimetre, infra-red and optical wavelengths, *JIERE*, **57**, pp 227 - 234

RAIN ATTENUATION MEASUREMENTS IN SOUTH-EAST ASIA

R. Lekkla¹, S.L. Lim², J. Wachja³, K.S. McCormick⁴

- ¹ - Communications Authority of Thailand, 12/46-48 Chaeng Wattana Road, Bangkok 10002, Thailand
Tel: +66-2-573-0099, ext. 3204, Fax: +66-2-573-7093
- ² - Singapore Telecommunications Pte., 500 Rifle Range Road, Singapore 2158, Republic of Singapore
Tel: +65-460-9205, Fax: +65-467-2061
- ³ - PT Telkom, Jl. Gegerkalong Hilir 47, Bandung, Indonesia
Tel: +62-22-212-259, Fax: +62-22-214-669
- ⁴ - Communications Research Centre, 3701 Carling Ave, Ottawa K2H 8S2, Canada
Tel: +613-998-2768, Fax: +613-998-9875, E-mail: stu.mccormick@crc.doc.ca

ABSTRACT

In South-East Asia, with its severe rain climates, significant attenuation will occur on earth-satellite paths in the 14/11 GHz bands. In August of 1993, at ISRP'93, the results from the first year of radiometric measurements of rain attenuation were presented for four locations in Thailand, Singapore and Indonesia. This paper describes the results from the second year of measurements, and compares them with the results obtained in the first year.

Keywords: Rain, Attenuation, Satellite.

1. INTRODUCTION

In 1989, an agreement was signed between the Association of South-East Asian Nations (ASEAN) and Canada to carry out a cooperative measurement program in the measurement of rain attenuation statistics on earth space paths. Of particular interest was the feasibility of using the Ku band frequencies of the INTELSAT Pacific Ocean Region (POR) satellites. The heavy rainfall conditions, combined with the relatively low elevation angles to the POR satellites, may make it impractical to use the higher frequency bands for certain satellite communications applications in the region.

Three countries are participating in the experiment: Thailand, Singapore and Indonesia, covering a wide geographical area. Part of Thailand lies in ITU-R rain climate zone N (tropical moderate) and part in rain climate zone P (tropical wet), while the other countries are entirely within rain climate zone P.

2. EXPERIMENTAL ARRANGEMENTS

In February 1992, measurement equipment was installed at Bangkok and Si Racha, Thailand, at Bukit Timah, Singapore, and at Bandung, Indonesia, as shown in Table 1. Another set of equipment was installed at Jakarta, but equipment problems at that site have not been resolved, and no data are available from Jakarta.

In Table 1, "Long." and "Lat." refer to the longitude and latitude of the measurement location, "Alt." is the altitude of the radiometer antenna above sea level, "Elev." and "Az." give the pointing angle to a satellite, "Rain" is the average annual rainfall amount, and "Rain Zone" is the ITU-R rain climate. The satellite position chosen was 174°E longitude except for Singapore, where an experiment was already in progress using an INTELSAT beacon from an Indian Ocean satellite, and the radiometer antenna was pointed in the direction of a satellite at 60°E.

The experimental equipment consists of radiometers operating at a frequency of 12.0 GHz. These are of the dual-slope type, using an antenna of 1.2m diameter. Measurements of sky noise temperature are made every two seconds, and stored in the radiometer memory. A tipping-bucket raingauge is mounted near each radiometer, and the time of each tip is also stored. Periodically, communications are established between the radiometer and a (remote) personal computer, and the radiometer memory is examined. If significant temperature fluctuations are found within a given hour, all the sky-noise measurements for that hour are transferred to the computer and recorded to disk. For quiescent

Table 1. Characteristics of the experimental locations

Location	Long.	Lat.	Alt. (m)	Elev. (deg)	Az. (deg)	Rain (mm)	Rain Zone
Bangkok	100.5°E	13.7°N	54	7.4	94.0	1460	N
Si Racha	100.8°E	13.1°N	30	7.9	93.9	1350	N
Bukit Timah	103.9°E	1.3°N	20	39.4	268.3	2285	P
Bandung	107.6°E	6.9°S	870	15.0	87.0	2164	P

periods, only the average noise temperature and its variance are retained for each hour. The times of all rain gauge tips are always saved. Since detailed recordings of sky noise temperature are retained only when there is significant activity, this recording procedure has proven quite efficient, in that only about five megabytes of data will be recorded for each site during a twelve-month period.

3. DATA ANALYSIS

This paper presents data for the two year period March 1992 to February 1993, and March 1993 to February 1994. At each experimental site, there were occasional equipment failures caused by lightning strikes, computer, and other equipment failures. Figure 1 shows the percentage of time that valid data were obtained for each of the sites. Severe equipment problems at Si Racha caused a complete loss of data for the months April through July 1993. Unfortunately, the data for Bandung for the period December 1993 to February 1994 were not received in time to be analyzed for this paper. For the two year period, the data availabilities from the experiments are 77%, 87%, 94%, and 78% for Bandung, Bangkok, Singapore and Si Racha, respectively. (When the data for Bandung are included, the figure will rise from 77% to 88%).

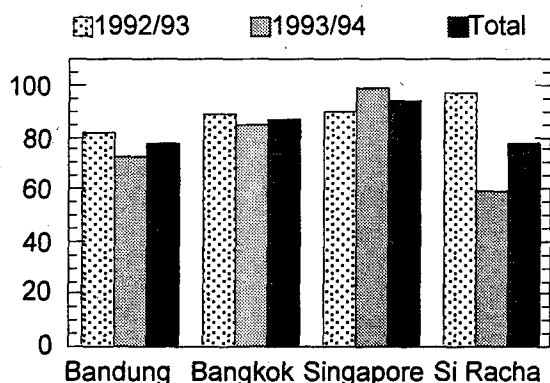


Figure 1. Percentage of time that valid data were obtained for each of the experimental sites.

The radiometric measurements of sky noise temperature were converted to path attenuations using the relation $A = 10\log(T_m - T_{cs}) / (T_m - T_a)$, where A is the attenuation in dB, T_{cs} is the sky noise temperature in the absence of precipitation, T_a is the measured noise temperature, and T_m is the 'effective' temperature of the absorbing medium. In this analysis, T_{cs} was assumed to be 30°K. Selecting a value for T_m is difficult since it varies from one rainstorm to another, and even within a single storm. Various authors have used different techniques to determine this quantity. In this analysis it was decided to examine all the attenuation events and to select those for which the

radiometer appeared to reach saturation (i.e. the measured sky noise temperature approached the effective medium temperature). These saturation temperatures were then plotted against the date on which they occurred, and a value of T_m was selected through examination of the values on the plot. This semi-quantitative approach yielded values of T_m equal to 280°K for Bangkok, Si Racha and Bandung, and 290°K for Singapore. From these values, time series of radiometrically-inferred attenuations were calculated from all the measured noise temperatures, and these data were then used to calculate monthly distributions of attenuation for each location.

The rain gauge data presented in this paper have not been integrated over one-minute periods. The times of each tip were simply used to calculate a time series of "instantaneous" rainfall rates, which were further processed to form cumulative distributions for each month.

4. RESULTS

The results of the data analysis for each location are given in Figures 2 and 3. Figure 2 shows distributions of rain rate, and Figure 3, distributions of attenuation.

In each of the plots of Figure 2, the label (a) refers to a pair of curves representing the distributions of measured rainfall rate for each of the one-year periods. In the first plot, for Bandung, the 1993/94 data are represented by the lower curve. In each of the other cases, the 1993/94 data are given by the upper curve of the pairs, indicating that 1993/94 tended to have more rain than the previous year. The curves associated with the label (b) are intended to represent "worst month" conditions. They were constructed from monthly distributions of rainfall rate by considering 1 mm/hr intervals, and selecting the largest of the monthly percentages for each interval. Curves N and P represent the distributions of rainfall rate given in ITU-R Recommendation 837 for rain climatic zones N and P.

The measured data for Bandung, Bangkok and Si Racha tend to lie closer to rain climate N than to climate P, while the data for Singapore lie between N and P. In all four cases, rain climate P seems to be a fairly good descriptor of the "worst month" data.

In each plot of Figure 3, the label (a) is associated with a pair of curves showing the 12 GHz attenuation inferred from the radiometer measurements. As in Figure 2, the lower curve of the pair represents the 1993/94 data for Bandung, while for the other three cases the lower curves show the 1992/93 values. Label (b) is again associated with "worst month" values, where in this case they were

derived by considering 0.1 dB intervals of attenuation, and choosing the greatest monthly percentage of time for each 0.1 dB interval. In each case, label (c) denotes the annual attenuation distribution predicted using the procedure in ITU-R Recommendation 618-2, for a frequency of 12.0 GHz, and the location data given in Table 1. In the calculation, the rain intensity for 0.01 percent of the year was taken to be 86 and 91 mm/hr for Bangkok and Si Racha, respectively, which are average values over the two years. For Bandung and Singapore, the measured 0.01% values were in excess of 100 mm/hr, so that 100 mm/hr was used as prescribed in the Recommendation.

In all cases, the measured attenuation distributions for the two years are reasonably close, and for Singapore they are indistinguishable. At the lower elevation angles, Bandung, Bangkok and Si Racha, the measured distributions agree fairly well with the prediction, but with the prediction tending to underestimate the measured values. For Singapore, where the elevation angle of the measurement is much larger, the agreement is poor with a severe underprediction of the measured values.

5. CONCLUSION

This paper presents results from an extensive experiment designed to obtain rain attenuation information relevant to the design of satellite communications systems, in the 14/11 GHz bands, in South-East Asia. Indications from each of two years of measurements are that the ITU-R attenuation prediction technique gives reasonable agreement with measurements at relatively small elevation angles, but that the method seriously underpredicts the attenuation at relatively large angles for small percentages of time.

6. ACKNOWLEDGMENT

This work was supported by the Canadian International Development Agency, under project number 149-12982.

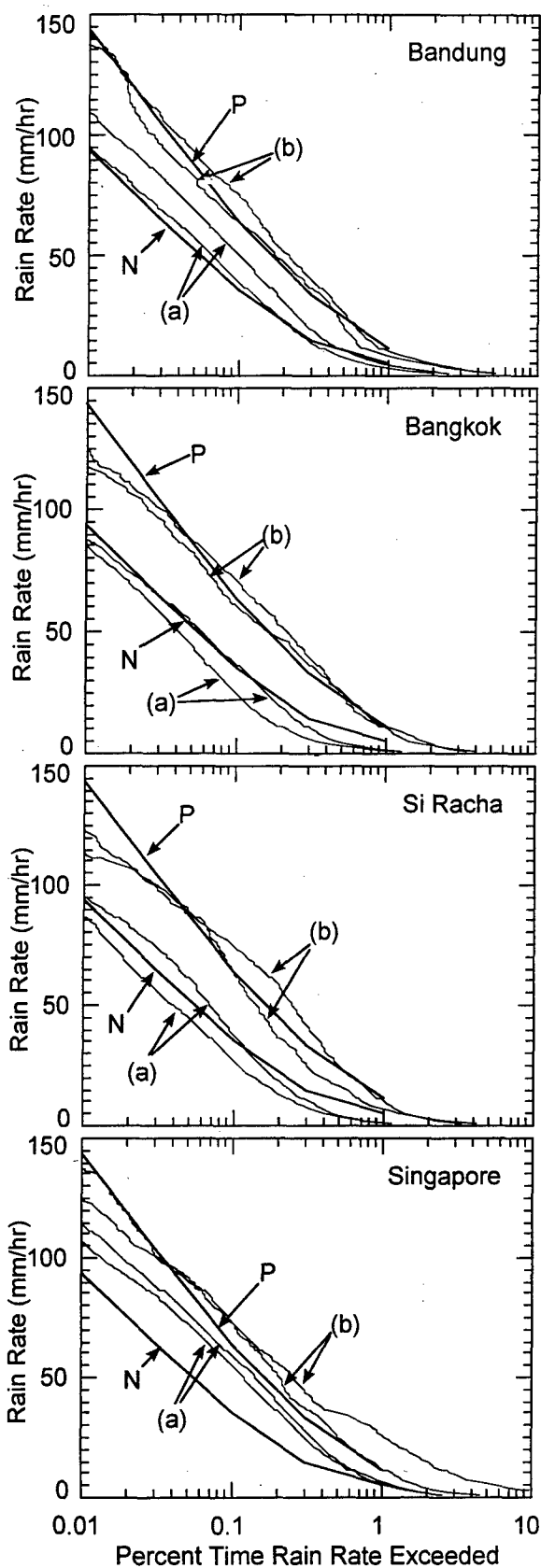


Figure 2. Measured rainfall rate distributions for each of the four experimental locations.

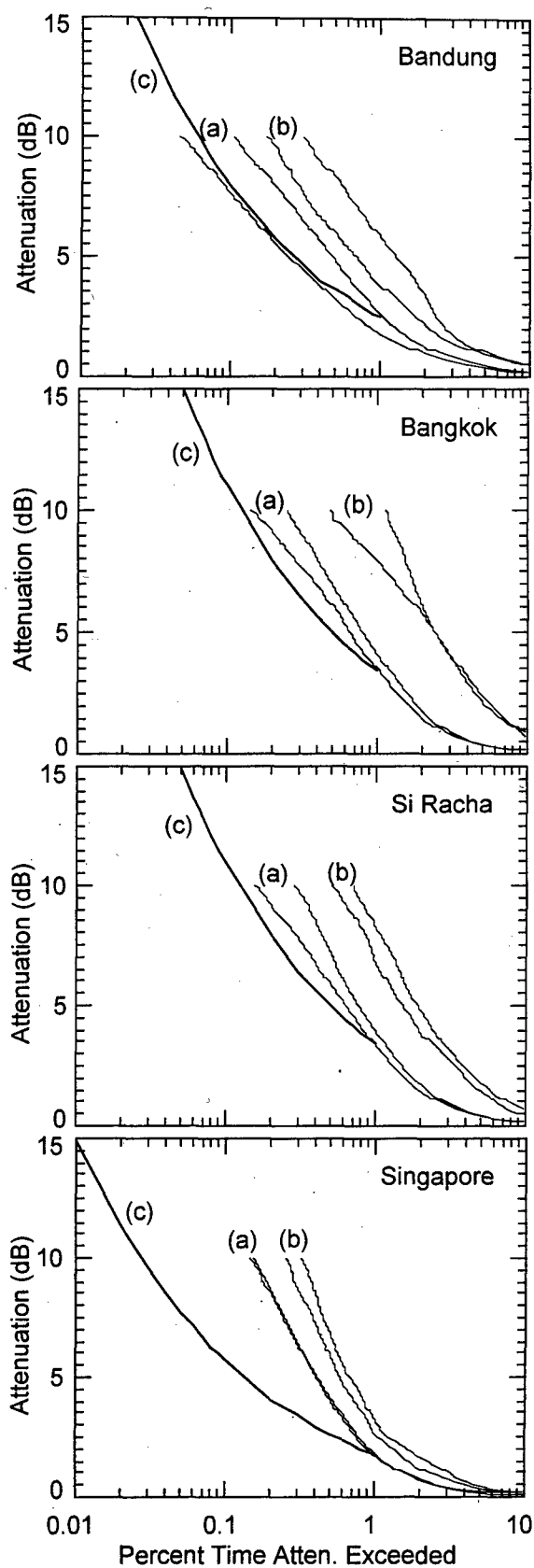


Figure 3. Distributions of attenuation at 12 GHz inferred from radiometer measurements at each of the four experimental locations.

Session 6: Clear air I

CLIMATIC PARAMETERS IN CLEAR-AIR PROPAGATION MODELLING

K.H. Craig¹, T. Tjelta² and B. Segal³

1-Rutherford Appleton Laboratory, Chilton, Didcot, OX11 0QX, U.K.

Tel: +44 235 445134, Fax: +44 235 446140, Email: ken.craig@rl.ac.uk

2-Norwegian Telecom Research, PO Box 83, N-2007 Kjeller, Norway

Tel: +47 63 80 92 03, Fax: +47 63 81 00 76, Email: terje.tjelta@tf.tele.no

3-Communications Research Centre, PO Box 11490, Ottawa, Ontario K2H 8S2, Canada

Tel: +613 998 2468, Fax: +613 998 4077, Email: bsegal@ramet.dgrc.doc.ca

ABSTRACT

This paper reviews the current status of climatic parameters in clear-air propagation modelling, and considers possible developments. Sources of radio wave propagation data and radiometeorological data are discussed. Analyses of surface, and radiosonde-derived duct, statistics are given.

Keywords: Climatic Parameters, Propagation Modelling, Propagation Datasets, Radiosondes, Ducting.

1. INTRODUCTION

1.1 Structure of the troposphere

The radio refractive index n determines the effect of the clear-air atmosphere on radio wave propagation. Because n is very close to unity, it is usual to work with the refractivity, N , which is the deviation of n from unity, in parts per million. N depends on the pressure P (mb), the absolute temperature T (K) and the partial pressure of water vapour e (mb):

$$N = 77.6 \frac{P}{T} + 3.73 \times 10^5 \frac{e}{T^2} \quad (1)$$

The first term is denoted N_{dry} while the second term (due to water vapour) is denoted N_{wet} .

P , T and e vary on several scales. Figure 1 shows contours of potential refractivity (i.e. refractivity reduced to a standard pressure level) derived from aircraft measurements made over the English Channel. The variations are about two orders of magnitude greater in the vertical direction than in the horizontal, and the troposphere can often be considered to be horizontally stratified on the largest scale (> 1000 km). On the medium scale (100 m–1000 km) the ground, meteorology (local or mesoscale) and climate can produce spatial and temporal variations; the influence of the coast at each side of the Channel are visible in the Figure.

On the smallest scale (< 100 m) turbulent mixing causes scattering and scintillation.

In the *standard* atmosphere, N decreases exponentially with height, although a linear decrease is a good approximation in the first kilometre. The surface refractivity N_s and the rate of decrease vary with season and from place to place.

1.1.1 Super-refraction and ducting

N decreases by about 40 N/km in the lower troposphere in average conditions at mid-latitudes. Meteorological conditions can give rise to non-standard propagation. *Sub-refraction* occurs for lapse rates less than 40 N/km, reducing the clearance above terrain on terrestrial paths. *Super-refraction* occurs for lapse rates exceeding 40 N/km, extending the radio horizon beyond the normal horizon. If the lapse rate of N exceeds 157 N/km, radio waves are bent towards the Earth more rapidly than the Earth's curvature, and this may give rise to *ducting*. Such large gradients are often associated with a layer at the interface between two air masses.

For very abrupt changes in refractivity, it may be more appropriate to consider the radio waves to be reflected by the layer, rather than refracted by it. The distinction is frequency dependent and a layer reflection model is more useful at the lower (VHF) frequencies.

Energy can become trapped between a boundary or layer in the troposphere and the surface of the Earth (*surface duct*) or between two boundaries in the troposphere (*elevated duct*). Ducting can cause multipath fading and enhancement on terrestrial, line-of-sight links and long range interference between services. Figure 2 shows an elevated duct profile in terms of *modified refractivity* M : $M = N + 0.157 z$, where z is the height above the ground in metres. A *ducting layer* is identifiable by a negative slope in the modified refractivity–height curve. The *duct* extends from the top of the ducting

layer down to the height at which the modified refractivity returns to the same value as at the top of the layer. In the case of a surface duct, it would extend down to the ground.

A ducting layer will only trap radio waves if certain geometrical constraints apply. In particular, the angle of incidence of electromagnetic energy at the layer must be very small, generally less than $0.5-1^\circ$. Even energy launched horizontally will intercept an elevated layer at a non-zero angle due to the Earth's curvature, and ducting layers will not significantly affect terrestrial radio links if the layers are higher than about 1 km above the path.

High refractivity lapse rates are caused by a rapid decrease in water vapour pressure with height and by temperature inversions; these often occur together. Differences of several tens of N-units over a height interval of tens of metres can occur between adjacent air masses, leading to the formation of a ducting layer. As these conditions depend on climate and topography, statistics of super-refraction and ducting will vary in different regions of the world.

The most widespread form of duct is the shallow (less than 30 m) surface duct caused by evaporation over large bodies of water. Although this has a major effect on ship-borne radar performance, it is less important for civil communication systems, except when located in low-lying coastal areas. Subsidence inversions and advection are the most important causes of extreme range interference on terrestrial paths, giving rise to deep (up to hundreds of metres thick) surface ducts, and strong elevated ducts. On overland paths, nocturnal radiation can give rise to strong temperature inversions; this is an important cause of multipath on line-of-sight links.

1.2 Climatic parameters in clear-air radio wave propagation modelling

In the design of radio systems the possible impairments from propagation effects have to be considered and taken into account. The design of a system requires radio frequencies and bandwidths and will often include an evaluation of service quality and availability as a function of path length or coverage area. In this picture the terrain and buildings etc. play a very important role. Furthermore, the atmosphere alone, or in combination with the terrain, has a major influence on propagation and hence on service quality. The different climates on the Earth produce quite different conditions for the design and operation of radio systems. It is therefore of great interest to

characterise the various clear air climates and derive parameters for propagation models.

Several prediction methods recommended by the International Telecommunication Union (ITU) use climate zones. The zones are, for example: mountain; desert; dry and humid; overland; over water; coastal areas etc. Some of these zones are also classified using meteorological characteristics of the refractive index for that climate.

A further step is to directly use the clear air radio meteorological parameters that are available from long term standard meteorological measurements, as part of the prediction procedure. The parameters currently selected for use in the prediction methods recommended by the ITU are:

- N_s : the refractivity at ground level;
- N_o : the value of N_s scaled to sea level;
- N_{wet} : the wet component of refractivity;
- ΔN : the difference between the values of refractivity at the ground and 1 km;
- β_o : the percentage of the time that the refractivity gradient in the lowest 100 m above the ground is less than -100 N/km;
- P_L : a (pseudo-)worst month value of β_o .

In the following we concentrate on modelling for communication systems only. The ITU-R Recommendations are to be found in [1].

1.2.1 Line-of-sight fading and enhancement parameters

P_L is used in the modelling of geoclimatic factors for the line-of-sight multipath propagation distribution (ITU-R Rec 530):

$$K = C P_L^{1.5} \quad (2)$$

C takes into account terrain characteristics (such as overland, mountainous area, medium and large bodies of water) and P_L is currently taken from ITU-R Rec 453 (based on [2]).

1.2.2 Parameters used for transhorizon, troposcatter and interference calculations

A normal mixed atmosphere makes it possible for the radio signals to propagate slightly beyond the geometric horizon. In super-refractive and ducting conditions the signal may propagate far beyond the horizon. Even under normal conditions there is a weak signal due to small scale inhomogeneities and troposcatter links exploit this mechanism.

The ITU-R troposcatter model (ITU-R Rec 617) is based on eight climatic zones which depend on the statistics of N_o .

ΔN and β_o are used in the evaluation of the influence of ducts and super-refractive layers on long range interference (ITU-R Rec 452). These can be obtained from maps (based on [2]), or in the European region, β_o can be calculated in terms of the radio climatic zones (inland/coastal/sea) which the path traverses. The troposcatter contribution to interference depends on N_o .

1.2.3 Parameters for other systems

Low angle satellite systems experience angle-of-arrival variations due to variations in the refractive index. The prediction of total deviation (ITU-R Rec 834) is given in terms of four climatic zones. The calculation of the effect of scintillation (ITU-R Rec 618) is based on statistics of N_{wer} .

2. DATA AVAILABLE

The only readily available database is that of the ITU-R, comprising various tables. The description of the data and entries are given in ITU-R Rec 311 and some information about the data that have been collected is found in ITU-R Doc 5C/88 (1993).

2.1 Line-of-sight radio propagation data

One of the ITU-R tables concerns measurements on multipath fading and enhancement, and currently contains 243 entries that include statistics. Table 1 lists country, number of entries, and some information, such as path lengths and radio frequencies, relevant to system design. The data given are average worst month statistics, and the number of calendar month distributions used to obtain the statistics ranges from few months to 8 years, with an average of 15 months.

The data collected are link information (such as transmitter and receiver locations), radio frequency, terrain profile (along with some derived characteristics) worst month signal statistics and worst month to annual ratio.

The European COST 235 project may add more radio wave propagation data to the European part of the database.

Propagation data are clearly required from regions of the world where none are now available: a large part of Asia, Australia, Africa, and America. For all parts of the world more data from types of links other than overland are required, such as overwater and in mountainous areas.

Continent	Country	No. of entries	Path length (km)	Frequency (GHz)
			min,max,mean	min,max,mean
America	Brazil	8	40.2, 68.0, 54.4	4.0, 7.7, 6.2
	Canada	33	15.7, 131.9, 62.0	0.5, 17.7, 5.2
Europe	Denmark	1	44.7	14.3
	Finland	12	41.2, 66.3, 50.9	6.0, 7.5, 6.3
	France	30	28.0, 95.3, 47.6	3.8, 14.5, 7.7
	Italy	50	32.6, 299.9, 97.2	0.9, 11.8, 5.3
	Norway	13	39.0, 93.8, 63.7	3.7, 7.5, 5.9
	Russia*	29	12.7, 74.9, 46.5	3.7, 29.3, 5.6
	Sweden	7	15.2, 73.0, 35.7	2.2, 36.0, 14.0
	Switzerland	10	53.7, 125.0, 98.0	2.3, 7.0, 4.2
	UK	33	7.5, 74.8, 42.8	1.8, 37.0, 9.8
	Egypt	7	24.5, 49.0, 39.8	6.0, 6.8, 6.5
Africa	Ghana	3	29.5, 60.1, 49.9	2.0, 7.7, 3.9
	Malawi	1	85.0	2.1
	Mozambique	1	112.6	2.1
	Senegal	3	25.4, 54.5, 43.1	6.5, 6.8, 6.6
	Zimbabwe	1	54.0	6.9
Asia*	Pakistan	1	12.0	13.0
Australia		0		
Total		243		

(* Former USSR: also includes data from Estonia, Belarus, Ukraine, Georgia, and Uzbekistan.

Note that the two latter countries and some Russian links are in Asia)

Table 1: Line-of-sight radio wave propagation data

The ITU database also includes a table (16 entries) on co- and cross-polar effects on line-of-sight links and tables on diversity reception improvement (25 entries) and radio channel characteristics (50 entries), of help in understanding line-of-sight propagation data related to clear-air phenomena.

2.2 Propagation data for the evaluation of interference

The ITU-R database includes a set of 201 links. A large amount of information is asked for and collected, including link parameters and radio-meteorological data (N_o , N_s , β_o). Links are also sorted by climatic zone. Table 2 gives the countries from which data are now available.

2.3 Meteorological data

A distinction is made here between sources of raw, unprocessed meteorological data, and data reduced to radiometeorological parameters that can be used in prediction models. The most convenient form of the latter is global and regional maps.

2.3.1 Raw data

Global networks of stations gather meteorological data on a regular basis for synoptic weather

forecasting. These data are regularly archived and are available from several world data centres. Surface weather conditions are monitored at more than 5000 sites worldwide, while a network of over 1000 stations carry out routine radiosonde observations (RAOBs) that permit vertical profiles of various meteorological parameters, including radio refractivity, to be calculated.

Surface data are recorded three-hourly, and many stations have data collected over a long time span (in some cases hundreds of years); these are a useful source of data for statistical studies of variability of meteorological parameters (spatial, diurnal and climatic).

Radiosondes measure (directly or indirectly) pressure, temperature and humidity, from which height and refractive index can be derived. Radiosonde stations make ascents twice daily (at 0000 and 1200 UT), and some stations also launch pilot balloons (wind data only) at 0600 and 1800.

The vertical resolution of modern radiosondes is excellent (about 10 m), but unfortunately the data are only reported and archived at "standard" pressure levels (1000 mb and 850 mb being the only levels normally relevant for radio purposes) and "significant" levels (i.e. those that show a

Continent	Country	No. of receivers	No. of transmitters	Path length (km) min,max,mean	Frequency (GHz) min,max,mean
America	Barbados	1	0	342	0.9
	Canada	4	5	228, 346, 295	0.5, 4.7, 2.9
	Cuba	0	1	299	0.9
	Trinidad&Tobago	0	1	342	0.9
	US	29	27	156, 554, 290	0.5, 9.4, 2.0
Europe	Denmark	2	5	138, 839, 466	1.3, 11.7, 6.4
	France	25	8	152, 483, 254	0.5, 11.6, 3.8
	Germany	19	14	93, 599, 295	0.5, 29.0, 4.4
	Italy	0	1	577	0.8
	Netherlands	29	14	100, 955, 329	0.6, 17.7, 2.7
	Russia	2	2	295	1.0, 4.5, 2.7
	Spain	1	1	380, 577, 479	0.8, 0.9, 0.8
	Sweden	0	2	957, 974, 966	1.3
	UK	66	98	66, 974, 308	0.1, 17.8, 2.5
	Morocco	1	0	380	0.9
Africa	China	3	3	140, 229, 196	2.8
	Japan	17	17	226, 438, 318	0.6, 3.0, 1.6
	Malaysia	1	0	598	1.0
	Singapore	0	1	598	1.0
	Thailand	0	1	722	1.8
	Viet Nam	1	0	722	1.8
Australia		0	0		9
Total		201	201		

Table 2: Radio wave propagation data for interference considerations

“significant feature” in the temperature or humidity profile). This means that the resolution in the first kilometre is rather poor.

Older types of radiosonde are inherently less accurate and have poorer vertical resolution. The sensors are not fast-response devices, and the time lag of the radiosonde instrumentation has two important effects. Firstly, it will tend to underestimate the magnitude of any refractivity changes so that (a) layers will have apparent gradients that are less extreme than they actually are, and (b) very thin structures may not be detected at all. Secondly, the indicated height for a refractive layer may appear to be higher than its true height.

The discrete launch times of radiosondes, and the fact that ascents are made at different local times in different parts of the world, serves to obscure details of the refractive conditions at a given location and makes it difficult to separate diurnal effects from genuine regional variations. The fact that many different types of radiosondes are in use worldwide, and that meteorological organisations occasionally change types may limit the usefulness of long time span datasets for statistical analyses.

Alternative methods of measuring the vertical refractive index profile exist, but none of them are as developed, as widely available or as inexpensive as the radiosonde. However they can give valuable insight into the atmospheric processes that cause anomalous propagation, and in the longer term may prove a better source of radiometeorological data than the radiosonde:

- the refractometer is an *in situ* measurement system, normally mounted on an aircraft or helicopter for detailed case studies; it has high accuracy and a very rapid response time;
- *remote sensing* is an active area of study. Doppler radars, lidars (laser sounders), sodars (acoustic sounders), and satellite-borne instruments have all been considered;
- numerical weather models hold out promise for the wide scale *forecasting* of refractivity; recent mesoscale models covering limited regions have good vertical and horizontal resolution.

2.3.2 Radioclimatological statistics

Statistical studies of radiorefractivity parameters based on surface and radiosonde data have been carried out since the 1950s by several workers. Two major studies of global coverage are:

- Bean et. al. [2] calculated statistics for four calendar months (February, May, August and November) based on 112 radiosonde stations with a 5-year time span in the late 1950s and early 1960s. They produced contour maps and cumulative probability distribution functions of surface refractivity and refractivity gradients over different height intervals. Their maps are the basis for the current ITU-R prediction procedures;
- Ortenburger of GTE Sylvania [3] carried out a larger study of surface, super-refracting layer and duct statistics based on 5 years of data (late 1960s and early 1970s) for all calendar months.

In their time, both these exercises were major tasks, and the results are still widely used. More recently, the raw data and the computing power needed to process them have become widely available, and several groups are actively involved in new analyses covering longer time spans with better resolution data.

3. NEW CLIMATIC PARAMETERS

3.1 Refractivity/duct-layer parameters

Clear-air anomalous propagation phenomena (such as multipath fading) are often considered to be the direct consequence of a radio duct in the troposphere. By itself this condition is neither necessary nor sufficient for anomalous propagation to be manifest. However, since the same holds true for any other pre-defined refractive configuration, the existence of a stratified tropospheric radio duct is arguably the best concomitant of anomalous line-of-sight propagation. The problems facing the modeller are

- (a) to define the exact ducting-layer probability statistics for a given location,
- (b) to determine which specific duct parameter(s) are the most relevant and useful ones, and
- (c) to determine which other refractivity-related meteorological quantities might usefully serve as proxies for, or adjuncts to, radio ducts.

This section examines several duct-layer quantities that might be used in propagation modelling.

(i) Probability of occurrence:

For obvious practical reasons, the only possible way in which duct occurrence statistics can be derived for the entire globe or for a large portion of it is through the analysis of existing radiosonde

archives. These contain data for more than 1000 different locations extending for a number of decades at some locations although developments relating to the instrumentation restrict the useful period to about 25 or 30 years. A data set of that size is required in order to provide the necessary statistical significance, especially if one hopes to provide predictions of propagation conditions on a monthly basis.

(ii) Heights of occurrence:

The height of occurrence of a duct is obviously an important parameter and one that has not received sufficient attention. If the layer is not penetrated by at least one of the signal ray trajectories then it cannot affect the propagation. The three heights associated with an idealised ducting layer are shown in Figure 2: the top and bottom of the ducting layer, and the bottom of the duct itself.

In a simple ray picture, the outer boundaries of a horizontally homogeneous duct represent the interval from within which a launched ray may become "trapped". The base of the ducting-gradient layer is the "optimal" level from which a pseudo-horizontally launched ray might become trapped. All three height levels are potentially significant in modifying propagation conditions and hence deserve some consideration as modelling parameters.

(iii) Duct intensity:

The intensity of the duct is defined in Figure 2. It may be thought of as providing a measure of how significant the duct might be in influencing propagation. Combined with the physical thickness of the duct, it helps define the minimum wave frequency that can be "trapped" within the duct boundaries. While actual "trapping" of a radio signal is important primarily for long terrestrial paths, the intensity of a layer may nonetheless be indicative of its importance in anomalous propagation.

3.2 Preliminary analyses

An analysis of duct layer thickness (based on Sylvania statistics) has been made for sites along the east and west coasts of Canada and for the UK and the European west coast. Differences are evident in the average thickness (especially for surface ducts) and in their daily and seasonal variability. All tend to be somewhat larger in North America.

An analysis of duct height and intensity is more problematic than that of probability of occurrence because of the poor vertical resolution and slow-response of the sensors discussed earlier. Statistics of duct parameters derived from RAOBs may be useful for propagation modelling, but care has to be taken in interpreting their meaning.

Figure 3 compares the monthly median heights (the vertical bars show the 25–75% exceedance interval) of surface ducts from stations in the Mediterranean and India (based on a new analysis of radiosonde data). The seasonal variations are clearly very different, in contrast to the probabilities of duct occurrence, which show a similar trend for the two stations; this indicates the potential of duct height as a climatic parameter.

Layers often form, move vertically and decay with a strong diurnal correlation. Twice-daily radiosonde ascents are insufficient to follow the trends. Because of this it might be preferable to make the *a priori* assumption that the occurrence of a duct is not a (strong) function of height. In this way the duct occurrence statistics might be enhanced by combining surface-based with elevated ducts up to some undetermined altitude. This approach is not without risk. For example, the data in Figure 4 indicate that surface ducts are somewhat more prevalent in the UK than in coastal Canadian regions, while the reverse holds true for elevated ducts. It is not clear whether this is a result of different local launch times in the two continents, or whether it is due to genuine climatic differences.

3.3 "Modified" radio ducts

A number of reasons have been outlined as to why one might seriously question the observations routinely produced by the global network of RAOB stations. While every reasonable effort should be made to correct and improve available RAOB readings, it is also appropriate to consider modifying the operational definition of a duct. Thus, we might presume the existence of a true duct when the vertical refractivity lapse rate as reported by a meteorological radiosonde falls below some less severe limit, such as 125 N/km, 100 N/km, or possibly even 80 N/km. It is not difficult to redefine a set of pseudo-duct parameters.

3.4 Non-radiosonde parameters

Having noted the difficulties associated with standard radiosonde data, it is tempting to consider the use of other meteorological information that might serve as a substitute for or supplement to

refractivity gradient statistics. Figure 5 shows the minimum temperature difference required to create a 10 m surface ducting layer with an intensity of 3 N-units: it indicates that surface ducts are more readily created under hot and humid conditions, although it is recognised that large-scale advection or nocturnal radiation cooling frequently creates strong and persistent ducts in Arctic and/or desert areas.

For most Temperate locations, however, it is likely that atmospheric water vapour, observable at the surface, constitutes the most critical antecedent of super-refraction. Thus, one might consider the surface value of such a quantity as a modelling parameter. The advantages of such a parameter include the fact that surface meteorological observations extend over a much longer period of time, are measured at a much greater number of sites worldwide, are measured more frequently than the twice-per-day radiosonde soundings, are much simpler to process, and most importantly they represent quasi-static measurements with inherently greater accuracy.

As an alternative, the water vapour parameter might be combined with surface temperature to give N_{wet} . Figure 6 shows the mean seasonal wet and dry components of the surface refractivity and their standard deviations for a mid- latitude temperate

location in southern Canada. Based on ten years' observations taken every three hours, these represent as much data as forty years of radiosonde observations and allow a complete diurnal analysis to be carried out. Of course careful analysis would be required to establish a correlation between surface water vapour or N_{wet} and duct or pseudo-duct statistics and, ultimately, with propagation data.

While no simple surface parameter could be applicable to all locations globally, it could provide a significant advantage in greater precision, in improved temporal and spatial resolution as well as in extending validated models to areas where reliable RAOBs are not available.

4. REFERENCES

- [1] ITU-R Recommendations, RPN series, Propagation in Non-Ionised Media, Geneva, 1994.
- [2] B.R. Bean, B.A. Cahoon, C.A. Samson and G.D. Thayer, A World Atlas of Atmospheric Radio Refractivity, ESSA Monograph 1, 1966.
- [3] L.N. Ortenburger, Radiosonde Data Analysis II, GTE/Sylvania Incorporated, 1977.

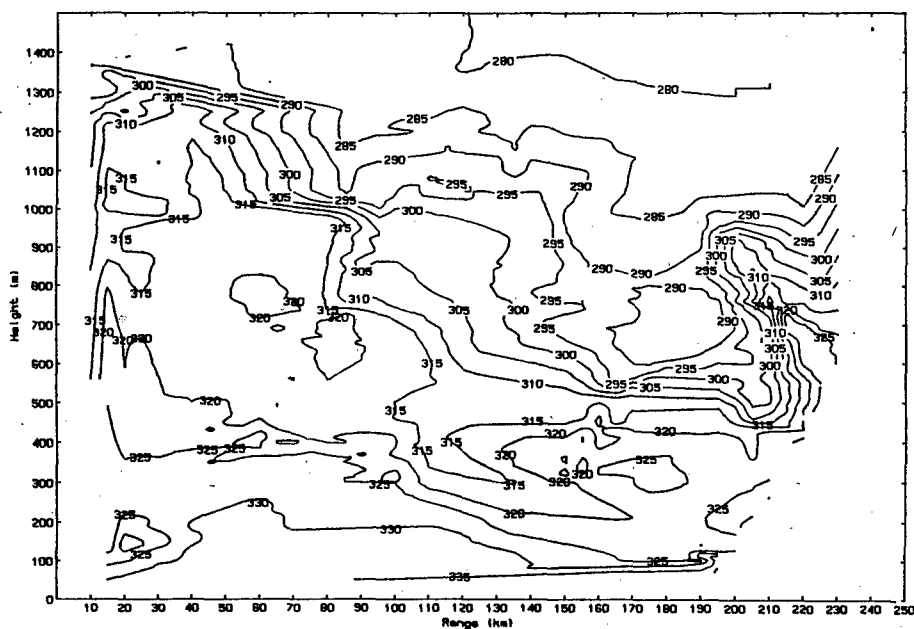


Figure 1: Contours of potential refractivity over the English Channel

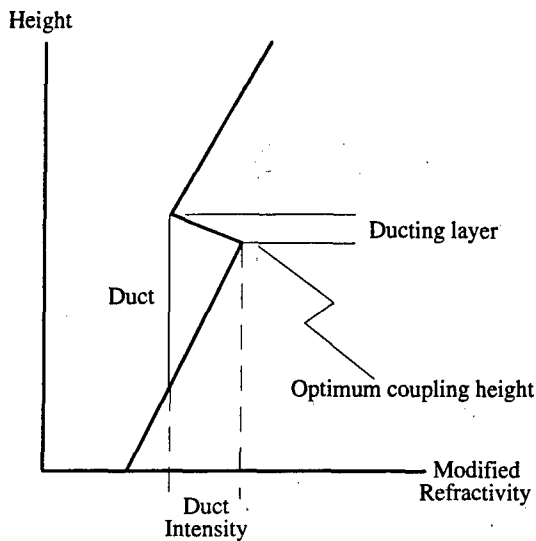


Figure 2: Refractivity profile and duct parameters

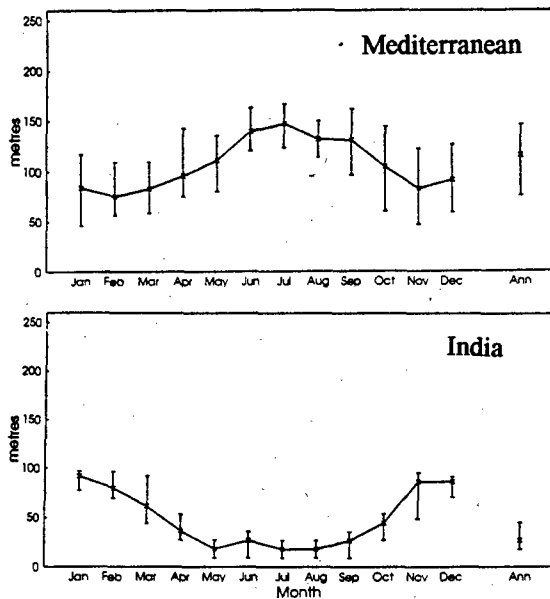


Figure 3: Surface duct height statistics

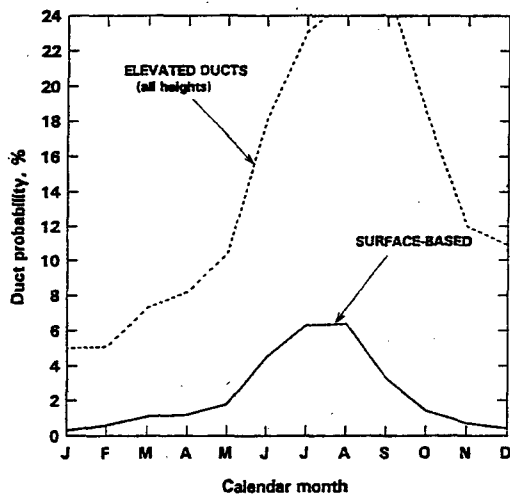


Figure 4a: Duct occurrence probability in Canada

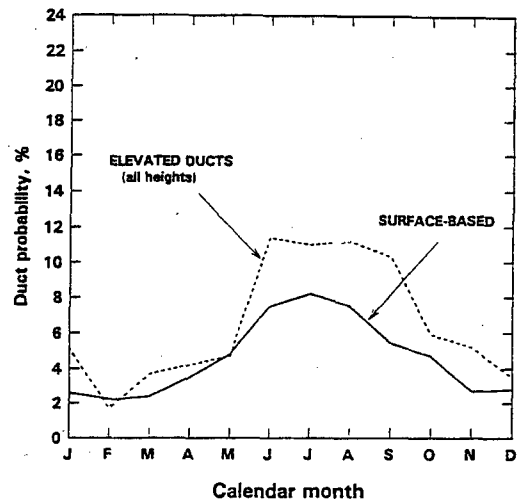


Figure 4b: Duct occurrence probability in the UK

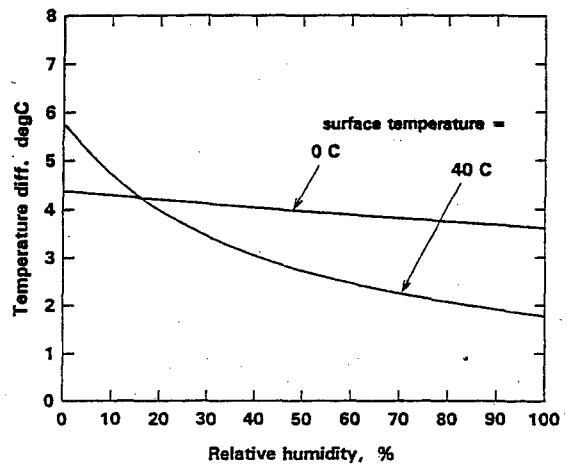


Figure 5: Humidity dependence of ducting layer formation

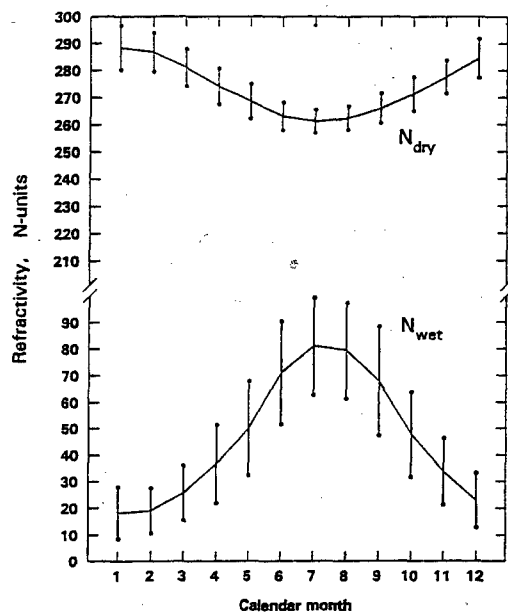


Figure 6: Mean and standard deviation of N_{dry} and N_{wet} in southern Canada

Investigation of climatic factor influence on abnormal radio propagation

V.N.Troitsky

NIIR, 16 Kazakova Str. Moscow, 103064, Russia
tel. 7 095 267 06 47 , fax. 7 095 261 00 90

Abstract

The investigation of correlation between probability of anomalous high EM field strength and different meteorological and radio sound data has been conducted in NIIR with the purpose of predicting of interference signal probability in various climatic regions.

1. Introduction

The prediction of interference signal level in different geographical regions is important and difficult problem. It is impossible to conduct radio propagation experiments in all climatic and geographical regions of the earth. Therefore it is important to get the reliable method evaluating of interference signal by means huge massive of meteorological data, which there is for almost all regions of earth. With this connection it is important to look for the dependence on high signal level with meteorological data, in particular, radio sound data. For this aim the special investigation has been conducted in NIIR.

2. Result of investigation

At first the correlation between high signal level beyond the horizon and the value of N has been investigated for some long distance paths. The correlation factor ρ between value A (signal level respect to free space level) and N_s has been about 0 for all paths for one month period. Only for period about one year the correlation factor gets marked value. Besides it decreases with a distance increasing. For example, ρ was about 0,5 for path Vologda—Taldom 303 km distance (frequency about 1 GHz). For path Magadan—Ochotsk (415 km, $f=1$ GHz) ρ was about 0,41 for one year period. It is interesting to remark, that correlation decreases for large signal level. The regression function is offered on Fig.1 for the path Magadan—Ochotsk. It is obvious from this figure, that regression factor $k = \frac{dA}{dN_s}$ decreases for large A value.

The experiments show, that there is not direct correlation between values A and N_s for large distances. There are only season dependence A , so as N_s , which causes different from 0 correlation factor. It is necessary to look for other meteorological parameters, which are more directly connected with appearance of high signal level on trans—horizon paths.

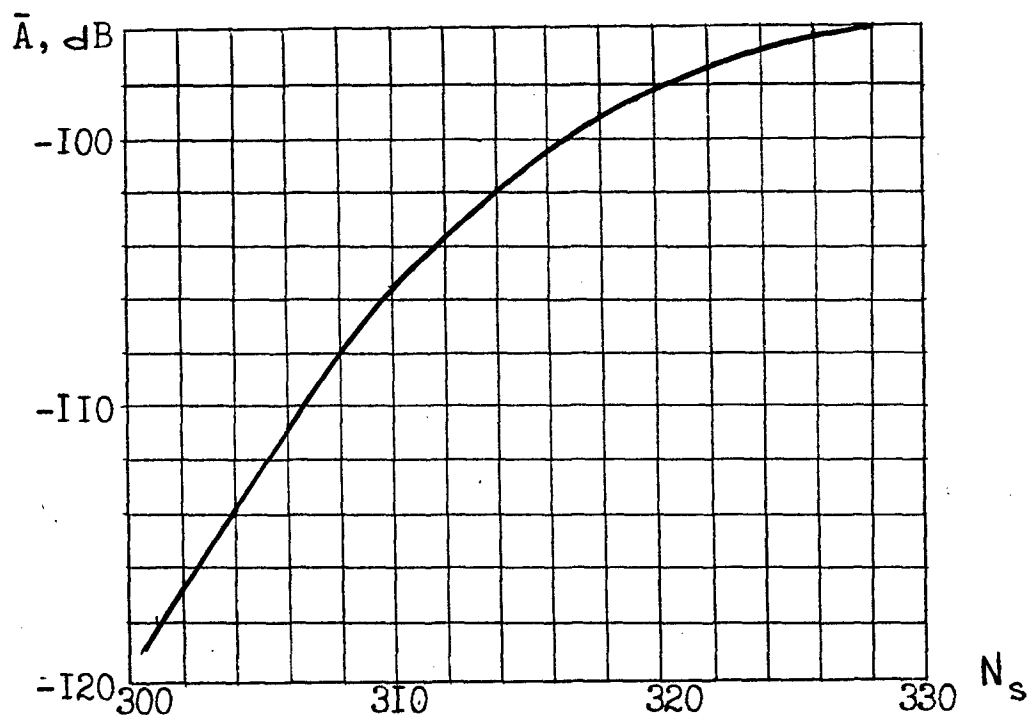


Fig. 1. Regression function $\bar{A}(N_s)$ for the path
Magadan-Ochotsk (415 km, 1 GHz)

The main cause of anomalous propagation is the ducting and the reflection from atmosphere layers. All this phenomenon connected with strong vertical gradients of N in atmosphere. The gradient $N = g$ may be obtained from radio sound data.

In the former Soviet Union regular radio sound measurements were conducted on all territory of the country during 30 or 50 years. Therefore it is possible to obtain large statistical material of values g for different geographical and climatic regions.

Majority of strong layer discontinuities of atmosphere is localized in lower part of the troposphere up to 3 km. Owing to this fact the comparison has been carried out between A on trans-horizon paths and following meteorological parameters in 3 km layer of atmosphere:

- 1) N_s — refractivity on the earth surface
- 2) \bar{g} — average gradient of N in 3 km layer
- 3) g_m — maximum gradient of N having been somewhere in 3 km layer
- 4) σ_g — root mean square deviation of g in 3 km layer.

Table 1 gives of correlation factor ρ for A and all above values for trans-horizon path 165 km length on frequency 203 and 543 MHz for one year period. In this table ρ is correlation factor medians for 3 hour value of A and N , \bar{g} , g , g_m and σ_g for radio sound, launched in the middle of each 3 hour term.

Tabl 1.

f, MGz Parametr	\bar{g}	σ_g	g_m	N_s
207 MHz	0,20	0,018	-0,049	0,059
543 MHz	0,11	0,100	0,105	0,151

As it is seen, there is not correlation between this values.

This fact may be explained, that the radio sounds were launching only on the terminals of path, and the data does not reflect atmosphere condition on the whole path in that moment.

It is possible to compare the statistical distribution of signal level and meteorological data for a term about 3 days. Such distributions reflects statistical characteristics of radio wave propagation and statistical characteristics of refractive inhomogeneities in the region of the path during this 3 days. The values A , exceeded 10 and 1% time were obtained from A distribution and value of N_s , \bar{g} , g_m and σ_g , exceeded 10% time were determined from the distribution of these values.

Table 2 gives correlation factor of value A , exceeded 10 and 1% time and values of N_s , \bar{g} , g_m and σ_g , exceeded 10% time.

Tabl 2

f, MGz	Parametr	\bar{g}	σ_g	g_m	N_s
207	(1%,10%)	0,817	0,514	0,784	0,715
	(10%,10%)	0,221	0,679	0,600	0,471
543	(1%,10%)	0,308	0,028	0,802	0,875
	(10%,10%)	0,059	0,832	0,782	0,606

Evidently the correlation factor in this case considerably more, than in the first case. The most significant correlation was obtained for value A and g_m .

The same results were obtained for other path. Experiments has been conducted, in particular, on two paths in Arctic zone on frequency about 1 GHz for two summer month. The path over the Laptev See has a length 433 km. Another path over the land in Jakutia has length 357 km. Correlation factor for value A and g_m (1%, 10%) was 0,7–0,8, but correlation factor for value A and N_s (1%,10%) was less 0,5.

Thus it gets obvious that value g_m may be used for field strength prediction at least for small percentage of time. Therefore it is important to get statistical data of g_m for different climatic zones for some years.

The treatment of radio sound data has been conducted in NIIR for getting g_m statistical data for different regions of the former Sovjet Union. Distributions of g_m for various climatic regions may be differ very strongly. For example, the cumulative distributions have been offered on Fig. 2. for two regions.

- a – for Rjazan district (Central Russia)
- b – for Land of Franz Iosiv (Arctic)

The heights of lowest point, where maximum gradient g_m was observed, were determined by radio sound data.

The distributions of such heights are given on Fig. 3. for two points:

- a – for Rjazan district
- b – for the Land of Franz Iosiv.

It is Possible to see, that maximum gradients are observed usually not near earth level but on the heights about some hundred meters.

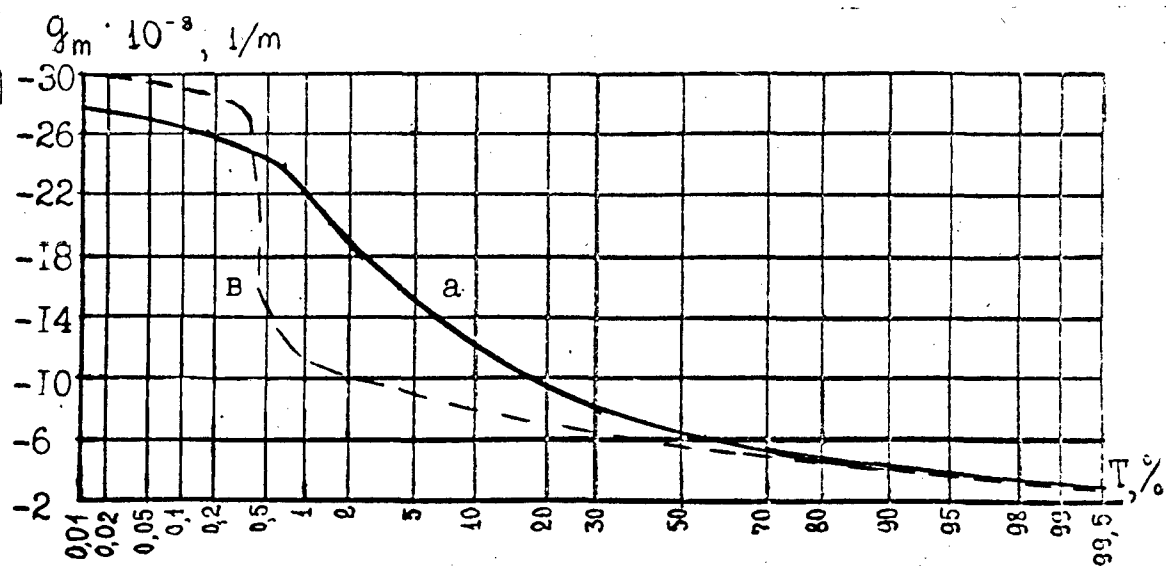


Figure 2: Maximum gradient g_m distribution for one year data
 a - Rjazan district
 b - Frans Iosif islands

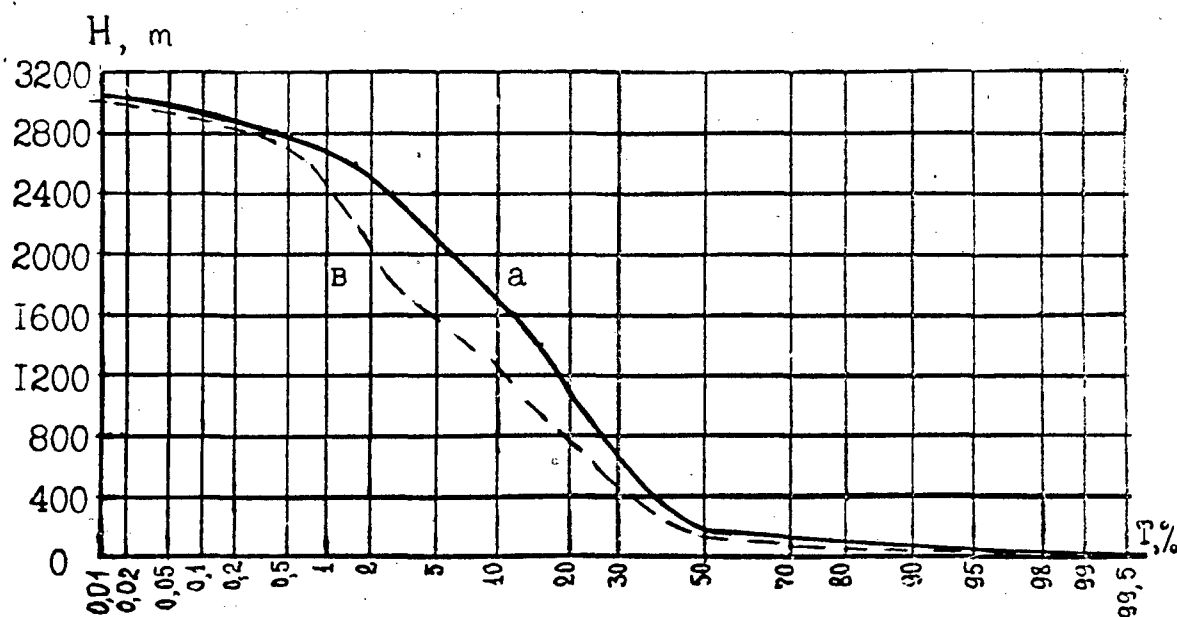


Figure 3: Hight of maximum gradient g layer distribution for one year data
 a - Rjazan district
 b - Franz Iosif islands

Session 7: Clear air II

ON ACOUSTIC REMOTE SENSING FOR CLIMATOLOGIC STUDY OF MICROWAVE PROPAGATION IN THE ATMOSPHERIC BOUNDARY LAYER

M. A. Kallistratova

IAP-RAS, Pyzhevskii 3, 109017 Moscow, Russian
Tel: +7-095-233-48-76, Fax: +7-095-233-16-52, E-mail: postmaster@iaph.msk.su

ABSTRACT

The method of acoustic sounding of the atmospheric boundary layer is described. The potential of the method for long-term continuous measurements of the parameters affecting the microwave propagation on line-of-sight links is discussed.

Keywords: acoustic sensing, microwave ducts, structure parameter of refractive index, atmospheric boundary layer.

1. INTRODUCTION

The atmospheric boundary layer (ABL), that occupies the lower several hundreds of meters above the underlying surface, is known to affect strongly the microwave communications. Within this layer high gradients of wave propagating velocity are observed which result in the waveguide or antiwaveguide effect. The ABL strong turbulization results in high frequency disturbance both phase and amplitude of a wave. Multilayered inversion structures initiate a multibeam propagation that results in deep fading.

The difficulties in estimating the ABL effect are engendered by a high spatial and time variability of this layer: strong seasonal and daily variations (who's range essentially depends on the orography) the variations that are due to synoptic processes are superimposed on. Therefore the fragmentary data on vertical profiles of the refractive index $n(z)$ and on the values of its structure parameter $C_n^2(z)$ are usually poorly representative.

Climatological data on the ABL structure obtained from long-term continuous measurements are necessary for estimating the quality and parameters of the routes of microwave links planned at a certain place and also in studying general regularities for generation of low-level ducts under different natural conditions.

The data regularly obtained by the Meteorological Service are seemingly best suited for this purpose. However, the meteorological standards (developed many years ago to meet the needs for a synoptical forecast and air navigation safety) are not adapted to determining the parameters of low-level ducts and of the ABL turbulence. The information gathered by radiosonde systems has poor vertical resolution; moreover, these measurements are taken only twice a day.

Most representative data on $n(z)$ can be obtained with radiometers and those of C_n^2

- from the measurements of microwave intensity fluctuations. However the data published are fragmentary since such measurements are too costly for continuous long-term study.

The remote acoustic sensing is the most available and cost-effective tool for climatological study of ABL. Design and applications of this method are carried out in the Institute of Atmospheric Physics, Russian Academy of Sciences since the early eighties (Ref. 1).

The potentials of the method in obtaining data on behavior of the ABL refractive index are discussed in the present paper.

2. ACOUSTIC SOUNDING METHOD

Acoustic sensing is based on a solid wave scattering from small-scale turbulent inhomogeneities of the atmosphere parameters (Ref. 2, 3).

The most popular monostatic sounding scheme draws on backscattering. The operation of an acoustic locator (sodar) is just similar to that of a clear air radar: a short impulse filled with carrier frequency is emitted by electro-acoustical reverser which then receives the scattered signal. Scattering is subject to the Bragg condition: backscattering depends on the turbulence spectrum component, whose spatial wave number $k_T = 2k_B$, where $k_B = 2\pi/\lambda_B$; λ_B is soundwave length. The carrier frequency of sodars is usually between 1 and 3 kHz, which correspond to the scales of turbulent irregularities $2\pi/k_T \sim 5-15$ cm.

Temperature irregularities make the major contribution to the backscattering cross section σ_{180} . For Kolmogorov's turbulent spectrum model which describes adequately enough the small-scale ABL turbulence

$$\sigma_{180} = 4 \cdot 10^{-3} k_B^{1/3} C_T^2 / \langle T \rangle^2, \quad (1)$$

where $\langle T \rangle$ is the mean temperature,

$$C_T^2 = \langle [T(\vec{r}_1) - T(\vec{r}_2)]^2 \rangle \cdot (r_1 - r_2)^{-2/3} \quad (2)$$

is the temperature structure parameter.

Basic difference between a sodar and a clear air radar are the following:

1. Speed of sound is more responsive to the changes in air temperature (by a factor of 10^3) than that of radiowave, which provides simplicity in design and lower operating cost of sodars.

2. Speed of sound is less than that of

radiowave propagation by a factor of 10^6 , which, first, simplifies considerably the processing of sodar signals and, second, results in a good spatial resolution (15-30 m) and a short dead zone of sodar.

3. Sound wave within the centimetre and decimetre ranges are readily absorbed by the air, therefore the sounding range is limited by a height of 500-1000 m.

These peculiarities of sodars make them particularly suitable for study of the ABL. Alongside with the quantitative measurements of the $C_T^2(z)$ (using Eq. 1) and velocity of wind due to Doppler effect this method make it possible to obtain facsimile records (echograms) of echo-signals on coordinates height - current time.

The echograms give a continuous time-space pattern of the structure of turbulent localities in the ABL. Numerous comparisons between such echograms and in situ measurements of the profiles of the ABL meteorological parameters allow one to determine the type of the atmospheric stratification and, in particular, to estimate the depth of surface and elevated inversion layers. Examples of such echograms obtained at different points under inversion conditions are given in Figs 1-6.

3. EMPLOYMENT OF THE METHOD TO DIAGNOSE THE CONDITIONS FOR MICROWAVE PROPAGATION

Different dependence of sound and microwave speeds on the air temperature and humidity seemingly prevent to use of sodar data to diagnose the microwave propagation conditions. In fact, a full expression for the effective (at backscattering) structure parameter of the sound refractive index C_S^2 has the following form (Ref. 4):

$$C_S^2 = 2.9 \cdot 10^{-6} C_T^2 - 0.4 R C_T C_q + 0.15 C_q^2 \quad (3)$$

and for radiowave (Ref. 5):

$$C_n^2 = 2 \cdot 10^{-12} C_T^2 - 2 \cdot 10^{-8} R C_T C_q + 5 \cdot 10^{-5} C_q^2 \quad (4)$$

Here q is the specific humidity; C_q^2 is the humidity structure parameter; $C_T^2 = (C_T^2)^{1/2}$; $C_q = (C_q^2)^{1/2}$; R is the correlation coefficient for temperature and humidity fluctuations; dimensional numerical coefficients are calculated for $T = 293$, $p = 1000$ mb.

As is seen from (3) and (4), a relative contribution of the values of C_q^2 and $R C_T C_q$ to C_n^2 is by one order of magnitude greater, than that to C_S^2 .

However, recall, that the first acoustical locators: Gilman's SODAR (Ref. 6) and McAllister's ECHOSOUNDER (Ref. 7) were devised just as a diagnostic tool for microwave line-of-sight links. Sodars observations performed over the past 10 years on several microwave links within the range between 7 and 11 GHz (Ref. 8-11) have demonstrated that sodars are a powerful instrument for the study of radiometeorology.

The matter is that over land, especially in winter, fluctuations of humidity are considerably less than those of temperature (Ref. 5):

$$C_q^2 \sim (10^{-5} - 10^{-6}) C_T^2;$$

$$R C_T C_q \sim (10^{-4} - 10^{-5}) C_T^2.$$

Moreover, there are similarity for the profiles of $C_T^2(z)$ and $C_q^2(z)$ (see Ref. 12). Therefore the height dependences $C_n^2(z)$ and $C_S^2(z)$ for such conditions are similar in character, and to estimate the behavior of C_n^2 the following relationship (Ref. 2) can be used:

$$C_n^2 \sim \left(\frac{79 \cdot p}{T^2}\right)^2 \cdot 10^{-12} C_T^2 \quad (5)$$

The support of this the estimation of C_n^2 , obtained from sodar data (Ref. 13) using equation (5) are in agreement by the order of magnitude with those, obtained from the measurements of microwave intensity fluctuations (Ref. 14, 15).

Elevated temperature inversion layers over the layer of convection (which provide moisture transport to the inversion basis) usually accompanied a heightened humidity. Surface radiation inversions, accompanied by dew or frost fall out, also result in increase of specific humidity with height. Therefore temperature and humidity profiles over land also demonstrate similarity and the temperature inversion corresponds to inversion of microwave propagation speed. So inversion layer, observed by sodar can be interpreted as microwave ducts.

But certainly, such estimations are too rough to be used for ocean, moist soil in summer and melting snow.

The results of the studies (Ref. 9, 10, 11) have show growth of a received signal (and, accordingly increase in the range of communication) at surface inversions, and also good correlation in the increase of microwave fadings and sodar observation of multilayered inversion structures.

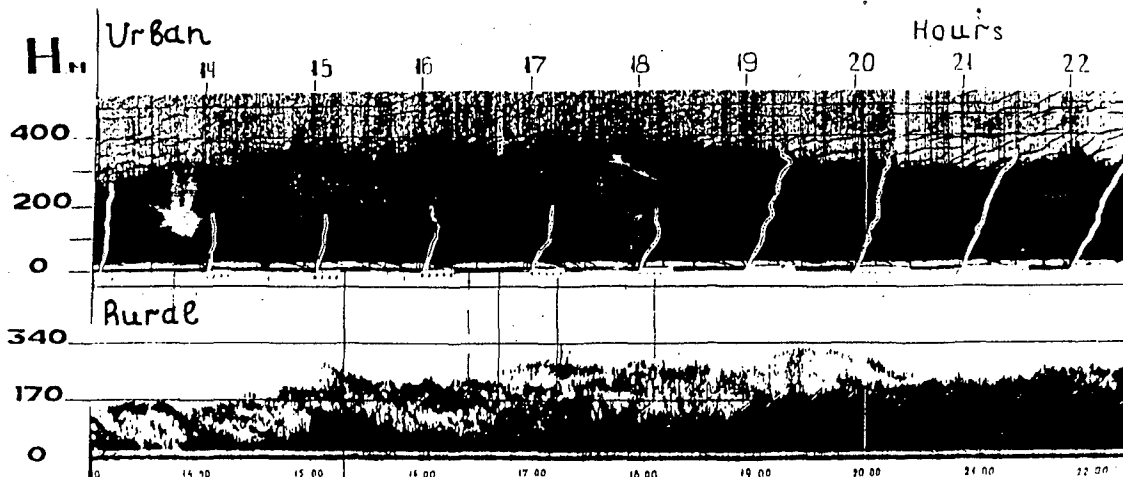


Figure 1. Sodar echograms, obtained simultaneously in two points: in the center of Moscow (top) and in the rural locality near Moscow (bottom). The difference in thickness and structure of the surface inversion layer in the two points is seen. The wind velocity profiles measured by sodar are plotted on the top record. February 01, 1991.

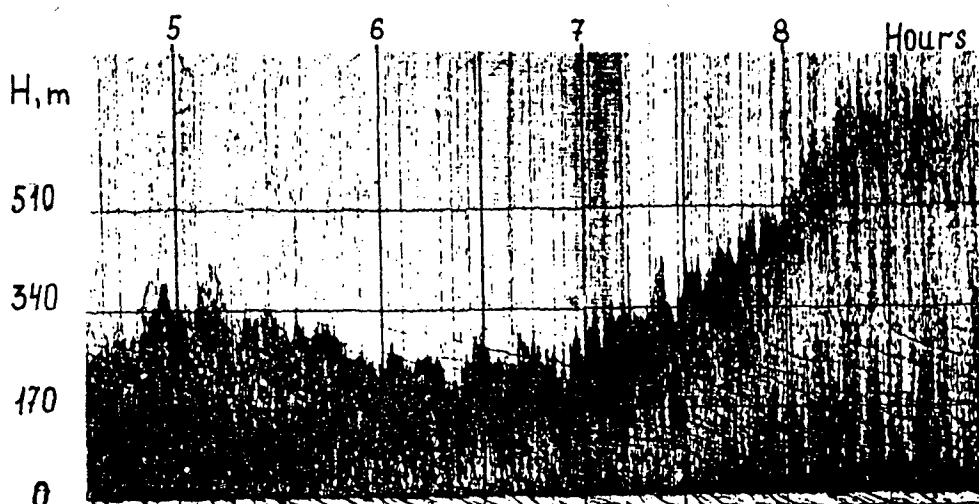


Figure 2. Same as in Fig. 1., obtained in the rural locality during the morning inversion-convection transition. A raise and dissipation of the nocturnal inversion layer above convection are seen. July 08, 1990.

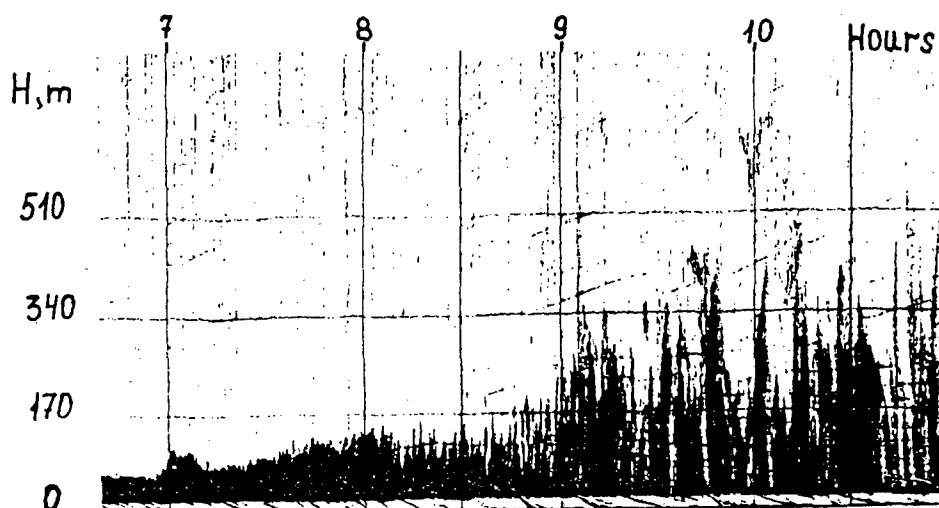


Figure 3. Same as in Fig. 2. But in this morning the inversion-convection transition was not accompanied by the rising inversion layer. July 10, 1990.

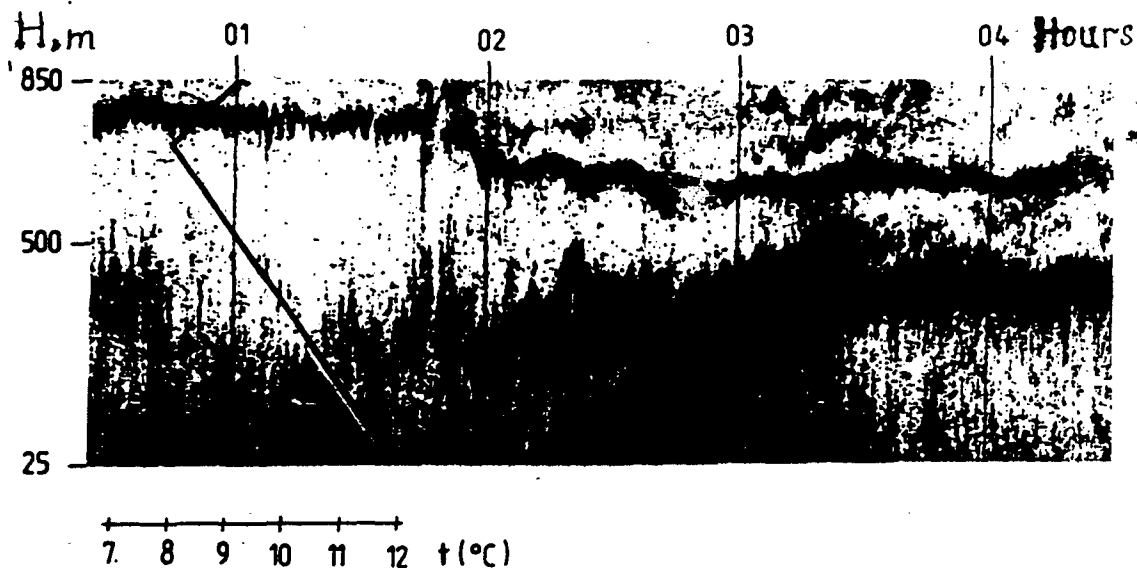


Figure 4. Sodar echogram, obtained under condition of multilayer inversion over Berlin. The temperature profile due to radiosonde is plotted on the record. May 05, 1985.

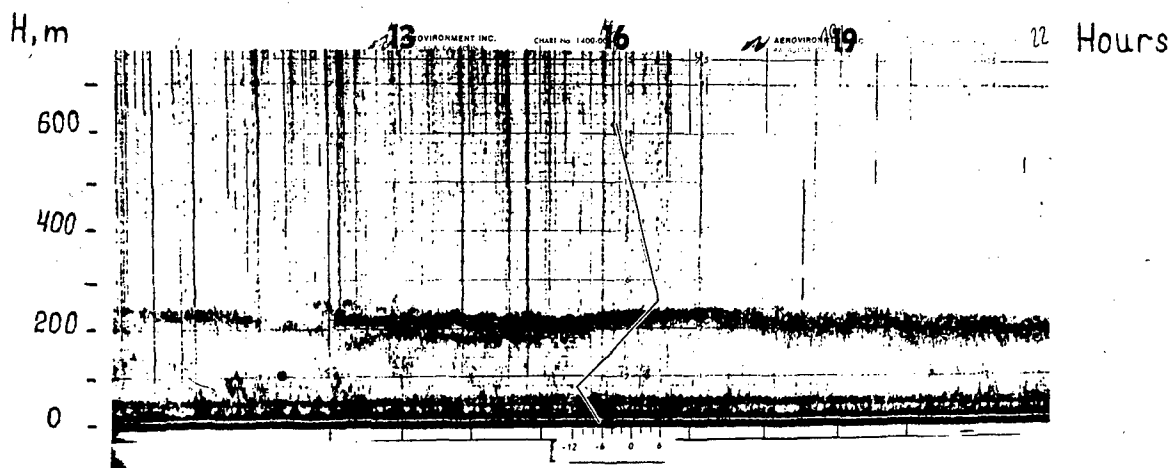


Figure 5. Same as in Fig. 4 under condition of elevated inversion, observed during 24 hours over the valley in the Grushny Gory (North-West of Czech Republic). March 20, 1986.

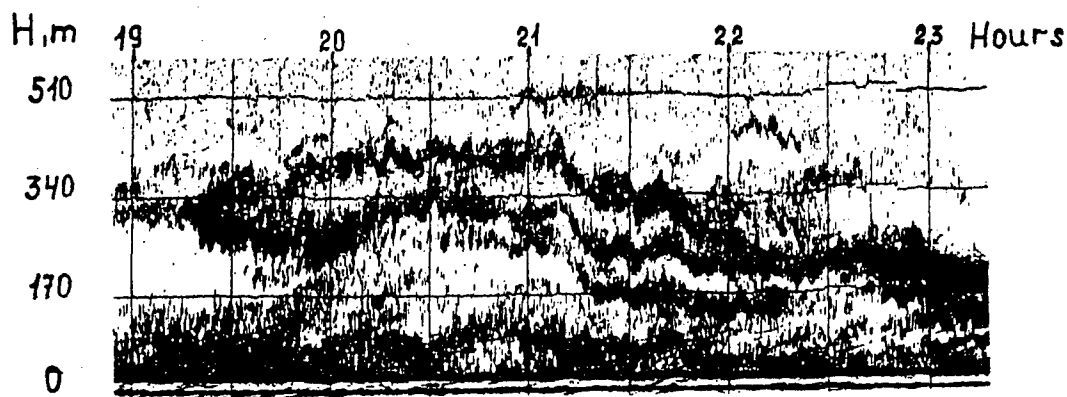


Figure 6. Sodar echogram, obtained in Alma-Ata (Kazakhstan), whose multilayer wavy structure is typical for this site. December 03, 1987.

The main advantages of sodars that they make it possible to take continuous round-the-year measurements under any weather conditions in the automatic mode with a minimum operating cost. Sodars are most suitable for obtaining climatological data, providing at the same time, the current, in real time-scale information about the changes of ABL structure. An example of a study of the behavior of the refractive index for a large city is given in (Ref. 13).

4. CONCLUSION

In spite of the fact that the relationship between the velocity of propagation and the air temperature and humidity is different for sound and microwave, sodars are particularly convenient for climatological studies of low-level microwave waveguides.

Sodars allow the statistical data to be obtained on daily and season variation in the occurrence of ducts, their thickness and duration. Moreover, using sodar observation it is possible to diagnose the inversion structures that encourage fadings, and also to estimate the values and time variations of the refractive index structure parameter.

It is a good reason for take using the sodar measurements to verify models prediction of microwave propagation for the particular line-of-sight links.

5. ACKNOWLEDGMENTS

This research was supported by the Russian Foundation for Fundamental Researches through Grant 93-05-08753 and also by International Scientific Foundation (project Es 2-3667-0925).

6. REFERENCES

1. Kallistratova M.A., Kar'ukin G.A. 1984, Sodars investigations of C_n^2 vertical profiles under inversion conditions, *Radiometeorology, Proc. of 6th all Union conference on radar meteorology*, Apr. 20-23 1982, Tallin, Hidrometeoizdat, Leningrad, pp. 341-344.
2. V.I. Tatarskii 1980, *Wave Propagation in a Turbulent Medium*, Dover Publication, Inc. New York, 285 pp.
3. Kallistratova M.A. 1994, Acoustic and radio-acoustic remote sensing in C.I.S (former USSR) - current status, *Int. J. Remote Sensing*, 15, 2, pp. 251-256.
4. Ostashev V.E. 1992, *Sound Propagation in Moving Media*, Nauka, Moscow, 206 p.
5. Kallistratova M.A., Kon A.I. 1985, *Radioacoustical Sensing of the Atmosphere*, Nauka, Moscow, 197 p.
6. Gilman G. W. et al. 1946, Reflection of sound signals in the troposphere, *J. Acoustic Soc. of America*, 18, pp. 274-283.

7. McAllister L. G. 1968, Acoustic sounding of the lower atmosphere, *J. Atmos. Terr. Phys.*, 30, pp. 1439-1440.

8. Gera B.S. and Sargar S.K. 1980, Sodars as an indicator of microwave propagation characteristics, *Indian J. Radio & Space Phys.*, 9, pp. 86-96.

9. Singal S. P. et al. 1981, Application of sodar derived boundary layer information in microwave communication, *J. Scientific Industrial Res.*, 40, pp. 765-777.

10. Rao D.N. et al. 1989, Sodars echograms and correlation with microwave propagation characteristics in hilly terrain, *Proc. ICAR, IEE (U.K.)*, Pub. No. 248, pp. 227-230.

11. Ghosh A.B. et al. 1990, Estimated values of various propagation parameters for a 11.5 GHz line-of-sight link using sodar structures and Kyttoon measurements, *Proc. of the 5th Int. Symp. on Acoustic Remote Sensing*, Feb. 6-9 1990, Tata McGraw-Hill PCL, pp. 526-530.

12. Monin A.S. and Yaglom A.M. 1971 *Statistical Fluid Mechanics*, vol.2, MIT Press, Cambridge, 769 p.

13. Bedulin A.N. et al. Climatologic study of microwave-active turbulence behavior over a big city by sodar, *This collection*, pp. - .

14. Zrazhevskii A. Yu. et al. 1984, An experimental investigation of refractive index structure parameter for millimeter range of wave in the atmosphere, *Radiometeorology, Proc. of 6th all Union conference on radar meteorology*, Apr. 20-23 1982, Tallin, Hidrometeoizdat, Leningrad, pp. 232-235.

15. Golunov V.A. et al. 1984, Results of measurement of refractive index structure parameter for 8-mm wave in the atmosphere, *Ibid.*, pp. 266-268.

MAPPING OF ZONES IN WHICH CLEAR-AIR FADING AND INTERFERENCE MAY OCCUR

Dr. Gerda Fengler (posthumous)
Mozartstr. 31, D-78194 Immendingen

ABSTRACT

Evaluation of three years of propagation measurements under special consideration of the meteorological situations indicated that the prevailing causes of fading and interference on line-of-sight paths are ground inversions. In order to forecast their occurrence, routinely gathered data on visibility was applied for the mapping of zones in which clear-air fading and interference may occur.

Keywords: mapping, prediction, ground inversions, visibility, fading

1. INTRODUCTION

The prediction of severe fading and interference, i.e. of anomalous propagation, for line-of-sight (LOS) paths in clear-air situations is a subject of current interest and was an obvious starting point for the COST 210 research program (Ref. 1, 2). The causes of fading and interference are meteorological conditions. Often, certain physical features along the path play an additional role depending on season and time of day (Ref. 1, 3). Therefore, meteorological forecasts and a knowledge of the terrain along a given path can be employed to predict anomalous propagation conditions. This is especially useful for areas in which propagation measurements have never been carried out before.

2. CAUSES OF ANOMALOUS PROPAGATION

On terrestrial paths anomalous propagation is characterized by fading depths of over 20 db up to over 50 db. The length of fading periods ranges from some minutes to 1 or 2 hours. The average field strength is enhanced by between 10 and 40 db, which leads to overshoots and to interference with other transmission links.

Anomalous clear-air propagation conditions are caused by widespread discontinuities or inhomogeneities in the lower atmosphere, that is by free and ground inversions and boundaries between two different masses of air. They appear as significant changes in the lapse rate of the height-profile of refractivity (N-profile).

Free inversions are mainly caused by subsidence, through the slow descent of air in areas of high-pressure (anticyclones), as long as wind speeds are low enough so as to prevent turbulences from arising that may disturb the stable stratification.

Ground inversions are formed over land towards evening. As the radiation from the sun decreases in the afternoon, the ground gets cooler and the air close to the ground emits more energy than it can absorb and cools off. This results in a layer of cool air near the ground bordered to the top by warmer air. This ground inversion continues to build up after sunset to a height of several hundred meters. As the ground heats up after sunrise, it changes to a free inversion before dissolving altogether. Necessary for the occurrence of ground inversions are calm and nearly cloudless nights as well as land with low heat-retaining capability.

Owing to the *evaporation* from the surface of the ocean, there is a considerable concentration of water vapour in the air directly above it. This leads to the formation of an evaporation duct (Ref. 4, 5). Over river beds, shallow water and moist soil, the effects of evaporation amplify ground inversions. *Advection* happens in the general circulation as well as locally in mountain and coastal areas, if a new air mass approaches the region under consideration and an overflow or underflow of the air mass is present.

3. ORIGINAL RESULTS OF OBSERVATIONS

The following paper is based on field strength values and fading characteristics that were observed during a period of three years, among others, along three overland transmission paths here called A, B and C. Radio-sonde measurements were carried out simultaneously with the above mentioned observations. The 2192 N-profiles that were gained through evaluation of the radio-sonde measurements were correlated case by case to the recorded field strength of the transmission paths and the other way around. In this way, the prevailing propagation mechanism could be identified for each case (Refs. 6, 7, 8, 9). The conclusions drawn from these measurements are not limited to the considered transmission paths. They have also been gained for other radio links (Ref. 10). Path A was a line-of-sight (LOS) link of 115 km length with a

terrain incursion. Paths B and C were transhorizon paths over distances of 202 km and 323 km respectively, with radiooptical horizons ($k = 3/4$) at 118 km and 129 km, respectively.

The analysis of the radio-sonde ascents yielded, among others, the following results. In 76,3 % of all cases considered, one or more inversions were present up at an altitude of 2000 m. There was no inversion in 23,7 % of all cases. In 26,0 % of all considered events, one of the inversions or the only one was a ground inversion (Ref. 8).

Correlation of field strength values with the altitude of the inversions showed, that for each path there is an *effective height intervall* for which, if the lower boundry of the inversion lies within it, the signal strength is several db higher than for inversions with the same gradient of refractivity at smaller or greater altitudes. In regard to ground inversions, the signal strength grows with increasing thickness of the inversion. Thin ground inversions are sufficient for an increase of the signal strength level for short paths, but longer paths require thicker ground inversions. A weaker inversion (smaller gradient of N) has to be thicker in order to be able to cause a signal strength equal to that of a stronger inversion (Ref. 9).

Anomalous propagation in the form of *fading* was observed as follows:

path A: 26,0 (36,5) % of time in winter(summer)

path B: 5,8 (6,7) % of time in winter(summer)

path C: 22,9 (5,4) % of time in winter(summer).

The percentage of occurrence of fading matches the one of ground inversions in the case of LOS path A. In the case of the transhorizon paths B and C the two percentages of occurrences are correlated. Ground inversions have a dominant influence on LOS paths and a considerable one on transhorizon paths, if the these inversions are thick and strong enough. Therefore, the forecast of ground inversions can be used to predict anomalous propagation conditions, in particular for LOS paths.

4. THE INFLUENCE OF TEMPERATURE AND HUMIDITY

The refractivity N is a function of pressure, temperature and water vapour pressure of the air (Ref. 1, 3). From this follows, that the influence of free and ground inversions on radio paths is only significant, if the average temperature of the inversion is greater than 20 °C and its humidity is high. This corresponds with the observation, that severe

fading is a warm weather phenomenon that often occurs in combination with fog. Fog occurs at a relative humidity of 100%. Ground inversions though, already form at relative humidities below 100 % and also occur without the presence of fog. The identification of zones where ground inversions occur requires data on temperature and humidity and their diurnal variations. This information is not always readily available.

5. VISIBILITY

Visibility is affected by the size of particles in the atmosphere. As long as humidity is high, the particles pick up water and increase in size, reducing visibility. A profound reduction of visibility occurs with the formation of haze, that is, depending on the type of particles present, if the relative humidity exceeds 70%. Further reduction of visibility occurs as mist develops at levels of relative humidity above 80%. In fog, that is if the relative humidity reaches 100%, visibility is reduced to under 1 km (Ref. 11).

Generally, visibility can be divided into three categories:

bad	visibility (fog, below 800 m)
medium	visibility (mist, haze)
good	visibility (above 8 km).

Every synoptic, aeronautical and climate station performs visibility measurements at least three times a day.

A record for each of the observation times, of the number of days per month with bad or medium visibility indicates the diurnal variations and the frequency of occurrence of fog as well as of mist and haze during this month. The diurnal variation shows the variation of temperature during the course of the day and indicates the formation and decomposition of ground inversions. In conclusion, from the number of days per month with bad and medium visibility and its diurnal variation, the frequency of formation of ground inversions, i.e. of anomalous propagation conditions, can be determined. For stations at high altitudes, the same conclusions can be drawn for elevated inversions because their altitude varies with the daytime. Bad and medium visibility that does not correspond to diurnal variation indicates advection of humid air. Using the monthly evaluations, the seasons in which anomalous propagation conditions are likely to occur can be identified for each station and its represented area. The average temperature of each month has to be considered.

Each station represents a certain area and has its own characteristic pattern of visibility which can be assessed with a grade. The grade indicates the probability of the occurrence of fading and interference for the represented area and serves as the base for the *mapping*. The grades can be condensed into several categories, in this case eight categories, indicating the probability of very frequent, frequent and rare occurrence and the season of occurrence of clear-air LOS fading and interference. There are *limitations* to the determination of fading and interference zones. The dominant presence of sea fog, produced by cold air above warm water, accounts for severe fading in coastal areas. The evaporation layers of lakes drift inland, leading to an increase of anomalous propagation in those areas. Also, the evaporation ducts over sea must be taken into account. As well, an exact comparison of the percentage of time in which anomalous propagation occurs to the percentage of time in which ground inversions occur has not yet been carried out, but has been estimated. Also, the boundaries of the represented area of the stations must be defined.

6. APPLICATION TO THE REGIONS OF CANADA

The mapping of zones in which clear-air fading and interference may occur was performed for Canada. The mapping was based on summaries of observations of pressure, temperature, humidity, cloud formation, visibility and wind published monthly for 262 stations (Ref. 12). These stations were located in the provinces and territories: British Columbia (46), Alberta (23), Saskatchewan (17), Manitoba (18), Ontario (37), Quebec (35), Newfoundland (19), New Brunswick (6), Nova Scotia (9), Prince Edward Island (2), Yukon Territory (8) and Northwest Territories (42). For each of the four observation times (midnight, morning, noon, evening) and for each station, the number of days per month with bad and medium visibility was recorded. The average number (of days with bad or medium visibility) was determined for each month, station and observation time for a period of two years. The resulting pattern over the year was graded for each station: for stations at lower altitudes in respect to the occurrence of ground inversions, for stations at high altitudes in respect to the occurrence of elevated inversions. The grades read as follow:

Grade	seasons of events	Days per month
A1	Sp,Su,F	1-3
A2	Sp,Su,F	4-5
A3	Sp,Su,F	5-9
A4	Sp,Su,F	10-14
A5	Sp,Su,F	over 14
B1	Sp,Su,F,W	1-3
B2	Sp,Su,F,W	4-5
B3	Sp,Su,F,W	6-9
B4	Sp,Su,F,W	over 9
C1	(Sp),F	1-3
C2	(Sp),F	4-5
D1	Sp,F,W	1-3
D2	Sp,F,W	4-5
D3	Sp,F,W	6-9
E	no events	
F	Sp,F	1-3
H1	Midsummer	1-3
H2	Midsummer	4-5
AC1	Sp,(Su),F	1-3
AC2	Sp,(Su),F	4-5
AF	Su	1-3
AH	Su*	1-3
BD1	Sp,(Su),F,W	1-3
BD2	Sp,(Su),F,W	4-5
BC	F,(Sp,Su,W)	1-3

Sp: Spring Su: Summer
F: Fall W: Winter
* T above 22° C

The grading of the stations in British Columbia reads as follows:

place	lattd.	longtd.	height ft	grade
Abbotsford	49 01	122 22	198	B3
Alert Bay	50 35	126 56	169	B1
Alta Lake	50 09	122 57	2190	B2
Blue River	52 07	119 18	2240	A3
Bull Harbour	50 55	127 57	45	B3
Burns Lake	54 14	125 46	2308	C1
Cape St. James	51 56	131 01	292	B3
Cape Scott	50 47	128 26	239	B3
Castlegar	49 18	117 38	1619	C2
Comox	49 43	124 54	75	D2
Cranbrook	49 36	115 47	3045	C1
Dawson Creek	55 44	120 11	2164	E
Dease Lake	58 25	130 00	2678	C
Estevan Point	49 23	126 32	20	B4
Ethalda Bay	53 03	129 41	20	B3
Fort Nelson	58 50	122 35	1230	A1
Fort St. John	56 14	120 44	2275	A1

Germansen Landing	55 47	124 42	2450	A1
Hope	49 23	121 26	152	B3
Kamloops	50 42	120 25	1133	C1
Langara	54 15	133 03	134	B3
Liard River	59 27	126 09	1523	E
Lytton	50 14	121 35	838	C1
Mackenzie	55 18	123 08	2394	C2
McInnes Island	52 16	128 43	75	B3
Merry Island	49 28	123 54	190	D1
Nanaimo	49 03	123 52	104	B2
Penticton	49 28	119 34	1211	D1
Port Albernt	49 16	124 50	10	D3
Port Hardy	50 41	127 22	47	B2
Prince George	53 53	122 40	2218	A2
Prince Rupert	54 18	130 26	110	B3
Princeton	49 28	120 31	2283	C1
Puntzi Mountain	52 07	124 05	2990	A1
Quesnel	53 04	122 31	1787	A2
Revelstoke	50 58	118 11	1467	C2
Sandspit	53 15	131 49	25	BC
Smithers	54 49	127 11	1718	C1
Spring Island	50 00	127 25	37	B4
Terrace	54 28	128 35	719	C3
Tofino	49 05	125 46	80	B4
Vancouver Interntl.	49 11	123 10	16	BC3
Victoria Gonzales	48 25	123 19	228	BD1
Victoria Intern.	48 39	123 26	67	BD2
Vict. Marine Radio	48 22	123 45	104	BD2
Williams Lake	52 11	122 04	3088	A2

The grading of the stations in Alberta reads as follows:

place	lattd.	longtd.	height ft.	grade
Banff	51 11	115 34	4583	C2
Brooks	50 33	111 51	2487	C1
Calgary Internat.	51 06	114 01	3540	C3
Cold Lake	54 25	110 17	1784	A2
Coronation	52 06	111 27	2618	A2
Edmonton Industr.	53 34	113 31	2219	AC
Edmonton Intern.	53 19	113 35	2358	AC2
Edmonton Nanao	53 40	113 28	2293	AC2
Edson	53 35	115 27	3035	Fh
Footner Lake	58 37	117 10	1104	Fh
Fort Chipewyan	58 46	111 07	749	Fh
Fort McMurray	56 39	111 13	1213	AF
Grande Prairie	55 11	118 53	2190	Fh
Jaspers	52 53	111 04	3480	C2
Lethbridge	49 38	112 48	3018	C2
Medicine Hat	50 01	110 43	2365	C2
Peace River	56 14	117 26	1866	F1
Pincher Creek	49 30	113 57	3790	F1
Reed Deer	52 11	113 54	2965	C2

Rocky Mtn House	52 23	114 55	3330	AF
Slave Lake	55 18	114 47	1915	F
Vermilion	53 21	110 50	2037	C1
Whitecourt	54 06	115 40	2430	A2

h: Predominant in Fall

The grading of the stations in Ontario reads as follows:

place	lattd.	longtd.	height ft.	grade
Armstrong	50 17	88 54	1065	A3
Atikokan	48 45	91 37	1289	A2
Chapleau	47 50	83 26	1405	A3
Dryden	49 50	92 45	1350	A2
Earlton	47 42	79 51	805	A3
Geraldton	49 42	86 54	1085	A3
Goderich	43 40	81 42	703	A5
Gore Bay	45 53	82 34	624	A4
Hamilton	43 10	79 56	808	A4
Kapuskasing	49 25	82 28	752	A3
Kenora	49 48	04 22	1345	A2
Kingston	44 13	76 36	295	A3
Landsdowne House	52 14	87 53	840	A2
London	43 02	81 09	912	A5
Mosinee	51 16	80 39	34	(A2)
Mount Forest	43 59	80 45	1360	A4
Muskoka	44 58	79 18	926	A4
North Bay	46 22	79 25	1210	A4
Ottawa int. Airt.	45 19	75 40	413	A4
Peterborough	44 14	78 21	627	A4
Red Lake	51 04	93 49	1245	A2
Sarnia	43 00	82 18	595	A5
Sault Ste Marie	46 29	84 30	620	A4
Simcoe	42 51	80 16	789	A5
Sioux Lookout	50 07	91 54	1227	A3
Sudbury	46 37	80 48	1121	A3
Thunder Bay	48 22	89 19	644	A3
Tiimens	48 34	81 22	965	A3
Toronto Downsview	43 45	79 29	650	A4
Toronto Int. Arprt.	43 41	79 38	578	A3
Toronto Island	43 38	79 24	267	A3
Trenton	44 07	77 32	266	A3
Trout Lake	53 50	89 52	675	A2
Waterloo Wellingt.	43 27	80 23	1027	A4
White River	48 36	85 17	1243	A4
Warton	44 45	81 06	720	A4
Windsor	42 16	82 58	637	A5

The grading was performed for the stations in the other provinces as well. The corresponding maps are shown in Figures 1 to 3. Here the grades were condensed into eight categories.

Cate- gory	Probability of anomalous propagation	Seasons of occurrence
8	very frequent	Sp, Su, Fall, (Wi)*
7	frequent	all year
6	frequent	Sp, Su, Fall
5	frequent	Su
4**	frequent	Sp, Fall
3	rare	Sp, Su, Fall
2	rare	Su
1	rare	Sp, Fall

Sp :Spring; Su: Summer; Wi: Winter

* Pacific region only

** for mountain-to-mountain paths

Percentage of time of occurrence during the seasons:

Very frequent : more than 10 %
Frequent : 1 to 10 %
Rare : less than 1 %

7. CONCLUSIONS

An analysis of the maps of zones in which fading and interference may occur leads to the following results. The coastal and lake areas are the zones most afflicted. Due to the general west wind drift, the western coasts are influenced all year round, while the eastern coastal areas and the areas around large lakes are not influenced in winter. For the same reason, the effects on the eastern shore of smaller lakes is usually greater than the effect on the western shore. The average temperature plays an important role. The further north a region is, the more the influence is reduced to summer. The occurrence of fading and interference in different areas obviously depends on the season. In mountain areas, the impact of large river beds is evident.

8. REFERENCES

1. COST 210 Influence of the atmosphere on interference between radio communications systems at frequencies above 1 GHz.
2. Lane, J.A., Prediction of interference levels and coordination distances for frequencies above 1 GHz, *Radio Waves* edited by MPM Hall and LW Barclay, 1989 Peter Peregrinus Ltd, pp.231-245
3. Rotheraram, S., Clear air aspects of the troposphere and their effects on propagation mechanisms from VHF to millimetre waves, *ibid.*, pp.150-172
4. Jeske, H., Die Ausbreitung elektromagnetischer Wellen im cm- bis m-Band unter besonderer Berücksichtigung der meteorologischen Bedingungen in der maritimen Grenzschicht der Atmosphäre, *Hamburger Geophysikalische Einzelschriften* 6, 1965
5. Früchtenicht, H.W., Tagesgang und Gezeitenabhängigkeit der Empfangsfeldstärke auf Richtfunkstrecken in der Deutschen Bucht, *Institut für Radiometeorologie, Universität Hamburg*, Report 13, 1968
6. Fengler, G., Investigations of electromagnetic wave propagation over land in the range of 500 MHz with particular consideration of meteorological conditions (in German), *ibid.*, Report 8, 1964
7. Fengler C. and Fengler G., V.H.F. and u.h.f. field strength variations corresponding to river beds, *Proc.IEE* 122 (1975), pp.44-47
8. Fengler, G., Dependence of 500 MHz field strength values and fading frequencies on meteorological parameters, *1964 World Conf. on Radio Meteorology, Boulder, Col.*, pp.84-87
9. Fengler, G., The influence of inversions on uhv-propagation over land, *idib.*, pp.80-83
10. Kuehn, U., Longterm measurements of tropospheric overshoots in Germany, *Rundfunktechnische Mitteilungen* 36 (1992), pp.73-88
11. Moeller, F., *Einführung in die Meteorologie*, Bibliographisches Institut AG, Mannheim 1973, p.159
12. *Monthly Record meteorological observations in Canada*, Environment Canada, Downsview, Ontario, Jan. 1972 - Dec. 1973

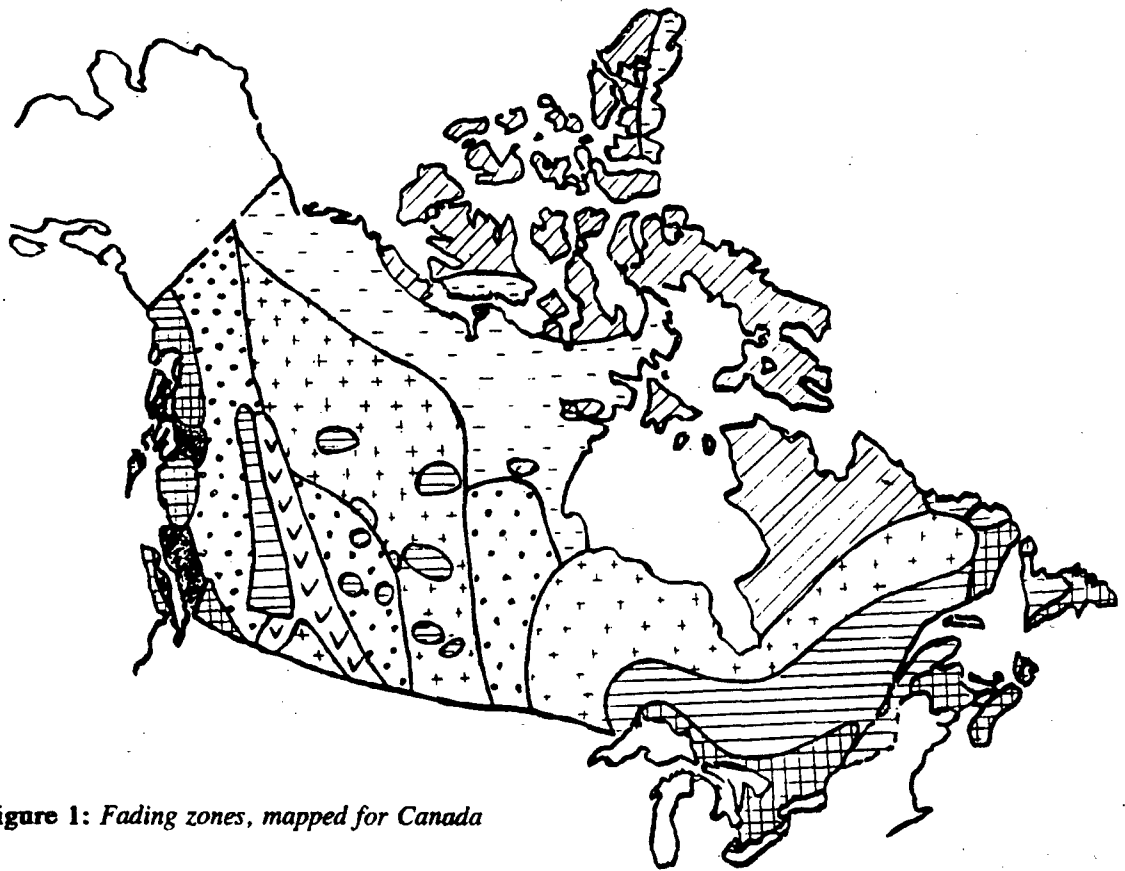


Figure 1: Fading zones, mapped for Canada

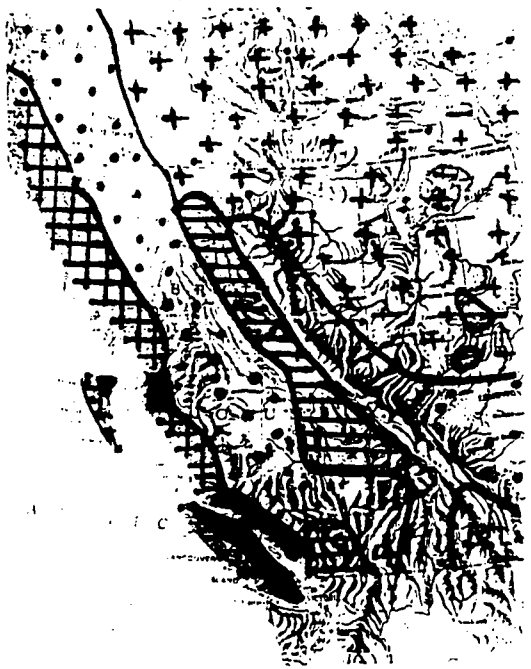


Figure 2: Enlarged section of Fig. 1: British Columbia

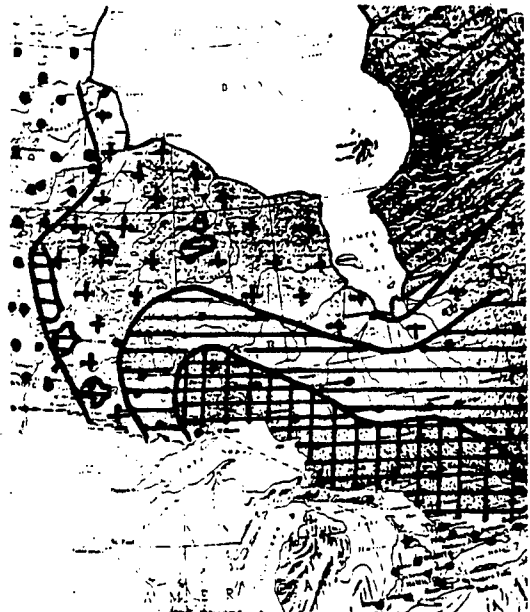
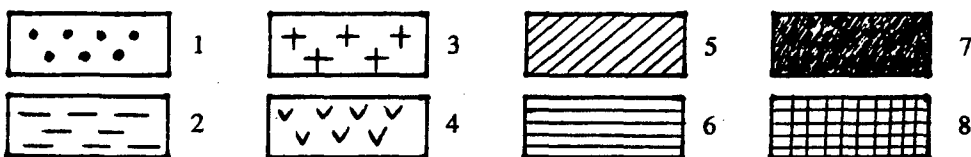


Figure 3: Enlarged section of Fig. 1: Ontario

Legend : Categories



CLIMATIC FACTOR IN STATISTICS OF THE FADE DURATION ON LINE-OF-SIGHT PATHS

L.V. Nadenenko

NIIR, 16, Kazakova Str., Moscow, 103064, Russia
Tel.: (095) 267-06-47, Fax: (095) 261-00-90, Telex: 411601 Rubin

ABSTRACT

This report gives the principal conformity to natural laws in statistics of fade duration, observed in different climatic regions of Russia and the former USSR. The results are necessary for development of the modern prediction methods of the error performance for digital radio-relay links.

1. INTRODUCTION

Radio - wave propagation conditions have the significant impact on the operation of line - of - sight digital radio-relay links. Effects of multipath fading which may distort and attenuate received signals are the dominant factor on the error performance of digital radio-relay systems operating at the frequencies below about 10 GHz. Also these effects can bring in the essential contribution to the performance of unavailability of radio-relay line.

In order to estimate the performance of digital radio-relay systems it is necessary to know not only the total outage time in the worst month as it was in analogue systems. Error performance objectives for real digital radio-relay links apply when the system is considered to be available in accordance CCIR Recommendations 557 and 634. This state includes periods of high bit error ratio which persist for duration less than ten consecutive seconds. Periods of high bit error ratio which persist for ten consecutive seconds duration or longer are taken into account of unavailability of radio-relay system.

So in accordance above mentioned in order to develop modern prediction methods, which may be used for guidance in radio link planning, it is necessary to know statistics of number and duration of fade dynamics in different climatic regions. In this report the generalized statistics and regularity concerning duration of fades are given.

2. RESULTS OF THE STUDIES

The studies were carried out in the frequency band 3.7-8 GHz on 26 different path with hop length from 35 to 63 km in the various climatic regions of the Union of Independent States (UIS) or the former USSR: the central, north-west and south regions of the European territory of Russia, Baltic coast, Ukraine, Byelorussia, the Crimea and Caucasian Black sea coast.

The investigation were performed during 1965-1989 for a total test period for statistical purposes of 30000 hours.

The studies showed that the results generally agree with the following points:

2.1. The fade duration depends on different factors as a frequency, a depth of fading, hop parameters, topographic and climatic conditions. The mean value of fade duration due to multipath mechanism decreases with the increase of path length and path clearance.

2.2. For a depth of fading $A \geq 20$ dB in an average worst month the fade duration is distributed according to a log-normal law without dependence on geographical location of paths. This result agrees with data of CCIR Report 338.

2.3. Parameters of the statistical distribution of the fade duration mean value $\bar{\tau}$ and median value τ_m joined by mean of the following expression

$$\bar{\tau} = \tau_m e^{2.65 \cdot 10^{-2} \sigma_r^2 [dB]}, \quad (1)$$

where σ_r – standard deviation.

On the basis of the measurements for single reception

$$\tau_m = C_m (10^{-A/10})^{0.5} \cdot \left(\frac{f}{3.7}\right)^{-0.5}, \quad [s] \quad (2)$$

where A, dB ; f, GHz.

C_m – empiric factor for climate and terrain effects on climate. Dependence value C_m at the frequency 3.7 GHz on the parameter ψ_r is given on Fig.1, where test results with number paths are shown (these numbers don't correspond to path numbers in the data bank of the former USSR).

Compare this result with CCIR 338 Report . From equation (2) $\alpha_2 = 0.5$, $\beta_2 = -0.5$. Another administrations (France, Denmark ,United States, Switzerland) gave $\alpha_2 = (0.33 - 0.5)$, $\beta_2 = -(0.5 - 1)$.

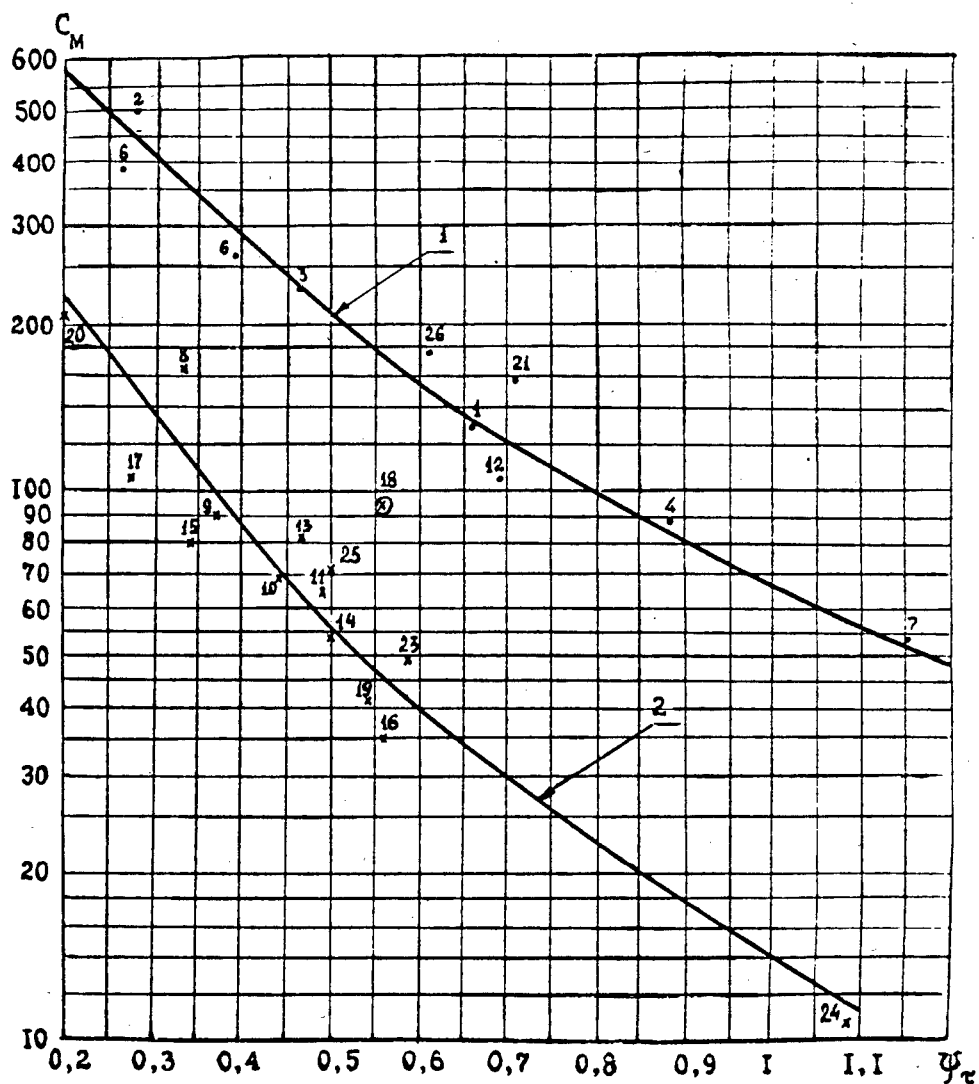


Figure1: C_m as a function of ψ_r for land and coastal or humidity regions

On Fig.1 the curve 1 represents the values C_m for land regions in terrain of average smoothness.

$$C_m = \frac{1}{0,001 + 0,0141 \psi_r^{1,85}} \quad (3)$$

The curve 2 represents the values C_m for maritime, coastal and also regions near water - reservoirs.

$$C_m = \frac{1}{0,0022 + 0,069 \psi_r^{2,15}} \quad (4)$$

The generalized parameter ψ_r is defined by the formula:

$$\psi_r = d^2 \cdot P(\bar{g}) \cdot 10^{-4}, \quad (5)$$

where:

d - path length, km ;

$P(\bar{g})$ - relative clearance on the path for average refraction

$$P(\bar{g}) = H(\bar{g}) / H_0, \quad (6)$$

$H(\bar{g})$ - hop clearance for mean effective gradient in the permittivity of the air \bar{g} on the area crossed by a path. On the territory of the UIS in summer months variations $\bar{g} = -(6-13) \cdot 10^{-8} 1/m$ or factor of the refraction $k_e = 1.23 - 1.7$.

H_0 - clearance on the path conforming to free space field strength. It is equal to at least 60 % of the radius of the first Fresnel zone.

The mean error in the prediction with using of the equation (3) $\bar{E} = -1.75\%$ and standard deviation of errors $\sigma_E = 13.4\%$. The accuracy of the equation (4): $\bar{E} = 4.4\%$, $\sigma_E = 22\%$.

Particular cases:

1) If the maritime or coastal paths have large difference of antenna heights Δh above sea level, the median fade duration corresponds approximately to the value τ_m for land paths (for example, Fig.1 the path 26, where $\Delta h = 300$ m). Probably this is due to additional specific, fairly slow signal attenuations, defined by the propagation wave through tropospheric ducts and layers.

2) If the wooded paths pass over marshes, in hot summer months the total statistics of the fade depth is the same as on coastal paths, but number of fades are in two times less and median duration of fades is in two times more than on coastal paths (for example, Fig.1 the path 18).

It should be noted that the basis of the above prediction method of the fade duration is the result of studies on paths in wide range of latitude of the territory of the former USSR: from $59,2^\circ$ to $42,9^\circ$ N.L. For example, for curve 2 on Fig.1 these paths pass on Baltic coast (13,14,15,16), above Cimlanskoje water reservoir (10), in region of Azov sea (9,22), on the Crimea and the Caucasus coast of the Black sea (24,25). Taking into account the sufficiently high accuracy of the approximation of the experimental data it would seem reasonable to assume that in the worst months there is no dependence of the median fade duration from latitude of the path location and the geoclimatic factor. Distinction may be in number of

such months in different climatic regions. So on Baltic coast there are 1–2 months and on south paths there are 2–3 or seldom 4 months.

2.4. The important parameter of the distribution of the fade duration is the standard deviation σ_r . It decreases with fade depth A. On the basis of average experimental data at the frequency 3.7 GHz for single reception dependence from A is given in Table:

A, dB	20	25	30	35	40
σ_r , dB	6,5	5,8	5,2	4,9	4,7

Compare this result with the data of CCIR 338 Report, where $\sigma_r = (6.9 - 4.3)$ dB for $A = (10 - 50)$ dB, but if $A = 30$ dB, $\sigma_r = 5.6$ dB.

Frequency dependence σ_r was defined by means of the simultaneous statistical measurements at the frequencies 3.7, 6 and 8 GHz. The results showed that the data in Table also may be used on overland paths at the frequency 6 and 8 GHz. For paths over large bodies of water (maritime, coastal regions and so on) standard deviation increases somewhat with frequency. This increase (average value) approximately is equal

$$\Delta\sigma_r = 5 \cdot \lg \frac{f}{3.7}, \quad (7)$$

where f, GHz.

Taking the above mentioned parameters of the log-normal distribution of the fade duration into account, for each hop of digital radio-relay link it is possible to calculate part of the outage time in an average worst month, caused by multipath fading with duration $\tau < 10$ s and $\tau \geq 10$ s. The first result defines error performance while the second result is taken into account of unavailability digital of radio-relay systems. In these cases for space diversity it is possible to apply the same improvement factor. Example of the calculation $P(\text{BER} \geq 10^{-3})$ for single reception at the frequency 6 GHz based on the prediction method of Russia are reproduced in Fig.2.

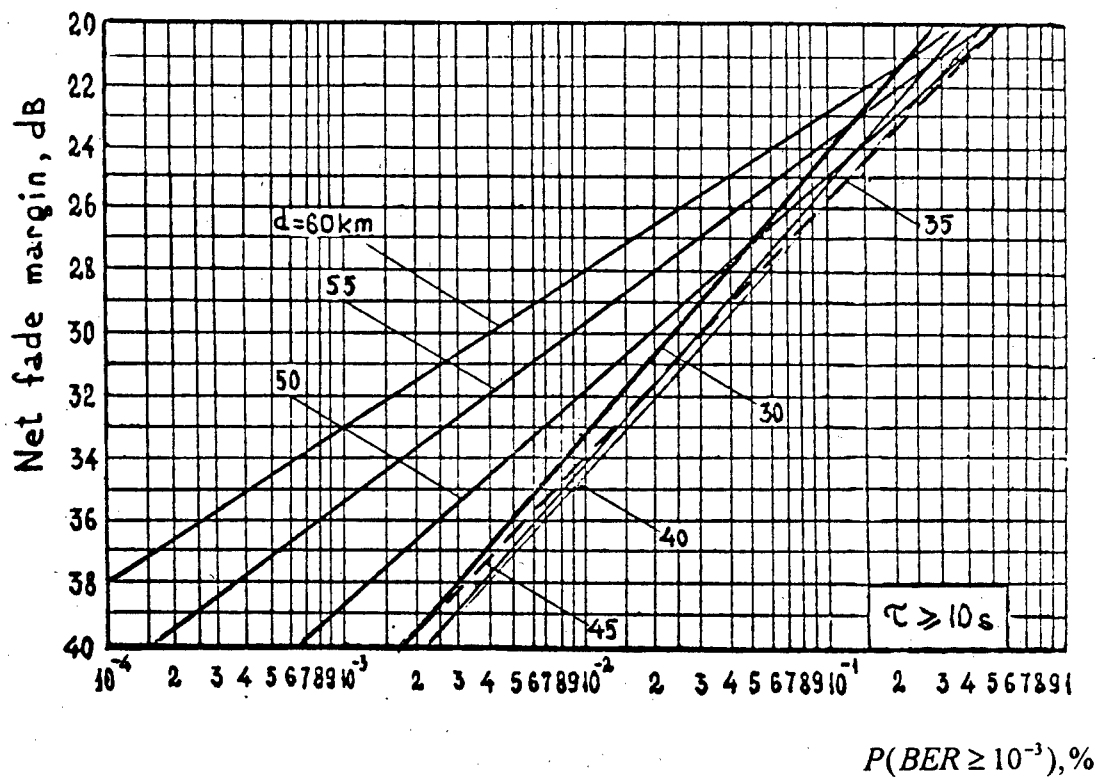
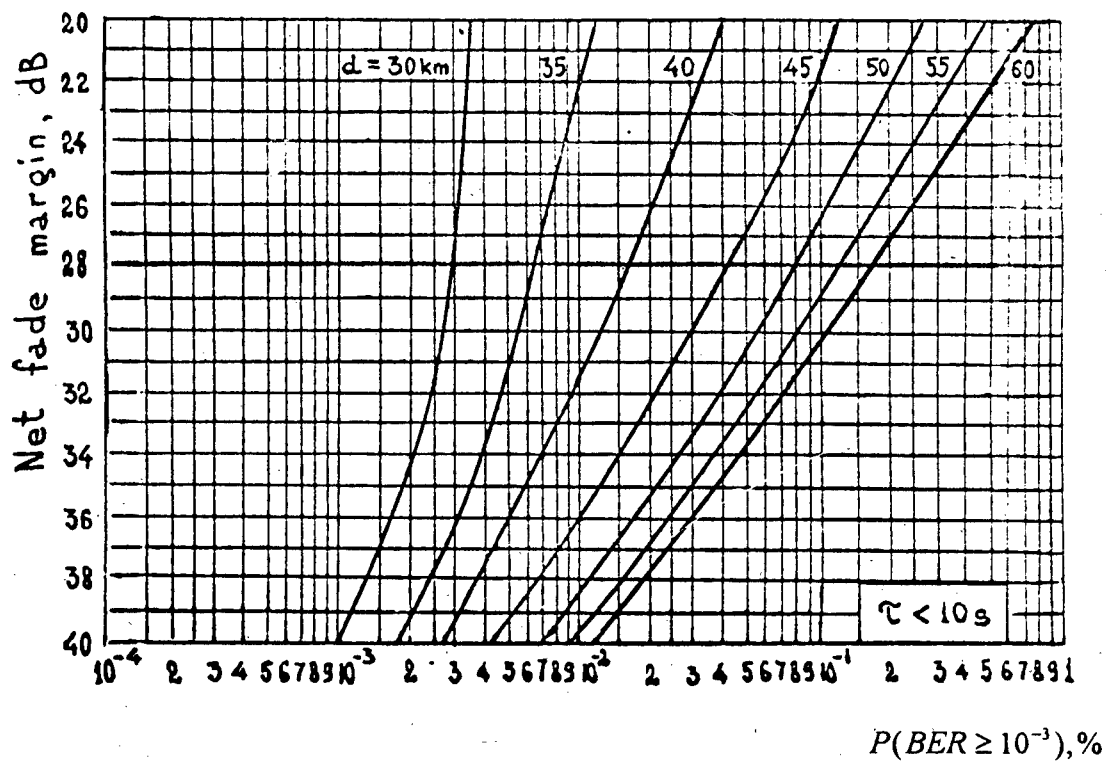


Figure2: $P(BER \geq 10^{-3})$ as a function of the net fade margin for coastal paths at the frequency 6 GHz

DATABASE OF RADIOMETEOROLOGICAL PARAMETERS

M.E.Rovkin

TACSR, 40, Lenin av., Tomsk, 634050, Russia,
tel: +7(3822)496488, Fax: +7(3822)223262, E-mail: root@orts.tiasur.tomsk.su

ABSTRACT

This paper messages about Data Base of Radio and Meteorological Parameters, that builds in TACSR. Data includes experiment processing results for transhorizon over-seas paths, listed below. In paper listed data characteristics and volumes. Data is original and based on measurements was build by TACSR in 1979-1993.

Keywords: propagation, transhorizon, over-seas, radioparameters, meteorological.

1. INTRODUCTION

Experimental research of transhorizon over-seas UHF radiowave propagation on base of Okhotsk Radiophysics Polygon of TACSR begins in 1979. Most of experiments was made in different bands simultaneously on single path, and was accompanied by meteomeasurements. Experiment scheme traditionally is: in standard times, when government states measures meteoparameters, four times per a day, there are measurement of radioparameters (in each situation different, dependably from task). Target of experiments was different, but in all we measurements energy parameters of transhorizon source signals was received. Experiments based, in most, on 1-2 «base» paths with length 30...600 km.

Data base (DB) have a target to concentrate in suitable form large arrays of experimental works of Radioengineering System Department (RSD) of TACSR. This paper can searched like small overview placed in our DB data. Work isn't ended in part of old data (before 1986), which we'll transference from PDP-11 to PC platform. Data structure and types lists below.

2. DATA TYPES

Data can be classified like: common, energy, nonenergy and meteo.

2.1 Common data

Common data includes data about paths sources and receivers. Source parameters includes: pulse transmitter power, [kW], pulse length time [us], pulse repetition time [us], wave length [m], transmitter antenna gain [dB], polarization [vertical, horizontal, circle], transmitter antenna evaluation [mrad], antenna type [paraboloid etc.], transmitter antenna beamwidth in vertical plane [mrad], transmitter antenna beamwidth in horizontal plane [mrad], transmitter high above sea [m], transmitter high above ground [m]. Receiver parameters includes: edge sensitivity [dB/W], bandwidth [MHz], receiver antenna gain [dB], antenna type [paraboloid], transmitter antenna beamwidth in vertical plane [mrad], transmitter antenna beamwidth in horizontal plane [mrad], transmitter high above sea [m], transmitter high above ground [m]. Path specification includes: path name, path type [over-seas, over-sea near-cost etc.], transmitter name, receiver name, stationarity-mobility, latitude and longitude of source, max path length (for mobile paths) [km], min path length (for mobile paths) [km]. Most of transmitters was placed on i. Sakhalin, receivers - on i. Sakhalin and i. Iturup (Kuril islands) or ships.

2.2. Energy parameters data

Energy parameters data includes primary data about received signals level values and secondary results processing of this data. Primary energy data includes date, time, source name, receiver name, path name, registration mode (time step and etc.) and received levels array. Secondary data includes processed from level arrays secondary arrays of averaged across 1-minute, 5-minutes, half-hour, day and month signal level for some path, transmitter and receiver. Interesting are data arrays of signals levels from different bands or different wave lengths, which transmitted and received with using transmitting and receive antennas with common phase centers, i.e. zero space- and direction- distanced. There are three forms of level data in different units: in dB/W, in mV and in mv/m (e/m field intensity). This class of data is most representative, because of all scheme experiments includes signal levels

measurements (with meteo). For example, old tables, released on PDP-11 includes near 3500 hours of level measurements. Standard report for data illustrates Table 1.

2.3. Nonenergy parameters data

Includes values for nonenergy signal parameters, such as radiopulse envelopment distortion, receiving time fluctuation, phase front fluctuation, direction to source fluctuations. Nonenergy parameters difficult to sort and processing. But some of this, such as time differences fluctuations characteristics in space-distanced points, phase differences fluctuation characteristics in space-distanced points presents in large volume.

2.4 Meteo data

Meteo parameters data includes data about meteostations and measuremented meteoparameters values. Each meteostation specification includes: station name, station coordinates (latitude and longitude), high above sea [m]. Primary meteo parameters measurement include such values: station name, date, time, temperature of the air [C], влажность [], atmosphere pressure [GPa], wind speed [m/s], wind direction [grad], refraction index [N-units], clouds index, hydrometeors presence [fog, rain, snow], temperature of the water surface [C]. Secondary meteo data includes: station name, date, time, refraction index (RI) at 250 m high gradient [N-units], RI on 1000 m high gradient [N-units], RI 2000 m high gradient [N-units], non-stability energy [J/kg], specific layer high [km], specific layer intensity [m], subrefraction layer high [m], subrefraction layer intensity [N-units], subrefraction layer width [m], 0-1km high refractive gradient [N-units]. If was made aerological measurements with using of aerozonds, database stores a high-profile arrays of RI.

3. DATA VOLUMES

3.1 Energy parameters data

Most interesting for looking are data for stationarity paths Energy parameters presence in volumes:

1983, may-june: total time (TT) = 150 hours (in 10cm, 180cm bands) 1983, october : TT = 130 hours (in 10cm, 180cm bands) 1984, march : TT = 100 hours (in 10cm, 180cm bands) 1984, july - september: TT= 300 hours (in 10cm, 180cm

bands) 1984, october-december: TT = 100 hours (in 10cm, 180cm bands) 1985, july - august: TT = 150 hours (in 10cm, 35cm, 180cm bands) 1986, jule - august: TT = 150 hours (in 10cm band only) 1987, may - june: TT = 170 hours (in 10cm band only) 1987, july - august: TT = 120 hours (in 10cm band only) 1987, september - october: TT = 260 hours (in 10cm band only) 1988, july-august: TT = 750 hours (in 10cm, 35cm, 180cm bands) 1989, august - october: TT = 240 hours (in 10cm, 35cm, 180cm bands) 1990, august - october TT = 450 hours (in 10cm, 35cm bands) 1991, february : TT = 80 hours (in 10cm band only) 1991, august - september: TT = 150 hours (in 10cm, 35cm bands) 1992, august - september: TT = 240 hours (in 10cm, 35cm, 180cm bands) 1993, august - september: TT = 320 hours (in 10cm, 35cm, 180cm bands)

Every measurements handled by meteo.

3.2 Nonenergy parameters data

Nonenergy parameters are presented in large volume too, but they are very difference and there are difficult to report about all of them in this paper. For example, in 1984 - 1993 systematically was measured the transmitter antenna directivity diagram fluctuation in different (10-cm and 35-cm) bands.

4. DATA EXAMPLE

In table 1 there are presented standard form for one measurement seance of transmissions loss in different bands.

5. CONCLUSION

Listed Radiometeorological Parameters DB we use for transhorizon radiowave propagation research and it can be used by other radio wave propagation in investigators and designers of radioengineering and communication systems which includes UHF transhorizon propagation over-seas paths. In [1] there are writing about same in application target database. Most difference from COST 210 DB is presence corresponding current meteoinformations. Today our DB don't compatible with this COST210 DB, but we can, if it's interesting for something, to present reformat data in COST210 database standard.

Table 1.

Example of Radiometeoparameter DataBase Standard Report

Transmitter Vzmorje (i.Sakhalin)			Receiver	Kurilsk (i.Itupup)	
Wave length,cm	10	35	Wavelength,cm	10	35
Pulse power, kW	700	230	Edge sens.db/w	-135	-137
Pulse length, us	2.6	1.6	Bandwidth MHz	1.6	1.6
Rep.time, ms	2.9	2.9	Antenna gain, dB	32	28
Antenna type	par/s	par	Polarization	ver	hor
Antenna gain ,dB	43	32	Ant.b/w in ver. pl.mrad	40	172
Ant.eval.mrad	1.2	1.7	Ant.b/w hor.pl.mrad	40	61
Antenna type	par	par	High a.sea ,m	32	31.2
Ant.b/w ver.pl.mrad	40	161.2	High a.ground ,m	3.8	1.9
Ant.b/w hor.pl.mrad	12.5	44	Signal frequency MHz	3001	786
High a.g. ,m	3.6	1.9			
High a.s. ,m	22	20.2			
Path length km 495.0			Over-seas part km 494.7		
Transmitter over-ground part m 290			Receiver over-ground part m 10		
Date 20:03:84			Meteoparameters (receiving point)		
Wave length,cm	10 cm	35 cm	RI	315	N-units
Time(msk)	Transhorizon transmission loss,dB		Gradient RI 0-1km	4	N-units/m
2:30	97	88.1	Gradient RI h=250m	37	N-units/m
3:35	96	82.1	Gradient RI h=1000m	33	N-units
4:35	95.5	83.1	Gradient RI h=2000m	31	N-units
5:35	95.3	84.4	Windspeed(a.p.850mBa	3.7	m/s
...	Wind speed (h=0)	2.2	m/s
			N/s energy	-875	J/kg
		

6.SOURCES

1.EUR 13407 - COST 210 - Influence of the atmosphere on interference between radio communi-

cations systems at frequencies above 1GHz Edited by:
E.Ballabio. Final report. Luxembourg: Office for
Official Publications of the European Communities
1991-XXIV, 624pp.,num.fig., tab. - 16.2x22.9cm

CLEAR AIR PROPAGATION MEASUREMENTS IN BRAZIL

N.R. Dhein, C.M. Einloft, M.S. Pontes, L.A.R. Silva Mello, G.L. Siqueira

CETUC-PUC/Rio, R. Marquês de S. Vicente 225, Rio de Janeiro, 22453-900, Brazil
Tel: +55-21-5299255, Fax: +55-21-2945748, E-mail: smello@cetuc.puc-rio.br

ABSTRACT

This paper presents results clear air propagation measurements performed in Brazil, aiming to provide data for clear air propagation predictions.

Keywords: Propagation measurements, multipath fading, refractivity.

1. INTRODUCTION

Several clear air propagation measurements' campaigns have been performed in tropical regions in Brazil, in the last 15 years. The experiments include:

- One year measurement of single frequency multipath fading in 12 line-of-sight microwave links.
- Measurement of multipath channel two-ray model parameters in the same 12 line-of-sight microwave links.
- One year measurements of refractivity gradient performed continuously using refractometers at 8 sites. Similar results, obtained from radio sonde, are available from 13 sites in Brazil and 2 sites in Argentina.
- Measurements of effective value of the earth's k factor in 5 diffracted links.

This paper presents a brief description of each experiment and examples of the results obtained. The data available can be useful to improve existing maps of climatic parameters for propagation predictions.

2. SINGLE FREQUENCY FADING

Cumulative distributions of single frequency multipath fading from continuous one year records of AGC level in line-of-sight analog microwave links. Examples of such distributions are shown in Figure 1. The link characteristics are described in Table 1.

In almost all cases, the measured distributions were well fitted by conditional Rayleigh distributions, allowing the determination of the multipath fading

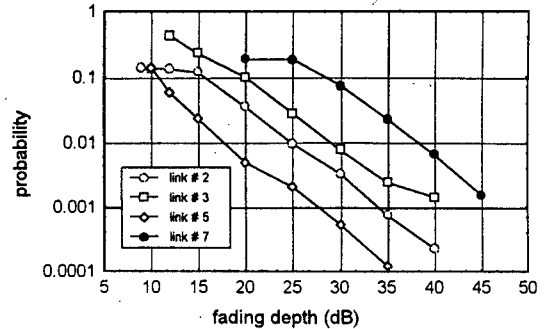


Figure 1: Cumulative distributions of single frequency multipath fading in line of sight microwave links.

occurrence factor r . This parameter is related to geo-climatic parameter K defined by the ITU-R (Ref. 1):

$$K = \frac{r}{d^{3.3} \cdot f^{0.93} \cdot (1 + |\epsilon_p|)^{-1.1} \cdot \varphi^{-1.2}} \quad (1)$$

where d is the path length in km, f the frequency in GHz, ϵ_p and φ in mradians are, respectively, the path inclination and the grazing angle, as defined in (Ref. 1). The values of K obtained are also shown in Table 1.

3. TWO-RAY MODEL PARAMETERS

Additionally to the AGC level, the continuity pilot level was detected and continuously recorded in the links described in Table 1. During the occurrence of multipath fading enhancements in the pilot level are observed that, together with the AGC level can be used (Ref. 2) to provide estimates for the parameters of the multipath channel transfer function:

$$H(f) = 1 + b \cdot e^{j2\pi(f-f_c)\tau} \quad (2)$$

Histograms of the maximum fade depth ($\lambda=1-b$) relative delay τ were obtained from the measured data. The histograms of the relative delay are, in almost all cases, well fitted by exponential density functions:

#	Link	Latitude	Longitude	Path length (km)	Frequency (GHz)	r (%)	$/\epsilon_p/$ (mrad)	ϕ (mrad)	K (%)	$\bar{\tau}$ (ns)
1	Contenda-Curitiba	23° 22' S	45° 32' W	44	6.3	0.93	0.23			1.27
2	M.Redondo-Curitiba	25° 15' S	49° 09' W	40.2	6.3	4.4	2.9	8.03	22×10^{-5}	0.59
3	C. Procópio-Londrina	23° 11' S	51° 05' W	54.5	7.5	9.3	0.72	5.91	4×10^{-5}	0.89
4	S. do Capivari-Curitiba	23° 00' S	47° 31' W	57.5	6.3	11	4.8			0.52
5	M. do Meio - Paranaguá	25° 19' S	48° 18' W	46.6	7.7	0.55	22.3	13.7	19×10^{-5}	
6	Carvalho- Ponta Grossa	25° 01' S	50° 05' W	68	7.5	25	0.62	3.68	2.7×10^{-5}	1.4
7	Tucuruvi-Curitiba	23° 17' S	43° 21' W	57.5	4	3.7	4.8			0.48
8	Para Pedro-Dourados	22° 13' S	54° 48' W	57.8	4	13	1.43	3.38	7.3×10^{-5}	0.67
9	M.Carmelo-M. Pedras	18° 43' S	47° 29' W	65.2	7.5	6.22	3.83	4.7	3.6×10^{-5}	0.76
10	P. Minas-Divinópolis	20° 09' S	44° 54' W	46	7.5	1.97	2.83	6.25	3.2×10^{-5}	0.13
11	Gonzaga-Ibituruna	19° 10' S	41° 52' W	57.5	7.5	12.04	0.6	19	1.7×10^{-4}	1.34
12	Serrania-Varginha	21° 33' S	45° 26' W	58.5	7.5	1.45	6.15	6.5	2.7×10^{-5}	0.29

Table1: Single frequency fading measurements

#	Site	Meas. Period	Statistics time basis	Latitude	Longitude	Meas. method	K_{med}	K_{min}	P_L	P_{Duct}
1	Caravelas	3 yrs.	year	17° 45' S	39° 15' W	Radio sonde	1.59	1.15		1
2	Salvador	3 yrs.	year	12° 59' S	38° 31' W	Radio sonde	1.61	0.97		1
3	Caroliña	3 yrs.	year	07° 20' S	47° 28' W	Radio sonde	1.81	1.01		1
4	Floriano	3 yrs.	year	06° 47' S	43° 01' W	Radio sonde	1.51	1.03		1
5	B.J.da Lapa	3 yrs.	year	13° 15' S	43° 25' W	Radio sonde	1.44	0.97		
6	Recife	3 yrs.	year	08° 03' S	34° 54' W	Radio sonde	1.68	0.97		1
7	S. Luiz	3 yrs.	year	02° 31' S	44° 16' W	Radio sonde	1.71	1.01		2
8	Petrolina	3 yrs.	year	09° 24' S	40° 30' W	Radio sonde	1.37	0.97		1
		1 yr.	month			Refractometer	2.18	<0.33	50	35
9	Trindade	5 yrs.	month	20° 31' S	29° 19' W	Radio sonde	3.57	0.52	75	26
10	Belém	6 yrs.	month	01° 27' S	48° 29' W	Radio sonde	2.87	0.99	68	16
		1 yr.	year			Refractometer	1.98	0.33		
11	Rio de Janeiro	5 yrs.	month	22° 54' S	43° 15' W	Radio sonde	2.07	0.93	38	14
		1 yr.	month			Refractometer	2.54	< 0.50	59	30
12	Campo Grande	6 yrs.	month	20° 27' S	54° 37' W	Radio sonde	1.34	0.94	3	
		1 yr.	year			Refractometer	1.86	0.76		9
13	Curitiba	6 yrs.	month	25° 25' S	49° 15' W	Radio sonde	1.51	0.83	18	1
14	Jiparaná	1 yr.	month	08° 03' S	62° 52' W	Refractometer	3.63	0.7	65	28
15	Cáceres	1 yr.	year	16° 04' S	57° 41' W	Refractometer	2.27	< 0.50	59	34
16	Goiânia	1 yr.	year	16° 40' S	49° 16' W	Refractometer	2.14	0.44		
17	Natal	6 yrs.	month	05° 24' S	35° 08' W	Radio sonde	3.34	1.2	52	23
18	Porto Alegre	6 yrs.	month	30° 02' S	51° 07' W	Radio sonde	1.8	0.8	29	5
19	Vilhena	6 yrs.	month	14° 14' S	60° 04' W	Radio sonde	1.65	1	15	
20	Manaus	6 yrs.	month	03° 09' S	60° 01' W	Radio sonde	2	1.07	22	5
21	Aracati	1 yr.	month	04° 21' S	37° 27' W	Refractometer	2.34	0.7	51	19

Table 2: Refractivity measurements

$$p_{\tau}(\tau) = \frac{1}{\bar{\tau}} e^{-\frac{\tau}{\bar{\tau}}}, \tau \geq 0 \quad (3)$$

The values of the average relative delay ($\bar{\tau}$), obtained for several links, are shown in Table 1. Strong correlation between $\bar{\tau}$ and the path length and inclination was observed. A preliminary expression for estimating the average delay as a function of these link parameters was derived:

$$\bar{\tau}(ns) = 0.05 \cdot d^{0.87} \cdot e^{-0.25|e_p|} \quad (4)$$

4. REFRACTIVITY GRADIENT

4.1 Radio sonde measurements

Results of radio sonde measurements at thirteen sites in Brazil, for periods between three and eight years, have been analysed to provide statistics of the refractivity gradient. The data correspond to radio sonde launches at 08:00 AM, local time. Average year cumulative distributions were obtained from data of eight sites. For the remaining five sites, average distributions for the months of February, May, August and November are available. The geographical coordinates of the sites and the measurements' periods are given in Table 2.

Several parameters used for propagation predictions can be derived from the refractivity gradient cumulative distributions. The earth's K factor is defined as a function of the refractivity (N) by:

$$K = \frac{1}{1 + a \frac{\Delta N}{\Delta H} \times 10^{-6}} \quad (5)$$

where $\frac{\Delta N}{\Delta H}$ is the vertical gradient of the refractivity (in N units/km) and a is the earth's radius (6370 km). The value of K exceeded during 99.9 % of the time (K_{min}) and the median value of K (K_{med}) are widely used in link design.

The distributions also provide the probability of occurrence of surface ducts, corresponding to refractivity gradients smaller than $-157 N$ units/km or negative values of K factor. For the sites where monthly distributions are available it is also possible to obtain the parameter p_L . This parameter, used in the prediction of single frequency multipath fading distributions (Ref. 1), is defined as the higher value of probability of occurrence of refractivity gradients smaller than

$-100 N$ units for the months of February, May, August and November.

The values of K_{min} , K_{med} , p_L and probability of occurrence of surface ducts, derived from radio sonde measurements are shown in Table 2.

4.2 Refractometer measurements

Measurements of refractivity vertical gradient were performed for periods of one year at 8 sites, using two-cavity refractometers. The measurement system consists of two refractometers positioned near the basis and near the top of a tower, with height difference between 60 and 100 m, depending on the site. The refractometer voltage are used as input for a differential amplifier which output is a voltage directly proportional to the refractivity gradient. This arrangement allows continuous measurements, eliminating the bias present in radio sonde measurements, that are made only once or twice a day.

An example of monthly cumulative distributions obtained with refractometers at Aracati, in Northwest of Brazil, is shown in Figure 2.

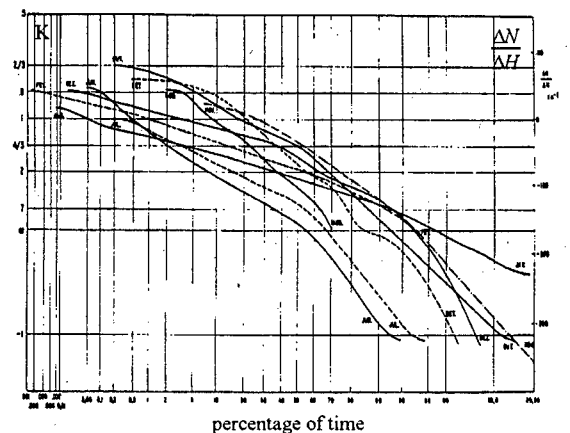


Figure 2: Cumulative distributions of refractivity gradient.

The measurement sites characteristics and the values of K_{min} , K_{med} , p_L and probability of occurrence of surface ducts, obtained from radiometer measurements are shown in Table 2.

Both refractometer and radio sonde data are available in 4 sites. The results obtained indicate that cumulative distributions of the refractivity gradient obtained from radio sonde measurements underestimate the occurrence of super-refraction and tropospheric ducts. It is also observed that the values of K_{min} derived from radio sonde data are much higher than those obtained with refractometers. Consequently, the occurrence of sub-refraction is also underestimated.

Link	Latitude	Longitude	Path length (km)	K_{med}	K_{min}
Carmo da Mata - Divinópolis	20° 09' S	44° 54' W	42.2	1.2	0.74
Cabo Verde - Poços de Caldas	21° 48' S	46° 34' W	38.1	1.3	0.72
Abadia dos Dourados - M. Carmelo	18° 43' S	47° 29' W	35.4	1.8	0.81
Dores de Campo - Barbacena	21° 14' S	43° 46' W	27.3	1.3	0.69
Francisco Sá - Montes Claros	16° 43' S	43° 52' W	51.2	1.7	0.67

Table 3: Measurements of effective K factor in diffracted links

5. EFFECTIVE K FACTOR

The excess attenuation due to diffraction in obstructed links is strongly dependent on the earth's K factor. Reliable methods (Ref. 3) are available for predicting the excess attenuation in such links, particularly when the obstruction is due to a single, isolated obstacle. The K factor can, thus, be estimated from excess attenuation measurements. This is an indirect method, which accuracy depends on the reliability of the attenuation prediction method chosen for inversion. On the other hand, it has the advantage of providing an effective value for the K factor, which includes the effect of horizontal variations of the refractive index.

Such an experiment was performed in 5 diffracted links, operating at 300 GHz. The site locations, path lengths are shown in Table 3. Figure 3 shows the cumulative distribution of received power measured in one of the links. Based on such distributions, the median and minimum values of the effective K factor were derived by inversion of the ITU-R method (Ref. 4) for calculation additional attenuation by diffraction. The results are shown in Table 3.

6. CONCLUSIONS

A significant amount of clear air propagation data from tropical climates was obtained in experiments carried out in Brazil in the last 15 years. In this paper, the experiments were briefly reviewed and examples of the its results were presented. The data available can be useful to improve existing maps of climatic parameters for propagation predictions.

7. REFERENCES

1. CCIR Rec. 618-2, SG-5 RPN Series , 1992, ITU, Geneva, Switzerland.
2. Taylor D P and Shafi M 1983, A Simple Method for Estimating Multipath Fade Parameters", *IEEE Trans. Comm.*, COM-31.
3. CCIR Rec. 526-1, SG-5 RPN Series , 1992, ITU, Geneva, Switzerland.

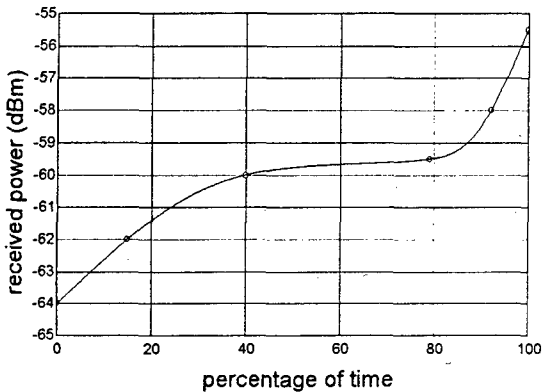


Figure 3: Cumulative distributions of received power level measured in a diffracted link operating at 300 MHz.

Session 8: Clear air III

CLIMATOLOGIC STUDY OF MICROWAVE-ACTIVE TURBULENCE BEHAVIOR OVER A BIG CITY BY SODAR

A. N. Bedulin, M. A. Kallistratova, M. S. Pekour, I. V. Petenko, E. A. Shurygin

IAP-RAS, Pyzhevskii 3, 109017 Moscow, Russia

Tel: +7-095-233-48-76, Fax: +7-095-233-16-52, E-mail: postmaster@iaph.msk.su

ABSTRACT

The results of continuous 24-hour observations of the atmospheric boundary layer carried out during 3 year are presented. All the measurements were made due to remote acoustic sounding. Data on thermic stratification, on occurrence and heights of inversion layers forming the microwave ducts are obtained. Data on daily variations of the vertical profiles of the refractive index structure parameter are also given. The structure of boundary layer over two districts of Moscow is compared with that over the Moscow region.

Keywords: acoustic remote sensing, sodar, microwave duct, climatology of the urban boundary layer.

1. INTRODUCTION

The usefulness of remote acoustic sensing for long-term regular investigations of the atmospheric boundary layer (ABL) parameters that affect the microwave communication links was discussed in (Ref. 1).

During 1989-1991 continuous 24-hour observations of the ABL structure were carried out over Moscow. The acoustic locator (sodar) was disposed at the Meteorological Observatory of the Moscow State University (MSU) on the Vorob'evy Gory. The facsimile records (echograms) of sodar echo-signals were processed by the methods described in (Ref. 2-4) to obtain

the occurrence of the atmospheric stratification types. The data on height distribution and time span of the inversion layers were also obtained.

The cyclic remote observations were also carried out in two other points: in the center of Moscow - on the roof of the building of the Institute of Atmospheric Physics (IAP) and in a country-side - at the Zvenigorod Scientific Station (ZSS) of the IAP 45 km West of Moscow. The comparison of simultaneous observations in the three points allowed the spatial inhomogeneity of the urban ABL to be found.

The daily variations and vertical profiles of the temperature structure parameter (which permits one to evaluate the index

refraction structure parameter C_n^2) were

obtained for summer and winter at the IAP point. The methods of such measurements are given in (Ref. 5,6).

2. APPARATUS

The ECHO-1 sodar installed at the MSU is a nondoppler vertical acoustic locator, which gives only the echograms of the echo-signal on the height-time coordinates. The sodar parameters are: carrier frequency $f=1660$ Hz, electric power $W=75$ W, range of sensing z is from 30 m to 800 m, spatial resolution $\Delta z=17$ m, period of sound pulses $\tau=10$ s.

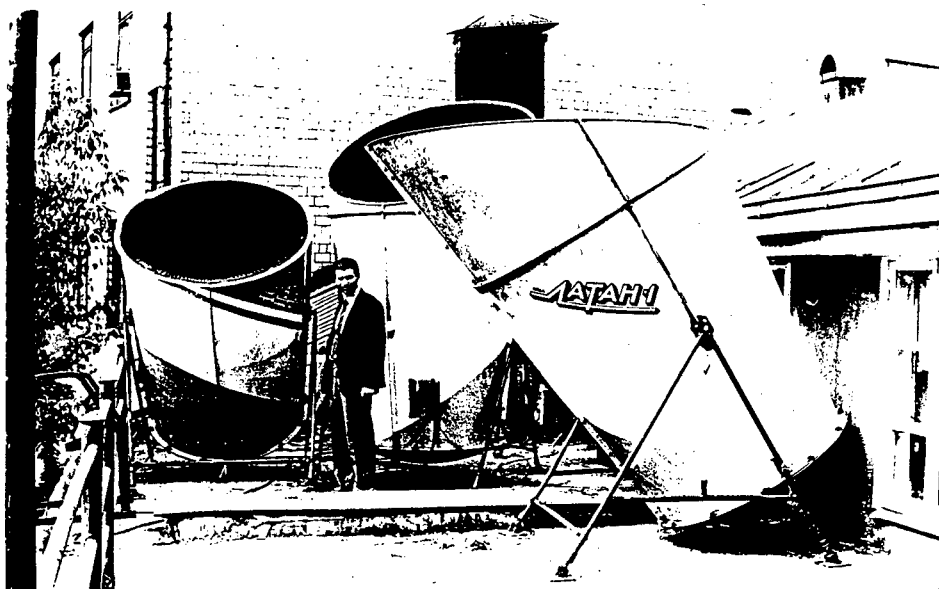


Figure 1: Antennae of LATAN-sodar on the roof of IAP building in the center of Moscow.

On the IAP building and at the ZSS the three-component Doppler LATAN sodars (designed at IAP) were used. LATAN sodar allows the profiles of temperature

structure parameter C_T^2 and vector of wind

velocity to be measured; echograms being also provided. The LATAN SODAR parameters are: $f=2000$ Hz, $W=100$ W, z is from 30 m to 600 m, $Az=17$ m, $\tau=10$ s. The photo of the LATAN sodar on the roof of the IAP is in Fig. 1.

3. Results

In Fig. 2 the examples of simultaneous echograms are given for the 3 points. The elevated layer of echo-signal, that corresponds to the elevated inversion layer (which is due to warm air advection), is similar for all the points. But the character and heights of the lower layer of the echo-signal, that corresponds to the surface radiation inversion, are noticeably different. As is seen from the long-term observations, the surface inversion thickness in the center of the city is always more by 100-150 m than that in its outskirts both in summer and winter.

Moreover, the type of the ABL thermic stratification is often different over different parts of the Moscow region. Table 1 gives the occurrence of types of stratification from the 3-year

observations at the MSU, and Table 2 demonstrates the distinctions for 3 points on basis of simultaneous measurements.

Table 1. Occurrence of different types of stratification over Moscow (in %)

Type of stratification		1989	1990	1991
Surface inversion	(I)	44	34	40
Multilayer inversion	(U)	4	4	10
Elevated inversion	(R)	8	8	9
Capped convection	(C)	2	2	4
Developed convection	(K)	15	16	15
Near neutral condition	(S)	27	36	22

Table 2. Occurrence of types of stratification in the center of the city, its outskirts and at the rural area (in %)

Type of stratification	May-June 1990			February 1991		
	IAP	MSU	ZSS	IAP	MSU	ZSS
(I)	26	42	39	37	51	39
(U,R)	14	7	20	17	18	31
(C)	6	3	5	2	2	6
(K)	34	33	26	4	2	7
(S)	20	15	10	40	27	18

Figs 3,4 and 5 give the occurrence of daily variations of the surface inversion, the distributions of their time span and the histograms of their thickness, respectively. As the microwave ducts occur only under the inversion conditions, these Tables and Figures allow the occurrence of

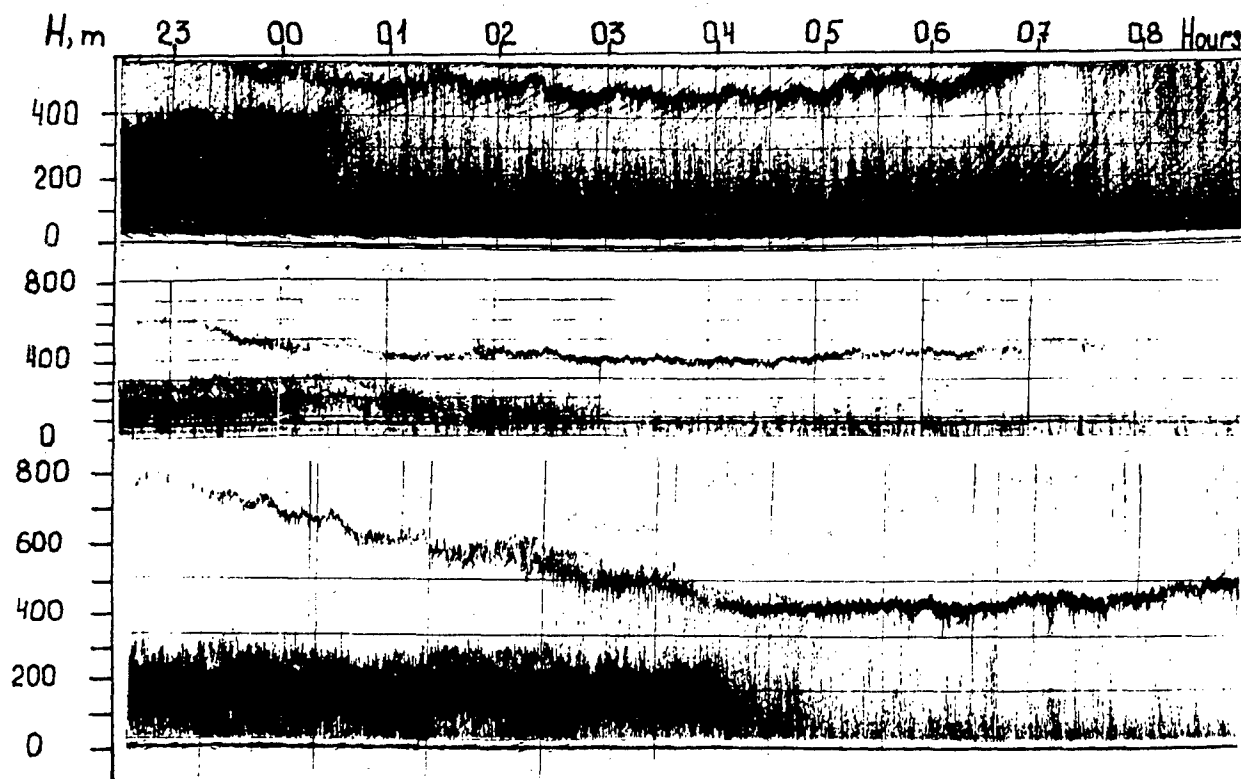


Figure 2: Sodar echograms obtained simultaneously in the center of Moscow (the upper one), at the MSU site and at the ZSS site (the lower one).

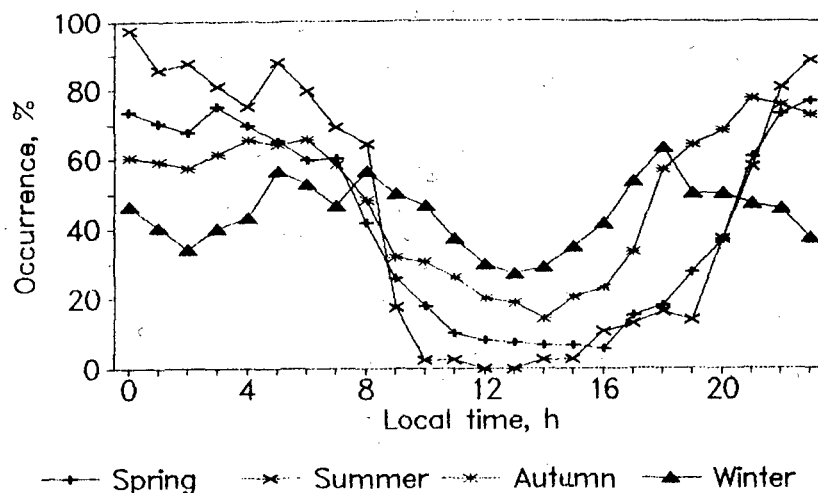


Figure 3: Daily variation of occurrences of the surface inversion averaged on each of four seasons (MSU site).

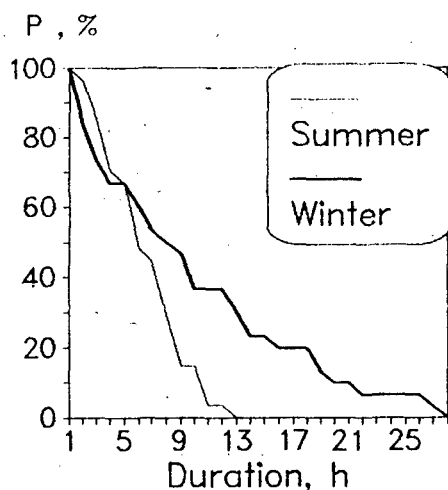


Figure 4: Probability distributions of surface inversion observation in the center of Moscow as a function of duration.

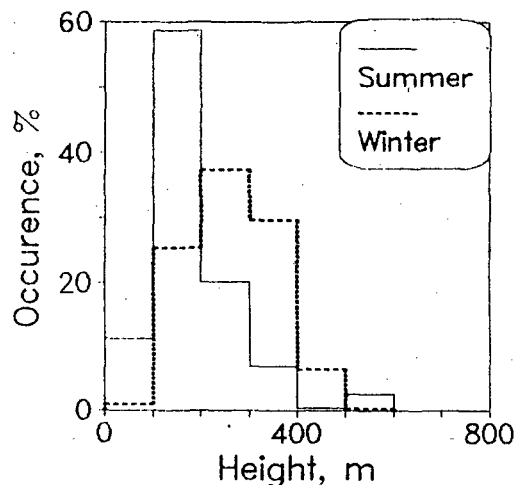


Figure 5: Frequency distribution of surface inversion thickness in the MSU site.

ducts to be evaluated for winter and summer over Moscow and its neighbourhood.

Figs 6 and 7 give monthly averaged profiles of the index refraction structure parameter, calculated from the temperature

structure parameter C_T^2 by the formula

$$C_n^2 = \left(79 \cdot 10^{-6} \frac{p}{T^2} \right)^2 C_T^2$$

(see Ref.1), which does not take into

account the input of humidity fluctuations in the refractive index. These data permit one to evaluate the high-frequency fluctuation of the intensity and angle of microwave arrival using the known formulae by Tatarskii (Ref. 7).

Moreover, the pattern of these profiles demonstrates that the optimum height for communication links (on which the turbulent distortions of wave parameters are minimal) over center of Moscow is in the range of 100-200 m above the ground level.

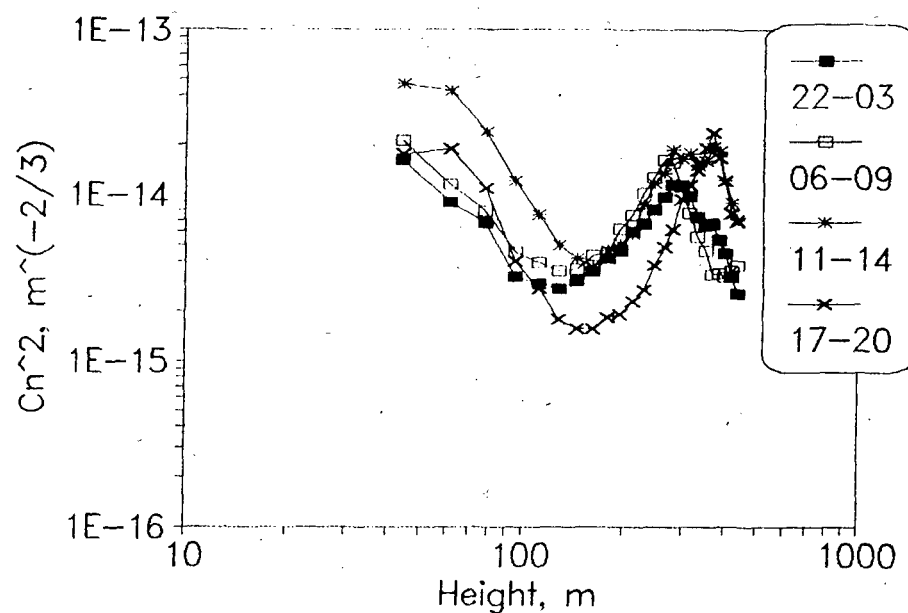


Figure 6: Monthly averaged profiles of $C_n^2(z)$ (February 1991) averaged over 4 period of 24 hours in the IAP site.

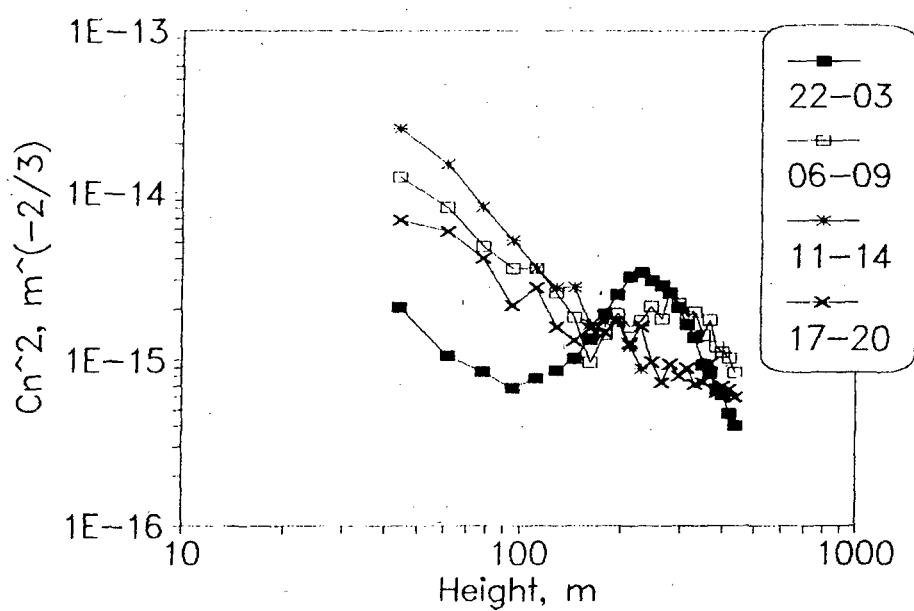


Figure 7: The same as in Figure 6 for July 1991.

4. CONCLUSION

The climatologic data on the occurrence of different types of the atmospheric thermal stratification over Moscow are obtained by acoustic remote sensing. This data allow one to evaluate the seasonal variation, the time span and thickness of microwave ducts.

The spatial inhomogeneity of the urban ABL structure is shown.

The vertical profiles of the structure parameter of temperature (which allow one to evaluate that of radiowave refractive index), are obtained for summer and winter. These profiles make it possible to evaluate the optimum height for line-of-sight links over Moscow as 100-200 m.

5. ACKNOWLEDGMENTS

This research was supported by the Russian Foundation for Fundamental Researches through Grant 93-05-08753 and also by International Scientific Foundation (project Es 2-3667-0925).

6. REFERENCES

1. Kallistratova M.A. 1994, On acoustic remote sensing for climatologic study of microwave propagation in the atmospheric boundary layer, *This collection*, pp. -
2. Pekour M.S. et al. 1994, Acoustic sounding study of the mixing layer over a city, in *SPIE vol. 2107 Optical Monitoring of the Environment*, pp. 169-193
3. Pekour M.S. and Kallistratova M.A. 1993, SODAR study of the boundary layer over Moscow for air-pollution application, *Appl. Phys.* B57, pp.49-55
4. Lokoshenko M.A. et al. 1993, Studies of the atmospheric boundary layer over Moscow by remote sensing and direct methods. *Meteorology and Hydrology*, No 9, pp. 20-33
5. Geras'uk N.E. et al. 1981, A sodar for investigation of atmospheric turbulence, *Izv. Acad. Sci USSR, Atmosp. and Ocean Phys.*, 17, pp. 73-76
6. Danilov S.D. et al. 1992, Acoustic calibration of sodars, *Meas. Sci. Technol.*, 3, pp. 1001-1007
7. V.I.Tatarskii 1971, *The effects of the turbulent atmosphere on wave propagation*, NTIS, Springfield, Va. 22151, 471 p.

LINE-OF-SIGHT MICROWAVE PROPAGATION AND CLEAR AIR CLIMATIC CONDITIONS FOR COASTAL REGIONS UNDER THE NORTHERN POLAR CIRCLE

T. Tjelta¹ and S. Lystad²

1-Norwegian Telecom Research, P.O. Box 83, N-2007 Kjeller, Norway

Tel: + 47 63 80 92 03, Fax: + 47 63 81 00 76, Email: terje.tjelta@tf.tele.no

2-Norwegian Meteorological Institute, P.O. Box 43 Blindern, N-0313 Oslo, Norway

Tel: + 47 22 96 31 73, Fax: + 47 22 96 30 50

ABSTRACT

Microwave links have to be designed such that propagation effects do not reduce the quality. Propagation measurements and meteorological measurements from coastal regions at latitude at about the Northern Polar circle are analysed and discussed. Climatic models for the coast of Helgeland is suggested, models for use in the interpretation of the propagation data and for future planning of microwave links.

Keywords: Multipath fading, Ducting layers

1. INTRODUCTION

Line-of-sight radio link networks are designed to meet very high quality objectives. The planning involves careful consideration of the actual path and the propagation effects to be expected on the path. A precise prediction of expected multipath fading and enhancement distribution is therefore important. Our knowledge of multipath propagation does currently best cover overland links. In mountainous regions and over-water coastal areas there is less information available [1].

Measured multipath propagation and meteorological data are studied for a coastal area at about 65° latitude in Norway. The general climate in this region is characterized by oceanic or suboceanic temperature regimes with mild to moderately cold winters and

moderately warm summers. This coastal area is open to invasion of the maritime zonal westerlies and the change eastwards from maritime to continental climate is very gradual.

This paper present and discuss propagation and meteorological data from this area at a latitude close to the Northern polar circle. Radio propagation data for 1993 is used along with meteorological data.

2. MULTIPATH FADING MEASUREMENTS

Norwegian Telecom has done measurements on the coast of Helgeland at about 65° latitude over the last years. Results are available from the three links on the coast of Helgeland. The links pass mostly over sea water. They are designed to meet standard recommendations by the International Telecommunication Union. That means there are enough clearance. No reflections from the surface of the sea are visible. However, the sea is illuminated by the transmitter on the two longest links, and the blocked reflection could be part of the multipath propagation mechanisms. Some characteristic data about the links are given in Table I.

The multipath fading cumulative distributions for 1993 for the link Gul-Mun are shown together with distributions of July 1993 for the other two links. The signal level is referenced to the median of the month, also given along with amount of available data.

Table I: Radio link characteristics

	Gjeltheia	Munken		Gulsvåg fjell		Åsen
Transmitter or Receiver	T	R	R	T	R	T
Path length (km)	73.3		93.8		54.1	
Radio frequency (GHz)	6.7		6.7		6.7	
Approximate bandwidth (MHz)	35		35		35	
Height (m) of ground above sea	519	91		728		60
Antenna height (m) above ground	71.0	75.0	75.0	60.8	41.6	19.5
Antenna diameter (m)	3.6 ¹⁾	3.6 ¹⁾	3.6 ¹⁾	3.6 ¹⁾	3.6	3.6
Measurement periods in 1993	June - September		April - December		July - September	

¹⁾ Two of these antennas are connected in parallel (beside each other) to achieve larger margin

Measured distributions 1993 Receivers at Mun and Gul

Reference: Median Days

Gul: April	-37.57	27.72
Gul: May	-38.84	28.64
Gul: June	-37.88	19.79
Gul: July	-38.51	21.25
Gul: August	-38.30	28.64
Gul: September	-38.34	21.68
Gul: October	-38.39	26.80
Gul: November	-37.85	27.72
Gul: December	-40.53	20.98
Gje: July	-33.46	21.25
Åsen: July	-28.55	24.01

Stations:
Gjeltheia (Gje)
Munken (Mun)
Gulsvågfjell (Gul)
Åsen

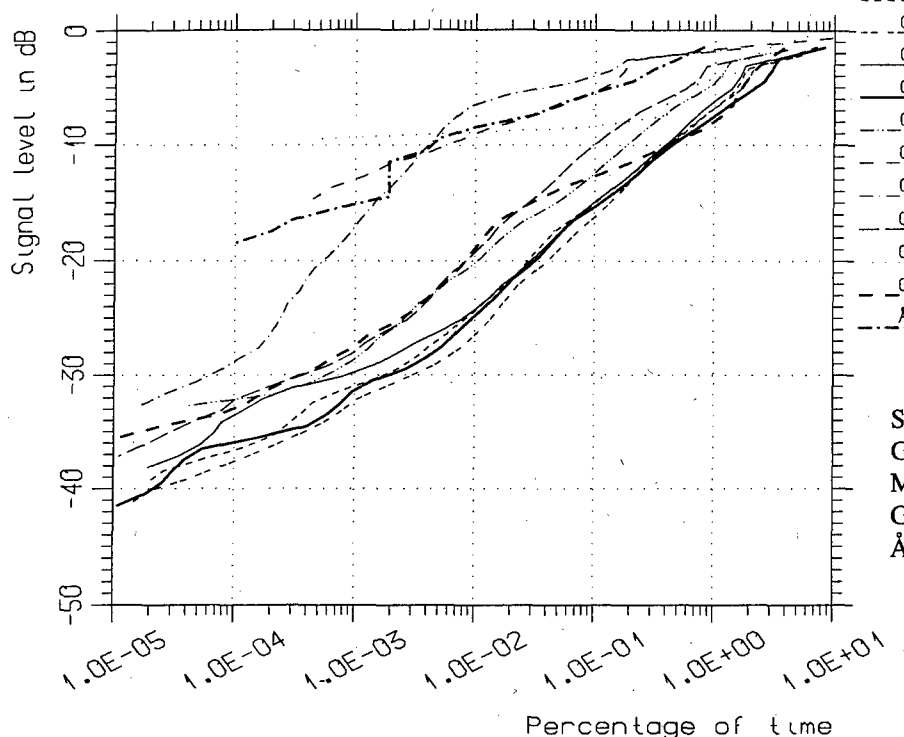


Figure 1. Fading distributions measured on 3 links at the coast of Helgeland

The 4 months distributions for the link Gje-Mun show similarities with those from Gul-Mun. The link Åsen-Gul show considerably less fading than the two others. The months Aug. and Sep. show less multipath activity for all the links than July. Since July is close to May, where May is the Gul-Mun worst month, it is probably close to the worst month for the two other links.

The enhancement distribution given in Fig. 2 show the general picture that the month with most fading also give most enhancement.

ITU-R Method 1 [2] predicts for the tail region of the worst month distribution 3 and 12 dB less fading for the links Gje-Mun and Åsen-Gul respectively compared with Gul-Mun. From Fig. 1 it is reasonable that the tail region starts at about 18 dB for all months and links except Sep., Oct., and Dec., and Åsen-Gul. The distribution of Sep. show approximately a 10 dB/decade slope beginning at 9 dB. Measured at 0.01% of the time (in the tail) the Gul-Mun distributions fall into three groups. One for the 4 months Apr.-Jul., another for Aug. and Nov., and a third for Sep., Oct., and Dec. The other links Gje-Mun and Åsen-Gul show less fading as predicted compared with Gul-Mun, where the first link show about 6 dB less fading compared with the predicted 3 dB. Åsen-Gul seems never to reach a acceptable tail-region for fair comparison with prediction.

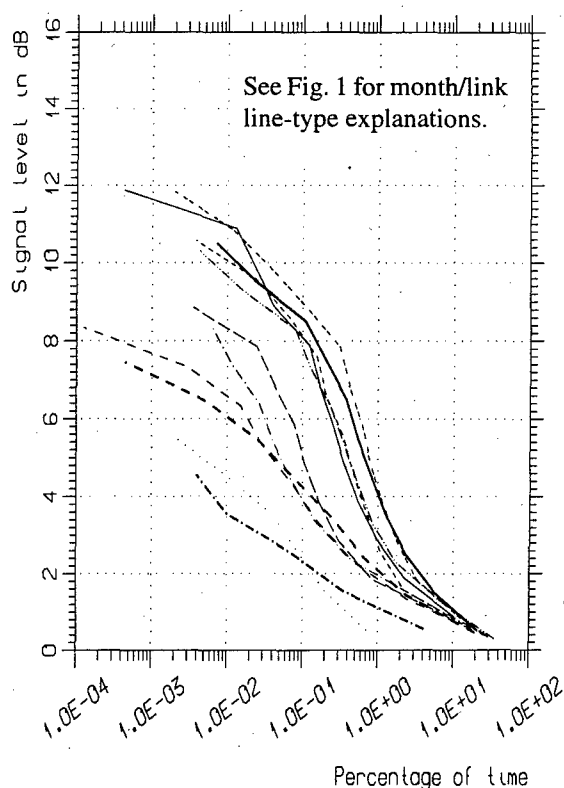


Figure 2. Enhancement distributions 1993

3. DESCRIPTION OF THE CLIMATE

3.1 Radiation and temperature.

Table II give the day length vs latitude is. At lower latitude, near 35°N the total incoming radiation over a year from sun and sky is about 150 Mcal/cm², 65% is due to direct solar radiation. At 70°N the total incoming radiation has is 70 Mcal/cm², 60% results from diffuse sky radiation.

Table II: Variation of day length

Latitude	21 Dec	21 June
70°N	-	24 h
60°N	5 h 52 m	18 h 52 m
50°N	9 h 4 m	16 h 23 m

This shift from direct to diffuse radiation reduce the influence of the angle of slope of land. The radiation totals is less important higher latitudes since diffuse radiation is received nearly equally on all slopes of moderate inclination giving more equal distribution of temperature.

Actual day to day temperatures in an area are partly correlated with the prevailing air mass. Berg [3] has defined an index of continentality $K = C \cdot 100 / R$ (%), where C is the frequency of continental air-masses and R is the frequency of all other air-masses.

K is shown in Fig. 3 and the Western part of Scandinavia has clearly, in spite of the high latitude, a maritime character. Because of the "even" distribution of the local scale temperature our inclination is that the major spatial variation in refractivity $N, N = N(P, T, e)$ where P is air pressure, T the temperature and e the vapour pressure of the air, is caused by the variation in e. This is again linked to the frequency of the type of prewailing air-mass and whether the type are continental or maritime.

3.2 Local effects.

Local effects along the western coast of Norway are due to the constant supply of temperate water by the Gulf-stream combined with cold and relatively dry air streams on local scale. Those are created by negative radiation balance in the high mountains and are moving down and out to the Norwegian sea.

This will often create a well defined system of air layers with different properties. The bottom layer is warm to moderately warm and humid, the layer above, due to the outstreaming air, is cold and moderately dry, whereas the top layer, provided by the westerlies, is moderately warm and humid.

The mutual interfaces of the layers are not stable, between the bottom layer and the middle layer an instability is caused by the thermal stratification, between the middle and the top layer by wind shear. Here the

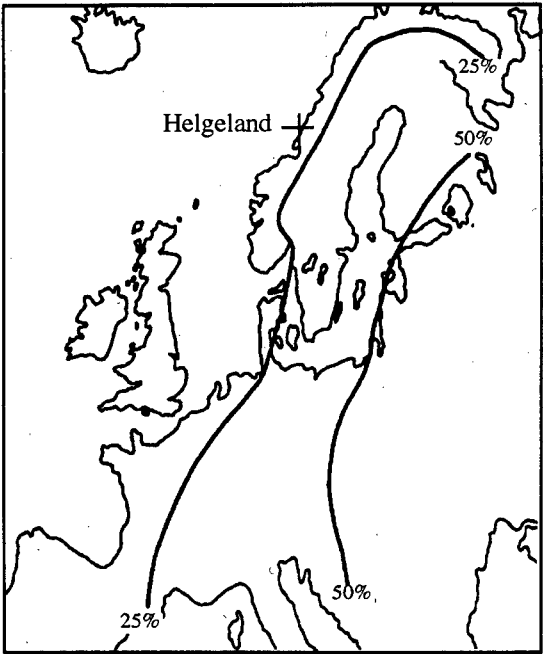


Figure 3. Continental air-masses over North West Europe (from [3])

interface is not so sharp defined, due to the turbulent mixing. Since the air is moving and the layers have different physical properties, we can also have instabilities of the Kelvin-Helmholtz type internal waves. The occurrence and "intensity" of this layers will have a daily as well as an annual variation, mainly due to the magnitude of the radiation balance. A nightly negative radiation balance in summer can create this local cool air-mass moving westwards. When the sun rises we get a positive radiation balance and a decay of the cold air production which disappears towards noon. The whole picture is more or less a "sea-land breeze".

In the winter when the radiation balance is negative this layering will prevail whether it is day or night. The major modifications to this picture is then due to the "intensity" of the physical properties of the east moving air mass supplied by the zonal current.

4. THE WEATHER CONDITIONS 1993

In January the weather was governed by a high pressure over the Baltic with a low pressure belt from Iceland to Svalbard. Numerous fronts passed over the north of Norway resulting in fair amounts of precipitation and cloudiness.

February had rather variable weather conditions resulting from the diminishing low pressure belt from January. Wind from west gave rain and snow showers in Northern Norway, but occasional wind from east resulted often in clear weather.

March had numerous frontal passages in the northern Norway with great amounts of precipitation,

amounts up to 400% of normal value.

April had wind from north which resulted in showers along the coast in northern and western Norway.

May had in the beginning a high pressure over the Baltic resulting in wind from north in northern Norway. In the end of the month a new high pressure area developed over Great Britain and this resulted in wind from the west with precipitation in the coastal areas.

June had passages of numerous weak fronts with little rain and in between periods with fair weather.

In July the Northern Norway had the best weather with high pressure conditions and sparse cloudiness. Maximum temperatures were well above the normal. In August unstable weather conditions was predominant in the whole country. The northern coast, however, had a fair amount of good weather.

In September low pressure systems arrived from the North sea giving wind mainly from east in the middle and the southern parts of the north of Norway.

October started with low pressure and a frontal system over England giving fair weather. Later on the frontal systems moved away northwards. This gave wind from northwest with rain sleet and snow on the northern coast and a rather stormy weather.

Two different frontal systems dominated the weather in November. One system from Iceland to Svalbard and a rather weak system over England and Denmark. This resulted in fair weather. The temperature at the coast of Helgeland was 2°C above the normal.

For December the weather was very variable due to many frontal passages. At Helgeland thunderstorms occurred in connection with cold front passages.

5. REFRACTIVITY MEASUREMENTS

Data from 1993 from 3 radiosonde stations; Ørland, station 1241, (63.7°N latitude, 9.4°E longitude, 10m height above mean sea level), Bodø, 1152, (67.3,14.4,8) and Mike-9661- (66.0,2.0,6) form the basis for computation of the atmospheric refractivity. The ascents are done twice a day at hours 00 and 12 GMT for all stations. In addition Mike does ascents at 06 and 18 GMT. Data consists of values of pressure, temperature and humidity. The sondes are Vaisala sondes of the Digicora type.

The refractivity is computed at given heights as reported by the sondes as well as a linear interpolation pr 100 m to obtain the gradients (dN/dz) for $z=100m$ and $1km$, see Table III. Fig. 4 gives the occurrence of $dN/dz < -100$ N-units. An investigation of ducts are done by means of the modified index M. Duct-types are split in surface/elevated surface ducts and elevated ducts. The condition for a surface duct is $(dM/dz) < 0$ for $z=0$, an elevated surface duct is defined by $(dM/dz) > 0$ for $z=0$, $(dM/dz) < 0$ for $z > 0$

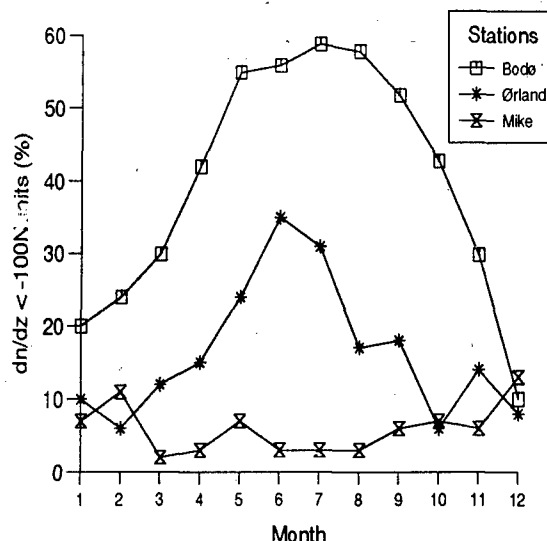


Figure 4. Refractivity gradient occurrences of three stations 1993 taken at 100m above ground

and $M(z > 0) < M(z = 0)$, and finally an elevated duct is characterized by $(dM/dz) < 0$ for $z > 0$ and $M(z > 0) > M(z = 0)$. The results are given in Tables IV-VI.

6. RADIOCLIMATIC MODELS

Looking at the refractivity values under consideration we find for the surface ducts at the Helgeland coast a typical vertical range from 60 to 80m with standard deviations ranging from 5 to 25m, highest values in summer and lowest in winter. We will look at two different situations: one with heating from "below" and the other with cooling from "below". Heating from below happens for instance as a result of solar radiation accumulated in ground. Convective air movement is the result with creation of three more or less layers, a surface layer with a definitely superadiabatic lapse rate, which increases as the ground is approached. Above is a thick central layer in which the lapse rate is very nearly adiabatic, and above is a stable layer. The central layer is characterized by an approximately standard M-profile. The superadiabatic bottom layer is superstandard if the surface is water or wet ground. If the surface is dry ground, there is no vapour gradient, thus the layer is substandard. In the stable top layer we usually have superstandard conditions, but occasionally an intense vapour inversion can make the layer substandard. The surface layer is characteristically shallow. If it is superstandard, the M-inversion is usually between a few meters up to 10-15 m. A common situation that gives heating from below occurs over water when there is an offshore wind and the surface air on land is colder than the water as a result of nocturnal cooling. The layer grows higher as the air

moves farther offshore. In spite of nearly negligible depth of this layer it can be of importance as refracting the rays hitting the sea surface. If we consider cooling from below we have no convection and the modification of the air can be effected only by mechanical turbulence and thus does not extend above the layer of frictional influence. In the case heating from below the air modifications may extend to great heights, if we look at cooling from below the effect is confined to about 100 to 150 m.

7. CONCLUSIONS

Coastal radio propagation and meteorological data from 1993 at a latitude of about 65°N have been presented. It is evident that spring/summer months show most multipath propagation events as well as most duct occurrences.

July had good weather with large temperature difference day and night. This compares well with July as the worst propagation month. November had also fair weather with rather high day temperatures and thermal energy loss at night created cold surface layers. The top height of ground based radio ducts range

from 60 (winter) to 80m (summer) and the variability suggest that some ducts reach as high as 200 m above ground during the summer.

Future work is needed to more exactly model the layer structures and use such models in theoretical evaluation of radio wave propagation.

8. REFERENCES

1. SG5 Database of the Int. Telecom. Union, 1994, Geneva.
2. CCIR Recommendations, RPN-Series Propagation in non-ionized media, Int. Telecom. Union, 1992, Geneva.
3. Berg H. *Die Kontentalitaet Europas und ihre Aenderung 1928/37 gegen 1888/97*. Anals Hydrogr. Berlin 124. 1940 Berlin.

ACKNOWLEDGMENTS

We are most grateful to those in Norwegian Telecom and Norwegian Meteorological Institute that provided the measured data, in particular Torbjørn Tanem and Ruth Arntzen.

Table III: Refractivity gradients (N-units) measured between ground and 0.1 and 1 km

	month	Jan.	Feb.	Mar.	Apr.	May	Jun.	Jul.	Aug.	Sep.	Oct.	Nov.	Dec.
Bodø	mean	-101.0	-94.0	-104.0	-113.4	-141.3	-158.1	-191.6	-169.1	-128.6	-112.3	-102.4	-81.2
	sd	43.7	31.4	25.8	27.2	38.8	38.0	43.1	43.4	53.1	26.4	30.3	22.3
	dN/dz	-40.0	-42.0	-49.0	-62.0	-43.0	-60.0	-59.0	-69.0	209.0	-35.0	-43.0	-34.0
	at 0.1	-251.0	-160.0	-161.0	-189.0	-261.0	-258.0	-336.0	-288.0	-210.0	-170.0	-179.0	-133.0
	mean	-39.7	-37.5	-37.1	-39.1	-43.2	-44.6	-49.5	-46.6	-40.9	-38.8	-39.6	-36.2
	sd	4.4	4.3	3.0	5.4	7.4	6.8	7.3	7.5	6.8	4.6	5.4	3.4
	dN/dz	-33.2	-29.0	-30.8	-28.6	-32.2	-32.1	-37.9	-34.3	-6.0	-30.4	-24.7	-29.7
	at 1	-53.7	-49.6	-43.3	-57.8	-64.2	-63.5	-67.1	-64.1	-51.0	-51.0	-52.3	-46.6
Ørland	mean	-69.0	-63.8	-74.0	-71.1	-96.5	-104.8	-104.5	-85.4	-86.0	-69.8	-78.6	-59.9
	sd	28.3	27.4	35.9	31.4	68.6	40.8	49.1	39.1	33.0	25.2	38.7	27.9
	dN/dz	-18.0	-1.0	-10.0	-35.0	103.0	-34.0	-31.0	-34.0	-20.0	-27.0	-34.0	-29.0
	at 0.1	-156.0	-151.0	-208.0	-158.0	-355.0	-255.0	-259.0	-199.0	-178.0	-150.0	-205.0	-143.0
	mean	-37.0	-37.7	-37.9	-40.1	-44.2	-42.8	-44.8	-44.6	-42.5	-39.7	-42.5	-38.6
	sd	3.9	4.6	5.1	6.4	10.9	7.4	6.9	5.7	5.3	4.1	8.6	5.5
	dN/dz	-27.6	-26.2	-25.3	-24.7	-19.1	-32.6	-29.8	-28.2	-30.1	-28.4	-27.0	-26.8
	at 1	-44.3	-51.8	-50.9	-63.5	-83.7	-65.5	-68.8	-61.2	-58.1	-49.2	-64.6	-58.1
Mike	mean	-49.5	-57.5	-48.7	-51.8	-53.0	-54.9	-47.7	-50.5	-58.5	-57.0	-55.3	-58.0
	sd	18.2	26.8	18.2	16.9	24.6	19.0	27.5	18.8	47.8	27.2	21.7	27.4
	dN/dz	-16.0	9.0	-15.0	-12.0	25.0	-13.0	53.0	-7.0	404.0	19.0	14.0	-21.0
	at 0.1	-123.0	-132.0	-164.0	-117.0	-193.0	-155.0	-251.0	-114.0	-168.0	-174.0	-138.0	-166.0
	mean	-35.6	-36.7	-37.2	-38.7	-42.8	-36.5	-41.6	-42.4	-40.5	-39.1	-39.2	-35.7
	sd	4.0	4.1	5.2	7.2	10.4	4.3	5.9	5.3	7.3	7.2	5.9	4.1
	dN/dz	-28.6	-29.1	-27.8	-28.2	-28.8	-28.5	-26.8	-28.6	0.1	-24.3	-28.1	-27.8
	at 1	-51.1	-50.5	-55.7	-69.1	-73.4	-52.0	-67.0	-57.3	-61.0	-68.6	-58.5	-51.3

Table IV: Measured duct occurrences, heights, and intensities. Bodø 1993 (h and sd in m, int in M-units)

mon	surface/elevated surface duct					elevated duct				
	no	h	sd	int	sd	no	h	sd	int	sd
Jan	19	62.3	9.5	-4.4	3.2	0	0.0	0.0	0.0	0.0
Feb	20	73.2	8.3	-3.1	1.9	0	0.0	0.0	-0.1	0.0
Mar	42	73.7	7.1	-2.7	2.1	1	1902.0	0.0	-3.2	0.4
Apr	45	76.1	6.8	-3.1	2.2	0	0.0	0.0	0.0	0.0
May	49	78.6	8.0	-5.6	3.3	5	1688.4	681.3	-6.2	2.5
Jun	56	76.9	8.8	-6.7	3.1	7	1630.0	244.1	-2.4	1.6
Jul	58	81.1	25.3	-9.6	4.5	5	1958.4	381.9	-3.8	2.5
Aug	53	78.3	18.3	-8.5	3.4	5	1850.0	268.5	-2.0	1.0
Sep	43	70.7	9.3	-5.7	2.7	4	1563.0	245.2	-1.8	1.5
Oct	49	70.9	7.1	-3.7	2.1	7	2094.9	612.4	-2.4	1.6
Nov	36	72.2	5.9	-3.5	2.7	2	1529.0	176.8	-2.0	0.1
Des	15	70.4	10.5	-1.8	1.4	0	0.0	0.0	0.0	0.0

Table V: Measured duct occurrences, heights, and intensities. Ørland 1993 (h and sd in m, int in M-units)

mon	surface/elevated surface duct					elevated duct				
	no	h	sd	int	sd	no	h	sd	int	sd
Jan	6	65.0	10.5	-1.4	1.5	1	1648.0	0.0	-0.7	0.0
Feb	3	62.7	17.0	-1.4	1.2	1	1792.0	0.0	-0.1	0.0
Mar	7	70.6	10.2	-3.0	2.3	2	2526.0	1026.7	-0.6	0.5
Apr	7	71.4	18.3	-1.2	0.8	2	783.0	258.8	-5.3	5.7
May	20	62.7	17.5	-4.2	5.7	10	1398.4	1196.0	-7.4	8.3
Jun	32	61.0	16.1	-3.7	3.2	6	1310.0	379.9	-3.8	2.9
Jul	26	69.9	22.2	-3.6	3.4	4	2447.0	1039.3	-3.9	3.9
Aug	14	67.4	17.5	-6.6	10.4	5	1650.8	1290.1	-3.3	3.8
Sep	15	66.1	20.1	-2.6	1.9	6	1815.7	956.8	-1.5	1.3
Oct	6	63.3	3.7	-2.0	1.2	3	1708.7	396.6	-3.2	3.4
Nov	5	80.8	26.8	-3.9	2.8	8	1376.5	744.9	-5.0	3.6
Des	7	63.7	8.1	-2.5	66.7	1	518.0	0.0	-0.2	0.0

Table VI: Measured duct occurrences, heights, and intensities. Mike 1993 (h and sd in m, int in M-units)

mon	surface/elevated surface duct					elevated duct				
	no	h	sd	int	sd	no	h	sd	int	sd
Jan	8	54.5	5.0	-1.6	1.1	3	972.7	221.9	-1.2	0.4
Feb	13	51.7	5.8	-2.2	1.5	4	1677.5	626.3	-2.0	2.0
Mar	3	59.3	5.0	-3.8	3.7	13	1541.7	432.2	-3.2	3.2
Apr	4	51.0	10.4	-2.1	1.3	16	1497.5	817.2	-7.7	7.2
May	5	63.6	17.2	-2.6	2.0	38	1100.0	747.9	-4.7	4.5
Jun	3	56.0	7.2	-3.7	2.7	16	1298.9	167.7	-6.4	3.3
Jul	2	77.0	35.4	-7.3	3.4	14	1715.7	1050.6	-3.2	4.9
Aug	1	58.0	0.0	-2.3	0.0	9	1189.8	479.4	-6.3	3.9
Sep	4	54.5	4.1	-5.1	2.8	19	1528.0	828.7	-4.4	3.7
Oct	5	71.2	44.2	-3.5	2.2	9	1348.7	539.3	-3.8	2.4
Nov	5	57.6	5.5	-2.8	1.1	17	1526.5	591.3	-4.3	3.1
Des	18	56.0	4.3	-2.3	2.2	5	1397.6	423.1	-3.0	1.5

THE EXPERIMENTAL RESULTS OF 11 - 35 GHZ RADIO WAVE ATTENUATION INVESTIGATIONS ON TERRESTRIAL LINKS IN BULGARIA, POLAND AND RUSSIA

E.Alexandrova¹, A.Kawecki², V.V.Svjatogor³, V.N.Pozhidayev⁴

1 - NIIS, 8 Hidushka Poljana, Sofia, BULGARIA

Tel: 359-522808, Fax: 359-800038, E-mail:

2 - ITMP, 1 Szachowa ul., PL-04894, Warszawa, POLAND

Tel: +48-22-128362, Fax: +48-22-129007, E-mail:

3 - NIIR, 16 Kazakova Str., Moscow, 103064, RUSSIA

Tel: (095) 261-02-73, Fax: (095) 261-02-73, E-mail:

4 - IRE, 11 Mokhovaja Str., Moscow, 103907, RUSSIA

Tel: (095) 203-49-96, Fax: (095) 203-60-78, E-mail: efr@ire.uucp.free.msk.su

ABSTRACT

The results of multi-year measurements of radio wave attenuation at the four terrestrial links are presented. Attenuation statistics due to rain, snowfalls or to abnormal air refractive index profiles are separated. The prediction methods for rain attenuation statistics are compared with the experimental data and the error estimations are given. The prediction methods in case of abnormal air refractive index profile over the link are analyzed and some comparisons with the experimental data have been carried out.

Keywords: Attenuation Statistics, Comparison with Prediction Models

1. DESCRIPTION OF EXPERIMENTS

This investigations had been carried out at the International Experimental area (Dubna) and the National test areas in Bulgaria and Poland as a part of "INTERCOSMOS" program.

1.1. Link # 1 (Bulgaria)

Hop length is 7.12 km, frequencies are 11.15, 19.15, 33.6 GHz. The link was placed between the building of Communication Institute in Sofia and mountain Vitosha slope, so the link was pointed at 7.5° over the hori-

zon. The only atmospheric phenomena affecting the link reliability were rains and fogs. The time periods for the attenuation statistics measurements were: 20435 hours for 11.15 GHz, 19678 hours for 19.15 GHz (1986-1990) and 11071 hours for 33.6 GHz (1986-1989). Rain rate measurements have been carried out at the terminals of the link. The rain rate statistics for all links are shown in Table 7.

The statistical distributions of radio wave attenuation in rains at this location had been calculated for each year. In Table 1 attenuation statistics both year-averaged and for the averaged worst-month are presented.

1.2. Link # 2 (Poland)

Hop length is 15.4 km, frequencies are 11.5, 18.6 GHz. The link is located not far from Warshaw over cross - country with some forests, therefore reflections from the Earth surface were absent. The heights of the link terminals are 144 m and 124 m above the sea level. According to link geometry the first Fresnel zone was slightly overlapped on both frequencies.

The measurements at 18.6 GHz have been carried out during 1986 - 1990 with dynamic range 40 dB. The measurements at 11.5 GHz have been started in 1989 with dynamic range

Table 1.

Probability, %	1986 - 1990				1986 - 1989	
	11.15 GHz		19.15 GHz		33.6 GHz	
	year	w.m.	year	w.m.	year	w.m.
1.0				3.3	2.3	6.9
0.5		2.8	2.4	4.7	4.2	10.2
0.3		3.5	3.2	5.9	6.8	13.5
0.2	2.1	4.2	3.9	7.5	8.8	16.5
0.1	2.9	5.5	5.2	11.3	13.0	24.6
0.05	3.8	8.0	6.9	15.3	17.3	>30.
0.03	4.6	9.5	8.7	18.5	22.5	
0.02	5.4	10.5	10.3	20.8	25.7	
0.01	7.4	11.9	14.1	26.0	>30.	
0.005	9.5	14.3	18.5	29.8		
0.003	10.6	16.0	21.8	>30.		
0.002	11.4		24.6			
0.001	12.8		29.2			
0.0005	14.5					
0.0003	16.0					

Table 2.

Probability, %	18.6 GHz						11.5 GHz			
	1986 - 1990				1987 - 1989		1989 - 1990			
	total att.		rains		multipath		total att.		rains	
	year	w.m.	year	w.m.	year	w.m.	year	w.m.	year	w.m.
5.0	2.2	4.7						4.1		
3.0	2.9	5.6						4.8		
2.0	3.6	6.4						5.4		1.1
1.0	4.7	8.3		3.8			4.2	6.9		2.0
0.5	5.8	11.9	2.0	6.2		3.4	5.2	8.6		3.3
0.3	7.0	14.6	3.4	8.7		6.5	5.9	9.8		4.2
0.2	8.2	17.0	4.6	10.5		8.1	6.7	11.0	2.5	5.2
0.1	11.4	21.3	6.9	15.0	3.6	11.4	8.0	14.3	3.5	7.2
0.05	15.7	29.1	9.6	25.0	7.3	15.2	9.9	18.4	4.7	10.0
0.03	18.5	36.6	12.2	36.6	9.5	16.8	11.5	20.5	5.7	13.1
0.02	20.9		15.0		11.5	18.2	13.9	21.2	6.5	16.5
0.01	26.6		21.8		14.3	20.7	17.6	24.0	8.8	23.3
0.005	35.4		33.0		16.5	23.6	20.9	32.0	11.7	
0.003	41.0		41.0		17.9	26.0	22.4		15.7	
0.002					19.0	28.6	23.5		19.7	
0.001					21.6		26.3		26.0	
0.0005					25.0		30.3		29.6	
0.0003					28.0					

from - 32 up to + 10 dB. Rain rate measurements have been carried out at 5 points along the route with the tipping bucket rain gauges (Ref.1). The attenuation on this link had

been caused by: hydrometeors (rain, fog, snowfalls), multipath propagation ducting due to the negative gradients. The summary of attenuation statistics measured on this

link is presented in Table 2.

1.3. Link # 3 (Russia)

Hop length is 12.65 km, frequencies are 11.5, 19.3, 29.3 GHz. The link is located in Dubna not far from the Moscow sea. The heights of the link terminals are 30 m above the Earth's surface. The Fresnel zones were not disturbed for all frequencies. The difference in the link terminal heights above the sea level is 12 m.

The measurements at 11.5 and 19.3 GHz have been carried out during 1983 - 1990 (up to 1985 - circular, after that - vertical polarization). The measurements at 29.3 GHz have been carried out in 1986 - 1990. The dynamic ranges were about 40 dB.

The radio wave attenuation statistics had been recorded during 66240 hours (97.5 % from the total period) at 11.5 GHz, during 62780 hours (92.4 %) at 19.3 GHz and during 40997 hours (93.6 %) at 29.3 GHz. The main sources of fading were: hydrometeors (rain, snowfall, fog), multipath propagation, reflection from layers arising between the link terminal heights, ducting due to the negative gradients. Both total attenuation statistics and statistics due to the different phenomena are presented at Tables 3, 4 and 5.

Besides the rain rate measurements the air refractive index gradient between the two heights at 2 and 30 m had been measured in Dubna at the link terminal during one summer. The strong time correlation between the large gradient values and the radio wave attenuation has been observed and these data have been used to test the prediction models.

1.4. Link # 4 (Russia)

The hop length is 0.7 km and the link is located in Dubna close to the link # 3. Frequency is 19.2 GHz

and polarization used is vertical. The measurements have been carried out during 1986-1990. The attenuation statistics has been recorded at 32838 hours (93.7 % of the total period). The fading occurs due to rain and snowfall only. The resulting statistics averaged over a year and over the worst month are presented in Table 6.

2. DATA ANALYSIS

2.1. Fading in hydrometeors

The most serious fading at the links # 1 and 4 has been caused by rains, and these data have been used to get some empirical relations and to test some prediction models for rain only. In a winter time the fading at the link # 4 has been usually 1.5 - 2.0 dB in snowfalls with peaks no more than 5 dB.

The fading at the link # 2 can be considered equal (very roughly) for both major phenomena and only separated parts of the total statistics can be used for the purposes mentioned above. In a winter time the fading in wet snowfalls has arisen up to 25 dB. The connection between the equiprobable attenuation values at 18.6 and 11.5 GHz in rains has been confirmed as:

$$A_{F2} = K_2 (A_{F1} / K_1)^{\alpha_2 / \alpha_1},$$

where the coefficients K_1 , K_2 , α_1 , α_2 are used for the specific attenuation calculations at the given frequencies.

The fading at the link # 3 had been investigated thoroughly with statistics separation due to the different phenomena. The ratio of the equiprobable attenuation values has been found as:

$$A_{F2} / A_{F1} = c A_{F1}^d,$$

Table 3.

Proba- bility, %	Attenuation, dB (frequency: 11.5 GHz, polar.: vert.)													
	1983 - 1990							1986 - 1990						
	total statist.		rains atten.		no rain		C	total statist.		rains atten.		D	multipath fading	
	year	w.m.	year	w.m.	year	w.m.		year	w.m.	year	w.m.	w.m.	year	w.m.
1.0	4.4	7.4		4.6	4.4	4.6		3.8	7.0		4.8	3.8		3.6
0.5	5.6	11.1		5.9	5.1	6.9		5.0	10.4	3.1	6.2	8.9		5.0
0.3	6.7	14.4	3.6	7.1	6.3	9.4		6.3	13.3	3.8	7.4	13.5		6.4
0.2	7.9	17.5	4.2	8.2	7.3	11.7		7.6	16.4	4.4	8.4	15.7	3.2	7.6
0.1	10.3	22.4	5.2	10.1	10.1	14.5		10.1	21.8	6.2	10.2	19.8	4.7	10.4
0.05	13.9	25.7	6.6	12.3	13.6	17.4		13.2	25.2	7.7	12.0	24.1	6.6	13.7
0.03	16.5	27.2	7.8	14.3	16.0	19.2		15.6	26.2	8.4	13.7	26.4	8.3	16.4
0.02	18.9	28.7	8.8	16.1	18.4	20.7		18.2	27.0	9.0	15.2	27.7	9.7	18.1
0.01	22.9	31.4	10.7	20.6	22.4	23.5		22.4	28.7	10.8	18.8	30.1	12.1	20.7
0.005	24.8	34.6	12.7	25.6	25.6	26.1		25.4	31.4	12.7	25.1	33.6	15.0	23.2
0.003	27.5	37.5	14.6	29.0	27.0	27.8		26.5	33.9	14.4	27.8	38.0	17.4	25.2
0.002	29.0	38.7	16.3	30.8	28.4	29.2		27.5	37.0	15.9	30.1		18.8	26.8
0.001	31.9		20.3	35.0	31.0	31.8		29.4		19.9	35.0		21.4	28.7
0.0005	35.0		24.6	38.4	33.9	33.8		33.0		24.5	39.0		23.8	31.5
0.0003	37.0		28.0		37.0	35.0		35.0		27.0			25.4	33.0
0.0002	39.0		30.2		39.0	35.7		39.0		29.1			26.7	33.7
0.0001			34.4			37.0				34.2			28.8	35.0

Table 4.

Proba- bility, %	Attenuation, dB (frequency: 19.3 GHz, polar.: vert.)													
	1983 - 1990							1986 - 1990						
	total statist.		rains atten.		no rain		C	total statist.		rains atten.		D	multipath fading	
	year	w.m.	year	w.m.	year	w.m.		year	w.m.	year	w.m.	w.m.	year	w.m.
1.0	5.8	9.2	3.8	6.8	4.8	5.9		4.9	8.7	3.8	6.7			4.3
0.5	7.2	13.3	4.9	9.0	6.1	8.8		6.6	13.5	5.0	8.6	7.3		6.6
0.3	8.7	16.4	6.0	11.5	7.2	10.7		8.2	17.5	6.2	10.5	14.3	2.8	9.0
0.2	10.1	20.1	7.1	14.3	8.3	12.6		9.6	20.3	7.1	13.3	18.3	3.7	10.7
0.1	13.3	24.9	9.1	20.6	10.6	16.1		13.0	25.0	9.1	19.5	23.6	5.9	13.6
0.05	17.5	30.8	12.0	28.2	14.0	19.5		17.4	29.9	11.9	27.3	27.6	8.4	16.3
0.03	20.8	36.6	15.1	34.4	16.9	21.7		20.7	35.4	14.9	34.0	29.7	10.6	19.0
0.02	23.4	>40.	18.0	39.0	19.0	23.5		23.4	>40.	17.7	>40.	31.3	12.2	21.1
0.01	28.1		24.2	>40.	22.5	26.7		27.8		23.6		34.0	14.5	25.2
0.005	33.5		30.6		25.5	30.4		32.5		30.2		36.8	17.6	29.4
0.003	37.5		35.3		27.5	32.7		36.5		36.6		38.3	20.2	32.1
0.002	>40.		39.0		29.2	34.2		>40.		38.8		>40.	22.6	33.7
0.001			>40.		32.5	37.0				>40.			26.5	36.2
0.0005					35.0	38.5							30.6	38.3
0.0003					37.0	>40.							33.3	>40.
0.0002					37.7								34.8	
0.0001					39.0								37.0	

Note: C means the multipath fading, D means fading due to the shielding layer between the heights of the link terminals (1988-1990 only).

Table 5.

Probabi- lity, %	Attenuation, dB (frequency: 29.3 GHz, polar.: vert.)						
	1986 - 1990						
	total stat.		rain atten.		C		D
	year	wor.m.	year	wor.m.	year	wor.m.	worst month
1.0	6.7	13.6	5.5	12.7		4.7	
0.5	9.6	19.4	7.8	16.5		6.6	9.5
0.3	12.0	26.1	10.1	20.6	3.2	8.3	15.8
0.2	14.3	34.6	12.2	24.2	4.0	9.7	19.8
0.1	19.2	>40.	15.9	36.6	5.6	12.0	25.5
0.05	26.0		21.1	>40.	7.7	14.3	30.0
0.03	33.0		26.2		9.5	16.0	32.8
0.02	39.0		31.8		11.0	17.3	34.1
0.01	>40.		>40.		13.0	19.0	37.5
0.005					15.0	21.2	>40.
0.003					16.8	23.1	
0.002					17.9	24.5	
0.001					19.7	27.0	
0.0005					21.9	29.3	
0.0003					23.7	30.3	
0.0002					24.8	31.0	
0.0001					27.6	33.0	

Table 6.

Attenu- ation, dB	
year	w.m.
1.6	2.5
2.0	3.1
2.4	3.5
2.7	3.7
3.2	4.2
3.9	4.7
4.1	5.1
4.3	5.5
4.7	6.4
5.2	7.6
5.6	8.3
5.9	8.7
6.7	9.2
7.7	9.6
8.3	9.9
8.6	10.1
9.2	

Note: Abbreviations C and D are the same as in Tables 3 and 4.

Table 7.

Proba- bility, %	Rain rate to be exceeded, mm/hours					
	Dubna		Warsaw		Sofia	
	year	w.month	year	w.month	year	w.month
1.0		4.6		3.7		3.4
0.5	3.0	7.4	2.5	5.2	1.8	5.2
0.3	3.9	9.9	3.4	7.3	3.1	8.2
0.2	4.6	13.4	4.2	9.6	4.1	10.6
0.1	7.3	22.1	6.0	15.3	7.4	18.8
0.05	10.8	33.8	9.0	25.0	11.6	31.1
0.03	15.1	42.7	12.5	33.8	14.4	40.0
0.02	19.8	49.2	15.9	42.0	18.0	46.5
0.01	31.0	62.9	24.2	60.1	27.5	61.6
0.005	41.6	82.7	34.9	77.0	38.1	91.7
0.003	49.0	94.0	43.3	97.1	47.8	109.0
0.002	56.0	101.0	50.3	104.0	52.8	144.0
0.001	70.0	110.0	64.1		70.0	163.6
0.0005	88.0		75.0		90.0	
0.0003	97.5		88.1		116.6	
0.0002	101.0		100.0		140.0	

where c and d are: 1.29 and 0.18 (Ref.2).
 for the pair 19.3/11.5 GHz and 1.84
 and 0.25 for the pair 29.3/11.5 GHz

2.2. Fading in the clear air

The fading in these conditions is caused by the abnormal air refractive index profiles, which can be divided into four groups: the large positive gradient, the large negative gradient, the reflecting layer above the link, the reflecting layer between the heights of the both terminals. The propagation phenomena considered are ducting, multipath propagation and "shielding" of one link terminal (Ref.3).

The worst-month attenuation statistics at the link # 2 due to multipath propagation can be approximated as:

$$P(A) = 1.25 \cdot 10^{-0.1A}, \%$$

where A is the attenuation in dB.

The worst-month attenuation statistics at the link # 3 due to multipath propagation can be approximated as:

$$P(A) = 0.08(38 - |F - 20.1|^{1.5}) \cdot 10^{-0.1A}, \%$$

where F is the frequency in GHz. As concerning the attenuation due to the "shields" of reflecting layers between the heights of link terminals, it has occurred only 1-2 times in a year. The curves showing the attenuation statistics can be approximated by log-normal distributions, or by the sum of two straight lines with the different slopes (Ref.4)

3. ATTENUATION STATISTICS PREDICTION

The prediction models for the attenuation statistics prediction have been tested by the comparison with the experimental statistics. The 8 rain prediction models have been tried. The estimation of r.m.s. has shown that the best methods for the year averaged and worst month predictions are those, proposed by C. Capsoni et al and E. Larin. The both r.m.s. values are about 24 %.

The probability distribution for the air refractive index gradient, measured from April till November, can be divided on the two parts and be approximated as (Ref.4):

$$P(g) = 0.47 \cdot \exp(-0.024g) \text{ for } g > +20, \%$$
$$P(g) = 0.89 \cdot \exp(0.0091g) \text{ for } g < -140, \%$$

where g is the gradient in N-unit/km. The prediction models for the worst month attenuation statistics in this case have been tested by the comparison with the experimental statistics only for Dubna (Ref 3,4).

As a result of this investigations the computer program for the attenuation statistics prediction on the terrestrial link has been developed.

REFERENCES

1. Kawecki A, Svjatogor V. 1993, Rain rate characteristics in Warsaw and in Dubna. *Ann. Telecommun.*, 48, 5-6, p.283.
2. Alexandrova E. et al. 1990, Terrestrial propagation experiments in the 11 - 30 GHz frequency band in the Dubna - Intercosmos international experimental area. *Proc. 20th Europ. Microwave Conf.* Budapest.
3. Alexandrova E. et al. 1991, Statistical characteristics of the attenuation of radio-waves with the frequencies above 10 GHz on terrestrial links, *Radiotechnica i elektronica*, 36, 4, p.689-700. (in Russian).
4. Pozhidayev V., Svjatogor V. 1992, Methods for calculations of radiowave attenuation probability distributions on terrestrial roots due to abnormalities of the air refractive index profiles, *Radiotechnica i elektronica*, 37, 7, p.1172. (in Russian).

**RADIOMETEOROLOGICAL PARAMETERS AND SIGNAL FLUCTUATION
CHARACTERISTICS OF THE TROPOSPHERIC PATHS OF
THE PACIFIC OCEAN'S COAST**

Batueva E.V., Darizhapov D.D

Buryat Nature Sciences Institute of Siberian Dept. of the Russia Academy of Sciences,
6 Sakhyanova, 670042 Ulan-Ude Russia

Tel. (8-30122) 3-62-60, Fax (8-30122) 3-28-41, E-mail Relcom: root@bien.buriatia.su

ABSTRACT

The necessity of providing VHF propagation under different physico - climatic conditions of the globe demands scrupulous study of radiometeorological parameters of atmosphere. It concerns also vast territories of the Pacific Ocean's coast scantily explored from this point of view.

Investigations of the lowest atmospheric layer values for refraction coefficient N and its vertical gradients G_n (to the height 3000 m above the station level) have been performed according to the average data during 10 years (1961-1970) for 21 stations of aerological radioexploring. Besides, integral statistic distributions N and G_n have been constructed according to direct data of the aerological radioexploring.

Types of seasonal and daily variations N and G_n have been revealed, statistic moments have been calculated, superrefractive conditions have been discovered and there have been shown mechanisms of its formation during the investigation.

Keywords: Refraction Coefficient, Signal, Vertical Gradient, Tropospheric

INTRODUCTION

The increase of effectivity and reliability of radioelectronic means for different purpose causes the necessity of investigation of atmosphere's refractive characteristics. On the other hand in recent years the interest towards results of these investigations has greatly increased because of the necessity of providing electromagnetic compatibility with radioelectronic means (EMC PET) just in quite different physioclimatic conditions of the globe.

If radiometeorological parameters of the troposphere in moderate climatic conditions are studied in detail, where seasonal variations N have simple motion with one maximum in summer and one minimum in winter, then in the regions, subjected to the atmospheric processes taking

place between the Asian continent and the Pacific ocean, such investigations have incomplete character. Only separate information concerning this problem in the coastal regions of the Far-East can be got from works of B.R.Bean and E.G.Dutton.

RADIOMETEOROLOGICAL PARAMETERS

The region of the Far East under investigation is characterised by large spectra of radiometeorological conditions and it's situated in the area from subarctic latitudes to moderate ones. In order to have characteristics of space - time distribution of radiometeorological parameters of troposphere, lowest atmospheric layer values for refractive coefficient N and its vertical gradients G_n have been found by virtue of data of hydro-meteorological stations and aerological exploring ones situated in different latitudes of the coast zone.

Both the lowest atmospheric layer values of refractive index and its vertical gradients have been obtained according to averaged data for 10 years (1961 - 1970). Radiometeorological parameters under consideration have been calculated according to data of more than 20 stations of aerological radiosounding.

As a result, seasonal variations of radiometeorological parameters and also daily allowance variations N and G_n have been plotted for different seasons of a year.

During analysis of obtained results we have revealed two types of seasonal variations N in regions under consideration. The first type is with 2 maximums (in winter and in summer) and two minimums (in spring and autumn) and coincides with seasonal variations N in sharply continental regions of moderate latitudes. Unlike the variation N in continental regions, the principal maximum in the coast zone is observed in summer. The second type has maximum in summer and one minimum in winter and so it's appropriate to the atmosphere of moderate climatic zone.

In these regions seasonal variations of th

vertical gradient G_n are characterized by two types. The first type is with two maximums (in winter and in summer) and two minimums (in spring and in autumn) and so it's analogous to the variation N of the first type. The second type is with two maximums (in spring and in autumn) and two minimums (in winter and in summer). This type of the seasonal variation seem to be opposite in phase to the variation G_n , observed in sharply continental regions.

Two types of daily variations have been revealed. Summer and winter daily and nightly maximums in spring and autumn are characteristic of the subarctic climatic zone, in other seasons summer morning maximums and nightly maximums are characteristic of the subarctic climatic zone, in other seasons summer morning maximums and nightly maximums are characteristic of the moderate climatic zone.

At the same time for obtaining principal statistic characteristics, integral distributions N and G_n have been plotted in virtue of direct data of aerological radiosounding performed during a year. Statistic integral distributions for stations of the subarctic climatic zone are submitted to the normal law of the distribution of accidental values.

As a result of this research, superrefractive conditions have been discovered at the station Marcovo. It has been observed in lowest atmospheric layer of the atmosphere of 100 metres wide and with probability of 10%, and the same was for the level of 200 metres wide and with probability of 4%. Super-refractive conditions are occurred mainly at night but there were cases when they are observed at day. It follows from the study of the mechanism of formation of super-refractive conditions in lowest atmospheric layer that atmospheric processes taking place under the influence of boundary land-sea have dominating character for this formation and also intensive freezing of earth surface at night and

intensive evaporation at day. In addition data of statistic moments of the second, third and fourth order are given.

These values obtained from integral distributions of values G_n in layer 2-200 m. that were constructed separately for every month for four stations of investigated region - Gyzhiga, Anadyr, Marcovo, Magadan. It is revealed the changing values range of refraction coefficients gradients G_n (1 - 99%). In winter median values G_n of subarctic Marcovo station according to absolute values are essentially higher than analogous values for other seasons. The median absolute values for this station exceed the gradient value for standard atmosphere. On the coastal subarctic stations Anadyr and Gyzhiga the winter median value G_n is less than on the continental Marcovo station. The median values of G_n for these stations are slightly exceed the normal atmosphere gradient. The south further the cyclone activity is became stronger and situation transformed. For Magadan station the absolute values of winter median G_n is less than summer one. All median values of G_n for this station are close to value for standard radioatmosphere.

SIGNAL FLUCTUATION CHARACTERISTICS

Investigation of the transhorizon tropospheric signal level are made on the 205 km radioline passed through the coast of Okhotsk sea. The equivalent distance for the normal refraction calculated by more precise methods, is equal 167 km. The standard apparatus "Horizont - M" are used for measurements.

The average signal level on given radioline has the seasonal variations with two maximums (in winter and in summer) and two minimums (in spring and in autumn). This is in good agreement with seasonal variations of radiometeorological parameters for mentioned region.

Session 9: Clear air IV

ALGORITHM FOR COMPUTING TRAJECTORY PARAMETERS OF EM WAVES IN A SPHERICALLY STRATIFIED ATMOSPHERE

V.A.Parshukov¹, A.Yu.Zrazhevsky², Ye.P.Novichikhin³

1,2,3-IRE, Mokhovaya St., 11, Moscow, 103907, Russia

Tel.:(095)202-50-49, Fax:(095)203-84-14, E-mail:<root@ire.msk.su>

ABSTRACT

The algorithm for computing trajectory parameters of EM waves between transmitter and receiver (departure and arrival angles, total angular refraction, geometric and apparent range) serves to determine all the possible paths between two points with any specified coordinates and under any profiles of the atmospheric refractive index $n(H)$.

Keywords: Refraction Effects

1. INTRODUCTION

Analysis shows that profile $n(H)$ within the atmospheric border layer may run through strata with different gradients of the refractive index ($g>0$, $g=0\dots-40$ N units/km, $g=-40\dots-157$ N units/km, and $g\leq-157$ N units/km) characterizing diverse types of refraction, and these strata may be located in a different order. In such an environment, there may be no connecting path between two points (transmitter and receiver), the ray path may change its direction vertically, and the two points may be connected by several paths as a result of refraction. The proposed method has been developed for these and any other conditions.

2. ALGORITHM

The input data are profile $n(H)$, the true coordinates of the receiver, and the true or apparent coordinates of the transmitter. The atmosphere is divided into spherical

layers with a constant gradient of the refractive index within each layer.

Our method implies a bending of the ray within each layer, without any refraction at the boundaries between the layers. The angular characteristics of the ray path are determined with the use of the geometrical optics ray-tracing technique.

The trajectory of ray i within the layer starting from level k is computed in accordance with Table 1, and is characterized by the following parameters:

1. Angles of ray departure from the respective level θ_k , θ_{k+1} or θ_{k-1} (elevation angles).
2. Total angular refraction τ_k or τ_{k-1} .
3. Angular distance ϕ_k or ϕ_{k-1} (angle at the earth's center).
4. Geometric distance along the ray path S_k or S_{k-1} .
5. Apparent distance L_k or L_{k-1} .

The trajectory depends on the value of this expression (Snell's law for a spherically stratified atmosphere):

$$y_{k\pm 1} = \frac{n_k \cdot (a + H_k) \cdot \cos \theta_k}{n_{k\pm 1} \cdot (a + H_{k\pm 1})},$$

where a is the earth's radius, and H is the height of the respective level; the $k+1$ subscript refers to the upward ray path, and the $k-1$ subscript, to the downward ray path.

The expressions in Lines 1, 2 and 3 of Table 1 are given in (Ref.1,2). The formula in Line 4 of Table 1

was obtained on the assumption that the ray trajectory within a layer constitutes an arc.

Table 1: Algorithm for Computing Trajectory Parameters ($j=k$ for upward path, $j=k-1$ for downward path)

$y_{k+1} < 1$	
1.	$\theta_{i,k+1} = \arccos y_{k+1}$
2.	$\tau_{i,j} = \frac{2 \cdot (n_j - n_{j+1})}{\operatorname{tg} \theta_{i,j} + \operatorname{tg} \theta_{i,j+1}}$
3.	$\phi_{i,j} = \tau_{i,j} - \theta_{i,j} + \theta_{i,j+1}$
4.	$S_{i,j} = \frac{\tau_{i,j} (a + H_{j+1}) \cdot \sin \phi_{i,j}}{2 \cdot \sin(\tau_{i,j} / 2) \cdot \cos \theta_{i,j}}$
5.	$L_{i,j} = S_{i,j} \cdot (n_j + n_{j+1}) / 2$
$y_{k+1} \geq 1$	
6.	$b_{i,k} = \frac{-(-1)^{j-k} \cdot \theta_{j,k}^2}{2[g_j / n_k + 1 / (a + H_k)]}$
7.	$H_{k+1}^* = H_k \pm b_{i,k}$
8.	$n_{k+1}^* = n_k \pm g_j \cdot b_{i,k}$
9.	$\theta_{i,k+1}^* = 0$

Total angular refraction and the angular, geometric and apparent distance between the two points are computed by summing up the respective values for each layer.

The condition $y_{k+1} > 1$ means that the ray cannot reach the next level, and that there is a change in the

vertical direction of the ray path. The turning points are marked by additional H_{k+1}^* levels, whose heights were determined by means of the technique given in (Ref. 2) for calculating the duct penetration angle ($y_{k+1}=1$). The parameters of the additional levels are determined in accordance with Lines 6-9 of Table 1.

The parameters of each entire path connecting the two points are computed layer by layer, from the lower to the upper point (transmitter or receiver). In order to detect all the paths connecting the points, use was made of elevation-angle scanning of the area around the upper point.

In mathematical terms, the task is to find the solutions of an equation of the form $F(x)=0$, which assumes the equality of two total angular distances. One of these is determined through path computation, and the other—through the specified coordinates of the two points.

A comparison of total angular refraction computed by means of our algorithm with that computed through the refraction integral (Ref. 2) shows that the accuracy of computations for the algorithm is approximately 1 sec of arc throughout the entire refracting atmosphere and across the whole range of elevation angles.

3. COMPUTATION EXAMPLE

To illustrate the potentialities of the algorithm, let us calculate the apparent elevation angles to the transmitter under the following conditions: receiver height - 60 m, transmitter height - 70 m, the distance between them - 10 km along the earth's surface, the earth's average radius - 6,371 km. Table 2 shows the refractive index profile constructed for this example, and Table 3, the results of computations.

Table 3 shows that in the given

conditions there are nine possible ray paths between the transmitter and the receiver.

Our method makes it possible to solve the problem of communication between two points under any conditions in a spherically stratified atmosphere. Refractive index profiles obtained from standard weather observations made on meteorological masts, from radiosonde data, or from various atmosphere refractivity models may be used in the computations.

Table 2: Refractive Index Profile

Height above the surface (m)	$N = (n-1) \cdot 10^6$ (N units)
2	182.0
30	280.0
40	315.0
60	326.0
70	325.6
90	304.0
105	247.0

Table 3: Apparent elevation angles to transmitter

Ray number	Angle (min)	Ray-turning height (m)
1	1.43	-
2	5.76	72.79
3	8.28	74.41
4	29.05	95.06
5	38.38	102.37
6	-3.15	59.41
7	-6.60	57.39
8	-30.09	33.39
9	-37.49	27.60

4. REFERENCES

1. Schulkin M. 1952, Average radio-ray refraction in the lower atmosphere, Proc. IRE, 40, 5, pp.554-561.
2. Bean B.R., Dutton E.J. 1966, Radio Meteorology, Boulder, National Bureau of Standards.

STATISTICAL CHARACTERIZATION OF RADIO REFRACTIVITY IN CAIRO

Amany K.Farrag¹ and Ahmed A.Hassan²

1-National Telecommunication Institute

Tel: +202 2636849, Fax: +202 2636802, E-mail: Amany@NTI.EG

2-Egyptian Meteorology Authority

Tel: +202 830053

ABSTRACT

This paper presents some of the obtained results describing the behaviour of the surface radio refractivity in Cairo. Average, minimum and maximum monthly values of N_s for two consecutive years are presented. Cumulative probability distribution of N_s for the four seasons of each year are also presented.

1.INTRODUCTION

The gaseous constituents of the atmosphere influence the propagation of radio waves by varying the refractive index in time and space causing refraction, reflection and guiding or scattering of the waves. This variation of the refractive index at a point in space is mainly due to the variation in temperature and water vapour concentration. It may occur on a short-term scale causing small-scale irregularities or turbulent fluctuations or on a longer time scale causing for example ducting. As these variations depend on the climatic condition one can not neglect the effect of topographical condition. Therefore, it is important to study the dynamic behavior of the refractive index all over the world.

In 1984 H.N Kheirallah et al. [1] presented a preliminary investigation of the behaviour of refractive index in

Marsa Matrouh. This study shows that Marsa Matrouh suffers from large refractive index variation. This is mainly due to the location of this city. It is bounded from the north by the sea (Medetirenian) and from the south by the desert (West Desert).

On the other hand multipath fading phenomena on microwave links in Egypt has been investigated in Egypt [2,3]. From the obtained results it has been concluded, that the dynamic behaviour of the refractive index in Egypt must be investigated.

Based on the above given conclusion, we decided to continue the study of the dynamic aspect of the refractive index started in 1984.

2.THE RADIO REFRACTIVITY FORMULA

It is well known that the atmosphere can be described by the radio refractive index n . As n is close to one, it is more convenient to utilize radio refractivity N , which can be expressed by [CCIR Rec. 453-3]

$$N = (n - 1)10^6 \\ = \frac{77.6}{T} \left[p + 4810 \frac{e}{T} \right] \quad (1)$$

where

p : atmospheric pressure (hPa)

e : water vapour pressure (hPa)

T : absolute temperature (K)

The relation ship between water vapour pressure e and relative humidity H is given by

$$e = \frac{He_s}{100}$$

with

$$e_s = a \exp \left[\frac{bt}{t+c} \right] \quad (2)$$

where,

H : relative humidity (%)

t : Celsius temperature($^{\circ}\text{C}$)

e_s : saturation vapour pressure in hPa at the temperature t and the coefficients are ($a = 6.1121$, $b = 17.502$, $c = 240.97$)

3.DESCREPTION OF THE DATA

The results presented in this paper are based on data collected by one weather station in Cairo. The station is located to the north of Cairo. The station is lying within the desert, but not far from the Nile valley. The data was collected each hour by using weather measuring instruments located on the ground of the station.

4.NUMERICAL RESULTS

The surface radio refractivity N_s were calculated for two calender year 1989 and 1990. Samples from the obtained results are presented in this section. In Fig.1and3 the minimum, maximum and average value N for each month for the two years is given. From this figure it is clear that the refractive index reaches its maximum value during the summer season (June, July, August) where the maximum value ($N_s = 381.25$ N unit) occurred in July and the minimum value ($N_s = 287.5$ N unit) occurred in May. Following the cumulative probability distribution for the four seasons given in

Fig.2 and4 we see that for the summer and autumn season about 50 % of the value of N_s is greater than (340-N unit). Diurnal distribution of the data shows that N_s reaches its maximum value during midnight or in the early morning. From Fig.5and 6 it is clear that the diffence between the maximum and minimum values of N_s during the winter months is much smaller than for summer months

5.CONCLUSION

The dynamic behaviour of the surface radio refractivity for two calandar years (1989-1990) in Cairo is presented.

The obtained results indicates that N_s reaches its minimum value during the winter season and the maximum value during the summer season. These results agree with those obtained previously [1].

6.REFERENCES

1. H.N. Keirallah et al. 1984, Refractive Index Statistics for Mersa Matrouh, 2nd National Radio Science Symposium, Cairo, March 1984, pp. 64-70
2. et al., Multipath fading Phenomena on Microwave L.O.S., 1st workshop Cairo 1988
3. O.L.El-Sayed et al., Multipath Fading Phenomena L.O.S. 2nd workshop Cairo 1989

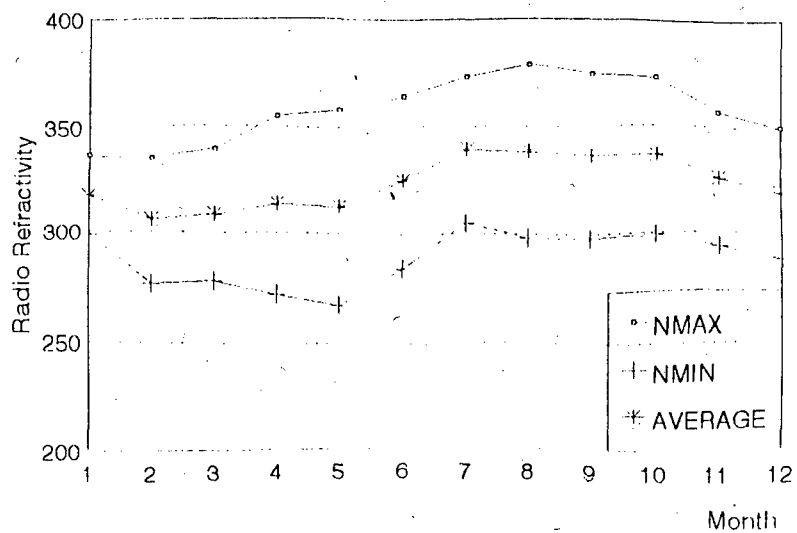


Fig. 1

YEAR-1989

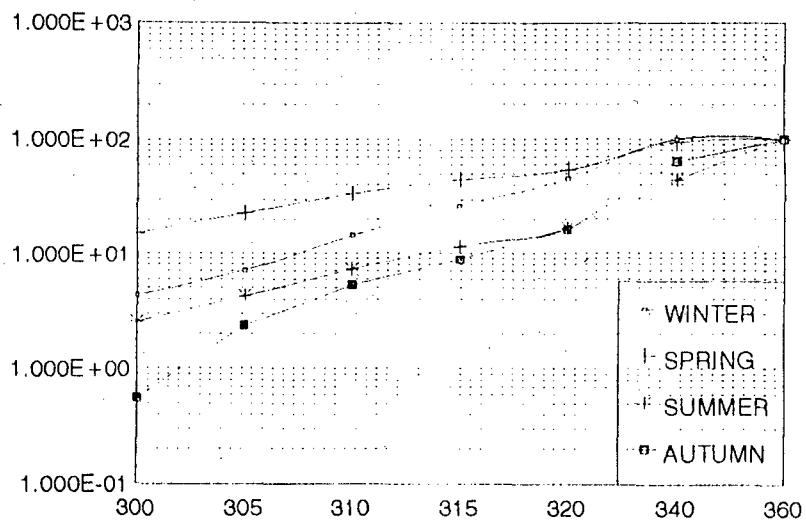


Fig. 2

YEAR-1990

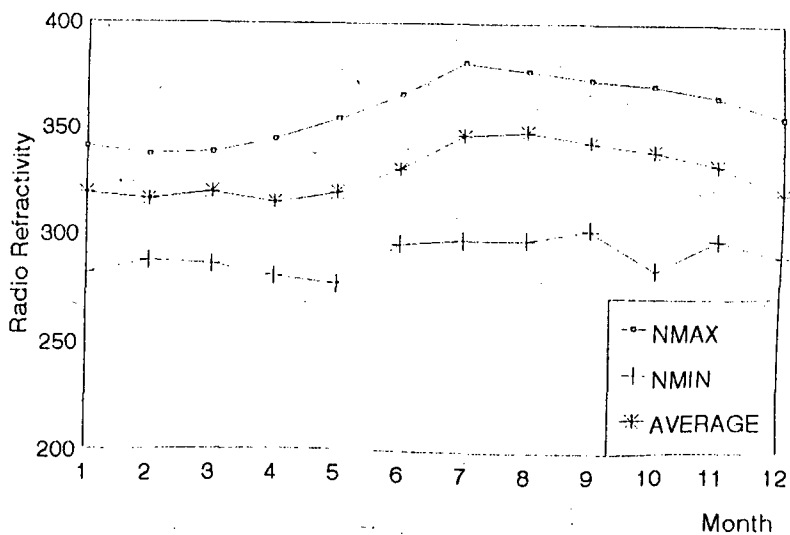


Fig. 3

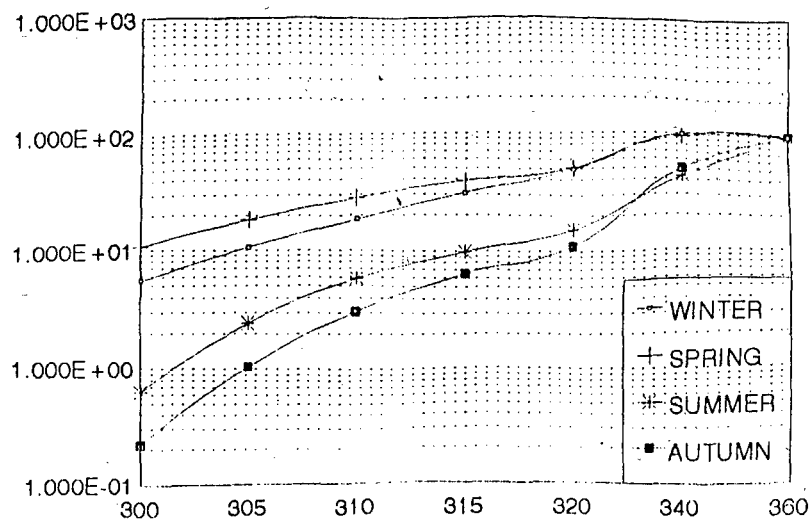


Fig. 4

JANUARY-1990

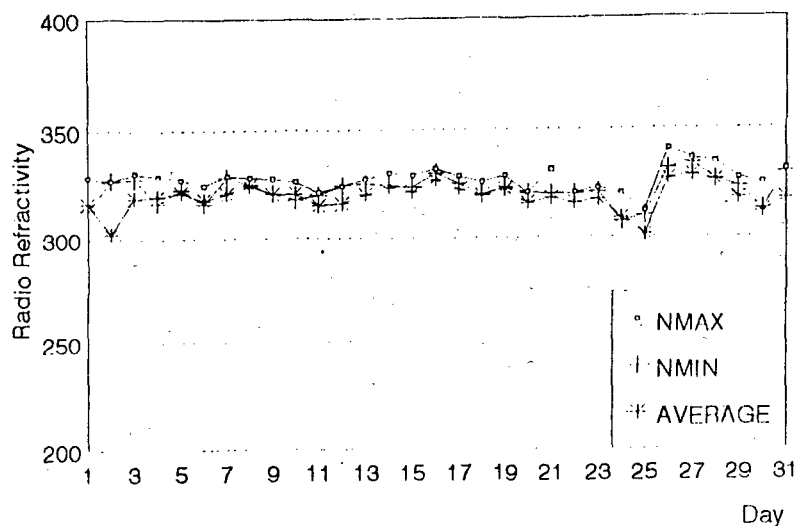


Fig. 5

JUNE-1990

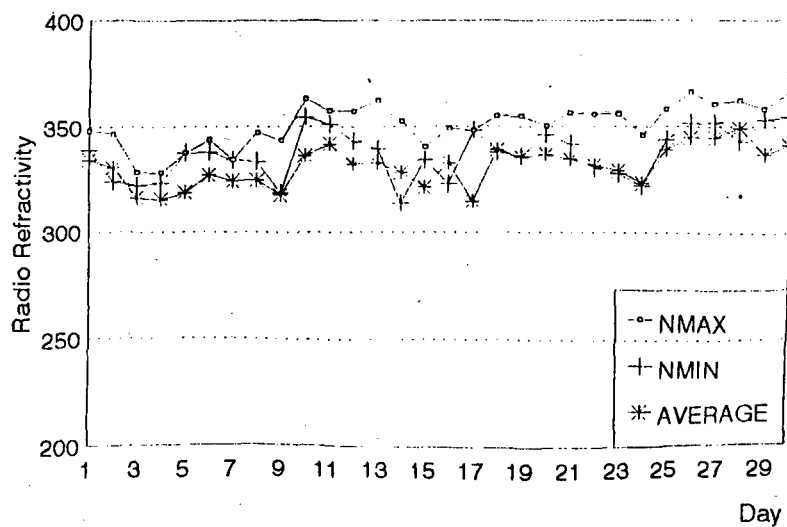


Fig. 6

RADIOMETEOROLOGICAL PARAMETERS MODEL OVER RUSSIA REGION

G. S. Zhamsuveva, D. D. Darizhapov

Buryat Nature Sciences Institute of Siberian Department of the Russia Academy of Sciences, 6 Sakhyanova, 670042 Ulan-Ude, Russia

Tel. (8-30122) 3-62-60, Fax (8-30122) 3-28-41, E-mail Relcom: root@bien.buriatia.su

ABSTRACT

This paper deals with the investigation of super-refractive conditions of VHF-propagation in high and moderate latitudes of the troposphere. For these regions expression describing radio duct occurrence is derived. It is necessary for the prediction of anomal high signal levels. Quantitive model of atmosphere's radio refractive index in time region is constructed. Also radiometeorological maps of effective earth's radius, maps of year's variations of radio refractive index and vertical gradients of radio refractive index over Russia region are given in this paper.

Keywords: Atmosphere, Refractive, Wave, Propagation

INTRODUCTION

Investigation of physical regularities of the formation of anomalous conditions and the study of troposphere signal fluctuation characteristics are closely connected with the problem of electromagnetic compatibility. Further work on this problem is, however, badly needed, especially in the case of high latitudes. Refraction influence on VHF-propagation is not significant in the troposphere similar to standard one. In regions with sharply continental climate considerable inversions can be appeared so that high values of the refraction coefficient will be observed. Therefore the refraction influence on VHF-propagation significantly increases. It was found that in sharply continental and extreme climatic conditions the winter season is the worst from the standpoint of electromagnetic compatibility.

SUPER-REFRACTIVE CONDITIONS

Statistical vertical gradient distributions of the refractive index in atmosphere's land layer up to

1000 m have been obtained according to the data of aerological radioexploring during 3 years. Measurements are performed at two stations situated in extreme climatic regions (Vakutsk, Verkhovansk). It was founded that in sharply continental and extreme climatic regions super-refractive conditions appear in winter owing to intensive inversions influenced by Asian anticyclone. A duct occurrence probability of super-refractive conditions in atmosphere's land layer is greater than in elevated one, decreases with the rise of its power and the height of lower boundary. At st. Vakutsk occurrence sum of radio duct in summer and winter is 25% from the total number of measurements. Maximum of radio duct occurrence is observed in February and is 11% from the number of winter measurements. Accordingly it was 6.2% and 3.8% in December and January. At the Verkhovansk maximum of radio duct occurrence is observed in February and is 8.6% from the number of winter measurements. Super-refractive conditions of VHF-propagation often are observed at night time. Besides surface atmospheric radio duct there are elevated radio duct. For example radio duct occurrence is observed in December about 2 percent for the total winter measurements. The distribution function for refractive index $F(g_n)$ can be approximated by exponential function both for upper layer and for atmosphere land layer (Refs. 1,2)

$$F(g_n) = \frac{1}{2} \exp(4(g - g_m)/3\sigma), \quad -\infty < g \leq g_p \\ F(g_n) = \frac{1}{2} \operatorname{erfc}(-(g - g_m)/\sqrt{2}\sigma), \quad g_p < g < +\infty$$

where $g_p = g_m - 1.48\sigma$, $g_m = \Delta N$, $\sigma = \sigma_{\Delta N} / \sqrt{\Delta h}$.

$\Delta N, \sigma_{\Delta N}$ average monthly values of refractive index and standard derivation for 1-km layer above terrestrial surface, Δh - thickness of the layer under consideration.

Radio duct occurrence probability can be denoted as the percentage of time that refractive index g is less than $-157 \cdot 10^6$ 1/km, or refractivity gradient is less than 0 NU/km. Therefore, distribution function for refractive index $F(g_n)$ of $g < 0$ is given by the following exponential function:

$$P_{<0} = \frac{1}{2} \exp \left(- \frac{4\bar{z} \sqrt{\Delta h}}{3\sigma_{\Delta N}} \right).$$

As a result of total analysis of super-refractive occurrence following expression describing the radio duct occurrence in extreme climatic regions is:

$$P = \frac{1}{2} \exp \left(- \frac{4\bar{z} \sqrt{0,052 - 0,464h}}{3\sigma_{\Delta N}} \right),$$

where $\bar{z} = \Delta N + 157$ (1/km)

According to this expression one can determine the radio duct occurrence for arbitrarily choosed value h when ΔN and $\sigma_{\Delta N}$ are given. The probability can be calculated for an arbitrarily selected g_{Δ} value.

Also radiometeorological maps describing regions with super-refractive conditions are given in this paper.

QUANTITATIVE MODEL

Numerical modelling of the conditions of electromagnetic wave propagation in the atmosphere is the most effective research method of particularities of radiowave propagation in the specific radiometeorological conditions. In the most broad outline the structure of the model includes initial meteorological data and fundamental equations describing physical processes realised as computer programs.

For mathematical description of seasonal variations of the radio-refractive index of air N at the earth surface actual data of 146 Russia stations of aerological radiosonding covering different physico-climatic zones and embracing ten-year period are used. Values of refractive index N for each station and each month are calculated by the averaged values of meteorological elements. Seasonal variations of N by amplitude and by nature of curve of the annual variations differ highly all over the territory of the Russia. This article is an attempt to generalize analitically particularities of VHF refraction in atmosphere's boundary layer which concern seasonal variations of physical processes in it, e.g. to construct a model satisfying seasonal and climatic fluctuations of the mean structure of atmosphere refractive index. Probability characteristics of atmosphere refractive index depend periodically upon the time with the period $T = 12$ months. Because of seasonal variations mean values of N (averaged for ten years) are periodic functions of time with the period of 12 months. Therefore they may be represented as Fourier's series.

Each realisation of the function $N(t)$ has the ergodic property. Under the fulfilment of ergodicity conditions, coefficients in the Eq.1 are determined over a isolated realisation $N(t)$ with time averaging. The suggested procedure allows to get in analitic form Eq.1 seasonal variations of statistic characteristics of the refractive index of air at the earth surface. Having solved the problem of an approximate representation of seasonal variations of N by trigonometric polynomial we find the coefficients and for each station. In the expansion of $N(t)$ in an infinite Fourier series only two first harmonics are of great importance. Then the Fourier's series Eq.1 gets a form as following:

$$N(t) = \frac{1}{2} a_0 + a_1 \cos \frac{2\pi}{T} t + a_2 \cos \frac{4\pi}{T} t + b_1 \sin \frac{2\pi}{T} t + b_2 \sin \frac{4\pi}{T} t \quad (1)$$

The amplitude of seasonal variations, the coefficients a_0, a_1, a_2, b_1, b_2 depend on the meteorological and climatic conditions of a region under investigation.

As a result of the substitution of the specific value of t in the equations mentioned above we can obtain mean values of N for a given month on the examined region. The calculation error of N is 1-2 N -units.

Such a form of representation of $N(t)$ corresponds to an analytical expression of region-seasonal model of the refractive index in boundary layer of atmosphere. The region-seasonal model of the refractive index in boundary layer of atmosphere may be used for prediction of VHF propagation conditions on near-earth paths, as well as in different automated design and control systems, using tropospheric radio-channels.

REFERENCES

1. Osami Sasaki and Tadashi Akiyama. In: IEEE Trans. Antennas Propagat., AP-30(1982), p.853
2. Tadashi Akiyama. In: Review of the Electrical Communication laboratories, 25(1977), p.79

TRANSHORIZON WAVE SCATTERING AND THE PROBLEM OF PREDICTION OF FIELD NONENERGY CHARACTERISTICS

Ju.P.Akulichev, V.A.But'ko, M.E.Rovkin

TACSR, 40, Lenin av., Tomsk, 634050, Russia,

Tel: +7(3822)496488, Fax: +7(3822)223262, E-mail: root@orts.tiasur.tomsk.su

ABSTRACT

The problem of prediction of the electromagnetic field nonenergy parameters (such as fading depth, spatial, frequency and temporal correlation intervals, cross-correlation function maximum shift) along transhorizon troposphere paths by length of 200-500 km over 100-3000 MHz frequency range are discussed. There are used both radiosonde and electromagnetic field measurements data.

There was discovered that the most useful information for the field parameters prediction is contained in the results of the crosspath wind velocity measurements in the scattering volume.

Keywords: Beyond-the-Horizon Wave Scattering, Prediction, Field Coherence.

1. INTRODUCTION

The principal peculiarity of the transhorizon troposphere channel is that the field $E(t, r)$ in point r , caused by the harmonic oscillation source with frequency ω placed in point r_s , is random and depends on all variables: t, ω, r, r_s . The most important characteristic of the channel is attenuation coefficient V_T . In experimental researches it is evaluated as

$$V_T = 10 \lg \int_0^T |E(t', r)|^2 dt' / |E_0(t, r)|^2, \quad (1)$$

where E_0 is the free space field under the same conditions.

In practice the problem of transhorizon wave scattering conditions prognosis are usually understood as the estimation of the attenuation coefficient. On the other hand there are lot of other parameters, which describe the spatial-frequency-temporal scattered field coherence and influence the efficiency of radioengineering systems using beyond-the-horizon radiowave propagation.

First, it's the parameter σ_x , which is numerically equal to r.m.s. fluctuations of the signal magnitude logarithm in temporal interval T . The value of σ_x depends on the signal fading depth.

Second, it's important to know the values of the correlation intervals corresponding the temporal diversity τ_0 , the frequency diversity F_0 and the horizontal crosspath diversity l_0 . Each of this intervals is usually determined as diversity which gives the received signals correlation coefficient equal to $1/e \approx 0.37$.

Third, when complex diversity is used it's necessary to find the formula for the multi-dimensional correlation function. The simplest case is when multi-dimensional correlation function is equal to the product of correlation functions describing the particular diversities. For example, for spatial-temporal diversity:

$$R(\Delta t, \Delta x) = R_t(\Delta t) R_x(\Delta x). \quad (2)$$

Obviously, that formula (2) can be true only in the absence of wind. The theoretical and experimental data show that there are shifts of two received signals cross-correlation function maximum, that depend on crosspath wind velocity.

It's clear, that nonenergy field parameters influence the efficiency and even the possibility of spatial-temporal coherence method of signal reception. These parameters change in time randomly due to variations of the radiowave propagation conditions.

The possibility of prediction of the expected values of this field parameters for frequencies 100-3000 MHz over transhorizon sea paths by length of 200 - 500 km is discussed in this paper.

Two ways of prediction are considered. The first is founded by using of radiosonde measurements. The second way is based on using measurements of some transhorizon source field parameters. Then some interpolation and extrapolation methods can be used for evaluation of expected parameter values.

2. FADING DEPTH

The joint measurements of electromagnetic field magnitude and troposphere characteristics by means of radiosondes had been carried out over the period of May, 1983 - December, 1984 over the paths by length of 440 - 495 km ($\lambda = 10$ cm) and 495 km

($\lambda = 185$ cm) over the Okhotsk Sea. All receivers were placed on the western coast of the Iturup Island. Receiving and transmitting antennas heights above the sea level were equal to 25 and 36 m respectively.

Radiosonde measurements were made in four points which were placed 100 - 200 km from the path ends. There had been made measurements of the refractive index, its gradient and wind velocity at different heights.

The maximum values of correlation coefficient σ_x with the «best» meteoparameter (the best ones appeared to be refractive index over the sea surface) are equal to 0.41, 0.52 and 0.56 for $T = 5$ min, 30 min and 3 hours respectively. These values are too small for σ_x prediction based on radiosonde measurements, i.e. the error of prediction isn't less than 83%. It can be noted for the comparison that the r.m.s. prediction error of the attenuation coefficient based on the same radiosonde data can be about 50 %. Probably this is caused by the fact that r.m.s. variations of σ_x were only 1.3 - 1.5 dB. Autocorrelation functions of V_T and σ_x variations are given in Figures 1 - 2 for both wave ranges ($T = 30$ min). One can see that if σ_x have been measured in some temporal point the prediction of the expected value of this parameter σ_x with error of 50 % is possible in 0.5-hour interval only in meter wave range.

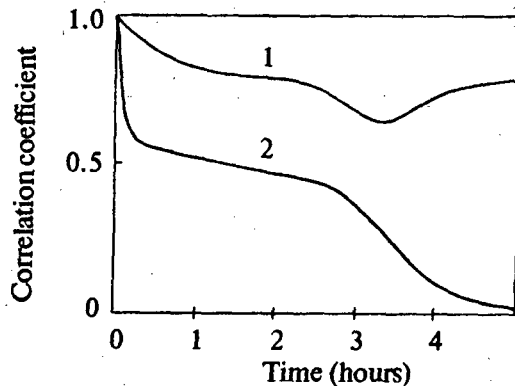


Figure 1: Autocorrelation function of the attenuation coefficient (1) and r.m.s. signal level variations (2), $\lambda = 10$ cm, $T = 30$ min

The dependence of σ_x on other field parameters (attenuation coefficient, correlation intervals) had not been detected.

3. CORRELATION INTERVALS

The experimental by found dependence between the field correlation intervals and radiosonde data

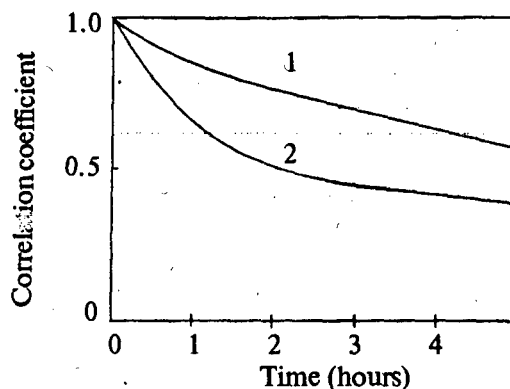


Figure 2: Autocorrelation function of the attenuation coefficient (1) and r.m.s. signal level variations (2), $\lambda = 185$ cm, $T = 30$ min

was not investigated. The measurements of the temporal correlation intervals for wavelength $\lambda_1 = 10$ cm, $\lambda_2 = 35$ cm, $\lambda_3 = 185$ cm were made over the beyond-the-horizon 495-km path over the Sea of Okhotsk in July-August 1985. The good approximation for empirical distribution function is

$$F(\tau_0) = 1 - \exp(-\tau_0/m), \quad \tau_0 \geq 0, \quad (3)$$

where $m = 0.6, 1.28$ and 16.1 s for λ_1, λ_2 and λ_3 ($T = 3-5$ min). The empirical distribution of the quotient of $\tau_0(\lambda_j)$ and $\tau_0(\lambda_k)$ for the different wavelengths λ_j and λ_k are given in Figures 3 - 5 where N is the number of experimental points. The mean value of this quotient corresponds to the formula

$$\overline{\tau_0(\lambda_j)/\tau_0(\lambda_k)} \approx \lambda_j/\lambda_k. \quad (4)$$

This fact is in agreement with the conclusion given by theory of wave multiple scattering from the small-scale tropospheric inhomogeneities (Refs.1,2) and with the experimental results obtained over the 225-km path over Black Sea for the same operating frequencies (Ref.3).

The spread in values of the quotient is rather large due to significant frequency diversity so it is impossible to point out now what is the accuracy of the τ_0 extrapolation in the frequency domain. Estimates of the spatial correlation intervals have been also made during the experiment and we can repeat the above mentioned conclusion with respect to l_0 . The features of the frequency correlation interval were studied worse.

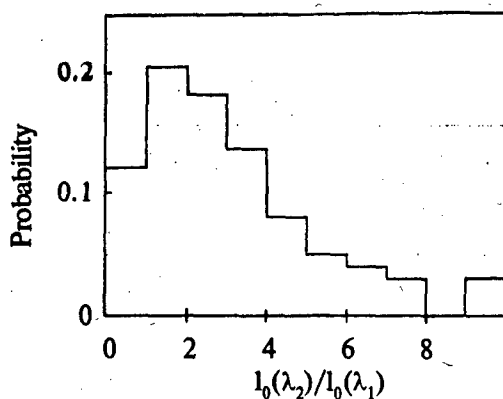


Figure 3: Empirical distribution of the quotient of $\tau_0(\lambda_1)$ and $\tau_0(\lambda_2)$, $\lambda_1 = 10$ cm, $\lambda_2 = 35$ cm, $N = 73$

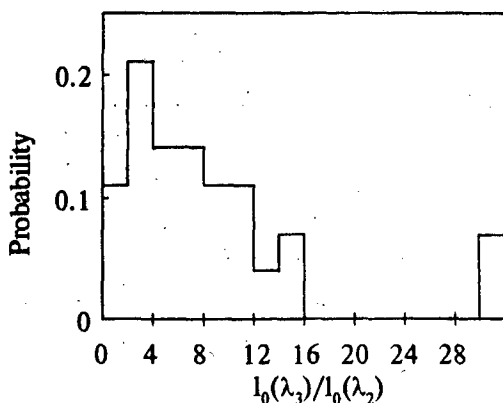


Figure 4: Empirical distribution of the quotient of $\tau_0(\lambda_2)$ and $\tau_0(\lambda_3)$, $\lambda_2 = 35$ cm, $\lambda_3 = 185$ cm, $N = 28$

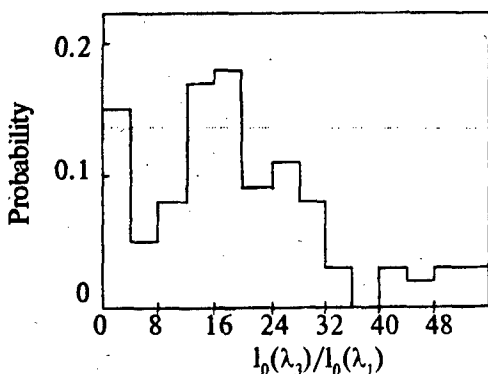


Figure 5: Empirical distribution of the quotient of $\tau_0(\lambda_1)$ and $\tau_0(\lambda_3)$, $\lambda_1 = 10$ cm, $\lambda_3 = 185$ cm, $N = 66$

4. PARAMETERS OF THE MULTIDIMENSIONAL CORRELATION FUNCTIONS

4.1 Joint spatial diversity of the transmitters and receivers

The experiments of such type have been made in period July-August 1985 over the the 495-km path

over the Sea of Okhotsk. The crosspath spatial diversity of two transmitters was $d_1 = d$ and the similar diversity of two receivers was $d_2 = \pm d$. The first observations have shown that a lot of information can be derived when $d = 90$ m for $\lambda = 185$ cm.

The empirical distribution functions of the correlation coefficient of two signals over the parallel, divergent (convergent) and crossed path are given in Figure 6 for $T = 5$ min. It is seen clearly that the propagation conditions varied during the period of observation.

The empirical distribution function of the value

$$\gamma = I_p/I_c, \quad (5)$$

where I_p and I_c are the estimates of the spatial correlation intervals over the the parallel ($d_1 = d_2$) and crossed ($d_1 = -d_2$) paths which have been made at the same moment, is shown in Figure 7.

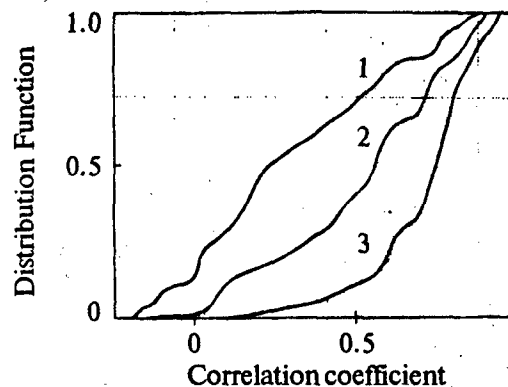


Figure 6: Distribution functions of the correlation coefficient of signals over the crossed (1), divergent (2) and parallel (3) paths

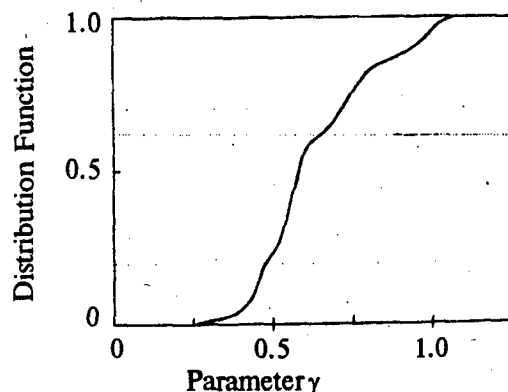


Figure 7: Distribution functions of parameter $\gamma = I_p/I_c$

The analysis of multiscatter problem in Markov's random process approximation (Ref.2) gave the restriction $\gamma < 1$ and showed that there was shift of the maximum of the mutual correlation function $R(d_2, d_1)$, i.e. correlation coefficient of two received signals was maximal when the diversity of receivers was equal

$$d_2' = -d_1[(1-\gamma^2)/(1+\gamma^2)]. \quad (6)$$

There had been noticed that γ grew little when the signal was strong. The comparison of d_2' , γ and radiosonde data wasn't carried out.

4.2 Joint spatial-temporary diversity

The three-dimensional correlation function $R(d_1, d_2, \Delta t)$ must be used for the description of the field fluctuations. It depends on γ and crosspath wind velocity V (Ref.2). The last dependence is very strong. The best illustration of this conclusion is the data of joint measurements of wind velocity by two methods.

The first is based on analysis of correlation function of two signals over the parallel paths, the second is the usual radiosonde method which gives the wind velocity at different heights. The largest value of correlation coefficient of two estimates is equal 0.88 and corresponds to the height of 4 km.

5. CONCLUSION

The problem of prediction the nonenergy field parameters over the beyond-the-horizon

tropospheric path appears to be more difficult task compared with the attenuation coefficient prediction. Two reasons can be named among the others. First, experiments show that values of nonenergy parameters are less stable in the frequency-temporal domain compared with the stability of the attenuation coefficient.

Second, the usual radiosonde measurements give very few information suitable for the prediction of nonenergy parameters. The exception is the cross-path wind velocity data. It is quite possible that there would be more useful the measurements of short-living smallscale refractive index inhomogeneities in the scattering volume including characteristics in the horizontal plane.

6. REFERENCES

1. Ishimaru A 1978, *Wave Propagation and Scattering in Random Media*, New York, San Francisco, London, Academic Press
2. Akulinichev Ju P et al. 1990, The limit form of the field coherence function in stratified inhomogeneous medium, *Optika atmosfery*, 3, 10, pp. 1060 -1063 (in Russian)
3. Sharygin G S 1983, *Statistical structure of UHF field beyond the horizon*, Moscow, Radio i Svyaz' (in Russian)

PREDICTION OF ATTENUATION FACTOR HOUR MEDIAN FOR UHF WAVE TROPOSPHERIC OVER SEA PROPAGATION USING METEOROLOGICAL PARAMETERS

Kiselev O. N., Dudko B. P., Kovalev V. N., Sharygin G. S.

TACSR, 40 Lenin av., Tomsk, 634050, Russia
Fax: +7-3822-224302, E-mail: root@tiasur.tomsk.su

ABSTRACT

Improved method to estimate the attenuation factor for over the sea beyond the horizon UHF signals is described. This method allows to predict hour median using several measured meteorological parameters deviations from their average value. Results of the experimental test are given.

KEYWORDS: Prediction, Sea, Meteoparameter, Norm, Hour Median.

1. INTRODUCTION

There are some well-known methods for attenuation factor prediction. Many of them use empirically observed correlation signal month median with some macroscale radiometeorological characteristics as refractive index, vertical refractive index gradient (Ref.1).

But to detect real correlation some parameters and signal it is necessary to exclude so called trends - regular functions. In case mentioned above it may be changing signal and refractivity month medians as functions of month medians. So to improve of prediction it is necessary to search statistic not signal and some meteoparameter but deviation every of them about its year function.

2. SCALES OF RADIOMETEOROLOGICAL PROCESSES

There is a certain minimum time interval with allows to detect a relationship between signal level median and meteoparameters. Usually the meteomeasurements are made in one site near radiopath. It is generally agreed that by some meaning the measurements rather well characterize radiopath environments. If take into account the range of the path, average of the wind velocity, it can be proved that hour median has some relationship with any meteoparameters. Therefore, there is a possibility to make the meteorology prediction any parameters of the signal. On the other hand, it is necessary to investigate radiometeorological correlation on annual and more prolonged inter-

vals, because there are the essential season differences of meteorological condition. In such case one can not use methods, based on the classical liner model. To get more reliable statistical conclusion about the attenuation factor it is better to use not any parameters themselves, but their relative deviations, called in meteorology norms (Ref.2).

3. PREDICTION MODEL

Attenuation factor F , when described statistically, may be represented as a sum of the regular component (norm) F_0 and the random component with the zero average and some variance. Characteristics of the random signal component are caused by several mechanisms of the refractivity field and therefore depend on several radiometeorological tropospheric parameters. They can be found using regression analysis. In this case the attenuation factor at the time t over the path range D can be described as follows:

$$\begin{aligned} F(t, D) &= F_0(t, D) + \sum_{m=1}^N K_m \cdot \{M_m(t) - \overline{M_m(t)}\} + \zeta(t) = \\ &= F_0(t, D) + \sum_{m=1}^N K_m \cdot \Delta M_m + \zeta(t), \end{aligned}$$

where K_m - regression index; $\Delta M_m = M_m(t) - \overline{M_m(t)}$ - deviation of the m -th meteoparameter from its regular season behaviour; $\zeta(t)$ - perturbation, describing random deviation from the regression line.

The regression index K_m could be found using the results of the training samples treatment for corresponding average per hour sequence of ΔF and ΔM . These training samples are meant to find experimentally unknown trace parameters of the regression equation. For this purpose in Tomsk Institute of ACS and Radioelectronics there were organized special experiments in 10 cm band over the stationary sea trace 495 km long in the Southern part of the Ochotsk sea. There were received results for all the year seasons from 1983 till 1986, on a whole 3580 hour sessions.

Meteorological data were measured simultaneously in both points: one point near the transmitter, another near the aerological station «Urup». Regression equations for two groups of meteorological parameters are:

$$\hat{F}_1 = F_0 + 0,18(N_s - \bar{N}_s) - 0,54(V - \bar{V}_s) \text{ [dB]},$$

$$\hat{F}_2 = F_0 + 0,14(N_s - \bar{N}_s) - 0,56(V_s - \bar{V}_s) -$$

$$-0,11(V_{850} - \bar{V}_{850}) - 0,18(\Delta N - \bar{\Delta N}) \text{ [dB]}$$

The first equation contains parameters, based on data measured over-the-ground (over-the-sea): N_s - refraction index, V_s - wind speed; the second equation - parameters, based on meteorological and aerological data: N_s , V_s , V_{850} - wind speed in the layer where pressure is 850 mB, ΔN - refraction index gradient in the lower one kilometer thick troposphere layer.

Meteoparameter and signal norm values (\bar{N}_s , \bar{V}_s ,

\bar{V}_{850} , $\bar{\Delta N}$, \bar{F}_0) may be found in Atlases and Handbooks as (Ref.3,4).

There was a version of the regression equation, which took into consideration characteristics of the troposphere stratified inhomogeneities and based on small quantity of experimental data.

4. TEST OF MODEL

Test of the predicting equations was made on independent experiments along sea traces. Distances between the transmitter and the receiver varied from 100 to 450 km. In the process of motion there were measured signal level, meteorological and aerological data, which allowed to count the attenuation factor and to compare it with the really observed signal attenuation. Efficiency of the suggested method for the attenuation factor hour median estimation is illustrated in fig. 1, where we show the fields correlation of measured and predicted data for two groups of meteoparameters. Numerical characteristics of the prediction error are shown in Table 1, where there are root-mean-square deviation of the predicted values from the measured ones. In order to compare the first column shows deviation of the measured values from the month median, received by long-term averaging.

Table 1
Error of the average per hour attenuation factor prediction

Quantity of meteoparam.	Without using meteoparamet.	2	4	9
σ_F , dB	8.7	6.6	5.6	4.5

5. CONCLUSIONS

Results of the radiometeorological experiments allow to make some conclusions.

1. The opinion about the opportunity to estimate the beyond the horizon troposphere signals level in limits of only month medians is the result of noncorrect processing of radiometeorological long series data samples. If the method could be changed one can expect better results and can estimate connections between meteorological data and radiosignals on averaging periods shorter than a month periods.
2. Using norms in regression equations shows new meaning of the extended radiometeorological experimental data accumulated in maps and in season plots of different parameters. The information could be more effectively used for prediction based on meteoparameters.
3. It looks fruitful to go on with investigation of beyond the horizon troposphere effects, especially in regions not enough investigated, in order to get statistically supported attenuation factor norms and to define available now radiometeorological maps.

6. REFERENCES

1. B. R. Bean, E. J. Dutton. *Radiometeorology*. - Central Radio Propagation Laboratory, NBS, Boulder, Colorado, 1966.
2. H. A. Panovsky, G. V. Brier. *Statistical methods in meteorology*. - 1972.
3. *Rept. 233*. International Radio Consultive Committee, Geneva, 1963.
4. *Атлас климатических характеристик температуры, плотности и давления воздуха, ветра и геопотенциала в тропосфере и нижней стратосфере Северного полушария*. - М.: Гидрометеониздат, 1974. (*Atlas of temperature, air density and pressure climatic characteristics in troposphere and low stratosphere of the Northern hemisphere*.)

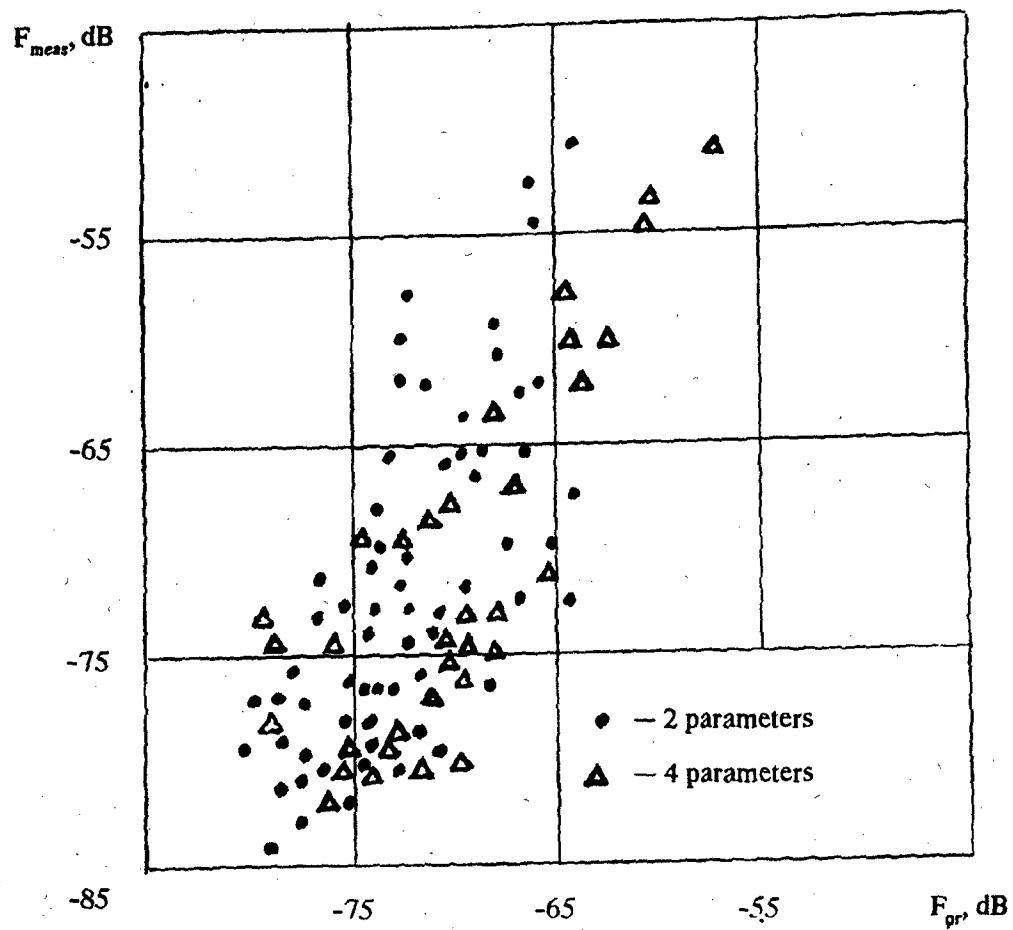


Figure 1: Efficiency of the suggested method.

THE RESULTS OF NON-STOP MEASUREMENTS OF ATMOSPHERIC BOUNDARY LAYER TEMPERATURE PROFILE BY USING 5 MM RADIOMETER

Khaikin M., Kadygrov E., Sorokin M.
Central Aerological Observatory, Russia

ABSTRACT

This report had described the method, equipment and results of operational temperature profile measurements of atmosphere in height range 0 - 600 m by using microwave radiometer with working frequency at 60 GHz.

Keywords: Microwave radiometer, temperature profile, atmospheric boundary layer.

1. INTRODUCTION

Many problems connected with radio wave propagation it is very important to know real temperature profile of atmospheric boundary layer. There is extremely wide variety of possible temperature profiles in the boundary layer: adiabatic, isothermal, with inversion, with elevated inversion. This important limit of atmosphere has variety not only in type but in time also. For forecasting conditions of wave propagation in slant path it is need to have operational information on variation of temperature profile.

Different methods had used for measurement of the boundary layer temperature profile, for example, in situ measurements: radiosond; tethered balloon; meteorological tower, and remote sensing measurements: sodar and microwave radiometers. Radiosond impossible to use for continuous measurements, tethered balloon and meteorological tower impossible to use near by aerodrome, sodar not give information about first hundred meter above Earth surface and have not good accuracy of absolute temperature measurement.

In this report had described the method and equipment for remote sensing of the boundary layer temperature profile by using microwave radiometers with working frequency at 60 GHz, near the centre of oxygen absorption band. Advantages of present system over other remote radio or acoustic remote temperature sensors are in size, portability, reliability, ruggedness, range of environmental conditions under which it can function, price, and simplicity of operation. Clouds, fog and week rain have not influence on measurements of temperature profile of atmosphere by means this method.

The results of measurements of temperature profile received in May-June and September-December

1993 Year and comparisons with time and space-coincident radiozond observations are given also. The examples of grate variety profile of temperature within two-three hours had discussed.

2. DESCRIPTION OF METHOD AND EQUIPMENT

The techniques that we use for microwave remote sensing of the atmospheric boundary layer temperature have based on measuring thermal radiation of atmosphere in the centre of the molecular oxygen absorption band near 60 GHz, where the skin depth is about 300 m (Refs.1,2).

Remote temperature sensing of the boundary layer has conducted by measurements of the radiobrightness temperature at different zenith angles from 0° to 90° (Refs.3-5). In this case depth of the contributing radiation layer changes in a range 0 to 300 m.

For retrieval processing we use iteration method of Chahine with original algorithm, permitting to receive temperature profile in real time [Ref.5].

A block diagram of the equipment for boundary layer temperature profile determination using microwave radiometric observation is shown in Fig.1.

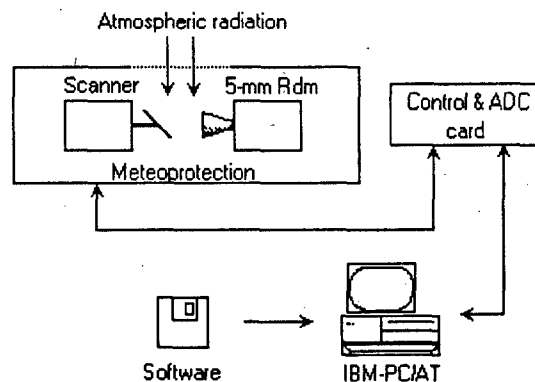


Figure 1: Block diagram of MTP-5

The main part of Microwave Temperature Profiler MTP-5 is the high-sensitivity all solid state super heterodyne receiver (5-mm Radiometer) at the central frequency 60 GHz. The sensitivity of this radiometer (without cooling) is 0,04° K with an integration time 1 sec.. The antenna is a scalar horn with beam width of about 3° or 6° and has a

small scattering coefficient outside the main lobe (less than 1%).

The calibration of the receiver has conducted by the internal noise generator. This noise generator produces the reference temperature step, which determine the scale of the instrument. For the absolute radiation measurements at least one additional point must be known. This known point was the emission temperature at horizontal direction, which equals to the air temperature near the earth surface.

For beam scanning we use rotating mirror in discrete scanning mode with variable reflection angle. The duration of temperature measurement cycle is about 2 minutes in complete automatic mode. The main characteristic of MTP-5 has shown in Table 1.

Table 1

Altitude range	0 - 600 m
Height resolution	30 - 60 m
Sensitivity	0.04° K
Antenna beam width	3° or 6°
Time of one profile measurement	120 s
Accuracy of temperature profile retrieval	0.3 - 0.5° C
Mass of hardware	10 kg
Power consumption	< 60 W (28V)
Outside temperature range	-40° C - +40° C

3. MEASUREMENTS

The discussed in these report measurements had carried out in May-October 1993 in Central Aerological Observatory (Dolgoprudny, Moscow region). The radiometric system MTP-5 has installed on the top of six-floor building on height 22 m over the ground. A set of temperature profile measurements had carried out for comparison with time and space coincident radiozond observations. Fig.2 shows the results of these comparisons. The available experimental evidence shows that the discrepancy of retrieval temperature profile with that received by radiozond for flat profile equals 0.2-0.3° C, and 0.4-0.5° C for profiles with temperature inversion in height. The difference between data of two simultaneously operating radiometers was less than 0.1° K.

As an example of strong changing temperature profile connected with the sunrise and sunset has shown in Fig.3: continuous measurements from 19 Moscow local time (MLT) May 12 to 9 MLT May 13, and in Fig.4, continuous measurements from 19 MLT May 13 to 9 MLT May 14.

Radiozond data received at 00:00 GMT May 13 shows the presence of temperature inversion with mean positive gradient 1.5° C/100 m at the first

200 m, and the negative one equalled 1.0° C/100 m higher 200 m.

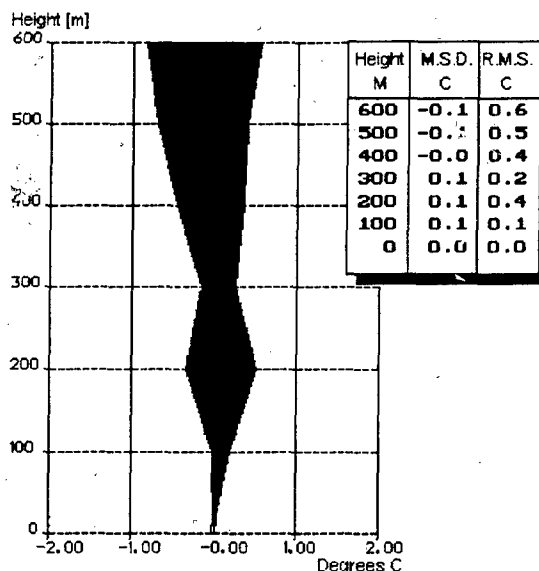


Figure 2: Results of the comparison between radiosond and MTP-5 data (71 set).

At 12:00 GMT May 13 according radiozond data the temperature profile has corresponded to dry adiabatic profile with gradient 1.0° C/100 m. At 00:00 GMT May 14 it has observed inversion again close that observed at 00:00 GMT May 13. The change of temperature profile from adiabatic to inversion has observed about 1,5 hour before the sunset (Fig.3). At 4:30 Moscow local time (MLT) the temperature profile has closed to isothermal. The conversion of temperature profile from inversion too adiabatic has observed for about 1 hour from 7:30 to 8:30 MLT about 3 hours after sunrise (Fig.4). The available experimental data shows that the strong changes of temperature profile of atmosphere boundary layer had observed as rule for time sunrise, sunset and time before and after that. And in this time it can be wait a great change of radio wave propagation conditions on slant path.

3. CONCLUSIONS

The results obtained by mean's microwave temperature profile MTP-5 was showed that the developed method and equipment allow:

- to carry out sounding of temperature profile of atmospheric boundary layer up to 600 m with vertical resolution 30-60 m and retrieval error not greater 0,5° C
- to record immediately and reliably the main features of temperature profiles and their dynamics
- to use data received by MTP-5 for forecasting of radiowave propagation conditions change.

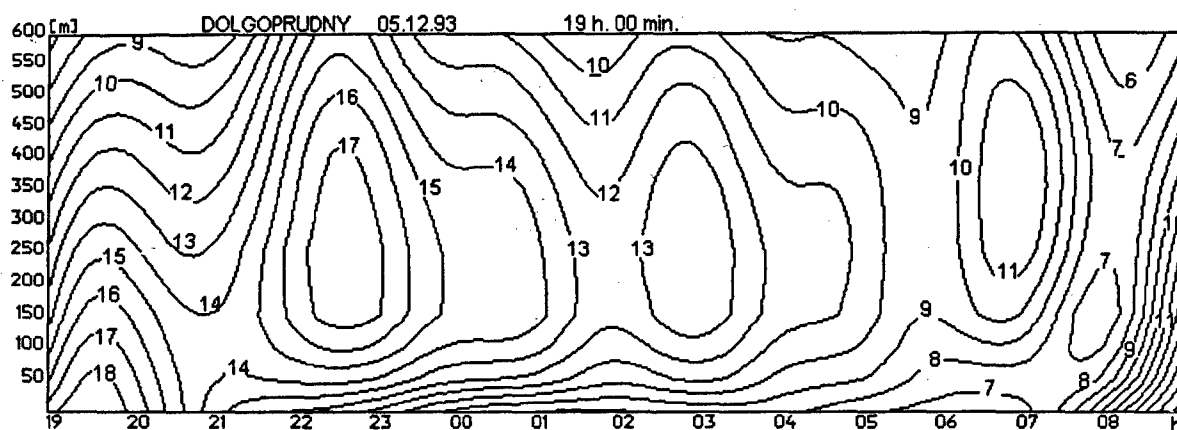


Figure 3: The variation in temperature profile of atmosphere boundary layer as a function of time on MTP-5 data (May 12-13)

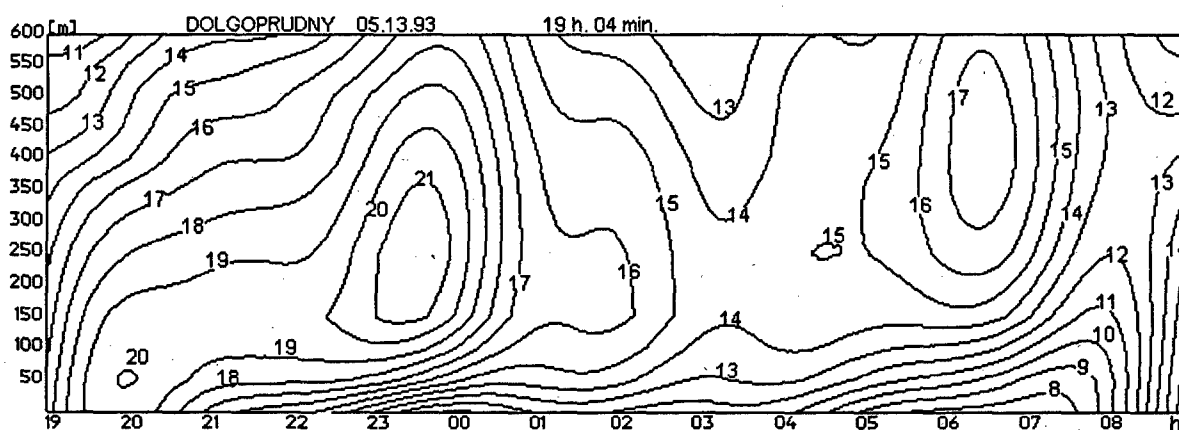


Figure 4: The same as in Fig.3, but for May 13-14.

4. ACKNOWLEDGEMENT

The authors would like to express their appreciation to S.Viazankin, A.Koldaev, and E. Miller without whose assistance this work would not be possible.

5. REFERENCES

1. Westwater E.R., 1972, Ground-based determination of low altitude temperature profiles by microwaves. *Monthly Weather Rev.*, vol. 100, pp. 15-22
2. Troitsky A.V., 1986, Remote definition of the atmosphere temperature from spectral radiometric measurements in the line 5 mm, *Izv. Vuzov, Radiofizika*, vol. 29, pp. 878-884
3. Gromov V.D., Kadyrov E.N., Kosov A.S., 1992, Remote sensing of atmospheric boundary layer at 5 mm wavelength, In: *Proc. Symp. Wave propagation and remote sensing*, Ravenskar, United Kingdom, 8-12 June, pp. 3.4.1 - 3.4.5
4. Troitsky A.V., Gajkovich K.P., Gromov V.D., Kadyrov E.N., Kosov A.S., 1993, Thermal Sounding of the Atmospheric Boundary Layer Temperature in the O2 Absorption Band Centre at 60 GHz, *IEEE Trans. on Geoscience and Remote Sensing*, vol. 31, N 1, pp. 116-120
5. Kadyrov E.N. et. al. 1990, Results of oxygen absorption coefficient laboratory measurements in the 5 mm band, *Izv. Acad. Sci. USSR, Atmosph. Ocean. Physics*, v. 26, N 7, pp. 734-738

THE ESTIMATION OF REFRACTIVITY STRUCTURE FUNCTION BY THE OPTICAL PROPAGATION ALONG THE SLANT PATH NEAR THE GROUND

T.I.Arsenyan¹, N.N.Fedotov¹, P.V.Korolenko¹, E.A.Kuliagina¹

1 - Moscow State University, Physics faculty; Lenin Hills, Moscow, 119899 Russia
Tel: (095) 939-1586; Fax: (095) 932-8820.

ABSTRACT

New method of the structure characteristic of the air refractivity C_n^2 estimation is suggested. It is based on the analysis of the interferometric pattern containing helical dislocations of the wave front.

1. INTRODUCTION

Electromagnetic signal fluctuations on a slant path near the ground are defined by the altitude profile of the meteorological parameters of the path. The structure characteristic of the refractive index C_n^2 is one of them.

The necessity of taking into account the turbulent motions when reckoning the paths of radio- and optical propagation both near the ground and in space initiated lately a lot of investigations for the purpose of measurement of the tropospheric turbulent motions (Ref.1). Theoretical approach allowing to calculate the practical applications is limited by the analytical expression defining the relation between the statistical characteristics of the atmospheric turbulence and the fluctuations of the refractive index. Limitations of "the 2/3 law" by the scope of the inertial interval as well as subsequent calculations with unavoidable using of approximate relations in the each stage of them give at present only semiquantitative estimation of the main characteristic of the turbulent inhomogeneities of the refractive index - C_n^2

2. METHODS OF ESTIMATION

Analysis shows that the C_n^2 modeling at the atmospheric paths may be performed only approximately and that it is necessary

to search more reliable ways for this characteristic estimations under the conditions of real paths. That is why the experimental results of C_n^2 measurements on different paths are of especial interest. There are different methods of C_n^2 estimations based on radio- and optical sounding of the troposphere. These methods are either connected with the estimation of intensity fluctuations or based on densitometric analysis of interference or diffraction patterns. The first of these methods enables to determine C_n^2 by measuring of the intensity fluctuations' logarithm according to the relation:

$$\sigma_{\ln I}^2 = A C_n^2 k^{7/6} L^{11/6} \quad (1)$$

where k is the wave number; L is the path's length; A is determined by the beam's shape.

The comparison of the meteorological data obtained at the receiving and transmitting points enables to get C_n^2 as a function of the Richardson's number, average path's height and temperature gradient in height. This method is rather simple for the technical realization. But it's practical usage is defined by the conditions of "the weak intensity fluctuations", that is why it's accuracy and field of applications have been limited.

Methods of C_n^2 estimations based on the interferometric measurements seemed to be more accurate (Ref.2). The analysis of the interferometric pattern obtained by means of two-ray interferometer with a large base enables to determine C_n^2 according to the relation between the visibility of the interferometric pattern and the structure function of phase fluctuations:

$$V = (I_{\max} - I_{\min}) / (I_{\max} + I_{\min}) = \exp(-D_\phi/2) \quad (2)$$

which in its turn happens to be connected with C_n^2 by the relationship:

$$D_\phi(l) = A C_n^2 k^2 L l^{5/3} \quad (3)$$

where l is the beams' separation.

Accuracy and high sensitivity of the interferometric methods are well known but they don't allow to perform estimations for the long paths because of unwanted overlapping of rays before their incidence on the second mirror of the interferometer due to diffractive divergence of the beams. In this case the measurements encounter difficulties because of side interferometric effects. Besides the interference pattern gives information on total action of space displacing and angle of arrival fluctuations. To separate these two effects the application of shadow schemes was put forward (Ref.2).

But the methods connected with the analysis of the intensity distribution in the Fraunhofer diffraction pattern seem to be more warranted. In this case

$$\begin{aligned} \langle |E_{xz}(U)|^2 \rangle = \\ = 2B \int_0^1 (1 - \cos \eta) \cos(2U\eta) e^{-\beta' \eta} d\eta \quad (4) \end{aligned}$$

where η is the separation of the observation points ξ_1 and ξ_2 ; $U = (ka^2/2) \sin \theta$; $B = A^2 S^2 E_0^2$ is the value proportional to E_0^2 - the intensity in the maximum of the interferometric pattern; S is the aperture; $\beta' = 2.3 k^2 L C_n^2 \eta^{5/3}$.

This expression holds for the inertial interval $l_0 \leq |\xi_1 - \xi_2| \ll L_0$ under the condition $|\xi_1 - \xi_2| \leq \sqrt{\lambda} L$.

The methods of C_n^2 determination described above hold true for the case of "the weak fluctuations". Such conditions are not feasible even on comparatively short paths (a few hundred meters length).

3. C_n^2 AND HELICAL DISLOCATIONS

A method based on the analysis of the interferometric pattern containing the helical dislocations is more preferable and allows to improve the possibilities of C_n^2

estimation. The evaluation of this method was carried out on a slant path near the ground. The receiving and transmitting devices were placed at a height of 40 m. The distance between the point of their location and the reflecting mirror (placed at a height of 160 m) was about 320 m. The angle of inclination was about 29 with respect to the horizon. The values of the wind velocity and temperature obtained at the ground level (at the MSU Observatory) and at the heights of 40 m and 160 m have been taken simultaneously with the measurements of the electromagnetic wave fluctuations. The number of helical dislocations was defined from the interferometric pattern obtained by the use of a shift interferometer.

Depending on the weather conditions of the path different regimes of turbulence have been realized. Conditions of "the strong fluctuations" on the path described took place under C_n^2 equal to $10^{-16} - 10^{-15} \text{ m}^{-2/3}$. In such cases the radius of the phase correlations of phase fluctuations happens to be smaller than the beam radius and helical dislocations of the phase appear on the wave front (Ref.3). The number of dislocations in interference pattern is determined with good approximation by the relation:

$$N = r_b^2 (C_n^2 k^2 L)^{6/5} \quad (5)$$

where r_b is the beam radius.

As it transpires from this formula, N is determined by the relationship between the beam cross-section and the area of the correlation zone. So the possibility of C_n^2 experimental estimation follows with the help of relationship:

$$C_n^2 = (N/r_b^2)^{5/6} k^2 L^{-1} \quad (6)$$

4. EXPERIMENTAL STUDIES

Several sets of observations have been carried out to study the behaviour of C_n^2 in different conditions. Some of the results are listed in the table 1. They allow to conclude that the difference between the

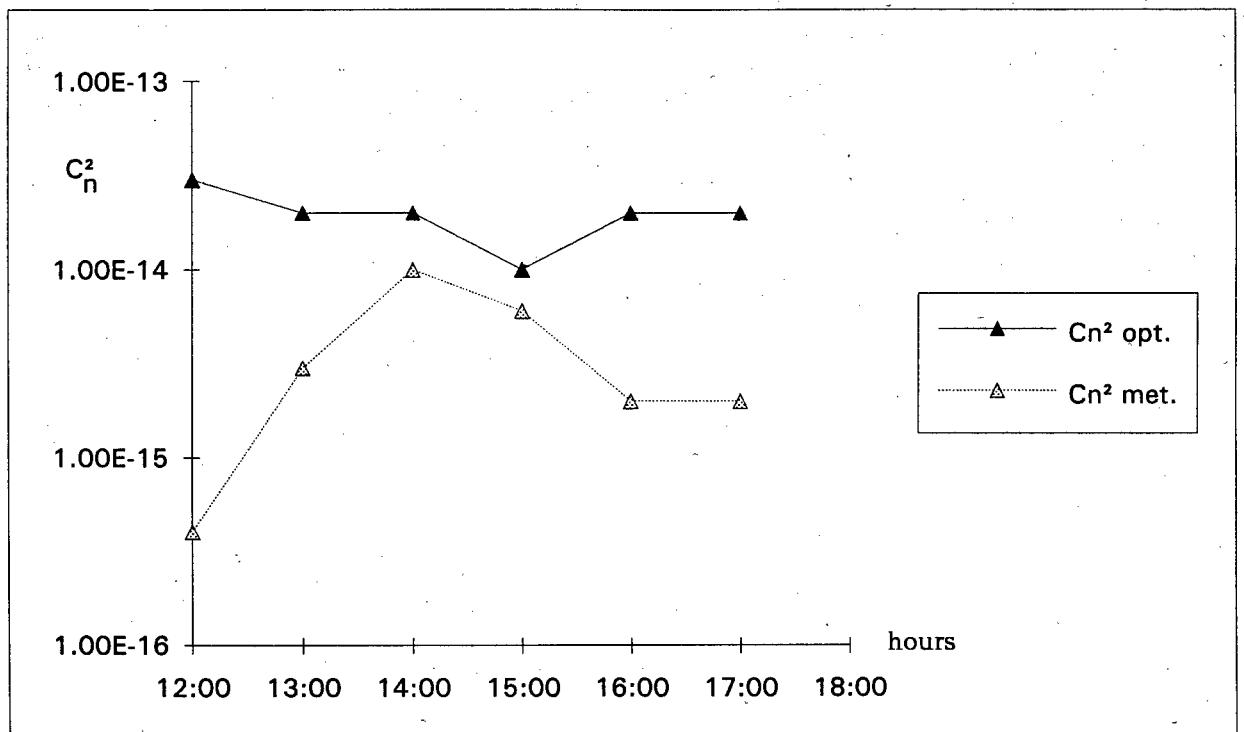
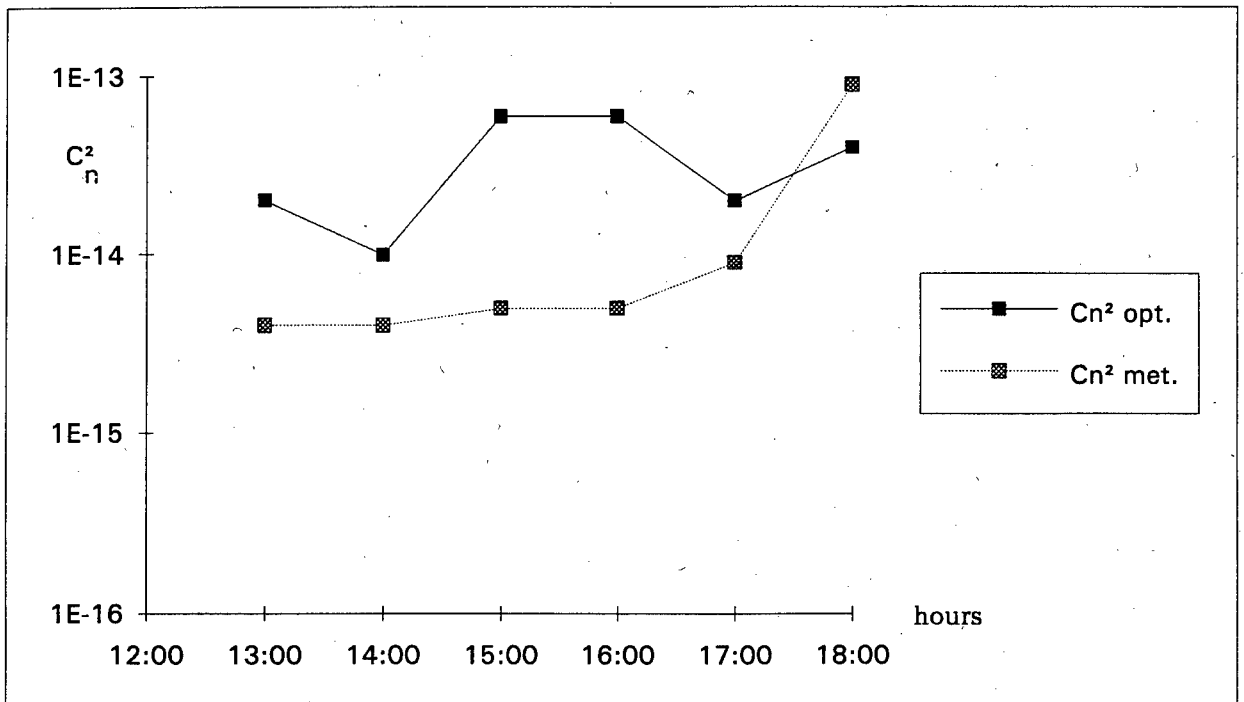


Figure 1: Behaviour of the structure characteristic of refractivity during the daytime (27.11.92 and 17.09.93).

values of C_n^2 got from meteorological data and from optical propagation experiments is rather small. As it is obvious from the table 1 practically always the effective value of C_n^2 obtained from the optical measurements appears to be greater than that obtained from meteorological data.

Analysis of different methods of C_n^2 definition leads to the same result. The method suggested allows to trace the time behaviour of C_n^2 . The examples are presented in fig.1.

Table 1.
Number of dislocations N and the structure characteristics of refractivity

Average number of dislocations	optical C_n^2	meteo C_n^2	Average number of dislocations	optical C_n^2	meteo C_n^2
1	$2 \cdot 10^{-14}$	$1 \cdot 10^{-14}$	3	$4 \cdot 10^{-14}$	$6 \cdot 10^{-15}$
2	$3 \cdot 10^{-14}$	$4 \cdot 10^{-15}$	4	$3 \cdot 10^{-14}$	$1 \cdot 10^{-15}$
2	$4 \cdot 10^{-14}$	$2 \cdot 10^{-14}$	4	$2 \cdot 10^{-14}$	$1 \cdot 10^{-15}$
2	$2 \cdot 10^{-14}$	$1 \cdot 10^{-14}$	4	$7 \cdot 10^{-14}$	$2 \cdot 10^{-14}$
2	$4 \cdot 10^{-14}$	$1 \cdot 10^{-15}$	4	$2 \cdot 10^{-14}$	$7 \cdot 10^{-16}$
2	$6 \cdot 10^{-15}$	$8 \cdot 10^{-17}$	5	$3 \cdot 10^{-14}$	$2 \cdot 10^{-14}$
2	$7 \cdot 10^{-15}$	$3 \cdot 10^{-15}$	5	$3 \cdot 10^{-14}$	$3 \cdot 10^{-15}$
2	$1 \cdot 10^{-14}$	$2 \cdot 10^{-14}$	5	$9 \cdot 10^{-15}$	$8 \cdot 10^{-16}$
3	$8 \cdot 10^{-14}$	$3 \cdot 10^{-14}$	5	$1 \cdot 10^{-14}$	$7 \cdot 10^{-14}$
3	$1 \cdot 10^{-14}$	$8 \cdot 10^{-16}$	6	$3 \cdot 10^{-14}$	$1 \cdot 10^{-13}$
3	$2 \cdot 10^{-14}$	$2 \cdot 10^{-15}$	7	$3 \cdot 10^{-14}$	$2 \cdot 10^{-15}$
3	$4 \cdot 10^{-14}$	$7 \cdot 10^{-16}$	7	$3 \cdot 10^{-14}$	$7 \cdot 10^{-16}$
3	$3 \cdot 10^{-14}$	$2 \cdot 10^{-14}$	7	$3 \cdot 10^{-14}$	$4 \cdot 10^{-15}$

5. DISCUSSION

It is simple to carry out the experiments using the method described. Its accuracy is defined by that of the estimation of the average beam radius and the number of helical dislocations in the beam cross-section. From the other side using the meteorological parameters one can define C_n^2 to a precision of the order of magnitude.

The advantage of the method suggested lies in the fact that it allows to carry out C_n^2 estimation for the paths of any length.

This research was sponsored by the Russian Foundation of Fundamental Investigations (project # 93-02-16048).

6. REFERENCES

1. Kravtsov Yu.A. 1992, *Progress in Physics*, 55, No 1.
2. Semenov A.A., Arsenyan T.I. 1978, *Electromagnetic Waves Fluctuations on the Paths near the Ground*. - Moscow, Nauka.
3. Arsenyan T.I., Korolenko P.V., Kuliagina E.A., Fedotov N.N. 1992, *Radiotekhnika i elektronika*, 37, No 10.

MILLIMETER-WAVE SCATTERING DUE TO ATMOSPHERIC TURBULENT INHOMOGENEITIES

G.A.Andreyev, E.V.Frolova

IRE RAS, Mokhovaya Str.11, Moscow, 103907, Russia,
Tel.: (7095)202-15-91, Fax: (7095)203-84-14,
E-mail: L112@IREUUCP.free.msk.su

ABSTRACT

The results of calculations and analysis of the differential cross section and scattering indicatrices of turbulent atmosphere inhomogeneities are given.

Keywords : Millimeter - Wave Scattering, Energetic Potential.

Beam amplitude, phase and direction fluctuations during millimeter-wave propagation in troposphere arise due to its natural turbulence. As distinct from optical waveband, the radius of the first Fresnel zone $\sqrt{\lambda L}$ in the MMW band on paths with length L is comparable with the external scale of turbulence L_0 which amounts to several metres in the lower level of the atmosphere above the ground. In that case the characteristics of wave fluctuations depend not only on structural characteristic of air refraction index fluctuations C but on the size of inhomogeneities L_0 [Ref.1]. Two types of measurements are necessary to evaluate structural characteristic C : the depth of chaotic amplitude modulation and mean square fluctuations of the phase difference.

The task was to evaluate the possibilities of determination of structural characteristics, path-averaged on accepted MMW scattering by

turbulent inhomogeneities.

In the millimetre waveband when fluctuations of the air refraction index are low ($\Delta n \ll 1$), scattered field is small as compared with the field of initial wave, that is why the method of small perturbations [Ref.2] is used for its description. In the approximation of the method the differential scattering cross section of a unit of volume $\sigma_\Omega(\vec{n}_s, \vec{n}_i)$ is expressed through spectral density of the refraction index fluctuations ϕ_n as [Ref.2]:

$$\sigma_\Omega(\vec{n}_s, \vec{n}_i) = \sigma_\Omega(\vartheta, \varphi) = \frac{1}{8} \pi k^4 \phi_n(\vec{K}_s) \quad (1)$$

where $k = \frac{2\pi}{\lambda}$ - wave number, \vec{n}_i and \vec{n}_s - directions of incident and scattered waves, ϑ, φ - polar and azimuth angles corresponding to direction \vec{n}_s , $\vec{K} = k(\vec{n}_s - \vec{n}_i)$ - vector of scattering, $|\vec{K}| = k \sin \vartheta/2$.

The spectrum corrected for the external scale of turbulence [Ref.2] is given by

$$\phi_n(x) = \frac{1}{4} 0,033 C_n^2 (x^2 + x_0^2)^{-11/3} \quad (2)$$

where $x = \frac{2\pi}{L_0}$ - spatial frequency corresponding to external scale of inhomogeneities L_0 .

The formula of the diffe-

rential scattering cross section (1) with spectrum (2) is brought in the following form:

$$\sigma_{\Omega}(\vartheta) = \frac{1}{8} 0,033 C_n^2 k^4 x_o^{-11/3} * [1 + (\frac{2k}{x_o} \sin \frac{\vartheta}{2})^2]^{-11/6} \quad (3)$$

The angular function of scattering is characterized by indicatrice $G(\vartheta) = \sigma_{\Omega}(\vartheta) / \sigma_v$ determinated as differential section $\sigma_{\Omega}(\vartheta)$ normalized on full scattering section of a unit of volume σ_v

$$\sigma_v = 2\pi \int_0^{2\pi} \sigma_{\Omega}(\vartheta) \sin \vartheta d\vartheta \quad (4)$$

Using (1) and (4) for section σ and indicatrice $G(\vartheta)$ the following formulae have been derived:

$$\sigma_v = 0,033 \frac{3\pi}{20} C_n^2 k^{1/3} x_o^{-5/3} \quad (5)$$

$$G(\vartheta) =$$

$$= \frac{5}{6\pi} (\frac{k}{x_o})^2 [1 + (\frac{2k}{x_o} \sin \frac{\vartheta}{2})^2]^{-11/6} \quad (6)$$

The analysis of the equation (6) demonstrates that the width of the indicatrice forms the estimate $\vartheta_i = \frac{\lambda}{L_o}$, which in the MM waveband constitutes 10^{-3} rad.

The section $\sigma_{\Omega}(\vartheta)$ as function of the angle of scattering ϑ is calculated on the formula (3) at wavelength $\lambda = 8 \cdot 10^{-3}$ m for $C_n^2 = 10^{-12} \text{ m}^{-2/3}$ at different L_o are presented at Fig.1 (1 - $L_o = 5$ m, 2 - $L_o = 2$ m, 3 - $L_o = 1$ m).

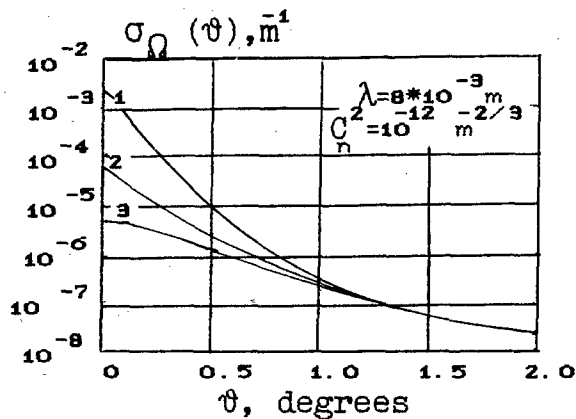


Fig 1. Differential scattering cross sections as functions of angle.

As follows from Eq.3 when the angles of scattering ϑ wider then the width of the indicatrice $\vartheta_i = \lambda / L_o$ the section $\sigma_{\Omega}(\vartheta)$ does not depend on the external scale of inhomogeneities L_o and is defined only by wavelength λ and structural characteristic C_n . At the approximation $\frac{2k}{x_o} \gg 1$ for angles $\vartheta > \lambda / L_o$ Eq.3 is transformed into

$$\sigma_{\Omega}(\vartheta) = 0,033 \frac{\pi}{8} C_n^2 k^{1/3} (2 \sin \frac{\vartheta}{2})^{11/3} \quad (7)$$

The scattered power P_s caught by the receiving antenna is connected with the cross section $\sigma_{\Omega}(\vartheta)$ and determined on the basis of radio communication equation with the angular separation of directional diagrams of receiving and transmitting antennae [Ref.3]:

$$P_s = P_o \int \frac{\lambda^2 G_1(\vec{n}_1) G_2(\vec{n}_s)}{(4\pi)^3 r_1^2 r_2^2} * \sigma_{\Omega}(\vec{n}_s, \vec{n}_1) dV \quad (8)$$

where

P - transmitting power,
 G° - gain of transmitting
 and 2 receiving antennae,
 r^1, r^2 - distances from the scat-
 tering volume element dV to
 the transmitter and the
 receiver. With narrow direc-
 tional diagrams and their
 Gaussian approximation the
 Eq.8 is transform into

$$P_s = 0,068 P_*$$

$$* \frac{\lambda}{L} \frac{2\rho_\circ}{\sigma_\Omega(\theta)} \frac{1}{\sin \theta/2} \quad (9)$$

where

$2\rho_\circ$ - diameter of antennae
 $L = 2r \cos(\theta/2)$ horizontal
 distance between the trans-
 mitter and receiver.

The energetic potential of
 the system P_* is determined as
 the ratio of the transmitting
 power P to the noise power
 brought to the input of the
 receiver. At the present level
 of signal/noise ratio at the
 input of the reseiver thro-
 ught the Eq.9 for energetic
 potential reduced to the
 following form:

$$P_* = 14,6 q_\circ^2 \frac{L \sin \theta/2}{\lambda \frac{2\rho_\circ}{\sigma_\Omega(\theta)}} \quad (10)$$

With the approximation (7)
 for angle of scattering
 $\theta > \lambda/L$ energetic potential P_*
 is given by

$$P_* = 7,83 \cdot 10^3 q_\circ^2 * \frac{L}{C_n^2 \lambda^{2/3} 2\rho_\circ} (\sin \theta/2)^{14/3} \quad (11)$$

Dependencies P_* on the path
 length L , calculated on the
 basis of the Eq.11 at wave
 length $\lambda = 8 \cdot 10^{-3}$ m with the
 diameter of antennae $2\rho_\circ =$
 0.45 m and observation angles
 $\alpha = \theta/2$, equal 5° ; 10° are

shown on Fig.2.

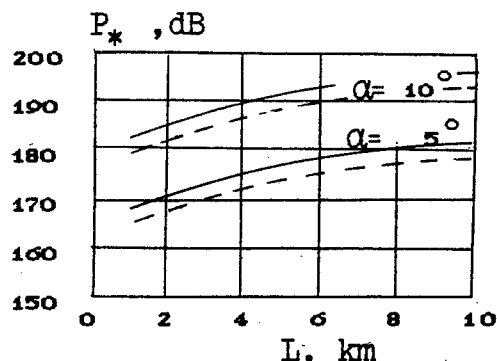


Fig.2. Energetic poten-
 tial as function of path
 length (— $C_n^2 = 0,5 \cdot 10^{-12}$
 $m^{-2/3}$, - - - $C_n^2 = 1,0 \cdot 10^{-12}$
 $m^{-2/3}$).

Signal/noise ratio was
 present at 10 dB. As follows
 from the estimates, the requ-
 ired energetic potential of
 the system for structural
 characteristic measurements
 $C_n^2 = (0,5-1,0) \cdot 10^{-12} m^{-2/3}$ on
 the path length $L=10$ km should
 constitute (180-177) dB and
 (194-191) dB for observation
 angles $\alpha = 5^\circ$ and 10° corres-
 pondingly. For example, the
 transmitter with power output
 $P = 130$ mW provides energe-
 tic potential $P_* = 180$ dB in the
 bandwidth $\Delta F = 10$ Hz at the
 receiver's noise temperature
 $T_n = 10^3$ K.

REFERENCES

1. Andreyev G.A. et al.
 The 2nd All-Union School-
 Symposium on MM and Sub-
 MM Wave Propagation in
 Atmosphere, Frunze:
 Illim, 1986, p.34.
2. Rytov Y.M. et al. 1978,
 Introduction to statis-
 tical radiophyzic., v.2,
 Moscow: Science.
3. Ishimaru A. 1981, Wave
 Propagation and Scat-
 tering in random media,
 v.1, Moscow: World.

Session 10: Mapping I

GLOBAL PRECIPITATION CLIMATOLOGICAL DATA BASE

Bruno Rudolf, Hubert Hauschild, Wolfgang R  th and Udo Schneider

All - Deutscher Wetterdienst, GPCC, Postfach 10 04 65, D-63004 Offenbach, Germany
Tel: +49-69-80622981, Fax: +49-69-80622993

ABSTRACT

The purpose of the Global Precipitation Climatology Project of the World Climate Research Programme is to provide global analyses of monthly precipitation based on all suitable observation techniques. As a central element of this project, the GPCC is operated by the Deutscher Wetterdienst (National Meteorological Service of Germany). Up to now, the GPCC has prepared gridded global data sets for 24 months (1987/1988), and the process is going on. The GPCC has installed a data bank for grid-related precipitation estimates containing also long-term means compiled by other authors, as Schutz and Gates, Jaeger, Legates, Hulme, and Schemm et al., numerical weather prediction results, and estimates derived by various algorithms from satellite data.

Keywords: Global Climate, Precipitation

1. BACKGROUND

Climate change is one of the most important environmental issues facing us. The element precipitation is especially important as its spatial distribution identifies the regions of maximum latent heat release which is the major driving force of the atmospheric circulation. Therefore, it is also a highly sensitive indicator of global climate change. Besides, precipitation is the main input quantity in the water balance of the earth's surface, whereas evaporation and runoff represent the main losses.

Global precipitation data sets are of general interest. Especially, analyses derived from observed data are necessary for the verification of global climate or general circulation models, and conventionally measured data are still inalienable to calibrate remotely sensed precipitation estimates. Since the observed precipitation data are used for the assessment of the earth's energy and water balances or for validation of satellite-based estimates or verification of climate models, the data need to be temporarily and spatially integrated, e.g. as monthly totals averaged over grid areas.

2. THE GPCP/GPCC

The Global Precipitation Climatology Project (GPCP) was initiated by the World Climate Research Programme in order to provide the investigators of the global climate, especially the modelers with gridded monthly global precipitation data sets based on conventional as well as remotely sensed observations for the period 1986-1995. The main components of this project are the both satellite-oriented groups evaluating infrared and microwave images, several calibration/validation activities and the Global Precipitation Climatology Centre (GPCC). Within this framework, the GPCC is carrying out the following itemized tasks:

- Collection and storage of all available conventionally measured precipitation data world-wide on a monthly basis.
- Quality-control of the conventionally measured data.
- Calculation of areal precipitation totals on a 2.5° grid over land based on the conventionally measured data using an objective analysis method.
- Correction of the analyses with regard to the systematic gauge measuring errors depending on the instruments used.
- Estimating the accuracy and error of the gridded data.
- Intercomparison studies for the gridded data from different sources (raingauges, satellites, model results).
- Merging the results from the different sources to obtain complete global gridded precipitation data sets.
- Publication of the results and dissemination of the gridded data sets to the ICSU-World Data Centres for Meteorology A (Asheville, USA) and B (Obninsk, Russia).

These functions of the GPCC are already operational and permanent. Therefore, it is proposed that the GPCC will take the role of a specified global data centre for precipitation in the Global

Climate Observing System (GCOS), but it will simultaneously cover its present functions in the WCRP. The GPCC also contributes to hydrological projects of the World Climate Programme - Water and cooperates with the Global Runoff Data Centre.

The components of the operational data processing system developed by the GPCC are summarized as follows. A description of more detail is given by Rudolf (1993).

2.1 Collection of in-situ data

Over the continental areas, conventional rain-gauge measurements are the main and most reliable data base. From CLIMAT and SYNOP reports, regularly disseminated via the World Weather Watch Global Telecommunication System (WWW-GTS), information from world-wide 4,500 stations is available. Recognizing the high spatial and temporal variability of precipitation, station networks of high density are necessary also for global-scale analyses. In order to derive monthly areal mean precipitation on a grid of 2.5° latitude by longitude with an error of most probably less than 10%, a number of 10 to 40 point measurements per grid is required (GPCC 1992). The required number of stations depends on climate (precipitation types) and the topography of the individual grid cell. This definition ends in the requirement of at least 40,000 stations for the total continental areas. In order to fulfill the requirements on the data density, the GPCC has undertaken all possible data acquisition. Up to early 1994, the collection includes monthly precipitation data from more than 30,000 stations of national networks of about 70 countries and additional data of several international projects of the FAO, UNESCO and UNEP.

2.2 Quality-control

The quality-control of the gauge-measured monthly precipitation totals up to now has been performed only for the data included in the analyses. An automatic quality-control of all gauge-measured data is supplemented by a manual revision of the data indicated as questionable by the automatic procedure.

2.3 Spatial interpolation

Based on an intercomparison study on different methods, Shepard's (1968) empirical weighting scheme was chosen as the interpolation method

being most suitable for the GPCC application. Following Willmott et al. (1985), who transferred the scheme to spherical coordinates, this method avoids some deficiencies which are typical for a pure distance weighting, 1) by using only the 4 to 10 nearest stations, 2) by clustering near neighbouring measurements (directional weighting), and 3) by the extrapolation of estimated gradients of the precipitation field to yield extrema being not covered by measurements. Using this code, the conventionally measured monthly precipitation depths from stations are interpolated on a 0.5° grid and areal means on a 2.5° grid are calculated by averaging of 25 interpolated values (Rudolf et al. 1992). This analysis is done for the anomalies, too.

2.4 Error assessment

The GPCC is planning to provide the gridded monthly precipitation with a supplement for the error size on each individual grid cell, whereby the total error has three components, the systematic rain-gauge-measuring error, the stochastic error resulting from errors of the individual data, and the methodic analysis uncertainty. The methodic error mainly depends on the station density, but is also influenced by the climatic conditions and the orographic structure of the individual grid cell as well as by the analysis method used. This component has been investigated based on the data from dense networks of Australia, Germany and the US (Rudolf et al. 1993). A study of the other error components is in preparation.

2.5 Compiling the global product

In order to obtain complete global products, the GPCC merges the data from different observation techniques. Preliminary, a blending scheme is used, whereby the grid values from the different data sources are selected by predefined priorities depending on the geographical location: analyses from conventional gauge-measurements are exclusively used for all land grids, infrared-microwave-mixed estimates over tropical oceans, microwave-only estimates over the subtropical and mid-latitude oceans and model results of the European Centre for Medium Range Weather Forecasts (ECMWF) over the high-latitude oceans, where no observed data are available (GPCC 1992, 1993). The satellite-based precipitation estimates are provided by the GPCP components operated at the NOAA (Janowiak 1993, GPI-approach from Arkin 1979) and at the NASA (Chang, method described by Wilheit et al. 1993).

Up to now, the GPCC has prepared gridded global data sets for 24 months (January 1987 to December 1988). An example is shown in Figure 1. The gridded monthly precipitation is provided also in digital form on diskettes together with a flag on the data source and the number of stations per the grid. This data set is still preliminary, since the continental results are based on a smaller raingauge data collection from about 6,700 stations only, and the simple blending scheme described in 2.5 has been used to fit in the satellite data. The data from the 30,000 stations (cf. 2.1) are being prepared to be included in the re-analysis planned to be carried out soon.

In order to derive results of highest possible reliability, the concept is the simultaneous use of all available information and minimizing the errors. An optimum estimation model could be the best method. As a precondition of the application of this approach, the error ranges have to be derived separately for each observation technique considering the dependency on space and time. The development of an advanced method for merging the results from different observation techniques is ongoing (Adler et al., 1993).

3. INTERCOMPARISON STUDIES

The GPCC preliminary results are compared to other gridded global and terrestrial climatologies provided by Schutz and Gates (1972), Jaeger (1976), Legates (1987), Leemans and Cramer (1990), Hulme (1991) and Schemm et al. (1992). Additionally, the ECMWF weather prediction model results (spectral model T106, daily 12-36h forecasts accumulated to monthly totals) are included in this intercomparison.

The terrestrial results of all of the climatologies are based on conventional data measured by rain-gauges. However, the estimates of the various authors are derived from different data collections and by different interpolation approaches. Also the goals of the authors differed in setting up time series of analyses based on homogeneous but smaller input data sets (5° grid-size, data time series from ca. 4,000 stations, Hulme 1991) or providing a gridded global long-term climatology of highest possible spatial resolution (0.5° grid-size, long-term means on dissimilar and partly unknown periods but of ca. 25,000 stations, Legates,

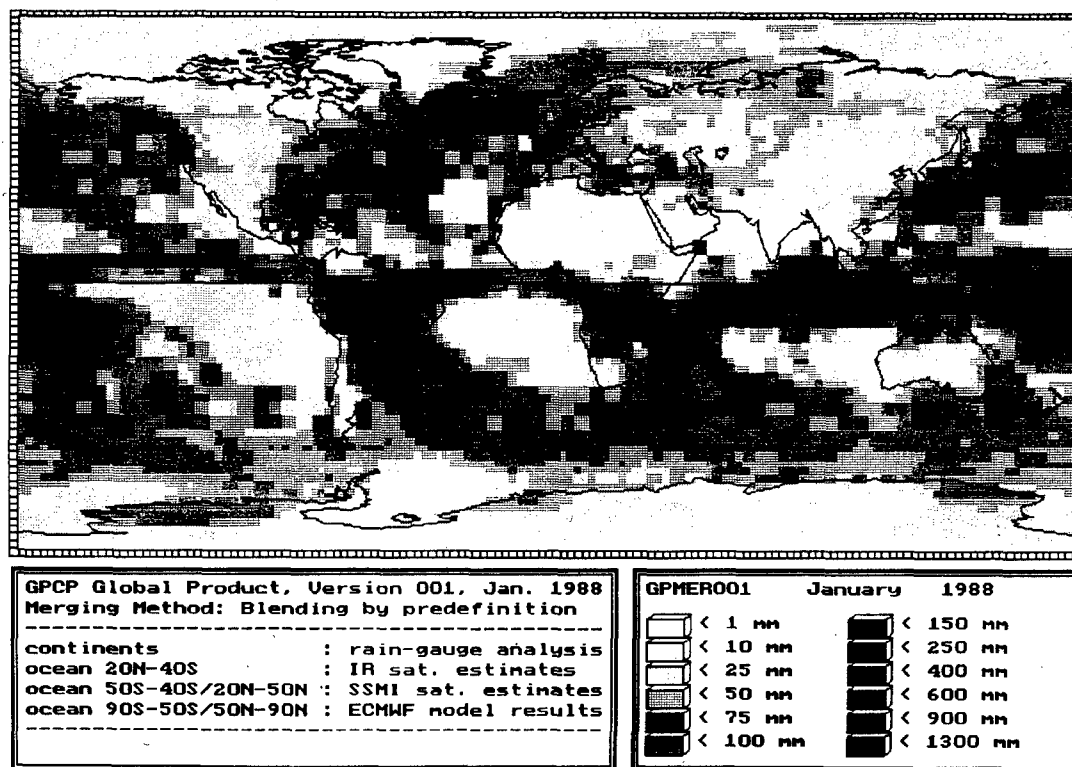


Figure 1: Example of the GPCP global product, as it is provided by the GPCC also in digital format on IBM-compatible diskettes.

1987). The IIASA data set prepared by Leemans and Cramer is based on the time series of the period 1931-1960 collected by Bradley et al. (1985). Hulme used the data compiled and quality-controlled by Eischeid et al. (1990) to set up monthly digital maps for the period 1951-1980. Both climatologies cover land areas only.

The authors of global data sets have used different sources of information on precipitation over the oceans: The Jaeger product was assembled from mean monthly precipitation maps for the period 1931-1960 from contemporary rainfall atlases including the isohyetal maps from the U.S. Marine Climatic Atlas. Legates included the estimates from ship weather observations published by Dorman and Bourke (1979, 1981), whereas Schemm et al. (1992) have based their oceanic data on MSU satellite observations and the GPCP is using infrared and microwave satellite data as well as numerical weather prediction results (Rudolf 1993).

Legate's gridded data are provided as two separate versions, the non-corrected "nc" data set derived from the point measurements as reported, and the "c" data set from the station related data which were corrected with regard to the systematic error from evaporation losses and rain drop and snow drift due to wind. The assessment of the size of this error (even if it can be done only roughly) is very important if the observed data are used for validation of satellite based estimates or climate model results.

An overall intercomparison is given by the annual global means, here derived from the monthly gridded data by yearly accumulation and grid-area related averaging: the results are

Jaeger	985 mm,
Legates (nc)	1,034 mm,
Legates (c)	1,140 mm,
GPCC for 1987	1,015 mm,
GPCC for 1988	1,025 mm,
ECMWF for 1987	1,205 mm,
ECMWF for 1988	1,230 mm.

If the systematic error is not considered, the annual global means of the climatologies based on observational data are on the same level with relative differences of less than 3% to the total mean (1,015 mm). The overall mean of Legates' corrected data is about 10% larger than the result from his data as measured. A comparison of the two Legates data sets, separately for the climatic

zonal belts and for the seasons, shows that the systematic gauge-measuring error is estimated to be highest and reaches its largest relative values with about 70% (absolute 15 mm/month) in the northern subpolar zone and more than 100% (absolute 30 mm/month) over Antarctica, in each case during the hemispheric winter season. In the tropics, the absolute error can also reach more than 10 mm/month, however, but the relative error is generally less than 5%.

The highest total precipitation results from the forecast model and is about 8% larger than the highest value of the observed data, which have been corrected with regard to the systematic measuring error. Arpe (1991) studied the characteristics of the ECMWF forecast model results and found a tendency of the contemporary model to overestimate convective rainfall.

The similarity of the climatological data sets and the model defect mentioned can also be seen by the comparison of the continental zonal means, plotted in Figure 2. For the northern summer as well as for the year, the ECMWF model yields the broadest ITCZ with highest precipitation, while the Hulme data indicate the lowest precipitation amounts in the tropics. Furthermore, there is a small shift in the location of the ITCZ between the model and the observation-based estimates in the northern winter season. In arid zones and in the northern hemisphere subtropics all results are in good agreement. In general, the largest differences between the observation-based climatologies are found in the southern hemisphere extratropics, what might be due to the sparse coverage with measured data.

The intra-annual variation of area-averaged precipitation is evaluated separately for the continental and oceanic areas. Figure 3 shows the climatological mean estimates periodically plotted versus time series of the GPCC and ECMWF results for the period of January 1987 to December 1988. Over land, the seasonal characteristics are visible in all data sets.

Over ocean, the temporal variations are smoother, only the Legates data indicate a pronounced maximum in November, December and January, which seems to be artificial with regard to the data used (mainly very rough estimates from ship weather observations). Generally, the model results are higher than all other data sets, clearly higher than the GPCC analyses (over ocean mainly based on satellite data).

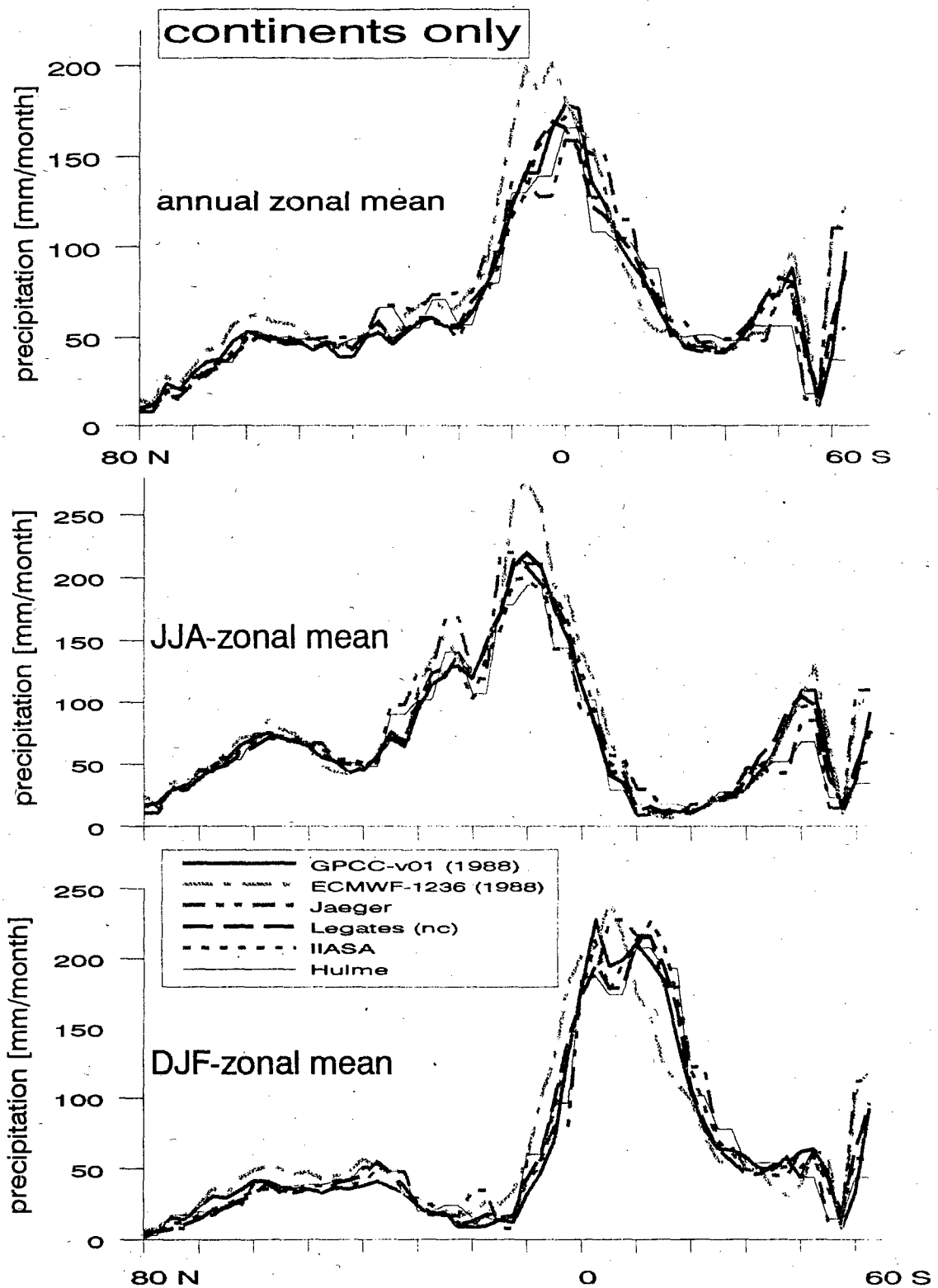


Figure 2: Latitudinal profile of zonal-mean precipitation in mm/month exclusively for the continental areas, for the climatological data sets of Hulme, Jaeger, Leemans/Cramer (ILASA) and Legates, and the 1988 analyses of the GPCC and the ECMWF forecast results (upper panel annual mean, mid panel northern summer and lower panel northern winter).

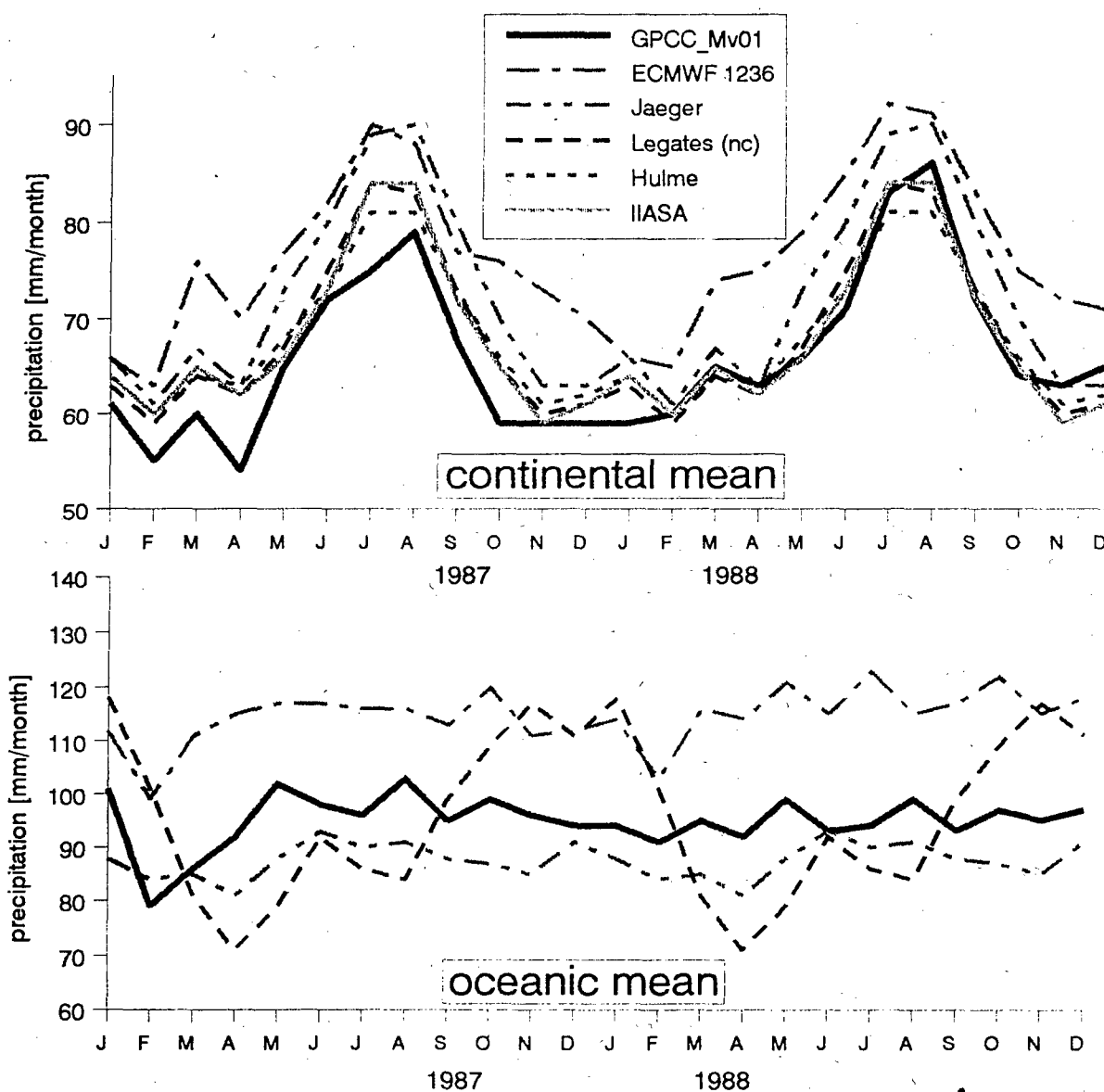


Figure 3: Terrestrial and oceanic area-averaged precipitation (mm/month) for the climatologies of Hulme, Jaeger, Leemans/Cramer (IIASA), and Legates, as well as for the GPCC analyses and ECMWF model results (years 1987 and 1988).

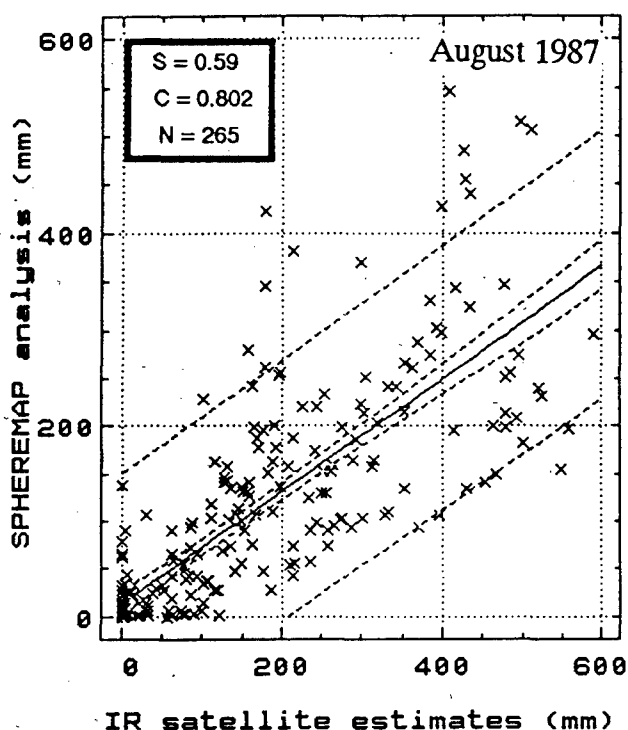


Figure 4: Scatter diagram for grid-area related monthly precipitation for August 1987, analysis from rain-gauge measurements versus estimates from IR satellite images, r = correlation coefficient, s = linear regression slope, n = number of grid pairs (only less complicated grid cells are used).

Finally, the estimates from satellite infrared images over land are gridwise compared to the GPCC results based on the in-situ measurements. In this study, "complicated" grid-cells are not included, which are defined by high mountains (mean grid terrain level more than 1000 m msl), coastal belts (water-covered grid area of 50% or more) and very poor in-situ data (less than two stations). The widely spread scattering as well as a strong bias is illustrated by Figure 4. Generally, IR-results overestimate the precipitation over the continents, and underestimate it over the oceans (GPCC 1992). However, relationships diverging from this rule are found over the eastern coasts of the continents and over cold upwelling water, west of the continental shelves. The structure of the spatial distribution of differences will have to be analysed in more detail when the GPCC's data set will cover a larger period and will be based on more conventional data.

4. CONCLUSIONS

In order to produce reliable quantitative area-means of the terrestrial precipitation, the incorporation of a sufficient density of in-situ observations is necessary. Remotely sensed information should be adjusted to the ground truth with regard to regional peculiarities, especially over land areas.

Oceanic and polar estimates still are the most uncertain part of the global precipitation climatology. At present, precipitation over ocean can be estimated best by satellite observations, even if the calibration is required. Further research on algorithms and intercomparison studies are necessary.

5. REFERENCES

- Arkin P A 1979: The relationship between fractional coverage of high cloud and rainfall accumulation during GATE over the B-scale array. *Month. Weath. Rev.* 107, 1382-1387.
- Adler R F, G J Huffman, P R Keehn, B Rudolf and U Schneider 1993: Global Precipitation Estimates Using a Combination of Satellite Data, Raingage Analysis and Model Precipitation Information. Contribution to the IAMAP/IAHS Joint International Meeting, Yokohama, July 1993.
- Arpe K 1991: The hydrological cycle in the ECMWF short range forecasts. *Dynamics of Atmospheres and Oceans* 16, 33-60.
- Bradley R S, P M Kelly, P D Jones, H F Diaz and C Goodess 1985: A Climatic Data Bank for the Northern Hemisphere Land Areas, 1851-1980. DOE Techn. Rep. No. TR017, US Dep. of Energy, Carbon Dioxide Res. Div., Washington D.C..

- Dorman C E and R H Bourke 1979: Precipitation over the Pacific Ocean, 30°S to 60°N. *Month. Weath. Rev.* 107 (7), 896-910.
- Dorman C E and R H Bourke 1981: Precipitation over the Atlantic Ocean, 30°S to 70°N.- *Month. Weath. Rev.* 109 (3), 941-948.
- Eischeid J K, H F Diaz, R S Bradley and P D Jones 1991: A Comprehensive Precipitation Data Set for Global Land Areas. U.S. Dep. of Energy Report No. DOE/ ER 69017T-H1, Washington D.C., 81 pp.
- GPCC 1992: Monthly Precipitation Estimates Based on Gauge Measurements on the Continents for the Year 1987 (Preliminary Results) and Future Requirements. Rep.-No. DWD/K7/WZN-1992/08-1, Offenbach/Main, August 1992, 24 pp (order from GPCC).
- GPCC 1993: Global Area-Mean Monthly Precipitation Totals on a 2.5° Grid for the Year 1988 (Preliminary Results, Derived from Rain-Gauge Measurements, Satellite Observations and Numerical Weather Prediction Results). Rep.-No. DWD/WZN-1993/07-1, Offenbach/Main, July 1993, 20 pp (order from GPCC).
- Hulme M 1991: An Intercomparison of Model and Observed Global Precipitation Climatologies. *Geophys. Res. Lett.* 18, 1715-1718.
- Jaeger L 1976: Monatskarten des Niederschlags für die ganze Erde. Bericht des Deutschen Wetterdienstes, Nr. 139 (Bd. 18), 33 pp and plates.
- Janowiak J 1993: Rainfall from remotely sensed infrared brightness temperature. In: *Proceedings of the GEWEX International Workshop Analysis Methods of Precipitation on a Global Scale*, Koblenz/Germany, Sept. 14-17, 1992, Annex A/41-44. WCRP-Report 81, WMO/TD-No. 558, Geneva, June 1993.
- Leemans R and W P Cramer 1990: The IIASA Database for Mean Monthly Values of Temperature, Precipitation and Cloudiness on a Global Terrestrial Grid. Working Paper WP-90-41, Biosphere Dynamics Project, Internat. Inst. for Applied Systems Analysis, Laxenburg, Austria, 62 pp.
- Legates D R 1987: A Climatology of Global Precipitation. *Publ. in Climatology* 40 (1), Newark, Delaware, 85 pp.
- Rudolf, B, H Hauschild, M Reiss, U Schneider 1992: Beiträge zum Weltzentrum für Niederschlagsklimatologie - Contributions to the Global Precipitation Climatology Centre, *Meteorologische Zeitschrift N.F.* 1(1), 7-84.
- Rudolf B, W Rueth and U Schneider 1993: The Spatial Sampling Error of Areal Mean Monthly Precipitation Totals Analyzed from Gauge Measurements. Fourth International Conference on Precipitation; Hydrological and Meteorological Aspects of Rainfall Measurement and Predictability, Iowa City, USA, 80-82. (see also Rudolf et al., this issue.)
- Rudolf B 1993: Management and Analysis of Precipitation Data on a Routine Basis. *Proceedings Intern. WMO/IAHS/ETH Symp. on Precipitation and Evaporation* (Ed. M. Lapin, B. Sevruck), Vol. 1, 69-76, Slovak Hydromet Inst., Bratislava, Sept. 1993.
- Schemm J, S Schubert and J Terry 1992: Estimates of monthly mean soil moisture for 1979-1989. NASA Technical Memorandum 104571, GSFC, Greenbelt, Maryland.
- Schutz C and W L Gates 1972-74: Global Climatic Data for the Surface: R-1029-ARPA (1972), R-915/1-ARPA (1972), R-1317-ARPA (1973), R-1425-ARPA (1974), RAND Corporation, Santa Monica.
- Shepard D 1968: A two-dimensional interpolation function for irregularly spaced data. *Proc. 23rd ACM Nat. Conf.*, Brandon/Systems Press, Princeton, NJ, 517-524.
- Wilheit T T, A T C Chang and L S Chiu 1991: Retrieval of Monthly Rainfall Indices from Microwave Radiometric Measurements Using Probability Distribution Functions. *J. Atm. Ocean. Tech.* 8, 118-136.
- Willmott C J, C M Rowe and W D Philpot 1985: Small-scale climate maps: A sensitivity analysis of some common assumptions associated with grid-point interpolation and contouring. *The American Cartographer* 12 (1), 5-16.

MAPPING OF SUPER-REFRACTIVE AND DUCTING LAYER STATISTICS FROM RADIOSONDE DATA

K.H. Craig and T.G. Hayton

Rutherford Appleton Laboratory, Chilton, Didcot, OX11 0QX, U.K.
Tel: +44 235 445134, Fax: +44 235 446140, Email: ken.craig@rl.ac.uk

ABSTRACT

This paper reports preliminary results from a new analysis of radiosonde data aimed at producing maps of duct-related parameters for use in radio wave propagation models. The sources, reduction and validation of the data are described. Boundary layer modelling was used to investigate apparent anomalies in the data.

Keywords: Radiosondes, Duct Statistics, Mapping, Boundary Layer.

1. INTRODUCTION

The maps of clear-air climatological parameters used by the current ITU-R recommended prediction procedures for line-of-sight paths and for interference between terrestrial stations are based on analyses of radiosonde ascents [1] made in the early 1960s. The study involved 112 radiosonde stations with a time span of 5 years (with only 4 months from each year included).

In collaboration with Norwegian Telecom Research and CRC, Canada, a fresh statistical analysis of recent, more extensive, radiosonde data has begun to look for new, physically-based parameters to characterise the atmosphere during anomalous propagation conditions. The overall goal is to improve the prediction accuracy of propagation models by incorporating these parameters and to validate them using radio link data banks available within the ITU and COST 235.

2. RADIOSONDE DATA SOURCES

2.1 Low resolution data

The only source of radiosonde data with global coverage and long time span is the WMO network of upper air sounding stations. The data are archived by several organisations.

All available radiosonde observation (RAOB) data for the ten years 1983–1992 were obtained from the

National Center for Atmospheric Research (NCAR) in the USA. The parameters available are pressure, temperature, dew point depression, geopotential height, and wind speed and direction. Balloons are launched twice daily, nominally at 0000h and 1200h UT.

All parameters are reported at *mandatory* levels: fixed pressure levels agreed by the WMO. Only the 1000 mb and 850 mb levels are normally relevant to terrestrial radio links, the lower pressures levels being too high. Pressure, temperature and dew point are also reported at *significant* levels: heights that show significant features (such as changes of slope) in the vertical profiles of temperature or dew point. There may be several significant levels below a height of 1000 m.

Many stations also launch pilot balloons (PIBALS) to give information on upper air winds at the intermediate times of 0600h and 1800h; these have not been used in the analysis as refractive index can not be derived from them.

The station level values of pressure, temperature and dew point temperature are also reported. A calculation of the ground value of refractivity is clearly very important for studies of ground-based layers and surface ducts. In this context, it is important to note that *the station values are normally obtained from ground-based sensors, and not from the radiosonde itself*. This is discussed further below.

One further piece of information is available in the NCAR data. Each parameter is marked with a "flag" showing the result of consistency checks applied to the data; these flags have been used when validating the refractivity profiles derived from the radiosonde data.

2.2 High resolution data

The mandatory and significant level data reported to the WMO are extracted from "raw" data transmitted back to a ground receiver from the radiosonde as it ascends. For modern radiosondes, the height resolution of this raw data is high; the

Vaisala sondes currently used by the UK Met Office send back data every 2 seconds, giving a height resolution of about 10 m. In the UK, this high resolution data is archived in digital form.

A complete year (1991) of high resolution data from Hemsby in the UK has been obtained in order to compare radiometeorological statistics obtained from the WMO-formatted data with those obtained from the raw data.

3. DATA REDUCTION AND VALIDATION

Reducing the low resolution RAOBS data to validated height-refractivity profiles is a major data processing task. The compressed and encoded WMO dataset amounts to over 6 Gb and is ordered by date, not by radiosonde station. Extracting and unpacking individual station files, containing all the ascents made in 10 years is a process equivalent to rotating a 6 Gb matrix. The availability of 20 Gb of disk space simplified this enormously. In all, there were over 4000 stations in the dataset, although less than 1000 contained a sufficient number of ascents for subsequent statistical analysis.

The next stage is to reduce the station files of meteorological parameters to files of height-refractivity profiles. The refractivity is obtained from the pressure, temperature and dew point depression. The height is obtained by integrating the hydrostatic equation and the equation of state of the air from the ground up to the level of interest. In this process, validity checks are made:

- (i) only data that have passed the tightest NCAR consistency checks are accepted;
- (ii) the heights calculated from the hydrostatic equation can be compared with geopotential heights given in the WMO data at mandatory reporting levels (calculated by the radiosonde system from the hydrostatic equation using all the "raw" ascent data). The difference between the two gives an indication of the quality of the radiosonde data, and a criterion based on the error distribution is used to reject ascents with poor height estimates.

4. RESULTS

In this section we report preliminary results based on analyses of the height-refractivity profiles from a subset of the radiosonde stations available, mainly in Europe.

None of the current ITU-R prediction methods make use of duct or ducting layer statistics: all the clear-air climatological maps are based on surface values or surface-based gradient statistics. Since ducts and reflecting layers are the main cause of multipath and long range interference, a preliminary study of duct parameter statistics has been made.

Our results have been compared with duct statistics from [2], based on 5 years' of radiosonde data from the late 1960s and early 1970s.

4.1 Duct statistics

Monthly and annual statistics of the probability of occurrence, and median values of the duct strength, thickness and height were obtained for surface and elevated ducts.

Figure 1 compares the monthly percentage of occurrence of surface ducts at Hemsby in the UK derived from the new low resolution data and from the Sylvania study. The incidence of ducting is greater in the summer months as expected. However, it is noticeable that the new data shows a higher incidence of ducting than the older data. This was true of most of the radiosonde stations considered. (There was good agreement between the two data sources for the statistics of duct height and strength).

The reason for these differences is not yet clear. It is more likely a result of the higher resolution, better accuracy and response times of the more modern radiosonde sensors than a change in the climate over the 20-year period between the datasets, but further investigation is required.

Figure 2 is a contour map of the annual percentage of occurrence of *elevated* ducts in Europe. The map is based on only the 16 stations indicated, although statistics from over 100 stations are available.

4.2 Comparisons of the high and low resolution data

Within the COST 235 framework, analyses of surface layer statistics (for example, the refractivity gradient in the lowest 100 m, which is needed in the calculation of the parameter β_0) have been made. It was found that different sources of radiosonde data (of different height resolutions, although both classed as low resolution) gave different results. There is no ducting in the majority of ascents: rather the refractivity profile in the first one or two kilometres is essentially linear, although with a slope which differs from ascent to ascent. The

differences in the statistics were caused by the station height value of refractivity being offset from the value that would be expected by simple extrapolation of the radiosonde data values to the ground; this had a significant effect on the gradients in the lowest 100 m which was different for the different height resolutions.

The Hemsby high resolution data were used to investigate the surface layer in more detail: the height resolution is about 10 m, and the first radiosonde point generally occurs at a height below 20 m. Three possibilities for the station value "offset" were considered:

- (i) calibration differences between the ground-based sensors and the radiosonde sensors;
- (ii) time lags and inadequate acclimatisation of the radiosonde before launch;
- (iii) boundary layer effects;

Figure 3 shows the distribution of the difference between the reported ground value and the ground value derived by extrapolating the first few radiosonde points. The distribution is strongly biased to positive values (i.e. higher refractivity measured at the ground than would be expected by extrapolating from the radiosonde data). This shows that the differences are unlikely to be due to calibration errors.

The quality control at Hemsby is known to be good. In the great majority of the ascents, the refractivity profiles were close to linear right from the lowest radiosonde point, with only the ground value offset, so it seems unlikely that poor acclimatisation or sensor time lags are the cause of the ground value offsets.

In the atmospheric boundary layer, the lowest 50–100 m forms a surface layer in which the wind structure is determined primarily by surface friction and the vertical gradient of temperature. The vertical transport of momentum, heat and moisture in this layer occurs by turbulent mixing, and the vertical fluxes of these quantities are proportional to the mean values of the gradients of wind velocity, potential temperature and specific humidity, respectively [3]. The vertical profiles of these quantities are almost always logarithmic in the lowest part of the surface layer.

To test whether this could explain the offsets in the surface values, the low resolution ascent of Figure 4a was used. Only two points occurred below 100 m: the station height, and significant level data at 24 m. It was assumed that the station

meteorological instruments were at a height of 1 m above ground level, and the potential temperature and specific humidity fluxes were calculated from the temperature and dew point values measured at these two heights. These fluxes were then used to predict the full modified refractivity profile between heights of 1 and 24 m, while the profile above this surface layer was assumed to be correctly represented by the low resolution data. The continuous line in Figure 4b shows the reconstructed profile. The values of modified refractivity measured by the high resolution radiosonde data have been overlaid: the agreement is excellent.

Although much more work is required, it appears that the ground value offsets in the data may be genuine and attributable to boundary layer effects.

5. CONCLUSIONS

Because of its global coverage and long time span, the WMO radiosonde network is at present the only available source of refractive index profile statistics. With modern computing resources, large scale statistical analyses are quite feasible, and these can be used to draw maps of parameters that are candidates for propagation prediction models.

However, further investigation of the accuracies and limitations of statistics based on radiosonde data is required. In particular, any statistics derived from gradients in the first few hundred metres (including surface duct, β_0 and P_L statistics) must be interpreted with caution due to the very high gradients that can exist in the lowest few tens of metres above the surface.

Mapping of super-refractive and ducting layer statistics is only the first step in improving propagation prediction models. These parameters have to be incorporated into the propagation models and validated against measured radio link data. This work is being carried out within COST 235 and the ITU.

6. REFERENCES

- [1] B.R. Bean, B.A. Cahoon, C.A. Samson and G.D. Thayer, A World Atlas of Atmospheric Radio Refractivity, ESSA Monograph 1, 1966.
- [2] L.N. Ortenburger, Radiosonde Data Analysis II, GTE/Sylvania Incorporated, 1977.
- [3] J.C. Kaimal and J.J. Finnigan, Atmospheric Boundary Layer Flows, OUP, 1994.

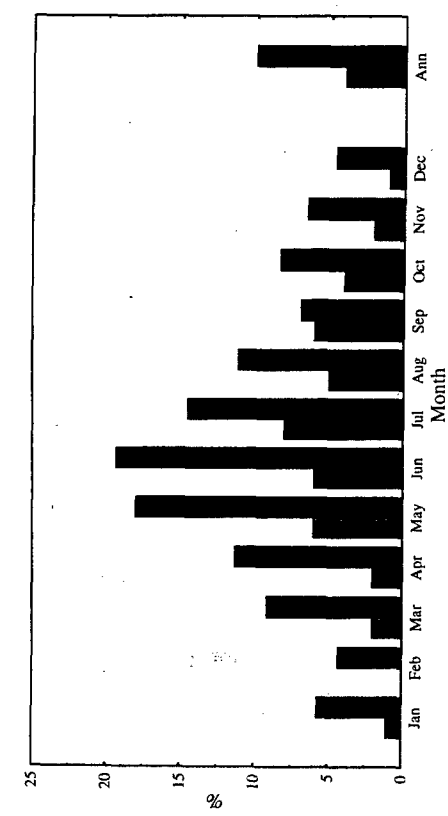


Figure 1: Percentage of occurrence of surface ducts at Hemsby (Solid bars: new data; shaded bars: Sylvania data [21])

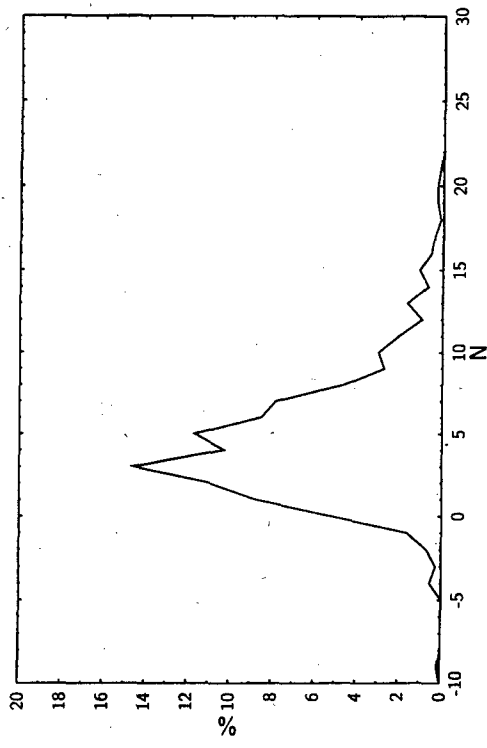


Figure 3: Distribution of radiosonde ground value offsets

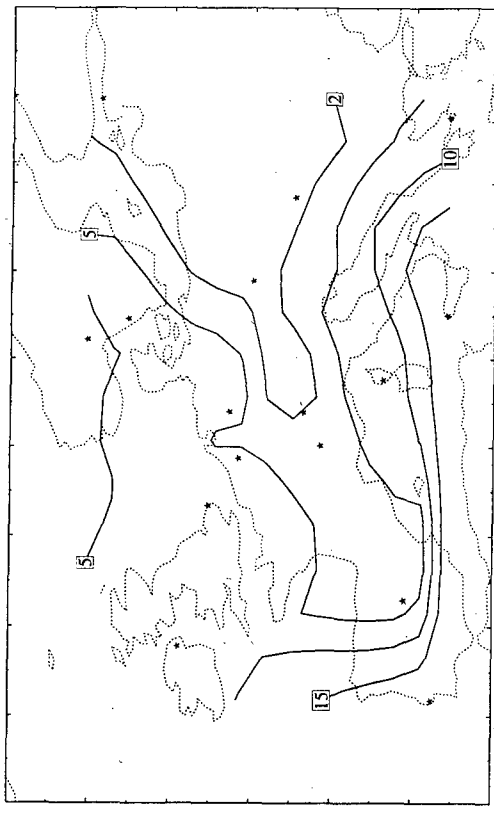


Figure 2: Annual percentage of occurrence of elevated ducts

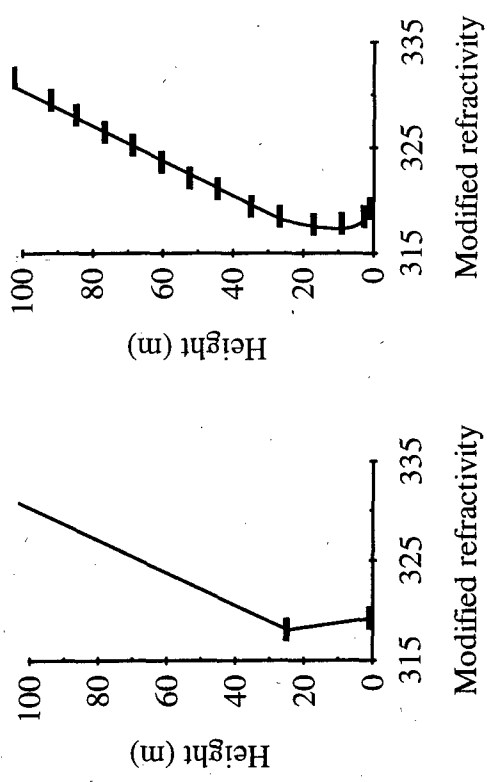


Figure 4: (a) Low resolution data
(b) High resolution data and boundary layer prediction

Session 11: Mapping II

RAIN RATE DISTRIBUTIONS IN SPAIN RELATED TO ITS CLIMATIC CHARACTERISTICS

L. Mercader¹ and A. Benarroch²

1- Public University of Navarra, ETSIT, 31006 Pamplona, Spain

Tel: +33-48-169311, Fax: +33-48-169281, E-mail: luismer@upna.es

2- Polytechnic University of Madrid, ETSIT, 28040 MADRID, Spain

Tel: +33-1-3367218, Fax: +33-1-3367350

ABSTRACT

In order to obtain a rainfall rate map of Iberia based on local data, raingauge records from more than 65 sites have been analyzed. As it is shown in this paper, the results obtained agree with the very different climatic peculiarities of the regions of Iberia, which are mostly due to the large amount of mountains and to the diverse influence of the Atlantic Ocean and the Mediterranean Sea.

Keywords: Atmospheric precipitation, Rainfall rate statistics, Spatial distribution, Spain, Europe.

1. INTRODUCTION

Raingauge records from over 65 meteorological stations located in every region, with an average of ten years per station, have been analyzed in order to obtain a rainfall rate distributions map of Iberia. This map, which is based on local data, will provide the required tool to make accurate rain attenuation predictions for satellite or terrestrial radiolinks. Moreover, the results obtained for Spain could help to elaborate the future climatic map of Europe. The extremely different climatic characteristics found throughout Iberia are due to the very different influence of the Atlantic Ocean and the Mediterranean Sea surrounding the Peninsula combined with the very complicated orography of the country (fig.1). Moreover, the obstructing effect of the Azores Islands high pressure system as well as the influence of the Sahara winds on the Mediterranean Coast are determining climatic factors (Ref. 1).

Some of the more significant features of Iberia are:

- 1) The very rainy north coast from the frontier of Portugal to the frontier of France separated from the interior by the Cantabrian range,
- 2) The large and high Duero region, which the Central range isolates from the lower Tago and Guadiana bassins,
- 3) The Guadalquivir Valley, wide open to the Atlantic Ocean but cut off from the Mediterranean Sea influence because of the very high Penibetic range,

- 4) The Mediterranean Coast, out of the reach of the Atlantic Ocean influence due to the Iberian range and to the continuous Coastal ranges,
- 5) The Ebro Valley, encircled by the Pyrenees at the north, the Iberian range at the west and south, and the Coastal range at the east, and,
- 6) The semideserts of Almeria in East Andalusia, the Monegros in Aragon, and the B ardenas Reales in the south of Navarra.

2. EXPERIMENTAL RESULTS

2.1. The North and Northwest

Due to the blocking effect of the Azores Islands high pressure system, low pressure systems forming in the North Atlantic Ocean move very often towards the european regions north of Spain, grazing the northern coast up to the Cantabrian Mountains and the Pyrenees. Moreover, since rainy fronts usually enter Iberia from the west, it is in the northwest (Galicia) and the northern regions of Iberia where rainfalls are more frequent. After studying 10 years of raingauge records from the meteorological stations in Fuenterrabia, San Sebastian, Bilbao, Santander, Gijon and Avil s (located along the northern coast), it has been found that their rain rate distributions are proportional to the CCIR distribution for zone G (Ref.2). The relative errors with respect to this distribution can be neglected provided a proportionality coefficient is considered in each case (fig. 2). From these distributions, it is inferred that the intensity exceeded 0.01% of an average year $R_{0.01\%}$ contour lines for 30, 35 and 40 mm/h must be plotted as shown in fig. 3. The highest rainfall rates concentrate in the inner corner of the Bay of Biscay, from San Sebastian to Biarritz, where $R_{0.01\%} > 40$ mm/h.

Similar results have been achieved from the raingauge records collected in La Coru a, Santiago and Vigo (Coast of Galicia) (fig. 4). In consequence, the 30 mm/h contour line must return from the Ocean towards the interior of Galicia (fig.3). The relative errors for Lugo and Orense, located in the mountainous interior of this region, show that the

orographic effect on the high rain rates is such that the experimental distributions are closer to the H distribution for the lower probabilities and to the G distribution for the higher probabilities (fig. 5)

2.2. The Duero Region

As the chains of mountains in the north (Cantabrian range, near the coast, the Pyrenees, in the frontier with France) act as barriers to the rain systems, south of them the behaviour of rain rates changes abruptly. The high plateau of Castilla-Leon, with approximately 1000 m. of altitude, shows a central ring where the intensity for the 0.01% of the year falls below 20 mm/h (fig. 3). The distributions derived using the raingauge records from the stations located in this region (Valladolid, Zamora, Salamanca, Burgos, Soria) are proportional to the H distribution, provided it is corrected both in $R_{0.1\%}=8.5$ mm/h and $R_{1\%}=1.5$ mm/h. The corresponding relative errors are shown in fig. 6. The influence of the mountains surrounding this region has been considered when plotting the contour lines for 20, 30 and 35 mm/h in the map of fig. 3.

2.3. The Ebro Valley

The Ebro bassin is even more strongly isolated from the Atlantic Ocean low pressure systems due to the Pyrenees and the Iberian range, which separates it from the Duero Bassin. Instead, the influence of the Mediterranean Sea is clearly observed, even though a mountain range near the coast reduces its effects. The distributions obtained from the sites investigated in this region (Logroño, Zaragoza, Daroca, Lerida) are similar to the L distribution, considering the corresponding proportionality coefficients (fig. 7). The contour lines for this region, for 35, 30, 25 and 20 mm/h have been plotted according to the results obtained. The 20 mm/h line circles two semideserts (Los Monegros and Bardenas Reales) in the central part of this region.

2.4. The Orographic Effect

The orographic effect is significant in several sites located in mountainous areas in the above commented regions. The rain rate distributions for Huesca (near the Pyrenees, north of the Ebro Bassin), Ponferrada, Oviedo (north of the Cantabrian range), and Avila (at an altitude of 1131 m, near the Central range) (fig. 8) show a significant increase of high intensities for the same probability levels with respect to other sites located in the same regions but farther away from the mountains. Unfortunately, meteorological stations located in mountainous areas are very scarce.

Therefore it is not feasible to define accurately the limits between one zone and another, or to determine with precision the corresponding contour lines.

2.5. The South

Because of the Azores Islands high pressure system, most of the rain that falls in the Southwest of Iberia is due to the low pressure systems forming between the Bay of Cadiz and the Canary Islands in Autumn. In consequence, the distributions obtained by processing the rainfall records from Huelva, Sevilla, Cádiz, (in the Low Guadalquivir Valley) and Málaga are proportional to the CCIR distribution for zone K (fig.9). Instead, the distributions for Córdoba and Jaen, in the central part of Andalusia, and Badajoz and Ciudad Real, in the Guadiana Bassin, are approximately proportional to the H distribution (fig. 10). Therefore, higher intensities are observed for sites more open to the Atlantic Ocean influence.

Completely different to the already described, and also one from the other, are the distributions for Granada (at an altitude of 683 m, in a valley encircled by mountains) and Almería (semidesert area on the Mediterranean Coast under the Sahara winds).

All the commented results have allowed plotting the 20, 25, 30 and 40 mm/h contour lines for the South of Iberia (fig. 3).

2.6. The Eastern Coast

The very peculiar results for the Eastern Coast can be observed in fig. 11. While the distribution for the site located more towards the north (Castellon) is approximately equal to the K distribution, a continuous decrease of rain intensities is noted for stations located moving south along the coast. The effect of the Sahara winds is also perceptible in sites north of Almeria, such as Murcia and San Javier, whose distribution has been considered as a reference for the southern part of this region. The errors relative to this distribution are plotted in fig. 12, including the distribution for Almería. The contour lines corresponding to this region have been deduced from these results (fig. 3).

3. REFERENCES

1. Font I. 1985, *Climatología de España y Portugal*, INM, Madrid.
2. CCIR Report 563-4, Radiometeorological data, Reports of the CCIR, Annex to Vol. 5, Geneva 1990.

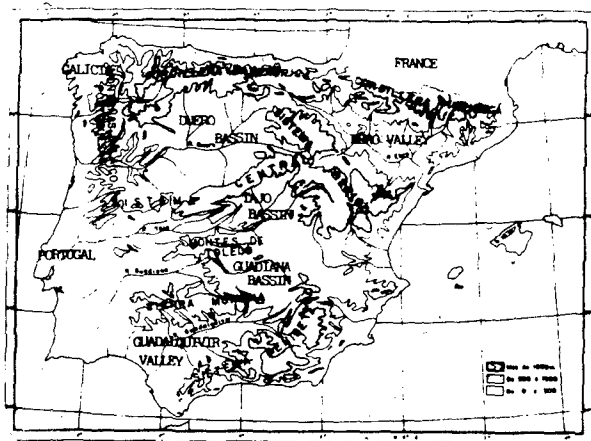


Figure 1. Orographic map of Iberia.

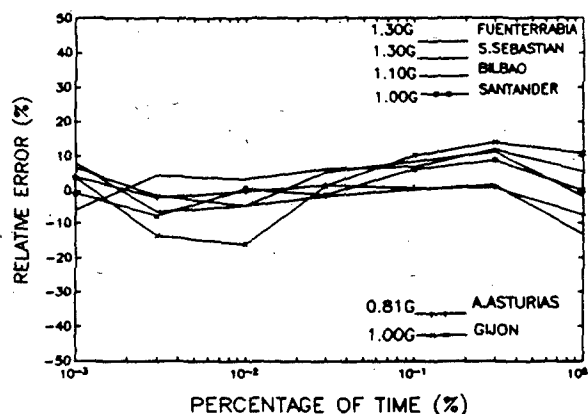


Figure 2. Relative errors for the North region with respect to the distribution for CCIR zone G.



Figure 3. $R_{0.01\%}$ Contour lines map of Iberia.

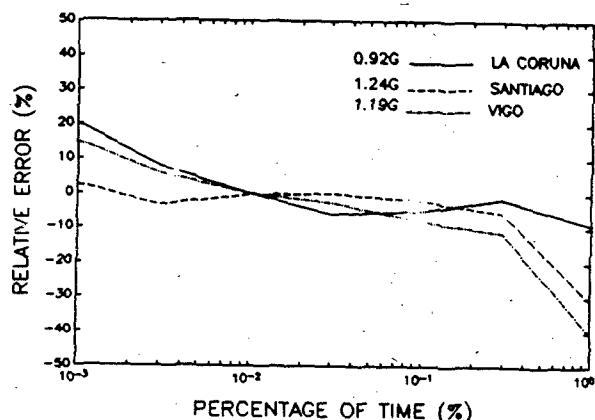


Figure 4. Relative errors for the Northwest with respect to the distribution for zone G.

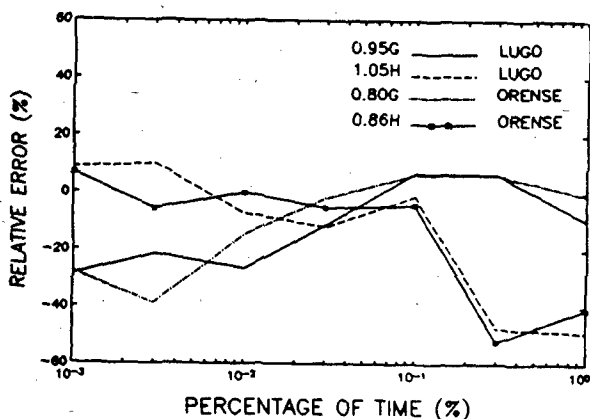


Figure 5. Relative errors for the mountainous interior of Galicia with respect to the distributions for zones G and H.

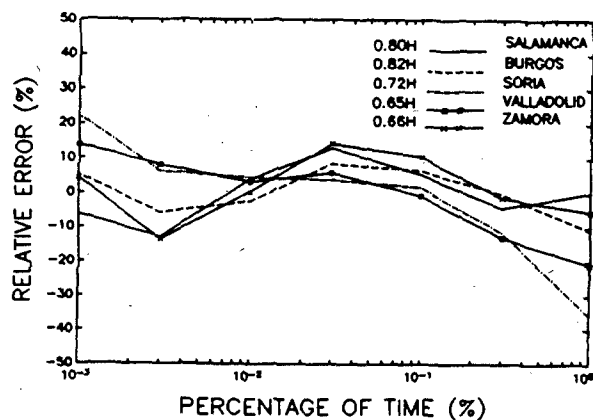


Figure 6. Relative errors for the Duero region with respect to the distribution for zone H.

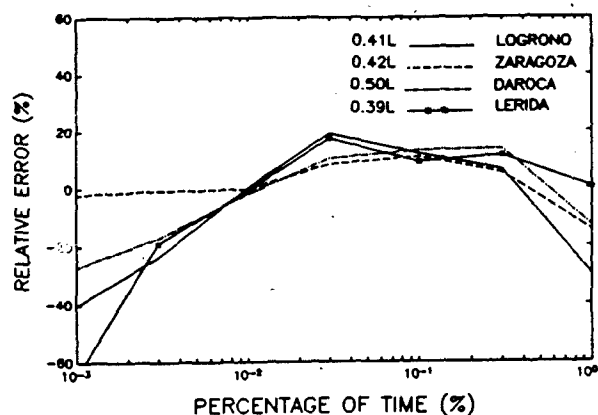


Figure 7. Relative errors for the Ebro Valley with respect to the distribution for zone L.

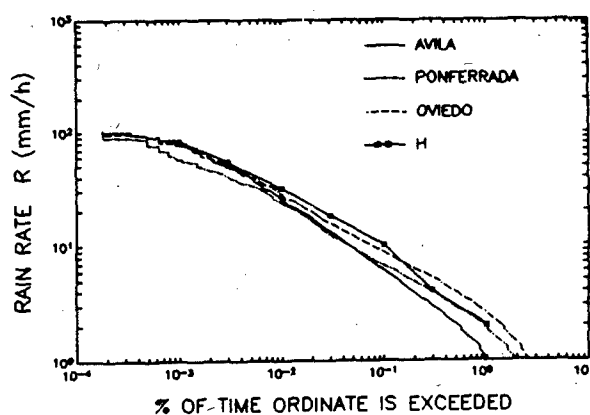


Figure 8. Rainfall rate distributions for sites in mountainous areas (compared to the distribution for zone H as a reference).

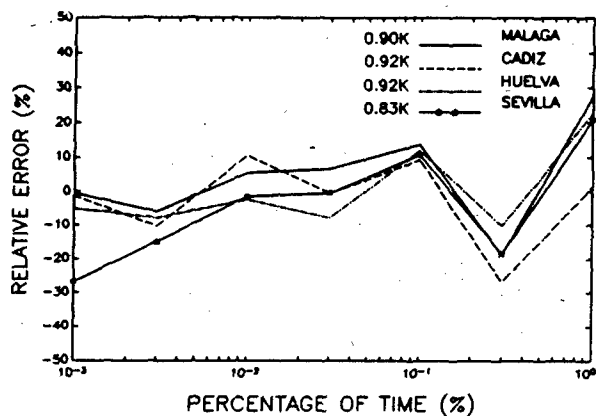


Figure 9. Relative errors for Western Andalusia with respect to the distribution for zone K.

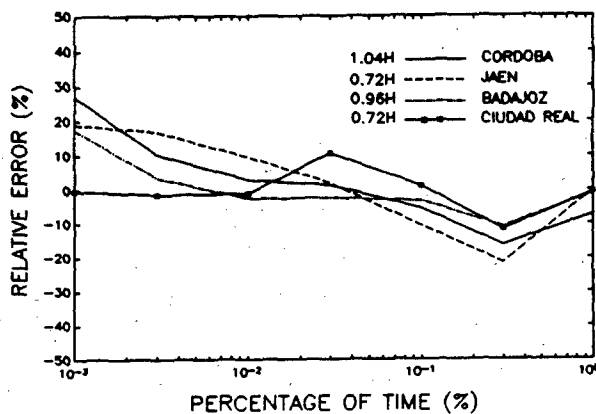


Figure 10. Relative errors for Central Andalusia and the Guadiana Bassin with respect to the distribution for zone H.

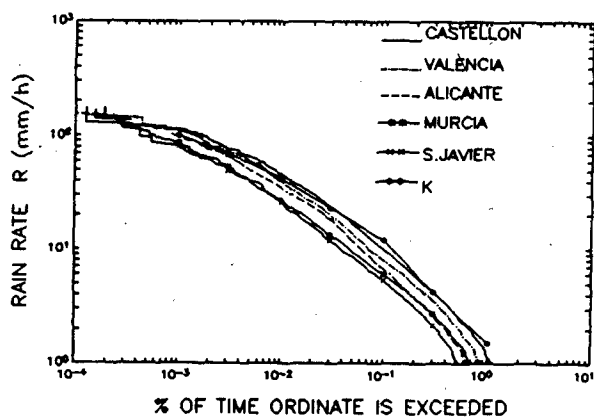


Figure 11. Rainfall rate distributions for the Eastern Coast.

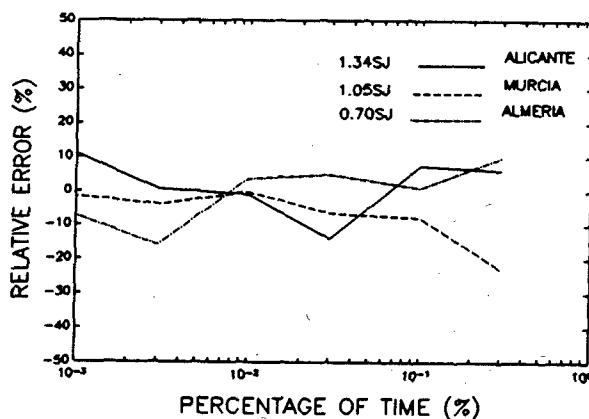


Figure 12. Relative errors for the Southeast with respect to the distribution for San Javier.

RADIOMETEOROLOGICAL DATABASE OF THE RUSSIA WITH GRAPHIC MAPPINGS

Darizhapov D.D., Batueva E.V., Zhamsueva G.S.

Buryat Nature Sciences Institute of Siberian Department of the Russia Academy of Sciences, 6 Sakhyanova, 670042 Ulan-Ude, Russia

tel. (8-30122) 3-62-60, Fax (8-30122) 3-28-41, E-mail Relcom: root@nien.buriatia.su

ABSTRACT

Radiometeorological database of the atmosphere over Russia territory has been obtained according to averaged data of 146 stations of aerological radiosounding for 10 years. Database is integrated into "Framework" environment. It included the characteristics of a vertical gradient of the atmosphere refractive index for different months of year and different hours of a day.

Keywords: Radiorefraction, Propagation, Database, Mapping

INTRODUCTION

The questions of planning and control modern telecommunication and information systems directly are connected with the problems of prognosis of tropospheric radio channel conditions. On this view the problem of construction the base of statistic characteristics of radiometeorological parameters of troposphere with dynamic and flexible systems is very actual. This system can be easily transformed to another parameters, for a example, first and second statistical moments of atmosphere's refractive index and it's vertical gradient.

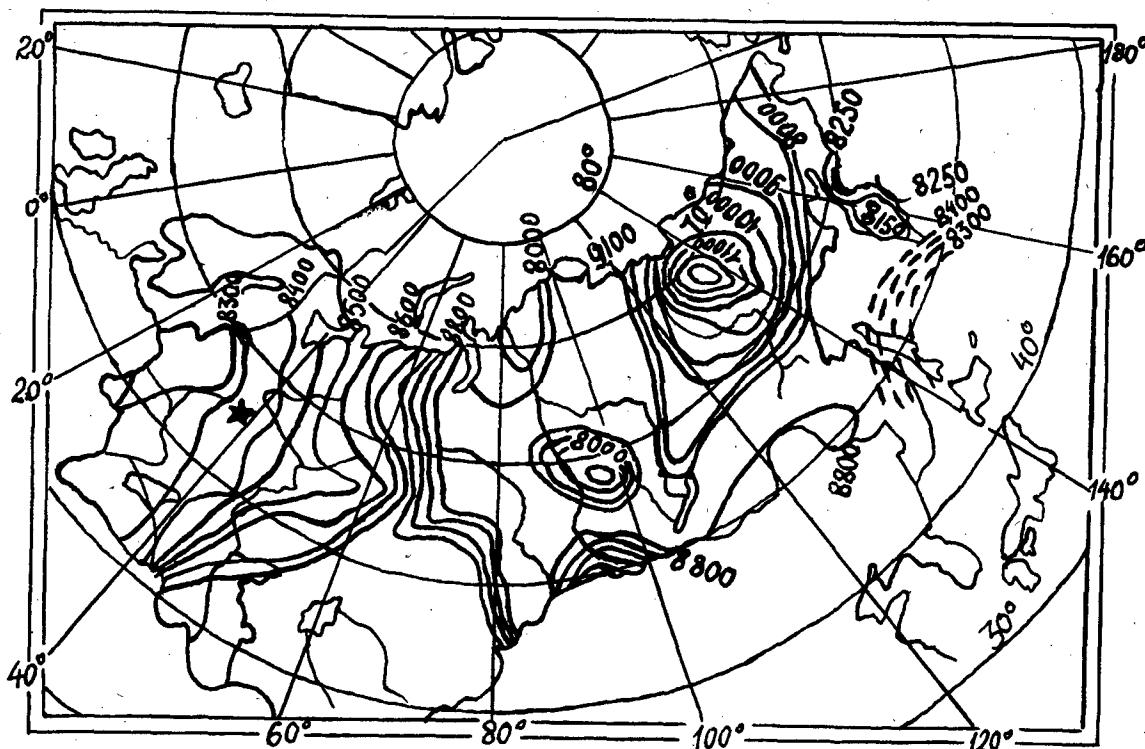


Fig. 1 Map of isopleths of monthly mean values of effective radius of Earth a for 1 km above the surface

RADIOMETEOROLOGICAL DATABASE

At present time creature atlas of radiorefractive parameters have been based on 306 stations of world and do not give a clear picture of radio-propagation conditions over Russia region, because only 40 stations are presented in mentioned radiorefractive atlas (Ref.1).

The tables of vertical gradients of refractive index over Russia territory on the basis of radiometeorological data of 51 station of Russia are constructed by method of approximate the refractive index of the atmosphere by exponential model (Ref.2). So the present radiometeorological charts and tables (Ref.1,2) do not give satisfy accuracy for practice.

In this paper radiometeorological database of the atmosphere over Russia territory has been obtained according to averaged data of 146 stations of aerological radiosounding for 10 year (from 1961 to 1970 years) (Ref.3). Database is integrated into "Framework" environment.

It included the characteristics of a vertical gradient of the atmosphere refractive index for different months of year and different hours of a day. Radiometeorological database can be easily transformed to another parameters. for a example, first and second statistical moments of atmosphere's refractive index and index and it's

vertical gradient. Also there is the possibility to prepare the monthly maps showing isopleths of refractive index for the layers between ground and 3000 m above sea level. For example map of isopleths of monthly mean values of effective radius of Earth a for 1 km above the surface (Fig.1). Figure 1 show that high mean values a are generally typical for sharp - continental region.

The centre of high mean values a strikingly reveals in extreme climatic zone of Russia (north - east) out of influence siberian anticyclone and strong cooling of surface air. Meridional distribution of a is observed in Europe part of Russia, where effective radius of Earth increase from west to east. Coast and island stations are characterized by move low means values of a .

REFERENCES

1. Bean B.R. et al. 1966. A world atlas of atmosphere radiorefractivity. Radio Science, 1, 9.
2. Rukina A.N. 1977. Index of refractivity in surface layer of air over USSR territory, 15 p.
3. New aeroclimatological reference book of frontier layer of atmosphere over USSR, 1986. 1, 1-10, p. 1-1802.

OCEANIC RAIN RATE PARAMETERS DERIVED FROM SSM/I

Long S. Chiu¹ and Alfred T. C. Chang

Hydrological Sciences Branch, NASA/GSFC, Greenbelt, Maryland 20771 U.S.A.

¹SAIC/General Sciences Corporation, Laurel, Maryland 20707 U.S.A.

ABSTRACT

Oceanic monthly rain rate parameters such as rain frequency, rain intensity, height of the rain column, and the no rain microwave brightness temperature threshold estimated for 5° by 5° latitude/longitude boxes from six and half years of SSM/I data are examined. Analyses show that the rain intensity and frequency tend to vary in phase zonally in the climatological mean pattern, whereas temporal variations of these parameters tend to correlate negatively. The zonal average rain column height shows a distinct seasonal cycle, with seasonal amplitude that increases with latitude. The rain column is a maximum of about 4.7 km in the tropics, and decreases to about 3.2-3.8 km at latitudes of about 50°.

Keywords: Rain frequency, rain intensity, rain column height, SSM/I

1. INTRODUCTION

Wilheit et al. (ref. 1) developed a technique (hereafter referred as WCC technique) for estimating monthly oceanic rain rates over 5° by 5° latitude/longitude boxes using microwave measurements taken by the Special Sensor Microwave Imager (SSM/I) on board the Defense Meteorological Satellite Program (DMSP) satellites. Six and a half years (July 1987 - December 1993, with December 1987 omitted due to missing data) of SSM/I data have been processed and monthly rain rates generated. Preliminary comparison showed that these oceanic rain rates are in good agreement with climatology and the GOES Precipitation Index (GPI) (ref. 2). Comparison with rain gauge data collected at the Pacific atoll stations showed a low bias of 8% and a r.m.s. difference of about 50% (ref. 3).

In addition to oceanic monthly mean rain rates, the WCC technique also computes other rain rate parameters such as rain probabilities, rain intensities, heights of the rain column, and the no rain microwave brightness temperature thresholds. This paper examines the various rain rate parameters in terms of the zonal average time mean rain pattern and how temporal variabilities of these parameters may affect climate variations of the zonally average rain patterns.

2. WCC TECHNIQUE

The WCC technique uses a combination of microwave brightness temperature (T) of twice the vertical polarization at 19 GHz minus that at 22 GHz of the SSM/I to reduce the effect of water vapor on the microwave signal. The histogram of T for a 5° by 5° latitude/longitude box is computed and matched iteratively to a theoretical microwave brightness temperature histogram which is derived from a mixed lognormal rain rate distribution (ref. 4). Wilheit et al.'s (ref. 5) rain rate (R) -microwave brightness temperature (R-T) relation is used in converting the rain rate distribution to the brightness temperature histogram. The mixed rain rate distribution consists of a no rain probability of (1-p) and a rain probability of p. The raining part of the mixed distribution is assumed to follow a lognormal distribution, with mean R_0 , and variance S. The non-raining part of the T histogram is modeled by a Gaussian distribution, with mean T_0 and standard deviation S_0 . Altogether, there are five relevant parameters that has to be estimated, p, R_0 , S, T_0 , S_0 . We shall refer to p as the rain frequency, R_0 the rain intensity, and T_0 the background brightness temperature. The total monthly rainfall is $RR = p * R_0$. In addition to these parameters, the height of the rain column, H_0 , is computed from the scattergram of 19 and 22 GHz using multi-channel information from these channels. A chi-square goodness-of-fit is computed for each monthly 5° by 5° box using ten intervals, and boxes with chi-square values in excess of 5000 are flagged missing.

3. ZONAL MEANS

Figure 1 shows the time averaged zonal mean rain rates for the global ocean (A), the Atlantic (B), Pacific (C), and Indian (D) ocean, respectively. Time averaging is performed for each month overall the years. Missing boxes are excluded from the zonal averaging. In the global mean, the region of maximum zonal mean precipitation appears in the tropics. A zonal maximum of 300 mm/month is found in the latitude belt of 5°-10°N in August. The maximum in the southern hemisphere is less well defined. Secondary maxima are found in the latitude

belts between 40° - 50° in the winter season in both hemispheres.

The seasonal cycle is less pronounced in the south Atlantic than the north Atlantic which shows a winter maximum in the high northern latitude belts. The belt of maximum zonal precipitation near the equator tracks the mean position of the Inter-Tropical Convergence Zone (ITCZ) quite well and follows the movement of thermal equator closely. The Atlantic also sees the maximum latitudinal gradient of zonal mean precipitation, from a maximum of about 275 mm/month at the equatorial peak, dropping to minimum of about 25 mm/month in the oceanic dry zones.

The pattern of the seasonal zonal mean precipitation in the Pacific is similar to that in the Atlantic. The latitudinal zonal gradient is smaller. In the latitude belt between 5° - 15°S, a seasonal amplitude of about 50 mm/month is seen. This seasonal feature is a manifestation of the South Pacific Convergence Zone (SPCZ). A seasonal cycle in the south Atlantic in these latitudes is lacking.

The seasonal cycle in the Indian Ocean is characterized by January (southern summer) maximum in the latitude belt 5°-10°S, and a June (northern summer) peak at latitude belts between 10°-20°N. The June peak, which occurs in the Bay of Bengal region, is indicative of the Indian summer monsoon.

The mean rain rate is given by the relation $RR = p * Ro$. If we let $\langle \rangle$ denotes time average over the years and $[]$ denotes zonal averaging, and primed (') and starred (*) quantities represents the departure from the time and zonal means, respectively, we can write

$$[\langle RR \rangle] = [\langle p Ro \rangle]$$

$$\begin{aligned} &= [\langle p \rangle][\langle Ro \rangle] \quad (\text{term 1}) \\ &+ [\langle p' Ro' \rangle] \quad (\text{term 2}) \\ &+ [\langle p' Ro^* \rangle] \quad (\text{term 3}) \end{aligned}$$

(1)

The first term represents the product of the time mean zonal average rain frequency and rain intensity. The second term is the covariance of zonal departure of the time mean p and Ro . At a given latitude belt, the second term is positive if high rain frequency regions tend to coincide with regions of high rain intensity in the time average p and Ro fields. The third term represents the zonal average of the temporal covariance of p and Ro , and arises because of interannual variations of the rain intensity and frequency.

Figure 2 shows the long term averaged zonal mean rain frequency $\langle p \rangle$, the rain intensity $\langle Ro \rangle$, the

height of the rain column $\langle Ho \rangle$, and the background (no rain threshold) brightness temperature $\langle To \rangle$. The pattern of $\langle p \rangle$ matches the total rain rate $\langle RR \rangle$ quite well, showing maximum $\langle p \rangle$ in excess of 0.45 in the latitude belts of 5°-10°N in the northern winter and in latitude belts of 40°-50°S and 35°-50°N. The northern hemisphere displays a more pronounced seasonal cycle in p , compared to the southern hemisphere.

The seasonal pattern of $\langle Ro \rangle$ is characterized by the maximum in July-August in the 5°-10° belt of over 20 mm/day, and another maximum in the northern high latitude in January-February. The position of maximum $\langle Ro \rangle$ coincides the $\langle p \rangle$ maximum in the low latitude. If we examine the relative contribution of the various terms in Eq. 1, the first term dominates. The second term is negative in the high northern latitudes in the winter time, but becomes positive at the low southern latitudes for most of the year. This indicates that the rain intensity and frequency regions are out of phase at the high northern latitudes. The third term is mostly negative, and tends to be large in the northern high latitudes.

The field of $\langle Ho \rangle$ shows a maximum of about 4.7 km near the equator which decreases poleward to about 4.2-4 km (3.8 km) in the northern (southern) summer hemispheres. The zonal average Ho shows a minimum of 3.2 km at 50° latitude during the winter in both hemispheres. The seasonal amplitude of $\langle Ho \rangle$ increases poleward.

A fairly smooth varying seasonal cycle is also seen in $\langle To \rangle$. The seasonal amplitude is less than 2°K at each latitude belts, whereas the equator to 50° latitude difference is about 10°K.

4. DISCUSSION

Techniques have been proposed (ref. 6) to combine the GOES Precipitation Index (ref. 7) (GPI) and microwave estimates to take advantage of the frequent sampling of the geosynchronous satellites. We demonstrated that the rain frequency and the rain intensity can be estimated independently to obtain the total rain amount. Since the GPI works best for convective rain and the Wilheit et al. R-T relation has been shown to satisfy stratiform rain conditions (ref. 8), a combination of the GPI and the WCC method, encompassing both convective and stratiform rain, may prove to be fruitful.

Wilheit et al. (Ref. 1) use an R-T relation which is fitted empirically to radiative calculations involving the height of the rain column, Ho , and the no rain threshold, To . Our study shows (not presented here) that the zonal and temporal variabilities of both To and Ho are small, and the $\langle To \rangle$ and $\langle Ho \rangle$ can be fitted to simple analytical expressions. These relations

can be applied to Wilheit et al.'s empirical R-T relation to derive a simple emission-based oceanic rain rate estimation method which may be applicable to climate-scale rainfall.

5. REFERENCES:

1. Wilheit, T., A. Chang, and L. Chiu, 1991: Retrieval of monthly rainfall indices from microwave radiometric measurements using probability distribution functions, *J. Atmo. Oceanic Tech.*, 8, 118-136.
2. Chiu, L., A. Chang, and J. Janowiak, 1993: Comparison of monthly rain rates derived from GPI and SSM/I using probability distribution functions, *J. Appl. Meteor.*, 32, 323-334.
3. Chang, A., L. Chiu, and T. Wilheit, 1993: Random errors of oceanic monthly rainfall derived from SSM/I using probability distribution functions, *Mon. Weath. Rev.*, 121, 2351-2354.
4. Kedem, B., L. Chiu, and G. North, 1990: Estimation of mean rain rates: Application to satellite observations, *J. Geophys. Res.*, 93, 3720-3728.
5. Wilheit, T., A. Chang, M. Rao, E. Rodgers, and J. Theon, 1977: A satellite technique for quantitatively mapping rainfall rates over the oceans. *J. Appl. Meteor.*, 16, 551-560.
6. Meisner, B., and P. Arkin, 1987: The relationship between large-scale convective rainfall and cold cloud over the western hemi-sphere during 1982-1984. *Mon. Weath. Rev.*, 115, 51-74.
7. Huffman, G., R. Adler, P. Keehn, A. Negri, 1993: Examples of global estimates from combined low orbit microwave and geosynchronous IR data, *Fourth Symp. on Climate Change Studies*, 17-20 January, 1993, Anaheim, California, 318-323.
8. Chang, A., A. Barnes, M. Glass, R. Kakar, and T. Wilheit, 1993: Aircraft observations of the vertical structure of stratiform precipitation relevant to microwave radiative transfer, *J. Appl. Meteor.*, 32, 1083-1091.

FIGURE CAPTIONS

Figure 1. Climatological seasonal variations of the zonal mean rain rate, [$\langle RR \rangle$], computed for the period July 1987 - December 1993, for the global ocean (top left panel), the Atlantic, the Pacific, and the Indian Ocean. Units are in mm/month.

Figure 2. Climatological seasonal variations of the zonal mean rain frequency [$\langle p \rangle$] (top left), rain intensity [$\langle Ro \rangle$] (upper right) in mm/day, height of rain column [$\langle Ho \rangle$] (lower left) in km, and the background brightness temperature [$\langle To \rangle$] (lower right panel) in $^{\circ}K$.

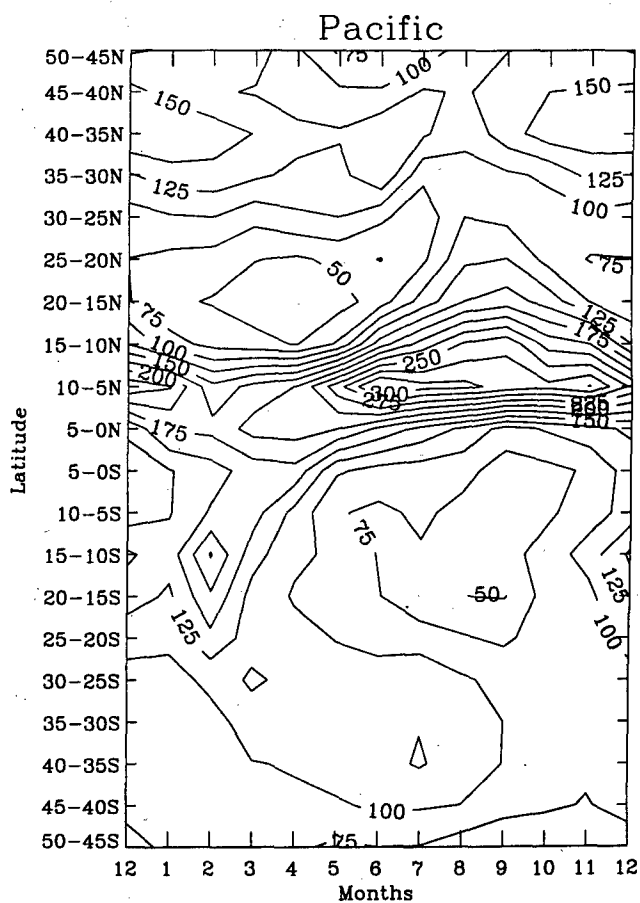
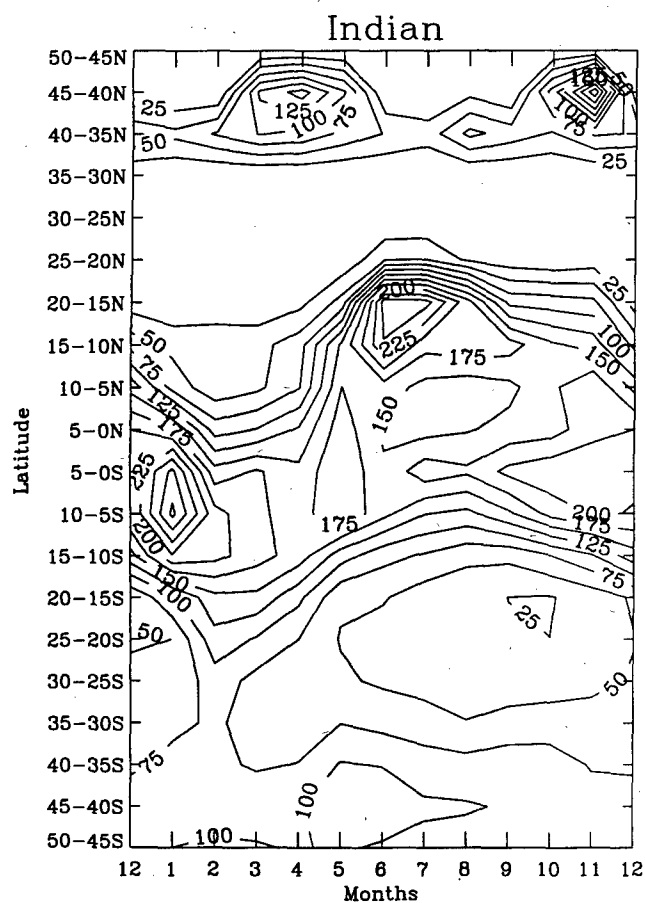
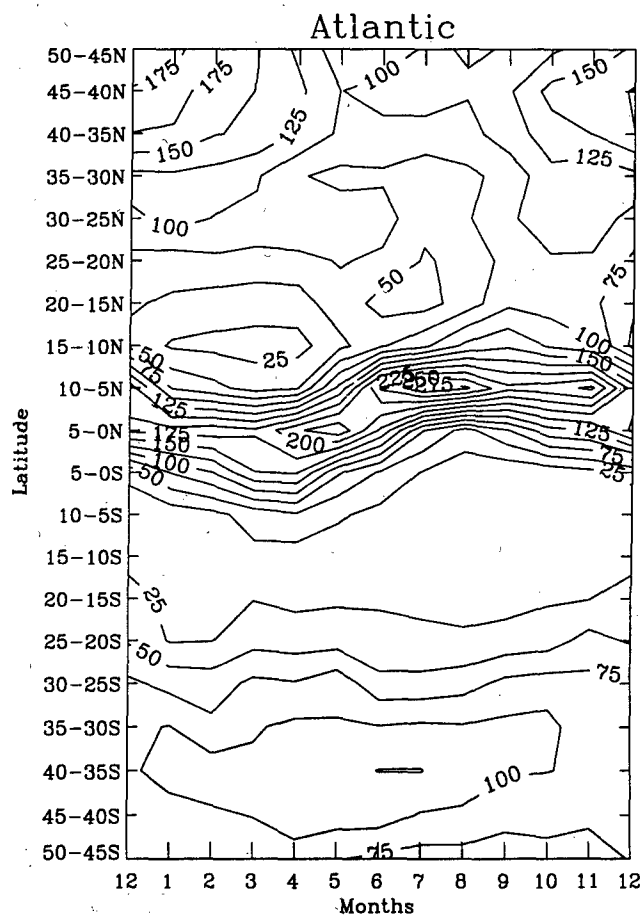
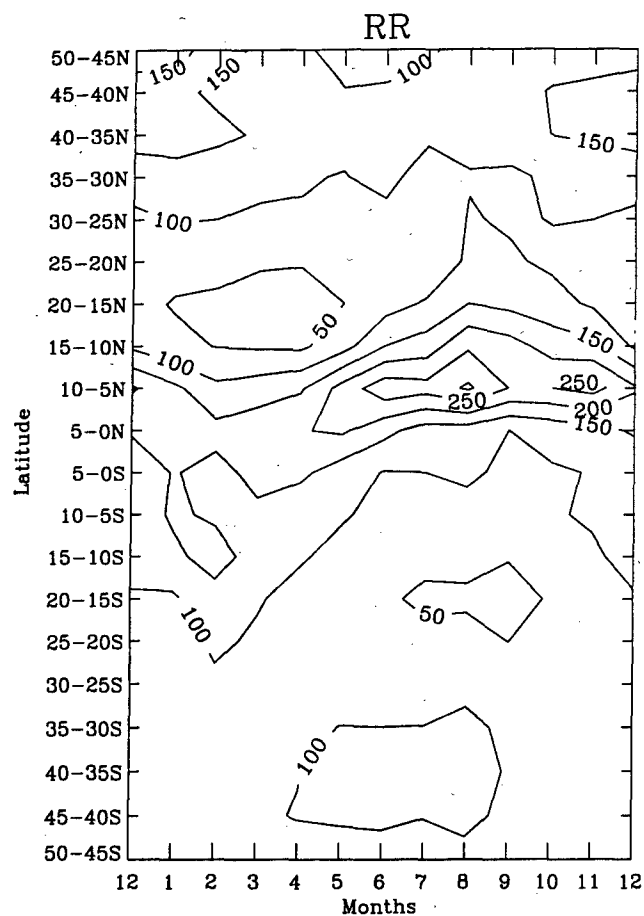


Figure 1

11.3.4

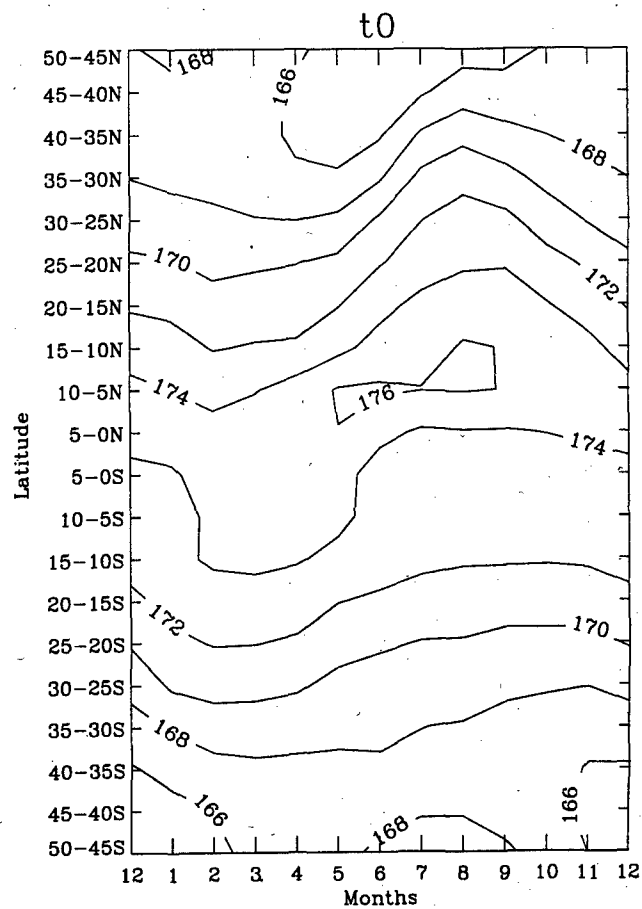
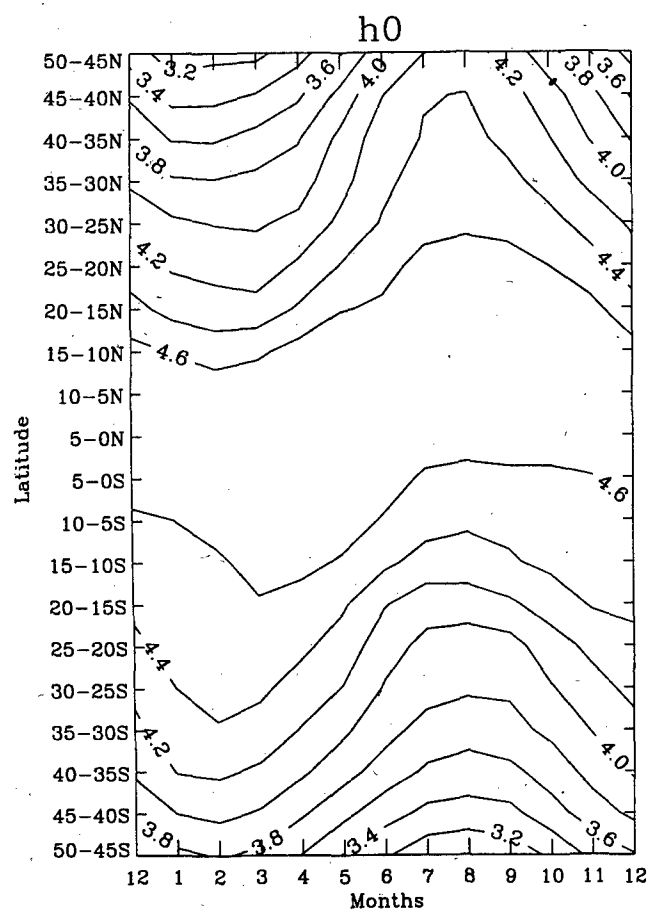
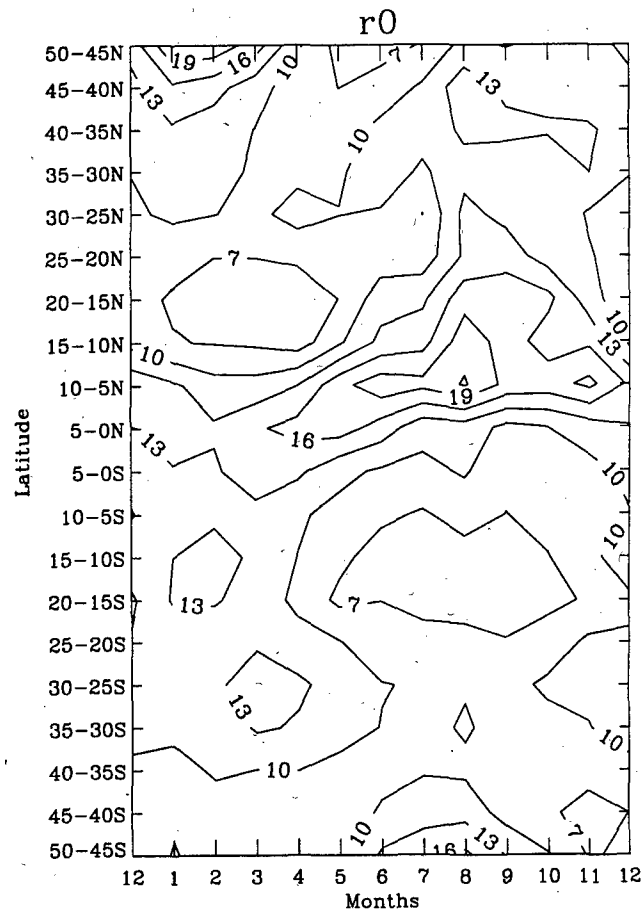
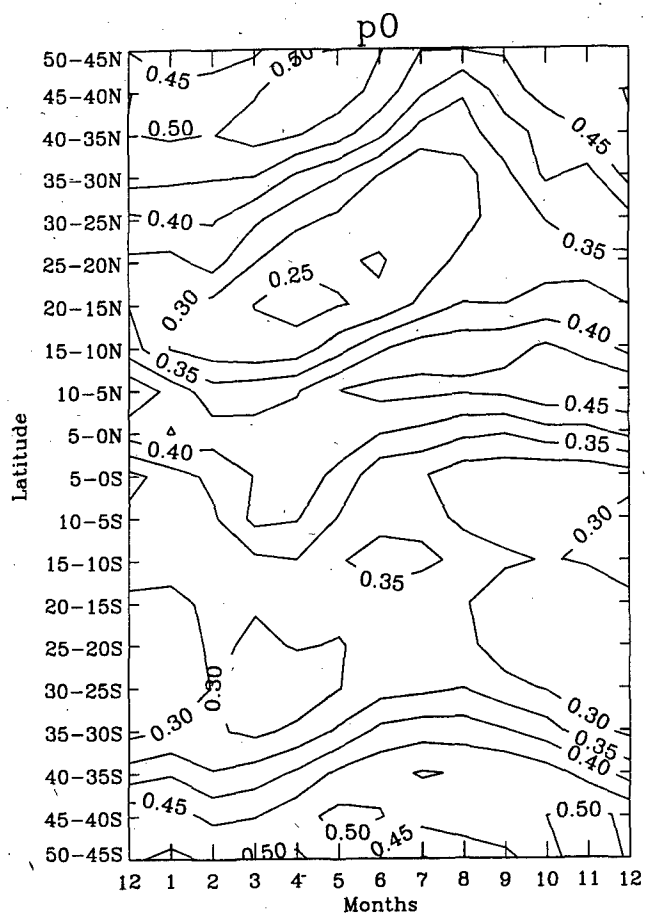


Figure 2

11.3.5

MESOSCALE MODELLING OF REFRACTIVE INDEX AND TROPOSPHERIC PATH-LOSS VARIATIONS

Kiselev O.N., Gosenchenko S.G., Mescheryakov A.A.

TACSR, 40 Lenin ev., Tomsk 634050, Russia.

Fax: +7 3822 224302, E-mail: root@tiasur.tomsk.su.

ABSTRACT

Results of mesoscale refractivity index above the ocean and their influence on UHF-radiosignal long-term variations searching by using structural functions are offered. The modelling of refractivity and path-loss variations is described.

KEYWORDS: Mesoscale, Long Term, Model, Ocean, Meteorology, Refractivity, Path Loss.

1. INTRODUCTION

There are not numerous data on state and changing of UHF-radiowave propagation conditions concerned with mesoscale atmospheric processes and corresponding time radiowave variations. Analysis of signal level samples and refractive index fields within macroscale (synoptical) inhomogeneities has shown the presence of periodic components with various typical periods. This fact allows quasiperiodic model of nonstationary random mesoscale processes to propose with taking into account both determinate and random components. The structural functions were used as a means of experimental samples analysis. As shown in (Ref.1) structural function method for detecting process periods is preferable to correlation-spectral one.

2. REFRACTIVE INDEX INHOMOGENEITIES

A mesoscale structure is a result of circulation cells above ocean because of background surface temperature variations. Mesoscale cells were detected experimentally with horizontal length about 100-200 of kilometers (Ref.2). Refractive index inhomogeneity field characteristics were estimated by using of searchship data. Measurements were made by simultaneous radiosounding by means two, three or four ships in some kilometers to 900 km spaced in south-west area of the Pacific Ocean northzone. Structural functions were represented as a sum of components with different scale for macro- (synoptical) and mesoinho-

mogeneities with assumption about Gaussian correlation function for synoptical component. As for mesoscale component the fact was taken into account that regular structures appear only till some distance determined as coherent interval. Then they appear as random ones. So the offered model is

$$B(l) = 2\sigma_s^2 \{1 - \exp(-l^2/l_s^2)\} + 2A_M^2 \sin^2(\pi l/L_C) \exp(-l^2/l_{CM}^2) + 2\sigma_M^2 \{1 - \exp(-l^2/l_{CM}^2)\} \quad (1)$$

where σ_s^2 - variance of refractive index because of synoptic inhomogeneity, l_s - space scale of synoptic inhomogeneity, A_M - a regular mesocomponent amplitude, L_C - a size of regular cell, l_{CM} - a coherent mesocomponent interval, σ_M^2 - variance of refractive index because of mesoinhomogeneity.

3. PATH-LOSS VARIATIONS

The signal characteristic studies were carried out on the base of processing half an hour medians derived from the data of two weeks experiment (for 3 hours 4 times a day) in the August 1988 over the sea 495 km tropospheric path in the south-east area of Okhotsk Sea in the 180 cm wavelength. The signal time variation model includes: a) two random components because of microscale and macroscale inhomogeneities, b) daily periodic component and c) synoptical component with quasiperiod of about 5 days:

$$B(\tau) = 2\sigma_p^2 \{1 - \exp(-\tau^2/\tau_p^2)\} + 2A_d^2 \sin^2(\pi\tau/T_d) + 2A_s^2 \sin^2(\pi\tau/T_s) + 2\sigma_h^2 \{1 - \exp(-\tau^2/\tau_h^2)\} \quad (2)$$

where σ_p^2 , σ_h^2 - variance of prolonged (some of hours) and large-term (some hundreds of hours) variations correspondingly; A_d , A_s - amplitudes of diurnal and synoptical variations, τ_p , τ_h - correlation intervals of corresponding random processes; T_d , T_s - periods of diurnal and synoptical variations.

4. RESULTS

The example of refractive index field modelling at 1 km height both separate components and experimental data is shown in Fig. 1. Analysis of calculated structural functions allow estimate component parameters. So refractivity r.m.s. of synoptical inhomogeneities changes from 6.1 to 17.3 N-units, size - from 670 km to 904 km for heights less of 5 km. As for mesoscalinhomogeneities, refractivity amplitude changes from 3.8 to 5.2 N-units, cell size - from 92 to 129 km, a coherent interval - from 141 to 246 km.

The studies of radiosignal has been carried out in the area of cyclone transmitting in the north the direction of Pacific Ocean. So, it should be expected the time signal characteristics are determined by inhomogeneities crossing the propagation path. The level signal structural function with its approximation are shown in Fig. 2. The synoptical period of 109 hours has been found out reliably. The intensity of this component is 1.8 dB in amplitude that is twice diurnal cycle amplitude (0.8 dB).

A global weather variation is due to atmospheric nonstable macrowhirl and has typical living time about 7 days. It agrees to our experiment. Part of turbulences was destructing in research region. That was a reason of rather intense random signal component with correlation interval about 1.8 hours.

5. CONCLUSION

The analysis of long-term radiosignal variations and large-scale refractivity inhomogeneities by using structural functions was carried out. The quasiperiodic components in structural functions were detected. The corresponding modeling was offered and relative contribution of some components was estimated. The time periods are in accordance with the size of corresponding mesoscale and macroscale inhomogeneities.

6. REFERENCES

1. Сергеев Г.А., Янутш Д.А., 1973. *Статистические методы исследования природных объектов*. Ленинград. Гидрометеониздат.
(Sergeev G.A., Yanutsh D.A. *The methods of statistical analysis of natural phenomena*).
2. Зверев А.С., 1968. *Синоптическая метеорология*. Ленинград, Гидрометеониздат
(Zverev A.S. *Synoptical meteorology*).
3. Насилов Д.П. 1966. *Радиометеорология*. Москва, Наука
(Nasilov D.P. *Radiometeorology*).

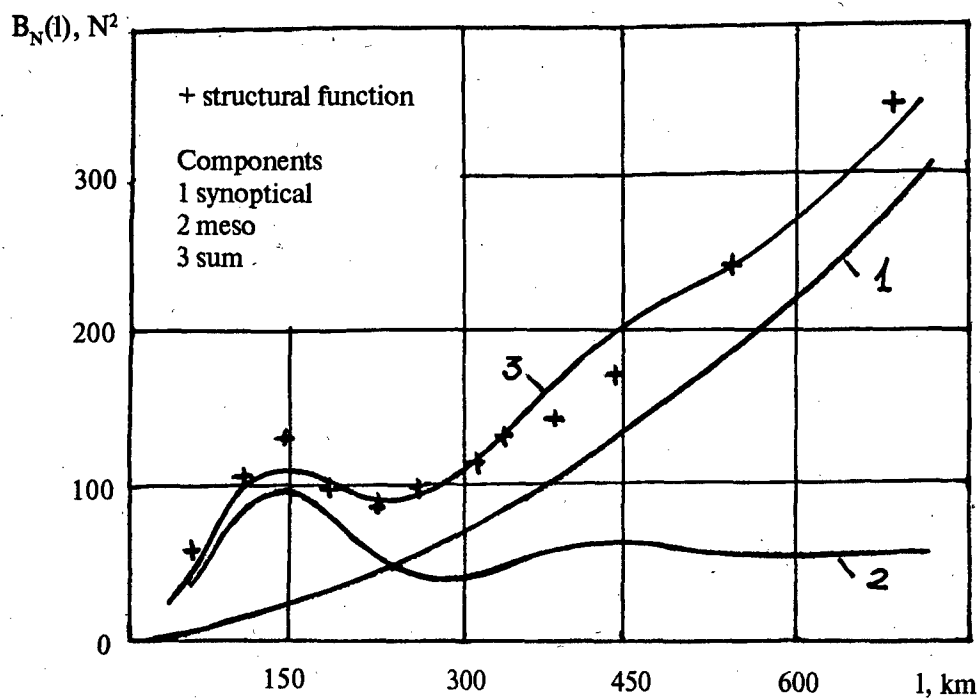


Figure 1: Results of refractive index modelling.

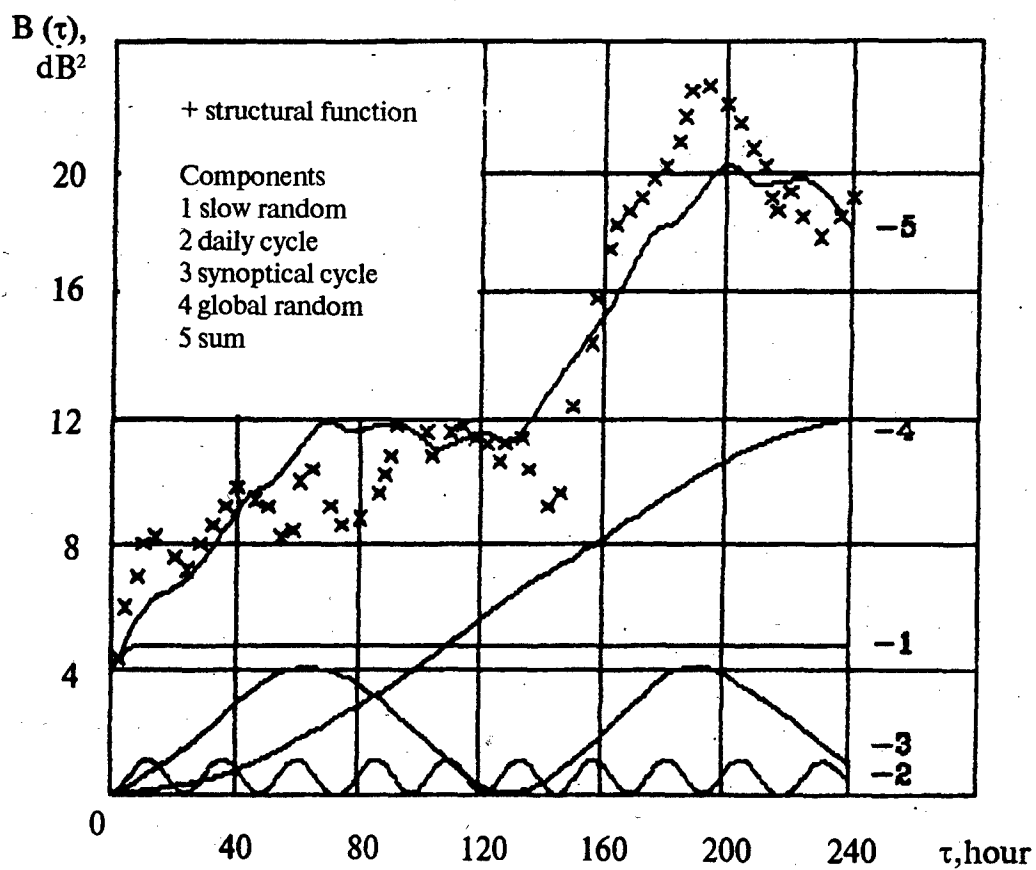


Figure 2: Results of signal level modelling.

Session 12: Mapping III

Data from Numerical Weather Forecast Systems - Useful Input for Propagation Predictions?

E. Salonen¹, S. Uppala², S. Karhu³ and J.P.V. Poiars Baptista⁴

¹ Technical University Helsinki, Radio Laboratorio, Otakaari 5A, SF - 02150 Espoo, Finland
Phone: +358-0-4512249 Fax: +358-0-460224 E-mail: erkki.salonen@hut.fi

² VTT, Otakaari 7B, SF - 02150 Espoo, Finland
Phone: +358-0-4512249 Fax: +358-0-460224 E-mail: seppo.karhu@vtt.fi

³ ECMWF, Shinfield Park, Reading, Berkshire RG2 9AX, UK
Phone: +44-734-876000 Fax: +44-734-869450

⁴ ESTEC, European Space Agency, Keplerlaan 1, NL-2200 AG Noordwijk, Netherlands
Phone: +31-1719-84319 Fax: +31-1719-84999 E-mail: pedro@xe.estec.esa.nl

ABSTRACT

This paper summarizes results recently obtained for the prediction of attenuation in low availability systems using data from the ECMWF numerical weather forecast system.

Keywords: Prediction Models, Attenuation, Low Availability

1. INTRODUCTION

In the design of communication systems it is essential to take into account the propagation losses. These have to be available before the actual design is carried out and for this purpose experimental campaigns of several years have to be carried out well ahead of the potential use a frequency band.

It is not conceivable, due to its costs, to carry out these campaigns wherever a communication link is to be established. For this purpose prediction models are used in the field of radio wave propagation where the propagation losses are calculated from available statistics of meteorological variables that induce the electromagnetic effects being calculated.

Recent developments in telecommunication systems have increased the interest of low fade margin systems due to their flexibility and lower cost. System operators have come to realise that with the growth of digital systems, users can tolerate systems (due to their lower cost) where non essential real-time communication can be delayed during a propagation outage and sent forward when the system becomes again available.

Currently available prediction models can not be extended *a priori* to low availability probabilities since they were never tested for these. Data for high outage is also not readily available because they are either of secondary importance or of no interest for

"classical" systems.

An example of this situation is, for example, the lack of reliable information in a wide scale for cloud attenuation, gaseous absorption and low rain rates.

In the past few years the European Space Agency has put a considerable effort in developing models, tools and data for modelling low availability propagation [Ref.1], [Ref.2] both in-house and through sponsoring research activities with research institutes and universities.

The present paper presents very recent results obtained by the Technical University Helsinki (TKK) and the Finnish Meteorological Institute (Ilmatieteen Laitos) in the frame of an activity sponsored by ESA. The activity concentrated mainly in obtaining continental or world -wide radiometeorological data and in developing or validating prediction models for all propagation effects.

2. RADIOMETEOROLOGICAL DATA

In a previous activity 6 years of European radiosonde and ground-based radiometric data were compared and validated. In a further stage these data were also compared with initialisation data from the ECMWF (European Center for Medium Range Weather Forecast) Global Circulation Model (GCM) in the form of attenuation at several frequencies and as meteorological variables (e.g. Liquid Water and Water Vapour Contents). The results obtained lead to the validation of the ECMWF data for yearly probabilities between 0.1% and 100% [Ref. 1]. This work concentrated on non precipitating phenomena in the European region.

In the present activity the effort was put on 1) obtaining a global non-precipitating radiometeorological data, 2) defining the rain climatology for the European region for high yearly probabilities (bigger than 0.1%) and 3) developing and

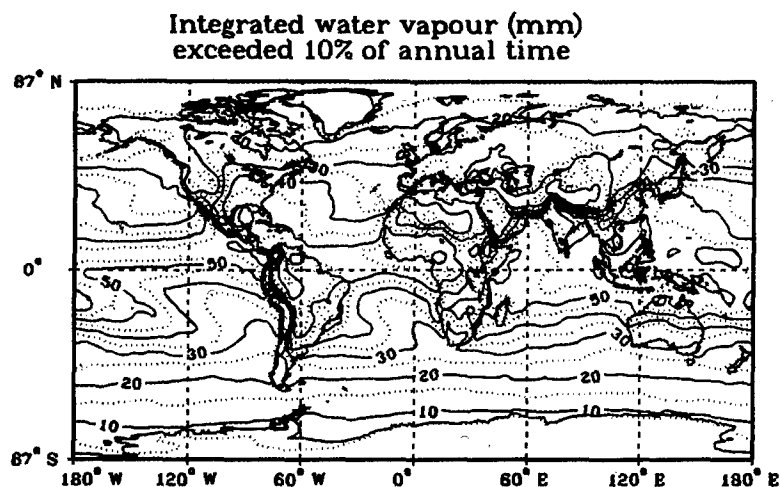


Figure 1 - Integrated Water Vapour Content exceeded for 10% of the year. Labels are in mm.

validating the associated prediction models.

For the purpose of the European rain climatology, 1 year (from 1989 to 1990) of ECMWF European data with a resolution of 1.5° in latitude and longitude were used. For the non-precipitating global climatology, ECMWF data from 1 July 1990 to 30 June 1991 with a resolution of 3° was extracted for each analysis time (00, 06, 12 and 18 UTC) at 14 pressure levels (1000, 850, 700, 500, 400, 300, 250, 200, 150, 100, 70, 50, 30 and 10 hPa).

2.1 Global non-precipitating results

Using the data described in the previous section and the models described in [Ref. 1], [Ref. 3], [Ref. 4] and [Ref. 5] the Integrated Water Vapour and Integrated

Liquid Water Contents were calculated for 1, 5, 10, 20, 50, 80, 90, 95, 98 and 99% exceedance probabilities of the year. Figure 1 shows, as an example, the Integrated Water Vapour Contents for 10% of the average year in mm.

Monthly rain amounts for convective and large-scale rain, as defined by the ECMWF GCM were also derived as well as the cumulative distributions of 6 hour time step with 0.1mm/h intervals for both types of rain.

Monthly averages for the height of the 0°C isotherm were also calculated as well as the yearly mean 0°C height weighted and unweighted with the rain amount of the GCM time interval 6h before and after the analysis time. Figure 2 shows the results for the latter case.

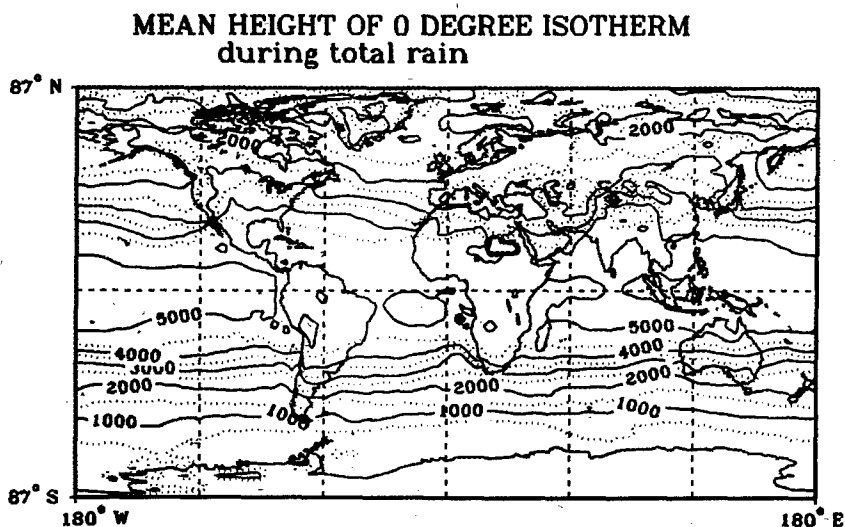


Figure 2 - Mean unweighted 0°C isotherm height during the occurrence of rain. Labels are in meters.

Having in mind the application of these data also for the calculation of dry air (no water vapour) absorption, zenith attenuation for 30, 40 and 50 GHz were also calculated for the same probability levels as for the Water Vapour.

2.2 European Region results

Results already obtained in [Ref. 1] were recalculated to increase the statistical sample. The data in the European regions covers now 3 years (from 1987 to 1990).

Precipitation in the ECMWF model is not taken into account as a model variable but as a diagnostic one. In practice it means that precipitation is not analysed "correcting" the most recent six-hour forecast. The forecast model physics produces precipitation within each time step from the simulated processes of the atmosphere. The precipitation amounts in mm are produced 4 times per day divided in three precipitation types: large scale rain, snowfall and convective rain.

The large scale rain is mainly produced when humid air ascends within a grid box and reaches the saturation point. The water released from the atmosphere in this form is called large scale rain. This process is usually associated to cyclones and their frontal systems where air ascend and descends over large areas. large scale rain rates are usually moderate

and do not account for the higher rain intensities. This process loosely reproduces widespread rain.

Convective rain is produced in the GCM in processes where a net inflow of humidity into a grid box occurs either from the surface layers or from the confining grid boxes. If the temperature structure of the grid box is suitable, the condensation process is assumed to occur and the humidity is released as convective rain. The rainfall amount is proportional to the net inflow of humidity. This process does not however, represent mesoscale showers and as a consequence does not represent the very heavy rainfalls.

However, the ECMWF GCM seems to represent accurately enough the rainfalls associated with low availabilities even in terms of its integration time (6 hours).

For the rain climatology needed for low availability systems, it was necessary to increase the probability range of the data in the ESA Climatic Map [Ref.6] (only 0.1% to 0.01% of the average year) and thus cover also yearly probabilities higher than 0.1%. For this purpose one year of rain amounts in 6 hour steps of ECMWF data were used. Several methods, Rice-Holmberg [Ref.7], Moupfouma [Ref.8], [Ref.9] and Watson [Ref.6] were tested to model the rain rate distribution and it was concluded that the Rice-

Rainfall rate exceeded 1% of annual time

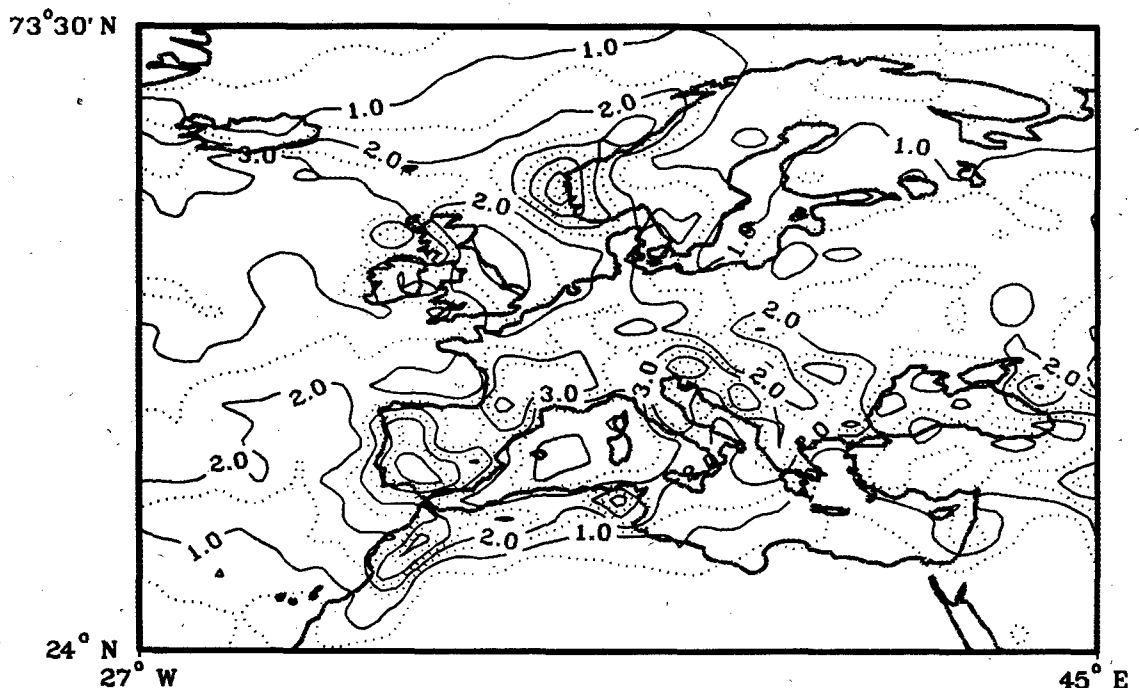


Figure 3 - Rainfall rate exceeded for 1% of the year calculated using Rice-Holmberg model and ECMWF data. Labels are in mm/h.

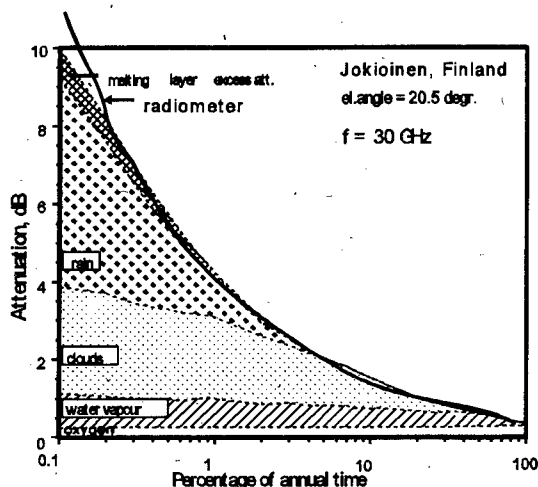


Figure 4 - The predicted distribution of the 30 GHz atmospheric attenuation for Jokioinen and the measured 29.3 GHz radiometer distribution (1985-1987) for Kirkkonummi.

Holmberg method may be used for low rainfall rates while the Moupfouma method may be applied to medium to high rain rates. A conversion of the rain cumulative statistics from a 6 hour integration time to 1 min integration time was carried out based on the Rice-Holmberg model however, due to the lack of measured rain data, the conversion method was only tested with data from Jokioinen, Finland.

Because both the Rice-Holmberg input parameters calculated from the ECMWF data and the six-hour distribution have the same error sources, the inaccuracy in the converted distribution may become larger than the one in the distribution computed directly from the Rice-Holmberg model.

For this reason the rain intensities for yearly probabilities higher than 0.1% were calculated directly the Rice-Holmberg model using the ECMWF data to derive its parameters. Figure 3 shows, by way of example, the values in the European region for one of these parameters.

3. PROPAGATION PREDICTION MODELS

As already shown in [Ref. 1] the models for predicting the attenuation in a non precipitating atmosphere work extremely well with the radiometeorological data obtained from the ECMWF analysis, Figure 4 is shown as an example of this behaviour. However mainly in the Mediterranean region the equiprobability method to calculate the total attenuation due to all the

Total atten. to Olympus, $f=30$ GHz, $p=1\%$

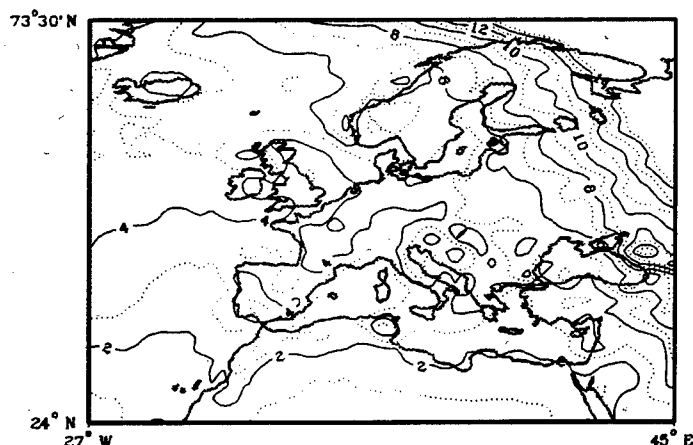


Figure 5 - Total attenuation for 1% of the year at 30 GHz for the Olympus satellite. Labels are in dB. The total attenuation was calculated using the models and data described in this paper.

effects introduces, in some cases, significant errors. For this reason, the exceeded zenith attenuations at 12, 20, 30, 40 and 50 GHz were calculated for all the European region and for 20, 50, 80, 90, 95, 98, 99 and 99.9% of the year using the original ECMWF dataset. Reliable values of predicted attenuation can be obtained for all the European region using the scaling law,

$$A(P, f_2) = \frac{A_{eq}(P, f_2)}{A_{eq}(P, f_1)} \cdot A_{coh}(P, f_1)$$

$$= \frac{a_2 V(P) + b_2 W_{red}(P) + A_{2,ox}(1-P)}{a_1 V(P) + b_1 W_{red}(P) + A_{1,ox}(1-P)} \cdot A_{coh}(P, f_1)$$

where f_2 is the frequency of interest, f_1 is the nearest frequency where "coherent" results are available, P is the probability level, $A_{n,ox}$ is the zenith attenuation due to dry air at frequency n , W_{red} is the Integrated Reduced Liquid Water and V is the Integrated Water Vapour Content. The coefficients a_1 , a_2 , b_1 and b_2 can be calculated from formula (8) of [Ref.10]. A_{eq} are the total attenuations calculated using the equiprobability method where the attenuations due to each meteorological phenomenon are summed for equal probabilities.

Regarding rain attenuation the Watson model was the best performer (in terms of accuracy, flexibility and complexity) in this activity as well as in the previous one.

Figure 5 shows the total attenuation for 1% of the average year predicted using all the radiometeorological data and models obtained during the activity.

A comparison of this results with Olympus measured data (Darmstadt-D, Albertslund-DK, Metsahovi-SF, Martlesham-GB and Lessive-B) and with COST 205 data, gave good results. Comparison results in the form used by ITU-R are in preparation.

4. CONCLUSIONS

Models and associated radiometeorological data for the prediction of low availability communication systems were developed with very positive results.

The ECMWF model data is a source of very useful radiometeorological input. Even the variables associated with rain, even if they are not assimilated in the model, demonstrated to be very useful.

5. REFERENCES

- /1/. Salonen, E. et al., 1992, Modelling and Calculation of Atmospheric Attenuation for Low-Fade-Margin Satellite Communications, ESA Journal, 92/3
- /2/. Watson, P.A. et al., 1993, Statistic Fade Compensation, Interim Report ESA/ESTEC Contract 10010/92/NL/PB
- /3/. Salonen, E. et al., 1991, Study of Propagation Phenomena for Low Availability Satellite Systems, Final Report ESA/ESTEC Contract N. 9025/88/NL/PR
- /4/. Salonen et al., 1994, Study of Improved Propagation Predictions, Final Report ESA/ESTEC Contract 9455/91/NL/LC(SC)
- /5/. Salonen, E. and Uppala, S., 1991, New Prediction Method of Cloud Attenuation, *Elec. Letters*, Vol. 27, N. 12, pp. 1106-1108.
- /6/. Watson, P.A. et al., 1987, Prediction of attenuation on satellite-earth links in the European region, *IEE Proc.*, Part F, Vol. 137, N. 6.
- /7/. Rice P.L., Holmberg N.R., 1973, Cumulative time statistics of surface-point rainfall rates, *IEEE Trans.* Vol. COM-21, N. 10, pp. 1131-1136
- /8/. Moupfouma F., 1987, More about rainfall rates and their prediction for radio systems engineering, *IEE Proc.*, Part H, Vol. 134, N. 6, pp.527-537
- /9/. Moupfouma F., Martin L., 1993, Point rainfall rate cumulative distribution function valid at various locations, *Elec. Letters*, Vol. 29, N. 17, pp. 1503-1505
- /10/. Salonen E., Uppala S., 1992, Water vapour attenuation on a slant path, Helsinki University of Technology, Report S 196, ISBN 951-22-1193-9

PREDICTION OF ATTENUATION ON SATELLITE-EARTH LINKS FOR SYSTEMS OPERATING WITH LOW FADE MARGINS

P A Watson¹, Y F Hu²

1 - Department of Electronics, University of York, Heslington, York, YO1 5DD
Tel + 0904 432338, Fax +0904 432335, E-mail paw@ohm.york.ac.uk

2 - Department of Electronic and Electrical Engineering, University of Bradford
Tel +0904 384031, Fax +0904 391521, E-mail y.f.hu@bradford.ac.uk

ABSTRACT

A new method for prediction of attenuation on satellite-earth links is presented, for systems operating with low fade margins. The method is based on modelling the physical structure of rainfall and includes, in order of importance, (i) an improved approach to combining components of fading, (ii) a non-uniform vertical on-average profile of rain specific-attenuation, (iii) the differing frequency dependencies of melting zone and rain components and (iv) contributions from widespread and showery rain. The method has been tested using 21 years of data covering the 11 to 30 GHz range and shows good agreement.

INTRODUCTION

In applications of the millimetre-wave bands in satellite-earth telecommunications links, systems are often considered for operation with low fade margins (ie ≤ 10 dB). This may be achieved by using fade-countermeasures such as adaptive time-division multiple access, uplink power control, by using time-diversity (in messaging systems) or by accepting a modest grade of service, for example in mobile systems.

For whatever system circumstances may apply, when interest lies in fade margins ≤ 10 dB for frequencies at and above 20 GHz, a much greater variety of contributory factors to attenuation must be considered than at 11/14 GHz. These include absorption from atmospheric gases, scintillation from atmospheric turbulence, attenuation by rain and attenuation from ice and water clouds.

This paper reports on a methodology for predicting link attenuation exceedences for low fade-margin systems and gives an assessment of the methodology using data from the Olympus satellite.

BACKGROUND

An earlier series of papers reported on a methodology for prediction of attenuation on earth-space radio links based on physical modelling of rain structure as interpreted from dual-polarisation radar data (see Leitao and Watson [1] and Watson

et al [2]). This prediction method was tested at 11/14 GHz against measurements obtained from OTS collected within the EEC COST 205 programme [3] giving excellent agreement (less than 25% rms error in attenuation for all the COST stations). However this method related specifically to the scenario of high availabilities and showery rain. Although the Leitao-Watson study [1] developed methods for prediction in rain for both widespread and showery rain, at 11/14 GHz for the exceedances in question, only the showery rain model was applied [2].

A more recent study (Salonen et al [4]) have examined the problem of prediction for low availabilities (typically 90% to 99% of the average year) for predictions at 20 and 30 GHz. Methodologies were outlined for inclusion of cloud, water vapour, melting zone and scintillation effects along with rainfall. For rainfall, Salonen et al have used the Leitao-Watson widespread rain model throughout the low availability range.

APPROACHES TO PREDICTION FOR LOW FADE MARGINS

Components of fading

Propagation factors contributing to fading at 20 and 30 GHz include attenuation from rain, melting particles and clouds, absorption from atmospheric water vapour and scintillation from turbulence. Absorption in the tail of the 60 GHz oxygen band is small at 20 and 30 GHz in absolute terms, (≤ 0.06 dB at 20 GHz and ≤ 0.1 dB at 30 GHz for zenith values). Summer to winter variability is also negligible (< 0.01 dB at 30 GHz).

Combination of fading components

Evidently the problem of prediction for low fade margins or low link availabilities is much more complex than that for high availabilities, purely in terms of the number of components to be included. The situation is further complicated by the fact that many of these fading processes can neither be regarded as entirely correlated or completely independent. The important question of how the contributions from each component are to be combined must thus be addressed.

In the 1990 study of Salonen et al [4] fading components were added on an equi-probability basis. This is unlikely to apply for all components, though it may be satisfactory for some. Overall it represents a worst case approach, but it does allow simple data processing to be applied.

As a step towards a more rigorous combination of components, we model rain and non-rain processes as two disjoint sets, adding exceedances. Within the rain process we include rain, melting zone, rain-cloud and water vapour contributions. For the latter we take a saturated water vapour contribution to the rain height and a melting zone thickness based on equi-probability rain intensity. For rain-cloud contributions we use the empirical model of Altshuler and Marr [5].

Within the non-rain processes, we model non-precipitating cloud, water vapour and scintillation effects as being highly correlated, adding attenuations for equal exceedances. Table 1 summarizes the situation.

There are thus two main parts to our total fading model; the rain-fading component and the non-rain component, ie:

$$P(A_T > a) = P(A_{\text{non-rain}} > a) + P(A_{\text{rain}} > a) \quad (1)$$

where A_T is the total attenuation, A_{fair} is the non-rain component and A_{rain} is the rainy weather component.

The non-rain component consists of attenuation due to water vapour, cloud and scintillation. These three factors are combined on an equiprobable basis. Thus, given non-raining conditions, $A_T(p)$ is given

by:

$$A_T(p) = A_{\text{water vapour}}(p) + A_{\text{cloud}}(p) + A_{\text{scint}}(p) \quad (2a)$$

$$\text{where } p = P(A_{\text{non-rain}} > a) \quad (2b)$$

$P(A_{\text{non-rain}} > a)$ can be rewritten as:

$$P(A_{\text{non-rain}} > a) = P(A_T > a_{\text{non-rain}})P(\text{non-rain}) \quad (3)$$

It has also been assumed that:

$$P(\text{non-rain}) = 1 - P(R > 0) \quad (4)$$

where R is rain intensity.

Data for prediction of exceedances for low fade margins

This represents a significant problem area, especially in the context of rainfall data. Many of the modern raingauges, designed with a focus on intense rainfalls, are quite inaccurate for rainfall rates ≤ 5 mm/hr. We thus cannot rely on direct measurements taken at the ground for light rainfalls and have to fall back onto a model-based approach, predicting low margin intensities from monthly and yearly figures such as used in the method developed by Rice and Holmberg [6] and later implemented by Dutton and Dougherty [7].

Regarding other meteorological inputs than rainfall intensity, here we have drawn on readily available meteorological database including the UK Met 0.856C data [8] and data from the European Centre for Medium Range Weather Forecasts (so called SYNOP and TEMP reports) as collated and presented by Salonen et al [4].

Table 1 Combination Of Fading Processes

Rain processes	rain attenuation melting zone saturated water vapour (up to rain height) rain - cloud	} added on an equi-probability basis	added as disjoint variables
Non-rain processes	cloud scintillation water vapour	} added on an equi-probability basis	(adding exceedances for equal fade thresholds)

CHARACTERISATION OF COMPONENTS OF FADING

Component models

For non-rain processes we have used models and data given in the published literature [4,11]. We will now describe in more detail our approach to rain process modelling.

Rain processes

Let the random variables A and R denote the rain attenuation (due to both types of rain) and the point rain rate respectively. The probability that A is greater than a given value a , is given by:

$$P(A > a) = P(A > a|S)P(S) + P(A > a|W)P(W) \quad (5)$$

where S and W denote showery rain and widespread rain respectively. The above equation can be written as:

$$P(A > a) = P(A > a|S)P(S) + P(A > a|W)P(W) \quad (6)$$

where r_1 and r_2 are values of the equiprobable point rain rate to give a for showery and widespread rain respectively. In the Rice-Holmberg rain rate prediction method, the probability that a point rain rate, R , is greater than a given value r , is given by a combination of the rain rate probabilities due to the two types of rain:

$$\begin{aligned} P(R > r) &= P(R > r, S) + P(R > r, W) \\ &= P(R > r|S)P(S) + P(R > r|W)P(W) \\ &= q_{1r}(R > r) \frac{T_{1r}(r)}{8766} + q_{2r}(R > r) \frac{T_{2r}(r)}{8766} \end{aligned} \quad (7)$$

where $T_{1r}(r)$ and $T_{2r}(r)$ are the total number of hours that there is more than 0.254 mm of rain in a t -min period due to showery and widespread rain respectively. Also $q_{1r}(R > r)$ and $q_{2r}(R > r)$ are the probabilities that the rainfall rate, R , is greater than a given value, r , by the showery and widespread rain respectively. Substituting equation(7) into (6) gives:

$$P(A > a) = q_{1r}(R > r) \frac{T_{1r}(r)}{8766} \quad (8)$$

Occurrence of showery and widespread rain

For availabilities near to 99.9% of the average year we expect that for many sites contributions will be made both from widespread and showery rain. This hypothesis was tested using the RH/DD mode 1 and mode 2 rains as the basis for weighting the application of Leitao-Watson widespread and showery rains (in Equation (8)). Figs 1a-1d

illustrate these tests for 4 European sites (Jokionen, Finland, Brindisi, Italy, Martlesham, UK and Graz, Austria). Identical rain-heights (from our published rain height map [2]), have been taken for both showery and widespread rains (in the absence of better data). These results thus need careful interpretation.

The predicted cross-over points between the dominance of showery and widespread rains occurs between 99.99% and 99.9% availabilities for 3 of the 4 sites. For Brindisi, Italy, the cross-over is close to 99.9% whereas for Martlesham it is above 99.99%. In all cases for availabilities $\leq 99\%$ widespread rain clearly dominates. Note, however, that there is some local evidence in the case of Martlesham that showery rain dominates availabilities close to 99.99%.

Rain height

The rain-height map published for the original Watson et al [2] prediction method was based on the 0° isotherm height plus seasonal and climatic adjustments. The seasonal adjustments were made by noting, for each station in the meteorological data base, the month during which the most intense rainfalls occurred (usually July/August in continental Europe, October in Mediterranean regions). The appropriate mean monthly 0° isotherm heights were then deduced. Climatic corrections were then made to account for increase or decrease in rain height associated with rain. For example in maritime climates with a preponderance of cold frontal showers, rain height was corrected downwards, in continental climates where intense rain is associated with strong convection, rain height was corrected upwards.

The use of this rain height map in the original study is based on two observations, neither of which entirely hold for low availabilities:

- (i) that showery rain dominates rain outages
- (ii) that the 0° isotherm height with seasonal and climatic corrections represents the rain height for modelling purposes and includes a region of melting particles (the melting zone) which can be modelled as rain.

Observation (i) is evidently not correct below 99.9% availability. However, we do not have a separate rain height map for widespread rain and it is not an easy task to prepare one. In this aspect the combination of showery and widespread rain intensity components as observed at the ground (for example as shown in Figs 1a to d) is suspect, in that on a slant path, if the widespread rain occurs mainly in the winter and the showery rain occurs mainly in the summer, too much emphasis is given to widespread rain for the prediction of attenuation owing to the lower rain height. This is believed to

be the explanation for the discrepancy noted earlier in relation to Martlesham.

In the absence of suitable data we have had to use the same rain height grid for both showery and widespread rains. This weakness could be addressed in future studies.

Observation (ii) includes a coincidence which applies at 11/14 GHz, but will not apply at 20/30 GHz. Leitao and Watson observed from radar data that there was an on-average tendency for specific attenuation in rain to decrease with height in agreement with observations by Foote and Du Toit on the variation of raindrop terminal velocities with barometric pressure [9]. This can lead to a 5-10% *overestimation* of attenuation if rain is modelled with a uniform vertical specific attenuation profile. On the other hand, if the melting zone occurring immediately below the 0° isotherm is modelled as a region of rain, then the attenuation for that region is marginally *underestimated*. Leitao and Watson found that at 11/14 GHz these two factors cancel out and by coincidence a good estimation of attenuation is achieved by taking the (seasonally and climatically adjusted) 0° isotherm height as the rain height. Because of the markedly different frequency dependence of specific attenuation in the rain and melting regions, observation (ii) should be modified for application to 20 and 30 GHz.

Rather than build in such empirical corrections to a prediction model for 20/30 GHz, we prefer to take a more physically based approach and model the rain region and melting zone entirely separately. We thus take the rain height as the 0° isotherm height minus the thickness of the melting zone (a rain intensity-dependent thickness taken from Russchenberg and Ligthart [10]) and make a correction for the variation of specific attenuation with height (an empirically determined factor of 0.95 from Leitao's radar study [11]).

Melting zone attenuation

Here we avoid using the excess zenith attenuation concept, in view of errors that would be introduced in the frequency-dependence of total rain attenuation model (see section on rain height). Instead we calculate the melting zone attenuation for a specific ground rainfall intensity, using the model of Russchenberg and Ligthart [10].

Total rain-process attenuation model

For widespread rain, the rain height is taken up to the bottom of the melting layer. The thickness of the melting layer (H_m) and the absolute value of the melting layer attenuation are obtained from the Russchenberg-Ligthart model and the melting layer attenuation is then added to the rain attenuation,

irrespective of the type of rain. (It is assumed that melting occurs somewhere, even though in showery rain a well-defined melting band may not be seen.) In addition, the attenuation due to a saturated water vapour column up to the rain height is included. Furthermore, the Leitao-Watson rain model overestimates the slant path attenuation in the rain region by 5%-10% [4] owing to the assumption of a uniform vertical profile of rain specific attenuation in the rain region. To compensate for this, a correction factor, C (≈ 0.95) is applied to the predicted attenuation in the rain region. So for a given point rain rate R , the attenuation, A , due to either showery rain or widespread rain together with the melting layer, a saturated water vapour column is :

$$A(p) = CA_{rain}(H_0 - H_m, R) + A_{bb}(H_m, R) + A_{water\ vapour}(H_0 - H_m) \quad (9)$$

The CCIR water vapour model [10] is used to obtain the attenuation of the saturated water vapour column. Finally, it is found that at 30 GHz and above, a correction for cloud attenuation, concurrent with rain, should be made.

VALIDATION AND TESTING OF APPROACH

Available records for testing

We have searched out the largest available data records for 20/30 GHz fading, considering only those stations with at least 5 years data. This rules out stations that have collected Olympus data *alone* but includes those that ran extended radiometer campaigns prior to and alongside Olympus. A good example here is the database collected by Howell et al [14] at British Telecom, bringing together satellite and radiometric measurements to give 21 years of extrapolated data for 20 and 30 GHz.

It is still early for many experimenters to have completed their data analysis for Olympus and as yet we have not been able to obtain other records of substantial length.

Comparison of predictions with measurements

The Martlesham data were gathered on all channels whenever the 3 dB threshold was exceeded at 30 GHz. It may thus be the case that the data should be compared with our total attenuation prediction model, rather than just rain attenuation. Figs 2a to 2d show such comparisons.

At 30 GHz predictions from our new approach are in remarkably good agreement with measurements (errors < 0.5 dB over the whole availability range

and no tendency to underestimate or overestimate). The equi-probability approach overestimates attenuation by 3 dB (50% error).

At 20 GHz the agreement is quite good though below 99.7% there is a tendency to overestimate, increasing to 0.5 dB at 99%. The equi-probability approach overestimates by 2 dB (60% error).

The agreement at 12 and 14 GHz is also quite good though for 12 GHz at 99.9% there is still a tendency to underestimate by 0.5 dB. (Note that the absolute accuracy of the measurements at 11 GHz below about 99.5% must be questioned, when the attenuation has fallen to <1dB.)

OVERALL CONCLUSIONS

An improved rain attenuation prediction method for low availabilities has been developed, tested and used for predictions at 20 and 30 GHz. The method gains most of its improvements over previous work in the following aspects (in descending order of importance):

- (i) Rain and non-rain fading processes are combined using a better statistical approach than that of adding equi-probability attenuations
- (ii) The vertical on-average profile of rain specific attenuation is taken into account
- (iii) The differing frequency dependencies of melting zone and rain components of attenuation are included
- (iv) Contributions from widespread and showery rain are included separately

The method has been tested only on a single European station with a sufficiently long data record of 20 and 30 GHz attenuation. Further comparisons with Olympus data should be made when these are available. The method also includes a known deficiency in relation to the rain height map used (that for showery rain only). Also the model for attenuation in the melting zone may require further improvement. However at 20 and 30 GHz these deficiencies appear to be of minor significance.

REFERENCES

- [1] Leitao M J M and Watson P A "Method for prediction of attenuation on earth-space links based on radar measurements of the physical structure of rainfall" IEE Proc Pt F, **133** 1986, 429-440.
- [2] Watson, P A, Leitao M J M, Sathiaselan V, Gunes M, Poyares Baptista JPV, Potter B A, Sengupta N, Turney S and Brussaard G "Prediction of attenuation on satellite-earth links in the European region", IEE Proc Pt F, **134** 1987, 583-596.

- [3] EEC COST 205. "Influence of the atmosphere on radio-propagation on satellite-earth paths at frequencies above 10 GHz" EEC Report EUR9923, 1984.
- [4] Salonen E, Karhu S, Jokela P, Zhang W, Jppala S, Aulamo H and Sarkkula S, Poyares Baptista, J.P.V., "Modelling and Calculation of Atmospheric Attenuation for Low-Fade-Margin Satellite Communications" ESA Journal 1992, **16**, 3 pp 299-317.
- [5] Altshuler EE and Marr R A "Cloud Attenuation at millimeter wavelengths". IEEE Trans Ant and Prop AP-37 (11), 1989, 1473-1479.
- [6] Rice P L and Holmberg N R "Cumulative time statistics of surface point rainfall rates", IEEE Trans Comms COM-21 (10), 1973, 1131-1136.
- [7] Dutton E J, Dougherty H T and Martin R F "Prediction of European rainfall and link performance coefficients at 8 to 30 GHz" Tech Report ACC-ACO-16-74, Institute for Telecommunication Sciences, USA, Aug 1974.
- [8] UK Meteorological Office, "Tables of temperature, relative humidity, precipitation and sunshine for the world". Met 0.856C, 1972.
- [9] Foote GB and Du Toit PS "Terminal velocities of raindrops aloft" J App Meteor. **8**, 1969, 249-253.
- [10] Russchenberg H W J and Lighthart L P "Backscattering by and propagation through the melting layer of precipitation" ESA/ESTEC Contract Final Report PO122859, 1993.
- [11] Leitao M J M "Propagation factors affecting the design of satellite communication systems" PhD thesis, University of Bradford, 1985.
- [12] Liebe H J "MPM - An atmospheric millimetre-wave propagation model". Int-Jour. Infrared and Millimeter W. **16**, (6) 1989
- [13] International Radio Consultative Committee (CCIR) "Effects of tropospheric refraction on radiowave propagation". Report 718-3 XVIIth, Plenary Assembly, Dusseldorf 1990.
- [14] Howell R G, Harris J W and Mehler M "Satellite co-polar measurements at BT Laboratories" BT Technology Journal **10** (4) 1992, 34-51.

ACKNOWLEDGEMENT

The authors gratefully acknowledge the support of the European Space Agency for this work which was funded via a sub-contract with TICRA (Denmark), and would especially like to thank Pedro Baptista and Stephano Badessi of ESA/ESTEC, for assistance throughout the study, and Hans-Henrik Viskum of TICRA for efficient contract management.

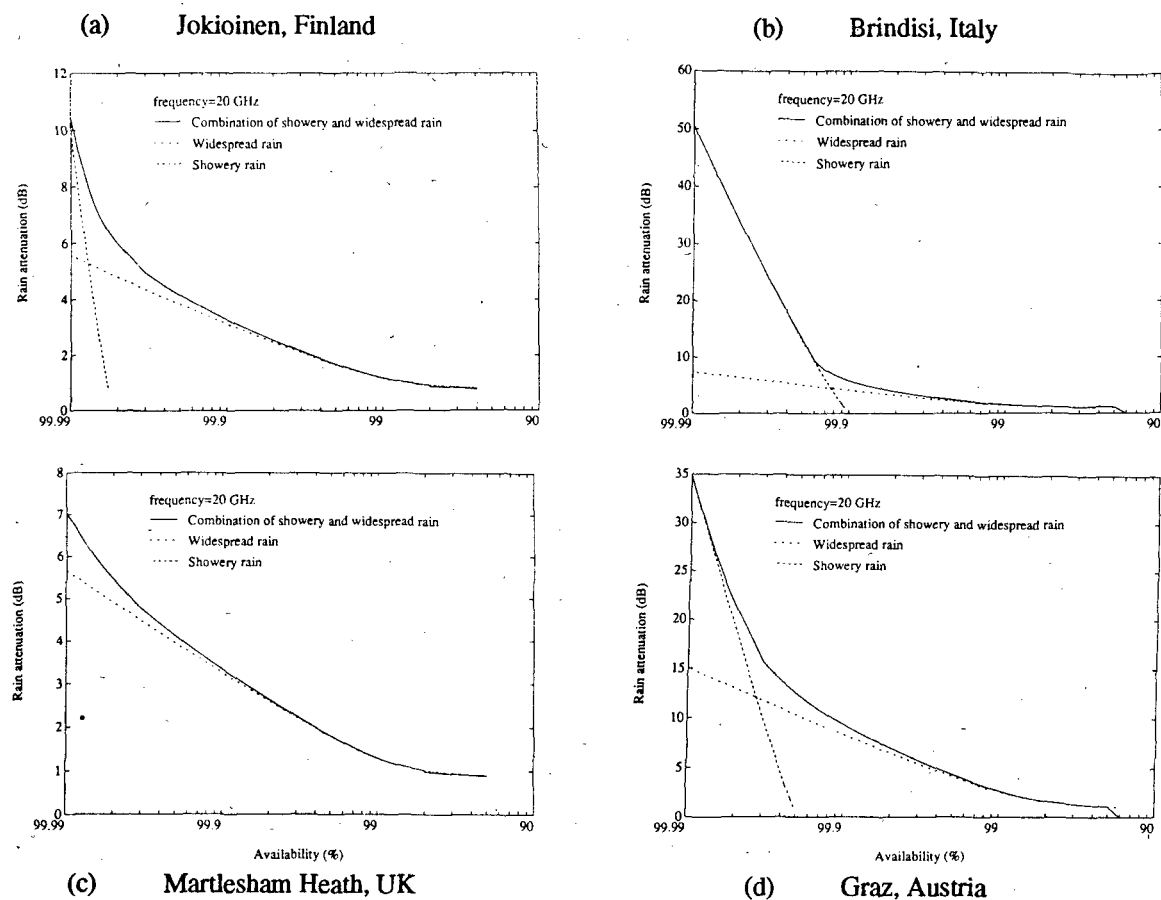


Fig 1 (a-d) Cumulative statistics of rain attenuation at 20 GHz for four European locations predicted using combined showery and widespread rain models (but excluding melting band, cloud and water vapour contributions).

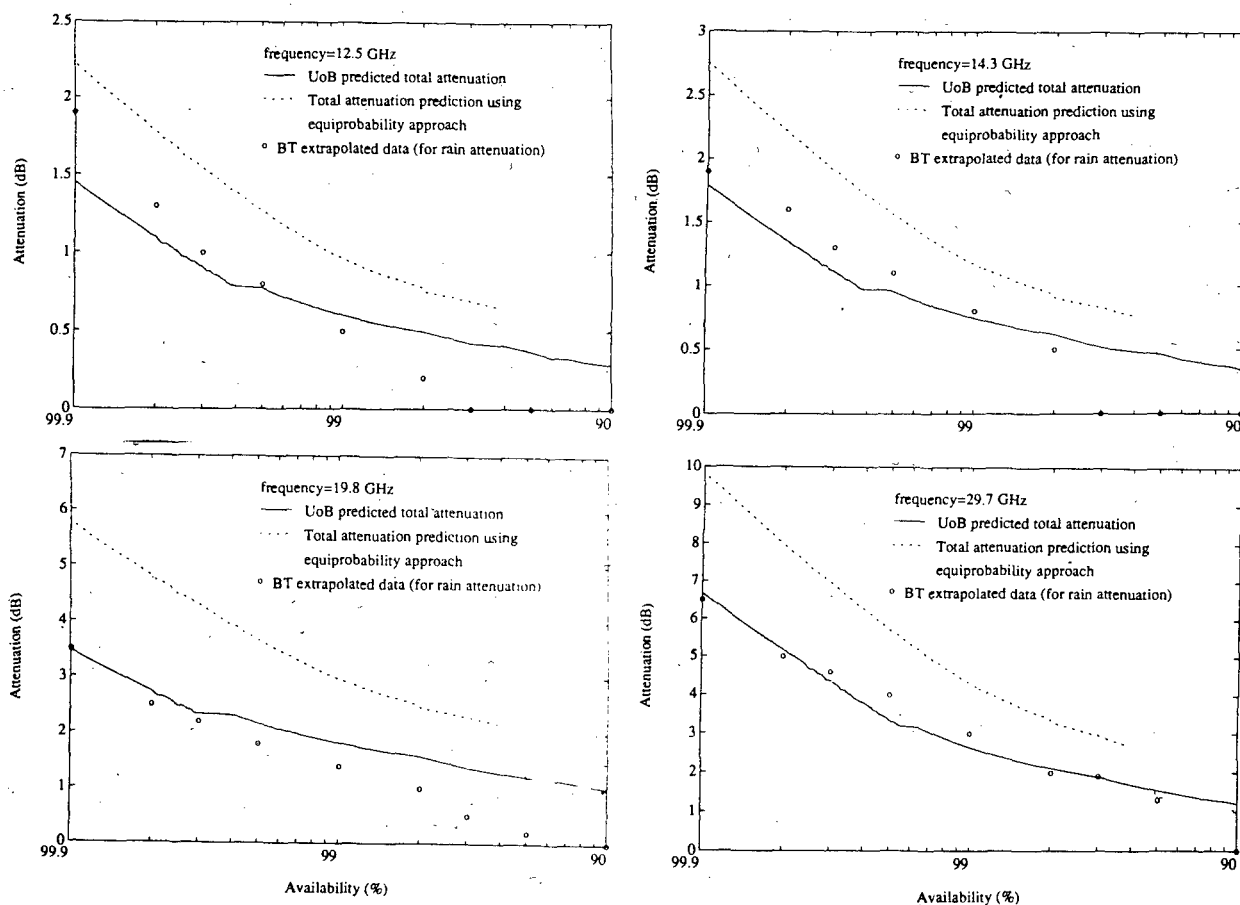


Fig 2(a-d) Comparison of predicted and measured cumulative statistics of total attenuation at 12.5, 14.3, 19.8 and 29.7 GHz for Martlesham Heath, UK. The predictions use our total attenuation model including all rain and non-rain fading processes (see text). Measured data are from Howell et al [18].

RADIOCLIMATIC MAPS OF UHF RADIOWAVE OVER-SEA PROPAGATION PARAMETERS FOR THE PACIFIC OCEAN

G.S.Sharygin, V.I.Slutski, B.P.Dudko, O.N.Kiselev, I.L.Korneev, M.V.Krutikov

TACSR, Lenin ave. 40, Tomsk, 634050, Russia

Tel: +7(3822)224302, Fax: +7(3822)223262, E-mail: gssh@tiasur.tomsk.su

ABSTRACT

The paper gives a description of radioclimatic maps of monthly average parameters of refractive index structure and radiowave characteristics for 3 cm - 3 m band in the region of the Pacific Ocean. Maps were formed using experiment results received at the sea prove ground and during research ships' services for many years. Methods of drawing up the maps are expounded.

Keywords: Radioclimatic Maps, Refractive Index, Tropospheric Radiowave Propagation, Pacific Ocean.

1. INTRODUCTION

The atlas of radioclimatic maps for Pacific Ocean region (1:60000000 scale) is formed by the Tomsk State Academy of Control Systems and Radioelectronics with participation of the Tomsk State University and the Far-East Research Hydrometeorological Institute. The atlas contains 58 maps with isolines of mean troposphere parameters affecting UHF propagation and 75 maps with characteristics of radiosignals for over-the-sea propagation up to 1000 km. Mapping process includes the systematization of many experimental data of radiometeorological parameters, the determination of monthly average values of each 10-degrees or 5-degrees latitudes and longitudes square, the calculation of deficit data of radiowave characteristics using familiar methods and tropospheric parameters. For making maps there were used about 68,000 meteorological, 10,000 aerological observations and radiosignal measurements during approximately 20,000 hours in central and north-west regions of the Pacific Ocean. There were also used data of the published radiometeorological maps and atlases. Nearly all the maps are made for the central months of the seasons: February, May, August, November.

2. RADIOMETEOROLOGICAL TROPOSPHERIC PARAMETERS

2.1. Refractive index near sea surface (8 maps)

The maps of the mean value and standard deviation of the refractive index at a height of 10-15 m were drawn up. The latitude and longitude resolution is 10 degrees, the interval between isolines of average values is 10 N-units, of standard deviation - 4 N-units. There were used integrated climatic data of temperature, moisture content, pressure (Refs. 1,2) and data measured by Soviet research ships during 1961-80 years. Fragments of maps are shown in fig. 1 and 2.

2.2. Evaporation ducts parameters (16 maps)

There were made up maps of the evaporation ducts mean heights and deficit for the central months of every season as well as their standard deviation with intervals between isolines 2 m, 1 M-unit, 1 m and 0.5 M-unit. Parameters were calculated using methods (Ref. 3) and data concerned water temperature, air temperature, moisture, pressure and the wind speed. A fragment of one of these maps is shown in fig. 3.

2.3. Vertical profile of the refractive index (20 maps)

The first 8 maps of this division shows parameters of the exponential model's vertical profile:

$$N(h) = N(0) \exp(-h/H),$$

where $N(0)$ - at the surface refractive index, H - the height scale. For finding $N(0)$ and H there were used average for many year data concerned the air temperature, the water vapour elasticity, geopotential and specific moisture at different isobar levels in the coordinate net knots with the 10-degrees step. Isolines of $N(0)$ are drawn with 5 N-units step, H - with 0.2 km step.

In addition to this the division contains maps of the standard deviation of the refractive index at 1 and 3 km height (fig. 4 for instance) and the maximum deviation of this index at the heights' interval 0-3 km. Data were received in 1960-85 while Soviet research ships made aerological sounding.

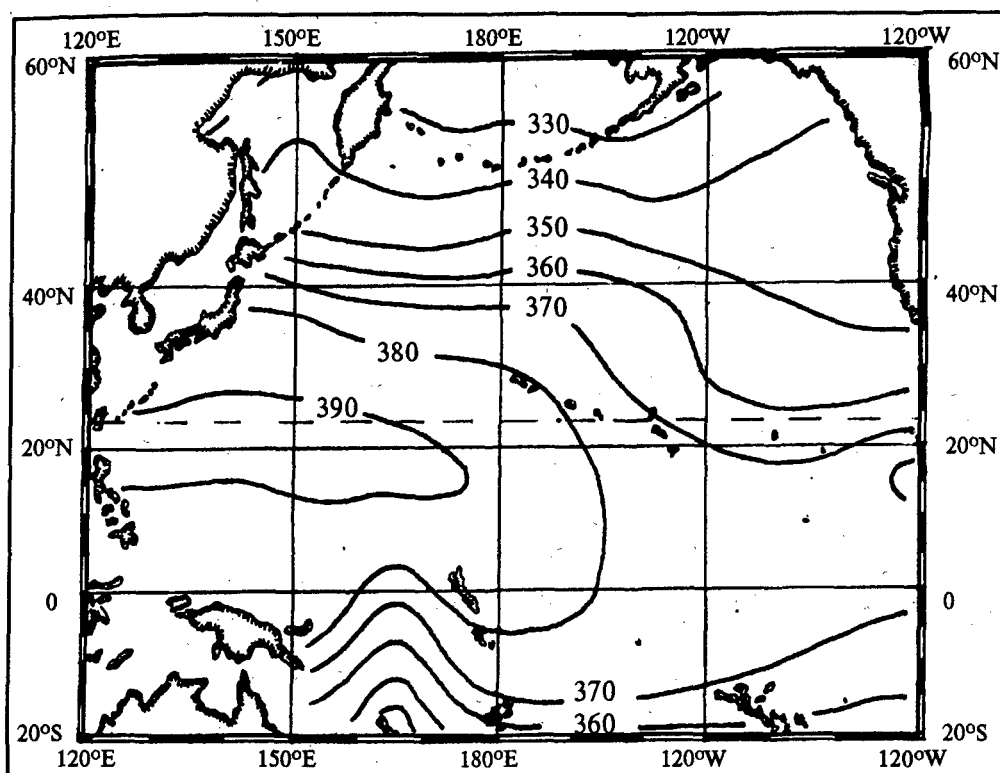


Figure 1: Refraction index in N-units near sea surface. August.

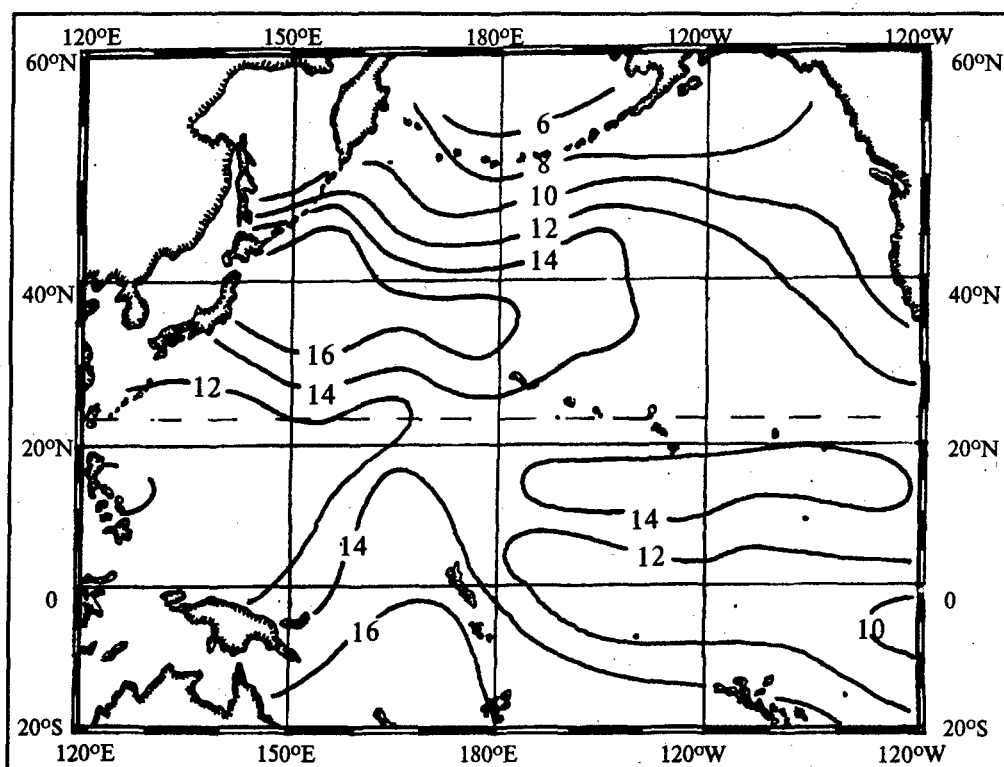


Figure 2: Standard deviation of refraction index in N-units near sea surface. August.

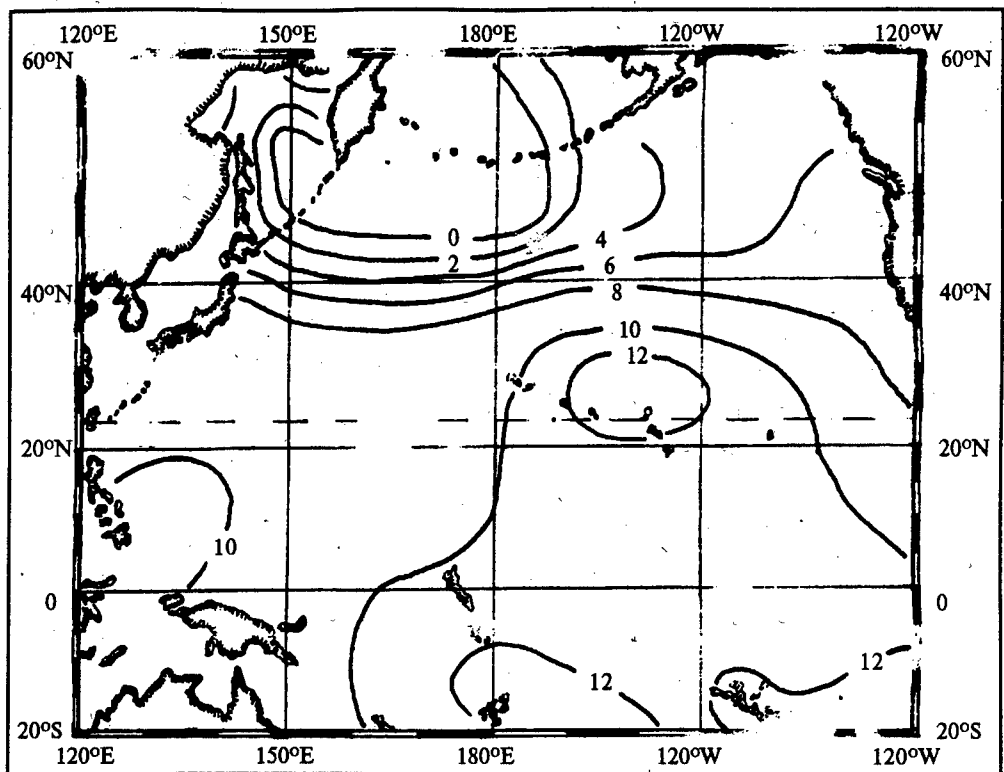


Figure 3: Average height of evaporation duct in meters. August.

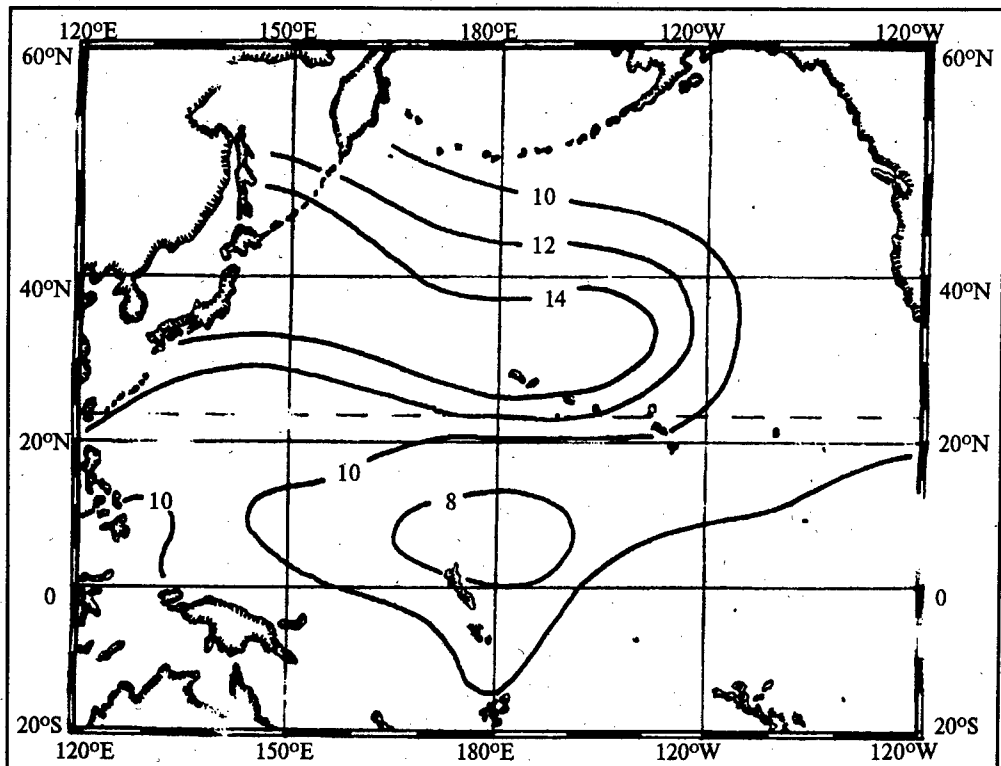


Figure 4: Standard deviation of refraction index at 1 km height in N-units. August.

2.4. Layers of the high refraction (6 maps)

There were made calculations of the repetition frequency, mean height, bottom boundary and the average power of the high refraction layers with the refractive index gradient $g < -80$ N-units/km for the height's interval 0.1-5.0 km. There were also calculated elevated layers of subrefraction with $g > 0$.

2.5. The average wind speed (8 maps)

There were made maps of the average wind speed at the sea surface and at the height 1500 m using aerological sounding data and the results of meteorological measurements made by the research ships.

3. RADIOWAVES PARAMETERS TROPOSPHERICALLY PROPOGATED OVER-THE-SEA

3.1. Radiohorizon range (4 maps)

For different seasons there are given isolines of the radiohorizon range, calculated for different antenna heights over the sea surface supposing the vertical profile of the refractive index linear and using mean for month difference of this index at the sea surface and at the height 0.2 km.

3.2. Attenuation index in rain (8 maps)

Calculations were made for 3 and 10 cm bands taking into consideration the mean quantity of precipitation, its average intensity and the typical size of the precipitation zones. There were used data of precipitation observations in 60 points of the Pacific Ocean. The attenuation factor was calculated for only one-way propagation of the signal from the range-sight to antenna put at 25 m height, using method (Ref. 4).

3.3. Frequency band of signals reflected from the sea surface (4 maps)

The frequency band was found for the band of 3 cm, using data about the wind speed. The main wind speed isolines are given for the angles 1 and 90 degrees. A fragment of one of these maps is shown in fig. 5.

3.4. Vertical antennas lobes (16 maps)

Parameters of the vertical antennas' lobes (the field level of the first maximum and minimum relating

to the free space) were calculated for horizontal polarization, bands 3 and 10 cm. These calculations were made after the intermediate estimation of the reflection from the sea surface index, taking into consideration the waves height and supposing that this height has gaussian distribution.

3.5. Attenuation index in the diffraction zone (4 maps)

There were made maps of the diffraction attenuation of the sight-line bound and of the full attenuation beyond this boundary. Isolines of this parameters were calculated for the antennas height 16 m, using approximate method, based on the well known diffraction formulae V.A. Fok (Ref. 6). There was used the Eath equivalent model and data about the reflection index gradient in the low atmosphere over the sea.

3.6. Attenuation index in the zone of far tropospheric propagation (13 maps)

In the zone of far tropospheric propagation there exists the range interval, where specific signal attenuation much smaller than in the diffraction zone. The border of this zone is 50-80 km beyond the horizon. The maps allow to make interval (fig. 6) and point (fig. 7) estimation of the attenuation index in the band of 10-200 cm when both antennas (transmitting and receiving) are situated at the height of 15 m, which means out of the evaporation duct. There were taken, as called standard functions of attenuation, average for the conditions over the whole ocean, to estimate longitudinal dependences. These curves were drawn using all experimental data with necessary correction, connected with regions and time of observation. Borders of intervals, put in every band according to histograms for different ocean regions and seasons, were the basis for interval estimations. Isolines of month deviations from standard curves (for point estimations) and zones of the most probable intervals are shown in the maps.

Estimation of attenuation index deviation without straight experimental data was done using month refraction index and refractive index gradient in the layer 0-1 km. It could be done after introduction of the special coefficients of validity. Borders of points for the interval estimation of the attenuation index in different bands were chosen to make apriory probability of the same points approximately equal. It allowed to make maps without distributing according to frequencies.

In order to estimate slow variations of the attenuation index for the two north-west regions of the

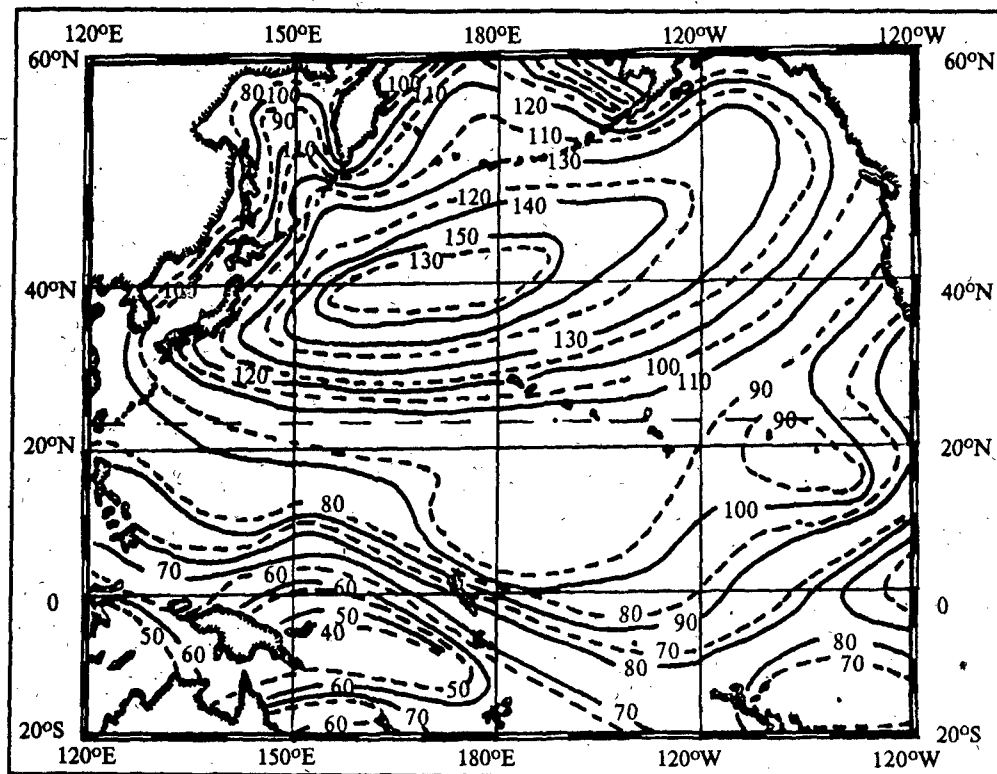


Figure 5: Doppler spectrum width of radar signals reflected from sea surface. Wavelength 3 cm. February. Angle of incidence, degrees: ---- 1; - - - 90.

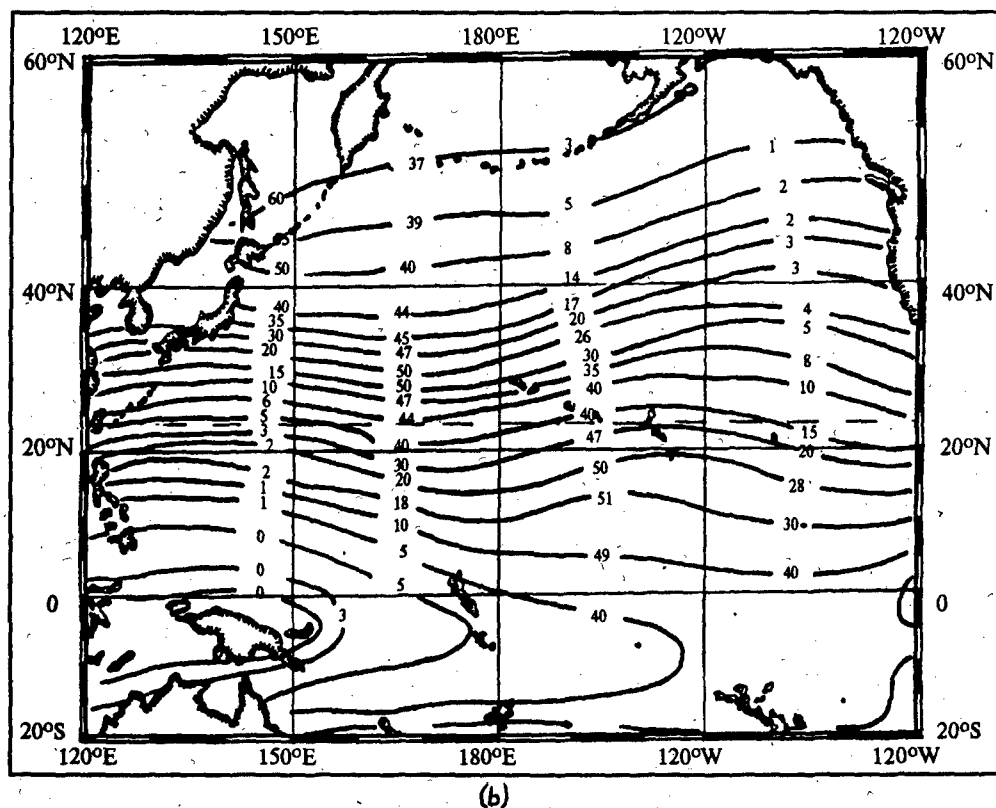
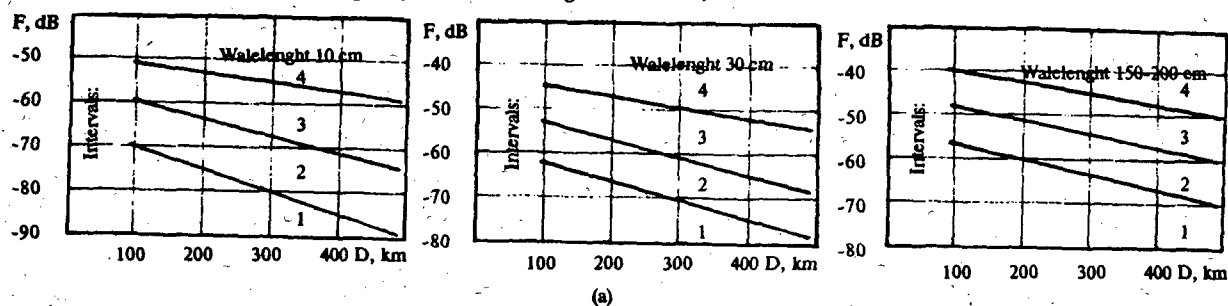


Figure 6: Interval estimate of attenuation factor. February.

(a) Interval boundaries (F - attenuation factor; D - path length).

(b) Interval probabilities isolines (from left to right - percents for 1, 2, 3 and 4th intervals).

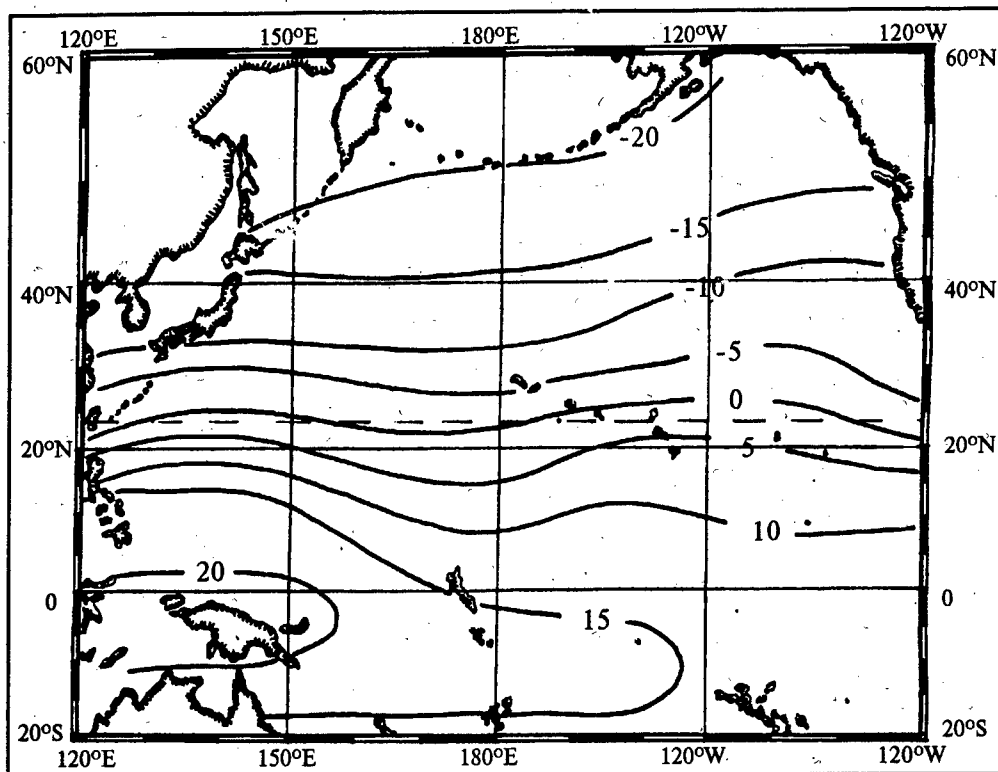


Figure 7: Attenuation factor departure from boundary between 2 and 3th intervals (fig. 6), dB. Wavelength 10 cm. February.

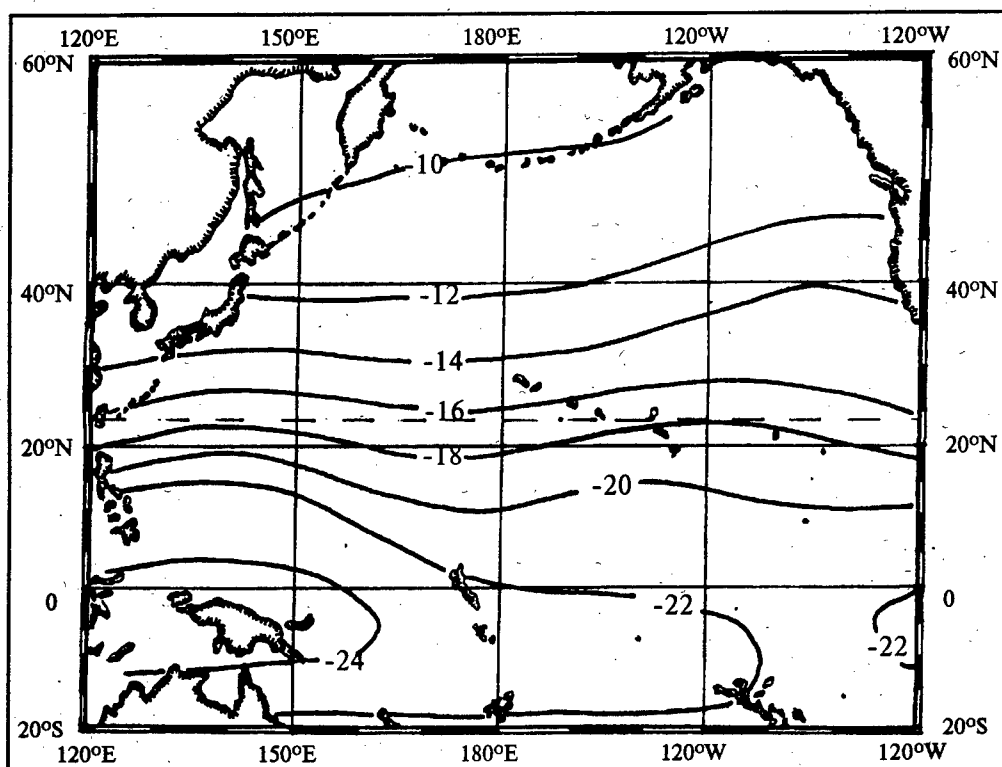


Figure 8: Relative level of cross-polarized wave in dB. Wavelength 10 cm. February.

Pacific Ocean there were built up structure functions, which turned out nearly the same for the time intervals up to 40-70 hours.

3.7. Coherence and correlation (16 maps)

Interval estimation of the coherence parameter (relation of regular and dissipated signals in 5-minutes intervals), radius of time and space (cross) correlation and standard deviation of the quick fluctuations for different ocean regions in the cm-band and the zone of far tropospheric propagation were represented as maps.

For each of these parameters and for different seasons in the maps are shown borders of intervals and isolines of their probability. While making the maps there were used experimental data and if these data were not enough productive there were done calculation, using coefficients of validity connected with the height gradient of the refractive index and with the wind speed.

3.8. Attenuation in the evaporation duct (4 maps)

Point estimation of the attenuation factor for different antenna's height (5 and 15 m) was done for paths of 200 km long and the band of 3 cm using method (Ref.7) and maps of evaporation ducts.

3.9. Signal depolarization in the zone of far tropospheric propagation (6 maps)

There are given maps of the mean relation of the signal cross and main components (example in fig. 8) and of the standard deviation of the cross component on the paths 300-500 km long in 10 cm band for the vertical transmitting signal polarization.

4. PROGNOSIS VALIDITY

Experimental tests of the estimations of the average radiometeorological parameters and characteristics of radiosignals presented in the maps are rather difficult because of the limited quantity of samples and of time and space of observation limits. Still there could be done indirect conclusion by comparison of standard deviation of measured parameters with the same deviations calculated after subtracting of prognosed values. Measurements of many parameters, made during research ships voyages (more than 10 voyages during 5 years), showed, that standard deviation of the prognosed values are 1,5-2,5 times smaller than the same deviations

without prognosis; for instance standard deviation of the hour attenuation factor over paths 200-600 km long in 10-cm band changes from 13,8 dB to 8,7 dB after using prognosed data.

5. CONCLUSION

Radiometeorological and radiophysical maps of the tropospheric atlas of the Pacific Ocean can be a basis for the long-term prognosis of characteristics of board and ground radiosystems. More accurate definition of the prognosis and spreading it on shorter periods (days, hours) can be done after using some additions defined by specific meteorological and radiomeasurements.

6. REFERENCES

1. *Атлас океанов. Тихий океан.* - М.: Военно-морской флот, 1974. - 302 с.
(*Atlas of oceans. Pacific Ocean.* - Moscow, 1974).
2. *Атлас климатических характеристик температуры, плотности и давления воздуха, ветра и геопотенциала в тропосфере и нижней стратосфере Северного полушария.* Ч. 1 и 2. - М.: Гидрометеониздат, 1975.
(*Atlas of climatic characteristics of troposphere and low stratosphere.* - Moscow, 1975).
3. Гаврилов А.С., Петров Ю.С. Метод расчета структуры приводного слоя атмосферы применительно к задачам радиолокации над океаном. - В сб: *Рассеяние и дифракция радиолокационных сигналов и их информативность.* - Л.: СЗПИ, 1984, с. 31-36.
(A.Gavrilov, J.Petrov. Method of calculation over-the-sea atmospheric structure. - Leningrad, North-West Polytechnical Institute, 1984).
4. J.Battesti, L.Boithias, P.Misme. *Determination de l'affaiblissement du a la pluie pour les frequences superieures a 10 GHz.* - Ann. telecomms, 1971. - 26.-No.11-12, 439-444.
5. Загородников А.А. Зависимость спектра радиолокационного сигнала, рассеянного морской поверхностью, от размеров

- облучаемого участка и бальности волнения. - *Радиотехника и электроника*, No.3, 1972.
(A.Zagorodnikov. Spectrum of radar signal, reflectioning by sea surface. - *Radiotekhnika i elektronika*, No.3, 1972).
6. Калинин А.И. *Расчет трасс радиорелейных линий*. - М.: Связь, 1964. (A.Kalinin. Calculation of radio relay paths. - Moscow, 1964).
7. Белоброва М.В., Кукушкин А.В., Левин М.Б., Фастовский Я.А. *Пакет программ для оценки условий распространения радиоволн УКВ-диапазона в пограничном слое атмосферы над морем*. - Харьков, РИАН УССР, 1989. Препринт No.31. (M.Belobrova, A.Kukushkin, M.Levin, J.Fastovski. *Software for estimate UHF propagation over-the-sea*. - Kharkow, Institute of Radioastronomy, Preprint No. 31, 1989).

FREEZING LEVEL CHARACTERISTICS AT SELECTED STATIONS ACROSS CANADA

B. Kochtubajda¹, and D.V. Rogers²

1- Department of Geography, Meteorology Division, University of Alberta,
Edmonton, Alberta, Canada

Tel: 403-492-9958, Fax: 403-492-7598, E-mail: bkochtub@geog.ualberta.ca

2- Radio Sciences Directorate, Communications Research Centre, Industry Canada,
Ottawa, Ontario, Canada

Tel: 613-998-5174, Fax: 613-998-4077, E-mail: dave.rogers@crc.doc.ca

ABSTRACT

Statistical information on the variability of the freezing level in the atmosphere is useful in the development of interference prediction models for hydrometeor-scatter. In this study, radiosonde data from eight stations across Canada were extracted from the digital archive of the Canadian Climate Centre for the period 1979-1990. Surface observations were extracted for the hour before and after each radiosonde release in order to examine freezing level height differences during precipitating and non precipitating events. This paper examines the seasonal, longitudinal, and latitudinal variations of the freezing level height among arctic, maritime, and continental stations.

Keywords: Freezing level height, interference prediction, precipitation.

1. INTRODUCTION

Statistical information on the variability of the freezing level and rain height is useful in the development of interference prediction models for hydrometeor-scatter effects on communication systems. One interference mechanism for which prediction techniques are required is scattering from wet snow in the melting layer.

Measured values of the freezing level height have been reported for tropical and equatorial regions [1], [2], and for Europe [3]. This study will discuss the seasonal, longitudinal and latitudinal variations of the freezing-level height among arctic, maritime, and continental stations in Canada.

2. FREEZING LEVEL STATISTICS

Twice a day, all over the world, balloon-borne radiosondes are released from the earth's surface to measure characteristics of the atmosphere. Currently, there are 32 stations that comprise Canada's upper air network. For this study, a subset of eight stations representing different regions of the country were selected for freezing level analyses for the period 1979-1990. Full periods of record observations were not available for some stations. The specific stations, their latitudes and longitudes, elevation and period of record used in this work are summarized in Table 1. The station locations are shown in Figure 1.

2.1 Data Preparation

The surface and upper air data used in the analyses of the freezing level were obtained from the digital archive of Canadian Climatological Data that is maintained by the Canadian Climate Centre. Data tapes of hourly records indicating the presence or absence of any type of precipitation and the twice daily upper air soundings (at 00 GMT and 12 GMT) were requested for each of the stations from 1979 to 1990.

The upper air tapes contained records of each radiosonde ascent, consisting of the station identification number, date, time and element number followed by the data, repeated for each level, from the lowest level to the termination of the ascent. For each ascent, the freezing level was extracted by selecting the 0 deg temperature measure, or determined by linear interpolation. If the surface temperature was below freezing, a melting level was not calculated and the record reflected the surface temperature. This record was kept to determine frequency of occurrence statistics.

Surface precipitation observations were extracted for the hour before, during, and after each radiosonde release in order to examine freezing level height differences during precipitating and non precipitating events. Precipitation can occur in the form of liquid, freezing, frozen or combinations of these. The simultaneous 3-hourly surface observations were combined with the file of freezing heights and sorted by month into 3 broad categories; RAIN (liquid or combinations with liquid), OTHER (freezing or frozen) and NORAIN.

3. DISCUSSION OF RESULTS

The annual distribution of the percentage frequency of occurrence of ascents with surface temperatures above 0°C, indicative of when freezing level observations in the atmosphere were possible, is shown in Figure 2. This figure shows a wide range of climate types.

The mild, maritime climate of the western coast of British Columbia is characterized by small seasonal temperature differences [4]. During the winter season (Dec-Jan-Feb), the surface temperature is above freezing at Port Hardy for about 85% of the time and from 90 to 100% during the rest of the year.

Conversely, the climate of the Northwest Territories is harsh. Temperatures are generally below -18°C for 5 months or more, and the annual range of temperatures is one of the greatest on the continent. Freezing levels occurred above the surface for less than 3% of the time from November to March at Inuvik. During the summer months (Jun-Jul-Aug), freezing levels could be determined over 90% of the time.

Between these two extreme profiles the other stations from Vernon, B.C., to Shelburne, N.S., exhibit similar seasonal variations in the frequency of occurrence of the freezing level. In the winter, measurable freezing levels occur between 5-40% of the time. As the weather begins to warm in the spring, the occurrence of measurable freezing levels rises accordingly. By early summer, occurrences of over 95% are reached and maintained until October. However, the occurrence of measurable freezing levels drops from around 75% to near 30% by the end of November.

The monthly average of all measured mean freezing level heights in the atmosphere (when the surface temperatures are above freezing) for

the selected stations across Canada is shown in Figure 3. On an annual basis, the lowest heights occur at Inuvik, NWT, at 1447 m above ground level (AGL) and the highest occur at Shelburne, N.S. (2412 m AGL). An examination of the seasonal variations in height indicates that, as expected, the heights peak in the summer months and are lower in the winter. The spatial variability indicates that the freezing levels are generally higher in eastern Canada than in the western part of the country.

An examination of the freezing level heights during precipitating and non precipitating events was conducted to determine if height differences existed in the presence of precipitation. The monthly average freezing level heights conditioned on the occurrence of rain/norain/other are presented in Figures 4 through 10. (Lack of surface data for Vernon precluded this analysis for this location).

In general, when the melting level observations were conditioned on the occurrence of freezing or frozen rain / norain surface observations (+/- 1 hr of ascent), the heights were significantly lower during precipitation for most of the selected stations. However, there were some observations where the opposite held true, namely, Inuvik (Feb+Mar), and Manawaki (Dec+Jan).

When the melting level observations were conditioned on the occurrence of rain / norain surface observations (+/- 1 hr of ascent), the height tendencies were again mixed. At Inuvik, Port Hardy, and Stony Plain (western Canada) melting level heights were generally lower when it was raining. At Shelburne, melting level heights were higher when it was raining than when it was not. In Ontario and Quebec, there were no significant height differences during the summer (Jun-Jul-Aug). Heights were greater when it was raining between October and May in Manawaki and between September to November and between January and May at Sept Isles.

These data indicate that the mean freezing level is not always lower during rainfall. Upper air circulations and synoptic disturbances, notably cyclones, account for the differences. Central and eastern Canada are often affected by tropical and sub-tropical airstreams originating in the Gulf of Mexico and the Atlantic.

Seasonal and latitudinal variations among arctic, maritime and continental stations were examined and compared with the ITU-R expression [5]. The ITU-R empirical relationship for the mean

height of the freezing level, H_{fr} (km), during rainy conditions is written for the Northern Hemisphere as:

$$H_{fr} = 5.0 \quad \text{for } 0 \leq \varphi \leq 23$$

$$= 5.0 - 0.075(\varphi - 23) \quad \text{for } \varphi > 23$$

where φ (degrees) is the latitude. The results are summarized in Table 2. The observed summer heights agree fairly well with the ITU-R formula except at high latitudes. However, the observed mean heights differ substantially in some cases.

4. CONCLUSIONS

Monthly, seasonal, and annual distributions of the freezing level height were examined for 8 radiosonde stations representing the arctic, maritime and continental climates across Canada. In addition, surface observations were extracted for the hour before and after each radiosonde release in order to examine freezing level height differences during precipitating and non precipitating events.

On an annual basis, the lowest heights occurred at Inuvik, Northwest Territories and the highest at Shelburne, Nova Scotia. As expected, the freezing level heights peak in the summer months and are lower in the winter. When the freezing level observations were conditioned on the occurrence of freezing rain / norain, at most of the selected stations, heights were found to be lower when it was precipitating. The height tendencies were mixed when conditioned on the occurrence of rain / norain surface observations. Freezing level heights in Western Canada were generally lower during rain events, but were found to be higher between late fall through spring in eastern Canada.

Comparisons of freezing height statistics with the ITU-R expression were made. The observed summer heights seemed to agree fairly well with the formula except at high latitudes, but otherwise the ITU-R expression tends to overestimate the height.

ACKNOWLEDGEMENTS

The authors gratefully acknowledge the contributions of Mr. Andrej Krol from the Alberta Research Council for providing the computing support, Mr. Jim Ross from the Prairie and Northern Region of Environment Canada for providing the upper air data, and Dr. R.L. Olsen of CRC for helpful discussions. The support of the Spectrum Management Branch of Industry Canada, particularly Mr. Vishnu Sahay, is much appreciated.

BIBLIOGRAPHY

- [1] Ajayi, G.O., and F. Barbaliscia, 1989: Characteristics of the 0°C isotherm height at locations in Italy and Nigeria. Proc 5th URSI Comm. F Symp, La Londe-les Maures, France. 8.2.1-8.2.4
- [2] Pontes, M.S. and R.S.L. Souza, 1991: Estimation of rain height for slant-path attenuation prediction in tropical and equatorial climates. IEE Conf. Publ. No. 333, Pt.2: Propagation, 746-749.
- [3] Watson, P.A., M.J. Leita, V. Sathaseelan, M. Gunes, J.P.V. Poyares Baptista, B.A. Potter, N. Sengupta, O. Turney and G. Brussaard, 1987: Prediction of attenuation on satellite-earth links in the European region. IEE Proc., Vol. 134, Pt.F, No.6, 583-596.
- [4] Phillips, D., 1990: The Climates of Canada. Supply and Services Canada, Ottawa, 176pp.
- [5] Recommendation 839, 1992: "Rain height model for prediction methods", CCIR Recommendations, RPN Series, ITU, Geneva, 207.

Table 1: Summary of Upper Air Station Locations and Period of Record

Station Name	Latitude (degrees)	Longitude (degrees)	Station Elevation (above MSL)	Period of Record
Inuvik, NWT	68 19 N	133 32 W	103 m	1979 - 1990
Maniwaki, Que	46 23	75 58	170	1979 - 1990
Moosonee, Ont	51 16	80 39	10	1979 - 1989
Port Hardy, B.C.	50 41	127 22	22	1979 - 1989
Sept-Isles, Que	50 13	66 15	52	1979 - 1990
Shelburne, N.S.	43 43	65 15	28	1979 - 1988
Stony Plain, Alta	53 33	114 06	766	1979 - 1989
Vernon, B.C	50 14	119 17	555	1979 - 1990

Table 2: Summary of seasonal average and annual average freezing level heights (km AGL) across Canada.

Station Name	Winter (D-J-F)	Spring (M-A-M)	Summer (J-J-A)	Fall (S-O-N)	Annual	ITU-R equation
Inuvik, NWT	1.26	1.12	2.13	1.27	1.45	1.60
Maniwaki, Que	1.44	1.82	3.22	2.20	2.17	3.25
Moosonee, Ont	0.84	1.61	2.86	1.62	1.73	2.88
Port Hardy, B.C.	1.25	1.43	2.83	2.18	1.92	2.92
Sept-Isles, Que	1.04	1.30	2.80	1.59	1.68	2.96
Shelburne, N.S.	1.43	1.61	3.67	2.61	2.41	3.45
Stony Plain, Alta	1.10	1.27	2.37	1.57	1.58	2.71
Vernon, B.C	0.89	1.42	2.71	1.78	1.70	2.96

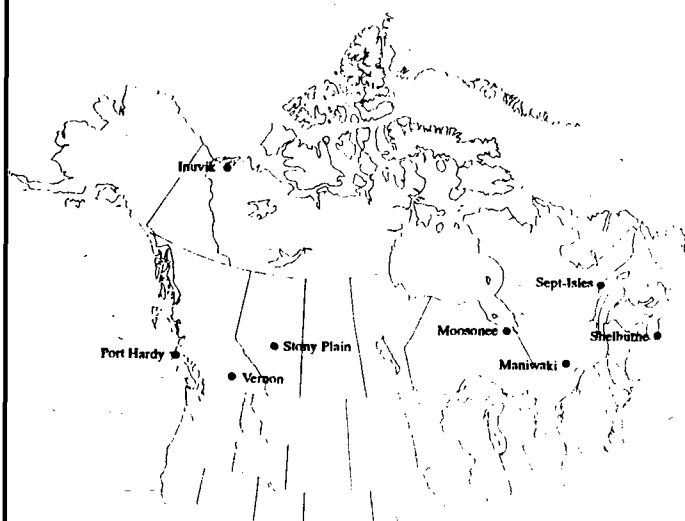


Figure 1: The locations of the radiosonde stations used in the study.

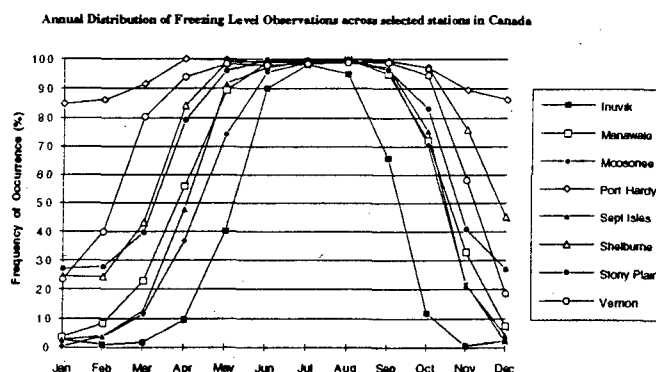


Figure 2: The annual distribution of the frequency of occurrence of upper air ascents with surface temperatures above 0°C for selected stations across Canada.

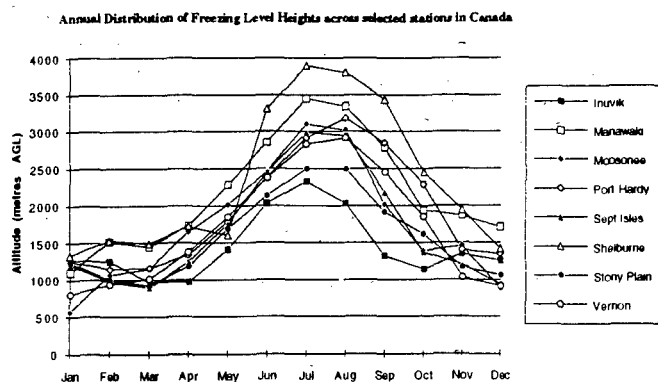


Figure 3: The monthly average freezing level heights in the atmosphere for selected stations across Canada.

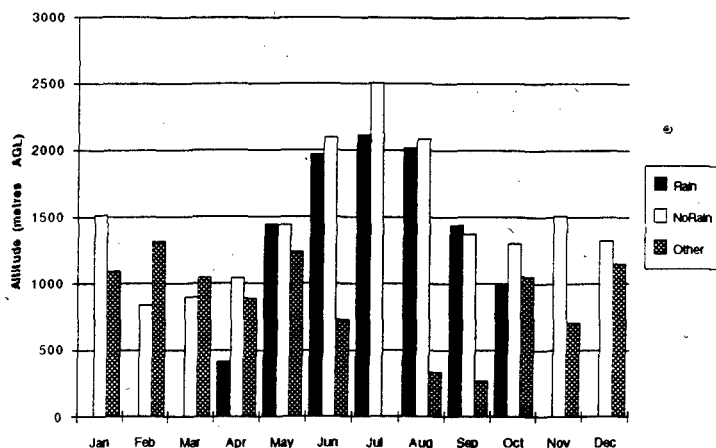


Figure 4: The monthly average freezing level height at Inuvik, Northwest Territories conditioned on the occurrence of rain / no rain / other surface observations (+/- 1 hr of ascent).

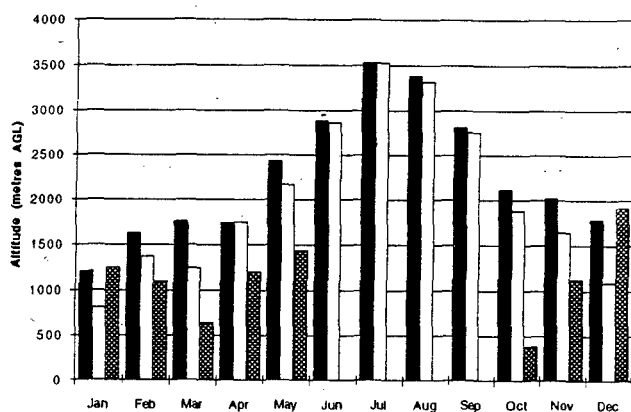


Figure 5: Same as fig.4, but for Manawaki Quebec.

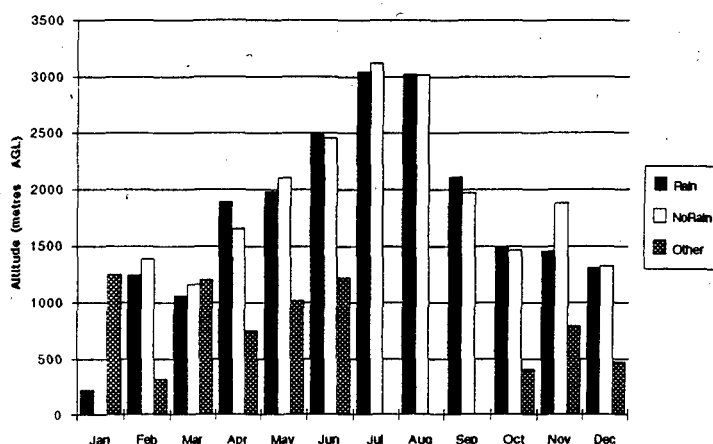


Figure 6: Same as fig.4, but for Moosonee, Ontario.

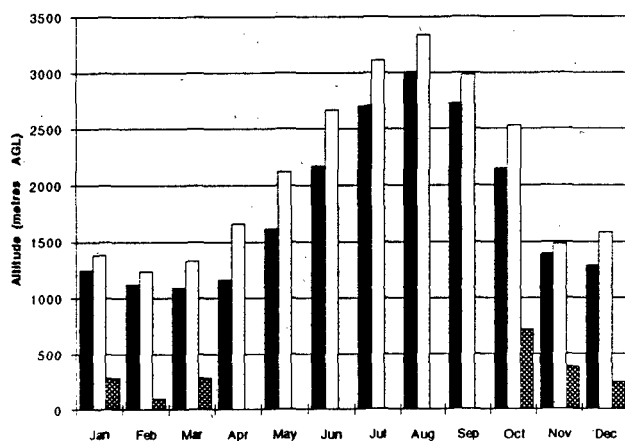


Figure 7: Same as fig.4, but for Port Hardy, British Columbia.

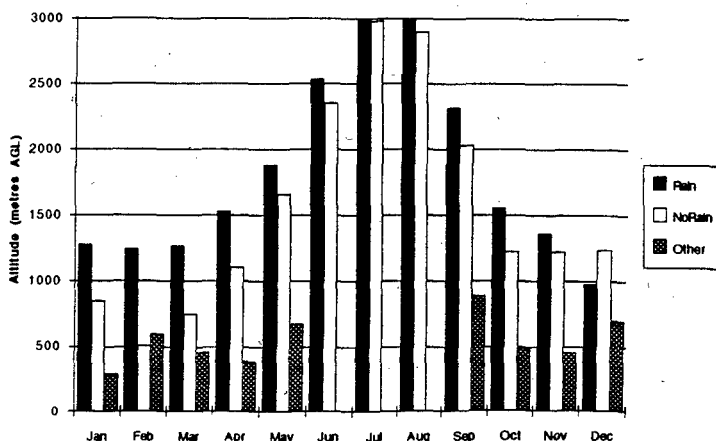


Figure 8: Same as fig.4, but for Sept Isles, Quebec.

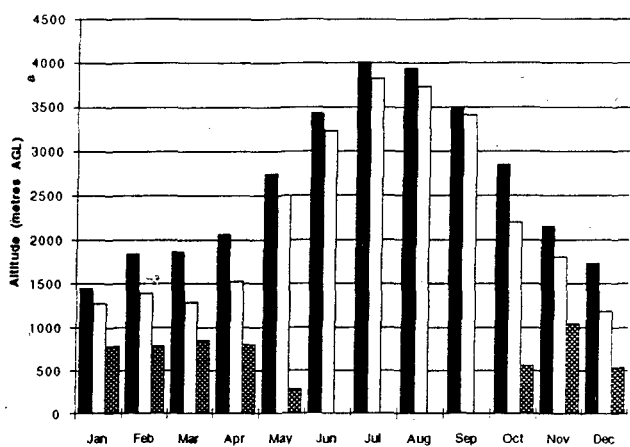


Figure 9: Same as fig.4, but for Shelburne, Nova Scotia.

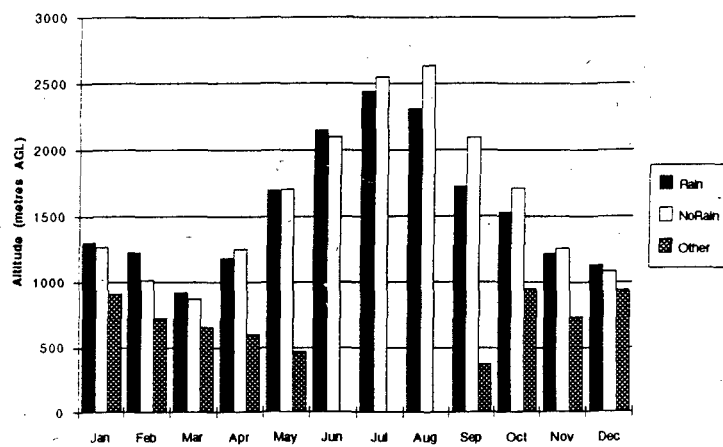


Figure 10: Same as fig.4, but for Stony Plain, Alberta.

Session 13: Mapping IV

APPLICATION OF MAXIMUM ENTROPY METHOD FOR PREDICTION MUTUAL CONTENT OF ATMOSPHERIC OZONE NEAR MOSCOW

A.V.Moshkov¹, V.V.Efremenko¹, K.G.Kirjanov², A.V.Shabelnikov¹

1 - IRE, 11 Mokhovaja Str., Moscow, 103907, RUSSIA

Tel: (095) 203-49-96, Fax: (095) 203-60-78, E-mail: efr@ire.uucp.free.msk.su

2 - University of Nizhny Novgorod, Gagarin prosp., 23, N-Novgorod, 603600, Russia.

Tel: (831) 265-03-67.

ABSTRACT

The maximum entropy method has employed for determination of spectrum and prognosis of temporal oscillation mutual content of atmospheric ozone near Moscow. It was shown, that during 20-monthly interval of time maximum average square mistake of prognosis does not exceed 10%. Temporal oscillations of mutual content of atmospheric ozone near Moscow, in general, offered by natural processes: the Earth's revolution round the Sun and the Sun System revolution round the Local center of stars.

Keywords: Maximum entropy method, Prognosis of mutual content of atmospheric ozone.

Authors have employed the maximum entropy method in the form of avto-regression model { AR-model } to determine the spectrum and predict the temporal oscillations of mutual amount of the atmospheric ozone near Moscow [1-4]:

$$x_n = - \sum_k a_k x_{n-k} + n_k, \quad (1)$$

where a_k - parameter of model, x_n - discrete series of numerical values of analyzed process in the given temporal interval t . The succession $\{n_k\}$ presents a realization of white noise with zero mean quantity and dispersion σ^2 . Within the limits AR-model signal is considered as a

result of determined component filtering from initial noise. In the case the estimation of power spectrum $S\{f\}$ of process {1} is determined by the relation [1]:

$$S(f) = \frac{\sigma^2 \Delta t}{\left| 1 + \sum_{k=1}^P a_k \exp(2\pi i f k \Delta t) \right|^2}, \quad (2)$$

where Δt - interval between initial data countings. Formula {2} was used for to calculate of power spectrum $S\{f\}$ of temporal oscillations of the total amount of the atmospheric ozone X {in ml.atmosph.sm.} during a 10-year interval 1973-1982 [5]. As initial series of monthly averaged meanings of X we used the data, received on the near Moscow ozonometric testing area $\{f=55.45', l=37.34'\}$. Methods of the value X measuring and also employed equipment were described in [6]. In Table 1 an experimental power spectrum $S\{f\}$ of temporal oscillation X is given. It is calculated by the formula {2} with $P=23$ and 30.

In the first column there are periods T_n^e of spectral components X in the Earth twenty-four hours, in the second column there are intensities of these components I in relative units. In the third column there are calculated values of spectral components periods X , received by the formula [7]:

$$T_n^T = T_1 / n^2, \quad (3)$$

Table 1

T_n^e , days	I, rel. units	T_n^T , days	n
2970	732	2905	2
1127	833	1291	3
680	1482	726	4
600	2093	465	5
366	211867	323	6
242	751	237	7
184	1419	182	8
144	291	143	9
127	231	116	10

Table 2

X_e , ml. atm. cm.	X_p , ml. atm. cm.
410	396
370	369
338	366
329	333
313	321
323	311
315	327
350	347
357	370
407	394
426	423
397	433
399	388
382	376
347	354
333	340
303	329
299	311
293	315
304	341

where $T_1=31,8$ years-the basic period of value X oscillations, $n=1,2,3,\dots$ -the whole numbers, given in the fourth column of Table 1. T_1 is one of components of oscillations spectrum of the Sun system parameters, caused by its revolution round the Local center of stars with the period $T=371$ thous. years [7]. The spectrum X analysis shows, that temporal oscillations offered, in general, by natural reasons. Annual changes X offered by the Earth's revolution round the Sun. Values X, on the average, during the examination period are maximum in March-April, when Earth's orbital speed is directed to the Galaxy center, and they are minimum in October-November, when the Earth's orbital speed is directed to opposite side. Between annual changes X are determined by the Sun system movement round the Local center of stars. Prognosis oscillations X near Moscow fulfilled by the formula {1} with $P=23$ during 20 months forward by 100-monthly initial massive of data and then was compared with measured values. In the first column of Table 2 measured values X is given, in the second column predicted values X, calculated by the formula {1} is given.

Table 2 shows, that maximum entropy method in the form of AR-model presents effective way of prognosis of temporal oscillations of different

natural process parameters. The maximum average mistake of prognosis does not exceed 10% during 20-monthly interval of time. We shall do brief deduction in conclusion:

1. The maximum entropy method was first applied for prognosis of monthly oscillations of total content of atmospheric ozone near Moscow.
2. Temporal oscillations of total content of atmospheric ozone near Moscow, in general, offered by natural processes: the Earth's revolution round the Sun and the Sun system revolution round the Local center of stars.
3. Proposed in this work method of prognosis can be used for any natural processes, having sufficient series experimental data.

REFERENCES

1. Marple S L 1987, Digital spectral analysis, New Jersey, Prentice-Hall, Inc.

2. Kay S M et al. 1981, Spectrum analysis. A modern perspective, *Proc. IEEE*, 69,11,pp.1380-1419
3. Marple S L 1980, A new autoregressive spectrum analysis algorithm, *IEEE Trans. SSP*, 28, 8,pp.441-454
4. Kay S M 1987, Modern spectral estimation, New Jersey, Prentice-Hall, Inc.
5. Gucshin G P 1976-1985, Total content of atmospheric ozone. Information data for USSR stations, Leningrad, Gidrometeoisdat
6. Gucshin G P et al. 1983, Total ozone in atmosphere, Leningrad, Gidrometeoisdat
7. Shabelnikov A V 1992, Impact of cosmophysical factors on the climate and biosphere of the Earth, *Biofizika*, 37, 3, pp.572-575

THE POTENTIAL OF A SPACEBORNE CLOUD RADAR TO MEASURE VARIOUS CLOUD TYPES AT 94 GHz

A.D.Papatsoris¹ and P.A.Watson²

1- University of York, Heslington, YORK YO1 5DD, United Kingdom
Tel: +44-904-432394, Fax: +44-904-432335, E-mail: adp@ohm.york.ac.uk
2- University of York, Heslington, YORK YO1 5DD, United Kingdom
Tel: +44-904-432338, Fax: +44-904-432335, E-mail: paw@ohm.york.ac.uk

ABSTRACT

The potential of a spaceborne cloud radar to aid global climate modelling via identification and quantification of the liquid water content of various multi-layered cloud structures is examined. Attenuation [dB] and reflectivity [dBZ] profiles are given for a wide collection of ice and water clouds, assuming a nadir-pointing radar configuration with sensitivity -30 dBZ in the presence of 5 dB of two-way atmospheric attenuation.

1. INTRODUCTION

The effect of clouds on the large scale circulation of the atmosphere is one of the major sources of uncertainty in predicting the climate change that will result from increased greenhouse gases. The vertical distribution of clouds, which is particularly poorly observed, affects the surface radiation balance and the profile of heat absorption and re-radiation through the depth of the atmosphere. These have important impacts on the hydrological and carbon cycles and on the climate both globally and regionally. Better global observation of clouds, especially on the vertical distribution, are required to improve understanding of the climate system and to develop and validate the general circulation models (GCM) used in climate description. It is generally believed that there is cooling from low level clouds such as the extensive areas of stratocumulus over the oceans whereas high level clouds result in heating. Millimetre-wave radars can be designed to detect most clouds. Unlike the optical radiation generated by lidars, millimetre-wave radiation can penetrate most non-precipitating clouds to give estimates of vertical cloud profiles. Millimetre-wave radar is thus the best available tool for measuring multiple cloud layers which are either not detected or identified ambiguously by other techniques. In the following, we give attenuation and reflectivity profiles resulting from various cloud structures which apply to a fixed beam nadir-pointing millimetre

tre wave radar operating at 94 GHz such that under consideration by the the UK GEWEX Forum (Ref. 1).

2. CLOUD PARTICLE SIZES AND CONCENTRATIONS

A wide collection of data and models for concentrations and size distributions of ice and water particles in clouds have been considered. Of particular interest and value are the general models of Feigelson (Ref. 6), AFGL (Ref. 2), the UK Met Office FIRE/ICE data for Cirrus (Ref. 9), the case studies of Foot (Ref. 7) and Nicholls (Ref. 8) for St and Sc, the studies of Bennets and Ouldrige (Ref. 12) for winter maritime Cb and those of Magono and Lee (Ref. 13) for snow clouds. Table II summarizes the data sources considered.

The size spectra of water droplets in clouds are given by the following general formulae:

$$n(r) = \begin{cases} A\left(\frac{r}{r_0}\right), & 0.1\mu\text{m} \leq r < r_{\min} \\ \frac{mN_0}{\Gamma(m+1)r_0^{m+1}}r^m e^{-\frac{r}{r_0}}, & r_{\min} \leq r < r_c \\ \frac{N_L(1-\beta)}{A}\left(\frac{A}{r}\right)^\beta, & r_c \leq r < r_{\max} \\ 0, & r > r_{\max}. \end{cases} \quad (1)$$

where the constants and parameters in Eq. 1 are given in Ref. 6.

The size spectra of ice particles in Ci clouds were studied by the Met Office C-130 aircraft during the ICE project. The collected data were analyzed and found to be best represented by the exponential $N(D) = N_0 \exp(-D/D_0^*)$. It must be noted however, that the probe used for these results could only size ice particles up to 800 μm in diameter. Another auxiliary device, suggested that the density of the ice particles was 0.9 gcm^{-3} for sizes less than 100 μm , but fell to 0.1 gcm^{-3} for particles 1 mm in diameter. The values of IWC (ice water content) inferred in the Ci clouds penetrated, ranged

Author	Date	Cloud Type
Silverman and Sprague (adapted later by AFGL) - Ref. 2	1970	Mid-latitude water clouds (St, Sc, As, Ns, Cu, various Cb)
Carrier et al (from various sources) - Ref. 3	1967	Mid-latitude water clouds (St/Sc, As, various Cu)
Ajvazyan (from various sources) - Refs. 4-5	1991	Water clouds containing super-large drops (St, Sc, Ac, As, various Cu, Cb)
Feigelson (reviews Russian authors) - Ref. 6	1984	Water clouds (detailed description of typical stratiform and convective cloud forms)
Foot - Ref. 7	1988	Detailed study of a Sc sheet
Nicholls - Ref. 8	1984	Detailed study of a marine Sc cloud
UK Met. Office - Ref. 9	1993	International Cirrus Experiment (ICE)
Foot - Ref. 10	1988	Detailed studies of a Cirrus cloud
Paltridge and Platt - Ref 11	1981	Detailed studies of several Cirrus decks
Bennetts and Oultridge - Ref. 12	1985	Study of an anvil of winter maritime Cb
Magono and Lee - Ref. 13	1967	Case studies of snow clouds

Table II: Data sources for various ice and water cloud models and other detailed case studies.

from 0.1 gm^{-3} down to 0.001 gm^{-3} , but were restricted to mid-latitude clouds and did not include the anvils from tropical storms. It is possible that much higher values up to 0.4 gm^{-3} can occur in the anvils of tropical Ci, but there are few data.

3. APPROACH TO CALCULATION OF CLOUD ATTENUATION AND REFLECTIVITY PROFILES

For our calculations we have assumed a monostatic, nadir-pointing radar with its beam uniformly filled. The range incrementation is taken 25 m for calculation purposes only. The conventional radar equation for volume scattering has been applied, including various components of atmospheric attenuation (clear air, cloud and rain), viz:

$$P_r = \frac{C \cdot |K|^2 \cdot Z_e}{r^2} e^{0.2 \ln 10 \cdot \int_0^r k(s) ds} \quad (2)$$

where P_r is the back-scattered power, C the radar constant, Z_e the radar equivalent reflectivity, $k(s)$ the attenuation coefficient in dB per unit length and r is the mid-point of the pulse volume. K is the associated dielectric factor of the scattering medium (At 94 GHz $|K|$ is 0.74 for water and 0.176 for ice at 5°C and -15°C , respectively). The calculations presented here refer to the equivalent radar reflectivity Z_e which is defined as:

$$Z_e = \frac{\lambda^4}{\pi^5 |K|^2} \int_D \sigma_b(D) N(D) dD \quad (3)$$

where $\sigma_b(D)$ is the radar cross section of a polydisperse medium described by a particle size distribution $N(D)$ reduced by the two-way attenuation

given by:

$$A = 2 \cdot \int_0^r k_{\text{clear air}} + k_{\text{cloud}} + k_{\text{rain}} ds \quad (4)$$

The zenith two-way clear air attenuation ranges typically from 1.1 dB to 3.0 dB for typical mid-latitude winter and summer atmospheres, respectively (results obtained from APM, see Ref. 14).

3.1 Particle scattering calculations

Mie scattering calculations have been used throughout. Cloud particles, either water droplets or ice crystals, have thus been modelled as spheres. For the prediction of attenuation and reflectivity resulting from water clouds, Mie scattering is an excellent approximation. For ice clouds, where very irregular shapes are encountered, the Mie scattering approach using equi-volume spheres should normally provide a reasonable estimation of attenuation and reflectivity for ice crystals less than $200 \mu\text{m}$ in diameter. The temperature has been taken 5°C for water droplets and -15°C for ice crystals.

Comparisons between Rayleigh and Mie scattering for ice and water spheres showed the Rayleigh approximation to be valid for water droplets less than $70 \mu\text{m}$ in radius and for ice spheres less than $145 \mu\text{m}$. Hence, for large ice particles and super-large drops an exact method for the calculation of the extinction and back-scattering cross sections is needed. Nevertheless, for most water clouds water droplets rarely exceed $40 \mu\text{m}$ in radius and the Rayleigh approximation can be used.

The importance of multiple scattering effects in clouds at millimetre wavelengths has been qualitatively investigated in Ref. 15. At 94 GHz it was

found that multiple scattering is negligible in water clouds. For thin Ci and ice forms of stratiform clouds without significant growth, multiple scattering -although present- is not expected to cause significant error in attenuation or reflectivity calculations. However, in convective clouds where ice particles and concentrations are much larger, multiple scattering is expected to be much more severe, but only a rigorous approach may provide quantitative results for both back-scattering and extinction.

The scattering properties of the larger ice particles found in Ci clouds, typically single or clustered hollow prisms ranging from 200 μm to 1 mm in length, have been modelled as bubble-like spheres (air core, ice shell) and approximated by solid ice spheres which exhibit similar scattering properties according to the relations:

$$r_{\sigma} = -8.28 \times 10^{-4} l_{Ci}^2 + 0.73 l_{Ci} + 32.7 \quad (5.a)$$

$$r_{C_{ext}} = -5.42 \times 10^{-4} l_{Ci}^2 + 0.64 l_{Ci} + 40.6 \quad (5.b)$$

where l_{Ci} is half the length of the Ci ice crystal in μm and r_{σ} and $r_{C_{ext}}$ are the radii of an equivalent solid ice sphere with same radar and extinction cross section in μm , respectively.

3.2 Modelling of cloud spatial inhomogeneity

In certain types of cloud the particle concentration, liquid or ice water content, size distribution and type of particles may vary significantly along the path of observation. In order to represent these variations, multi-layer models have been adopted with a single segmentation rule, namely that a linear relationship holds between the cloud parameters and the cloud depth. Thus, typical St/Sc and Cu are best represented by a two layer model whereas other more complex vertically extensive structures may require three or more layers. As an extreme example, we mention the case of the snow cloud described in Ref. 13 where 5 layers were considered.

4. ATTENUATION AND REFLECTIVITY PROFILES FOR VARIOUS CLOUDS

4.1 Water clouds

Generally attenuation from water clouds is simple to calculate. Since the cloud droplets are so small, the Rayleigh approximation is applicable and the attenuation is directly proportional to the total mass of the cloud. Attenuation is weakly only affected by temperature variations, but increases rapidly with the onset of precipitation. Typically the two-way attenuation for rain rates 2.5 and 10

mm/hour is 5, 10 and 16 dB, respectively. It is therefore sensible not to expect to take accurate cloud measurements when the precipitation rain rate exceeds 5 mm/hour.

An analysis of the observed droplet spectra from a C-130 aircraft during 3200 km of cloud penetrations during ASTEX (Atlantic Stratocumulus Transition Experiment) suggested the relationship (Ref. 16):

$$Z_e = 0.02 \cdot (LWC)^{1.2} \quad (6)$$

between the observed liquid water content and the resultant reflectivity, assuming Rayleigh scattering. Consequently, if the minimum Z_e value detected by the cloud radar was -30 dBZ then this would be equivalent to a LWC of about 0.08 gm^{-3} . Other computations related the effective cloud radius to the radar reflectivity according to the following empirical formula (Ref. 16):

$$Z_e = -61 + 37 \log(r_{eff}) \quad (7)$$

where the reflectivity Z_e is given in dBZ and the effective cloud radius r_{eff} in μm .

Attenuation and reflectivity profiles using Mie theory including the effect of super-large drops in clouds have been calculated and graphically illustrated along the cloud depth in Ref. 17. Here we summarize the results in Table III, below.

Cloud type	Attenuation (dB/km)	Reflectivity (dBZ)
St	0.7 to 2.2	-17 to -32
large drops	10% increase	+20 dBZ
Sc	1.0 to 2.7	-16 to -24
large drops	10% increase	+17 dBZ
Precipitation rain rate	2.5 to 5 2-5 mm/hour	0 to 20
As	0.5 to 2	-22 to -25
Ns	1.4 to 4.7	-12 to -15
large drops	10% increase	+19 dBZ
Cu (various)	0.6 to 8.5	-9 to -33
large drops	5 % increase	+13 dBZ
Cb	7 to 31	0 to +20
large drops	40% increase	+20 dBZ

Table III: Range of values of attenuation and radar reflectivity resulting from various water clouds.

4.2 Ice clouds

For Ci clouds, models from the UK Met Office (Ref. 9) along with special case studies from Refs. 10 and 11 have been considered. Detailed calculations and graphical illustrations for selected Cirrus cloud models have been given in Ref. 15. Generally, these calculations gave reassuringly low values for the resultant attenuation ($< 0.3 \text{ dB/km}$ even for

Ci with large IWC) and reflectivity values ranging from -15 to 15 dBZ for clouds bearing IWC between 0.025 and 0.377 gm^{-3} , respectively. Observations of Ci particle spectra during the ICE project predict the following empirical relationship between IWC and reflectivity (Ref. 16):

$$IWC = 0.07 \cdot Z_e^{0.7} \quad (gm^{-3}) \quad (8)$$

over the range of IWC from 0.001 to 0.1 gm^{-3} . Other ice clouds considered here include the study by Bennetts and Ouldrige (Ref. 12) of an anvil of winter maritime cumulonimbus and the studies of snow clouds of Magono and Lee (Ref. 13). A detailed description of the microphysical and thermodynamic structure of the anvil as recorded by the MRF C-130 aircraft is given in Ref. 12. Here, in Fig. 1 we give the corresponding attenuation and reflectivity profiles resulting from radar sampling along selected paths of the anvil. High reflectivity values are observed along the path crossing the core of the anvil, starting from -3 dBZ near the cloud edges and reaching 27 dBZ in the centre of the core. A similar pattern is observed for path BB' where at 4 km altitude, $Z_e = 17$ dBZ. At the right-hand edge of the anvil (CC') Z_e varies from -10 dBZ at the edges to 0 dBZ in the centre.

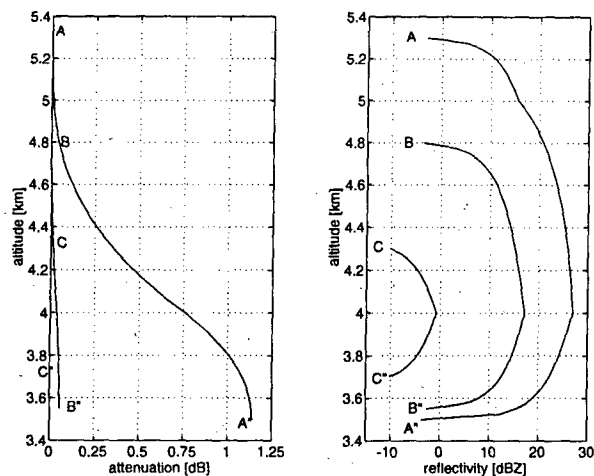


Fig. 1. Attenuation and reflectivity profiles for the maritime Cb anvil of Bennetts and Ouldrige along vertical paths AA' (core), BB' (off-core) and CC' (right-hand edge) of the anvil.

The multi-layer snow cloud model abstracted from the data of Magono and Lee has been used to calculate the attenuation and reflectivity profiles plotted in Fig. 2. As expected, attenuation is low, but reflectivity is consistently above 5 dBZ. The unusual fluctuation observed at 1.5 km is related to the very small ice water content reported by the authors at this altitude.

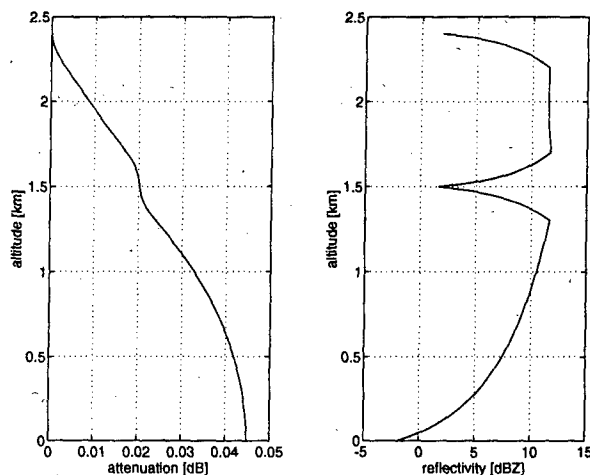


Fig. 2. Attenuation and reflectivity profiles for the snow cloud of Magono and Lee during the decaying phase.

The results are now summarized in table IV.

Cloud type	Attenuation (dB/km)	Reflectivity (dBZ)
Ci	< 0.3	-15 to 15
Cb ice anvil	0.1 to 0.7	-10 to 27
Snow (dry)	< 0.1	-3 to 13

Table IV: Range of values of attenuation and radar reflectivity resulting from various ice clouds.

5. DETECTION OF CLOUD LAYERS AND VERTICAL MAPPING

The most important objective of the spaceborne millimetre-wave radar is the detection and identification of multiple cloud layers. Particularly important, from a radiative point of view are extensive horizontal structures of St/Sc systems which may be not detected by other IR or VIS instruments when Ci clouds are present. From the previous analysis it is obvious that the radar should be able to "see" through Ci other cloud layers lying underneath. Most of the radiatively important St/Sc clouds should be identifiable, although in some cases the sensitivity of the radar may just not be enough to detect the cloud base. Nevertheless, it is evident that vertical mapping will be constrained here by the gate width. It might be important to reduce this below 450 m, though sensitivity trade offs are involved and gate-width diversity might be considered. Other stratiform clouds such as As and Ns can be more easily mapped in their vertical extent, since the associated reflectivity lies above the sensitivity

limit for most of the time.

Mapping of clouds with significant vertical extent can be problematic. The high attenuation usually associated with these clouds, reduces dramatically the observed reflectivity and will not allow the base of the cloud to be observed. Typically, reflectivity is -30 dBZ for a 2 km deep cumuliform cloud.

Ice anvils can be very well mapped in the horizontal as well as in their vertical extent. Furthermore, the resultant low attenuation (less than 0.75 dB/km), means that information about the underlying cloud layers should be obtainable. Snow clouds should likewise be penetrable to the point where melting occurs. The relatively high reflectivity of these structures should also help in identification.

5.1 Cloud identification

Knowledge of the reflectivity height profile should provide enough information to be able to identify many types of clouds from the radar alone. Ambiguities are introduced when attenuation becomes excessive or when reflectivities may become unusually high owing to the presence of super-large drops or drizzle drops. More information is needed on the frequency of occurrence of such drops in clouds.

The presence of precipitation under St/Sc can be easily detected, through enhanced reflectivity, provided that attenuation remains sufficiently low and the range gate is sufficiently narrow. Only the presence of very light precipitation under the cloud and the presence of super-large drops in the cloud volume can then confuse the detection of the cloud base.

6. CONCLUSIONS

Attenuation and reflectivity profiles for a wide collection of ice and water clouds at 94 GHz have been given. Various important associated problems such as multiple scattering and spectra of super-large drops have been examined and assessed in the context of a spaceborne cloud radar operating at 94 GHz. The -30 dBZ sensitivity limit implied by the preliminary specification, appears to be just adequate for the mapping of the vertical distribution of most important cloud structures. Nevertheless, the analysis clearly revealed the desirability of increasing sensitivity ideally by a further 10 dBZ or more realistically by 5 dBZ, in order to reduce uncertainties related to the detection of cloud bases and improve the penetration capability.

7. REFERENCES

1. UK GEWEX Forum, 1993, "A contribution to the World Climate Research Programme's Global Energy and Water Cycle Experiment - (GEWEX)", The Royal Society, UK.
2. Silverman B A, and Sprague E D, 1970, "Airborne measurements of In-Cloud visibility", National Conference on Weather Modification of the American Meteorological Society, April 6-9, Santa Barbara, California.
3. Carrier L W, Cato G A and Essen von K J, 1967, "The back-scattering and extinction of visible and infrared radiation by selected major cloud models", *Applied Optics*, Vol 6, No 7, pp. 1209-1261.
4. Ajvazyan H M, 1991, "Extinction and radar reflection coefficients for mm and sub-mm waves in clouds", *International Journal of Infrared and Millimetre Waves*, Vol 12, No 2, pp. 177-190.
5. Ajvazyan H M, 1991, "Extreme values of extinction and radar reflection coefficients for mm and sub-mm waves in clouds", *International Journal of Infrared and Millimetre Waves*, Vol 12, No 2, pp. 157-175.
6. Feigelson E M, 1984, *Radiation in a cloudy atmosphere*, Atmospheric Sciences Library, D Reidel Publishing Company.
7. Foot J S, 1988, "Some observations of the optical properties of clouds. I: Stratocumulus", *QJR Meteorol Soc*, Vol 114, pp. 129-144.
8. Nicholls S, 1984, "The dynamics of Stratocumulus aircraft observations and comparisons with a mixed layer model", *QJR Meteorol Soc*, Vol 110, pp. 783-820.
9. Illingworth A J, 1992, Ice spectra from the FIRE/ICE studies, Private Communication.
10. Foot J S, 1988, "Some observations of the optical properties of clouds. II: Cirrus", *QJR Meteorol Soc*, Vol 114, pp. 145-164.
11. Paltridge G W and Platt C M R, 1981, "Aircraft measurements of solar and infrared radiation and the microphysics of Cirrus cloud", *QJR Meteorol Soc*, Vol 107, pp. 367-380.
12. Bennetts D A and Oultridge M, 1984, "An observational study of the anvil of a winter maritime Cumulonimbus cloud", *QJR Meteorol Soc*, Vol 110, pp. 85-103.
13. Magono C and Lee C W, 1973, *J Meteor Soc Japan*, Vol 51, p 176.

14. Papatsoris A D and Watson P A, 1993, "Calculation of the absorption and dispersion spectra of atmospheric gases at millimetre-wavelengths", *IEE Proceedings-H*, Vol 140, No 6, pp. 461-468.
15. Papatsoris A D and Watson P A, 1993, Spaceborne Cloud Radar Feasibility Study - Study Topic: Target Definition, Mid-study report, contribution to the UK spaceborne cloud radar science team, RAL, January.
16. Fox N I and Illingworth A J, 1993, "Estimation of effective radius of cloud particles from the radar reflectivity", 26th Int Conference on Radar Meteorology.
17. Papatsoris A D, 1993, "Improvements to the modelling of radiowave propagation at millimetre wavelengths", PhD Thesis, Dept of Electronic and Electrical Engineering, Bradford University, UK.

SATELLITE PROBING OF EARTH'S OZONE LAYER
AT MILLIMETER WAVELENGTHS

G.M.Strelkov

Institute of Radioengineering and Electronics of Russian Academy of Sciences, Vvedensky sq., 1, Fryazino, Moscow region, 141120, Russia. Fax: (095) 2038414

ABSTRACT

The goal of the report is to propose a new method of active remote sensing of Earth's ozone layer which offers a possibility of institute controlling over layer state on a global scale. The method is based on using two satellites. One of them carries transmitter and receiver is on the other. The frequency of emitting signal coincides with that of one of strong ozone absorption lines located in millimeter-wave range. In process of setting one of satellites under horizon propagation path's optical depth as a function of shortest distance of the path to Earth's surface is measured. The following reducing the data of measurements together with ballistic ones and height distributions of temperature, pressure and oxygen and water vapour contents in the atmosphere enables to find ozone molecule concentration as a function of height. The method proposed is free of shortcomings peculiar to existing ones of ozone layer remote sensing both radiophysical and optical.

Keywords: Atmospheric ozone, Active sensing, Millimeter waves, Absorption line.

Studying of the Earth's ozone layer is now constituent part of investigations which are directed to compre-

hensive understanding of global ecological situation (Ref. 1). For this reason forecasting of layer behavior in near future turns now not only academic task but practical one. For reliable description of ozonosphere state trends it is needed to have as far as possible accurate data on its characteristics all over the Earth's surface and on their correlation with both geoheliophysical and anthropogenic factors. Information on ozone layer characteristics is received by different methods of remote sensing. However available methods do not permit to receive necessary extent of data owing to a number of reasons. Nowadays, balloon platform-based (Refs. 2,3) and surface-based (Ref. 4) radiophysical investigations of the ozonosphere give the data on its local parameters regarding to a region which is directly over the measurement point. It is impossible to cover the Earth's surface by radiometric measuring points, in particular because of very high absorption of the thermal radioemission by atmosphere in the large humidity regions (in tropics and so on). Optical methods both ground-based and satellite-based have also a number of principal shortcomings. For example they are not all-weather, cirrus and silver clouds or stratospheric aerosols influence on precision of optical measurements (Refs. 5,6). As a consequence it does not

permit finding of correlation of ozone layer characteristics with events of natural and man-made catastrophes (vulcan eruption, big fire and so on), what is independent and major problem.

So one can say that it is necessary to find alternative effective means of the global and correct control of differential and integral characteristics of ozone layer in real time. In the work it is described a new method of active remote sensing of the layer on a global scale which is free of shortcomings peculiar to existing methods both radiophysical and optical.

The method proposed is based on active layer radio-translucence using two Earth's artificial satellites. A transmitter is mounted on the one satellite and a receiver is on another. The transmitter emits a signal power P_t at a frequency coincided with the central one of a rotary absorption line of ozone in millimeter wave band. The receiver indicates a signal when one of the satellites sinks under the horizon. The received power P_r is equal

$$P_r(r) = \frac{P_t G_o A}{4\pi D^2} X \exp(-\tau(p)), \quad (1)$$

where

G_o - gain coefficient of transmitting antenna;

A - effective area of receiving antenna;

D - distance between transmitter and receiver;

X - refractory attenuation;

τ - optical depth of path depended on sight distance p , the same as the shortest distance from the path to

Earth's surface.

The quantity τ consists of partial optical depths caused by radiation absorption in oxygen, water vapour and ozone so that

$$\tau = \tau_{O_2} + \tau_{H_2O} + \tau_{O_3}. \quad (2)$$

Further the indicated dependence $P_r(p)$ is processed together with ballistic data and height distributions of temperature T , pressure P_a and O_2 and H_2O concentrations (contents) in the atmosphere that are known from standard models of different Earth's regions. As result a height dependence of ozone part τ_{O_3} of the path optical depth can be found.

Taking into account the path geometry (configuration) the τ_{O_3} quantity may be represented by

$$\tau_{O_3}(p) = \int_p^{\infty} \frac{\gamma_{O_3}(r)(r+R)dr}{\sqrt{(r+R)^2 - (p+R)^2}}, \quad (3)$$

where R - Earth's radius;

γ_{O_3} - absorption coefficient of ozone at working frequency.

The last is defined by following

$$\gamma_{O_3}(r) = \frac{8\pi^3 \gamma_{lm} N(r)}{3hc} \cdot \frac{1}{G(T)}$$

$$G(T) = \left(e^{-E_l/kT} - e^{-E_m/kT} \right).$$

$$|\mu_{lm}|^2 = \frac{1}{\pi \Delta \nu_{lm}(P_a, T)}. \quad (4)$$

where N-concentration of ozone molecules; $G(T)$ - rotary sum of ozone molecule; ν_{lm} - resonance transition frequency of zone molecule (carrier frequency);

$|\mu_{lm}|^2$ - squared matrix element of zone molecule for transition at frequency ν_{lm} ;

$\Delta\nu_{lm}$ - halfwidth of the line;

E_m and E_l - energy levels (upper and lower) of resonance transition at frequency ν_{lm} ; h -Planck constant;

c - velocity of light;

k - Boltzmann constant.

Using Abel transform of (3) with taking into account (4) gives a dependence of ozone molecule concentration in the atmosphere upon height:

$$N(p) = - \left[\frac{8\pi^3 \nu_{lm}}{3hc} \frac{1}{G(T)} (e^{-E_l/kT} - e^{-E_m/kT}) \frac{|\mu_{lm}|^2}{\pi \Delta \nu_{lm} (P_a, T)} \right]^{-1} \frac{1}{R+p} \frac{d}{dp} \int_p^\infty \frac{\tau_{O_3}(r)(r+R)dr}{\sqrt{(r+R)^2 - (p+R)^2}}, \quad (5)$$

Preliminary estimations show that within atmospheric transparency windows at 2 and 3 mm the τ_{O_3} quantity runs

into a few nepers and is by orders of magnitude greater than oxygen and water vapour parts of τ . Therefore the method proposed is to be expected to enable reliable measurements of ozone concentration in the atmosphere more over at any time of day and weather conditions. It is needed to say that method's accuracy and resolving ability on height scale will to a

great extent depend on the reliability of standard atmosphere models and ballistic data used in processing the results of measurements.

REFERENCES

1. Zurer P.S. Ozone Depletion's Recurring Surprises Challenge Atmospheric Scientists. *News focus*. 1993. May, 24. p.p.8-18.
2. Gibbins C.J., Dawkins A.W. J., Maddison B.M. 1988, Microwave remote sensing measurements of upper atmospheric water vapour and ozone from balloon-borne platform. *Planet. Space Sci.*, 36, 6, p.p.607-620.
3. Kadygrov E.N., Sorokin M. G., Vlasov A.A. 1993, Ozone concentration determination by microwave measurements from balloons in the stratosphere, *Earth research from space*, n.3, p.p.102-106. (In Russian).
4. Solomonov S.V., Kropotkina E.P., Lukin A.M., Ponomarenko M.I., Rozanov S.B., Ellder J. 1991, Some features of vertical ozone distribution from millimeter wave measurements at Pushkino and Onsala observations. Moscow: Physical Institute of Russian Academy of Sciences. Preprint N.101, 32p.
5. Khrgian A.Kh. 1973, *Physics of atmospheric ozone*. Leningrad, Gidrometeoizdat. -291p. (In Russian).
6. Khrgian A.Kh., Kuznetsov G.I. 1981, *Problems of observations and investigations of atmospheric ozone*. Moscow, Moscow State University. -216p. (In Russian).

ANALYSIS OF RAIN RATE STATISTICS IN THE NORTH COAST OF SPAIN

I.F. Anitzine¹, C.S. Yoldi², A. Benarroch³, L. Mercader⁴

- 1 - UPV Basque Country University
- 2 - UPV Basque Country University
- 3 - Polytechnic University of Madrid
- 4 - UPNA Public University of Navarre

ABSTRACT

In this paper, the rainfall rate statistics of Bilbao are studied. The results suggest that Bilbao and other places in the North coast of Spain, belong to G Zone instead of E Zone. A new coefficient is included here referred to hydrometeorological zones.

Keywords: Rainfall Rate Statistics, Hydrometeorological Zones, Cumulative Distribution.

1. INTRODUCTION

Until now, UIT-R climatic maps have been used to calculate the effect of rain on the design of radiolinks, in the North of Spain. As the number of radiolinks working at frequencies higher than 10 GHz is increasing, more accurate knowledge of rain attenuation is required.

2. RAIN RATE STATISTICS OF BILBAO

The data rain corresponding to the eight last years period (1985-1993) stored in Sondika, airport of Bilbao, have been analyzed. After sampling each 5 minutes time, digitalizing data, and carrying out a statistical study, the results obtained are shown in Table I. This table presents the percentage of time of the period for which the corresponding rain rate has been superated.

Nevertheless CCIR suggests that rain rate data with an integration time of at least 1 minute R_1 should be employed to calculate attenuation. Therefore conversion factors published by Fedi (Ref. 1) in 1979 have been used here, to convert rain rate data with an integration time of 5 minutes R_5 , in rain rate data with an integration time of 1 minute R_1 , at the same probability.

Rain intensity R_5 mm./h.	Percentage of total period
0	6.8
5	0.47
10	0.11
20	0.024
30	0.009
40	$3.4 \cdot 10^{-3}$
50	$1.8 \cdot 10^{-3}$
60	$1.2 \cdot 10^{-3}$
70	$9.4 \cdot 10^{-4}$
80	$5.3 \cdot 10^{-4}$
90	$2.6 \cdot 10^{-4}$

Table I

Table II shows some values of the cumulative distribution $T_v(R_1)$, corresponding to the average year of Sondika airport.

$T_v(R_1)$, %	R_1 , mm./h.
0.001	75.4
0.003	47.3
0.010	31.8
0.030	20.6
0.100	12.3
0.300	6.8
1.000	3.1

Table II

Both figures 1a and 1b show this cumulative distribution. On the one hand, figures 1 compare the experimental distribution with the ones of E and G hydrometeorological zones, proposed by UIT-R. It can be easily noticed, looking at the figure, that the experimental distribution and the one of E zone are very different. Nevertheless it's very similar to that of G zone.

Figure 1b on the other hand, shows the same distributions but a semilog scale has been used now. We can conclude then that Bilbao (and the

North Coast of Spain) belongs to G hydrometeorological zone.

In figure 2, relative errors between these two distributions are shown.

A very important fact to remark is that although these results have been obtained in Basque Country University with independence from the ones obtained in Polytechnics University of Madrid, both are in complete accordance. In Basque Country University, rain data of Sondika were obtained from a tipping-bucket raingauge. However in Madrid, rain data from syphon raingauges located in Igeldo (San Sebastián), Fuenterrabia, Santander, Gijón, and Asturias airport., were studied. Moreover, register papers from the locations and workers who processed data were also different. Figure 3 shows relative errors between the distributions corresponding to these locations and G zone, multiplied by its corresponding coefficients.

Similar results were obtained (figure 4) for La Coruña, Santiago de Compostela and Vigo, in the coast of Galicia.

3. CONCLUSIONS

From the results obtained we can conclude that North coast of Spain presents a cumulative distribution of rain rate similar to the one of G zone, proposed by UIT-R.

These results also seem to be very efficient, because although have been obtained in different ways, are in good accordance.

4. REFERENCES

1. Fedi F. 1979, Rainfall characteristics across Europe, *Alta Frequenza*, English Issue; 2, Vol. LXVI, No. 4, pp 158-166.

Figure 1a

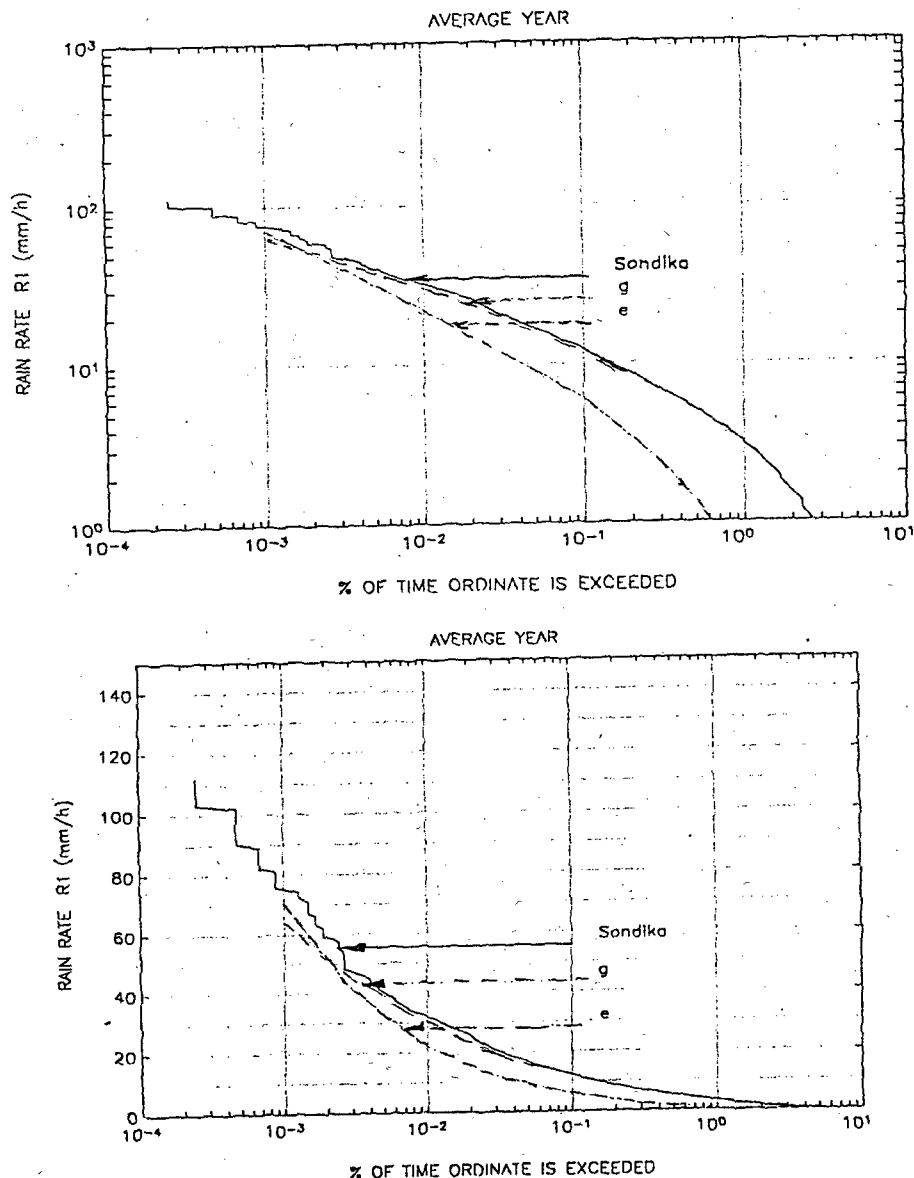


Figure 2

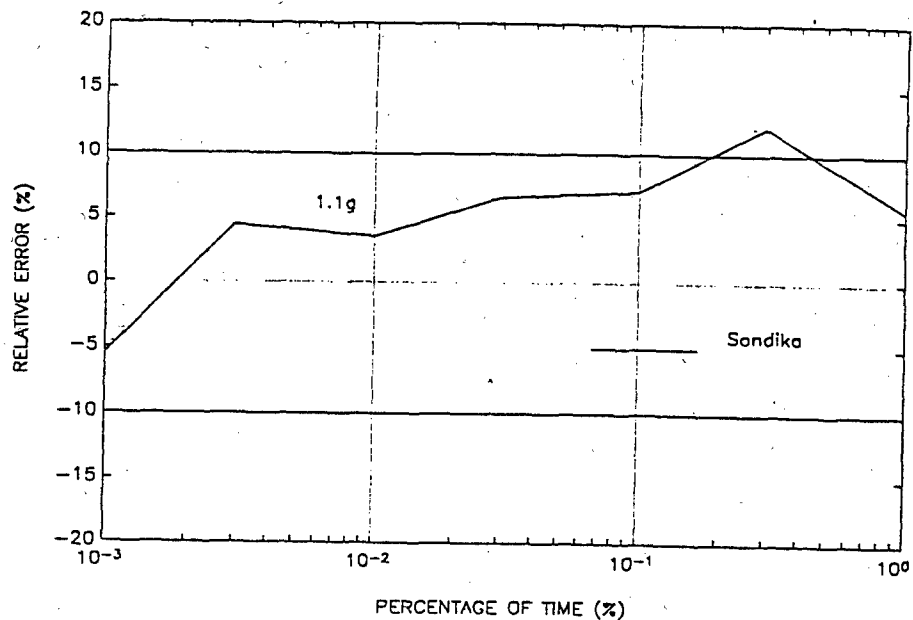


Figure 3

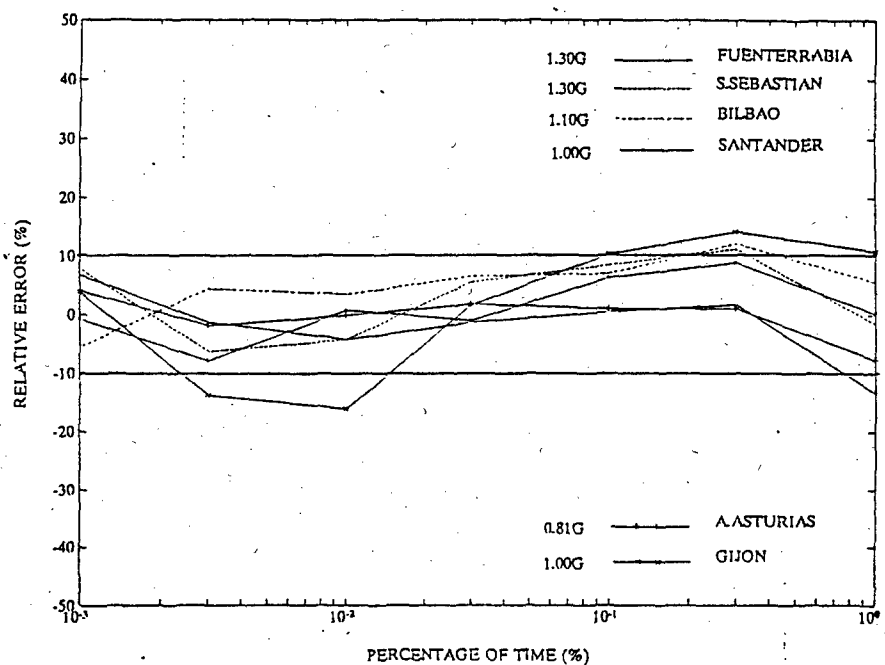
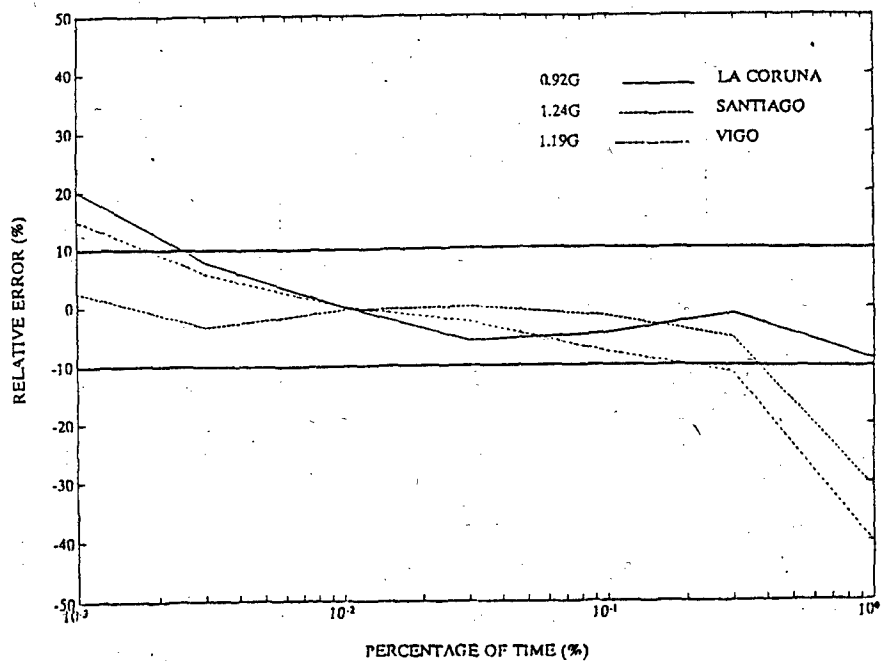


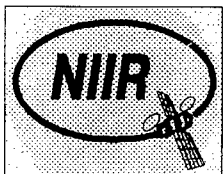
Figure 4



1. Prof I F Anitzine, ETSII & T of the UPV
Alameda de Urquijo, s/n; Bilbao, 48013 (SPAIN)
Phone: +34 4 427 8055; Fax: +34 4 441 4041.

2. Prof Luis Mercader, ETSIL & T of the UPN
Campus de la Arrosadia, s/n; Pamplona, 31006 (SPAIN)
Phone: +34 48 169 311; Fax: +34 48 169 169.

Session 14: Concluding Session



RADIO RESEARCH & DEVELOPMENT INSTITUTE (NIIR)

16, Kazakova str., 103064 Moscow, RUSSIAN FEDERATION

☎ +7(095) 975 22 48, Fax +7(095) 261 00 90, Telex (064) 411601Rubin

STRATEGY, SYSTEMS, SERVICES AND CONSULTANCY IN TELECOMMUNICATION AND EMC TECHNOLOGY

The Radio Research Institute (NIIR) was created in 1949 as an independent scientific research institute and was the main analytical scientific center of the USSR Telecommunication Administration in the field of telecommunications. Now NIIR is the major analytical and system development center of the Russian Telecommunication Administration and became the same for the Regional Communication Collaboration (RCC), which are involved Telecom Administrations of practically all CIS countries. Additionally NIIR was granted by Russian government the status of main radiocommunication type approval and certification center of Russia. NIIR has gained a wide experience in

- applying analytical solution of communication and information theories to radiocommunication problems;
- planning telecommunication networks;
- solving EMC compatibility problems between different applications radio equipment in both theoretical and practical fields;
- conducting frequency planning of telecommunication networks;
- managing radio spectrum and GSO both at the national and international levels;
- developing a wide-range of radio facilities for microwave links, satellite communication and radio broadcasting systems as well as for the other radiocommunication systems.

The most specific features of NIIR is that it is very familiar with different aspects of ITU, IFRB and, in particular, of the CCIR's activities as NIIR is the main consultative and executive body of the Russian Telecommunication Administration and provides all scientific and technical preparatory work for Administrative Radio Conferences, Plenary Assemblies of the CCIR and Plenipotentiary Conferences of the ITU. NIIR actively participates in the work of CCIR Study Groups, has provided many contributions and takes part in the Study Groups meetings. All Russian Chairmen and Vice-Chairmen of CCIR Study Groups were or are NIIR's staff members. Also, a large number of NIIR's experts are Chairmen and active participants of national preparatory groups for CCIR.

Within the above fields, NIIR is well prepared for providing a wide range of consultancy services, such as:

- tackling different, including science-intensive, problems involving communication and information theories in the context of telecommunication;
- designing standard acts on type approval and certification for radiocommunication and broadcasting systems;
- planning national, regional and local telecommunication networks;
- designing and testing different equipment for line-of-sight and tropospheric scatter microwave links, satellite radiocommunication, broadcasting and other terrestrial radiocommunication and broadcasting systems, designing relevant links and networks (a detailed list of the equipment can also be provided additionally);
- experimental investigation of the potential for allocating additional TV and Sound broadcasting channels for areas with specific terrain problems;
- designing special-purpose monitoring and test equipment required for the development, adjustment and operation of above radiocommunication and broadcasting systems and the appropriate networks;
- development of specialized facilities for processing and generating speech signals, such as vocoders, solid-state speech answer-back systems, etc;

clearing up various organizational, methodological and technical difficulties of spectrum management, including the establishment of national spectrum management systems together with their hardware and software support;

- developing procedures for the EMC analysis of radio facilities to any degree of complexity defined by the customer's request, and also appropriate models for representing equipment and propagation parameters, together with software support for both main frame and personal computers;

- developing, installing and putting into operation fixed monitoring centers, using small earth stations, which are used for monitoring the emissions from space stations;

- statistical measurements of radiowave propagation conditions in different climatic zones, including complex statistical treatment of the measurement results.

As a result of the activities conducted by NIIR, integrated networks for terrestrial and satellite radiocommunication and broadcasting have been established and which are now in operation in Russia, their efficiency and quality is fully compatible with investment made in establishing them. Without going into detail concerning the main radiocommunication and broadcasting systems developed and introduced by NIIR, it is sufficient to mention such well-known systems as MOLNIYA, ORBITA which were the world's first and were put into operation in 1963 and 1967 respectively, also advanced systems such as LUTCH, and GORISONT (used by the INTERSPUTNIK international organization), and also EKRAK, MOSKVA and a complex of unified versatile microwave links KURS, etc.

NIIR's activities have made it possible to establish a highly-effective national frequency management system which makes extensive use of computer technology, and to provide bilateral and multilateral international coordination of frequency assignments of radio facilities in different services covering, among other aspects, the problems of frequency assignment notification in the IFRB. The work carried out by NIIR formed a basis for standardized procedures of analyzing EMC between radio facilities of various services. These are recommended for use within the country by the Russian Telecommunication Administration and may be applied both to the analysis of mutual interferences between individual radio facilities and to frequency planning of radiocommunication and broadcasting networks. These procedures are helpful in tackling problems of frequency sharing by radio facilities in different services. Frequency plans for various radiocommunication and broadcasting networks have been developed and put into services; these plans are being steadily improved.

Having extensive experience in international cooperation, NIIR has rendered support to a great number of developing and East-European countries concerning to the development and modification of equipment and networks intended for the terrestrial and satellite radiocommunication and broadcasting. Among major projects, the establishment of earth station networks in the INTERSPUTNIK member-countries, and the design and implementation of microwave links in some other countries, are worthy of notice.

As for radio spectrum management issues, the assistance provided to Sudan in the introduction, - to Bulgaria in the modification, - and to Cuba in the automation of their national frequency management systems, should be mentioned. The aid has also given to Nicaragua and Cuba in developing frequency plans for the TV and sound broadcasting networks.

If you are interested obtaining cooperation in any of the above fields of expertise, please contact:

Dr. Alexandre Koushtouev
First Deputy Director
Radio Research Institute (NIIR)
16, Kazakova str.,
103 064 Moscow, Russia
Telex: 411601 RUBIN
Fax: 7095 261-00-90
Tel: 7095 975-22-48